IFS DOCUMENTATION – Cy50r1
Operational implementation 12 May 2026

PART IV: PHYSICAL PROCESSES

European Centre for Medium-Range Weather Forecasts
Shinfield Park, Reading, RG2 9AX, UK

DOCUMENTATION REVISION HISTORY

Changes from CY49R2 to CY50R1

- Chapter 3. Added description of prognostic TKE scheme.
- Chapter 6. Added description of handover of convective rain and snow to resolved scale.
- Chapter 7. Included changes to clouds/precipitation (ice fallspeed, convective precip handover, precipitation evaporation, cloud evaporation)

Changes from CY49R1 to CY49R2

- Chapter 2. Added description of solar eclipses computations.
- Chapter 3. Added description of changes to diffusion above the tropopause in stable conditions.

Changes from CY48R1 to CY49R1

- Chapter 8. (i) Added The new soil moisture stress function, (ii) Modified the vegetation related lookup tables for the minimum stomatal resistance, the roughness length and the veg fraction to follow the new vegetation maps (LULC and LAI), (iii) scaled the LAI with cveg (rvcov) for the canopy resistace computaton, (iv) modified the snow albedo for tile 7 to be explicitly from Obs climatology and (v) corrected a typo in the runoff equation8.88.
- Chapter 11. Update of Land use/ land cover maps, LAI maps and disaggregation method for low and high vegetation components of the LAI maps.

Changes from CY47R3 to CY48R1

- Chapter 2. Rewritten to reflect the introduction of the ecRad radiation scheme.
- Chapter 8. Added (i) mention of ECLand new plateform and open source, (ii) description of Snow multi-layers parametrization and (iii) description of Farquhar photosythesis module.
- Chapter 7. Added new microphysical processes. Revised precipitation type.
- Chapter 10. Updated to describe the Hybrid Linear Ozone (HLO) scheme.
- Chapter 11. Update of land-sea-mak, Glacier mask, Lake cover, Lake depth, handling of mean orography and subgrid orography fields and addition of C3/C4 photosythesis types map.

Changes from CY47R1 to CY47R3

- In most chapters corrected description of cp moist to cp dry.
- Chapter 1. Updated overview of physics.
- Chapter 3. Revised and simplified moist boundary-layer part. Clear air turbulence. Revised visibility, wind gust description.
- Chapter 6. Added moisture convergence closure, expanded coupling to the cloud scheme. Added descriptions and derivations for new Grib fields (new CAPE/CIN, tropopause height)
- Chapter 7. Revised cloud scheme section, precipitation type description.
- Chapter 8. Updated cool skin parametrization
- Chapter 12. Thoroughly revised and expanded, including saturation adjustment, enthalpy budget and flux, correction of many errors.

Changes from CY46R1 to CY47R1

- Chapter 11. Albedo climatological field revision: 6-component MODIS land-surface albedo climatology providing a solar-zenith-angle-dependent albedo in the UV/Vis and Near-IR bands and related plots.
- Chapter 8. Fixes in tables 8.2 and 8.3 as coded in the IFS

Changes from CY45R1 to CY46R1

- Chapter 2. Corrected and expanded descriptions of the cloud droplet and ice particle effective radii in the radiation scheme.

Changes from CY43R3 to CY45R1

- Chapter 6. Updates to parcel perturbations, phase of shallow clouds, positiveness of CAPE closure denominator, typos in previous versions. Added description of lightning parametrization.
- Chapter 8. Updates for HRES now being coupled to NEMO.

Changes from CY43R1 to CY43R3

- Chapter 2. Aerosol climatological revision.
- Chapter 6. Updates to sections on Large-scale budget equations, Freezing in convective updraughts, Generation of precipitation, Fallout of precipitation, Melting and freezing of precipitation, Link to the cloud scheme.
- Chapter 7. New section on Cloud height.
- Chapter 11.Climatological data plots have been updated to new cubic octahedral grid and text modified accordingly.

Changes from CY41R2 to CY43R1

- Convection chapter updates in sections: Detrainment rates; Deep convection; Freezing in convective updraughts; Generation of precipitation; Melting and freezing of precipitation; Temporal discretization; Diagnostics for postprocessing.
- Climatological data chapter updates in section: Ozone
- Surface parametrization chapter updates in sections: Sea Ice and Ocean Boundary Conditions.
- Clouds chapter updates: New section on 'Description of output fields. Addition of 3 new figures.
- Turbulent transport chapter updates: Removal of reference to ice in cloud description in section Outer Layer; section on Description of output fields changed to Diagnostic computations for post-processing and added to; corrections to equations in section Solution of the EDMF equations.

Chapter 1

Overview

Table of contents

1.1 Introduction
1.2 Overview of the code

1.1 INTRODUCTION

The physical processes associated with radiative transfer, turbulent mixing, convection, clouds, surface exchange, subgrid-scale orographic drag and non-orographic gravity wave drag have a strong impact on the large scale flow of the atmosphere. However, these mechanisms are often active at scales smaller than the resolved scales of the model grid. Parametrization schemes are then necessary in order to properly describe the impact of these subgrid-scale mechanisms on the large scale flow of the atmosphere. In other words the ensemble effect of the subgrid-scale processes has to be formulated in terms of the resolved grid-scale variables. Furthermore, forecast weather parameters, such as two-metre temperature, precipitation and cloud cover, are computed by the physical parametrization part of the model. This part (Part IV 'Physical processes') of the IFS documentation describes the physical parametrization package.

The radiation scheme (Chapter 2) performs computations of the short-wave and long-wave radiative fluxes using the predicted values of temperature, humidity, cloud, and monthly-mean climatologies for aerosols and trace gases. Internally the IFS uses the 'ecRad' radiation scheme (Hogan and Bozzo, 2018), which has multiple options for the treatment of sub-grid cloud structure and the optical properties of gases, aerosols and clouds. The operational configuration computes gas optical properties using the Rapid Radiation Transfer Model for GCMs (RRTMG, Mlawer *et al.*, 1997; Iacono *et al.*, 2008) and treats

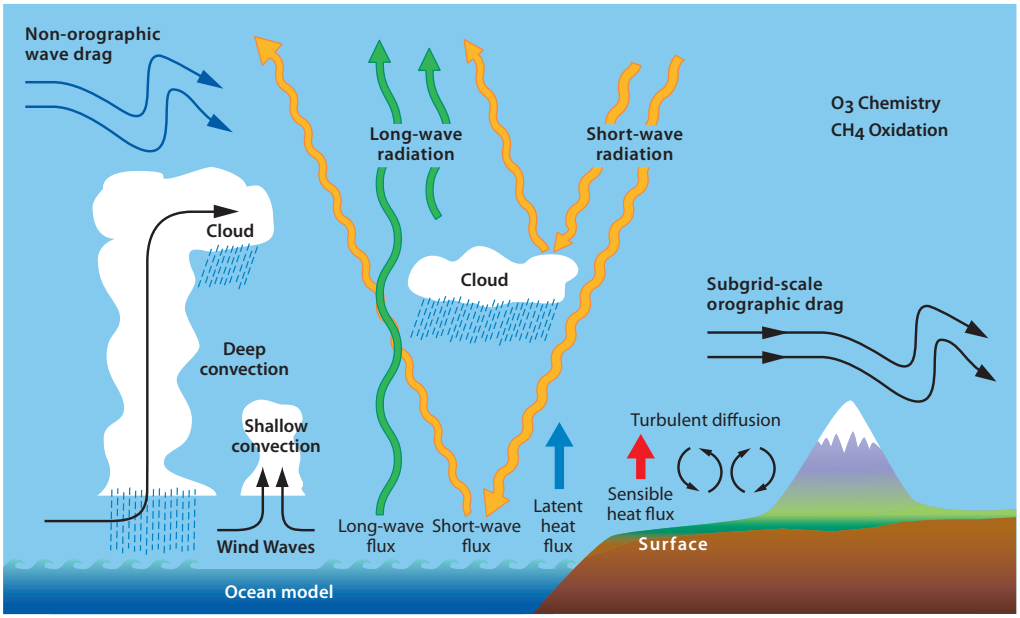

Figure 1.1 *Schematic diagram of the different physical processes represented in the IFS model.*

cloud sub-grid structure using the Monte Carlo Independent Column Approximation (McICA, Pincus *et al.*, 2003). To reduce the overall computational cost of the radiation scheme, full radiation calculations are performed on a reduced (coarser) radiation grid and/or on a reduced time frequency. The results are then interpolated back to the original grid.

The turbulent diffusion scheme (Chapter 3) represents the vertical exchange of heat, momentum and moisture through sub-grid scale turbulence. The vertical turbulent transport is treated differently in the surface layer and above. In the surface layer, the turbulence fluxes are computed using a first order K-diffusion closure based on the Monin–Obukhov (MO) similarity theory. Above the surface layer a K-diffusion turbulence closure is used everywhere, except for unstable boundary layers where an Eddy-Diffusivity Mass-Flux (EDMF) framework is applied, to represent the non-local boundary layer eddy fluxes (Köhler *et al.*, 2011). The scheme is written in moist conserved variables (liquid static energy and total water). Convective clouds are treated separately by the shallow convection scheme.

The effects of unresolved orography on the atmospheric flow are parametrized as a sink of momentum (drag). The turbulent diffusion scheme includes a parametrization in the lower atmosphere to represent the turbulent orographic form drag induced by small scale (< 5 km) orography (Beljaars *et al.*, 2004b). In addition, in stably stratified flow, the orographic drag parametrization (Chapter 4) represents the effects of low-level blocking due to unresolved orography (blocked flow drag) and the absorption and/or reflection of vertically propagating gravity waves (gravity wave drag) on the momentum budget (Lott and Miller, 1997).

The non-orographic gravity wave drag parametrization (Chapter 5) accounts for the effects of unresolved non-orographic gravity waves. These waves are generated in nature by processes like deep convection, frontal disturbances, and shear zones. Propagating upward from the troposphere the waves break in the middle atmosphere, comprising the stratosphere and the mesosphere, where they exert a strong drag on the flow. The parametrization uses a globally uniform wave spectrum, and propagates it vertically through changing horizontal winds and air density, thereby representing the wave breaking effects due to critical level filtering and non-linear dissipation. A description of the scheme and its effects on the middle atmosphere circulation can be found in Orr *et al.* (2010).

The moist convection scheme (Chapter 6) is based on the mass-flux approach and represents deep (including congestus), shallow and mid-level (elevated moist layers) convection. The distinction between deep and shallow convection is made on the the basis of the cloud depth (≤ 200 hPa for shallow). For deep convection the mass-flux is determined by assuming that convection removes Convective Available Potential Energy (CAPE) over a given time scale. The intensity of shallow convection is based on the budget of the moist static energy, i.e. the convective flux at cloud base equals the contribution of all other physical processes when integrated over the subcloud layer. Finally, mid-level convection can occur for elevated moist layers, and its mass flux is set according to the large-scale vertical velocity. The scheme, originally described in Tiedtke (1989), has evolved over time and amongst many changes includes a modified entrainment formulation leading to an improved representation of tropical variability of convection (Bechtold *et al.*, 2008), a modified CAPE closure leading to an improved diurnal cycle of convection (Bechtold *et al.*, 2014) and an additional closure dependence on total moisture convergence that improves mesoscale organisation (Becker *et al.*, 2021).

Clouds and large-scale precipitation (Chapter 7) are parametrized with a number of prognostic equations for cloud liquid, cloud ice, rain and snow water contents and a sub-grid fractional cloud cover. The cloud scheme represents the sources and sinks of cloud and precipitation due to the major generation and destruction processes, including cloud formation by detrainment from cumulus convection, condensation, deposition, evaporation, collection, melting and freezing. The scheme is based on (Tiedtke, 1993) but with an enhanced representation of mixed-phase clouds and prognostic precipitation (Forbes and Tompkins, 2011; Forbes *et al.*, 2011). Supersaturation with respect to ice is commonly observed in the upper troposphere and is also represented in the parametrization (Tompkins *et al.*, 2007).

The surface parametrization scheme (Chapter 8) represents the surface fluxes of energy and water and corresponding sub-surface quantities. The scheme is based on a tiled approach (TESSEL) representing different sub-grid surface types for vegetation, bare soil, snow and open water. Each tile has its own

properties defining separate heat and water fluxes used in an energy balance equation which is solved for the tile skin temperature. Four soil layers are represented as well as snow mass and density. The evaporative fluxes consider separately the fractional contributions from snow cover, wet and dry vegetation and bare soil. An interception layer collects water from precipitation and dew fall, and infiltration and run-off are represented depending on soil texture and subgrid orography (HTESSEL, Balsamo *et al.*, 2009, Balsamo *et al.*, 2011a). A carbon cycle is included and land-atmosphere exchanges of carbon dioxide are parametrized to respond to diurnal and synoptic variations in the water and energy cycles (CHTESSEL, Boussetta *et al.*, 2013a).

Chapter 9 'Methane oxidation' describes a simple parametrization of the upper-stratospheric moisture source due to methane oxidation. A parametrization representing photolysis of vapour in the mesosphere is also included.

Chapter 10 'Ozone chemistry parametrization' gives a brief description of the Hybrid Linear Ozone (HLO) scheme, which assumes that chemical changes in ozone can be described by a linear relaxation towards a photochemical equilibrium. HLO uses the same formulation as Cariolle and Déqué (1986), but with the coefficients derived from both an ozone reanalysis and from a full chemistry model.

Chapter 11 'Climatological data' describes the distributions of climatological fields, including land sea mask, orography (mean, standard deviation, anisotropy, orientation and slope), land use, soil type, vegetation type, leaf area index, albedo, aerosols, ozone and trace gases.

1.2 OVERVIEW OF THE CODE

The physics parametrization package is called by the IFS after the explicit dynamical computations. The physics computations are performed only in the vertical. The input information for the physics consists of the values of the gridbox mean prognostic variables (wind components u/v, temperature T, specific humidity q, cloud fraction a, water contents for cloud liquid q_l, cloud ice q_i, rain q_r, and snow q_s), the provisional dynamical tendencies for the same variables and various surface fields, both fixed and variable.

The time integration of the physics is based on the following:

(i) It has to be compatible with the adiabatic part of the IFS.
(ii) The tendencies from the different physical processes are computed in separate routines.
(iii) As a general approach, the value of a prognostic variable is updated with the tendency from one process and the next process starts from this updated value, in what is usually referred to as the 'method of fractional steps' (details are different for different processes).
(iv) Implicit schemes are used when needed for stability.

CALLPAR is the routine that controls the physical parametrization package with the exception of the main radiation routine RADINTG. RADINTG controls the computation of the short-wave transmissivities and the long-wave fluxes. RADINTG is called outside CALLPAR because of the need to make the radiation space interpolation compatible with the distributed memory version of the IFS. GP_MODEL is a high level routine that controls all computations in grid-point space. It calls both CALLPAR via interface routines EC_PHYS_DRV, EC_PHYSG, EC_PHYS and RADINTG via driver RADDRV.

In CALLPAR the physics routines are called in the following order:

SURFRAD_LAYER	Computes radiative properties of the surface.
RADFLUX_LAYER	Calls RADHEATN to compute the temperature tendencies and the downward radiation fluxes at the surface with updated (every time-step) values for the zenith angle.
CONVECTION_LAYER	Interface to call CUCALLN/CUMASTRN that controls the computation of the tendencies for u, v, T, q, chemical tracers and the cloud detrainment term due to the parametrization of moist convective processes.
CLOUD_SATADJ	Performs subgrid cloud saturation adjustment due to tendencies of T, q from dynamics, radiation, turbulence and convection. Computes tendencies of T, q, a, q_l and q_i.
CLOUD_LAYER	Calls CLOUDSC to compute tendencies for T, q, a, q_l, q_i, q_r and q_s due to the parametrization of cloud and precipitation processes.
GWDRAGWMS_LAYER	Calls GWDRAG_WMS to compute the tendencies for u, v and T due to the parametrization of non-orographic gravity waves.
SLTEND_LAYER	Optionally average tendencies from radiation, convection and cloud in time and space along the semi-Lagrangian trajectory.
GWDRAG_LAYER	Computes the tendencies for u, v and T due to the parametrization of subgrid-scale orographic drag. It also computes subgrid orographic coefficients for use in VDFMAIN.
TURBULENCE_LAYER	Calls VDFOUTER/VDFMAIN in two sub time steps for numerical stability. VDFMAIN computes the vertical exchange of u, v, T, q, a, q_l, q_i by turbulence.
METHOX	Computes tendencies for q due to methane oxidation and water vapour photolysis.
O3CHEM	Computes tendencies for O_3 due to ozone chemistry.
SURFTSTP_LAYER	Calls SURFTSTP to control the soil/surface scheme.
STOCHPERT_LAYER	Optionally add stochastic perturbations to physics tendencies.

Chapter 2

Radiation

Table of contents

2.1 Introduction
2.2 The pre-Cy32r2 Short-Wave Radiation Scheme
2.2.1 Spectral integration
2.2.2 Vertical integration
2.2.3 Multiple reflections between layers
2.2.4 Pre-CY32R2 cloud short-wave optical properties
2.3 The pre-Cy22r3 Long-Wave Radiation Scheme
2.3.1 The pre-cycle Cy22r3 scheme
2.3.2 Vertical integration
2.3.3 Spectral integration
2.3.4 The incorporation of the effects of clouds
2.4 Inputs to the radiation scheme
2.4.1 Model variables
2.4.2 Clouds
2.4.3 Aerosols
2.4.4 Greenhouse and other gases
2.4.5 Surface albedo and emissivity
2.4.6 Solar irradiance and zenith angle
2.5 The ecRad radiation scheme
2.5.1 Overview
2.5.2 Gas optics
2.5.3 Aerosol optics
2.5.4 Cloud optics
2.5.5 Solver
2.6 Solar eclipses
2.7 Spatial and temporal interpolation
2.7.1 The radiation grid
2.7.2 Approximate radiation updates: short-wave
2.7.3 Approximate radiation updates: long-wave
2.8 Radiation diagnostics
2.8.1 Conventions
2.8.2 Surface fluxes
2.8.3 Top-of-atmosphere fluxes
2.8.4 Other variables
2.9 Code
Appendix A. List of symbols

2.1 INTRODUCTION

Table 2.1 gives the timeline of the major changes affecting the representation of the radiation transfer (RT) in the ECMWF model since the late 80s; see Table 2 of Hogan *et al.* (2017) for additional details.

Table 2.1 *Major changes in the representation of radiation transfer in the ECMWF forecasting system.*

Cycle	Implementation date	Description
Morcrette scheme		
SPM 32	02/05/1989	RT schemes from Univ. Lille
SPM 46	01/02/1993	Optical properties for ice and mixed phase clouds
IFS 14r3	13/02/1996	Revised LW and SW absorption coefficients from HITRAN'92
IFS 16r2	15/05/1997	Voigt profile in long-wave RT scheme
IFS 16r4	27/08/1997	Revised ocean albedo from ERBE
IFS 18r3	16/12/1997	Revised LW and SW absorption coefficients from HITRAN'96
IFS 18r5	01/04/1998	Seasonal land albedo from ERBE
Morcrette scheme with RRTMG$_{LW}$		
IFS 22r3	27/06/2000	RRTMG$_{LW}$ as long-wave RT scheme short-wave RT scheme with 4 spectral intervals
IFS 23r4	12/06/2001	Hourly, instead of 3-hourly, calls to RT code during data assimilation cycle
IFS 25r1	09/04/2002	Short-wave RT scheme with 6 spectral intervals
IFS 26r3	07/10/2003	New aerosol climatology adapted from Tegen et al. (1997), new radiation grid
IFS 28r3	28/09/2004	Radiation called hourly in high resolution forecasts
McRad scheme		
IFS 32r2	05/06/2007	McICA approach to RT with RRTMG$_{LW}$ and RRTMG$_{SW}$ revised cloud optical properties, 60-km MODIS land albedo
IFS 35r3	08/09/2009	GEMS climatology for ozone and other gases
IFS 41r1	12/05/2015	MACC climatology for ozone and other gases, Updated RRTMG coefficients, 5-km MODIS land albedo
IFS 41r2	08/03/2016	Approximate updates to mitigate coastal temperature errors
IFS 43r1	22/11/2016	CAMS climatology for ozone, total solar irradiance (TSI) set to 1361 $\pm$ solar cycle
ecRad scheme		
IFS 43r3	11/07/2017	Replace McRad with ecRad (gas optics unchanged)
IFS 46r1	11/06/2020	Turned on long-wave scattering for clouds
IFS 47r1	30/06/2020	CMIP6 for long-term trends in greenhouse gases and TSI, MODIS land albedo uses solar zenith angle dependence
IFS 48r1		Radiatively interactive prognostic ozone from 'HLO' scheme

The original Morcrette (1991) radiation scheme, which was operational in the high-resolution 10-day forecasts from May 1989 to June 2000, is still described in this document as it forms the basis for the linearized schemes for short-wave (Section 2.2) and long-wave (Section 2.3) radiation transfer used in data assimilation.

In 2007, with Cycle 32r2 of the ECMWF IFS operational libraries, a new approach to the inclusion of sub-grid cloud effects on radiation fields (the Monte-Carlo Independent Column Approximation, McICA) was introduced in the IFS (the McRad radiation scheme, Morcrette *et al.*, 2008a). McRad also included both the long-wave and short-wave gas-optics treatment from the Rapid Radiation Transfer Model for GCMs (RRTMG), originally developed at AER, Inc. (Mlawer *et al.*, 1997; Iacono *et al.*, 2008).

In 2017, the ecRad radiation scheme was introduced (Hogan and Bozzo, 2018), which improved computational efficiency, as well as providing much more flexibility with regard to the treatment of gas, aerosol and cloud optical properties, and the selection of different solvers for treating cloud structure. An offline version of ecRad is available from GitHub (`https://github.com/ecmwf-ifs/ecrad`) and has since been incorporated into other models such as ICON, AROME and MesoNH. The inputs to the radiation scheme are described in Section 2.4, followed by a description of ecRad in Section 2.5

The radiation scheme has traditionally been a relatively expensive part of the model, so the IFS reduces the overall cost by the use of a coarser-resolution radiation grid (Morcrette *et al.*, 2008b) and by calling the full radiation scheme only every hour rather than every timestep. These reduced radiation configurations are described in Section 2.7 together with the approximate update scheme used for obtaining the radiative fluxes at every grid point and every time step for the relevant instantaneous temperature profile and solar zenith angle. Finally, Section 2.8 describes the radiation diagnostics that can be output from the IFS and Section 2.9 outlines the structure of the code.

The radiation scheme is configured via the NAERAD namelist group. Throughout this section when namelist options are described they are parameters in this group. Data files used by the radiation scheme are read from the `ifsdata` subdirectory of the directory provided in the DATA environment variable in the IFS. At ECMWF the files for Cycle 48r1 can be found in `/home/rdx/data/48/ifsdata`.

2.2 THE PRE-CY32R2 SHORT-WAVE RADIATION SCHEME

Please note that this section refers to a very old version of the radiation scheme that is only used in the linearized physics used in data assimilation. The symbols used here may differ from those in the other sections of this chapter.

The rate of atmospheric heating by absorption and scattering of short-wave radiation is

$$\frac{\partial T}{\partial t} = -\frac{g}{c_p}\frac{\partial \mathcal{F}_{\mathrm{SW}}}{\partial p} \tag{2.1}$$

where $\mathcal{F}_{\mathrm{SW}}$ is the net total short-wave flux (the subscript SW will be omitted in the remainder of this section).

$$\mathcal{F}(\delta) = \int_0^\infty \mathrm{d}\nu \left[\int_0^{2\pi} \mathrm{d}\phi \left\{ \int_{-1}^{+1} \mu \mathcal{L}_\nu(\delta, \mu, \phi)\, \mathrm{d}\mu \right\} \right] \tag{2.2}$$

is the diffuse radiance at wavenumber ν, in a direction given by the azimuth angle, ϕ, and the zenith angle, θ, with $\mu = \cos\theta$. In (2.2), we assume a plane parallel atmosphere, and the vertical coordinate is the optical depth δ, a convenient variable when the energy source is outside the medium

$$\delta(p) = \int_p^0 \beta_v^{\mathrm{ext}}(p')\, \mathrm{d}p' \tag{2.3}$$

$\beta_\nu^{\mathrm{ext}}(p)$ is the extinction coefficient, equal to the sum of the scattering coefficient β_ν^{sca} of the aerosol (or cloud particle absorption coefficient β_ν^{abs}) and the purely molecular absorption coefficient k_ν. The diffuse radiance $\mathcal{L}_\nu$ is governed by the radiation transfer equation

$$\begin{aligned} \mu \frac{\mathrm{d}\mathcal{L}_\nu(\delta, \mu, \phi)}{\mathrm{d}\delta} = {} & \mathcal{L}_\nu(\delta, \mu, \phi) - \frac{\varpi_\nu(\delta)}{4} P_\nu(\delta, \mu, \phi, \mu_0, \phi_0) \mathcal{E}_\nu^0 \exp(-\delta/\mu_r) \\ & - \frac{\varpi_\nu(\delta)}{4} \int_0^{2\pi} \mathrm{d}\phi' \left\{ \int_{-1}^{+1} \Phi_\nu(\delta, \mu, \phi, \mu', \phi') \mathcal{L}_\nu(\delta, \mu', \phi')\, \mathrm{d}\mu' \right\} \end{aligned} \tag{2.4}$$

$\mathcal{E}_\nu^0$ is the incident solar irradiance in the direction $\mu_0 = \cos\theta_0$, ϖ_ν, is the single scattering albedo ($= \beta_\nu^{\mathrm{sca}}/k_\nu$) and $\Phi(\delta, \mu, \phi, \mu', \phi')$ is the scattering phase function which defines the probability that radiation coming from direction (μ', ϕ') is scattered in direction (μ, ϕ). The short-wave part of the scheme, originally developed by Fouquart and Bonnel (1980) solves the radiation transfer equation and integrates the fluxes over the whole short-wave spectrum between 0.2 and 4 µm. Upward and downward fluxes are obtained from the reflectances and transmittances of the layers, and the photon-path-distribution method allows to separate the parametrization of the scattering processes from that of the molecular absorption.

2.2.1 Spectral integration

Solar radiation is attenuated by absorbing gases, mainly water vapour, uniformly mixed gases (oxygen, carbon dioxide, methane, nitrous oxide) and ozone, and scattered by molecules (Rayleigh scattering), aerosols and cloud particles. Since scattering and molecular absorption occur simultaneously, the exact

amount of absorber along the photon path length is unknown, and band models of the transmission function cannot be used directly as in long-wave radiation transfer (see Section 2.2). The approach of the photon path distribution method is to calculate the probability $\Pi(\mathcal{U})\,\mathrm{d}\mathcal{U}$ that a photon contributing to the flux $\mathcal{F}_{\mathrm{cons}}$ in the conservative case (i.e., no absorption, $\omega_\nu = 1, k_\nu = 0$) has encountered an absorber amount between $\mathcal{U}$ and $\mathcal{U} + \mathrm{d}\mathcal{U}$. With this distribution, the radiative flux at wavenumber v is related to $\mathcal{F}_{\mathrm{cons}}$ by

$$\mathcal{F}_v = \mathcal{F}_{\mathrm{cons}} \int_0^\infty \Pi(\mathcal{U}) \exp(-k_\nu \mathcal{U})\,\mathrm{d}\mathcal{U} \tag{2.5}$$

and the flux averaged over the spectral interval $\Delta\nu$ can then be calculated with the help of any band model of the transmission function $t_{\Delta\nu}$

$$\mathcal{F} = \frac{1}{\Delta\nu}\int_{\Delta\nu} \mathcal{F}_\nu\,\mathrm{d}\nu = \mathcal{F}_{\mathrm{cons}} \int_0^\infty \Pi(\mathcal{U}) t_{\Delta\nu}(\mathcal{U})\,\mathrm{d}\nu \tag{2.6}$$

To find the distribution function $\Pi(\mathcal{U})$, the scattering problem is solved first, by any method, for a set of arbitrarily fixed absorption coefficients k_1, thus giving a set of simulated fluxes $\mathcal{F}_{k_1}$. An inverse Laplace transform is then performed on (2.5) (Fouquart, 1974). The main advantage of the method is that the actual distribution $\Pi(\mathcal{U})$ is smooth enough that (2.5) gives accurate results even if $\Pi(\mathcal{U})$ itself is not known accurately. In fact, $\Pi(\mathcal{U})$ needs not be calculated explicitly as the spectrally integrated fluxes are

$$\begin{array}{ll} \mathcal{F} = \mathcal{F}_{\mathrm{cons}} t_{\Delta v}(\langle \mathcal{U} \rangle) & \text{in the limiting case of weak absorption} \\ \mathcal{F} = \mathcal{F}_{\mathrm{cons}} t_{\Delta v}(\langle \mathcal{U}^{1/2} \rangle) & \text{in the limiting case of strong absorption} \end{array}$$

where $\langle \mathcal{U} \rangle = \int_0^\infty \Pi(\mathcal{U})\mathcal{U}\,\mathrm{d}\mathcal{U}$ and $\langle \mathcal{U}^{1/2} \rangle = \int_0^\infty \Pi(\mathcal{U})\mathcal{U}^{1/2}\,\mathrm{d}\mathcal{U}$.

The atmospheric absorption in the water vapour bands is generally strong, and the scheme determines an effective absorber amount $\mathcal{U}_{\mathrm{e}}$ between $\langle \mathcal{U} \rangle$ and $\langle \mathcal{U}^{1/2} \rangle$ derived from

$$\mathcal{U}_{\mathrm{e}} = \ln(\mathcal{F}_{k_{\mathrm{e}}}/\mathcal{F}_{\mathrm{cons}})/k_{\mathrm{e}} \tag{2.7}$$

where k_{e} is an absorption coefficient chosen to approximate the spectrally averaged transmission of the clear sky atmosphere

$$k_{\mathrm{e}} = \frac{1}{\mathcal{U}_{\mathrm{tot}}/\mu_0} \ln(t_{\Delta v}(\mathcal{U}_{\mathrm{tot}}/\mu_0)) \tag{2.8}$$

where U_{tot} is the total amount of absorber in a vertical column and $\mu_0 = \cos\theta_0$. Once the effective absorber amounts of H_2O and uniformly mixed gases are found, the transmission functions are computed using Padé approximants

$$t_{\Delta\nu}(\mathcal{U}) = \frac{\sum_{i=0}^N a_i \mathcal{U}^{i-1}}{\sum_{j=0}^N b_j \mathcal{U}^{j-1}} \tag{2.9}$$

Absorption by ozone is also taken into account, but since ozone is located at low pressure levels for which molecular scattering is small and Mie scattering is negligible, interactions between scattering processes and ozone absorption are neglected. Transmission through ozone is computed using (2.6) where $\mathcal{U}_{\mathrm{O_3}}$ the amount of ozone is

$$\begin{array}{ll} \mathcal{U}^{\mathrm{d}}_{\mathrm{O_3}} = M \displaystyle\int_p^0 \mathrm{d}\mathcal{U}_{\mathrm{O_3}} & \text{for the downward transmission of the direct solar beam} \\ \mathcal{U}^{\mathrm{u}}_{\mathrm{O_3}} = r \displaystyle\int_{p_{\mathrm{s}}}^0 \mathrm{d}\mathcal{U}_{\mathrm{O_3}} + \mathcal{U}^{\mathrm{d}}_{\mathrm{O_3}}(p_{\mathrm{surf}}) & \text{for the upward transmission of the diffuse radiation} \end{array}$$

$r = 1.66$ is the diffusivity factor (see Section 2.2), and M is the magnification factor (Rodgers, 1967) used instead of r to account for the sphericity of the atmosphere at very small solar elevations

$$M = 35/\sqrt{\mu_0^2 + 1} \tag{2.10}$$

To perform the spectral integration, it is convenient to discretize the solar spectrum into subintervals in which the surface reflectance, molecular absorption characteristics, and cloud optical properties can be

considered as constants. One of the main causes for such a spectral variation is the sharp increase in the reflectivity of the vegetation in the near-infrared. Also, water vapour does not absorb below 0.69 μm nor do liquid water clouds. Till June 2000, the ECMWF short-wave scheme considered only two spectral intervals, one for the visible (0.2–0.69 µm), one for the near-infrared (0.69–4.00 µm) parts of the solar spectrum. From June 2000 to April 2002, the near-infrared interval was sub-divided into three intervals (0.69–1.19–2.38–4.00 µm) to account better for the spectral variations of the cloud optical properties. Till April 2002, all the molecular absorption coefficients (for O_3, H_2O, uniformly mixed gases) were derived from statistical models of the transmission function using spectroscopic parameters derived from various versions of the HITRAN database (Rothman *et al.*, 1986, 1992). In April 2002, following the recomputation of all the molecular absorption coefficients from an updated version of the short-wave line-by-line model of Dubuisson *et al.* (1996) using spectroscopic data from HAWKS (2000), the ultraviolet and visible part of the spectrum are now considered in three spectral intervals (0.20–0.25–0.69 µm) making the scheme having a total of six spectral intervals over which the aerosol and cloud optical properties are also defined. The cut-off at 0.69 µm allows the scheme to be more computational efficient, in as much as the interactions between gaseous absorption (by water vapour and uniformly mixed gases) and scattering processes are accounted for only in the near-infrared interval(s).

2.2.2 Vertical integration

Considering an atmosphere where a fraction $C_{\rm cld}^{\rm tot}$ (as seen from the surface or the top of the atmosphere) is covered by clouds (the fraction $C_{\rm cld}^{\rm tot}$ depends on which cloud-overlap assumption is assumed for the calculations), the final fluxes are given as a weighted average of the fluxes in the clear sky and in the cloudy fractions of the column

$$\mathcal{F}^{-}(j) = C_{\rm cld}^{\rm tot}\mathcal{F}_{\rm cld}^{-}(j) + (1 - C_{\rm cld}^{\rm tot})\mathcal{F}_{\rm clr}^{-}$$

where the subscripts 'clr' and 'cld' refer to the clear-sky and cloudy fractions of the layer, respectively. In contrast to the scheme of Geleyn and Hollingsworth (1979), the fluxes are not obtained through the solution of a system of linear equations in a matrix form. Rather, assuming an atmosphere divided into homogeneous layers, the upward and downward fluxes at a given layer interface j are given by

$$\begin{aligned} \mathcal{F}^{-}(j) &= \mathcal{F}_0 \prod_{k=j}^{N} \mathcal{T}_{\rm bot}(k) \\ \mathcal{F}^{+}(j) &= \mathcal{F}^{-}(j)\mathcal{R}_{\rm top}(j-1) \end{aligned} \tag{2.11}$$

where $\mathcal{R}_{\rm top}(j)$ and $\mathcal{T}_{\rm bot}(j)$ are the reflectance at the top and the transmittance at the bottom of the jth layer. Computation of the values of $\mathcal{R}_{\rm top}$ starts at the surface and works upwards, whereas determining values of $\mathcal{T}_{\rm bot}$ starts at the top of the atmosphere and works downward. $\mathcal{R}_{\rm top}$ and $\mathcal{T}_{\rm bot}$ account for the presence of cloud in the layer by using

$$\begin{aligned} \mathcal{R}_{\rm top} &= C_{\rm cld}\mathcal{R}_{\rm cld} + (1 - C_{\rm cld})\mathcal{R}_{\rm clr} \\ \mathcal{T}_{\rm bot} &= C_{\rm cld}\mathcal{T}_{\rm cld} + (1 - C_{\rm cld})\mathcal{T}_{\rm clr} \end{aligned} \tag{2.12}$$

where $C_{\rm cld}$ is the cloud fractional coverage of the layer within the cloudy fraction $C_{\rm cld}^{\rm tot}$ of the column.

(*a*) *Cloudy fraction layer*

$\mathcal{R}_{t_{\rm cdy}}$ and $\mathcal{R}_{b_{\rm cdy}}$ are the reflectance at the top and transmittance at the bottom of the cloudy fraction of the layer calculated with the Delta-Eddington approximation. Given $\delta_{\rm c}$, $\delta_{\rm a}$, and $\delta_{\rm g}$, the optical thicknesses for the cloud, the aerosol and the molecular absorption of the gases ($= k_{\rm e}U$), respectively, and $g_{\rm c}$ and $g_{\rm a}$ the cloud and aerosol asymmetry factors, $\mathcal{R}_{t_{\rm cdy}}$ and $\mathcal{R}_{b_{\rm cdy}}$ are calculated as functions of the total optical thickness of the layer

$$\delta = \delta_{\rm c} + \delta_{\rm a} + \delta_{\rm g} \tag{2.13}$$

of the total single scattering albedo

$$\omega^{*} = \frac{\delta_{\rm c} + \delta_{\rm a}}{\delta_{\rm c} + \delta_{\rm a} + \delta_{\rm g}} \tag{2.14}$$

of the total asymmetry factor

$$g^* = \frac{\delta_c}{\delta_c + \delta_a} g_c + \frac{\delta_a}{\delta_c + \delta_a} g_a \tag{2.15}$$

of the reflectance $\mathcal{R}_-$ of the underlying medium (surface or layers below the jth interface), and of the cosine of an effective solar zenith angle $\mu_{\text{eff}}(j)$ which accounts for the decrease of the direct solar beam and the corresponding increase of the diffuse part of the downward radiation by the upper scattering layers

$$\mu_{\text{eff}}(j) = [(1 - C^{\text{eff}}_{\text{cld}}(j))/\mu + rC^{\text{eff}}_{\text{cld}}(j)]^{-1} \tag{2.16}$$

with $C^{\text{eff}}_{\text{cld}}(j)$ the effective total cloudiness over level j

$$C^{\text{eff}}_{\text{cld}}(j) = 1 - \prod_{i=j+1}^{N} (1 - C_{\text{cld}}(i)E(i)) \tag{2.17}$$

and

$$E(i) = 1 - \exp\left[-\frac{(1 - \varpi_c(i)g_c(i)^2)\delta_c(i)}{\mu}\right] \tag{2.18}$$

$\delta_c(i), \varpi_c(i)$ and $g_c(i)$ are the optical thickness, single scattering albedo and asymmetry factor of the cloud in the ith layer, and r is the diffusivity factor. The scheme follows the Eddington approximation first proposed by Shettle and Weinman (1970), then modified by Joseph *et al.* (1976) to account more accurately for the large fraction of radiation directly transmitted in the forward scattering peak in case of highly asymmetric phase functions. Eddington's approximation assumes that, in a scattering medium of optical thickness δ^*, of single scattering albedo ω, and of asymmetry factor g, the radiance $\mathcal{L}$ can be written as

$$\mathcal{L}(\delta, \mu) = \mathcal{L}_0(\delta) + \mu\mathcal{L}_1(\delta) \tag{2.19}$$

In that case, when the phase function is expanded as a series of associated Legendre functions, all terms of order greater than one vanish when (2.2) is integrated over μ and ϕ. The phase function is therefore given by

$$P(\Theta) = 1 + \beta_1(\Theta)\mu$$

where Θ is the angle between incident and scattered radiances. The integral in (2.2) thus becomes

$$\int_0^{2\pi} d\phi' \left\{ \int_{-1}^{+1} p(\mu, \phi, \mu', \phi')\mathcal{L}(\mu', \phi')\, \mathrm{d}\mu' \right\} = 4\pi(L_0 + \pi\mathcal{L}_1) \tag{2.20}$$

where

$$g = \frac{\beta_1}{3} = \frac{1}{2}\int_{-1}^{+1} P(\Theta)\mu\, \mathrm{d}\mu$$

is the asymmetry factor.

Using (2.20) in (2.2) after integrating over μ and dividing by 2π, we get

$$\mu\frac{\mathrm{d}}{\mathrm{d}\delta}(\mathcal{L}_0 + \mu\mathcal{L}_1) = -(\mathcal{L}_0 + \mu\mathcal{L}_1) + \varpi(\mathcal{L}_0 + g\mu\mathcal{L}_1) + 1/4\varpi\mathcal{F}_0 \exp(-\delta/\mu_0)(1 + 3g\mu_0\mu) \tag{2.21}$$

We obtain a pair of equations for $\mathcal{L}_0$ and $\mathcal{L}_1$ by integrating (2.21) over μ

$$\begin{aligned} \frac{\mathrm{d}\mathcal{L}_0}{\mathrm{d}\delta} &= -3(1 - \varpi)\mathcal{L}_0 + \frac{3}{4}\varpi\mathcal{F}_0 \exp(-\delta/\mu_0) \\ \frac{\mathrm{d}\mathcal{L}_1}{\mathrm{d}\delta} &= -(1 - \varpi g)\mathcal{L}_1 + \frac{3}{4}\varpi g\mu_0\mathcal{F}_0 \exp(-\delta/\mu_0) \end{aligned} \tag{2.22}$$

For the cloudy layer assumed non-conservative ($\varpi < 1$), the solutions to (2.21) and (2.22), for $0 \le \delta \le \delta^*$, are

$$\begin{aligned} \mathcal{L}_0(\delta) &= C_1 \exp(-K\delta) + C_2 \exp(+K\delta) - \alpha \exp(-\delta/\mu_0) \\ \mathcal{L}_1(\delta) &= P\{C_1 \exp(-K\delta) - C_2 \exp(+K\delta) - \beta \exp(-\delta/\mu_0)\} \end{aligned} \tag{2.23}$$

where

$$K = \{3(1-\varpi)(1-\varpi g)\}^{1/2}$$
$$P = \{3(1-\varpi)/(1-\varpi g)\}^{1/2}$$
$$\alpha = 3\varpi F_0\mu_0\{1+3g(1-\varpi)\}/\{4(1-K^2\mu_0^2)\}$$
$$\beta = 3\varpi F_0\mu_0\{1+3g(1-\varpi)\mu_0^2\}/(4(1-K^2\mu_0^2))$$

The two boundary conditions allow to solve the system for C_1 and C_2; the downward directed diffuse flux at the top of the atmosphere is zero, that is

$$\mathcal{F}^-(0) = \left[\mathcal{L}_0(0) + \frac{2}{3}\mathcal{L}_1(0)\right] = 0$$

which translates into

$$(1+2P/3)C_1 + (1-2P/3)C_2 = \alpha + 2\beta/3 \tag{2.24}$$

The upward directed flux at the bottom of the layer is equal to the product of the downward directed diffuse and direct fluxes and the corresponding diffuse and direct reflectance ($\mathcal{R}_\mathrm{d}$ and $\mathcal{R}_-$, respectively) of the underlying medium

$$\begin{aligned}\mathcal{F}^+(\delta^*) &= \left\{\mathcal{L}_0(\delta^*) - \frac{2}{3}\mathcal{L}_1(\delta^*)\right\}\\ &= \mathcal{R}_-\left\{\mathcal{L}_0(\delta^*) + \frac{2}{3}\mathcal{L}_1(\delta^*)\right\} + \mathcal{R}_\mathrm{d}\mu_0\mathcal{F}_0\exp(-\delta^*/\mu_0)\end{aligned}$$

which translates into

$$\begin{aligned}&\{1-\mathcal{R}_- - 2(1+\mathcal{R}_-)P/3\}C_1\exp(-K\delta^*) + \{1-\mathcal{R}_- + 2(1+\mathcal{R}_-)P/3\}C_2(+K\delta^*)\\ &\quad = \{(1-\mathcal{R}_-)\alpha - 2(1+\mathcal{R}_-)\beta/3 + \mathcal{R}_\mathrm{d}\mu_0\mathcal{F}_0\}\exp(-\delta^*/\mu_0)\end{aligned} \tag{2.25}$$

In the Delta-Eddington approximation, the phase function is approximated by a Dirac delta function forward-scatter peak and a two-term expansion of the phase function

$$P(\theta) = 2f(1-\mu) + (1-f)(1+3g'\mu)$$

where f is the fractional scattering into the forward peak and g' the asymmetry factor of the truncated phase function. As shown by Joseph *et al.* (1976), these parameters are

$$\begin{aligned}f &= g^2\\ g' &= g/(g+1)\end{aligned} \tag{2.26}$$

The solution of the Eddington's equations remains the same provided that the total optical thickness, single scattering albedo and asymmetry factor entering (2.21) and (2.25) take their transformed values

$$\begin{aligned}\delta'^* &= (1+\varpi f)\delta^*\\ \omega' &= \frac{(1-f)\varpi}{1-\varpi f}\end{aligned} \tag{2.27}$$

Practically, the optical thickness, single scattering albedo, asymmetry factor and solar zenith angle entering (2.21)–(2.25) are δ^*, ϖ^*, g^* and μ_eff defined in (2.15) and (2.16).

(*b*) *Clear-sky fraction of the layers*

In the clear-sky part of the atmosphere, the short-wave scheme accounts for scattering and absorption by molecules and aerosols. The following calculations are practically done twice, once for the clear-sky fraction ($1 - C_\mathrm{cld}^\mathrm{tot}$) of the atmospheric column μ with equal to μ_0, simply modified for the effect of

Rayleigh and aerosol scattering, the second time for the clear-sky fraction of each individual layer within the fraction $C_{\rm cld}^{\rm tot}$ of the atmospheric column containing clouds, with μ equal to $\mu_{\rm e}$.

As the optical thickness for both Rayleigh and aerosol scattering is small, $\mathcal{R}_{\rm clr}(j-1)$ and $\mathcal{T}_{\rm clr}(j)$, the reflectance at the top and transmittance at the bottom of the jth layer can be calculated using respectively a first- and a second-order expansion of the analytical solutions of the two-stream equations similar to that of Coakley Jr. and Chylek (1975). For Rayleigh scattering, the optical thickness, single scattering albedo and asymmetry factor are respectively $\delta_{\rm R}$, $\varpi_{\rm R}=1$ and $g_{\rm R}=0$, so that

$$\begin{aligned}\mathcal{R}_{\rm R} &= \frac{\delta_{\rm R}}{2\mu+\delta_{\rm R}}\\ \mathcal{T}_{\rm R} &= \frac{2\mu}{(2\mu+\delta_{\rm R})}\end{aligned} \tag{2.28}$$

The optical thickness $\delta_{\rm R}$ of an atmospheric layer is simply

$$\delta_{\rm R} = \delta^*\{p(j)-p(j-1)\}/p_{\rm surf} \tag{2.29}$$

where $\delta_{\rm R}^*$ is the Rayleigh optical thickness of the whole atmosphere parametrized as a function of the solar zenith angle (Deschamps *et al.*, 1983)

For aerosol scattering and absorption, the optical thickness, single scattering albedo and asymmetry factor are respectively $\delta_{\rm a}$, $\varpi_{\rm a}$, with $1-\varpi_{\rm a}\ll 1$ and $g_{\rm a}$, so that

$$\begin{aligned}{\rm den} = 1 &+ \{1-\varpi_{\rm a}+{\rm back}(\mu_{\rm e})\varpi_{\rm a}\}(\delta_{\rm a}/\mu_{\rm e})\\ &+ (1-\varpi_{\rm a})\{1-\varpi_{\rm a}+2\,{\rm back}(\mu_{\rm e})\varpi_{\rm a}\}(\delta_{\rm a}^2/\mu_{\rm e}^2)\end{aligned} \tag{2.30}$$

$$\begin{aligned}\mathcal{R}(\mu_{\rm e}) &= \frac{({\rm back}(\mu_{\rm e})\varpi_{\rm a}\delta_{\rm a})/\mu_{\rm a}}{\rm den}\\ \mathcal{T}(\mu_{\rm e}) &= 1/{\rm den}\end{aligned} \tag{2.31}$$

where ${\rm back}(\mu_{\rm e})=(2-3\mu_{\rm e}g_{\rm a})/4$ is the backscattering factor.

Practically, $\mathcal{R}_{\rm clr}$ and $\mathcal{T}_{\rm clr}$ are computed using (2.31) and the combined effect of aerosol and Rayleigh scattering comes from using modified parameters corresponding to the addition of the two scatterers with provision for the highly asymmetric aerosol phase function through Delta-approximation of the forward scattering peak (as in (2.22) and (2.23)).

$$\begin{aligned}\delta^+ &= \delta_{\rm R}+\delta_{\rm a}(1-\varpi_a g_a^2)\\ g^+ &= \frac{g_{\rm a}}{1+g_{\rm a}}\frac{\delta_{\rm a}}{(\delta_{\rm R}+\delta_{\rm a})}\\ \varpi^+ &= \frac{\delta_{\rm R}}{\delta_{\rm a}+\delta_{\rm a}}\varpi_{\rm R}+\frac{\delta_{\rm a}}{\delta_{\rm R}+\delta_{\rm a}}\frac{\varpi_{\rm a}(1-g_{\rm a}^2)}{1-\varpi_{\rm a}g_{\rm a}^2}\end{aligned} \tag{2.32}$$

As for their cloudy counterparts, $\mathcal{R}_{\rm clr}$ and $\mathcal{T}_{\dot{\rm c}\rm lr}$ must account for the multiple reflections due to the layers underneath

$$\mathcal{R}_{\rm clr} = \mathcal{R}(\mu_{\rm e})+\mathcal{R}_-\mathcal{T}(\mu_{\rm e})(1-\mathcal{R}^*\mathcal{R}_-) \tag{2.33}$$

and $\mathcal{R}_-$ is the reflectance of the underlying medium $\mathcal{R}_-=\mathcal{R}_t(j-1)$ and r is the diffusivity factor.

Since interactions between molecular absorption and Rayleigh and aerosol scattering are negligible, the radiative fluxes in a clear-sky atmosphere are simply those calculated from (2.9) and (2.27) attenuated by the gaseous transmissions (2.7).

2.2.3 Multiple reflections between layers

To deal properly with the multiple reflections between the surface and the cloud layers, it should be necessary to separate the contribution of each individual reflecting surface to the layer reflectance and

transmittances in as much as each such surface gives rise to a particular distribution of absorber amount. In the case of an atmosphere including N cloud layers, the reflected light above the highest cloud consists of photons directly reflected by the highest cloud without interaction with the underlying atmosphere, and of photons that have passed through this cloud layer and undergone at least one reflection on the underlying atmosphere. In fact, (2.4) should be written

$$\mathcal{F} = \sum_{i=0}^{N} \mathcal{F}_{\mathrm{cl}} \int_0^{\infty} \mathcal{P}_1(\mathcal{U}) t_{\Delta v}(\mathcal{U}) \mathrm{d}v \tag{2.34}$$

where $\mathcal{F}_{\mathrm{cl}}$ and $\mathcal{P}_1(\mathcal{U})$ are the conservative fluxes and the distributions of absorber amount corresponding to the different reflecting surfaces.

Fouquart and Bonnel (1980) have shown that a very good approximation to this problem is obtained by evaluating the reflectance and transmittance of each layer (using (2.21) and (2.27)) assuming successively a non-reflecting underlying medium ($\mathcal{R}_- = 0$), then a reflecting underlying medium ($\mathcal{R}_- \neq 0$). First calculations provide the contribution to reflectance and transmittance of those photons interacting only with the layer into consideration, whereas the second ones give the contribution of the photons with interactions also outside the layer itself.

From those two sets of layer reflectance and transmittances ($\mathcal{T}_{\mathrm{t0}}, \mathcal{T}_{\mathrm{b0}}$) and ($\mathcal{R}_{\mathrm{t}\neq}, \mathcal{T}_{\mathrm{b}\neq}$) respectively, effective absorber amounts to be applied to computing the transmission functions for upward and downward fluxes are then derived using (2.5) and starting from the surface and working the formulas upward

$$\begin{aligned}
\mathcal{U}^-_{\mathrm{e0}} &= \ln\left(\mathcal{T}_{\mathrm{b0}}/\mathcal{T}_{\mathrm{bc}}\right)/k_{\mathrm{e}} \\
\mathcal{U}^-_{\mathrm{e}\neq} &= \ln\left(\mathcal{T}_{\mathrm{b}\neq}/\mathcal{T}_{\mathrm{bc}}\right)/k_{\mathrm{e}} \\
\mathcal{U}^+_{\mathrm{e0}} &= \ln\left(\mathcal{R}_{\mathrm{t0}}/\mathcal{R}_{\mathrm{tc}}\right)/k_{\mathrm{e}} \\
\mathcal{U}^+_{\mathrm{e}\neq} &= \ln\left(\mathcal{R}_{\mathrm{t}\neq}/\mathcal{R}_{\mathrm{tc}}\right)/k_{\mathrm{e}}
\end{aligned} \tag{2.35}$$

where $\mathcal{R}_{\mathrm{tc}}$ and $\mathcal{T}_{\mathrm{bc}}$ are the layer reflectance and transmittance corresponding to a conservative scattering medium.

Finally the upward and downward fluxes are obtained as

$$\mathcal{F}^+(j) = \mathcal{F}_0\{\mathcal{R}_{t0} t_{\Delta\nu}(\mathcal{U}^+_{\mathrm{e0}}) + (\mathcal{R}_{t\neq} - \mathcal{R}_{\mathrm{t0}}) t_{\Delta\nu}(\mathcal{U}^+_{\mathrm{e}\neq})\} \tag{2.36}$$

$$\mathcal{F}^-(j) = \mathcal{F}_0\{\mathcal{T}_{b0} t_{\Delta\nu}(\mathcal{U}^+_{\mathrm{e0}}) + (\mathcal{T}_{b\neq} - \mathcal{T}_{\mathrm{b0}}) t_{\Delta\nu}(\mathcal{U}^-_{\mathrm{e}\neq})\} \tag{2.37}$$

2.2.4 Pre-CY32R2 cloud short-wave optical properties

As seen in Subsection 2.2.2(a), the cloud radiative properties depend on three different parameters: the optical thickness δ_{c}, the asymmetry factor g_{c}, and the single scattering albedo ϖ_{c}.

In this older scheme the cloud optical properties were derived from Fouquart (1987) for the water clouds, and Ebert and Curry (1992) for the ice clouds.

The optical thickness δ_{c} is related to the cloud liquid water amount U_{LWP} by

$$\delta_{\mathrm{c}} = \frac{3\mathcal{U}_{\mathrm{LWP}}}{2r_{\mathrm{e}}}$$

where r_{e} is the mean effective radius of the size distribution of the cloud water droplets.

In an older formulation of this scheme, r_{e} was parametrized as a linear function of height from 10 μm at the surface to 45 μm at the top of the atmosphere, in an empirical attempt at dealing with the variation of water cloud type with height. Smaller water droplets are observed in low-level stratiform clouds whereas larger droplets are found in mid-level cumuliform water clouds. This parametrisation was then revised, using the formulation of Martin *et al.* (1994) to compute the effective radius of the liquid water cloud particles from the cloud liquid water content and specified concentrations of cloud condensation

nuclei over land and ocean. For ice clouds, the effective dimension of the cloud particles was diagnosed from temperature using a revision of the formulation by Ou and Liou (1995).

In the two-, four-, and six-spectral interval versions of the short-wave radiation scheme, the optical properties of liquid water clouds were defined from Fouquart (1987) and those for ice clouds from Ebert and Curry (1992). Alternative optical properties were also available for liquid water clouds (Slingo, 1989) and ice clouds (Fu, 1996).

2.3 THE PRE-CY22R3 LONG-WAVE RADIATION SCHEME

Please note that this section refers to a very old version of the radiation scheme that is only used in the linearized physics used in data assimilation. The symbols used here may differ from those in the other sections of this chapter.

As already noted, since cycle Cy22r3, two long-wave radiation schemes have been available in the ECMWF model, the pre-cycle Cy22r3 by Morcrette (1991), and the current long-wave radiation transfer scheme, the Rapid Radiation Transfer Model (RRTMG).

The rate of atmospheric cooling by emission-absorption of long-wave radiation is

$$\frac{\partial T}{\partial t} = \frac{g}{c_p}\frac{\partial \mathcal{F}_{\mathrm{LW}}}{\partial p} \tag{2.38}$$

where $\mathcal{F}_{\mathrm{LW}}$ is the net long-wave radiation flux (the subscript 'LW' is omitted in the remainder of this section).

Assuming a non-scattering atmosphere in local thermodynamic equilibrium, $\mathcal{F}$ is given by

$$\mathcal{F} = \int_{-1}^{1} \mu \, \mathrm{d}\mu \left[\int_{0}^{\infty} \mathrm{d}v \left\{ \mathcal{L}_v(p_{\mathrm{surf}}, \mu) t_v(p_{\mathrm{surf}}, p, \mu) + \int_{p'=p_{\mathrm{surf}}}^{0} \mathcal{L}_v(p', \mu) \, \mathrm{d}t_v \right\} \right] \tag{2.39}$$

where $\mathcal{L}_v(p, \mu)$ is the monochromatic radiance at wavenumber v at level p, propagating in a direction θ (the angle that this direction makes with the vertical), where $\mu = \cos\theta$ and $t_v(p, p'; r)$ is the monochromatic transmission through a layer whose limits are at p and p' seen under the same angle θ, with $r = \sec\theta$. The subscript 'surf' refers to the earth's surface.

2.3.1 The pre-cycle Cy22r3 scheme

After separating the upward and downward components (indicated by superscripts $+$ and $-$, respectively), and integrating by parts, we obtain the radiation transfer equation as it is actually estimated in the long-wave part of the radiation code

$$\begin{aligned} \mathcal{F}_v^+(p) &= [B_v(T_{\mathrm{surf}}) - B_v(T_{0+})] t_v(p_{\mathrm{surf}}, p; r) + B_v(T(p)) + \int_{p'=p_{\mathrm{surf}}}^{p} t_v(p, p'; r) \, \mathrm{d}B_v \\ \mathcal{F}_v^-(p) &= [B_v(T_\infty) - B_v(T_{\mathrm{top}})] t_v(p, 0; r) + B_v(T(p)) + \int_{p'=p}^{0} t_v(p', p; r) \, \mathrm{d}B_v \end{aligned} \tag{2.40}$$

where, taking benefit of the isotropic nature of the long-wave radiation, the radiance L_v of (2.39) has been replaced by the Planck function $B_v(T)$ in units of flux, Wm^{-2} (here, and elsewhere, B_v is assumed to always includes the π factor). T_{surf} is the surface temperature, T_{0+} that of the air just above the surface, $T(p)$ is the temperature at pressure-level p, T_{top} that at the top of the atmospheric model. The transmission t_v is evaluated as the radiance transmission in a direction θ to the vertical such that $r = \sec\theta$ is the diffusivity factor (Elsasser, 1942). Such an approximation for the integration over the angle is usual in radiative transfer calculations, and tests on the validity of this approximation have been presented by Rodgers and Walshaw (1966) and Liu and Schmetz (1988) among others. The use of the diffusivity factor gives cooling rates within 2% of those obtained with a 4-point Gaussian quadrature.

2.3.2 Vertical integration

The integrals in (2.40) are evaluated numerically, after discretization over the vertical grid, considering the atmosphere as a pile of homogeneous layers. As the cooling rate is strongly dependent on local

conditions of temperature and pressure, and energy is mainly exchanged with the layers adjacent to the level where fluxes are calculated, the contribution of the distant layers is simply computed using a trapezoidal rule integration, but the contribution of the adjacent layers is evaluated with a 2-point Gaussian quadrature, thus at the ith level

$$\int_{p'=p_{\text{surf}}}^{p_i} t_v(p,p';r)\,\mathrm{d}B_v = \sum_{l=1}^{2} \mathrm{d}B_v(l) w_l t_v(p_i,p_l;r) + \frac{1}{2}\sum_{j=1}^{i-2} \mathrm{d}B_v(j)[t_v(p_i,p_j;r) + t_v(p_i,p_{j-1};r)] \tag{2.41}$$

where p_l is the pressure corresponding to the Gaussian root and w_l is the Gaussian weight. $\mathrm{d}B_v(j)$ and $\mathrm{d}B_v(l)$ are the Planck function gradients calculated between two interfaces, and between mid-layer and interface, respectively.

2.3.3 Spectral integration

The integration over wavenumber v is performed using a band emissivity method, as first discussed by Rodgers (1967). The long-wave spectrum is divided into six spectral regions.

(i) 0–350 cm^{-1} and 1450–1880 cm^{-1}
(ii) 500–800 cm^{-1}
(iii) 800–970 cm^{-1} and 1110–1250 cm^{-1}
(iv) 970–1110 cm^{-1}
(v) 350–500 cm^{-1}
(vi) 1250–1450 cm^{-1} and 1880–2820 cm^{-1}

corresponding to the centres of the rotation and vibration-rotation bands of H_2O, the 15 µm band of CO_2, the atmospheric window, the 9.6 µm band of O_3, the 25 µm 'window' region, and the wings of the vibration-rotation band of H_2O, respectively. Over these spectral regions, band fluxes are evaluated with the help of band transmissivities pre-calculated from the narrow-band model of Morcrette and Fouquart (1985) – See Appendix of Morcrette *et al.* (1986) for details.

Integration of (2.40) over wavenumber ν within the kth spectral region gives the upward and downward fluxes as

$$\begin{aligned}\mathcal{F}_k^+(p) = {} & \{B_k(T_{\text{surf}}) - B_k(T_{0+})\} t_{B_k}\{r\mathcal{U}(p_{\text{surf}},p), T_{\mathcal{U}}(p_{\text{surf}},p)\} + B_k(T_p) \\ & + \int_{p'=p_{\text{surf}}}^{p} t_{\mathrm{d}B_k}\{r\mathcal{U}(p,p'), T_{\mathcal{U}}(p,p')\}\,\mathrm{d}B_k\end{aligned} \tag{2.42}$$

$$\begin{aligned}\mathcal{F}_k^-(p) = {} & \{B_k(T_0) - B_k(T_\infty)\} t_{B_k}\{r\mathcal{U}(p,0), T_{\mathcal{U}}(p,0)\} - B_k(T_p) \\ & - \int_{p'=p}^{0} t_{\mathrm{d}B_k}\{r\mathcal{U}(p',p), T_{\mathcal{U}}(p',p)\}\,\mathrm{d}B_k\end{aligned} \tag{2.43}$$

The formulation accounts for the different temperature dependencies involved in atmospheric flux calculations, namely that on T_p, the temperature at the level where fluxes are calculated, and that on $T_{\mathcal{U}}$, the temperature that governs the transmission through the temperature dependence of the intensity and half-widths of the lines absorbing in the concerned spectral region. The band transmissivities are non-isothermal accounting for the temperature dependence that arises from the wavenumber integration of the product of the monochromatic absorption and the Planck function. Two normalized band transmissivities are used for each absorber in a given spectral region: the first one for calculating the first right-hand-side term in (2.40), involving the boundaries; it corresponds to the weighted average of the transmission function by the Planck function

$$t_B(\overline{\mathcal{U}p}, T_p, T_{\mathcal{U}}) = \frac{\int_{v_1}^{v_2} B_v(T_p) t_v(\overline{\mathcal{U}p}, T_{\mathcal{U}})\,\mathrm{d}v}{\int_{v_1}^{v_2} B_v(T_p)\,\mathrm{d}v} \tag{2.44}$$

the second one for calculating the integral term in (2.40) is the weighted average of the transmission function by the derivative of the Planck function

$$t_{\mathrm{d}B}(\overline{\mathcal{U}p}, T_p, T_{\mathcal{U}}) = \frac{\int_{v_1}^{v_2} \{\mathrm{d}B(T_p)/\mathrm{d}T\} t_v(\overline{\mathcal{U}p}, T_{\mathcal{U}})\,\mathrm{d}v}{\int_{v_1}^{v_2} \{\mathrm{d}B(T_p)/\mathrm{d}T\}\,\mathrm{d}v} \tag{2.45}$$

where $\overline{\mathcal{U}p}$ is the pressure weighted amount of absorber.

The effect on absorption of the Doppler broadening of the lines (important only for pressure lower than 10 hPa) is included simply using the pressure correction method of Fels (1979). A finite line width (assumed to represent the Doppler half-width of the line) is retained under low pressure conditions where the pure Lorentz line width (proportional to pressure) would normally become negligible (Giorgetta and Morcrette, 1995).

In the scheme, the actual dependence on T_p is carried out explicitly in the Planck functions integrated over the spectral regions. Although normalized relative to $B(T_p)$ or $\mathrm{d}B(T_p)/\mathrm{d}T$, the transmissivities still depend on $T_{\mathcal{U}}$, both through Wien's displacement of the maximum of the Planck function with temperature and through the temperature dependence of the absorption coefficients. For computational efficiency, the transmissivities have been developed into Padé approximants

$$t(\overline{\mathcal{U}p}, T_u) = \frac{\sum_{i=0}^{2} c_i \mathcal{U}_{\mathrm{eff}}^{i/2}}{\sum_{j=0}^{2} d_j \mathcal{U}_{\mathrm{eff}}^{i/2}} \tag{2.46}$$

where $\mathcal{U}_{\mathrm{eff}} = r(\overline{\mathcal{U}p})\Psi(T_{\mathcal{U}}, \overline{\mathcal{U}p})$ is an effective amount of absorber which incorporates the diffusivity factor r, the weighting of the absorber amount by pressure $\overline{\mathcal{U}p}$, and the temperature dependence of the absorption coefficients. The function $\Psi(T_{\mathcal{U}}, \overline{\mathcal{U}p})$ takes the form

$$\Psi(T_{\mathcal{U}}, \overline{\mathcal{U}p}) = \exp[a(\overline{\mathcal{U}p})(T_{\mathcal{U}} - 250) + b(\overline{\mathcal{U}p})(T_{\mathcal{U}} - 250)^2] \tag{2.47}$$

The temperature dependence due to Wien's law is incorporated although there is no explicit variation of the coefficients c_i and d_j with temperature. These coefficients have been computed for temperatures between 187.5 and 312.5 K with a 12.5 K step, and transmissivities corresponding to the reference temperature the closest to the pressure weighted temperature $T_{\mathcal{U}}$ are actually used in the scheme.

2.3.4 The incorporation of the effects of clouds

The incorporation of the effects of clouds on the long-wave fluxes follows the treatment discussed by Washington and Williamson (1977). Whatever the state of the cloudiness of the atmosphere, the scheme starts by calculating the fluxes corresponding to a clear-sky atmosphere and stores the terms of the energy exchange between the different levels (the integrals in (2.40)) Let $\mathcal{F}_0^+(i)$ and $\mathcal{F}_0^-(i)$ be the upward and downward clear-sky fluxes. For any cloud layer actually present in the atmosphere, the scheme then evaluates the fluxes assuming a unique overcast cloud of emissivity unity. Let $\mathcal{F}_n^+(i)$ and $\mathcal{F}_n^+(i)$ the upward and downward fluxes when such a cloud is present in the nth layer of the atmosphere. Downward fluxes above the cloud, and upward fluxes below the cloud, are assumed to be given by the clear-sky values

$$\begin{aligned} \mathcal{F}_n^+(i) &= \mathcal{F}_0^+(i) \quad \text{for } i \le n \\ \mathcal{F}_n^-(i) &= \mathcal{F}_0^-(i) \quad \text{for } i > n \end{aligned} \tag{2.48}$$

Upward fluxes above the cloud ($\mathcal{F}_n^+(k)$ for $k \le n+1$) and downward fluxes below it ($\mathcal{F}_n^-(k)$ for $k > n$) can be expressed with expressions similar to (2.41) provided the boundary terms are now replaced by terms corresponding to possible temperature discontinuities between the cloud and the surrounding air

$$\begin{aligned} \mathcal{F}_n^+(k) &= \{\mathcal{F}_{\mathrm{cld}}^+ - B(n+1)\}t(p_k, p_{n+1}; r) + B(k) + \int_{p'=p_{n-1}}^{p_k} t(p_k, p'; r)\,\mathrm{d}B \\ \mathcal{F}_n^-(k) &= \{\mathcal{F}_{\mathrm{cld}}^- - B(n)\}t(p_k, p_n; r) + B(k) + \int_{p'=p_k}^{p_n} t(p_k, p'; r)\,\mathrm{d}B \end{aligned} \tag{2.49}$$

where $B(i)$ is now the total Planck function (integrated over the whole long-wave spectrum) at level i, and $\mathcal{F}_{\mathrm{cld}}^+$ and $\mathcal{F}_{\mathrm{cld}}^-$ are the long-wave fluxes at the upper and lower boundaries of the cloud. Terms under the integrals correspond to exchange of energy between layers in clear-sky atmosphere and have already been computed in the first step of the calculations. This step is repeated for all cloudy layers. The fluxes for the actual atmosphere (with semi-transparent, fractional and/or multi-layered clouds) are

derived from a linear combination of the fluxes calculated in previous steps with some cloud overlap assumption in the case of clouds present in several layers. Let N be the index of the layer containing the highest cloud, $C_{\rm cld}(i)$) the fractional cloud cover in layer i, with $C_{\rm cld}(0) = 1$ for the upward flux at the surface, and with $C_{\rm cld}(N+1) = 1$ and $\mathcal{F}^-_{N+1} = \mathcal{F}^-_0$ to have the right boundary condition for downward fluxes above the highest cloud.

Whereas the maximum and random overlap assumptions are also available in the code (Morcrette and Fouquart, 1986), the maximum-random overlap assumption is used in this version of the radiation scheme, and the cloudy upward $\mathcal{F}^+$ and downward $\mathcal{F}^-$ fluxes are obtained as

$$\begin{aligned}
&\mathcal{F}^+(i) = \mathcal{F}^+_0(i) && \text{for } i = 1\\
&\mathcal{F}^-(i) = C_{\rm cld}(i-1)\mathcal{F}^+_{i-1}(i-) + \sum_{n=0}^{i-2} C_{\rm cld}(n)\mathcal{F}^+_n(i) \prod_{l=n+1}^{i-1}\{1 - C_{\rm cld}(l)\} && \text{for } 2 \le i \le N+1\\
&\mathcal{F}^+(i) = C_{\rm cld}(N)\mathcal{F}^+_N(i) + \sum_{n=0}^{N-1} C_{\rm cld}(n)\mathcal{F}^+_n(i) \prod_{l=n+1}^{N}\{1 - C_{\rm cld}(l)\} && \text{for } i \ge N+2
\end{aligned} \tag{2.50}$$

In the case of semi-transparent clouds, the fractional cloudiness entering the calculations is an effective cloud cover equal to the product of the emissivity due to the condensed water and the gases in the layer by the horizontal coverage of the cloud layer, with the emissivity, $\varepsilon_{\rm cld}$, related to the condensed water amount by

$$\varepsilon_{\rm cld} = 1 - \exp(-k_{\rm abs}\mathcal{U}_{\rm LWP}) \tag{2.51}$$

where $k_{\rm abs}$ is the condensed water mass absorption coefficient (in $\mathrm{m^2 kg^{-1}}$) following Smith and Shi (1992).

2.4 INPUTS TO THE RADIATION SCHEME

2.4.1 Model variables

Temperature values are needed at the boundaries of the layers (half-levels), where the fluxes are computed. This is because the long-wave equations are solved in each model layer assuming the Planck function varies linearly with optical depth through the layer. They are derived from the model's full-level temperatures with a pressure-weighted interpolation:

$$T_{k+1/2} = T_k \frac{p_k(p_{k+1} - p_{k+1/2})}{p_{k+1/2}(p_{k+1} - p_k)} + T_{k+1}\frac{p_{k+1/2}(p_{k+1/2} - p_k)}{p_{k+1/2}(p_{k+1} - p_k)}. \tag{2.52}$$

Hogan and Bozzo (2016) investigated several options for how to treat the temperature of the base of lowest atmospheric layer, $T_{n+1/2}$ (where n is the number of model layers):

(i) Extrapolate linearly from the temperature at the half-level at the top of this layer, $T_{n-1/2}$, and the full-level temperature, T_n, which has the advantage that it respects the mean temperature of the layer. This can lead to a large discontinuity with the skin temperature, T_s, but it should be noted that in reality the temperature is far from linear in the lowest 20 m of the atmosphere represented by the lowest model layer.
(ii) Set it equal to the skin temperature T_s, thereby avoiding the discontinuity but not conserving the layer-mean temperature.
(iii) Set it equal to half-way between options (i) and (ii).

The impact on 2-m temperature forecasts between options (i) and (iii) can be as much as 4 K (Hogan and Bozzo, 2016), primarily due to the very strong 15-μm CO_2 band which makes the downwelling long-wave radiation sensitive to atmospheric temperature very close to the surface. The IFS currently uses option (iii), which lies between options (i) and (ii) in terms of impact. A potential avenue for future model improvement would be to investigate how to represent a more realistic vertical profile of temperature than linear in the lowest model layer.

2.4.2 Clouds

Cloud fraction and the mass mixing ratios of liquid, ice, rain and snow (q_l, q_i, q_r and q_s), are provided in all layers by the cloud scheme. These are used to calculate the effective radius for cloud water drops and ice particles required for the calculation of cloud-affected radiative fluxes. Note that 'in-cloud' water contents are used in all the effective radius equations (i.e. gridbox mean divided by the cloud fraction).

Internally, the radiation scheme only knows about two cloud types, 'liquid' and 'ice'. The liquid cloud mixing ratio fed to radiation comes only from the model's q_l variable, but rain mixing is used in the computation of liquid effective radius. The ice cloud mixing ratio fed to radiation is the sum of the model's ice and snow, i.e. $q_l + q_s$.

For both phases, effective radius is defined as

$$r_e = \frac{3V}{4A}, \tag{2.53}$$

where V is the total volume of liquid or ice in a given volume of air, and A is the total projected area of the particles in the same volume of air. Thus, r_e relates what the model provides (the mass of liquid or ice) to what radiation is primarily sensitive to when particles are much larger than the wavelength (the projected area). For liquid clouds this may be written as

$$r_e = \frac{3}{4}\frac{\mathrm{LWC}}{\rho_l A}, \tag{2.54}$$

where LWC is the liquid water content and ρ_l is the density of liquid water. A similar expression may be used for ice clouds using IWC and the density of solid ice.

(*a*) *Cloud droplet effective radius*

The formulation of the liquid cloud drop effective radius follows Martin *et al.* (1994) and Wood (2000). The liquid water content, LWC (equal to $q_l \rho_{\mathrm{air}}$), of a population of spherical cloud droplets can be written as an integral of the volume of the water drops over the droplet size distribution:

$$\mathrm{LWC} = \frac{4}{3}\pi\rho_w \int_0^\infty n_d(r) r^3 dr,$$

where ρ_w is the density of water and $n_d(r)dr$ is the number density of droplets of radius between r and $r + dr$. The average droplet radius (or volume radius) r_v in a unit volume of air with a droplet number density N_d can then be written as

$$r_v = \left(\frac{3\mathrm{LWC}}{4\pi\rho_w N_d}\right)^{1/3}.$$

The effective radius, r_e, of a cloud droplet population can be expressed as a function of its volume radius r by a factor k dependent on the shape of the cloud droplet size spectrum:

$$r_e^3 = \frac{r_v^3}{k},$$

so that

$$r_e = \left(\frac{3\mathrm{LWC}}{4\pi\rho_w k N_d}\right)^{1/3}. \tag{2.55}$$

The constant k can be formulated in terms of the relative dispersion D of the droplet size distribution. This is a normalised measure of the width of the distribution, equal to the standard deviation divided by the mean. The relationship is defined as

$$k = \frac{(1+D^2)^3}{(1+3D^2)^2}.$$

In the IFS, the spectral dispersion is given a value of $D = 0.33$ over ocean corresponding to $k = 0.77$. Over land, $D = 0.43$ and therefore $k = 0.69$. The values of the constant k are both close to the values given in Martin *et al.* (1994) from maritime and continental observations of stratocumulus.

Wood (2000) proposed an adjustment to the parametrization of effective radius in Martin *et al.* (1994) due to observations of an increased relative dispersion in the drop size spectra (a broader spectrum) when drizzle drops are present in the cloud. This formulation was introduced to the IFS in Cycle 36r4. The effective radius enhancement factor accounting for this increased dispersion follows Eq. 19 of Wood (2000):

$$E_d = \frac{1+\phi^{2/3}}{1+0.2(k_r/k)^{1/3}\phi},$$

where $\phi = \text{RWC/LWC}$ is the ratio of rain water content to liquid water content, k_r represents the large drops and is set to a constant 0.222, and k for the small droplets is defined from the dispersion D above. The enhancement factor, E_d, multiplies the effective radius in Eq. 2.55 and the in-cloud liquid water content LWC includes both cloud liquid and rain drops to give:

$$r_e = \left[\frac{E_d 3(\text{LWC}+\text{RWC})}{4\pi\rho_w k N_d}\right]^{1/3}. \tag{2.56}$$

The effective radius is then limited to be in the range 4 μm to 30 μm. The remaining unknown is the number concentration of cloud droplets, N_d, described below. Note that even though RWC appears in the definition of r_e, the rain water content is not used elsewhere in the radiation scheme (in contrast to snow, which is added to the ice water content).

The cloud droplet number concentration (cm^{-3}) (due to activated CCN) is parametrized in the IFS following Martin *et al.* (1994). The formulation is based on extensive aircraft observations of stratocumulus clouds from both maritime and continental regions of the world. Over the sea the parametrization is:

$$N_d = -1.15\times10^{-3}{N_a}^2 + 0.963N_a + 5.30, \tag{2.57}$$

and over land

$$N_d = -2.10\times10^{-4}{N_a}^2 + 0.568N_a - 27.9, \tag{2.58}$$

where N_d is the cloud droplet number concentration (assumed to be equal to the number of activated cloud condensation nuclei) and N_a is the aerosol number concentration in the size range 0.05 to 1.5 μm just below cloud base.

Before IFS Cycle 31r2, the aerosol concentration was fixed in time with $N_a = 50$ cm^{-3} over sea and $N_a = 900$ cm^{-3} over land. From Cycle 31r2 onwards, a more complex parametrization of the aerosol number concentration was introduced to better represent the spatial and temporal variability of aerosol. The near surface aerosol mass concentration (q_a) is calculated with a parametrization for the injection of aerosol from the surface into the atmosphere based on the 10-m wind speed. The formulation follows a parametrization derived for sea salt aerosol concentrations (Erickson *et al.*, 1986; Genthon, 1992):

$$q_a = e^{aW_s+b}, \tag{2.59}$$

where W_s is the 10-m wind speed (m s^{-1}) predicted by the model with coefficients depending on the wind speed; $a = 0.16$ and $b = 1.45$ for wind speeds less than 15 m s^{-1}, and $a = 0.13$ and $b = 1.89$ otherwise. This is applied over both ocean and land, with q_a limited to a value of 327 μg m^{-3} for wind speeds greater than 30 m s^{-1} over the ocean.

The conversion of aerosol mass concentration q_a to a number concentration N_a then follows an empirical formulation as described by Boucher and Lohmann (1995), Lowenthal *et al.* (2004) and others:

$$N_a = 10^{c+d\log_{10}(q_a)}. \tag{2.60}$$

In the IFS, the coefficients are $c = 1.2$, $d = 0.5$ over ocean and $c = 2.21$, $d = 0.3$ over land. This N_a is then used in Eqns. 2.57 and 2.58 to calculate the final cloud droplet number concentration. For very low wind speeds N_d is equal to 120 cm^{-3} over land and 40 cm^{-3} over sea, with increasing values as wind speed increases.

Note that the above formula in Boucher and Lohmann (1995) and Lowenthal *et al.* (2004) is derived to give the number of activated cloud condensation nuclei rather than the aerosol number concentration, so there is some inconsistency in the use of both Eq. 2.60 and Eqns. 2.57 and 2.58. A major revision of the effective radius calculation is planned for a future update.

(*b*) *Ice cloud effective radius*

For ice clouds, the effective dimension is a function of temperature, T (K), and in-cloud ice water content, IWC (g m^{-3}), based on Sun and Rikus (1999) with a revision from Sun (2001). Wherever there is ice cloud present, the snow water content is added to the ice to form a total ice water content as input to the scheme and therefore the same optical properties are currently assumed for both ice and snow. The ice particle effective diameter, D_e^{ice} (μm), is defined as

$$D_e^{\text{ice}} = 1.2351 + 0.0105(T - T_0)\,[a(\text{IWC}) + b(\text{IWC})(T - 83.15)]\,, \tag{2.61}$$

where $T_0 = 273.15$ K, $a(\text{IWC}) = 45.8966\text{IWC}^{0.2214}$ and $b(\text{IWC}) = 0.7957\text{IWC}^{0.2535}$. The effective diameter is then limited between a maximum of 155 μm and a latitude dependent minimum varying between 20 μm at the poles to 30 μm at the Equator, defined by $20 + 10\cos(\text{latitude})$. The ice particle effective radius (μm) is then defined as

$$r_e^{\text{ice}} = \frac{3\sqrt{3}}{8} D_e^{\text{ice}} = 0.64952 D_e^{\text{ice}}, \tag{2.62}$$

as suggested by Sun and Rikus (1999).

(*c*) *Cloud overlap*

The radiation scheme requires as input a profile of 'overlap parameter' α, on half-levels, defining the overlap of clouds in adjacent layers between the limits of 'maximum' ($\alpha = 1$) and 'random' overlap ($\alpha = 0$) overlap. Following the formulation of Hogan and Illingworth (2000), we compute this from decorrelation length, z_0, such that

$$\alpha = \exp(\Delta z / z_0),$$

where Δz is the vertical distance between the midpoints of the adjacent layers. This is often referred to as 'exponential-random' overlap, since clouds in adjacent layers have an overlap parameter with an exponential dependence on separation, but if clouds in two layers are separated by a clear layer between them then their overlap is random.

The IFS offers three means to specify Δz. If namelist parameter NDECOLAT=0 then a fixed value of $z_0 = 2$ km is used. Shonk *et al.* (2010) analysed data from cloud radar sites at a range of latitudes and proposed the following dependence on latitude (ϕ), in degrees, which is obtained with NDECOLAT=1:

$$z_0[\text{km}] = 2.899 - 0.0259|\phi|.$$

The larger decorrelation lengths in the tropics are consistent with the greater prevalence of convective clouds and the tendency for reduced wind shear compared to the mid-latitudes. The IFS default (NDECOLAT=2) uses a formulation that is consistent with the same radar observations, but has a smooth dependence with latitude across the equator:

$$z_0[\text{km}] = 0.75 + 2.149\cos^2\phi.$$

The radiation also needs to know how cloud sub-grid heterogeneities are correlated in the vertical. Hogan and Illingworth (2003) presented radar observations of ice clouds that suggested the vertical decorrelation length for cloud heterogeneities was half that for cloud boundaries, z_0, so in the absence of more specific information for different cloud types, this value of one half is used for all cloud types.

2.4.3 Aerosols

In the ECMWF forecast system from Cycles 26r3 to 43r1 the aerosol fields were provided by the Tegen *et al.* (1997) climatology. This is still used in the linearized version of the Morcrette (1991) radiation scheme used in data assimilation, but in other configurations of the IFS, the radiation scheme takes as input the mass mixing ratios of the 11 aerosol species from the Copernicus Atmospheric Monitoring System (CAMS). In CAMS air-quality forecasts, these values come directly from the 3D prognostic aerosol species after passing through the interpolation to the radiation grid. In other IFS configurations, we use a monthly mean 3D climatology derived from a CAMS aerosol reanalysis. As with trace gases

Table 2.2 *Summary of the properties of the aerosol species used in the CAMS system, either in prognostic or climatological configuration, taken from Bozzo et al. (2020) except where updates have been made. The size distribution is described by the modal radius r_{mod} and the geometric standard deviation σ; values are for dry aerosol apart from sea salt which is given for a relative humidity of 80%.*

Aerosol type (code)	Bin	Hydro-phylic?	Radius range (μm)	Optical model	Density ρ (g cm^{-3})	r_{mod} (μm)	σ
Sea salt (SU)	1 2 3	Y Y Y	0.03–0.5 0.5–5.0 5.0–20	OPAC	1.183	0.1992, 1.992†	1.9, 2.0†
Desert dust (DU)	1 2 3	N N N	0.03–0.55 0.55–0.9 0.9–20	Woodward or Composite‡	2.61	0.29	2.0
Organic matter (OM)	1 2	Y N	0.005–20	OPAC	See Bozzo *et al.* (2020)		
Black carbon (BC)	1 2	N* N	0.005–0.5	OPAC	1.0	0.0118	2.0
Sulfate (SU)	–	Y	0.005–20	GACP	1.76	0.0355	2.0

†Sea salt is described by a bimodal lognormal distribution with a 23.33 times larger number concentration in the small mode than the large.

‡Desert dust is treated using Woodward's refractive indices when used in a climatological configuration, and 'Composite' refractive indices when used in a prognostic configuration.

*Black carbon bin 1 is treated as hydrophilic in the CAMS aerosol scheme but as hydrophobic in the radiation scheme.

(discussed in Section 2.4.4), the time interpolation is done linearly assuming the climatology data correspond to the 15th of each month.

The details of the implementation together with the comparison against the Tegen *et al.* (1997) climatology and the impact on the model performance were discussed by Bozzo *et al.* (2020); a summary of the properties of the aerosol species is given in Table 2.2. See Section 11.7 for a visualization of the seasonal aerosol optical depth (AOD) of the CAMS climatology.

2.4.4 Greenhouse and other gases

Molecular oxygen is assigned a global-mean volume mixing ratio of 0.20944. Naturally, water vapour is taken directly from the model's prognostic variable. From Cycle 48r1, the model's prognostic ozone variable is used in the radiation scheme. The formulation of the linear ozone chemistry scheme follows the description in Chapter 10, but from the same cycle has changed from using the Cariolle coefficients to using coefficients derived to best fit the CAMS ozone analyses; this is known as the Hybrid Linear Ozone (HLO) scheme.

The five well-mixed greenhouse gases treated by the radiation scheme (CO_2, CH_4, N_2O, CFC-11 and CFC-12) are derived from a monthly/zonal-mean climatology defined in the file `greenhouse_gas_climatology_48r1.nc`. The file name may be overridden by setting namelist parameter CGHGCLIMFILE. This file also contains a climatology of ozone, which may be used instead of the prognostic ozone by setting namelist parameter LEPO3RA to `false` (default `true`).

The long-term trends in the five well-mixed greenhouse gases are treated by another file, `greenhouse_gas_timeseries_CMIP6_SSP370_CFC11equiv_47r1.nc`, which implements CMIP6 Shared Socioeconomic Pathway SSP3-7.0, covering observed and projected surface concentrations for the years 0–2500 CE, and including a scaling-up of the concentration of CFC-11 to approximately represent the radiative forcing of all other minor greenhouse gases. There are a number of namelist parameters that allow the forcing to be changed in the IFS:

- CGHGTIMESERIESFILE: specify an alternative file, in which case NGHGCMIP and NCP below are ignored.
- NGHGCMIP: select the version of CMIP from 0 (CMIP3), 5 (CMIP5) or 6 (CMIP6, default).
- NRCP: select the scenario from 1 (SSP1-2.6), 2 (SSP2-4.5), 3 (SSP3-7.0, the default) or 4 (SSP5-8.5). If NGHGCMIP=4 then the approximately equivalent scenario from CMIP5 is selected. Note that the values of NGHGCMIP and NRCP are used to select the timeseries file to read.
- NCMIPFIXYR: specify a fixed year for the forcing (default -1, which means use the current year).

2.4.5 Surface albedo and emissivity

The surface module of the IFS prepares the albedo and emissivity to be provided to the radiation scheme. Six bands are used to store albedo ($\lambda < 0.25$ μm, 0.25–0.44 μm, 0.44–0.69 μm, 0.69–1.19 μm, 1.19–2.38 μm and $\lambda > 2.38$ μm), although only sea ice uses different values for all six. Separate albedos are provided for diffuse and direct solar radiation. The albedos are computed separately for each tile, then averaged in proportion to the tile fraction.

The snow-free land-surface albedo is taken from a monthly-mean albedo climatology derived from the MODIS dataset described by Schaaf *et al.* (2002). It is pre-averaged to the model grid, and stored in two spectral bands (split at 0.7 μm) with three components for each band referred to as the isotropic, volumetric and geometric albedos. These are used to represent the solar-zenith-angle dependence of the albedo to direct solar radiation as described by Schaaf *et al.* (2002). The 2-band direct and diffuse albedos computed from this climatology and the current solar zenith angle are then modified to add the contribution from snow according to the snow cover and the prognostic snow albedo (see Section 8.4.4). Since the latter is a broadband value in the absence of vegetation, it is split into the same two bands and modified according to the presence of high or low vegetation using the data of Moody *et al.* (2007). More information on the original data and plots of the monthly mean albedo are shown in Chapter 11.

The ice sheets of Antarctica, Greenland and some glaciers are are designated as 'permanent snow'; rather than using the prognostic snow albedo, they are assigned a fixed broadband value of 0.82. This is divided into two bands in the same way as the prognostic snow. The value may be overriden using the namelist parameter RALFMINPSN in namelist group NAEPHY.

Over open water, the surface albedo for diffuse radiation is set as a wavelength-independent value of 0.06, while the albedo for direct parallel radiation is a fit to low-flying aircraft measurements over the ocean given by Taylor *et al.* (1996):

$$\alpha_{\mathrm{sp}} = \frac{0.037}{1.1\mu_0^{1.4} + 0.15}. \tag{2.63}$$

For sea ice, monthly values based on Ebert and Curry (1993) albedos for the Arctic Ocean, for each of the six bands, are interpolated to the forecast time. The bare sea-ice albedo value in Ebert and Curry is taken as a representative value for summer, and the dry-snow albedo value is used for the winter months. Values for the Antarctic are shifted by six months.

The thermal emissivity of the surface outside the 800–1250 cm^{-1} spectral region is assumed to be 0.99 everywhere. In the window region, the spectral emissivity is constant at 0.99 for open water, 0.98 for sea ice and 0.98 for snow tiles. For low and high vegetation and for shaded snow the emissivity depends on the water content in the top soil layer. Emissivity decreases linearly from 0.96 for soils at or above field capacity to 0.93 for soils at or below permanent wilting point. The same formulation is used for bare ground, except for desert areas ($\alpha_{\mathrm{sb}} > 0.3$), where a value of 0.93 is used independently of the soil water content.

2.4.6 Solar irradiance and zenith angle

The solar irradiance, S^0, is the instantaneous flux of solar radiation incident at the Earth, and is computed from Total Solar Irradiance (TSI) and the Sun-Earth distance. TSI is the annual-mean solar irradiance and varies primarily with the 11-year solar cycle as described in the file `total_solar_irradiance_CMIP6_47r1.nc` which includes an observational reconstruction from 1850 to 2014 CE and the CMIP6 recommended scenario from 2015 to 2300. This file may be overridden with

Table 2.3 *Spectral distribution of the absorption by atmospheric gases in RRTMG$_{LW}$. Note: CCl_4 and CFC-22 ($CHClF_2$) are presently not accounted for in the ECMWF model.*

		Gases included	
Spectral intervals cm^{-1}	**Number of g-points**	**Troposphere**	**Stratosphere**
10–350	8	H_2O	H_2O
350–500	14	H_2O	H_2O
500–630	16	H_2O, CO_2,N_2O	H_2O, CO_2,N_2O
630–700	14	H_2O, CO_2	O_3, CO_2
700–820	16	H_2O, CO_2, O_3, CCl_4	O_3, CO_2, CCl_4
820–980	8	H_2O, CO_2	CFC-11, CFC-12
980–1080	12	H_2O, O_3, CO_2	O_3, CO_2
1080–1180	8	H_2O, CFC-12, CFC22, CO_2,O_3,N_2O	O_3, CFC-12, CFC-22, CO_2,N_2O
1180–1390	12	H_2O, CH_4, N_2O	CH_4, N_2O
1390–1480	6	H_2O	H_2O
1480–1800	8	H_2O, O_2	H_2O, O_2
1800–2080	8	H_2O	
2080–2250	4	H_2O, N_2O	O_3
2250–2380	2	CO_2	CO_2
2380–2600	2	N_2O, CO_2	
2600–3250	2	H_2O, CH_4	CH_4

namelist parameter CSOLARIRRADIANCEFILE. Solar irradiance is then computed from TSI correcting for the changing Sun-Earth distance through the year.

Equations to compute the annual variation of the solar declination δ_s and the difference between solar time and official time (the Equation of Time) can be found in Paltridge and Platt (1976). These equations are used to give the cosine of the solar angle at the ground. Because of the curvature of the Earth, the zenith angle is not quite constant along the path of a sun ray. Hence the correction applied to μ_0^a to give an average μ_0 for the atmosphere is

$$\mu_0 = \frac{\frac{H}{a}}{\sqrt{(\mu_0^a)^2 + \frac{H}{a}\left(2 + \frac{H}{a}\right)} - \mu_0^a}. \tag{2.64}$$

where a is the earth radius and H is the atmospheric equivalent height. H/a is fixed at 0.001277.

The cosine of solar zenith angle, μ_0, is actually used twice in the model: (1) once per radiation timestep by the radiation scheme itself (including computing sea albedo in Eq. 2.63), and (2) at every intervening model timestep to scale the fluxes according to the instantaneous incoming top-of-atmosphere radiation (Eq. 2.109). In case (2), the value is computed as the average across the model timestep (using $\mu_0 = 0$ for parts of the model timestep when the sun is below the horizon), in order that when evolving temperature from timestep n to $n+1$, the most accurate mean fluxes are used. In case (1), Hogan and Hirahara (2016) showed that for the most accurate fluxes and stratospheric temperatures, the value of μ_0 used in the radiation scheme itself should be the average value only over the sunlit part of the radiation timestep. They provided the formula for computing the average μ_0 over a particular time interval, and this is implemented in the IFS.

2.5 THE ECRAD RADIATION SCHEME

2.5.1 Overview

A top-level scientific description of ecRad and the impact it had when introduced in the IFS was provided by Hogan and Bozzo (2018). The earlier memo by Hogan and Bozzo (2016) provided more of an architectural overview. Here we provide an overview of the mathematical formulation of ecRad,

Table 2.4 *Spectral distribution of the absorption by atmospheric gases in RRTMG$_{SW}$.*

		Gases included	
Spectral intervals cm^{-1}	**Number of g-points**	**Troposphere**	**Stratosphere**
800–2600	12	H_2O	CO_2
2600–3250	6	H_2O, CH_4	
3250–4000	12	H_2O, CO_2	H_2O, CO_2
4000–4650	8	H_2O, CH_4	CH_4
4650–5150	8	H_2O, CO_2	CO_2
5150–6150	10	H_2O, CH_4	H_2O, CH_4
6150–7700	10	H_2O, CO_2	H_2O, CO_2
7700–8050	2	H_2O, O_2	O_2
8050–12850	10	H_2O	
12850–16000	8	H_2O, O_2	O_2
16000–22650	6	H_2O	
22650–29000	6		
29000–38000	8	O_3	O_3
38000–50000	6	O_3, O_2	O_3, O_2

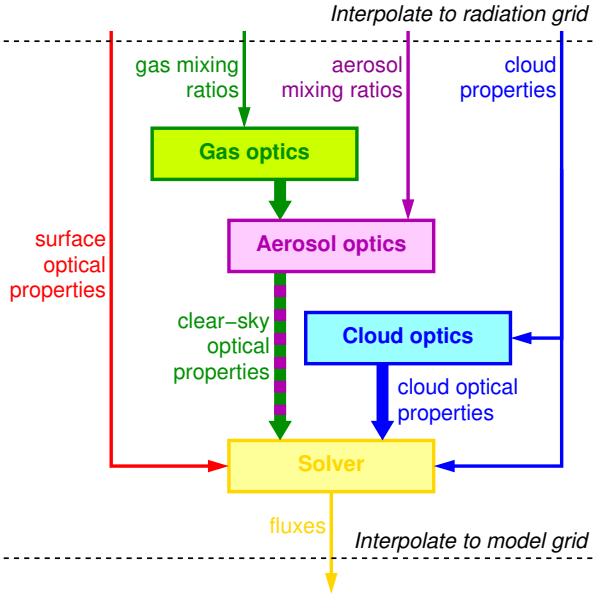

Figure 2.1 *Schematic of the four main components of ecRad and the flow of data between them.*

and details of how to configure it from the IFS. The code for the ecRad radiation scheme within the IFS resides in radiation/module, while RRTMG gas-optics routines and the code for preparing inputs to ecRad resides in arpifs/phys_radi. Hogan (2022) describes the full set of options for ecRad that may be configured via the RADIATION namelist group, while here we describe the more limited set of options intended for use in the IFS via the NAERAD namelist group; namelist options mentioned in the text refer to the NAERAD group. Fig. 2.1 depicts the four main components of ecRad, which are described in sections 2.5.2–2.5.5.

2.5.2 Gas optics

The gas-optics module determines the spectral discretization used by the entire radiation scheme. Up to and including Cycle 48r1, the only gas-optics model available is RRTMG (Mlawer *et al.*, 1997; Iacono *et al.*, 2008), which has been extensively validated against observations, principally at the ARM Southern Great Plains site. It uses 16 spectral bands in the long-wave and 14 in the short-wave. It is a correlated

k-distribution scheme, which means that within each band the cumulative probability distribution of molar absorption coefficient, k, is discretized into g-points, each of which represents a similar range of absorptions but which may not be contiguous in wavelength space. Since an independent radiative transfer calculation is required for each g-point, the computational cost of the entire radiation scheme scales with the total number of g-points. The original RRTM scheme sub-divided each band into 16 'g-points', but it was found that a more efficient scheme could be used by reducing the number of g-points in bands that either accounted for less radiative energy, or those with a weaker variation in gas absorption. This led to the development of RRTMG (the GCM-optimized version of RRTM), with the bands and number of g-points shown in Table 2.3 and Table 2.4; the total number of g-points in the long-wave and short-wave is 140 and 112, respectively. Note that there is some spectral overlap between the long-wave and the short-wave; this is because rather than defining these two regions by some arbitrary wavelength, we define the former as all radiation originating from emission by the surface or atmosphere, and the latter as all radiation originating from the sun. This separation makes the subsequent solvers more efficient since only the long-wave solver needs to treat atmospheric emission and only the short-wave solver needs to treat an additional 'direct' path of radiation through the atmosphere at the angle from the sun.

The gas-optics module takes as input the mass-mixing ratios of H_2O, O_2, O_3, CO_2, CH_4, N_2O, CFC-11 and CFC-12. Some gas-optics models support additionally N_2, CCl_4 and/or HCFC-22, but these are not currently used in the IFS version of ecRad. The source of these mixing ratios, whether from prognostic variables, a climatology or a global constant, is described in Section 2.4.4. The module is also fed the temperature and pressure at half-levels (i.e. at the interfaces between layers), $T_{i+1/2}$ and p_{i+1}, and the skin temperature T_s. Additionally it is provided with the solar irradiance, S^0, which varies through the year according to the varying sun-earth distance, and through the 11-year solar cycle. From these it computes the following variables:

- Short-wave absorption optical depth τ_a and Rayleigh scattering optical depth τ_s of each layer and g-point. These are converted to the extinction optical depth $\tau = \tau_a + \tau_s$ and the single-scattering albedo $\omega = \tau_s/\tau$.
- Long-wave absorption optical depth τ of each layer at each g-point, making use of the mid-point pressure and the pressure-weighted mean temperature of the layer. Rayleigh scattering is so weak in the long-wave that it may be neglected.
- The solar irradiance associated with each g-point, calculated from the assumed solar spectrum which in the case of RRTMG is the Kurucz spectrum.
- The Planck function at each half-level and long-wave g-point, $B_{i+1/2}$, i.e. the power emitted by a black body at temperature $T_{i+1/2}$ that is attributable the wavelengths associated with that g-point. Thus, if all g-points were summed we would expect to recover the total power emitted by a black body ($\sigma T_{i+1/2}$, where σ is the Stefan-Boltzmann constant).
- The Planck function at at the surface in each long-wave g-point, B_s.

Since version 1.5, the offline version of ecRad also supports the ECMWF Correlated K-Distribution (ecCKD) gas-optics scheme of Hogan and Matricardi (2022), in which the number of g-points is more flexible. This will be introduced into the IFS in a future cycle.

2.5.3 Aerosol optics

Whether produced from an aerosol climatology or the CAMS prognostic aerosol package, the radiation scheme is passed profiles of aerosol mass mixing ratios for a number of different aerosol species. As part of the setup phase of ecRad, each aerosol species is mapped to pre-computed aerosol optical properties stored in a netCDF file[1] These properties are computed using Mie theory as described by Bozzo *et al.* (2020) and pre-averaged to the RRTMG bands (16 in the long-wave and 14 in the short-wave); for aerosol species j they are (in both the long-wave and short-wave) the mass-extinction coefficient β_j (in $m^2\ kg^{-1}$), the single scattering albedo ω_j and the asymmetry factor g_j. Some of the species are hydrophilic, which means that their optical properties are stored in the file as a function of relative humidity in bins of width

[1]The latest aerosol optical property file `aerosol_ifs_rrtm_48r1_v2.nc` is available from the ecRad web site: https://confluence.ecmwf.int/display/ECRAD/.

10% (except between 80 and 100% where they are stored in bins of width 5%). When optical properties are computed for these species, the nearest bin is selected according to the relative humidity.

The aerosol optical depth in a layer is computed as the sum of the contribution from each species

$$\tau = \frac{\Delta p}{g^0} \sum_j^{n_{\text{aer}}} q_j \beta_j, \tag{2.65}$$

where q_j is the mass mixing ratio of aerosol species j, Δp is the pressure difference between the top and base of the layer, and g^0 is the acceleration due to gravity. The mean single scattering albedo and asymmetry factor are the weighted average of the contributions of the n_{aer} species, where ω is weighted by extinction coefficient and g is weighted by scattering coefficient:

$$\omega = \frac{\sum_j^{n_{\text{aer}}} q_j \beta_j \omega_j}{\sum_j^{n_{\text{aer}}} q_j \beta_j}; \tag{2.66}$$

$$g = \frac{\sum_j^{n_{\text{aer}}} q_j \beta_j \omega_j g_j}{\sum_j^{n_{\text{aer}}} q_j \beta_j \omega_j}. \tag{2.67}$$

The scattering patterns of both aerosol and cloud particles can exhibit strong forward scattering, which is not well captured in the two-stream paradigm used in ecRad. Therefore, Joseph *et al.* (1976) proposed 'delta scaling' of the optical properties: a fraction f of the scattering distribution is approximated as an infinitesimally narrow delta function at a scattering angle of 0°, essentially treating it as if it had not been scattered at all. They showed that a reasonable fit to more accurate calculations could be obtained with the assumption that $f = g^2$, leading to the following transformation:

$$\tau' = \tau(1 - \omega g^2); \tag{2.68}$$

$$\omega' = \omega \frac{1 - g^2}{1 - \omega g^2}; \tag{2.69}$$

$$g' = \frac{g}{1 + g}, \tag{2.70}$$

where the delta-scaled quantities τ', ω' and g' are used in all subsequent calculations.

If long-wave aerosol scattering is turned off then only the optical depth of aerosols is required: the single-scattering albedo is implicitly set to zero. For the emission rate to be correct we require the absorption optical depth rather than extinction optical depth, and hence replace (2.65) with

$$\tau = \frac{\Delta p}{g^0} \sum_j^{n_{\text{aer}}} q_j \beta_j (1 - \omega_j). \tag{2.71}$$

Once the combined, delta-scaled optical properties of aerosols are computed in each band, they are mapped to each g-point and combined with the existing optical properties of gases in the same way, i.e. optical depth is summed, single-scattering albedo is weighted by extinction coefficient (or equivalently by optical depth) and asymmetry factor is weighted by scattering coefficient.. Note that gases only absorb in the long-wave (so the ω of gases is zero) and their scattering is isotropic in the short-wave (so the g of gases is zero).

2.5.4 Cloud optics

The optical properties of clouds in each layer are also described by τ, ω and g in the cloudy part of each layer and band. For liquid clouds we use the 'SOCRATES' method to parametrize these optical properties in each band as a function of effective radius using Eqs. 6–8 of Hogan and Bozzo (2016). This approach originates from the Met Office radiation scheme. For ice clouds we use the 'Fu' scheme, which again parametrizes the properties versus effective radius, combining Fu (1996) in the short-wave and Fu *et al.* (1998) in the long-wave.

As with aerosol, delta scaling (Eqs. 2.68–2.70) is applied, but the resulting optical properties are not immediately added to the clear-sky properties on g-points; rather they are passed to the solver which deals with sub-grid cloud heterogeneity.

2.5.5 Solver

(*a*) *Overview*

The solver takes as input the clear-sky (gas plus aerosol) optical properties of each layer at each g-point, and the cloud optical properties of the cloudy layers in each band, and computes profiles of upwelling and downwelling short-wave and long-wave fluxes at each half-level. Several solvers are available in ecRad, which differ in the way that sub-grid cloud is treated; they are controlled by the namelist parameters NLWSOLVER and NSWSOLVERS. A value of 0 indicates the Monte Carlo Independent Column Approximation (McICA) solver, the default in the IFS, while 3 indicates 'Tripleclouds'. A value of 2 yields the 'SPARTACUS' solver, which can approximately represent the effects of 3D radiative transfer, but this is still an experimental code and is not perfectly stable in single precision.

In addition to the choice of overarching solver, a detail of the long-wave solver that can be specified is how scattering is treated: the namelist option NLWSCATTERING may be 0 to indicate no scattering is represented, 2 to indicate that both cloud and aerosol scattering is represented, or 1 (the default) to indicate that cloud scattering is represented but not aerosol. As described by Hogan and Bozzo (2018), the latter is almost as fast as if scattering is not represented, yet achieves most of the accuracy of the full-scattering treatment.

(*b*) *McICA cloud generator*

Originally proposed by Pincus *et al.* (2003) and used by a large fraction of weather and climate models worldwide, the idea of McICA is to feed each g-point with a stochastically generated (i.e. Monte Carlo) profile of cloud properties, with each sub-column treated independently by an efficient radiative transfer algorithm that assumes the cloud to be horizontally uniform (i.e. the Independent Column Approximation). The profiles are generated such that for a large number of samples, the generated clouds will respect the input variables controlling sub-grid cloud geometry, specifically the profiles of cloud fraction, a, the fractional standard deviation of in-cloud water content, FSD, and the overlap parameter between each layer, α. By default FSD is set to 1 everywhere, but this value can be overridden with namelist parameter RCLOUD_FRAC_STD.

The IFS originally used the cloud generator proposed by Räisänen *et al.* (2004), but with the introduction of ecRad this was changed to the scheme described by Hogan and Bozzo (2018), which is more efficient via the use of fewer random numbers, and introduces less stochastic noise in the fluxes via the exact enforcement of the total cloud cover, which is computed from the profiles of cloud fraction and overlap parameter as described in section 3.2 of Hogan and Bozzo (2018). If the gas-optics scheme specifies n_g g-points are needed to represent either the long-wave or short-wave spectrum, then the cloud generator produces n_g profiles of the cloud scaling factor O. This contains zeros for layers to be treated as cloud-free, while for cloudy layers the in-cloud-mean optical depth is multiplied by O before being merged with the clear-sky optical properties. Over a sufficiently large number of samples, the non-zero values of O in a layer have a mean of unity and a standard deviation of FSD. Note that inhomogeneity is enacted by scaling both cloud water content and optical depth up and down by the same factor, while leaving cloud effective radius unchanged.

(*c*) *Tripleclouds*

The concept of the Tripleclouds solver was originally described by Shonk and Hogan (2008): each cloudy layer is divided horizontally into three regions, one clear-sky, one optically thin cloudy region and one optically thick cloudy region. The optical depths and area fractions of the two cloudy regions are chosen such that the cloud has the same mean in-cloud optical depth as specified by the input data, and the same FSD. The fractional overlap of each region in one layer with each region in the layer below is computed in a way that is explicitly consistent with the specified overlap parameter. Shonk and Hogan

(2008) described in detail how the two-stream radiative transfer equations could be solved subject to this geometry.

(*d*) *Long-wave layer properties*

The long-wave two-stream equations express the relationship between upwelling and downwelling fluxes ($F^{\uparrow}$ and $F^{\downarrow}$, in W m^{-2}) for a particular g-point:

$$-\frac{dF^{\uparrow}}{d\tau} = -\gamma_1 F^{\uparrow} + \gamma_2 F^{\downarrow} + B; \tag{2.72}$$

$$\frac{dF^{\downarrow}}{d\tau} = -\gamma_1 F^{\downarrow} + \gamma_2 F^{\uparrow} + B, \tag{2.73}$$

where τ is the optical depth of the atmosphere measured down from top-of-atmosphere for that g-point, treated as a vertical coordinate, and B is the black-body emission for the same g-point (in W m^{-2}). The terms on the right-hand-side of each expression represent, respectively, loss of radiation by scattering into the other stream and absorption, gain of radiation by scattering from the other stream, and emission. The exchange terms are given by (e.g. Fu *et al.*, 1997)

$$\gamma_1 = D\left[1 - (1+g)\omega/2\right]; \tag{2.74}$$

$$\gamma_2 = D(1-g)\omega/2, \tag{2.75}$$

where ω and g are the combined single-scattering albedo and asymmetry factor of the gases, aerosol and cloud in the volume, and $D = 1.66$ is the 'diffusivity' of the atmosphere (Elsasser, 1942), i.e. the approximate factor by which the atmosphere is more optically thick to diffuse long-wave radiation than it is to radiation propagating directly up or down.

These equations are solved exactly in each layer under the assumption that the scattering properties are constant vertically through the layer, but that B varies linearly with τ across the layer. These solutions are expressed in terms of four properties. The reflectance and transmittance of the layer to diffuse incident radiation are given by Eqs. 25 and 26 of Meador and Weaver (1980):

$$R = \gamma_2 G\left[1 - \exp(-2k\tau_1)\right]; \tag{2.76}$$

$$T = 2kG\exp(-k\tau_1), \tag{2.77}$$

where τ_1 is the optical depth of the layer and

$$k = \left[(\gamma_1 - \gamma_2)(\gamma_1 + \gamma_2)\right]^{1/2}; \tag{2.78}$$

$$G = \left[k + \gamma_1 + (k - \gamma_1)\exp(-2k\tau_1)\right]^{-1}. \tag{2.79}$$

The other two layer properties are the rates of emission from the layer (in W m^{-2}) in an upward and downward direction (e.g. Eqs. 5 and 12 of Stackhouse and Stephens, 1991):

$$S^{\uparrow} = (B_{i-1/2} + C) - (B_{i-1/2} - C)R - (B_{i+1/2} + C)T; \tag{2.80}$$

$$S^{\downarrow} = (B_{i+1/2} - C) - (B_{i+1/2} + C)R - (B_{i-1/2} - C)T, \tag{2.81}$$

where $B_{i-1/2}$ and $B_{i+1/2}$ are the black-body emission rates at the top and bottom of the layer, and

$$C = \frac{B_{i+1/2} - B_{i-1/2}}{\tau(\gamma_1 + \gamma_2)}. \tag{2.82}$$

(*e*) *Long-wave adding method*

Given the four variables, R_i, T_i, $S_i^{\uparrow}$ and $S_i^{\downarrow}$ for each model layer i, we compute fluxes using the 'Adding Method', which successively adds the contribution of a new layer to the previous ones, accounting for multiple reflections between the layers being added. The calculations described here are repeated for each g-point. The surface which has an albedo of $A_{n+1/2} = 1 - \epsilon_s$ (where ϵ_s is the surface emissivity and

n is the number of layers) and an upward emitted flux of $E_{n+1/2} = \epsilon_s B_s$. We then loop up through the layers of the atmosphere computing $A_{i-1/2}$, which is the albedo of the entire surface-atmosphere system below half-level $i-1/2$, and $E_{i-1/2}$, which is the upwelling flux at half-level $i-1/2$ originating from emission below that half-level (e.g. Eqs. 9 and 11 of Shonk and Hogan, 2008):

$$A_{i-1/2} = R_i + \frac{T_i^2 A_{i+1/2}}{1 - R_i A_{i+1/2}}; \tag{2.83}$$

$$E_{i-1/2} = S_i^{\uparrow} + T_i \left(E_{i+1/2} + \frac{A_{i+1/2} S_i^{\downarrow}}{1 - R_i A_{i+1/2}} \right). \tag{2.84}$$

This is repeated up to top-of-atmosphere (half-level $1/2$). The denominator in each equation is the result of a geometric series representing multiple reflections between the new layer (with reflectance R_i) and the layers below (with reflectance $A_{i+1/2}$).

At top-of-atmosphere we have no downwelling long-wave radiation ($F_{1/2}^{\downarrow} = 0$) and the upwelling is equal to the total emission ($F_{1/2}^{\uparrow} = E_{1/2}$). We now pass back down through the atmosphere computing up- and down-welling fluxes at each half-level (e.g. Eqs. 12 and 14 of Shonk and Hogan, 2008):

$$F_{i+1/2}^{\downarrow} = \frac{T_i + F_{i-1/2}^{\downarrow} + R_i E_{i+1/2} + S_i^{\downarrow}}{1 - R_i A_{i+1/2}}; \tag{2.85}$$

$$F_{i+1/2}^{\uparrow} = A_{i+1/2} F_{i+1}^{\downarrow} + E_{i+1/2}. \tag{2.86}$$

This is repeated down to the surface, after which the fluxes from each g-point are summed to obtain the broadband fluxes. The upward-then-downward passes through the atmosphere are mathematically equivalent to solving a tridiagonal system of equations by Gaussian elimination followed by back-substitution, but with the benefit that the intermediate terms always have a physical meaning.

The method described here allows for the possibility of scattering in all layers. If long-wave aerosol scattering is turned off then the reflectance R_i in clear-sky becomes zero and the computation may be simplified, as described by Hogan and Bozzo (2018).

(*f*) *Short-wave layer properties*

The short-wave two-stream equations are as in the long-wave except that they include an additional 'direct' or 'unscattered' solar flux, F^0 (defined as the power into a plane perpendicular to the solar direction), which acts as a source term for the diffuse fluxes:

$$\frac{dF^0}{d\tau} = \frac{F^0}{\mu_0}; \tag{2.87}$$

$$-\frac{dF^{\uparrow}}{d\tau} = -\gamma_1 F^{\uparrow} + \gamma_2 F^{\mathrm{diff}\downarrow} + \omega\gamma_3 F^0; \tag{2.88}$$

$$\frac{dF^{\mathrm{diff}\downarrow}}{d\tau} = -\gamma_1 F^{\mathrm{diff}\downarrow} + \gamma_2 F^{\uparrow} + \omega\gamma_4 F^0, \tag{2.89}$$

where μ_0 is the cosine of the solar zenith angle, and we use expressions for the γ coefficients originating from Zdunkowski *et al.* (1980):

$$\gamma_1 = 2 - \omega\frac{5+3g}{4}; \tag{2.90}$$

$$\gamma_2 = \frac{3}{4}\omega(1-g); \tag{2.91}$$

$$\gamma_3 = \frac{1}{2} - \frac{3}{4}\mu_0 g; \tag{2.92}$$

$$\gamma_4 = 1 - \gamma_3. \tag{2.93}$$

In (2.88) and (2.89) we use $F^{\mathrm{diff}\downarrow}$ to indicate the diffuse component of the downwelling, to distinguish from the total downwelling $F^{\downarrow} = F^{\mathrm{diff}\downarrow} + \mu_0 F^0$ (whereas in the long-wave there is no direct beam so

$F^{\downarrow} = F^{\text{diff}\downarrow}$). As in the long-wave case we seek exact solutions to these equations for individual layers under the assumption that the scattering properties are constant vertically through the layer. The diffuse reflectance, R, and transmittance, T, are already given by (2.76) and (2.77). The unscattered transmittance to direct solar radiance is simply the solution to (2.87):

$$T^0 = \exp(-\tau_1/\mu_0). \tag{2.94}$$

We also require the reflectance to direct incoming radiation, R^{dir}, and the equivalent transmittance T^{dir}, but note that the latter is the fraction of direct flux at the top of the layer that emerges as diffuse radiation at the base of the layer (adapted from Meador and Weaver, 1980):

$$\begin{aligned} R^{\text{dir}} = G^{\text{dir}} \Big[&(1-k\mu_0)(\alpha_2+k\gamma_3) - (1+k\mu_0)(\alpha_2-k\gamma_3)\exp(-2k\tau_1) \\ &- 2k\exp(-k\tau_1)(\gamma_4-\alpha_2\mu_0)T^0 \Big]; \end{aligned} \tag{2.95}$$

$$\begin{aligned} T^{\text{dir}} = G^{\text{dir}} \Big\{ &2k\exp(-k\tau_1)(\gamma_4+\alpha_1\mu_0) \\ &- T^0\left[(1+k\mu_0)(\alpha_1+k\gamma_4) - (1-k\mu_0)(\alpha_1-k\gamma_4)\exp(-2k\tau_1)\right] \Big\}, \end{aligned} \tag{2.96}$$

where

$$G^{\text{dir}} = \frac{\mu_0\omega}{1-k^2\mu_0^2}G; \tag{2.97}$$

$$\alpha_1 = \gamma_1\gamma_4 + \gamma_2\gamma_3; \tag{2.98}$$

$$\alpha_2 = \gamma_1\gamma_3 + \gamma_2\gamma_4. \tag{2.99}$$

The denominator of (2.97) can in principle go to zero, and inaccurate results can occur in the vicinity of zero. This is avoided by detecting when $k\mu_0 \simeq 1$ and then perturbing μ_0 very slightly to avoid the singularity.

(g) *Short-wave adding method*

Given the five variables R_i, T_i, R_i^{dir}, T_i^{dir} and T_i^0 for each model layer i, we compute fluxes using the short-wave version of the Adding Method. As in the long-wave, we propagate the diffuse albedo $A_{i-1/2}$ from half-level to half-level up through the atmosphere, but rather than also propagating an emitted flux $E_{i-1/2}$ which would be zero at solar wavelengths, we propagate the direct albedo $D_{i-1/2}$, which is the albedo of the entire surface-atmosphere below half-level $i-1/2$ to incoming direct solar radiation. The radiation scheme is provided with diffuse surface albedo α and direct surface albedo α^{dir}. The surface values of the propagated variables are therefore simply $A_{n+1/2} = \alpha$ and $D_{n+1/2} = \mu_0\alpha^{\text{dir}}$, where the factor of μ_0 is necessary because the direct flux F^0 is defined to be into a plane perpendicular to the solar direction whereas the reflected flux $F^{\uparrow}$ is for a horizontal plane. Diffuse albedo is propagated exactly as in (2.83), whereas direct albedo uses

$$D_{i-1/2} = R_i^{\text{dir}} + T_{i+1/2}\frac{T_i^0 D_{i+1/2} + T_i^{\text{dir}} A_{i+1/2}}{1 - R_i A_{i+1/2}}. \tag{2.100}$$

At top-of-atmosphere the downwelling direct solar radiation is the solar irradiance for the specific g-point ($F_{1/2}^0 = S^0$) and there is no downwelling diffuse solar radiation ($F_{1/2}^{\text{diff}\downarrow} = 0$). We pass back down through the atmosphere computing fluxes using

$$F_{i+1/2}^0 = T_i^0 F_{i-1/2}^0; \tag{2.101}$$

$$F_{i+1/2}^{\text{diff}\downarrow} = \frac{T_i F_{i-1/2}^{\text{diff}\downarrow} + F_{i-1/2}^0 (T_i^0 D_{i+1/2} R_i + T_i^{\text{dir}})}{1 - R_i A_{i+1/2}}; \tag{2.102}$$

$$F_{i+1/2}^{\uparrow} = F_{i+1/2}^0 D_{i+1/2} + F_{i+1/2}^{\text{diff}\downarrow} A_{i+1/2}. \tag{2.103}$$

As in the long-wave, the fluxes from each g-point are summed to obtain the broadband values.

2.6 SOLAR ECLIPSES

From cycle 49r2 onwards, the effect of solar eclipses is included in the IFS by default (via the switch LSOLAR_ECLIPSES in namelist NAEPHY).

The prediction of solar eclipses requires accurate calculations of the positions of Sun and Moon relative to Earth (performed in COMPUTE_ASTRONOMY and SOLAR_ECLIPSE). Since an accuracy of a few kilometres should be sufficient in all current IFS applications, the choice was made to use:

- the VSOP87D solutions proposed by Bretagnon and Francou (1988) for Sun's position;
- the ELP-MPP02 solutions of Chapront and Francou (2003) for Moon's position;
- formulas for Dynamical Time and Greenwich Mean Sidereal Time definition, nutation corrections in longitude and obliquity, and aberration correction from Meeus (1998);
- formulas for ΔT (namely the difference between Dynamical Time and Universal Time) from NASA (see https://eclipse.gsfc.nasa.gov/SEcat5/deltatpoly.html);
- the GRS80 ellipsoid, to account for the impact of Earth's polar flattening.

The VSOP87D and ELP-MPP02 solutions only rely on a few external ASCII data files, which contain all coefficients required to calculate orbital positions for the selected date and time. One should note that only dates after 1900 are considered in the current IFS implementation of solar eclipses, since it was deemed unlikely that any reanalysis would ever be performed prior to that year. However, if needed, the latter limitation could be easily alleviated by implementing the appropriate formulas for ΔT for the desired period. One should also stress that the accuracy of eclipse predictions is expected to degrade for dates several centuries into the future, partly because of the impact of accumulated uncertainties in Earth's rotation on the evolution of ΔT.

Fig. 2.2 displays various statistics (mean, standard deviation, 5% and 95% quantiles) for the error of the umbra's central location predicted by IFS relative to NASA's reference path. Statistics include all 132 total eclipses of the period 1900 to 2100 and are stratified against solar elevation. Besides, IFS and NASA's eclipse paths are compared every 2 minutes, from the beginning to the end of each eclipse. The additional purple curve in Fig. 2.2, which shows the population in each 3° bin of solar elevation, indicates that the majority of cases involved in the statistics have solar elevations between 15° and 75°. For solar elevations above 20°, the mean and standard deviation errors are a few kilometres at most. The larger errors for solar elevations below 10° are likely due to the associated stretching of the eclipse's umbra on Earth's surface; in such cases, even tiny errors in the lunar or solar angular positions may translate into larger positional errors; however, one should stress that when the sun is very low over the horizon, the radiative (and meteorological) impact of the eclipse will be negligible. Therefore, the level of accuracy of the proposed IFS eclipse path computations is deemed sufficient for all currently envisaged applications.

Once the eclipse path has been calculated, the fractional area of Sun's disc eclipsed by the Moon, f_{eclip}, is computed as

$$f_{eclip} = \begin{cases} 1 & \text{if } \tau \leq \epsilon_M - \epsilon_S \\ \frac{1}{\pi\epsilon_S^2}\left(\epsilon_S^2 \arccos\left(\frac{\tau^2+\epsilon_S^2-\epsilon_M^2}{2\tau\epsilon_S}\right) + \epsilon_M^2 \arccos\left(\frac{\tau^2+\epsilon_M^2-\epsilon_S^2}{2\tau\epsilon_M}\right) \ldots \right. & \\ \left. -0.5\sqrt{(\epsilon_S+\epsilon_M-\tau)(\tau+\epsilon_S-\epsilon_M)(\tau-\epsilon_S+\epsilon_M)(\tau+\epsilon_S+\epsilon_M)}\right) & \text{if } \tau > \epsilon_M - \epsilon_S \text{ and } \tau < \epsilon_M + \epsilon_S \\ \frac{\epsilon_M}{\epsilon_S}^2 & \text{if } \tau \leq \epsilon_S - \epsilon_M \\ 0 & \text{otherwise} \end{cases} \tag{2.104}$$

where ϵ_M and ϵ_S respectively denote the angular sizes of the Moon and the Sun as viewed from the selected location on Earth, at the selected time; τ is the angular distance between the centres of the lunar and solar discs. Note that the first, second and third cases in Eq.2.104 correspond to the phase of totality, the partial phase, and the annular phase, respectively. The geographically and time dependent fraction f_{eclip} varies between 0 (no eclipse) and 1 (total eclipse). The impact of the eclipse is taken into account by simply multiplying the incoming solar flux at the top of the atmosphere by f_{eclip}, at each time step

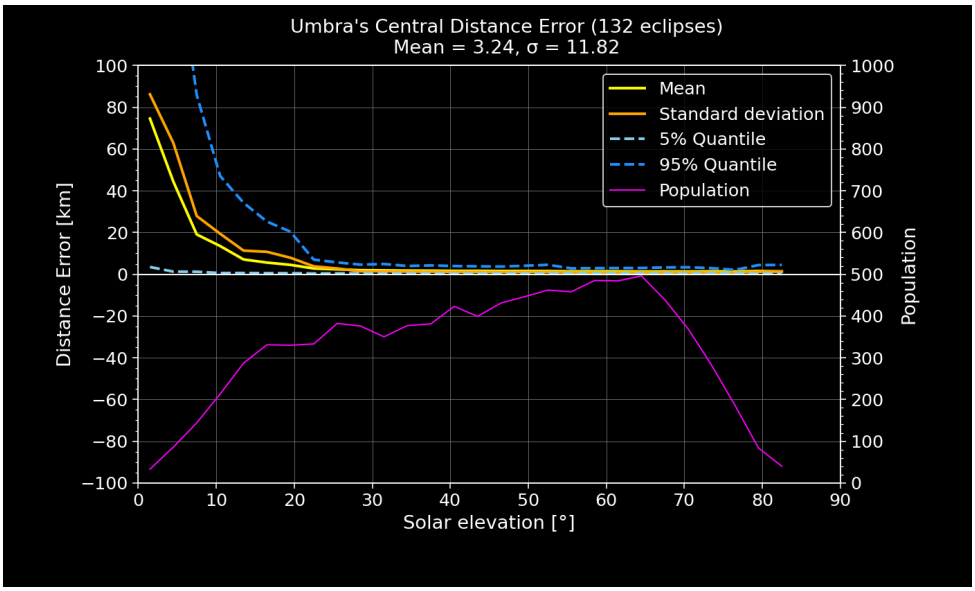

Figure 2.2 *Error statistics for the umbra's central location (in km) predicted by IFS with respect to NASA's reference path: mean (solid yellow line), standard deviation (solid orange line), 5% quantile (dashed cyan line) and 95% quantile (dashed blue line). Statistics include all 132 total solar eclipses between 1900 and 2100, and are binned according to solar elevation (x-axis). Population in each solar elevation bin is displayed with the purple line (labels along the right y-axis).*

of the IFS forecast (in routine RADHEATN). All meteorological impacts of a given eclipse in the IFS will stem from this modulation of the incoming solar flux.

One should note the following simplifications or possible sources of uncertainty in the current implementation of solar eclipses (even though their impact in the IFS is expected to be very small):

- Solar limb's darkening is currently ignored (mainly relevant near totality);
- Lunar limb's irregularities due to the combination of lunar orography, librations and flattening are not considered;
- The influence of observer's altitude on Earth is neglected;
- Our knowledge of the solar disc's size and shape is slightly uncertain.

It is worth stressing that the additional computational cost of solar eclipses is negligible compared to IFS dynamical and physical calculations, since no 3D quantities are involved.

A full report on the validation of solar eclipse computations and their impact on IFS forecasts (and analyses) can be found in Lopez (2024).

2.7 SPATIAL AND TEMPORAL INTERPOLATION

As stated in the introduction, the radiation scheme is called intermittently in time and on a lower-resolution spatial grid. The grid is described in Section 2.7.1. The fluxes are interpolated back to the full model grid and are then available at each intervening model timestep between calls to the radiation scheme.

The time between calls to the radiation scheme may be set by namelist parameter NRADFR: a positive number indicates the number of model timesteps between calls, whereas a negative number indicates the number of hours. The default is hourly.

At each model gridbox and timestep, surface fluxes are fed into the surface scheme to evolve surface temperature, and atmospheric radiative heating rates are computed as the divergence of net radiation

Table 2.5 *Summary of the default mapping from model to radiation grid (expressed as the spectral truncation number) and the corresponding coarsening factor, both in terms of the increase in distance between gridpoints, and the average area notionally represented by a gridpoint.*

Grid		Coarsening	
Model	Radiation	Distance	Area
47	31	1.50	2.25
63	31	2.00	4.00
79	31	2.50	6.25
95	31	3.00	9.00
127	47	2.67	7.11
159	79	2.00	4.00
199	79	2.50	6.25
255	79	3.20	10.24
319	127	2.50	6.25
399	159	2.50	6.25
511	199	2.56	6.55
639	255	2.50	6.25
799	399	2.00	4.00
911	399	2.28	5.20
1023	399	2.56	6.55
1279	399	3.20	10.24
1599	511	3.12	9.77
1999	511	3.91	15.26
2559	1023	2.50	6.25
3999	1023	3.91	15.26
7999	1023	7.81	61.04

fluxes F^{net} so that

$$\left(\frac{\partial T}{\partial t}\right)_{\text{rad}} = -\frac{g^0}{c_p}\frac{\partial F^{\text{net}}}{\partial p} \tag{2.105}$$

where c_p is set to the specific heat at constant pressure of dry air $c_{p_{\text{dry}}}$. However, before they are used the flux profiles need to be modified to minimize errors due to the radiation scheme being called at a lower resolution in time and space. The modifications in the short-wave are described in Section 2.7.2 and account for the change in solar zenith angle with time and variations in surface albedo in space. The modifications in the long-wave are described in Section 2.7.3 and account for changes of surface temperature in both time and space. The impacts of these modifications were examined in detail by Hogan and Bozzo (2015).

2.7.1 The radiation grid

The radiation grid is computed as a standard IFS model grid but with coarser resolution than the current model grid. Interpolation between model and radiation grids is performed using interfaces existing within the IFS libraries and as a result helps reduce code maintenance. Then radiation computations are done, and output fluxes are interpolated back to the reduced grid, at times of full radiation computations. The interpolation is controlled by namelist parameter NRADINT: a value of 0 indicates that radiation is to be called on the same grid as the full model, 2 indicates that bi-linear interpolation is to be used with a 4-point stencil, and 3 indicates that cubic interpolation is to be used with a 12-point stencil. Note that interpolation is used in both directions; we do not average multiple model columns together to produce variables on the coarser grid. The cubic interpolation can exhibit overshoots and undershoots close to sharp changes in curvature, so physical limits are imposed on interpolated variables as appropriate (e.g. cloud fraction to lie between 0 and 1).

Table 2.5 depicts the degree of coarsening for various IFS model resolutions. It can be seen that for HRES forecasts at $\text{T}_{\text{Co}}1279$ resolution, the radiation grid is a factor of 3.2 coarser in each horizontal direction,

meaning that radiation is called at 10.24 times fewer columns globally than the full model. For ensemble forecasts at $T_{Co}639$ resolution, as well as seasonal forecasts at lower resolutions than this, the coarsening factor is 2.5 in each horizontal direction.

The radiation grid may be overridden with the NRADRES namelist parameter, but the truncation number applied will be $(\text{NRADRES}+1)/2+1$, so to obtain a radiation grid of $T_{Co}399$ requires setting $\text{NRADRES}=799$.

2.7.2 Approximate radiation updates: short-wave

Three adjustments are performed to the short-wave flux profiles before they are used to compute heating rates each model timestep.

(i) When the short-wave flux profiles are first interpolated back from the radiation grid to the full grid, the net fluxes at the surface are not consistent with the local surface albedo. Consider a desert coastline: the low albedo of the sea leads to a large net flux into the surface, but spatial interpolation can lead to desert points at the coast receiving too large a flux that in turn can lead to them heating up too much during the day. Hogan and Bozzo (2015) proposed a solution that eliminated this problem, and is implemented in the IFS. Just after the fluxes are interpolated onto the full grid, the broadband surface and top-of-atmosphere (TOA) upwelling and downwelling fluxes are used to estimate an approximate transmittance (T) and reflectance (R) of the entire atmosphere:

$$T = \frac{F^{\uparrow}_{\text{surf}} F^{\downarrow}_{\text{TOA}} - F^{\uparrow}_{\text{surf}} F^{\uparrow}_{\text{TOA}}}{(F^{\downarrow}_{\text{TOA}})^2 - (F^{\uparrow}_{\text{surf}})^2}; \tag{2.106}$$

$$R = \frac{F^{\uparrow}_{\text{TOA}} F^{\downarrow}_{\text{TOA}} - F^{\uparrow}_{\text{surf}} F^{\downarrow}_{\text{surf}}}{(F^{\downarrow}_{\text{TOA}})^2 - (F^{\uparrow}_{\text{surf}})^2}. \tag{2.107}$$

Note that $F^{\downarrow}$ here refers to the total downwelling short-wave flux (diffuse plus direct), not just the diffuse as in earlier sections. The corrected net surface flux is then computed from the local broadband albedo (α) as

$$F^{\text{net}}_{\text{surf}} = F^{\downarrow}_{\text{TOA}} \frac{T(1-\alpha)}{1-\alpha R}. \tag{2.108}$$

The difference between the original and the new surface net flux is then used to modify the entire net-flux profile by a constant amount in order that the atmospheric heating rates are unchanged by this change to surface net flux. These operations are performed once per radiation timestep, with the assumption that the surface albedo is constant during this time. This scheme can be disabled by setting namelist parameter LAPPROXSWUPDATE=`false`.

(ii) If the top-of-atmosphere solar irradiance is S^0, then the top-of-atmosphere downwelling flux is

$$F^{\downarrow}_{\text{TOA}} = \mu_0 S^0, \tag{2.109}$$

where μ_0 is the cosine of the solar zenith angle, which can change significantly between calls to the radiation scheme. To account for this, the net flux profiles from the radiation scheme are normalized before being stored, such that they are the fluxes that would have been computed for $F^{\downarrow}_{\text{TOA}}=1$. Then at each model timestep, the local value of μ_0 is computed and the net flux profile is multiplied by $\mu_0 S^0$ before computing heating rates.

(iii) While the previous method accounts for the change in the incoming solar radiation at the top of atmosphere, it does not account for the change in path length of the direct solar beam through the atmosphere. Therefore we also apply the method of Manners *et al.* (2009) to update the instantaneous surface direct and diffuse solar fluxes. Denoting μ_0 as the cosine of the solar zenith angle used in the radiation scheme, and μ_0' as the more precise value at the model timestep, we may correct the *normalized* surface direct downwelling flux with the following approximate formula (where the normalization is such that $F^{\downarrow}_{\text{TOA}}=1$):

$$F^{\downarrow}_{\text{surf,dir}}(\mu_0') = F^{\downarrow}_{\text{surf,dir}}(\mu_0)^{\mu_0/\mu_0'}. \tag{2.110}$$

This leads to a difference in surface direct radiation and we need to decide what happens to this excess: does it reach the surface as diffuse radiation, get reflected back to space, or get absorbed in the atmosphere? Manners *et al.* (2009) made the assumption that half is scattered down to the surface and half scattered back to space, which leads to the following formula for the modified normalized surface total (direct plus diffuse) downwelling flux:

$$F^{\downarrow}_{\text{surf}}(\mu_0') = F^{\downarrow}_{\text{surf}}(\mu_0) + \frac{1}{2}\left[F^{\downarrow}_{\text{surf,dir}}(\mu_0)^{\mu_0/\mu_0'} - F^{\downarrow}_{\text{surf,dir}}(\mu_0)\right]. \tag{2.111}$$

Again, the entire net-flux profile is then shifted by a constant amount in order that the atmospheric heating rates are unchanged by this change to surface fluxes. This scheme can be disabled by setting namelist parameter LMANNERSSWUPDATE=`false`.

2.7.3 Approximate radiation updates: long-wave

Originally, the net long-wave fluxes were simply kept constant at the values given by the full radiation calculation, but this was found to lead to forecasts of night-time coastal 2-m temperature sometimes being too cold by in excess of 10 K. This is due to the averaging of the surface temperature field onto the coarser radiation grid before being input to the radiation scheme, leading to the upwelling long-wave radiation output at coastal land points being overestimated due to contamination by warmer sea points in the vicinity. The solution is to modify the local upwelling broadband long-wave radiation to be equal to thermal emission according to the local value of skin temperature (using the Stefan-Boltzmann law), plus reflection:

$$F^{\uparrow}_{\text{surf}} = \epsilon\sigma T^4_{\text{skin}} + (1-\epsilon)F^{\downarrow}_{\text{surf}}, \tag{2.112}$$

where ϵ is the long-wave emissivity of the surface. This change is not in itself sufficient, since we need to decide where any excess emitted flux ends up. This is achieved following the method of Hogan and Bozzo (2015): in addition to computing fluxes, the long-wave radiation scheme has been modified to also compute the partial derivative of upwelling long-wave flux at each model half-level with respect to the surface, $\partial F^{\uparrow}/\partial F^{\uparrow}_{\text{surf}}$. This way, the fraction of the excess radiation emitted from the surface that penetrates to different heights in the atmosphere can be estimated, and hence its effect on atmospheric heating rates. A further approximate modification is performed to account for the fact that the near-surface atmospheric temperature responds rapidly to changes in the surface temperature, resulting in a near-immediate change to the surface downwelling long-wave flux. Hogan and Bozzo (2015) found that this could be represented approximately by making the change to the downwelling flux a small fraction of the change to upwelling flux: $\Delta F^{\downarrow}_{\text{surf}} = 0.2\Delta F^{\uparrow}_{\text{surf}}$. The long-wave update scheme may be disabled by setting namelist parameter LAPPROXLWUPDATE=`false`.

2.8 RADIATION DIAGNOSTICS

This section summarizes the single-level radiation diagnostics that can be output from the IFS and are available in GRIB format in most operational forecast streams.

2.8.1 Conventions

The following conventions are employed in the storage of fluxes by the ECMWF model:

(i) Archived fluxes are either *downward* or *net*. Energy entering the Earth's atmosphere-surface system is taken as a positive quantity, and therefore downward fluxes are positive and net flux refers to the downward flux minus the upward flux. To obtain the upward flux ($F^{\uparrow}$) from the downward flux ($F^{\downarrow}$) and net flux (F^{net}), use $F^{\uparrow} = F^{\downarrow} - F^{\text{net}}$.

(ii) Physical fluxes archived by the ECMWF model are *accumulated* since the start of the relevant forecast, and therefore in units of J m^{-2} (or W m^{-2} s). Thus, a daily mean (in W m^{-2}) is obtained by retrieving the accumulated fluxes at $t_1 = t$ and $t_2 = t + 24$ hours (where t is the time of the start of the forecast), taking the difference and dividing by 86400, the number of seconds in a day.

(iii) As an exception to rule (ii), output from ERA5 is stored as hourly accumulations (units of W m^{-2} hr), so an hourly-mean flux in (W m^{-2}) is obtained by dividing by 3600 s. This also

Table 2.6 *Summary of surface accumulated flux diagnostics from the IFS, and the symbols/equations relating them to flux variables in this chapter, except replacing F by S or L depending on whether we are considering short-wave or long-wave fluxes. All fluxes here, except DSRP, are into a horizontal plane, and the μ_0 term is the cosine of the solar zenith angle and is needed to convert from the direct flux into a plane oriented perpendicular to the Sun's rays.*

Param. ID	Short name	Name	Symbol/equation
169	SSRD	Surface solar radiation downwards	$S^{\downarrow}_{\text{surf}} = \mu_0 S^{0}_{\text{surf}} + S^{\text{diff}\downarrow}_{\text{surf}}$
176	SSR	Surface net solar radiation	$S^{\text{net}}_{\text{surf}} = S^{\downarrow}_{\text{surf}} - S^{\uparrow}_{\text{surf}}$
210	SSRC	Surface net clear-sky solar radiation	$S^{\text{net}}_{\text{surf,clear}}$
47	DSRP	Direct surface solar radiation (perp. to Sun)	S^{0}_{surf}
228021	FDIR	Direct solar radiation at the surface	$\mu_0 S^{0}_{\text{surf}}$
228022	CDIR	Clear-sky direct solar radiation at surface	$\mu_0 S^{0}_{\text{surf,clear}}$
175	STRD	Surface thermal radiation downwards	$L^{\downarrow}_{\text{surf}}$
177	STR	Surface net thermal radiation	$L^{\text{net}}_{\text{surf}} = L^{\downarrow}_{\text{surf}} - L^{\uparrow}_{\text{surf}}$
211	STRC	Surface net clear-sky thermal radiation	$L^{\text{net}}_{\text{surf,clear}}$
58	PAR	Photosynthetically active radiation	
20	PARCS	Clear-sky photosynthetically active radiation	

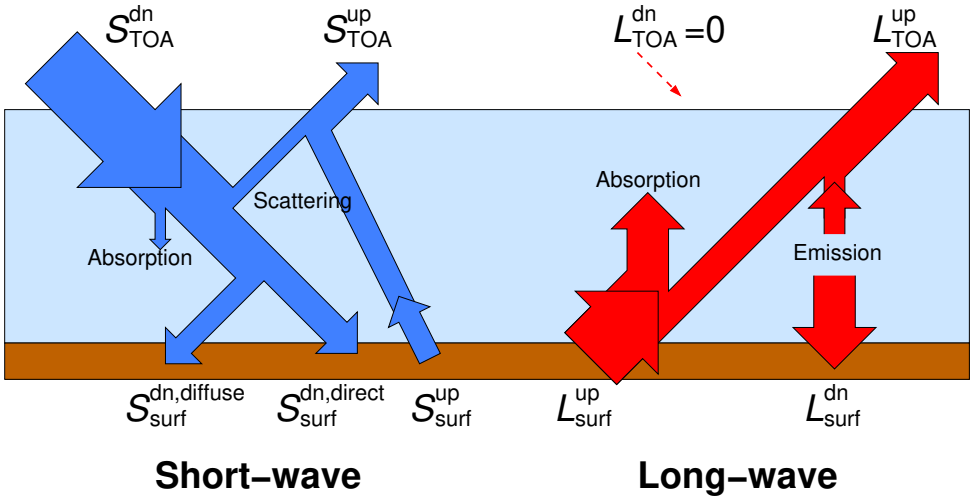

Figure 2.3 *Schematic of the short-wave and long-wave radiative energy flows in the atmosphere.*

means that to obtain a daily mean flux one must download all hourly accumulations, compute the corresponding fluxes, then average them.

(iv) *Clear-sky* quantities are computed for exactly the same atmospheric conditions of temperature, humidity, ozone, trace gases and aerosol, but assuming that the clouds are not there.

(v) *Solar* or *short-wave* refers to radiation emitted by the Sun, then scattered, absorbed or transmitted by the atmosphere and reflected or absorbed by the surface. It corresponds roughly to the 0.2–4 μm or 50,000–2600 cm^{-1} part of the spectrum. *Thermal, terrestrial* or *long-wave* refers to radiation emitted and absorbed by the surface or by gases, clouds and particles within the atmosphere. It corresponds roughly to the 4–100 μm or 2600–10 cm^{-1} part of the spectrum. Note that there is some spectral overlap between the two, which is fully represented in the model, so the division between solar and thermal radiation should not be thought of as simply radiation with a wavelength shorter or longer than 4 μm, but rather as radiation originating from the sun versus originating from emission by the Earth or its atmosphere.

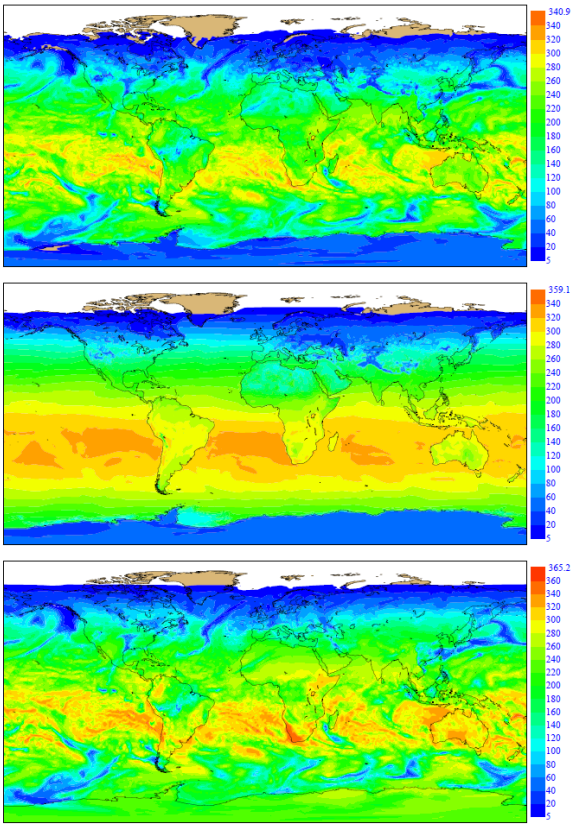

Figure 2.4 *Example of diagnostic fluxes (in W m^{-2}) computed from the first 24-hour accumulations from a forecast started at 12 UTC on 15 February 2012. From top: surface net solar radiation (SSR), surface net clear-sky solar radiation (SSRC) and surface solar radiation downwards (SSRD).*

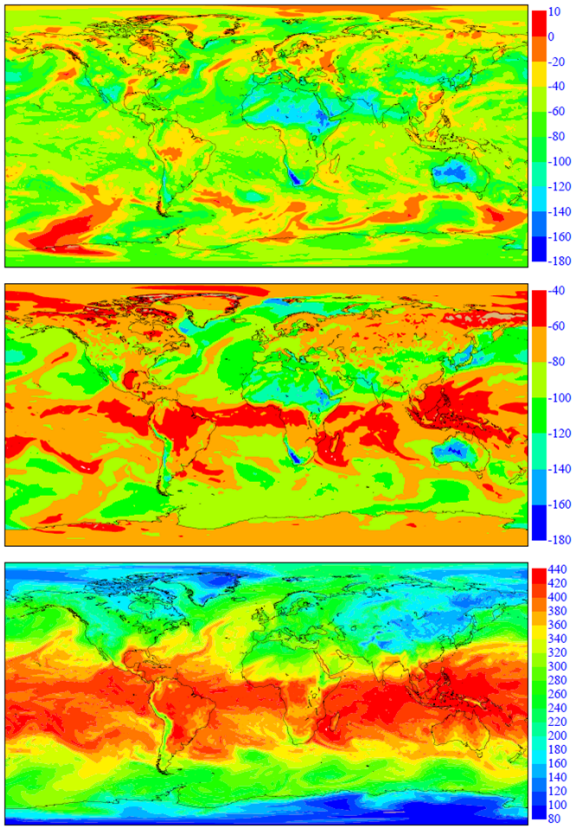

Figure 2.5 *As Fig. 2.4 but for the following variables (from top): surface net thermal radiation (STR), surface net clear-sky thermal radiation (STRC) and surface thermal radiation downwards (STRD).*

2.8.2 Surface fluxes

The accumulated fluxes available at the surface are shown in Table 2.6. The surface fluxes are accumulated from the start of the forecast in J m^{-2} (or 1-hour accumulations in the case of ERA5). See Fig. 2.3 to put these in the context of atmospheric energy flows, and Fig. 2.4, Fig. 2.5 and Fig. 2.6 for examples. There are several points to note:

- All quantities are at ground level in the model, according to the model's representation of orography. Some users ask if this is somehow corrected to be the value that would be observed at mean sea level if the Earth had no orography. The answer is no.
- To a reasonably good approximation, SSRD can be considered to be what would be measured by a global pyranometer at the surface, and SSRD − FDIR can be considered to be what would be measured by a diffuse pyranometer. But be aware that because of the use of delta-scaling of particle scattering properties described in Section 2.5.3, the direct (i.e. unscattered) solar radiation in the model actually includes radiation that has been scattered by cloud and aerosol particles by several degrees. Delta scaling is is performed because in the two-stream paradigm it is more accurate for the resultant total fluxes if the narrow forward-scattering peak in the scattering distribution is treated as if it had not been scattered at all A further point is that the diffuse downwelling radiation from the model includes diffuse radiation in the direction of the sun, which would be excluded from the radiation measured by a diffuse pyranometer that uses a shadow band to exclude direct radiation. Further discussion of this issue was provided by Räisänen and Lindfors (2019).

Table 2.7 *As Table 2.6 but for top-of-atmosphere (TOA) accumulated flux diagnostics.*

Param. ID	Short Name	Name	Symbol/Equation
212	TISR	Top incident solar radiation	$S^{\downarrow}_{\mathrm{TOA}} = \mu_0 S^{0}_{\mathrm{TOA}}$
178	TSR	Top net solar radiation	$S^{\mathrm{net}}_{\mathrm{TOA}} = S^{\downarrow}_{\mathrm{TOA}} - S^{\uparrow}_{\mathrm{TOA}}$
208	TSRC	Top net clear-sky solar radiation	$S^{\mathrm{net}}_{\mathrm{TOA,clear}}$
179	TTR	Top net thermal radiation	$L^{\mathrm{net}}_{\mathrm{TOA}} = -L^{\uparrow}_{\mathrm{TOA}}$
209	TTRC	Top net clear-sky thermal radiation	$L^{\mathrm{net}}_{\mathrm{TOA,clear}}$

Table 2.8 *Additional radiation variables available from the IFS.*

Param. ID	Short name	Name	Units
189	SUND	Sunshine duration	s
243	FAL	Forecast surface albedo	0-1

- The direct fluxes FDIR and CDIR are into a horizontal plane whereas DSRP is into a plane oriented perpendicular to the Sun's rays. A pyrheliometer generally measures the latter, but unfortunately DSRP is not yet available from all IFS streams. If DSRP is not available then it can be estimated to a good approximation from hourly FDIR with DSRP $=$ FDIR$/\mu_0$. This requires an accurate calculation of the cosine of the solar zenith angle μ_0, but reproducing the IFS's computation of μ_0, including the Equation of Time (see Section 2.4.6), can be difficult. One simple method is to obtain the corresponding global field of top-of-atmosphere incoming solar radiation, TISR, and applying $\mu_0 =$ TISR$/\max($TISR$)$. Here the maximum TISR value occurs at the sub-solar point and is therefore very close to the solar irradiance S^0 in Section 2.4.6. It should be noted that attempting to convert from FDIR to DSRP over longer periods than one hour will be less accurate because of the change in the solar angle during the averaging period.
- Photosynthetically active radiation (PAR) is the total downward accumulated flux into a horizontal plane associated with wavelengths in the range 0.4–0.7 μm. Note that before Cycle 43r1, PAR was computed from the wrong bands and hence was underestimated by around 30%.

2.8.3 Top-of-atmosphere fluxes

Top-of-atmosphere (i.e. for a half-level pressure of 0 hPa) accumulated flux diagnostics are shown in Table 2.7 and are put in context in Fig. 2.3. Some examples are shown in Fig. 2.7.

A frequently required quantity from global models is *Outgoing Long-Wave Radiation* (OLR), equal to $L^{\uparrow}_{\mathrm{TOA}}$. The downward long-wave (non-solar) flux from space is tiny (e.g. the cosmic background amounts to only 3×10^{-6} W m^{-2}) so may safely be neglected, i.e. $L^{\downarrow}_{\mathrm{TOA}} = 0$. Therefore TTR represents the negative of the outgoing long-wave radiation: OLR $=$ $-$TTR.

2.8.4 Other variables

Table 2.8 lists some additional radiation quantities available from the IFS. Sunshine duration is defined as the number of seconds since the start of the forecast that the direct solar flux at the surface into a plane perpendicular to the Sun's rays exceeded 120 W m^{-2}, matching the WMO definition. It is therefore an accumulated field. As explained in section 2.8.2, this uses ecRad's definition of 'direct' radiation, which includes some forward scattered radiation due to the use of delta scaling.

At each timestep an additional instantaneous broadband albedo is computed for diagnostic purposes only, and stored as 'FAL'. This variable includes the contribution from snow and sea-ice, but is computed as a weighted average of the *diffuse* albedos in the UV-visible and the near-infrared, weighted according to the fixed *top-of-atmosphere* spectral distribution of incoming solar radiation rather than the variable surface spectral distribution. The neglect of the difference between diffuse and direct radiation, and the use of a fixed spectral weighting, means that FAL differs somewhat from the true broadband all-sky

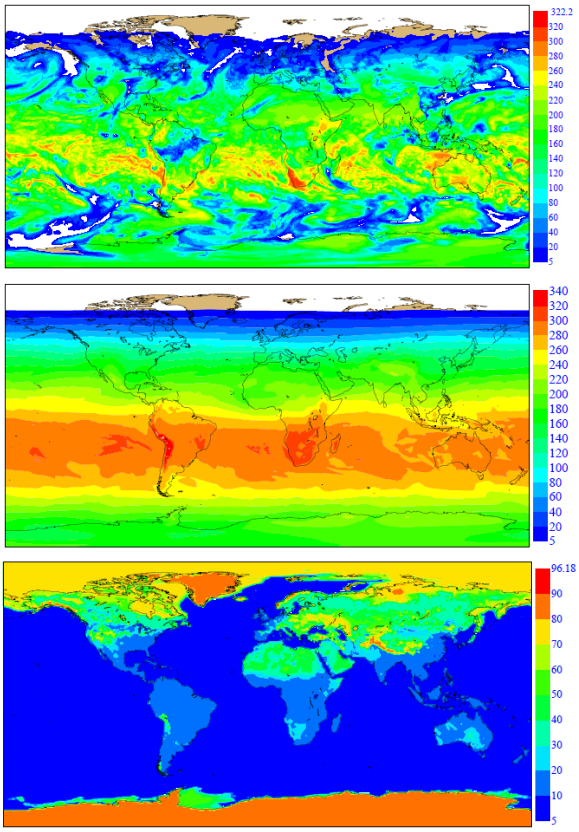

Figure 2.6 *As Fig. 2.4 but for the following variables (from top): surface direct solar radiation (FDIR) and surface direct clear-sky solar radiation (CDIR). The bottom panel depicts forecast albedo (FAL) as a percentage, 24-hr into the forecast.*

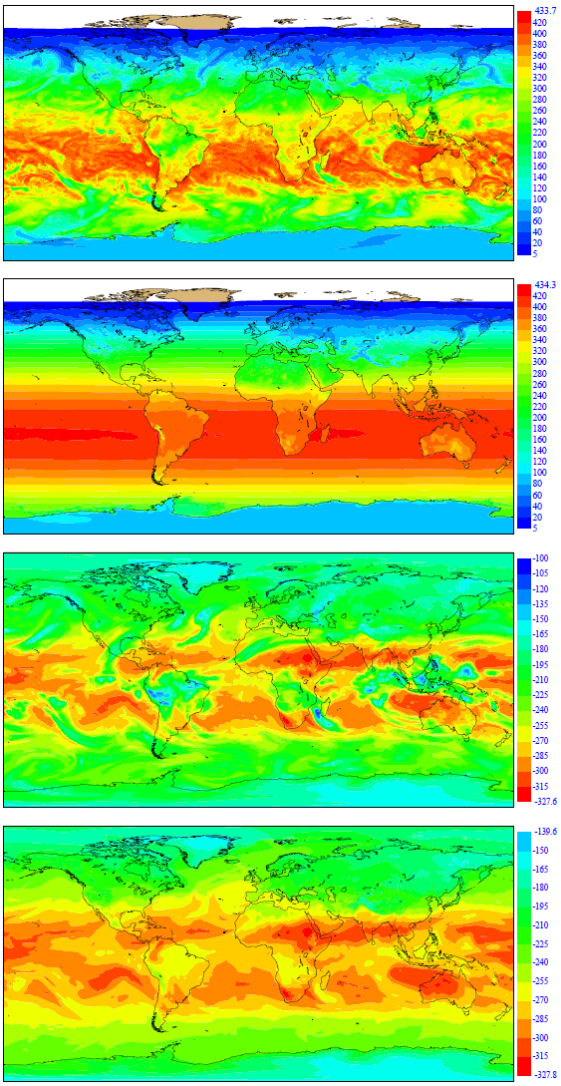

Figure 2.7 *As Fig. 2.4 but for the following variables (from top): top-of-atmosphere (TOA) net solar radiation (TSR), TOA net clear-sky solar radiation (TSRC), TOA net thermal radiation (TTR) and TOA net clear-sky thermal radiation (TTRC).*

albedo in the model, defined as

$$\alpha = S^{\uparrow}_{\text{surf}} / S^{\downarrow}_{\text{surf}}. \tag{2.113}$$

Noticeable differences between FAL and α occur particularly over snow and ice where there is a large difference in albedo between the two spectral regions. Users who wish to know α as defined by (2.113) are advised to calculate it directly from the archived surface fluxes using $\alpha = 1 - \text{SSR}/\text{SSRD}$. Since SSR and SSRD are accumulated, this will give the effective albedo averaged over the duration of the forecast up to that point in time. Of course, it will only produce reliable results over points that have been sunlit at some point during the forecast up to that point, i.e. SSRD > 0. An advantage of FAL as a diagnostic is that it can be computed at night, as shown in the example in Fig. 2.6.

As explained in Section 2.4.5, albedo in the IFS is computed from a land-surface snow-free albedo climatology that is then modified to add land snow, sea ice and open ocean. The individual components of the climatology are also output from the IFS and named AL*XXY*, where *XX* may be 'UV' indicating the UV-Visible part of the spectrum or 'NI' indicating the Near-Infrared part (with the split at 0.7 μm).

Y may be 'D' indicating the diffuse albedo, or 'I', 'V' or 'G' indicating the isometric, volumetric or geometric components as defined by Schaaf *et al.* (2002). Since these albedo components are purely climatological with no prognostic content, and they omit land snow, it is recommended that they are not used.

2.9 CODE

The ecRad code is stored in the IFS subdirectory radiation/module, and is a near exact copy of the offline radiation scheme freely available on GitHub. Each file is prefixed with radiation and describes a Fortran module of the same name. The routines preparing input to the ecRad and interpreting the fluxes afterwards, as well as the RRTMG gas optics scheme, are mostly stored in the IFS subdirectories arpifs/phys_radi and arpifs/module.

The module YOERAD stores the setup options of the radiation scheme. The routine SUECRAD sets the default values of these options and reads the namelist NAERAD to optionally override them. It then calls SETUP_RADIATION_SCHEME from the RADIATION_SETUP module which configures the ecRad-specific settings, before reading the RADIATION namelist to optionally override the ecRad specific features that are not exposed as options in NAERAD (note that normally the RADIATION namelist would not be used in the IFS). This in turn calls ecRad's SETUP_RADIATION routine from its RADIATION_INTERFACE module; this configures ecRad by, for example, reading in the relevant netCDF files.

Surface properties are computed from the SURFRAD_CTL routine in the SURFRAD_CTL_MOD module (in the surf/module subdirectory of the IFS). Full radiation computations are launched from RADDRV, which in turn calls RADINTG. The latter is a large routine that first interpolates the model fields to the radiation grid, and then computes climatological values from within this coarser grid, calling RADACA for the aerosol climatology and RADGHG for the greenhouse gas climatology. It then calls RADIATION_SCHEME to compute radiative fluxes which are then interpolated back to the model grid, including the short-wave updates described in Section 2.7.2.

The purpose of RADIATION_SCHEME is to translate the IFS fields on the radiation grid into ecRad structures, compute liquid and ice effective radius via calls to LIQUID_EFFECTIVE_RADIUS and ICE_EFFECTIVE_RADIUS, and then pass them to the RADIATION routine, also part of ecRad's RADIATION_INTERFACE routine. The structure of ecRad itself was described by Hogan and Bozzo (2016).

RADHEATN is called every model timestep from beneath CALLPAR and makes use of the stored fluxes at the last call to the radiation scheme to compute heating rate profiles and surface fluxes. It makes use of the position of the sun in the sky at the exact timestep to scale the incoming short-wave radiation to match the top-of-atmosphere value. It also applies the 'Manners' short-wave update described in Section 2.7.2 and the long-wave updates described in Section 2.7.3.

APPENDIX A. LIST OF SYMBOLS

$A_{i+1/2}$	albedo to diffuse radiation of the entire Earth-atmosphere system below half-level $i+1/2$
B	black-body flux for an individual g-point (in W m^{-2}), i.e. Planck function multiplied by π
a	cloud fraction
c_p	specific heat at constant pressure of moist air
$c_{p_{\text{dry}}}$	specific heat at constant pressure of dry air
$D_{i+1/2}$	albedo to direct radiation of the entire Earth-atmosphere system below half-level $i+1/2$
$E_{i+1/2}$	upward emission of the entire Earth-atmosphere system below half-level $i+1/2$
F^0	direct solar flux into a plane perpendicular to the sun
$F^{\uparrow}$	diffuse upwelling radiative flux
$F^{\text{diff}\downarrow}$	diffuse downwelling radiative flux

$F^{\downarrow}$	total downwelling radiative flux (including direct in short-wave)
F^{net}	net flux (down minus up)
f	fractional scattering into the forward peak
g^0	acceleration due to gravity
g	asymmetry factor for particle scattering, equal to the mean of the cosine of the scattering angle
k	molar absorption coefficient (except in Section 2.5.5 where it is an intermediate value in the solution to the two-stream equations)
p	pressure
q_j	mass mixing ratio of hydrometeor species j, or of aerosol species number j
D	diffusivity factor
r_e	mean effective radius of cloud water droplets or ice particles
R_i	reflectance of layer i to diffuse radiation
R_i^{dir}	reflectance of layer i to direct radiation
S^0	solar irradiance at top-of-atmosphere into a plane perpendicular to the solar direction
$S_i^{\uparrow\downarrow}$	emission rate by layer i in the upward or downward directions (W m^{-2})
T_i	transmittance of layer i to diffuse radiation
T_i^0	fraction of direct radiation entering the top of layer i that emerges unscattered from the base of the layer
T_i^{dir}	fraction of direct radiation entering the top of layer i that emerges from the base of the layer as diffuse radiation
T	temperature (K)
α	surface albedo to diffuse radiation
α^{dir}	surface albedo to direct radiation
τ	optical depth from top-of-atmosphere as a vertical coordinate
τ_1	optical depth of an individual layer
ϵ	surface long-wave emissivity
μ_0	cosine of solar zenith angle
ω	single-scattering albedo

Chapter 3

Turbulent transport and interactions with the surface

Table of contents

3.1 Introduction
3.2 The surface layer
3.2.1 Surface fluxes
3.2.2 Surface layer stability functions
3.2.3 Computation of the Obukhov length
3.2.4 Roughness lengths
3.3 The outer layer
3.3.1 The exchange coefficients in the mixed layer
3.3.2 The exchange coefficients in stable conditions and in unstable layers situated above the mixed layer
3.4 Turbulent orographic form drag (TOFD)
3.5 Solution of the EDMF equations
3.6 The surface energy balance
3.7 Tracer diffusion
3.8 Tendency calculations and energy dissipation
3.9 Prognostic turbulence kinetic energy scheme
3.10 Description of output fields: Boundary layer
3.10.1 Diagnostic boundary layer height
3.10.2 Temperature and humidity at the 2 m level
3.10.3 Wind at 10, 100 and 200 m level and friction velocity
3.10.4 Wind gusts
3.10.5 Clear air turbulence (CAT)
3.10.6 Visibility
3.11 Code
Appendix A. List of symbols

3.1 INTRODUCTION

The parametrization scheme described in this chapter represents the turbulent transfer of heat, momentum and moisture between the surface and the lowest model level (i.e. within the surface layer) and the turbulent transport of the same quantities plus liquid and ice water between model levels (i.e. in the outer layer). The scheme computes the physical tendencies of the six prognostic variables (u, v, T, q, q_l and q_i) due to the vertical exchange by turbulent processes. These tendencies are obtained as the difference between the results of an implicit time-step from t to $t+1$. All the diagnostic computations (such as the calculation of the exchange coefficients, etc.) are done at time t. The surface boundary condition is formulated separately for ten different tiles: water, ice, wet skin, low vegetation, exposed snow, high vegetation, snow under vegetation, bare soil, lakes and urban. The different tiles have their own surface energy balance and their own skin temperature. In this version of the IFS, the mixture of land and ocean tiles is still not used, i.e. a grid box is either 100% ocean (water + ice) or 100% land (tile 3 to 8). Details about tiles are given in Chapter 8.

The vertical turbulent transport is treated differently in the surface layer and in the outer layer. In the surface layer, the turbulence fluxes are computed using a first order K-diffusion closure. In the outer layer, a K-diffusion turbulence closure is used everywhere (i.e. stable or unstable layers), except in the well-mixed part of unstable boundary layers (i.e. further referred to as the mixed layer) where an Eddy-Diffusivity Mass-Flux (EDMF) framework is applied.

The equation for the vertical turbulent transport of any conservative quantity ϕ is described by

$$\frac{\partial \phi}{\partial t} = \frac{1}{\rho}\frac{\partial}{\partial z}\left(\rho K_\phi \frac{\partial \phi}{\partial z} - M(\phi_u - \overline{\phi})\right) = \frac{1}{\rho}\frac{\partial J_\phi}{\partial z} \tag{3.1}$$

The vertical turbulent flux J_ϕ (positive downwards, i.e. $J_\phi = -\rho\overline{\phi' w'}$) is written using a first-order turbulence closure, where K_ϕ is the exchange coefficient, to which a mass-flux component is added in the mixed layer to describe the strongest eddies. Because the mass-flux is zero at the surface and the top of the mixed layer, boundary conditions are satisfied by vertical diffusion

$$\begin{aligned} K_\phi \frac{\partial \phi}{\partial z} &= 0 \quad \text{at} \quad p = p_{\text{top}} \\ K_\phi \frac{\partial \phi}{\partial z} &\rightarrow \sum_{i=1}^{N_T} F_i C_{\phi i} |U(z)| (\phi(z) - \phi_{i,\text{surf}}) \text{ as } z \rightarrow 0 \end{aligned} \tag{3.2}$$

where p_{top} is the pressure at the top of the atmosphere. For heat and moisture the surface boundary condition is provided tile by tile and fluxes are averaged over the N_T tiles, weighted by their fraction F_i. The transfer coefficient $C_{\phi i}$ at the lowest model level depends upon the static stability and wind. The variable ϕ_{surf} represents the value of ϕ at the surface. For heat and moisture, ten tiles are used (see Chapter 10). For wind, a single tile is used with a no slip condition at the surface.

The vertical turbulent transport processes are applied to the two horizontal wind components, u and v, the specific total water q_t and the generalised liquid water static energy h_l,

$$q_t = q + q_l + q_i \tag{3.3}$$

$$h_l = gz + c_p T - L_{\text{vap}} q_l - L_{\text{subl}} q_i \tag{3.4}$$

where q, q_l, q_i are the specific humidity, specific liquid water and specific ice water, c_p is the specific heat at constant pressure of dry air, g is the constant of gravity, and L_{vap} and L_{subl} are the latent heats of condensation and deposition respectively. Note that the influence of water vapour on c_p is neglected throughout the formulation of vertical turbulent fluxes (as is also done in the other physics components).

The exchange coefficients (with the dimension of a pressure thickness) are then computed for momentum and for heat (sensible plus latent) (the subscripts 'M, 'H' and 'Q' are used to identify the exchange coefficient for momentum, heat and total water), with different formulations for the stable and the unstable cases. The mass-flux term is calculated based on an entraining plume model closed at the surface. The implicit linear equations for the fluxes of momentum, firstly for u and v and secondly for h_l and q_t, are solved by a Gaussian-elimination/back-substitution method, described in Section 3.5.

The surface boundary condition is applied between the downward scanning elimination and the upward scanning back substitution. It involves a no-slip condition for u and v and the tile-by-tile solution of the surface energy balance for the boundary condition of q and dry static energy

$$s = gz + c_p T \tag{3.5}$$

The water tile is an exception as it ignores the surface energy balance and uses the specified SST and the saturation specific humidity as boundary conditions.

Finally, the tendencies of temperature and water vapour are derived from the tendencies of q and h_l without applying a saturation adjustment, as the saturation adjustment is done subsequently as part of the cloud scheme together with the computation of a corresponding cloud fraction change.

$$\frac{\partial q}{\partial t} = \frac{\partial q_t}{\partial t} - \frac{\partial q_l}{\partial t} - \frac{\partial q_i}{\partial t} \tag{3.6}$$

$$\frac{\partial T}{\partial t} = \frac{1}{c_p}\left(\frac{\partial h_l}{\partial t} + L_{\text{vap}}\frac{\partial q_l}{\partial t} + L_{\text{subl}}\frac{\partial q_i}{\partial t}\right) \tag{3.7}$$

where the liquid and ice water tendencies remain unmodified by the diffusion scheme and correspond to the input tendencies.

The temperature is further modified by the effects of local dissipation (it is assumed that there is no storage of turbulence kinetic energy). The tiled surface fluxes of heat and moisture are also computed for later use by the surface scheme.

3.2 THE SURFACE LAYER

The surface layer approximation is applied between the lowest model level (about 10 m above the surface in the 137 level models) and the surface and for each tile separately. It is assume that the turbulent fluxes are constant with height and equal to the surface values. They can be expressed, using Monin–Obukhov similarity theory, in terms of the gradients of wind, dry static energy and specific humidity, which are assumed to be proportional to universal gradient functions of a stability parameter:

$$\begin{aligned}\frac{\kappa z}{u_*}\frac{\partial u}{\partial z} &= \Phi_{\mathrm{M}}\left(\frac{z}{\mathcal{L}}\right)\\ \frac{\kappa z}{s_*}\frac{\partial s}{\partial z} &= \Phi_{\mathrm{H}}\left(\frac{z}{\mathcal{L}}\right)\\ \frac{\kappa z}{q_*}\frac{\partial q}{\partial z} &= \Phi_{\mathrm{Q}}\left(\frac{z}{\mathcal{L}}\right)\end{aligned} \tag{3.8}$$

The scaling parameters u_*, s_* and q_* are expressed in terms of surface fluxes J_ϕ by

$$\begin{aligned}\rho u_*^2 &= J_{\mathrm{M}}\\ \rho u_* s_* &= J_{\mathrm{s}}\\ \rho u_* q_* &= J_{\mathrm{q}}\end{aligned} \tag{3.9}$$

The stability parameter $\mathcal{L}$ is the Obukhov length defined as

$$\mathcal{L} = -u_*^3 \Big/ \left(\frac{\kappa g}{T_n} Q_{0\mathrm{v}}\right) \quad \text{with} \quad Q_{0\mathrm{v}} = \frac{u_* s_*}{c_p} + \varepsilon T_n u_* q_* \tag{3.10}$$

$Q_{0\mathrm{v}}$ is the virtual temperature flux in the surface layer, κ is the Von Kármán constant $(= 0.4)$, T_n is a reference temperature taken as a near-surface temperature (the temperature of the lowest atmospheric level n) and $\varepsilon = (R_{\mathrm{vap}}/R_{\mathrm{dry}}) - 1$, where R_{vap} and R_{dry} are the gas constants for water vapour and dry air, respectively.

In the surface layer, the gradient functions (3.8) can be integrated to profiles

$$u = \frac{\tau_x}{\kappa\rho u_*}\left\{\log\left(\frac{z_n + z_{0\mathrm{M}}}{z_{0\mathrm{M}}}\right) - \Psi_{\mathrm{M}}\left(\frac{z_n + z_{0\mathrm{M}}}{\mathcal{L}}\right) + \Psi_{\mathrm{M}}\left(\frac{z_{0\mathrm{M}}}{\mathcal{L}}\right)\right\} \tag{3.11}$$

$$v = \frac{\tau_y}{\kappa\rho u_*}\left\{\log\left(\frac{z_n + z_{0\mathrm{M}}}{z_{0\mathrm{M}}}\right) - \Psi_{\mathrm{M}}\left(\frac{z_n + z_{0\mathrm{M}}}{\mathcal{L}}\right) + \Psi_{\mathrm{M}}\left(\frac{z_{0\mathrm{M}}}{\mathcal{L}}\right)\right\} \tag{3.12}$$

$$s - s_{\mathrm{surf}} = \frac{J_s}{\kappa\rho u_*}\left\{\log\left(\frac{z_n + z_{0\mathrm{M}}}{z_{0\mathrm{H}}}\right) - \Psi_{\mathrm{H}}\left(\frac{z_n + z_{0\mathrm{M}}}{\mathcal{L}}\right) + \Psi_{\mathrm{H}}\left(\frac{z_{0\mathrm{H}}}{\mathcal{L}}\right)\right\} \tag{3.13}$$

$$q - q_{\mathrm{surf}} = \frac{J_q}{\kappa\rho u_*}\left\{\log\left(\frac{z_n + z_{0\mathrm{M}}}{z_{0\mathrm{Q}}}\right) - \Psi_{\mathrm{H}}\left(\frac{z_n + z_{0\mathrm{M}}}{\mathcal{L}}\right) + \Psi_{\mathrm{H}}\left(\frac{z_{0\mathrm{Q}}}{\mathcal{L}}\right)\right\} \tag{3.14}$$

$z_{0\mathrm{M}}$, $z_{0\mathrm{H}}$ and $z_{0\mathrm{Q}}$ are the roughness lengths for momentum, heat and moisture. The stability profile functions Ψ are derived from the gradient functions (3.8) with the help of the relationship $\Phi = 1 - \zeta(\partial\Psi/\partial\zeta)$. These profiles are used for the surface atmosphere interaction as explained in the following sections and also for the interpolation between the lowest model level and the surface (post-processing of 10 m wind and 2 m temperature and moisture).

In extremely stable or weak wind situations, i.e. for very small positive $\mathcal{L}$, the ratio $z/\mathcal{L}$ is large, resulting in unrealistic profile shapes with standard stability functions. Therefore the ratio $z/\mathcal{L}$ is limited to 5 by

defining a height h such that $h/\mathcal{L} = 5$. If $z < h$, then the profile functions described above, are used up to $z = h$ and the profiles are assumed to be uniform above that. This modification of the profiles for exceptionally stable/ weak wind situations is applied only to the surface transfer formulation and not the post-processing of near-surface variables (since Cy49r1).

3.2.1 Surface fluxes

Surface fluxes for heat and moisture are computed separately for the different tiles, so most of the surface layer computations loop over the tile index. Here a general description is given of the aerodynamic aspects of the transfer between the surface and the lowest model level. The description of the individual tiles can be found in Chapter 8.

Assuming that the first model level above the surface is located in the surface boundary layer at a specified height z_n, the gradient functions (3.8) can be integrated to profiles for wind, dry static energy and specific humidity. The surface fluxes are expressed in terms of differences between parameters at level z_n and surface quantities (identified by the subscript 'surf'; the tile index has been omitted in this general description) so

$$\begin{aligned} J_{\mathrm{M}} &= \rho C_{\mathrm{M}} |U_n|^2 \\ J_{\mathrm{s}} &= \rho C_{\mathrm{H}} |U_n| (s_n - s_{\mathrm{surf}}) \\ J_{\mathrm{q}} &= \rho C_{\mathrm{Q}} |U_n| (\alpha_n q_n - \alpha_{\mathrm{surf}} q_{\mathrm{surf}}) \end{aligned} \tag{3.15}$$

where $q_{\mathrm{surf}} = q_{\mathrm{sat}}(T_{\mathrm{surf}})$, α_n and α_{surf} are provided by the land scheme, and $s_{\mathrm{surf}} = c_p T_{\mathrm{surf}}$, (the humidity equation simplifies over water where $\alpha_n = 1$ and $\alpha_{\mathrm{surf}} = 1$).

The transfer coefficients can be expressed as

$$C_{\mathrm{M}} = \frac{\kappa^2}{\left[\log\left(\frac{z_n+z_{0\mathrm{M}}}{z_{0\mathrm{M}}}\right) - \Psi_{\mathrm{M}}\left(\frac{z_n+z_{0\mathrm{M}}}{\mathcal{L}}\right) + \Psi_{\mathrm{M}}\left(\frac{z_{0\mathrm{M}}}{\mathcal{L}}\right)\right]^2} \tag{3.16}$$

$$C_{\mathrm{H}} = \frac{\kappa^2}{\left[\log\left(\frac{z_n+z_{0\mathrm{M}}}{z_{0\mathrm{M}}}\right) - \Psi_{\mathrm{M}}\left(\frac{z_n+z_{0\mathrm{M}}}{\mathcal{L}}\right) + \Psi_{\mathrm{M}}\left(\frac{z_{0\mathrm{M}}}{\mathcal{L}}\right)\right]\left[\log\left(\frac{z_n+z_{0\mathrm{M}}}{z_{0\mathrm{H}}}\right) - \Psi_{\mathrm{H}}\left(\frac{z_n+z_{0\mathrm{M}}}{\mathcal{L}}\right) + \Psi_{\mathrm{H}}\left(\frac{z_{0\mathrm{H}}}{\mathcal{L}}\right)\right]} \tag{3.17}$$

$$C_{\mathrm{Q}} = \frac{\kappa^2}{\left[\log\left(\frac{z_n+z_{0\mathrm{M}}}{z_{0\mathrm{M}}}\right) - \Psi_{\mathrm{M}}\left(\frac{z_n+z_{0\mathrm{M}}}{\mathcal{L}}\right) + \Psi_{\mathrm{M}}\left(\frac{z_{0\mathrm{M}}}{\mathcal{L}}\right)\right]\left[\log\left(\frac{z_n+z_{0\mathrm{M}}}{z_{0\mathrm{Q}}}\right) - \Psi_{\mathrm{Q}}\left(\frac{z_n+z_{0\mathrm{M}}}{\mathcal{L}}\right) + \Psi_{\mathrm{Q}}\left(\frac{z_{0\mathrm{Q}}}{\mathcal{L}}\right)\right]} \tag{3.18}$$

The wind speed $|U_n|$ is expressed as

$$|U_n|^2 = u_n^2 + v_n^2 + w_*^2 \tag{3.19}$$

with w_* the free convection velocity scale defined by

$$w_* = \left(z_{\mathrm{i}} \frac{g}{T_n} Q_{\mathrm{ov}}\right)^{1/3} \tag{3.20}$$

The parameter z_{i} is a scale height of the boundary layer depth and is set to constant value of 1000 m, since only the order of magnitude matters. The additional term in equation (3.19) represents the near surface wind induced by large eddies in the free-convection regime. When the surface is heated, this term guarantees a finite surface wind-forcing in the transfer law even for vanishing u_n and v_n, and prevents $|U_n|$ and $\mathcal{L}$ from becoming zero. Beljaars (1994) showed that this empirical term, when added into the standard Monin–Obukhov scaling, is in agreement with scaling laws for free convection. When used with the roughness lengths defined below, it provides a good fit to observational data, both over land and over sea.

3.2.2 Surface layer stability functions

The empirical forms of the dimensionless gradient functions Φ (given by (3.8)) have been deduced from field experiments over homogeneous terrain.

(i) *Unstable conditions* ($\zeta = z/\mathcal{L} < 0$). The gradient functions proposed by Dyer and Hicks are used (Dyer, 1974; Hogström, 1988). Therefore

$$\begin{aligned}\Phi_M(\zeta) &= (1-16\zeta)^{-1/4}\\ \Phi_H(\zeta) &= \Phi_Q(\zeta) = (1-16\zeta)^{-1/2}\end{aligned} \tag{3.21}$$

These functions can be integrated to the universal profile stability functions, Ψ, (Paulson, 1970) so that

$$\begin{aligned}\Psi_M(\zeta) &= \frac{\pi}{2} - 2\,\mathrm{atan}(x) + \log\frac{(1+x)^2\cdot(1+x^2)}{8}\\ \Psi_H(\zeta) &= \Psi_Q(\zeta) = 2\log\left\{\frac{1+x^2}{2}\right\}\end{aligned} \tag{3.22}$$

with $x = (1-16\zeta)^{1/4}$. The Ψ-functions are used in the surface layer and the Φ-functions for unstable stratification are used above the surface layer for local closure.

(ii) *Stable conditions* ($\zeta = z/\mathcal{L} > 0$). The gradient function Φ_M as documented by Hogström (1988), and Φ_H as derived from the Ellison and Turner relation for the ratio Φ_M/Φ_H are:

$$\begin{aligned}\Phi_M(\zeta) &= 1+5\zeta\\ \Phi_H(\zeta) &= \Phi_Q(\zeta) = (1+4\zeta)^2\end{aligned} \tag{3.23}$$

These functions, know an 'short-tail' functions, were previously used for local closure above the surface layer but provided insufficient mixing. Instead, Richardson number dependent functions are used in the outer layer and these 'short-tail' functions are used above the tropopause (see Section 3.3.2 on exchange coefficients above the mixed layer).

The stable profile functions as used in the surface layer, are assumed to have the empirical forms proposed by Holtslag and Bruin (1988), with a modification to allow for the effects of a critical flux Richardson number for large ζ.

The profiles are given by

$$\begin{aligned}\Psi_M(\zeta) &= -b\left(\zeta - \frac{c}{d}\right)\exp(-d\zeta) - a\zeta - \frac{bc}{d}\\ \Psi_H(\zeta) &= \Psi_Q(\zeta) = -b\left(\zeta - \frac{c}{d}\right)\exp(-d\zeta) - \left(1+\frac{2}{3}a\zeta\right)^{1.5} - \frac{bc}{d} + 1\end{aligned} \tag{3.24}$$

where $a = 1$, $b = 2/3$, $c = 5$, and $d = 0.35$.

3.2.3 Computation of the Obukhov length

The transfer coefficients needed for the surface fluxes require the estimation of stability parameter ζ, itself a function of the surface fluxes. Therefore, an implicit equation, relating ζ to bulk Richardson number Ri_{bulk}, is solved using

$$Ri_{\mathrm{bulk}} = \zeta\cdot\frac{\left[\log\left(\frac{z_n+z_{0M}}{z_{0H}}\right) - \Psi_H\left(\frac{z_n+z_{0M}}{\mathcal{L}}\right) + \Psi_H\left(\frac{z_{0H}}{\mathcal{L}}\right)\right]}{\left[\log\left(\frac{z_n+z_{0M}}{z_{0M}}\right) - \Psi_M\left(\frac{z_n+z_{0M}}{\mathcal{L}}\right) + \Psi_M\left(\frac{z_{0M}}{\mathcal{L}}\right)\right]^2} \tag{3.25}$$

with

$$Ri_{\mathrm{bulk}} = \left(\frac{g}{\theta_v}\right)\frac{z_n(\theta_{vn} - \theta_{v\mathrm{surf}})}{|U_n|^2} \tag{3.26}$$

where θ_{vn} and $\theta_{v\mathrm{surf}}$ are the virtual potential temperatures at level z_n and at the surface, and θ_v is a virtual potential temperature within the surface layer. Equation (3.26) can be expressed in terms of dry static energy:

$$Ri_{\mathrm{bulk}} = \frac{gz_n}{|U_n|^2}\left[\frac{2(s_n - s_{\mathrm{surf}})}{(s_n + s_{\mathrm{surf}} - gz_n)} + \varepsilon(q_n - q_{\mathrm{surf}})\right] \tag{3.27}$$

Knowing Ri_{bulk} at time t, a first guess of the Obukhov length is made from fluxes computed at the previous time step. Equation (3.25) is solved numerically using the Newton iteration method to retrieve ζ.

In contrast to the previous formulation used in the model (Louis *et al.*, 1982), the present scheme allows a consistent treatment of different roughness lengths for momentum, heat and moisture.

3.2.4 Roughness lengths

The integration constants $z_{0\text{M}}$, $z_{0\text{H}}$ and $z_{0\text{Q}}$, in the equations for the transfer coefficients C_{M}, C_{H} and C_{Q} ((3.16) to (3.18)) are called roughness lengths because they are related to the small scale inhomogeneities of the surface that determine the air–surface transfer.

(i) *Over land*. The roughness lengths over land are assumed to be fixed and related to the land surface cover. At every time step the dominant tile is determined and the roughness lengths are set according to a table that relates the roughness length to vegetation type or to land cover (bare soil and exposed snow). The roughness length for momentum is different from the one for heat, but the ones for heat and moisture are assumed to be the same (See Chapter 8 for the tables).

(ii) *Over sea*. The specification of surface roughness lengths is particularly important over the sea. Because of the fixed boundary conditions for temperature and moisture the sea is, in principle, an infinite source of energy to the model. Following Beljaars (1994) the surface roughness lengths are expressed by

$$\begin{aligned} z_{0\text{M}} &= \alpha_{\text{M}}\frac{\nu}{u_*} + \alpha_{\text{Ch}}\frac{u_*^2}{g} \\ z_{0\text{H}} &= \alpha_{\text{H}}\frac{\nu}{u_*} \\ z_{0\text{Q}} &= \alpha_{\text{Q}}\frac{\nu}{u_*} \end{aligned} \tag{3.28}$$

These expressions account for both low and high wind regimes.

- At low wind speed the sea surface becomes aerodynamically smooth and the sea surface roughness length scales with the kinematic viscosity ν ($= 1.5 \times 10^{-5}\text{m}^2\text{s}^{-1}$).
- At high wind speed the Charnock relation is used. The chosen constants are $\alpha_{\text{M}} = 0.11$, $\alpha_{\text{H}} = 0.40$, and $\alpha_{\text{Q}} = 0.62$ (Brutsaert, 1982). The Charnock coefficient is provided by the wave model as the IFS has an active wave model component. If the wave model was deactivated, α_{Ch} is set equal to 0.018.

The smooth-surface parametrization has been retained in high wind speed regimes for heat and moisture until CY49R1 because observations indicated that the transfer coefficients for heat and moisture have very little wind-speed dependence above 4 ms^{-1} (Miller *et al.*, 1992; Godfrey and Beljaars, 1991). In (3.28) friction velocity u_*, is calculated from

$$u_* = C_{\text{M}}^{1/2}(u_n^2 + v_n^2 + w_*^2)^{1/2} \tag{3.29}$$

with w_* from (3.20) using fluxes from the previous time step.
However, from CY49R1, based on the work of (Janssen, 1997) and (Janssen and Bidlot, 2018), a sea state dependency has been added, as it can be shown that ocean waves contribute to the exchange of heat and moisture for high winds. Define

$$\begin{aligned} z_{\text{m}} &= \beta_{\text{hq}}(\alpha_{\text{Ch}}\frac{u_*^2}{g} - z_{\text{b}}) \\ z_\nu &= \alpha_{\text{i}}\frac{\nu}{u_*}, i = H, Q \\ z_\pm &= -(z_{\text{m}} + 0.5z_\nu) \pm \{z_{\text{m}}^2 + (0.5z_\nu)^2\}^{\frac{1}{2}} \end{aligned} \tag{3.30}$$

Then the roughness length scale for heat ($i = H$) and moisture ($i = Q$) is given by

$$z_{0\text{i}} = f_{zz}(z_{\text{m}}, z_+, z_-)f_{zz}(z_{\text{m}}, z_-, z_+), i = H, Q \tag{3.31}$$

with the function f_{zz}

$$f_{zz}(z_m, a, b) = |a|^{\frac{(z_m+a)}{(a-b)}} \tag{3.32}$$

where $\beta_{hq} = 0.25$ is a tuning coefficient added to the original formulation of (Janssen, 1997), to adjust the impact of this change with the rest of the physics parameterisation. Until CY49R1, the background roughness z_b due to gravity-capillary waves was modelled with a Charnock relation with a small coefficient $\hat{\alpha}$.

$$z_b = \hat{\alpha}\frac{u_*^2}{g} \tag{3.33}$$

where $\hat{\alpha}$ is given in section 3.2 of part VII of the IFS documentation on the wave model. With CY49R1, a simplified model for the role of the gravity-capillary waves was introduced. For more details, please refer to part VII.
As given in (Janssen and Bidlot, 2018), (3.31) can be approximated as follows. It is what is used for the simplified physics and hence the TL/AD.

$$z_{0i} = \{z_\nu z_{0M}\}^{\frac{1}{2}}, i = H, Q \tag{3.34}$$

(iii) *Sea ice*. The roughness length for momentum is assumed to depend on the sea ice concentration c_i, reflecting evidence that with partial ice cover, sea ice is more likely to be broken up resulting in increased form drag. With no other information than sea ice concentration, (Andreas *et al.*, 2010) proposed a formulation for the drag coefficient with larger values for partial ice cover. Adapting this approach in terms of roughness length ((Bidlot *et al.*, 2014)) gives (the roughness lengths for for heat and moisture remains constant)

$$\begin{aligned} z_{0M} &= max\left(10^{-3}, 0.93.10^{-3}(1-c_i) + 6.05.10^{-3} exp\left[-17(c_i-0.5)^2\right]\right) \\ z_{0H} &= 10^{-3} \\ z_{0Q} &= 10^{-3} \end{aligned} \tag{3.35}$$

3.3 THE OUTER LAYER

The computation of the exchange coefficients depends on the stability regimes (locally and at the surface) and on the vertical location above the surface. Fig. 3.1 summarises the various areas where each scheme (e.g. EDMF with non-local K-profiles in the mixed layer, local diffusion dependent on the Richardson number following Louis *et al.* (1982) or local diffusion with Monin–Obukhov functions) is applied.

3.3.1 The exchange coefficients in the mixed layer

The Eddy-Diffusivity Mass-Flux (EDMF) approach is used to compute the exchange coefficients within the well mixed part of unstable (convective) boundary layers (Tompkins *et al.*, 2004; Köhler, 2005; Köhler *et al.*, 2011). The decision whether the boundary layer is stable or unstable is based on the stability at the surface: if the buoyancy flux at the surface is positive the boundary layer is unstable and convective, otherwise it is stable.

EDMF concept

The concept behind the EDMF approach is to describe the strong large-scale organised updraughts with mass fluxes and the remaining small-scale turbulent part with diffusion. The up/down-draughts described by the mass flux term allow for non-local mixing, while the local mixing described by the diffusion term is limited to down gradient transports. Siebesma and Cuijpers (1995) arbitrarily define a strong updraught as a fixed small fractional area a_u containing the strongest upward vertical motions. The horizontal distribution of a field ϕ can then be described with perturbation terms in both updraught and environment areas separately

$$\phi_u = \phi'_u + \overline{\phi_u}^u \qquad \text{and} \qquad \phi_e = \phi'_e + \overline{\phi_e}^e \tag{3.36}$$

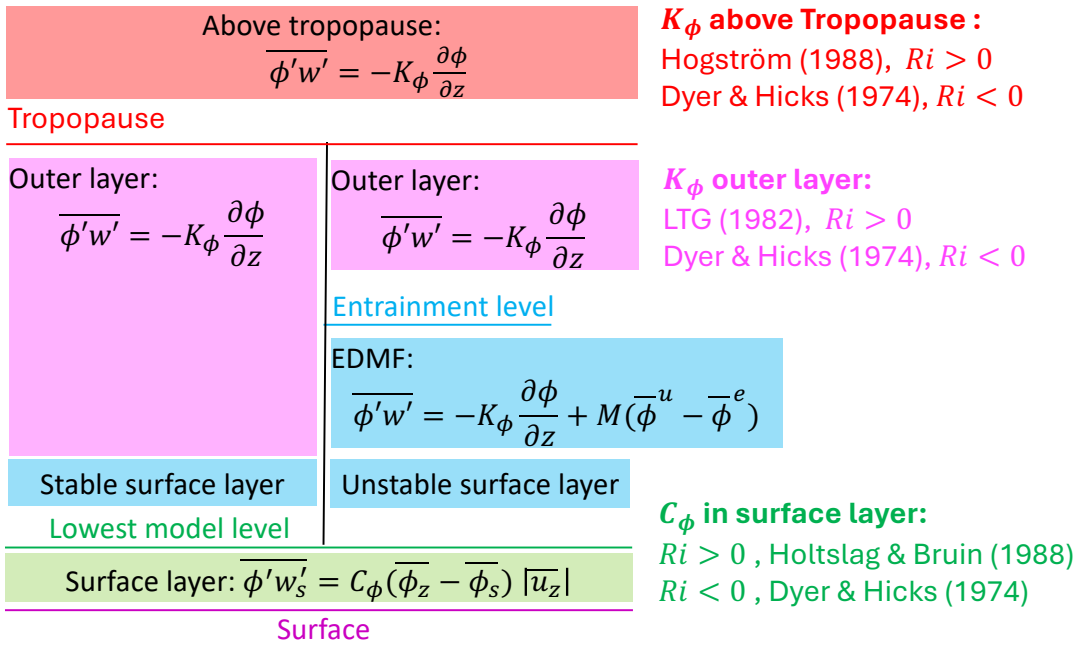

Figure 3.1 *Schematic diagram of the functions currently used under different stability regimes.*

where u and e refer to the updraught and environment areas both for the field and the averaging operator. The domain average then becomes

$$\overline{\phi} = a_u \overline{\phi_u}^u + (1 - a_u)\overline{\phi_e}^e \tag{3.37}$$

After some manipulation, the vertical turbulent flux breaks into three terms

$$\overline{w'\phi'} = a_u \overline{w'\phi'_u}^u + (1 - a_u)\overline{w'\phi'_e}^e + \frac{M}{\rho}(\phi_u - \phi_e) \tag{3.38}$$

where $M_u = \rho a_u w_u$ is the mass flux of the strongest updraughts. It is assumed $a_u \ll 1$ while $\overline{w'\phi'_u}^u$ and $\overline{w'\phi'_e}^e$ are of same order of magnitude. This permit the first term on the RHS to be neglected and $\phi_e \simeq \overline{\phi}$. The second term on the RHS can be approximated by diffusion with a coefficient of K_ϕ. Then

$$-\rho\overline{w'\phi'} = J_\phi = \rho K_\phi \frac{\partial \overline{\phi}}{\partial z} - M_u(\phi_u - \overline{\phi}) \tag{3.39}$$

Equation (3.39) is the basic equation for vertical turbulent transport of ϕ and will be considered for the moist conserved variables of generalised liquid water static energy s_l and total water mass mixing ratio q_t.

Plume model, convective boundary layer height and dry mass flux

The convective plume model serves to compute the top of the convective boundary layer z_i as well as the convective fluxes in the dry convective boundary layer. The convective fluxes in the cloudy boundary layer are computed by the shallow convection scheme (chapter 6). The convective plume model used by the turbulent diffusion scheme is that provided by the convection scheme for the surface parcel in section 6.4 and (6.18)-(6.20) with the only extension that the entrainment is increased inside the cloud layer by a factor of 3.

The boundary layer height z_i is determined as the uppermost level where the updraft vertical velocity $w_u > 0$ and the local Richardson number $Ri < 50$. However, in a stratocumulus (Sc) boundary layer more turbulent mixing is required inside the cloud layer and we set z_i equal to the convective cloud top level. This requires to distinguish between Sc and cumulus (Cu) type boundary layers. As proposed by Wood and Bretherton (2006) a useful predictor for the type of convective boundary layer is the so called estimated inversion strength EIS. Marquet and Bechtold (2020) developed a simple and efficient definition of EIS based on the moist entropy variable proposed by Marquet (2011) which is more continuous across the inversion. Approximating the moist entropy through the moist static energy as

$$h_e = h_l + c_p T * 5.87 q_t \tag{3.40}$$

we define the inversion strength as the variation of h_e across the boundary layer

$$\text{EIS} = max(h_{e,700} - h_{e,950}, h_{e,950} - h_{e,surf}) \tag{3.41}$$

where the subscripts denote specified pressure levels in hPa. Then for EIS>5 we assume a Sc boundary layer and diffusive mixing is applied up to convective cloud top.

The convective mass flux is initialised at the first model z_n as the product of an area fraction, atmospheric density and the fluctuation of vertical velocity σ_w, which is empirically derived from atmospheric data, tank measurements and LES data (Holtslag and Moeng, 1991)

$$M_{u,surf} = 0.1 \rho \sigma_w; \qquad \sigma_w = 1.2 \left(u_*^3 + 1.5 \kappa w_*^3 \frac{z_n}{z_{i,cb}} \right)^{1/3} \left(1 - \frac{z_n}{z_{i,cb}} \right)^{1/2} \tag{3.42}$$

where $\kappa = 0.4$ is the Von Kármán's constant, $u_* \equiv (\overline{u'w'}^2_{surf} + \overline{u'w'}^2_{surf})^{1/4}$ is the friction velocity, w_* the free convective velocity scale (3.20), $z_{i,cb} = z_i$ in the case of a dry boundary layer and is set to the convective cloud base height z_{cb} otherwise. The mass flux inside the dry convective boundary layer is then defined as

$$M_u = M_{u,surf} \frac{z}{z_n} \left(1 - \frac{z}{z_{i,cb}} \right)^2 \tag{3.43}$$

Convective transport is only applied to scalars and not for momentum.

Diffusion component

A first-order closure specifies the turbulent flux of a given quantity ϕ at a given model level proportional to the vertical gradient of that quantity. Therefore the diffusion component in the EDMF framework can be written as

$$J_\phi^k = \rho K_\phi \frac{\partial \phi}{\partial z}. \tag{3.44}$$

The exchange coefficients K_ϕ are estimated at half model levels.

In unstable surface conditions (positive buoyancy flux), the exchange coefficients are expressed as integral profiles for the entire convective mixed layer. This K-profile closure is based on the form proposed by Troen and Mahrt (1986). This approach is more suitable than the local diffusion one when the length scale of the largest transporting turbulent eddies have a similar size as the boundary layer height itself (unstable and convective conditions). It also allows for an explicit entrainment parametrization in the capping inversion (Beljaars and Viterbo, 1999).

In a dry boundary layer the mixing is due to surface driven eddies, while in a stratocumulus capped boundary layer, the turbulent mixing is also due to cloud top driven eddies. So in these cases the eddy-diffusion coefficients are the sum of the surface and a cloud top driven K-profile, and are overwritten with an explicit BL top entrainment at cloud top. For the surface driven diffusion a simple K-profile is specified (Troen and Mahrt, 1986; Holtslag, 1998):

$$\begin{aligned} K_{H,surf} &= \kappa u_* \Phi_{H0}^{-1} z \left(1 - \frac{z}{z_i} \right)^2 \\ K_{M,surf} &= \kappa u_* \Phi_{M0}^{-1} z \left(1 - \frac{z}{z_i} \right)^2 \end{aligned} \tag{3.45}$$

In the presence of convective clouds and a Bowen ratio< 0.25 (typical over water) the exchange coefficients are modified to yield less aggressive mixing in the upper part of the boundary layer

$$\begin{aligned} K_{\mathrm{H,surf}} &= \kappa u_* \Phi_{\mathrm{H0}}^{-1} z \left[\left(1 - \frac{z}{z_{\mathrm{cb}}}\right)^2 + \left(1 - \frac{z}{z_{\mathrm{i}}}\right)^4 \right] \\ K_{\mathrm{M,surf}} &= \kappa u_* \Phi_{\mathrm{M0}}^{-1} z \left[\left(1 - \frac{z}{z_{\mathrm{cb}}}\right)^2 + \left(1 - \frac{z}{z_{\mathrm{i}}}\right)^4 \right] \end{aligned} \tag{3.46}$$

The stability functions Φ_{H0} and Φ_{M0} are given by

$$\begin{aligned} \Phi_{\mathrm{H0}} &= \left(1 - 39\frac{z}{\mathcal{L}}\right)^{-1/3} \\ \Phi_{\mathrm{M0}} &= \left(1 - 15\frac{z}{\mathcal{L}}\right)^{-1/3} \end{aligned} \tag{3.47}$$

and $\mathcal{L} = -u_*^3 (\kappa \overline{w'\theta'_{\mathrm{v}}} g/\theta_{\mathrm{v}})^{-1}$ is the Obukhov length.

Furthermore, for the Sc boundary layer cloud top driven diffusion is described after Lock *et al.* (2000) as

$$K_{\mathrm{H,top}} = 0.85 \kappa v_{\mathrm{rad}} \frac{(z - z_{\mathrm{mb}})^2}{z_{\mathrm{i}} - z_{\mathrm{mb}}} \left(1 - \frac{z - z_{\mathrm{mb}}}{z_{\mathrm{i}} - z_{\mathrm{mb}}}\right)^{1/2} \tag{3.48}$$

where z_{i} is the inversion height or cloud top and z_{mb} is the level below cloud base to which the top driven mixing extends. A value of $z_{\mathrm{mb}} = 0$ is assumed, implying a strong coupling between the cloud layer and the sub-cloud layer. Parameter v_{rad} is a velocity scale due to radiatively driven entrainment at cloud top

$$v_{\mathrm{rad}}^3 = \frac{g}{\theta_0} z_{\mathrm{i}} \Delta R / (\rho c_p) \tag{3.49}$$

after Lock (1998), where ΔR is the radiative flux jump at cloud top.

Boundary layer top entrainment at $z = z_{\mathrm{i}}$ is explicitly specified as driven by surface for all boundary-layer types and in addition driven by radiation for the Sc layer.

$$\overline{w'\theta'_{\mathrm{v}}}^{\mathrm{entr}} = -0.2\overline{w'\theta'_{\mathrm{v}}}_{\mathrm{surf}} - 0.2 \triangle R / (\rho c_p) = -K_{\mathrm{H,e}} \frac{\partial \theta_{\mathrm{v}}}{\partial z} \approx -K_{\mathrm{H}}^{\mathrm{e}} \frac{\Delta \theta_{\mathrm{v}}}{\Delta z} \equiv w_{\mathrm{e}} \Delta \theta_{\mathrm{v}} \tag{3.50}$$

where w_{e} corresponds to the top entrainment velocity and where the buoyancy jump $\Delta\theta_{\mathrm{v}}$ is discretized using upstream differencing.

For both top driven and entrainment diffusion coefficients the turbulent Prantl number is $Pr = 1.$, i.e.

$$K_{\mathrm{M}} = K_{\mathrm{H}} \tag{3.51}$$

Within the PBL the total diffusion coefficient for h_{l} and q_{t} is specified as

$$K_{\mathrm{H}} = K_{\mathrm{H,surf}} + K_{\mathrm{H,top}} \tag{3.52}$$

while at the top of the PBL

$$K_{\mathrm{H}} = K_{\mathrm{H,e}} \tag{3.53}$$

is used.

3.3.2 The exchange coefficients in stable conditions and in unstable layers situated above the mixed layer

General

In all stable layers (i.e. within or above the boundary layer) and in unstable layers situated above the mixed layer (free-shear layers), the turbulent transports are determined based on local stability with a

first order closure (see Fig. 3.1). The diffusion coefficients depend on shear, on a mixing length and some stability functions of the local Richardson number. The local Richardson number is computed in each vertical layer using

$$\begin{aligned} |\Delta U|^2_{k+1/2} &= (u_k - u_{k+1})^2 + (v_k - v_{k+1})^2 \\ \left(\frac{\Delta s_v}{c_p T}\right)_{k+1/2} &= \frac{2(s_k - s_{k+1})}{(s_k - gz_k + s_{k+1} - gz_{k+1})} + \varepsilon(q_k - q_{k+1}) \\ Ri_{k+1/2} &= (gz_k - gz_{k+1})\frac{\{(\Delta s_v)/(c_p T)\}_{k+1/2}}{|\Delta U|^2_{k+1/2}} \end{aligned} \tag{3.54}$$

In the outer layer, the mixing length used in the surface layer ($l = \kappa z$) is bounded by introducing an asymptotic length scale λ (Blackadar, 1962):

$$\frac{1}{l} = \frac{1}{\kappa z} + \frac{1}{\lambda}. \tag{3.55}$$

The underlying idea is that vertical extent of the boundary layer, or of the free-shear unstable layer, limits the turbulence length scale. The asymptotic length scale has different values in stable and in unstable layers (see below).

The exchange coefficients

(*a*) *M–O similarity for unstable layers with* $Ri < 0$

In these statically unstable layers situated above the mixed layer, the exchange coefficients K_ϕ are based on local similarity (Nieuwstadt, 1984) stating that the expressions of the surface layer similarity can be used in the outer layer (strictly speaking only valid for stable conditions):

$$\begin{aligned} K_M &= \frac{l^2}{\Phi_M^2} \cdot \left|\frac{\partial U}{\partial z}\right| \\ K_H &= \frac{l^2}{\Phi_M \Phi_H}\left|\frac{\partial U}{\partial z}\right| \end{aligned} \tag{3.56}$$

with Φ_M and Φ_H specified in (3.21), where ζ is set to the local Richardson number R_i. The asymptotic mixing length is equal to $150m$.

(*b*) *Revised Louis scheme for stable layers with* $Ri > 0$

The exchange coefficients in the stable layers above the surface are given by

$$\begin{aligned} K_M &= l^2 f_M \left|\frac{\partial U}{\partial z}\right| \\ K_H &= l^2 f_H \left|\frac{\partial U}{\partial z}\right| \end{aligned} \tag{3.57}$$

Below the tropopause, the function for momentum $f_M = f_{LTG,M}$ and heat/humidity $f_H = f_{LTG,H}$ are the Louis, Tiedtke, Geleyn (LTG) stability functions of Ri (Louis *et al.*, 1982), revised by Beljaars (1995); Beljaars and Viterbo (1999); Viterbo *et al.* (1999) in order to enhance turbulent transport in stable layers. These functional dependencies with Ri for momentum $f_{LTG,M}$ and heat/moisture $f_{LTG,H}$ are given by:

$$\begin{aligned} f_{LTG,M}(Ri) &= \frac{1}{1 + 2bRi(1 + dRi)^{-1/2}} \\ f_{LTG,H}(Ri) &= \frac{1}{1 + 2bRi(1 + dRi)^{1/2}} \end{aligned} \tag{3.58}$$

with $b = 5$ and $d = 1$.

Since Cy50r1, the exchange coefficients in stable layers above the tropopause are given by the 'short-tail' functions, such that:

$$f_{\mathrm{M}} = \frac{1}{\Phi_{\mathrm{M}}^2(Ri)}$$
$$f_{\mathrm{H}} = \frac{1}{\Phi_{\mathrm{M}}(Ri)\Phi_{\mathrm{H}}(Ri)} \tag{3.59}$$

where Φ_{M} and Φ_{H} are given by equations 3.23, and ζ is set to the local Richardson number R_i. Note that, unlike equation 3.21 where the relation in equation 3.25 becomes $Ri \equiv \zeta$, equation 3.23 requires us to assume that $Ri \sim \zeta$ above the tropopause in stable conditions, which is a reasonable approximation. The tropopause height is diagnosed at everytime step using the stability definition described in Chapter 6 section 6.12. The $f_{\mathrm{LTG,M}}$ and $f_{\mathrm{LTG,H}}$ functions are then blended with the 'short-tail' functions (equation 3.59) over a depth set by TROP_PRESS_DIFF (currently set to 20hPa) across the tropopause, then returning back to the $f_{\mathrm{LTG,M}}$ and $f_{\mathrm{LTG,H}}$ functions at an altitude set by RDIFF_STRATO_UPPER (currently set to 10hPa). The choice was made to reduce the diffusion across the tropopause in this way in order to improve the amplitude of the winds in the quasi-biennial oscillation in the tropics and to reduce excessive moisture transport across the tropopause in the extratropics.

The asymptotic mixing length is now equal to 10% of the boundary layer height in stable boundary layers; which means that it is small in very stable and shallow boundary layers and it is bigger in weakly stable deeper boundary layers. The boundary layer height is diagnosed as the height where the bulk Richardson number becomes larger than 0.25. In stable layers situated above the boundary layer, the asymptotic mixing length is constant and equal to 30m, a value closer to that used in other NWP models (i.e. UK Metoffice, NCEP GFS) and to observational evidence (Tjernstrom, 1993).

3.4 TURBULENT OROGRAPHIC FORM DRAG (TOFD)

With the introduction of CY31R1, the orographic contribution to the aerodynamic roughness length has been replaced by an explicit specification of stress on model levels due to turbulent orographic form drag (TOFD). The TOFD scheme is based on the work of Wood and Mason (1993) in which the orographic surface drag is parametrized for sinusoidal hills and on the suggestion by Wood *et al.* (2001) to distribute this drag explicitly in the vertical. It is further inspired by the notion that fine scale data sets with sufficient horizontal resolution to compute slope or silhouette parameters on a global scale, are not available. The TOFD scheme, as described in detail by Beljaars *et al.* (2004b), has three key aspects.

First,the orographic spectrum is parameterised and the effect of all the scales is obtained by integrating over the spectrum (5 km down to 10 m). The standard deviation of filtered orography σ_{flt} is used as input for the scheme. It is defined in such a way that it can be measured from the available data at 1 km resolution (see appendix describing the climatological fields).

Secondly, the total drag is represented as a spectral integral over all wave numbers contributing to the variance of the slope. Drag, due to small horizontal orography scales is distributed over a shallow layer, whereas large scales affect deep layers. Convergence problems associated with the variance of the slope when computed as the integral over the spectrum, have been alleviated by including the wind forcing level in the spectral integral. Physically, it means that smaller horizontal scales have a wind forcing at a lower level than the large horizontal scales.

Thirdly, simplifications are applied to avoid explicit evaluation of the integral over the orographic spectrum. For numerical stability it is also necessary to have an implicit formulation that can be solved as part of the vertical diffusion tridiagonal solver.

The parametrization results in the following additional tendency (stress divergence) in the equations for the horizontal wind vector $\vec{U}$

$$\frac{\partial}{\partial z}\vec{\tau}_o/\rho = -2\alpha_{\mathrm{tofd}}\,\beta_{\mathrm{tofd}}\,C_{\mathrm{md}}C_{\mathrm{corr}}\,|\vec{U}(z)|\vec{U}(z)\,\int_{k_o}^{k_\infty}\frac{k^2}{l_{\mathrm{w}}}F_o(k)\,e^{-z/l_{\mathrm{w}}}dk \tag{3.60}$$

with

$$
\begin{aligned}
l_{\mathrm{w}} &= \min(2/k, 2/k_1), \\
F_o(k) &= a_1 k^{n_1}\ , \text{ for } k_o < k < k_1, \\
F_o(k) &= a_2 k^{n_2}\ , \text{ for } k_1 < k < k_\infty, \\
n_1 &= -1.9\ , & n_2 &= -2.8, \\
a_1 &= \sigma_{\mathrm{flt}}^2 (I_H k_{\mathrm{flt}}^{n_1})^{-1}\ , & a_2 &= a_1 k_1^{n1-n2}, \\
k_o &= 0.000628\ \mathrm{m}^{-1}\ , & k_1 &= 0.003\ \mathrm{m}^{-1}, \\
k_{\mathrm{flt}} &= 0.00035\ \mathrm{m}^{-1}\ , & k_\infty &= 2\pi c_{\mathrm{m}}/z_o, \\
I_{\mathrm{H}} &= 0.00102\ \mathrm{m}^{-1}\ , & c_{\mathrm{m}} &= 0.1, \\
\alpha_{\mathrm{tofd}} &= 35\ , & \beta_{\mathrm{tofd}} &= 1, \\
C_{\mathrm{md}} &= 0.005\ , & C_{\mathrm{corr}} &= 0.6.
\end{aligned}
\tag{3.61}
$$

The parameter α_{tofd} was determined from LES data as 12. But during extensive testing an optimal value of $12(1.7)^2 = 35$ was determined that reflects a 70% increase in the standard deviation of filtered orography σ_{flt}. Spectrum $F_o(k)$ of the sub-grid orography is represented with empirical power laws (power n_1 and n_2) in two different scale ranges. The integral of the right hand side of (3.60) can be pre-computed for different heights, without giving a computational burden. However, with hybrid vertical coordinates (as in the ECMWF model), model level heights vary with surface pressure, and therefore it is more convenient to have an analytical expression. A good approximation of (3.60) is

$$
\frac{\partial \vec{U}}{\partial t} = \frac{\partial}{\partial z}\vec{\tau}_{\mathrm{xo}}/\rho = -\alpha_{\mathrm{tofd}}\ \beta_{\mathrm{tofd}}\ C_{\mathrm{md}} C_{\mathrm{corr}}\ |\vec{U}(z)|\vec{U}(z)\ 2.109\ e^{-(z/1500)^{1.5}} a_2 z^{-1.2}
\tag{3.62}
$$

The use of (3.62) rather than (3.60) gives virtually identical results in single column simulations.

The two components of the stress divergence are included in the momentum equations and solved together with the turbulent transport equations. An implicit formulation is needed for stability. The standard way of time stepping a non-linear problem with implicit equations is by evaluating the non-linear part at the old time level and keeping the linear part for the new time level. In this case it means that the absolute wind speed $|U|$ is taken from the old time level and that the $U(z)$ and $V(z)$ components are evaluated implicitly.

With (3.62), and the constants in (3.61), the entire parametrization depends on a single geographical parameter namely the standard deviation of the filtered orography σ_{flt}. Equation (3.62) is written as

$$
\begin{aligned}
\frac{\partial \vec{U}}{\partial t} &= -C_{\mathrm{tofd}}|\vec{U}(z)|\vec{U}(z)\ , \\
C_{\mathrm{tofd}} &= -\alpha_{\mathrm{tofd}}\ \beta_{\mathrm{tofd}}\ C_{\mathrm{md}} C_{\mathrm{corr}}\ 2.109\ e^{-(z/1500)^{1.5}} a_2 z^{-1.2}
\end{aligned}
\tag{3.63}
$$

The expression in (3.63) is computed in subroutine VDFTOFDC. Output $C^*_{\mathrm{tofd}} = C_{\mathrm{tofd}}\alpha\Delta t|\vec{U}(z)|$ is passed to the implicit solver in VDFDIFM.

3.5 SOLUTION OF THE EDMF EQUATIONS

The equations for turbulent transfer are solved simultaneously for diffusion, mass fluxes, TOFD, the implicit and explicit terms from the sub-grid orography scheme ($\beta_{\mathrm{so}}\phi$ and α_{so}), and the tendencies from the adiabatic (subscript 'dyn') and radiative processes (subscript 'rad') as source terms in the right-hand side:

$$
\frac{\partial \phi}{\partial t} = -g\frac{\partial J_\phi}{\partial p} - C_{\mathrm{tofd}}|\vec{U}|\phi - \beta_{\mathrm{so}}\phi + \alpha_{\mathrm{so}} + \left.\frac{\partial \phi}{\partial t}\right|_{\mathrm{dyn}} + \left.\frac{\partial \phi}{\partial t}\right|_{\mathrm{rad}}
\tag{3.64}
$$

Flux J_ϕ (defined down-ward) has a diffusive part and a massflux term:

$$
J_\phi = \rho K\frac{\partial \phi}{\partial z} - M(\phi_{\mathrm{u}} - \phi)
\tag{3.65}
$$

Since the thickness of the model layers Δz is small near the ground and the time step is long, the time-stepping procedure must be implicit in order to avoid numerical instability ($K\Delta t/(\Delta z)^2 > 1$). The advantage of doing the implicit computation with as many processes as possible in a single equation (3.64) is to maintain balance between processes which avoids time step dependence for long time steps. (Beljaars, 1991, Janssen *et al.*, 1992, Beljaars *et al.*, 2004a). Several time discretizations including explicit and implicit solutions can be written by defining a general time level $\hat{\phi}$ and the implicitness factor α.

$$\hat{\phi} \equiv \alpha\phi^{t+1} + (1-\alpha)\phi^t \tag{3.66}$$

For $\alpha = 0$ the scheme is explicit, for $\alpha = 0.5$ we have a Crank–Nicholson and for $\alpha = 1$ we have an implicit backward scheme. In the model, $\alpha = 1.5$, to avoid non-linear instability from the K-coefficients. The diffusion coefficients, mass fluxes and other coefficients are computed from the mean variables at $t-1$ making them explicit. The time tendency can then be written as

$$\frac{\partial\phi}{\partial t} = \frac{\phi^{t+1}-\phi^t}{\triangle t} = \frac{\hat{\phi}-\phi^t}{\alpha\triangle t} = f(\hat{\phi}) + g(\phi^t) \tag{3.67}$$

with implicit terms $f(\hat{\phi})$ and explicit terms $g(\phi^t)$. Equation (3.64) is written in discrete form for $1 < k < n$ model levels using upwind differencing in the mass-flux term:

$$\begin{aligned}\frac{\hat{\phi}-\phi^t}{\alpha\triangle t} = \frac{\Delta\phi_{\rm dyn}}{\triangle t} + \frac{\Delta\phi_{\rm rad}}{\triangle t} &- C_{\rm tofd}|\vec{U}|\hat{\phi}_k - \beta_{\rm so}\hat{\phi}_k + \alpha_{\rm so} \\ &+ \frac{g}{\triangle p_k}\Big(\rho_{k-\frac{1}{2}}K_{k-\frac{1}{2}}\frac{\hat{\phi}_{k-1}-\hat{\phi}_k}{\triangle z_{k-\frac{1}{2}}} - M_{k-1}(\phi_{u,k-1}-\hat{\phi}_{k-1}) \\ &\quad -\rho_{k+\frac{1}{2}}K_{k+\frac{1}{2}}\frac{\hat{\phi}_k-\hat{\phi}_{k+1}}{\triangle z_{k+\frac{1}{2}}} + M_k(\phi_{u,k}-\hat{\phi}_k)\Big)\end{aligned} \tag{3.68}$$

with $\triangle z_{k+\frac{1}{2}} = z_k - z_{k+1}$ (note that z decreases with k) and $\triangle p_k = p_{k+\frac{1}{2}} - p_{k-\frac{1}{2}}$ (note that p increases with k). This can be rewritten as

$$\hat{\phi}_{k-1}A + \hat{\phi}_k B + \hat{\phi}_{k+1}C = RHS \tag{3.69}$$

$$\begin{aligned}A &= \frac{1}{\triangle p_k}\Big(-K^*_{k-\frac{1}{2}} - M^*_{k-1}\Big) \\ B &= \frac{1}{\triangle p_k}\Big(+K^*_{k-\frac{1}{2}} + K^*_{k+\frac{1}{2}} + M^*_k\Big) + 1 + C_{\rm tofd}|\vec{U}|\alpha\Delta t + \beta_{\rm so}\alpha\Delta t \\ C &= \frac{1}{\triangle p_k}\Big(-K^*_{k+\frac{1}{2}}\Big) \\ RHS &= \phi^t_k - \frac{1}{\triangle p_k}M^*_{k-1}\phi_{u,k-1} + \frac{1}{\triangle p_k}M^*_k\phi_{u,k} + \alpha\Delta\phi_{\rm dyn} + \alpha\Delta\phi_{\rm rad} + \alpha_{\rm so}\alpha\Delta t\end{aligned}$$

leading to the inversion of a tridiagonal matrix to solve for $\hat{\phi}$. The coefficients K and M area rescaled for convenience as $K^*_{k+1/2} = K_{k+1/2}\alpha\rho_{k+1/2}\big(\frac{g\Delta t}{\Delta z_{k+1/2}}\big)$ and $M^* = Mg\alpha\Delta t$.

At the lowest level ($k = n$) equation (3.69) is modified for scalars to include the surface fluxes which are obtained in the surface energy balance routine by averaging over $N_{\rm T}$ tiles:

$$\begin{aligned}A &= \frac{1}{\triangle p_n}\Big(-K^*_{n-\frac{1}{2}} - M^*_{n-1}\Big) \\ B &= \frac{1}{\triangle p_n}\Big(+K^*_{n-\frac{1}{2}} + K^*_{n+\frac{1}{2}} + M^*_n\Big) + 1 + C_{\rm tofd}|\vec{U}|\alpha\Delta t + \beta_{\rm so}\alpha\Delta t \\ C &= 0 \\ RHS &= \phi^t_n - \frac{1}{\triangle p_n}M^*_{n-1}\phi_{u,n-1} + \frac{1}{\triangle p_n}M^*_n\phi_{u,n} + \alpha\Delta\phi_{\rm dyn} + \alpha\Delta\phi_{\rm rad} + \alpha_{\rm so}\alpha\Delta t - \frac{g\alpha\Delta t}{\Delta p_n}J_\phi\end{aligned} \tag{3.70}$$

Note that the term $K^*_{n+\frac{1}{2}}$ in B is only used for momentum but not for scalars with a flux boundary condition. The surface flux is a weighted average over the tiles

$$\frac{g}{\Delta p_n}\bar{J}_\phi = +\sum_{i=1}^{N_T} F_i \frac{C^*_{\phi i}}{\alpha \Delta p_n}\{A_{ni}\hat{\phi}_n - A_{\text{surf}i}\hat{\phi}_{\text{surf}i}\} \tag{3.71}$$

with $C^*_{\phi i} = C^{t-1}_{\phi i}|U_n| g\rho\alpha\Delta t$ and

$$\begin{array}{llll} \phi = 0 & A_n = 1 & A_{\text{surf}} = 1 & N_T = 1 \text{ for } \phi = \text{u, v} \\ \phi_{\text{surf}i} = s_{\text{skin}i} & A_{ni} = 1 & A_{\text{surf}i} = 1 & N_T = 8 \text{ for } \phi = \text{s} \\ \phi_{\text{surf}i} = q_{\text{sat}}(T_{\text{skin}i}) & A_{ni} = \alpha_{ni} & A_{\text{surf}i} = \alpha_{\text{surf}i} & N_T = 8 \text{ for } \phi = \text{q} \end{array} \tag{3.72}$$

The downward elimination of the tridiagonal matrix results in linear relations between the lowest model level dry static energy and specific humidity and their fluxes

$$\begin{aligned} \hat{s}_n &= A_s\bar{J}_s + B_s \\ \hat{q}_n &= A_q\bar{J}_q + B_q \end{aligned} \tag{3.73}$$

Coefficients (A's and B's) are passed to the surface energy balance computation for the different tiles, and the resulting weighted fluxes are returned to the tridiagonal solver for upward back-substitution (see Section 3.6).

At the top of the atmosphere $(k = 1)$ turbulent fluxes are set to zero resulting in a modification of equation (3.69) as

$$\begin{aligned} A &= 0 \\ B &= \frac{1}{\triangle p_1}\left(K^*_{1+\frac{1}{2}} + M^*_1\right) + 1 + C_{\text{tofd}}|\vec{U}|\alpha\Delta t + \beta_{\text{so}}\alpha\Delta t \\ C &= \frac{1}{\triangle p_1}\left(-K^*_{1+\frac{1}{2}}\right) \\ RHS &= \phi^t_1 + \frac{1}{\triangle p_1}M^*_1\phi_{u,1} + \alpha\Delta\phi_{\text{dyn}} + \alpha\Delta\phi_{\text{rad}} + \alpha_{\text{so}}\alpha\Delta t \end{aligned} \tag{3.74}$$

The tridiagonal matrix equation is solved by a downward elimination scan followed by back substitution in an upward scan (Press *et al.*, 1992, pp 42–43).

To safeguard against instabilities for the mass-flux term a relaxed CFL criteria of 3 is enforced for M_u

$$M_u < 3\rho\frac{\triangle z}{\triangle t} \tag{3.75}$$

3.6 THE SURFACE ENERGY BALANCE

The surface energy balance is satisfied independently for each tile by calculating its skin temperature. The skin layer represents the vegetation layer, the top layer of the bare soil, or the top layer of the snow pack, has no heat capacity and therefore responds instantaneously to changes in, e.g. radiative forcing. In order to calculate the skin temperature, the surface energy balance equation is linearized for each tile leading to an expression for the skin temperature. This procedure is equivalent to the Penmann–Monteith approach which can be derived by eliminating the skin temperature from the surface energy balance equation assuming that the net radiation minus ground heat flux is known (e.g. Brutsaert, 1982). The approach followed here is an extension to the Penmann–Monteith derivation in the sense that it allows for coupling with the underlying soil (or snow, ice). Because of the short time scale associated with the skin layer, the equation for its temperature is solved implicitly together with the vertical turbulent transport in the boundary layer. In a fully implicit approach, the skin temperatures depend on each other and can not be solved independently. We follow the approach suggested by Best *et al.* (2004) which allows for such a solution. The coupling strategy of Best *et al.* (2004) also provides a well defined

(universal) interface between atmosphere and land surface models, making it possible to have a stand alone library of the land surface code.

The following general discussion applies to each tile but the parameters are tile dependent as discussed in the land surface part of the documentation (Chapter 8). The surface energy balance equation can be written as:

$$\mathfrak{R}_{\rm SW} + \mathfrak{R}_{\rm LW} + H + LJ_q = \Lambda_{\rm skin}(T_{\rm sk} - T_{\rm s}) \tag{3.76}$$

where $\mathfrak{R}_{\rm SW}$ and $\mathfrak{R}_{\rm LW}$ are the net short-wave and long-wave radiation fluxes at the surface and the right-hand side represents the ground heat flux through coupling with the underlying soil, snow or ice with temperature T_s. The turbulent sensible and latent heat fluxes are

$$H = J_{\rm s} \tag{3.77}$$
$$J_{\rm s} = \rho C_{\rm H}|U_n|\{s_n - s_{\rm sk}\} \tag{3.78}$$
$$J_{\rm q} = \rho C_{\rm Q}|U_n|\{\alpha_n q_n - \alpha_{\rm surf} q_{\rm sat}(T_{\rm sk})\} \tag{3.79}$$

The equations for $J_{\rm s}$ and $J_{\rm q}$ are linearized

$$J_{\rm s} = \rho C_{\rm H}|U_n|\{(\hat{s}_n - \hat{s}_{\rm sk}) \tag{3.80}$$
$$J_{\rm q} = \rho C_{\rm Q}|U_n|\left\{\alpha_n \hat{q}_n - \alpha_s q_{\rm sat}(T^t_{\rm sk}) - \alpha_s \frac{dq_{\rm sat}}{dT}\left(\frac{\hat{s}_{\rm sk}}{c^t_p} - T^t_{\rm sk}\right)\right\} \tag{3.81}$$

and written as

$$\begin{aligned} J_{\rm s} &= C_{Js1}S_n + C_{Js2}q_n + C_{Js3}S_{\rm sk} + C_{Js4} \\ J_{\rm q} &= C_{Jq1}S_n + C_{Jq2}q_n + C_{Jq3}S_{\rm sk} + C_{Jq4} \end{aligned} \tag{3.82}$$

with coefficients

$$\begin{aligned} C_{Js1} &= \rho C_{\rm H}|U_n|\,, & C_{Jq1} &= 0 \\ C_{Js2} &= 0\,, & C_{Jq2} &= \rho C_{\rm Q}|U_n|\alpha_n \\ C_{Js3} &= -\rho C_{\rm H}|U_n|\,, & C_{Jq3} &= \rho C_{\rm Q}|U_n|\alpha_s \tfrac{dq_{\rm sat}}{dT} c_p^{-1}\,, \\ C_{Js4} &= 0\,, & C_{Jq4} &= -\rho C_{\rm Q}|U_n|\alpha_s(q_{\rm sat}(T^t_{\rm sk}) - \tfrac{dq_{\rm sat}}{dT}T^t_{\rm sk}) \end{aligned}$$

Substitution of the expression for dry static energy and moisture fluxes in the surface energy balance equation, and linearization of the long wave radiation leads to the following expressions

$$\mathfrak{R}_{\rm SW} + \mathfrak{R}_{\rm LW} + J_{\rm s} + LJ_{\rm q} = \Lambda_{\rm skin}(\hat{T}_{\rm sk} - T_{\rm s}) \tag{3.83}$$

$$\begin{aligned} R_{\rm SW} + R^{\rm trad}_{\rm LW} + \frac{dR_{\rm LW}}{dT_{\rm sk}}(\hat{s}_{\rm sk}/c^t_p - T^{\rm trad}_{\rm sk}) + C_{Js1}\hat{s}_n + C_{Js3}\hat{s}_{\rm sk} + +L(C_{Jq2}\hat{q}_n + C_{Jq3}\hat{s}_{\rm sk} + C_{Jq4}) \\ = \Lambda_{\rm sk}(\hat{T}_{\rm sk} - T_{\rm s}) \end{aligned} \tag{3.84}$$

which is written in the following form

$$\hat{s}_{\rm sk} = D_{ss1}\hat{s}_n + D_{ss2}\hat{q}_n + D_{ss4} \tag{3.85}$$

The coefficients are (using $\hat{s}_{\rm sk} = c^t_p \hat{T}_{\rm sk}$)

$$\begin{aligned} D_{ss1} &= -C_{Js1}Z^{-1} \\ D_{ss2} &= -C_{Jq2}LZ^{-1} \\ D_{ss4} &= (-R_{\rm SW} - R^{-\rm trad}_{\rm LW} + \frac{dR_{\rm LW}}{dT_{\rm sk}}T^{\rm trad}_{\rm sk} - LC_{Jq4} - \Lambda_{\rm sk}T_{\rm s})Z^{-1} \\ Z &= (\frac{dR_{\rm LW}}{dT_{\rm sk}} - \Lambda_{\rm sk})c_p^{-1} + C_{Js3} + LC_{Jq3} \end{aligned} \tag{3.86}$$

With (3.84), $\hat{s}_{\rm sk}$ can be eliminated and the flux equations can be written in the following form.

$$\begin{aligned} J_{\rm s} &= D_{Js1}\hat{s}_n + D_{Js2}\hat{q}_n + D_{Js4} \\ J_{\rm q} &= D_{Jq1}\hat{s}_n + D_{Jq2}\hat{q}_n + D_{Jq4} \end{aligned} \tag{3.87}$$

with

$$\begin{aligned} D_{Js1} &= C_{Js1} + C_{Js3}D_{ss1}\,, \quad D_{Jq1} = C_{Jq1} + C_{Jq3}D_{ss1} \\ D_{Js2} &= C_{Js2} + C_{Js3}D_{ss2}\,, \quad D_{Jq2} = C_{Jq2} + C_{Jq3}D_{ss2} \\ D_{Js4} &= C_{Js3}D_{ss4} + C_{Js4}\,, \quad D_{Jq4} = C_{Jq3}D_{ss4} + C_{Jq4} \end{aligned}$$

With equation (3.87), a linear expression of fluxes is available in terms of lowest model level variables. The grid box average can be obtained by taking the weighted average of the coefficients over the tiles.

$$\begin{aligned} \bar{J}_\mathrm{s} &= \hat{s}_n \sum_i Fr^i D^i_{Js1} + \hat{q}_n \sum_i Fr^i D^i_{Js2} + \sum_i Fr^i D^i_{Js4}\,, \\ \bar{J}_\mathrm{q} &= \hat{s}_n \sum_i Fr^i D^i_{Jq1} + \hat{q}_n \sum_i Fr^i D^i_{Jq2} + \sum_i Fr^i D^i_{Jq4}\,. \end{aligned} \tag{3.88}$$

The over-bar indicates the grid box average of the fluxes. Equation (3.88) can be written as

$$\begin{aligned} \bar{J}_s &= E_{Js1}\hat{s}_n + E_{Js2}\hat{q}_n + E_{Js4}\,, \\ \bar{J}_q &= E_{Jq1}\hat{s}_n + E_{Jq2}\hat{q}_n + E_{Jq4}\,. \end{aligned} \tag{3.89}$$

where the E-coefficients are the grid box averages of the D-coefficients. After the downward elimination of the tridiagonal solver of the vertical turbulent transport a linear relation exists between the lowest model level $\hat{s}_n$, $\hat{q}_n$ and the surface fluxes in the form of equation (3.73).

Together with equation (3.89) it is straightforward to solve for $\bar{J}_\mathrm{s}$,$\bar{J}_\mathrm{q}$, $\hat{s}_n$, and $\hat{q}_n$. With the latter two, back substitution can be started in an upward scan of the vertical turbulent transport equation.

With the lowest model level dry static energy and specific humidity known, it is also possible to solve for all the tile dependent fluxes and skin temperatures using (3.86) and (3.87).

3.7 TRACER DIFFUSION

A detailed description on the modelling of atmospheric composition in the IFS can be found in Part 8 Atmospheric Composition, but a brief description of the turbulent diffusion of tracers is given here. Tracers are diffused in the same way as heat and moisture, but no mass flux term is used. This means that the turbulent diffusion of a tracer with mass mixing ratio C (kg/kg) is given by

$$\frac{\partial C}{\partial t} = \frac{1}{\rho}\frac{\partial}{\partial z}\left(\rho K_C \frac{\partial C}{\partial z}\right) \tag{3.90}$$

Above the surface layer, the exchange coefficient $K_\mathrm{C} = K_\mathrm{H}$, such that the exchange coefficient for tracers is identical to that of heat. The surface boundary condition consists of an externally specified surface flux J_C (positive downwards), but is modified to account for dry deposition using turbulent quantities. The total surface flux is modified thus

$$J_\mathrm{C,Tot} = J_C + \rho V_D C_n \tag{3.91}$$

Here, C_n is the tracer mass mixing ratio at the lowest model level and V_D is the deposition velocity (see section 3.2.1 of Part 8 Atmospheric Composition), given by

$$V_D = \frac{1}{r_a + r_b + r_c} \tag{3.92}$$

$r_a = \frac{1}{C_\mathrm{C}|U_n|}$ is the aerodynamic resistance, which is computed using the first model level windspeed and the surface exchange coefficient for tracers C_C

$$C_\mathrm{C} = \frac{\kappa^2}{\left[\log\left(\frac{z_n+z_{0\mathrm{M}}}{z_{0\mathrm{M}}}\right) - \Psi_\mathrm{M}\left(\frac{z_n+z_{0\mathrm{M}}}{\mathcal{L}}\right) + \Psi_\mathrm{M}\left(\frac{z_{0\mathrm{M}}}{\mathcal{L}}\right)\right]\left[\log\left(\frac{z_n+z_{0\mathrm{M}}}{z_{0\mathrm{M}}}\right) - \Psi_\mathrm{H}\left(\frac{z_n+z_{0\mathrm{M}}}{\mathcal{L}}\right) + \Psi_\mathrm{H}\left(\frac{z_{0\mathrm{H}}}{\mathcal{L}}\right)\right]} \tag{3.93}$$

note the small difference between C_C and C_H from equation 3.17. $r_b = \frac{2}{\kappa u_*}\left(\frac{\epsilon}{D_x}\right)^{2/3}$ is the quasi-laminar resistance, with ϵ being the thermal diffusivity of air and D_x the diffusivity of tracer x in air. Here, u_* is the friction velocity, computed in the post-processing routines using

$$u_* = F_{blend}\frac{\kappa}{\left[\log\left(\frac{z_{blend}+z_{0M}}{z_{0M}}\right) - \Psi_M\left(\frac{z_{blend}+z_{0M}}{\mathcal{L}}\right) + \Psi_M\left(\frac{z_{0M}}{\mathcal{L}}\right)\right]} \tag{3.94}$$

where F_{blend} is the wind at the blending height z_{blend}, see section 3.10.4 for a more detailed description of this. Finally, r_c is the ground/canopy resistance, which depends on the underlying surface and vegetation properties.

As with momentum, heat and moisture the implicit solver uses the dynamics tendency as a source term to obtain balance and small time step dependence for long time steps. The specified surface flux J_C, the deposition velocity ρV_D, the tracer mixing ratios C, the exchange coefficient $K_C = K_H$ and the dynamics tendency of the tracers are all passed to VDFDIFC where the total surface flux $J_{C,\mathrm{Tot}}$ is computed and equation 3.64 is solved for tracers (without contributions from orographic drag or radiation). The implicitness factor α is set to 1, because a higher value is not necessary for stability. It can be demonstrated that implicitness factors larger than 1 can lead to negative tracer mass mixing ratios due to the combination with the dynamics source term.

3.8 TENDENCY CALCULATIONS AND ENERGY DISSIPATION

Total tendencies for wind and total water after the vertical transport (including diffusion and mass-flux terms and also dynamics, radiation, TOFD, and sub-grid orography tendencies) are

$$\begin{aligned}\frac{\partial u}{\partial t} &= \frac{u^{t+1}-u^t}{\Delta t}\\ \frac{\partial v}{\partial t} &= \frac{v^{t+1}-v^t}{\Delta t}\\ \frac{\partial q_t}{\partial t} &= \frac{q_t^{t+1}-q_t^t}{\Delta t}\end{aligned} \tag{3.95}$$

The tendencies and model level fluxes are also computed separately for each process for diagnostic purposes. The surface fluxes of turbulent diffusion plus total TOFD (vertically integrated) are post-processed as turbulent surface drag. The vertically integrated tendency of the sub-grid orography scheme is post-processed as gravity wave stress.

The kinetic energy loss by the mean flow through the diffusion process, and TOFD (E_{diss}), is

$$E_{\mathrm{diss}} = 2\Delta t\left.\frac{\partial u}{\partial t}\right|_{\mathrm{turb+TOFD}}\left(\frac{u^{t+1}+u^t}{2}\right) + 2\Delta t\left.\frac{\partial v}{\partial t}\right|_{\mathrm{turb+TOFD}}\left(\frac{v^{t+1}+v^t}{2}\right) \tag{3.96}$$

The kinetic energy lost is assumed to be transformed locally into internal energy. This procedure by-passes the sub-grid scale energy cascade, but it allows a closed energy cycle in the model (the term is generally small). Therefore

$$\left.\frac{\partial s_l}{\partial t}\right|_{\mathrm{turb+dyn+rad}} = \frac{s_l^{t+1}+E_{\mathrm{diss}}-s_l^t}{\Delta t} \tag{3.97}$$

3.9 PROGNOSTIC TURBULENCE KINETIC ENERGY SCHEME

The prognostic Turbulence Kinetic Energy (TKE) scheme is a higher-order extension of the first-order closure scheme described in Section 3.3. Namely, one second-order moment prognostic equation is used, for the TKE, e_k. TKE represents the sum of sub-grid-scale variances of the wind components:

$$e_k = \frac{1}{2}\left(\overline{u'^2}+\overline{v'^2}+\overline{w'^2}\right). \tag{3.98}$$

Currently, the prognostic TKE scheme is available in the code, but it is deactivated (LECT=.FALSE.) in the operational setup.

The TKE formulation in the IFS model follows the TKE scheme from the ARPEGE model (Cuxart *et al.*, 2000; Marquet, 2008). The exchange coefficients depend on the prognostic TKE according to (Bašták Ďurán *et al.*, 2014):

$$K_M = C_K\, L\, \chi_3\left(Ri_f\right)\sqrt{e_k}, \tag{3.99}$$

$$K_H = C_3\, C_K\, L\, \phi_3\left(Ri_f\right)\sqrt{e_k}, \tag{3.100}$$

where $C_3 = 1.44$ is the inverse Prandtl number at neutrality, $C_K = 0.126$ is a closure constant, and Ri_f is the flux Richardson number:

$$Ri_f = Ri\,\frac{K_H}{K_M}. \tag{3.101}$$

The exchange coefficients computed by the TKE scheme are used in the diffusive part of Eq. 3.1. The mass-flux component of the EDMF method is not affected by the TKE scheme.

Prognostic TKE

The evolution of TKE is governed by

$$\frac{\partial e_k}{\partial t} + ADV(e_k) = \frac{\partial}{\partial z}\left(K_{e_k}\frac{\partial e_k}{\partial z}\right) + ST + BT - \epsilon_k, \tag{3.102}$$

$$ST \equiv -\overline{u'w'}\,\frac{\partial u}{\partial z} - \overline{v'w'}\,\frac{\partial v}{\partial z} = K_M S^2 = K_M\left[\left(\frac{\partial u}{\partial z}\right)^2 + \left(\frac{\partial v}{\partial z}\right)^2\right], \tag{3.103}$$

$$BT \equiv \frac{g}{\theta_v}\,\overline{\theta_v' w'} = -K_H N^2, \tag{3.104}$$

$$\epsilon_k = C_\epsilon\,\frac{e_k^{3/2}}{L}. \tag{3.105}$$

Here $ADV(e_k)$ denotes the advection of TKE by dynamics, ϵ_k is the dissipation rate of TKE, ST is the shear production term, BT is the buoyancy term, S is the vertical wind shear, and $K_{e_k} = 2.7\,K_M$ is the turbulent exchange coefficient for TKE.

To prevent underestimation of shear-generated TKE in strong-shear conditions due to temporal discretization, the source terms are partially replaced by their equilibrium counterparts:

$$ST = \left(R_{eq}K_M^{eq} + (1 - R_{eq})K_M\right)S^2, \tag{3.106}$$

$$BT = \left(R_{eq}K_H^{eq} + (1 - R_{eq})K_H\right)N^2, \tag{3.107}$$

where K_M^{eq} and K_H^{eq} are first-order closure estimates computed according to Section 3.3, and $R_{eq} = 0.5$ is a calibration constant.

Turbulence length scale

The length scale L is computed from its main component, L_{BL}, which is based on the non-local parcel displacement L_{AVG} (Hrastinski *et al.*, 2025):

$$L_{BL} = \frac{\kappa\, C_\epsilon}{\nu_k^3}\, L_{AVG}, \tag{3.108}$$

where $C_\epsilon = 0.871$ and $\nu_k = 0.52$ are closure constants.

The non-local displacement follows Bougeault and Lacarrere (1989): a parcel is lifted or lowered from each model level with TKE as the initial kinetic energy until buoyancy of the environment stops the

motion. This yields upward and downward displacements, L_{up} and L_{dw}, which provide a good measure of the maximum eddy size. Shear effects are added following Rodier *et al.* (2017):

$$\int_{z}^{z+L_{up}} \frac{g}{\theta_{vr}} \left(\theta_v(z) - \theta_v(z') + C_0\sqrt{e_k}\, S(z')\right) dz' = e_k(z), \tag{3.109}$$

$$\int_{z-L_{dw}}^{z} \frac{g}{\theta_{vr}} \left(\theta_v(z) - \theta_v(z') + C_0\sqrt{e_k}\, S(z')\right) dz' = e_k(z), \tag{3.110}$$

where θ_{vr} is a reference virtual potential temperature, and $C_0 = 0.55$ is a calibration constant.

The upward and downward displacements are combined into a single measure:

$$L_1 = \left(C_{up,1} L_{up}^{-2/3} + C_{dw,1} L_{dw}^{-2/3}\right)^{-3/2}, \tag{3.111}$$

$$L_2 = \left(C_{up,2} L_{up}^{-2/3} + C_{dw,2} L_{dw}^{-2/3}\right)^{-3/2}, \tag{3.112}$$

$$L_{AVG} = \max(L_1, L_2), \tag{3.113}$$

where $C_{up,1}$, $C_{up,2}$, $C_{dw,1}$, and $C_{dw,2}$ are calibration constants.

The final length scale is constrained in the surface layer using the von Kármán relationship (L_{surf}), and outside the PBL it transitions to a background length scale (L_b) that represents top entrainment and free-atmospheric turbulent mixing.

$$L = \max\left(\min(L_{surf}, L_b), L_{BL}\right), \tag{3.114}$$

$$z < C_{L1} H_{BL}: \quad L_{surf} = \frac{\kappa\, C_\epsilon}{\nu^3} z, \tag{3.115}$$

$$z > C_{L1} H_{BL}: \quad L_{surf} = 0, \tag{3.116}$$

$$z < C_{L2} H_{BL}: \quad L_b = 0, \tag{3.117}$$

$$z > C_{L2} H_{BL}: \quad L_b = L_{b,0} - \max\left(0, (z_{Lm} - z)\, \frac{L_{b,0} - L_{b,s}}{z_{Lm}}\right), \tag{3.118}$$

where H_{BL} is the boundary-layer height (see Section 3.10), $C_{L1} = 0.12$ is the H_{BL}-relative depth of the surface layer, $C_{L2} = 1.2$ is the H_{BL}-relative depth above the PBL, $z_{Lm} = 10^4$,m, and $L_{b,s} = 65$ m.

Stability parameter

The gradient Richardson number is computed by accounting for the influence of phase changes of water on the Brunt–Väisälä frequency (Marquet and Geleyn, 2013):

$$Ri = \frac{N^2}{S^2}, \tag{3.119}$$

$$N^2 = g\, M(C)\, \frac{c_{pd}}{c_p}\, \frac{\partial \ln \theta_s}{\partial z} + g\, \frac{\partial \ln \theta_s}{\partial z} \tag{3.120}$$

$$+ g\, M(C) \left[F(C) \left(1 + \frac{q}{1-q}\right) \frac{R_{vap}}{R_{dry}(1-q) + R_{vap} q} - 5.87\right] \frac{\partial q_t}{\partial z}, \tag{3.121}$$

$$M(C) = \frac{1 + D_C}{1 + D_C F(C)}, \tag{3.122}$$

$$F(C) = 1 + C^{C_e} \left[\frac{L_{vap}(T) \left(R_{dry}(1-q) + R_{vap} q\right)}{c_p\, T\, R_{vap}} - 1\right], \tag{3.123}$$

$$D_C = \frac{T}{p - e_{sat}(T)}\, \frac{\partial e_{sat}(T)}{\partial T}. \tag{3.124}$$

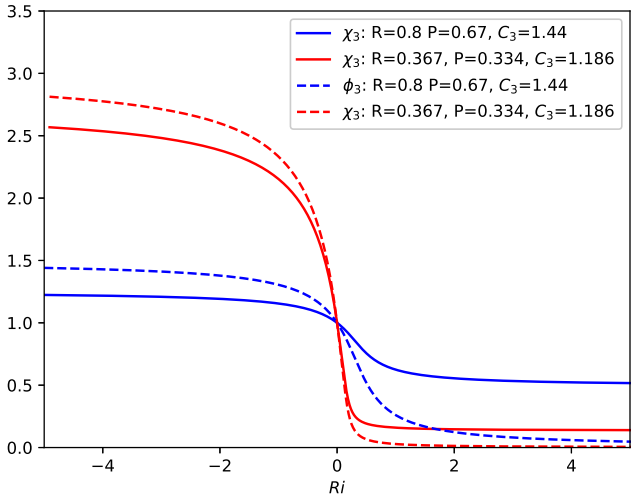

Figure 3.2 *Stability dependency functions for $R = 0.8$, $P = 0.67$, and $C_3 = 1.44$ (blue) and for $R = 0.367$, $P = 0.334$, $C_3 = 1.186$ (red).*

Here C is the prognostic cloud fraction, e_{sat} is the saturation vapor pressure over liquid water, and

$$\theta_s = \theta \exp\left(-\frac{L_{vap} q_l + L_{subl} q_i}{c_{pd} T}\right) \exp(5.87\, q_t) \tag{3.125}$$

is the moist-entropy potential temperature; θ is the potential temperature and c_{pd} is the specific heat of dry air at constant pressure.

The C_e exponent introduces skewness into the cloud-cover–BVF relationship within the convective regime, with the transition controlled by the EIS index:

$$\begin{aligned} \text{Shallow convection:} \quad & EIS < EIS^{\text{StCuL}}: \quad C_e = 0.5, \\ \text{Stratocumulus:} \quad & EIS > EIS^{\text{StCuL}}: \quad C_e = 1.0, \end{aligned}$$

Stability-dependence functions

The stability-dependence functions χ_3 and ϕ_3 follow Bašták Ďurán *et al.* (2014):

$$\chi_3(Ri_f) = \frac{1 - Ri_f/R}{1 - Ri_f}, \tag{3.126}$$

$$\phi_3(Ri_f) = \frac{1 - Ri_f/P}{1 - Ri_f}, \tag{3.127}$$

with $R = 0.8$ and $P = 0.67$ being shape parameters (see Fig. 3.2 for the impact of the shape parameters) satisfying the necessary condition:

$$0 < P < R < 1. \tag{3.128}$$

This yields the following relationship between Ri_f and Ri, where Ri is computed according to Eq. 3.119:

$$\frac{Ri}{Ri_f} = \frac{P\,(R - Ri_f)}{C_3\, R\,(P - Ri_f)}. \tag{3.129}$$

Interaction with the convection scheme

To suppress convective activity and increase cloud cover in stratocumulus regimes, the entrainment rate, ϵ, and cloud-base mass flux, M_{Base}, are modified for mid-level and shallow convection as a function of the EIS index:

$$X_{EIS} = \frac{EIS - EIS^{\text{StCuL}}}{EIS^{\text{StCuH}} - EIS^{\text{StCuL}}}, \tag{3.130}$$

$$S_C = \min\left(1.0, \max\left(0.0, \frac{1.1}{1.0 + 50\,X_{EIS}^2 + 50\,X_{EIS}^3} - 0.1\right)\right), \tag{3.131}$$

$$\epsilon^* = \frac{\epsilon}{\max\left(0.05, S_C\right)}, \tag{3.132}$$

$$M_{\text{Base}}^* = M_{\text{Base}}\,S_C, . \tag{3.133}$$

Additionally, the turbulence length scale is increased between cloud base, z_{Base}, and cloud top, z_{Top}, when the deep-convection parameterization is triggered, to account for enhanced turbulence associated with deep convective activity:

$$L_{DC} = \min\left(L_{DC}^0, z - z_{\text{Base}}, z_{\text{Top}} - z\right), \tag{3.134}$$

$$L^* = \max\left(L, L_{DC}\right), \tag{3.135}$$

where $L_{DC}^0 = 100.0$ m is the maximal turbulence length scale in deep-convection cloud.

3.10 DESCRIPTION OF OUTPUT FIELDS: BOUNDARY LAYER

3.10.1 Diagnostic boundary layer height

Grib code	Short Name	Description	Units
159.128	BLH	Boundary layer height	(m)

Because of its importance for applications (e.g. in air pollution modelling), the boundary layer height is diagnosed and made available for post-processing. The parametrization of the mixed layer uses a boundary layer height from an entraining parcel model. But in order to get a continuous field, also in neutral and stable situations a bulk Richardson method is used as a diagnostic, independent of the turbulence parametrization. This method follows the conclusions of the recent study by Seidel *et al.* (2012).

Seidel *et al.* (2012) evaluated a large number of methods proposed in the literature for estimating the boundary layer height and found that an algorithm based on the bulk Richardson number, originally proposed by Vogelezang and Holtslag (1996), is the most appropriate for application to radiosondes, reanalysis and climate model data sets. Several approximations are applied to the original algorithm, so that it can be consistently applied for both radiosondes and model output. Thus, since the friction velocity is not known from radiosonde data, the surface frictional effects are ignored in the computation of the bulk shear. Similarly, because radiosonde observations do not include winds close to the surface (at 2m), winds at 2m are set to zero. With these assumptions, the boundary layer height h_{BL} is defined as the lowest level at which the bulk R_i reaches the critical value of 0.25. Seidel *et al.* (2012) showed that this algorithm is suitable for both convective and stable boundary layers, identifies a nonnegative height in all cases, and is not strongly dependent on the sounding vertical resolution.

In IFS, the bulk Richardson number is computed as follows.

$$\begin{aligned} |\Delta U|^2 &= u_{\text{hbl}}^2 + v_{\text{hbl}}^2 \\ s_{\text{v}n} &= c_p T_n (1 + \varepsilon q_n) + g z_n \\ s_{\text{vhbl}} &= c_p T_{\text{hbl}} (1 + \varepsilon q_{\text{hbl}}) + g h_{\text{bl}} \\ Ri_{\text{b}} &= H_{\text{bl}} \frac{2g(s_{\text{vhbl}} - s_{\text{v}n})}{(s_{\text{vhbl}} + s_{\text{v}n} - g h_{\text{bl}} - g z_n)|\Delta U|^2} \end{aligned} \tag{3.136}$$

where index n indicates the lowest model level and $H_{\rm bl}$ indicates the boundary layer height, i.e the level where $Ri_{\rm b} = 0.25$. The virtual dry static energy from the lowest level s_{vn} is compared to the virtual dry static energy at the boundary layer height $h_{\rm bn}$. For the buoyancy parameter g/T, T is computed from s and averaged between the lowest model level and the boundary layer height. The boundary layer height is found by a vertical scan from the surface upwards. If the boundary layer height is found to be between two levels a linear interpolation is done to find the exact position.

3.10.2 Temperature and humidity at the 2 m level

Grib code	Short Name	Description	Units
167.128	2T	2m temperature	(K)
168.128	2D	2m dewpoint	(K)
26.228	MX2T3	Maximum temperature at 2m in the last 3 hours	(K)
27.228	MN2T3	Minimum temperature at 2m in the last 3 hours	(K)
121.128	MX2T6	Maximum temperature at 2m in the last 6 hours	(K)
122.128	MN2T6	Minimum temperature at 2m in the last 6 hours	(K)

Computation of temperature and moisture at the 2 m level is based on interpolation between the lowest model level and the surface making use of the same profile functions as in the parametrization of the surface fluxes. In model cycles prior to CY49R1, a limiter on the value of $\frac{z_2+z_{0\rm ma}}{\mathcal{L}}$ was applied, to avoid unrealistic profile shapes with standard stability functions and large temperature errors in case of cloud errors. This had the practical effect that for $\frac{z_2+z_{0\rm ma}}{\mathcal{L}} > 5$, quantities at 2 metre were set equal to the lowest model level ones. Since CY49R1, a modified interpolation function is used, avoiding the abrupt jump to the lowest model level value at a fixed value of stability.

The expressions for s_2 and q_2 are

$$s_2 = s_{\rm surf} + (s_n - s_{\rm surf})\,\alpha_{s_2} \tag{3.137}$$

$$q_2 = q_{\rm surf} + (q_n - q_{\rm surf})\,\alpha_{q_2} \tag{3.138}$$

The interpolation factors, α, are defined as

$$\alpha_i = \beta_i\,(1 - f_{2\rm m}) + \lambda_{2\rm m}\,f_{2\rm m} \quad i = s_2, q_2, \tag{3.139}$$

with

$$f_{2\rm m} = \frac{2}{\pi}\arctan\left(\gamma_{2\rm m}\,\frac{z_2 + z_{0\rm ma}}{\mathcal{L}}\right). \tag{3.140}$$

$\lambda_{2\rm m} = 0.75$ and $\gamma_{2\rm m} = 0.3$ are tunable parameters and the expressions for β are derived from equations (3.13) and (3.14), such that

$$\beta_{s_2} = \frac{\log\left(\frac{z_2+z_{0\rm ma}}{z_{0\rm HWMO}}\right) - \Psi_{\rm H}\left(\frac{z_2+z_{0\rm ma}}{\mathcal{L}}\right) + \Psi_{\rm H}\left(\frac{z_{0\rm HWMO}}{\mathcal{L}}\right)}{\log\left(\frac{z_n+z_{0\rm ma}}{z_{0\rm HWMO}}\right) - \Psi_{\rm H}\left(\frac{z_n+z_{0\rm ma}}{\mathcal{L}}\right) + \Psi_{\rm H}\left(\frac{z_{0\rm HWMO}}{\mathcal{L}}\right)} \tag{3.141}$$

$$\beta_{q_2} = \frac{\log\left(\frac{z_2+z_{0\rm ma}}{z_{0\rm QWMO}}\right) - \Psi_{\rm H}\left(\frac{z_2+z_{0\rm ma}}{\mathcal{L}}\right) + \Psi_{\rm H}\left(\frac{z_{0\rm QWMO}}{\mathcal{L}}\right)}{\log\left(\frac{z_n+z_{0\rm ma}}{z_{0\rm QWMO}}\right) - \Psi_{\rm H}\left(\frac{z_n+z_{0\rm ma}}{\mathcal{L}}\right) + \Psi_{\rm H}\left(\frac{z_{0\rm QWMO}}{\mathcal{L}}\right)} \tag{3.142}$$

with $z_2 = 2$ m. The new approach results in a continuous evolution of the interpolation factor α, avoiding the abrupt change at a fixed value of stability (see also Ingleby *et al.* (2023)).

s_2 and q_2 are computed for each tile, using the surface characteristics of each tile for $z_{0\rm HWMO}$, $z_{0\rm QWMO}$, $s_{\rm surf}$, $q_{\rm surf}$, $\mathcal{L}$. The roughness length for momentum $z_{0\rm ma}$ is the aggregated one as defined in section 8.2.2.

The latter was introduced in CY41R1 (12 May 2015) to keep sufficient mixing for turbulent heat flux in clearings of forests.

Temperature T_2 is derived from s_2 with (3.5). Also the dew point is computed from q_2 and surface pressure. The dew point uses the saturation formulation with respect to water to be consistent with WMO reporting practice. If the resulting dew point is lower than temperature T_2, the dew point is set equal to temperature.

Over land, the output values are tile-averaged. For instance, the diagnostic output of 2 metre temperature is computed as

$$T_2 = \frac{\sum_i Fr^i \; T_{2,i}}{\sum_i Fr^i} \tag{3.143}$$

with Fr the fraction of the grid-box covered by each tile and the sum performed over the active tiles over land. For water tiles (ocean and sea-ice) the dominant tile, with the largest fractional cover, is output.

3.10.3 Wind at 10, 100 and 200 m level and friction velocity

Grib code	Short Name	Description	Units
165.128	10U	10 metre u-wind speed	(m s^{-1})
166.128	10V	10 metre v-wind speed	(m s^{-1})
246.228	100U	100 metre u-wind speed	(m s^{-1})
247.228	100V	100 metre v-wind speed	(m s^{-1})
239.228	200U	200 metre u-wind speed	(m s^{-1})
240.228	200V	200 metre v-wind speed	(m s^{-1})
003.228	ZUST	Friction velocity	(m s^{-1})

Wind at the 10 m level is computed for post-processing because it is the standard level for SYNOP observations. It can be obtained rather easily by vertical interpolation between the lowest model level and the surface, making use of profile functions (3.11) and (3.12). This procedure is appropriate over the ocean or in areas where the surface is smooth and homogeneous. However, the postprocess-ed field is meant to be comparable to wind from SYNOP observations and for observations over land WMO requires SYNOP stations to be in open terrain in order to be well exposed to wind. So the SYNOP wind observations are not necessarily compatible with the wind that is representative for a large area (i.e. a grid box from the model). Over inhomogeneous terrain, the problem can be particularly serious, because the "aerodynamic roughness length" in the model is adjusted to provide sufficient drag at the surface which is dominated by the rough elements. This approach leads to a low area-averaged wind speed which is not comparable to the "open-terrain" wind speed as observed by WMO stations.

In order to make the postprocess-ed wind compatible with SYNOP observations, the concept of exposure correction is introduced. The open-terrain wind is obtained by taking the wind information from such a height above the surface that it is less influenced by the underlying terrain. This height is called the blending height $z_{\rm blend}$ and for the interpolation to 10 m an aerodynamic roughness length is used that is typical for open terrain with grassland.

The interpolation procedure is as follows. First the blending height and the interpolation roughness length are set dependent on the model roughness length field using

$$\begin{array}{llll} z_{\rm blend} = 40 & z_{\rm 0MWMO} = 0.03 & F_{\rm blend} = (u^2_{\rm blend} + v^2_{\rm blend})^{1/2} & \text{if } z_{0M} > 0.03 \\ z_{\rm blend} = z_n & z_{\rm 0MWMO} = z_{\rm 0M} & F_{\rm blend} = (u^2_n + v^2_n)^{1/2} & \text{if } z_{\rm 0M} < 0.03 \end{array} \tag{3.144}$$

$$F_{10} = F_{\rm blend} \frac{\log\left(\frac{z_{10}+z_{\rm 0MWMO}}{z_{\rm 0MWMO}}\right) - \Psi_{\rm M}\left(\frac{z_{10}+z_{\rm 0MWMO}}{\mathcal{L}}\right) + \Psi_{\rm M}\left(\frac{z_{\rm 0MWMO}}{\mathcal{L}}\right)}{\log\left(\frac{z_{\rm blend}+z_{\rm 0MWMO}}{z_{\rm 0MWMO}}\right) - \Psi_{\rm M}\left(\frac{z_{\rm blend}+z_{\rm 0MWMO}}{\mathcal{L}}\right) + \Psi_{\rm M}\left(\frac{z_{\rm 0MWMO}}{\mathcal{L}}\right)} \tag{3.145}$$

where $z_{10} = 10$ m, $u_{\rm blend}$,$v_{\rm blend}$ are the wind components at the blending height after interpolation from model levels to 40 m or copied from the lowest model level, $u_{\rm n}$,$v_{\rm n}$, are the wind components at the

lowest model level, F_{blend} is the horizontal wind speed at the blending height, and F_{10} is the resulting horizontal wind speed at 10 m.

The 10-metre equivalent-neutral wind is calculated as:

$$F_{10}^{n} = F_{\text{blend}} \frac{\log\left(\frac{z_{10}+z_{0\text{MWMO}}}{z_{0\text{MWMO}}}\right)}{\log\left(\frac{z_{\text{blend}}+z_{0\text{MWMO}}}{z_{0\text{MWMO}}}\right) - \Psi_{\text{M}}\left(\frac{z_{\text{blend}}+z_{0\text{MWMO}}}{\mathcal{L}}\right) + \Psi_{\text{M}}\left(\frac{z_{0\text{MWMO}}}{\mathcal{L}}\right)}, \tag{3.146}$$

and the friction velocity u_* as:

$$u_* = F_{\text{blend}} \frac{\kappa}{\log\left(\frac{z_{\text{blend}}+z_{0\text{MWMO}}}{z_{0\text{MWMO}}}\right) - \Psi_{\text{M}}\left(\frac{z_{\text{blend}}+z_{0\text{MWMO}}}{\mathcal{L}}\right) + \Psi_{\text{M}}\left(\frac{z_{0\text{MWMO}}}{\mathcal{L}}\right)}. \tag{3.147}$$

The wind speed from (3.145, 3.146) is converted to components by making use of the wind direction from the lowest model level.

Finally, the wind components at the 100 and 200 m levels have been added in order to provide wind forecasts at a typical wind turbine height. The u and v wind components at the 100 and 200 m level are simply obtained by a linear interpolation in height of the wind components at the respective two adjacent model levels.

3.10.4 Wind gusts

Grib code	Short Name	Description	Units
29.228	I10FG	Instantaneous 10m wind gust	(m s^{-1})
28.228	10FG3	Maximum 10 metre wind gust in the last 3 hours	(m s^{-1})
123.128	10FG6	Maximum 10 metre wind gust in the last 6 hours	(m s^{-1})

The computation of gusts is intended to be compatible with WMO observing practice for wind extremes. In order to get uniform observations, WMO defines a wind gust as the maximum of the wind averaged over 3 second intervals.

To simulate gusts, the standard deviation of the horizontal wind is estimated on the basis of the similarity relation by Panofsky *et al.* (1977)

$$\begin{aligned} \sigma_{\text{u}} &= 2.29 u_* f(z_{\text{i}}/\mathcal{L}) && \text{for } \mathcal{L} < 0 \\ \sigma_{\text{u}} &= 2.29 u_* && \text{for } \mathcal{L} > 0 \\ f(z_{\text{i}}/\mathcal{L}) &= \left(1 - \tfrac{0.5}{12}\tfrac{z_{\text{i}}}{\mathcal{L}}\right)^{1/3} \end{aligned} \tag{3.148}$$

with $z_{\text{i}} = 1000$ m. The difference between the gust and F_{10} is proportional to σ_{u}, where the multiplier has been determined from universal turbulence spectra for a 50% exceeding probability of the three-second wind gust (see Beljaars, 1987). The resulting wind gust is

$$F_{\text{gust}} = F_{10} + C_{\text{ugn}} u_* f(z_{\text{i}}/\mathcal{L}) \tag{3.149}$$

with parameter $C_{\text{ugn}} = 7.2$ (7.71 before Cy47r3) and u_* from the surface stress as computed in the vertical turbulent transport code. The value of C_{ugn} is obtained from the gust model with a time series length of 2200 s which corresponds to a horizontal length scale of 22 km at 10 m/s following the Taylor frozen turbulence assumption.

From the controlling parameters it is clear that the effects of surface friction (through surface roughness) and stability are captured. However, the approach is not adequate for gusts in baroclinic situations and where gusts are due to strong convective events. Therefore, in the presence of deep convection, a convective contribution as a function of the vertical wind shear (Bechtold and Bidlot, 2009) is added to the turbulence gustiness (3.149) so that the total gustiness becomes

$$F_{\rm gust} = F_{10} + C_{\rm ugn} u_* f(z_{\rm i}/\mathcal{L}) + C_{\rm conv} \max(0, U_{850} - U_{950}) \tag{3.150}$$

where the convective mixing parameter $C_{\rm conv} = 0.3$ (0.6 prior to Cy47r3), and U_{850} and U_{950} are the wind speeds at 850 and 950 hPa, respectively. Parameter $F_{\rm gust}$ is computed every time step (I10FG) and its maximum during the last post-processing period calculated (10FG3, 10FG6).

3.10.5 Clear air turbulence (CAT)

Grib code	Short Name	Description	Units
290.260	CAT	Turbulence parameter in units of eddy dissipation rate	($m^{2/3}$ s^{-1})

A clear air turbulence (CAT) parameter that is equivalent to the cube root of the eddy dissipation rate (EDR) has been implemented in Cy47r3 based on the total dissipation rate of the IFS. The development of this parameter and its evaluation using civil aircraft data is described in (Bechtold *et al.*, 2021). CAT comprises contributions from the vertical diffusion scheme (vdf), including turbulent mixing, orographic wave drag and orographic blocking, as well as dissipation due to convective momentum transport (cu) and convective gravity wave drag (GWD).

$$\mathrm{DISS} = \left| u \frac{\partial u}{\partial t}|_{\rm vdf} + v \frac{\partial v}{\partial t}|_{\rm vdf} \right|^{1/3} + \left| u \frac{\partial u}{\partial t}|_{\rm cu} + v \frac{\partial v}{\partial t}|_{\rm cu} \right|^{1/3} + \mathrm{GWD} \tag{3.151}$$

While the convective momentum tendencies correspond to that defined in (6.1), the GWD term is a scaled form of (5.13)

$$\mathrm{GWD} = \left(\left| u \frac{\partial u}{\partial t}|_{\rm gwd} + v \frac{\partial v}{\partial t}|_{\rm gwd} \right| \hat{T}_{\rm cu} \right)^{1/3}; \quad \hat{T}_{\rm cu} = -\frac{c_{\rm p}}{\hat{T}_0} \int_{p=500}^{top} \frac{\partial T}{\partial t}|_{\rm cu} \frac{dp}{g} \tag{3.152}$$

where the subscript gwd denotes the tendencies (wave drag) from the non-orographic wave scheme and the subscript cu the temperature tendency from the convection parametrization; $\hat{T}$ is normalised by $\hat{T}_0$ =1 W m^{-2}.

The dissipation is projected onto the climatological distribution of the EDR as observed by civil aircraft following the method proposed by Sharman and Pearson (2017). We precomputed the climatological distribution of DISS on model levels and then fitted a log-normal probability distribution to its climatological distribution (see Figure 1 in Bechtold *et al.* (2021))

$$Y = \frac{1}{\sqrt{2\sigma^2 \pi}} \exp\left(-\frac{(X-\mu)^2}{2\sigma^2} \right); \quad \mu = < \ln(x) > \tag{3.153}$$

where X=ln(x), x=DISS. The parameters μ and σ^2 represent the mean and variance, respectively and have been determined as $\mu = -3.30$ and $\sigma^2 = 0.60$.

Having precomputed the log-normal fits the projection onto the climatological EDR is then obtained as

$$\ln(y^*) = a + b \ln(x); \quad y^* = e^a \ x^b \tag{3.154}$$

where y* is the final, projected value of DISS onto the climatological EDR using the transformation coefficients

$$b = \frac{c2}{\sigma}; \quad a = c1 \ - b \ \mu \tag{3.155}$$

and $c1 = -2.57$ and $c2 = 0.51$ are constants representing the climatological mean and standard deviation of the EDR as proposed in Sharman and Pearson (2017).

Finally, an additional calibration is applied to obtain CAT as CAT=0.66 y^*.

Grib code	Short Name	Description	Units
003.020	VIS	Visibility	(m)

3.10.6 Visibility

A visibility diagnostic was introduced in IFS Cycle 41r1, operational at ECMWF from 12 May 2015. The diagnostic represents near surface horizontal visibility, equivalent to the visibility observations recorded in SYNOP reports.

A number of meteorological factors influence visibility, including the presence of small droplets (fog), precipitation and aerosol. The impact of aerosol is dependent on the environmental humidity as hygroscopic aerosol can increase in size through condensational growth to form small haze particles. The IFS predicts water vapour, cloud liquid water content, ice water content, rain and snow, but relies on a seasonally varying climatological distribution of aerosol species (organic, sulphate, sea salt, dust, black carbon). So in principle the IFS is able to represent the reduced visibility effects of fog, precipitation and humidity (based on a seasonally varying aerosol climatology), but not local deviations of the aerosol fields such as significant air pollution in high pressure situations over land.

Fog, in particular, is an extremely important but difficult weather hazard to predict. The new diagnostic includes information on the reduced visibility in fog, which is usually defined as visibility less than a kilometre. However, correctly predicting the formation and breakup of fog is dependent on an accurate representation of the surface characteristics (e.g. soil moisture and temperature), dynamic and thermodynamic conditions in the boundary layer and interactions with the radiation. Fog can be highly variable in space and time, often tied to orographic features that are not resolved by the model, so the representativity errors may be locally significant even if the mean conditions on the resolved scales of the model are accurately predicted. Given the large uncertainties if fog prediction, a probabilistic approach using the ensemble members will be of most benefit.

Visibility is diagnosed for the lowest model level (at 10 m, nominally representing the lowest 20 m of the atmosphere) by calculating a total extinction coefficient, β_{tot}, for optical wavelengths in the atmosphere, and assuming a visual range defined by a fixed liminal contrast ϵ. The visibility, V (in metres), is defined as

$$V = -(ln\ \epsilon)/\beta_{tot} \tag{3.156}$$

where ϵ is set to 0.02, a value originally proposed by Koschmieder (1924) and widely used since then for visibility definition. The total extinction coefficient is a sum of components from clean air, aerosol, cloud and precipitation,

$$\beta_{tot} = -\beta_{air} + \beta_{aerosol} + \beta_{cloud} + \beta_{precip} \tag{3.157}$$

These extinction coefficients contain the overall effect of the complexities of the aerosol and hydrometeor size spectra and scattering properties on the optical wavelengths.

The extinction coefficient of clean air is small and has little practical value, so following Clark *et al.* (2008) it is taken to be equivalent to a visibility of 100 km (10^5 m), which defines the maximum visibility that can be diagnosed,

$$\beta_{air} = (ln\ \epsilon)/10^5 \tag{3.158}$$

The extinction coefficient for aerosols contains a contribution from different aerosol species, including sea salt, dust, black carbon, organic, sulphates and includes a fixed term that represents unspecified tropospheric background aerosol,

$$\beta_{aerosol} = \beta_{seasalt} + \beta_{dust+} + \beta_{blackcarbon} + \beta_{organic} + \beta_{sulphates} + \beta_{background} \tag{3.159}$$

The operational IFS does not currently have prognostic aerosol species, but relies on a seasonally varying climatology for the direct radiative impact of aerosols in the radiation scheme. In IFS Cycle 43r1, the 2D monthly mean aerosol optical thickness climatology from Tegen *et al.* (1997) is used and is extended into the vertical assuming a fixed function that decays with height. The aerosol optical thickness (for a wavelength band of 0.44 to 0.63 μm) in the lowest model layer is used for the visibility diagnostic,

consistent with the aerosol used in the radiation parametrization. A different (fixed) relative humidity (with respect to water) is assumed for the computations of the relevant optical properties for each aerosol type: sea salt (95%), dust (50%), black carbon (80%), organic (80%), sulphates (95%). The background aerosol is assumed to have a fixed optical thickness of 0.03.

The extinction coefficients for cloud and precipitation are expressed as a sum of the extinction coefficients for the four prognostic grid-box mean variables in the IFS: cloud liquid water, cloud ice, rain and snow.

$$\beta_{cloud} + \beta_{precip} = \beta_{liq} + \beta_{ice} + \beta_{rain} + \beta_{snow} \tag{3.160}$$

The formulation of the extinction coefficients changed in Cycle 47r3 and both sets are described below.

(a) IFS Cycle 41r1 to Cycle 47r2

The extinction coefficient for cloud and precipitation hydrometeors uses the same formulation as the radiation scheme in the IFS. The parametrization takes the following functional form:

$$\beta_{liqice} = Q(a_0 + a_1/r_e) \tag{3.161}$$

where Q is the hydrometeor water content (g m^{-3}), r_e is the effective radius (μm) of the particle size distribution, and the coefficients a_0 (m^2 g^{-1}) and a_1 (μm m^2 g^{-1}) are obtained by numerical fitting to the single scattering properties computed from accurate light scattering and absorption calculations for the visible wavelength band (0.48 - 0.52μm).

For liquid cloud (fog), based on Slingo (1989) and Slingo and Schrecker (1982),

$$\beta_{liq} = Q_l(0.02672 + 1.32/r_e) \tag{3.162}$$

where Q_l is the predicted cloud liquid water content and a fixed effective radius of r_e = 10 μm is assumed, although this is probably an overestimate for the typical size of fog particles.

For cloud ice (freezing fog), the extinction formulation in the radiation scheme is also used for the visibility calculation. This follows Fu (1996) and has the same form as Eq. (3.161), except using the ice water content (g m^{-3}) and coefficients,

$$\beta_{ice} = Q_i(-9.45458 \times 10^{-5} + 2.52061/r_e) \tag{3.163}$$

where Q_i is the predicted cloud ice water content and a fixed effective radius of r_e = 60 μm is assumed

The formulation and coefficients used for cloud liquid and ice are also used for rain (β_{rain}) and snow (β_{snow}) respectively, but with a much larger particle size (1000 μm for rain and 2000 μm for snow).

(b) IFS Cycle 47r3 onwards

For liquid cloud (fog), the extinction coefficient (m^{-1}) is based on Gultepe *et al.* (2006),

$$\beta_{liq} = -\frac{ln\,\epsilon}{1.002 \times 10^3}(Q_l N_l)^{0.6473} \tag{3.164}$$

where Q_l is the predicted cloud liquid water content (in kg m^{-3}) and N_l is the number concentration of cloud droplets (in m^{-3}), assumed to be a constant 50 cm^{-3} (= 50×10^6 m^{-3}).

For ice cloud (fog), the extinction coefficient (m^{-1}) is based on Stoelinga and Warner (1999). The relationship is derived from the mass-diameter relationship of Rutledge and Hobbs (1983) assuming randomly oriented two-dimensional plates.

$$\beta_{ice} = 163.9 \times 10^{-3} Q_i \tag{3.165}$$

where Q_i is the predicted cloud ice content (kg m^{-3}).

For rain, the extinction coefficient (m^{-1}) is based on Stoelinga and Warner (1999) but with the leading constant increased from 2.24 to 5.0 to better fit the observed visibility,

$$\beta_{rain} = 5.0 \times 10^{-3} Q_r^{0.75} \tag{3.166}$$

where Q_r is the predicted cloud ice content (kg m^{-3}).

For snow, the extinction coefficient (m^{-1}) is based on Stallabrass (1985) and Stoelinga and Warner (1999) but with the leading constant reduced from 10.4 to 4.0 to better fit the observed visibility,

$$\beta_{snow} = 4.0 \times 10^{-3} Q_s^{0.78} \tag{3.167}$$

where Q_s is the predicted cloud ice content (kg m^{-3}).

3.11 CODE

Vertical turbulent transports, which affect temperature, velocities and specific humidity, is performed in subroutine VDFMAIN called by VDFOUTER which, in turn, is called by CALLPAR. All the routines for the surface energy balance and for the interaction between the lowest model level and the surface, are in the SURF library. Transfer of information between the IFS and the SURF library is limited to a few interaction routines. The other SURF routines can not be called by the IFS.

At the start of the model integration the following setup routines are called to initialize modules specific to the vertical transport code:

- SUVDF. Setup routine for a number of parametrization constants.
- SUVDFS. Setup routine for constants and tables related to the stability functions. Stability functions are included as statement functions from fcvds.h.
- SUSVEG. Is part of the SURF library and sets a number of vegetation and tile parameters.
- SU0PHY. Activation (LECT) and adjustment of the prognostic TKE scheme.
- SUPHY0. If the prognostic TKE scheme is activated (LECT=.TRUE.) this routine sets a number of parametrization constants.

The main subroutine (VDFMAIN) does a sequence of computations and subroutine calls:

- SURFEXCDRIVER. This is the first call to the SURF library to prepare all the necessary parameters for exchange with the surface. The tiled surface fluxes and tiled skin temperatures are cycled from time step to time step (fluxes are needed for the first guess of stability parameters), but are not available at the start of the forecast. For the first time step, neutral transfer coefficients are used to estimate momentum fluxes, the tiled skin temperatures are set equal to the grid box averaged skin temperature from the initial condition, and the sensible and latent heat fluxes needed as a first guess for the Obukhov length computation are set to zero. SURFEXCDRIVER calls a number of subroutines from the SURF library.
  - VUPDZ0. This routine computes roughness lengths for momentum, heat and moisture over ocean surfaces according to (3.28). It also computes surface buoyancy flux and Obukhov length from the fluxes of the previous time level.
  - VSURF. This routine prepares the surface boundary conditions for temperature and humidity and is called for every tile. The following quantities are computed: the surface specific humidity at saturation, the derivative of the saturation humidity curve at the surface, surface dry static energy, and vegetation stomatal resistances (see Chapter 8).
  - VEXCS. This routine determines the transfer coefficients between the surface and the lowest model level with the thermal stability expressed as function of the Obukhov length. It is called for every tile. The implicit relation between $z/\mathcal{L}$ and the Richardson number Ri_{bulk} is solved iteratively (using the Newton method with the derivative approximated in finite differences). Pre-computed tables defined in subroutine SUVDFS are used to obtain the first guess in stable conditions ($Ri > 0$) at the first time step. Transfer coefficients are multiplied by a constant factor $\alpha\rho g \frac{\Delta t}{\Delta z}$.
  - VEVAP. This routine computes for each tile the equivalent evapo-transpiration efficiency and the corresponding parameters a_n and a_{surf} defined by the land surface scheme (see chapter 8). Dry static energy at the surface at time level t is estimated as well.
  - VSFLX. This routine computes surface fluxes for each tile (heat flux, evaporation, momentum flux and virtual heat flux) at time t for later use in similarity functions and for the estimation of the diagnostic boundary layer depth.
- VDFDPBL. This routine diagnoses the boundary layer height for time level t. This boundary layer height is for post-processing only and is not used by the parametrization.
- VDFHGHTN. This routine calls an entraining plume model to determine updraught properties, cloud base and cloud top and computes convective boundary layer height and convective mass flux.
  - CUININ. Initializes environmental half levels.

  - CUBASEN. Computes parcel ascent and updraught properties.
- VDFEXCU. This routine determines the turbulent diffusion coefficients between the model levels above the surface layer.
- VDFTKE. This routine determines the turbulent diffusion coefficients between the model levels above the surface layer if the prognostic TKE scheme is activated (LECT=.TRUE.). It calls :
  - ACTKEIFS. This routine is an interface routine between VDFTKE and the ARPEGE code TKE scheme subroutines:
    * ACBL89. This routine computes the turbulence length scale, stability parameter and stability dependency functions.
    * ACTURB. This routine computes the turbulence exchange coefficients.
    * ACEVOLET. This routine solves the prognostic TKE equation.
- VDFTODC. This routine computes coefficients for turbulent orographic form drag.
- VDFDIFM. This routine solves the diffusion equation for momentum, by Gaussian elimination of the tridiagonal matrices.
- VDFDIFH. This routine solves the EDMF equations for total water and liquid water static energy. A downward elimination scan is done through the tridiagonal matrices, and coefficients A_s, B_s, A_q, and B_q are computed. Then, a call is made to SURF routine SURFSEB to compute the surface fluxes for heat and moisture. Also the tiled fluxes are returned.
- VDFDIFC. Routine solves the diffusion equations for passive tracers. A specified flux at the surface is used as a boundary condition.
- VDFINCR. This routine computes the tendencies of the prognostic variables and estimates the kinetic energy dissipation.
- VDFFBLEND. This routine computes the blending height.
- SURFPP. This is the routine from the SURF library for the interpolation of SYNOP parameters. It calls:
  - SPPCFL. This routine computes the surface 2 metre temperature and humidity (dew point and specific humidity), the wind at 10 m, the equivalent-neutral wind at 10m, and the friction velocity.
  - SPPGUST. This routine computes wind gusts as they are typically observed by standard WMO SYNOP stations.
  - VDFVINT. This routine computes the wind components at the 100 and 200 m level, respectively.

APPENDIX A. LIST OF SYMBOLS

a_{u}	updraught fraction
C	prognostic cloud fraction
C_0	calibration constant
C_3	inverse Prandtl number at neutrality
$C_{dw,1}$	calibration constant
$C_{dw,2}$	calibration constant
C_e	cloud cover skewness parameter
C_ϵ	closure constant
$C_{up,1}$	calibration constant
$C_{up,2}$	calibration constant
C_{H}	transfer coefficient for heat
C_{K}	closure constant
C_{L1}	H_{BL}-relative depth of the surface layer
C_{L2}	H_{BL}-relative depth above the PBL
C_{M}	transfer coefficient for momentum (drag coefficient)
C_{Q}	transfer coefficient for moisture
C_{C}	transfer coefficient for tracers
c_p	specific heat at constant pressure of moist air

c_{pd}	specific heat of dry air at constant pressure
E_{diss}	kinetic energy lost by the diffusion process
e_{k}	Turbulence Kinetic Energy (TKE)
e_{sat}	saturation vapor pressure over liquid water
EIS^{StCuL}	lowest value of EIS for StCu region
EIS^{StCuH}	highest value of EIS for StCu region
f	Coriolis parameter
F_{blend}	horizontal wind speed at blending height (for pp of 10 m wind)
F_{10}	horizontal wind speed at 10 m level (for pp)
g	acceleration of gravity
h_{l}	generalized liquid water static energy
h_{e}	generalized moist entropy
H_{BL}	diagnosed boundary layer height
J_ϕ	vertical turbulent flux of ϕ
J_{q}	surface humidity flux
J_{s}	surface flux of dry static energy
J_{M}	surface momentum flux
K_ϕ	turbulent exchange coefficient for ϕ
K_{e_k}	turbulent exchange coefficient for TKE
K_{H}	turbulent exchange coefficient for heat
K_{H}^{eq}	equilibrium turbulent exchange coefficient for heat
K_{M}	turbulent exchange coefficient for momentum
K_{M}^{eq}	equilibrium turbulent exchange coefficient for momentum
K_{Q}	turbulent exchange coefficient for moisture
$\mathcal{L}$	Obukhov length
L	turbulence length scale
L_{AVG}	non-local parcel displacement
L_b	background turbulence length scale
$L_{b,s}$	asymptotic value for background turbulence length scale
L_{BL}	Bougeault and Lacarrere turbulence length scale
L_{DC}^0	maximal turbulence length scale in deep convection cloud
L_{surf}	surface layer turbulence length scale
L_{up}	upward displacement
L_{dw}	downward displacement
L_{vap}	latent heat of vaporisation
L_{subl}	latent heat of sublimation
l_{H}	mixing length for heat
l_{M}	mixing length for momentum
M	mass flux
M_{Base}	cloud base mass flux
N_{T}	number of tiles
p	pressure
P	shape parameter for stability function for heat and moisture
Pr	Prandtl number
q	specific humidity
q_l	specific liquid water
q_{i}	specific ice water
q_{t}	specific total water $= q + q_l + q_{\text{i}}$
q_{sat}	saturated specific humidity
q_*	$= J_{\text{q}}/(\rho u_*)$
ΔR	radiative flux jump at cloud top
$Q_{0\text{v}}$	virtual temperature flux in the surface layer
R	shape parameter for stability function for momentum
R_{eq}	calibration constant
R_{dry}	gas constant for dry air

R_{vap}	gas constant for water vapour
$\mathfrak{R}_{\text{LW}}$	net long-wave radiation at the surface
$\mathfrak{R}_{\text{SW}}$	net short-wave radiation at the surface
RH_{surf}	relative humidity at the surface
Ri	local Richardson number
Ri_f	flux Richardson number
Ri_{bulk}	bulk Richardson number for the surface layer
s	dry static energy
S	vertical wind shear
s_{v}	virtual dry static energy
s_*	$= J_{\text{s}}/(\rho u_*)$
T	temperature
t	time
$\lvert U\rvert$	horizontal wind speed
u, v	horizontal wind components
v_{rad}	radiative velocity scale
u_*	friction velocity $= (J_{\text{M}}/\rho)^{1/2}$
w_*	free convection velocity scale
w_{e}	entrainment velocity
$z_{0\text{M}}$	roughness length for momentum (aerodynamic roughness length)
$z_{0\text{H}}$	roughness length for heat
$z_{0\text{Q}}$	roughness length for moisture
z_{i}	scale height of the boundary layer
z_{cb}	height of convective cloud base
z_{blend}	blending height (for pp of 10 m wind)
z_{Lm}	height at which L_b reaches asymptotic value
z_n	height of the lowest model level n
$z_{0\text{MWMO}}$	roughness length for momentum at SYNOP station
$z_{0\text{HWMO}}$	roughness length for heat at SYNOP station
$z_{0\text{QWMO}}$	roughness length for moisture at SYNOP station
z_2	height of screen level observation (2 m)
z_{10}	height of surface wind observation (10 m)
α	implicitness factor for diffusion equation
α_{Ch}	Charnock parameter
β	scaling parameter for asymptotic mixing length
Δt	time step
Δz	vertical grid length
ε	$= (R_{\text{vap}}/R_{\text{dry}}) - 1$
ε	parcel entrainment
ϵ_k	dissipation rate of TKE
θ_{v}	virtual potential temperature
θ_{vr}	reference virtual potential temperature
κ	Von Kármán's constant
λ	asymptotic mixing length
Λ_{skin}	thermal conductivity of air
ν	kinematic viscosity
ν_k	closure constant
ρ	density
σ_{qt}	standard deviation of total water
σ_{u}	standard deviation of horizontal wind
σ_{w}	standard deviation of vertical wind
ζ	$= z/\mathcal{L}$
ϕ	symbolic reference to a conservative quantity
Φ_{M}	universal gradient stability function for wind
Φ_{H}	universal gradient stability function for temperature

Φ_Q	universal gradient stability function for moisture
Ψ_M	universal profile stability function for wind
Ψ_H	universal profile stability function for temperature
Ψ_Q	universal profile stability function for moisture

Subscripts:

i	tile index
k	level index (counted from model top downwards)
n	referring to lowest model level
skin	referring to the skin layer
surf	referring to the surface
u	referring to the updraught
e	referring to the environment

Superscripts:

t	index for old time level, indicating beginning of time step
$t+1$	index for new time level, indicating end of time step
trad	index referring to the latest full radiation time step

Special symbols:

$\hat{\phi}$	implicit variable ϕ defined by equation (3.66)

Chapter 4

Subgrid-scale orographic drag

Table of contents

4.1 General principles
4.2 Description of the scheme
4.2.1 Blocked-flow drag
4.2.2 Gravity-wave drag
4.3 Specification of subgrid-scale orography
4.4 Code
4.4.1 GWSETUP
4.4.2 GWPROFIL
4.4.3 GWDRAG
Appendix A. List of symbols

4.1 GENERAL PRINCIPLES

The subgrid-scale orography intersects model levels, and consequently influences the momentum of the atmosphere, and hence other parts of the physics. In the model stably stratified flow over the subgrid-scale orography creates drag through a combination of low-level flow blocking (i.e. blocked-flow drag) and the absorption and/or reflection of vertically propagating gravity waves (i.e. gravity-wave drag). The parameterisation scheme is described in detail in Lott and Miller (1997).

The scheme is based on ideas presented by Baines and Palmer (1990), combined with ideas from bluff-body dynamics. The assumption is that the mesoscale-flow dynamics can be described by two conceptual models, whose relevance depends on the non-dimensional height of the mountain via

$$H_{\mathrm{n}} = \frac{NH}{|U|} \tag{4.1}$$

where H is the maximum height of the obstacle, U is the wind speed and N is the Brunt–Väisälä frequency of the incident flow.

At small H_{n} most of the flow goes over the mountain and gravity waves are forced by the vertical motion of the fluid. Suppose that the mountain has an elliptical shape and a height variation determined by a parameter b in the along-ridge direction and by a parameter a in the cross-ridge direction, such that the mountain anisotropy $\gamma = a/b \leq 1$, then the geometry of the mountain can be written in the form

$$h(x,y) = \frac{H}{1 + x^2/a^2 + y^2/b^2} \tag{4.2}$$

In the simple case when the incident flow is at right angles to the ridge the surface stress due to the gravity wave has the magnitude

$$\tau_{\mathrm{wave}} = \rho_0 bGB(\gamma)NUH^2 \tag{4.3}$$

provided that the Boussinesq and hydrostatic approximations apply. In (4.3) G is a function of the mountain sharpness (Phillips, 1984), and for the mountain given by (4.2), $G \approx 1.23$. The term $B(\gamma)$ is a function of γ, and can vary from $B(0) = 1$ for a two-dimensional ridge to $B(1) = \pi/4$ for a circular mountain.

At large H_n, the vertical motion of the fluid is limited and part of the low-level flow is blocked and goes around the mountain. The depth, Z_{blk}, of this blocked layer, when U and N are independent of height, can be expressed as

$$Z_{blk} = H \times \max\left(0, \frac{H_n - H_{n_{crit}}}{H_n}\right) \tag{4.4}$$

where $H_{n_{crit}}$ is a critical non-dimensional mountain height of order unity. The depth Z_{blk} can be viewed as the upstream elevation of the isentropic surface that is raised exactly to the mountain top. At each level below Z_{blk} the flow streamlines divide around the obstacle, and it is supposed that flow separation occurs on the obstacle's flanks. Then, the drag, $D_{blk}(z)$, exerted by the obstacle on the flow at these levels can be written as

$$D_{blk}(z) = -\rho_0 C_d l(z) \frac{U|U|}{2} \tag{4.5}$$

Here $l(z)$ represents the horizontal width of the obstacle as seen by the flow at an upstream height $z < Z_{blk}$, and for an elliptical mountain is given by,

$$l(z) = 2b\left(\frac{Z_{blk} - z}{z}\right)^{1/2} \tag{4.6}$$

C_d represents the drag coefficient, which according to the free streamline theory of jets in ideal fluids is a constant having a value close to 1 (Kirchoff, 1876; Gurevitch, 1965). However, observations show C_d can be nearer 2 in value when suction effects occur in the rear of the obstacle (Batchelor, 1967). Here, this drag is applied to the flow, level by level, and will be referred to as the 'blocked-flow drag', D_{blk}. Unlike the gravity-wave drag computation (4.3), the total stress exerted by the mountain on the 'blocked' flow does not need to be known *a priori*.

In (4.6), it is assumed that the level Z_{blk} is raised up to the mountain top, with each layer below Z_{blk} raised by a factor H/Z_{blk}. This leads, effectively, to a reduction of the obstacle width, as seen by the flow when compared with the case in which the flow does not experience vertical motion as it approaches the mountain. Then applying (4.5) to the fluid layers below Z_{blk}, the stress due to the blocked-flow drag is obtained by integrating from $z = 0$ to $z = Z_{blk}$, viz.

$$\tau_{blk} \approx C_d \pi b \rho_0 Z_{blk} \frac{U|U|}{2} \tag{4.7}$$

Moreover, the blocked layer results in a reduction of the mountain height which produces gravity waves, meaning the mountain height used in (4.3) is replaced with a lower effective (or cut-off) mountain height, i.e.

$$H_{eff} = 2(H - Z_{blk}) \tag{4.8}$$

The factor 2 was added later (in Cy32r2) because diagnostics indicated that without the factor 2, the gravity wave activity was too weak. In the present scheme the value of C_d is allowed to vary with the aspect ratio of the obstacle, as in the case of separated flows around immersed bodies (Landweber, 1961), while at the same time setting the critical number $H_{n_{crit}}$ equal to 0.5 as a constant intermediate value.

4.2 DESCRIPTION OF THE SCHEME

Following Baines and Palmer (1990), the subgrid-scale orography over one grid-point region is represented by four parameters μ, γ, σ and θ which stand for the standard deviation, the anisotropy, the slope and the geographical orientation of the orography, respectively. These four parameters have been calculated from the GTOPO30 data set at $30''$ (about 1000 m) resolution (Gesch and Larson, 1998), averaged to $2'30''$ resolution so as to remove scales less than 5000m. At sub-grid horizontal scales less than 5000 m, small surface obstacles generate additional turbulence or turbulent orographic form drag (TOFD).

The scheme uses values of wind velocity, U_H, Brunt–Väisälä frequency, N_H, and fluid density, ρ_H, which are evaluated by averaging between μ and 2μ above the model mean orography, i.e. representative

of flow incident to the subgrid-scale orography. Following Wallace *et al.* (1983), 2μ is interpreted as the envelope of the subgrid-scale mountain peaks above the model orography. The evaluation of the blocking height $Z_{\rm blk}$ is based on a very simple interpretation of the non-dimensional mountain height $H_{\rm n}$. To first order in the mountain amplitude, the obstacle excites a wave, and the sign of the vertical displacement of a fluid parcel is controlled by the wave phase. If a fluid parcel ascends the upstream mountain flank over a height large enough to significantly modify the wave phase, its vertical displacement can become zero, and it will not cross the mountain summit. In this case $Z_{\rm blk}$ is the highest level located below the mountain top for which the phase change between $Z_{\rm blk}$ and the mountain top exceeds a critical value $H_{\rm n_{crit}}$, i.e.

$$\int_{Z_{\rm blk}}^{3\mu} \frac{N}{U_{\rm p}} {\rm d}z \geq H_{\rm n_{crit}} \tag{4.9}$$

In the inequality (4.9), the wind speed, $U_{\rm p}(z)$, is calculated by resolving the wind, $U(z)$, in the direction of the flow U_H. Then, if the flow veers or backs with height, (4.9) will be satisfied when the flow becomes normal to U_H. Levels below this 'critical' altitude define the low-level blocked flow. The inequality (4.9) will also be satisfied below inversion layers, where the parameter N is very large. These two properties allow the new parametrization scheme to mimic the vortex shedding observed when pronounced inversions occur (Etling, 1989). The upper limit in the equality (4.9) was chosen to be 3μ, which is above the subgrid-scale mountain tops. This ensures that the integration in equality (4.9) does not lead to an underestimation of $Z_{\rm blk}$, which can occur because of the limited vertical resolution when using 2μ as an upper limit (a better representation of the peak height), but this upper limit could be relaxed given better vertical resolution.

In the following subsection the drag amplitudes will be estimated combining formulae valid for elliptical mountains with real orographic data. Considerable simplifications are implied and the calculations are, virtually, scale analyses relating the various amplitudes to the sub-grid parameters.

4.2.1 Blocked-flow drag

Within a given layer located below the blocking level $Z_{\rm blk}$, the drag is given by (4.5). At a given altitude z, the intersection between the mountain and the layer approximates to an ellipse with eccentricity of

$$(a', b') \approx (a, b) \left(\frac{Z_{\rm blk} - z}{z + \mu} \right)^{\frac{1}{2}} \tag{4.10}$$

where, by comparison with (4.6), it is also supposed that the level $z = 0$ (i.e. the model mean orography) is at an altitude μ above the mountain valleys. If the flow direction is taken into account, the length $l(z)$ can be written approximately as

$$l(z) \approx 2 \max(b \cos\psi, a \sin\psi) \left(\frac{Z_{\rm blk} - z}{z + \mu} \right)^{\frac{1}{2}} \tag{4.11}$$

where ψ is the angle between the incident flow direction θ. For one grid-point region and for uniformly distributed subgrid-scale orography, the incident flow encounters $L/(2a)$ obstacles is normal to the ridge $(\psi = 0)$, whereas if it is parallel to the ridge $(\psi = \pi/2)$ it encounters $L/(2b)$ obstacles, where L is the length scale of the grid-point region. If we sum up these contributions, the dependence of (4.11) on a and b can be neglected, and the length $l(z)$ becomes

$$l(z) = L \left(\frac{Z_{\rm blk} - z}{z + \mu} \right)^{\frac{1}{2}} \tag{4.12}$$

Furthermore, the number of consecutive ridges (i.e. located one after the other in the direction of the flow) depends on the obstacle shape: there are approximately $L/(2b)$ successive obstacles when the flow is along the ridge, and $L/(2a)$ when it is normal to the ridge. If we take this into account, together with the flow direction, then

$$l(z) = \frac{L^2}{2} \left(\frac{Z_{\rm blk} - z}{z + \mu} \right)^{\frac{1}{2}} \max\left(\frac{\cos\psi}{a}, \frac{\sin\psi}{b} \right) \tag{4.13}$$

Relating the parameters a and b to the subgrid-scale orography parameters $a \approx \mu/\sigma$ and $a/b \approx \gamma$ and, allowing the drag coefficient to vary with the aspect ratio of the obstacle as seen by the incident flow, we have

$$r = \frac{\cos^2\psi + \gamma \sin^2\psi}{\gamma \cos^2\psi + \sin^2\psi} \tag{4.14}$$

and the drag per unit area and per unit height can be written as

$$D_{\rm blk}(z) = -C_{\rm d} \max\left(2 - \frac{1}{r}, 0\right) \rho \frac{\sigma}{2\mu} \left(\frac{Z_{\rm blk} - z}{z + \mu}\right)^{\frac{1}{2}} \max(\cos\psi, \gamma \sin\psi) \frac{U|U|}{2} \tag{4.15}$$

The drag coefficient is modulated by the aspect ratio of the obstacle to account for the fact that $C_{\rm d}$ is twice as large for flow normal to an elongated obstacle as it is for flow round an isotropic obstacle. The drag tends to zero when the flow is nearly along a long ridge because flow separation is not expected to occur for a configuration of that kind. It can be shown that the term $\max(\cos\psi, \gamma \sin\psi)$ is similar to a later form used for the directional dependence of the gravity-wave stress. For simplicity, this later form has been adopted, so that

$$D_{\rm blk}(z) = C_{\rm d} \max\left(2 - \frac{1}{r}, 0\right) \rho \frac{\sigma}{2\mu} \left(\frac{Z_{\rm blk} - z}{z + \mu}\right)^{\frac{1}{2}} (B \cos^2\psi + C \sin^2\psi) \frac{U|U|}{2} \tag{4.16}$$

with the constants (Phillips, 1984)

$$B = 1 - 0.18\gamma - 0.04\gamma^2,\ C = 0.48\gamma + 0.3\gamma^2,\ C_{\rm d} = 2 \tag{4.17}$$

The difference between (4.15) and (4.16) has been shown to have only a negligible impact on all aspects of the model's behaviour.

In practice, (4.16) is suitably resolved and applied to the component from of the horizontal momentum equations. This equation is applied level by level below $Z_{\rm blk}$ and, to ensure numerical stability, a quasi-implicit treatment is adopted whereby the wind velocity U in (4.16) is evaluated at the updated time $t + {\rm d}t$, while the wind amplitude, $|U|$, is evaluated at the previous time step.

4.2.2 Gravity-wave drag

This gravity-wave part of the scheme is based on the work of Miller *et al.* (1989) and Baines and Palmer (1990), and takes into account some three-dimensional effects in the wave stress amplitude and orientation. For clarity and convenience, a brief description is given here. On the assumption that the subgrid-scale orography has the shape of one single elliptical mountain, the gravity wave surface stress (4.3) can be written as (Phillips, 1984)

$$(\tau_1, \tau_2) = \rho_H U_H N_H H_{\rm eff}^2 b G (B \cos^2\psi_H + C \sin^2\psi_H, (B - C) \sin\psi \cos\psi_H) \tag{4.18}$$

where ψ_H is the mean value between $z = \mu$ and $z = 2\mu$. Furthermore, when b or a are significantly smaller than the length L, characteristic of the gridpoint region size, there are, typically, $L^2/(4ab)$ ridges inside the grid-point region. Summing all the associated forces we find the stress per unit area, viz.

$$(\tau_1, \tau_2) = \rho_H U_H N_H (H_{\rm eff}^2/4)(\sigma/\mu) G \{B \cos^2\psi_H + C \sin^2\psi_H, (B - C) \sin\psi_H \cos\psi_H\} \tag{4.19}$$

where a has been replaced by μ/σ.

It is worth noting that, since the basic parameters ρ_H, U_H, N_H are evaluated for the layer between μ and 2μ above the mean orography that defines the model's lower boundary, there will be much less diurnal cycle in the stress than in previous formulations that used the lowest model levels for this evaluation. The vertical distribution of the gravity-wave stress will determine the levels at which the waves break and slow down the synoptic flow. Since this part of the scheme is active only above the blocked flow, this stress is now constant from the bottom model level to $Z_{\rm blk}$. Above this height, up to the top of the model, the stress is constant until the waves break (by the top of the model the gravity wave must have

broken completely). This occurs when the total Richardson number, Ri, falls below a critical value $Ri_{\rm crit}$, which is of order unity. When the non-dimensional mountain height is close to unity, this algorithm will usually predict wave breaking at relatively low levels (i.e. immediately above the 'blocked' layer). This is not surprising since the linear theory of mountain gravity waves predicts low-level breaking waves at large non-dimensional mountain heights (Miles and Huppert, 1969). In reality, the depth over which gravity-wave breaking occurs is more likely to be related to the vertical wavelength of the waves. For this reason, when low-level wave breaking occurs in the scheme, the corresponding drag is distributed (above the blocked flow), over a layer of thickness Δz, equal to a quarter of the vertical wavelengths of the waves, i.e.

$$\int_{Z_{\rm blk}}^{Z_{\rm blk}+\Delta z} \frac{N}{U_{\rm p}} {\rm d}z \approx \frac{\pi}{2} \tag{4.20}$$

Above the height $Z_{\rm blk}+\Delta z$ are waves with an amplitude such that $Ri > Ri_{\rm crit}$. The remaining part of the momentum flux above 9.9 Pa is spread between this level and the top of the model.

4.3 SPECIFICATION OF SUBGRID-SCALE OROGRAPHY

For completeness, the following describes how the subgrid-scale orography fields were computed by Baines and Palmer (1990). The mean topographic height above mean sea level over the grid-point region is denoted by $\bar{h}$, and the coordinate z denotes elevation above this level. Then the topography relative to this height $h(x,y)-\bar{h}$ is represented by four parameters, as follows.

(i) The net variance, or standard deviation, μ, of $h(x,y)$ in the grid-point region. This is gives a measure of the amplitude and 2μ approximates the physical envelope of the peaks.
(ii) A parameter γ which characterises the anisotropy of the topography within the grid-point region.
(iii) An angle ψ, which denotes the angle between the direction of the low-level wind and that of the principal axis of the topography.
(iv) A parameter σ which represents the mean slope within the grid-point region.

The parameters γ and ψ may be defined from the topographic gradient correlation tensor

$$H_{ij} = \overline{\frac{\partial h}{\partial x_i}\frac{\partial h}{\partial x_j}}$$

where $x_1 = x$, and $x_2 = y$, and where the terms be calculated (from the USN data-set) by using all relevant pairs of adjacent gridpoints within the grid-point region. This symmetric tensor may be diagonalized to find the directions of the principal axes and the degree of anisotropy. If

$$K = \frac{1}{2}\left\{\overline{\left(\frac{\partial h}{\partial x}\right)^2} + \overline{\left(\frac{\partial h}{\partial y}\right)^2}\right\}, \quad L = \frac{1}{2}\left\{\overline{\left(\frac{\partial h}{\partial x}\right)^2} - \overline{\left(\frac{\partial h}{\partial y}\right)^2}\right\} \quad \text{and} \quad M = \overline{\frac{\partial h}{\partial x}\frac{\partial h}{\partial y}} \tag{4.21}$$

the principal axis of H_{ij} is oriented at an angle θ to the x-axis, where θ is given by

$$\begin{aligned} \theta &= \frac{1}{2}\arctan(M/L) \quad if \quad L>0 \\ \theta &= \frac{1}{2}\arctan(M/L) + \pi/2 \quad if \quad L<0 \; and \; M>0 \\ \theta &= \frac{1}{2}\arctan(M/L) - \pi/2 \quad if \quad L<0 \; and \; M<0 \end{aligned} \tag{4.22}$$

This gives the direction where the topographic variations, as measured by the mean-square gradient, are largest. The corresponding direction for minimum variation is at right angles to this. Changing coordinates to x', y' which are oriented along the principal axes $x' = x\cos\theta + y\sin\theta$ and $y' = y\cos\theta - x\sin\theta$, the new values of K, L, and M relative to these axes, denoted K', L' and M', are given by

$$K' = K, \quad L' = (L^2+M^2)^{\frac{1}{2}} \quad \text{and} \quad M' = 0$$

where K, L and M are given by (4.21). The anisotropy of the orography or 'aspect ratio'. γ is then defined by the equations

$$\gamma^2 = \overline{\left(\frac{\partial h}{\partial y'}\right)^2} \Big/ \overline{\left(\frac{\partial h}{\partial x'}\right)^2} = \frac{K' - L'}{K' + L'} = \frac{K - (L^2 + M^2)^{1/2}}{K + (L^2 + M^2)^{1/2}} \tag{4.23}$$

If the low-level wind vector is directed at an angle φ to the x-axis, then the angle ψ is given by

$$\psi = \theta - \varphi \tag{4.24}$$

The slope parameter, σ, is defined as

$$\sigma^2 = \overline{\left(\frac{\partial h}{\partial x'}\right)^2} \tag{4.25}$$

which is the mean-square gradient along the principal axis.

4.4 CODE

The principal routine is GWDRAG, which is called from CALLPAR. GWDRAG first calls GWSETUP to define all the basic input values required for the evaluation of the blocking drag and gravity wave stress. It then computes the surface gravity wave stress and calls GWPROFIL to calculate its vertical distribution. GWDRAG then computes the momentum tendency coefficients (rather than the actual momentum tendencies). The coefficients are passed back to CALLPAR where they are solved in the vertical diffusion scheme as a joint implicit calculation with TOFD momentum tendency coefficients. The joint implicit calculation introduces some degree of dependency into these coupled processes, and so reduces the time step sensitivity which would have existed if each scheme had evaluated its tendencies independently (Beljaars *et al.*, 2004b).

4.4.1 GWSETUP

This routine defines various reference model levels for controlling the vertical structure of the calculations, and sets up a number of derived atmospheric variables and geometric calculations required to run the scheme.

(i) The definition of the Brunt–Väisälä frequency on half levels

$$N^2_{k-1/2} = \frac{2g^2}{c_{p_{\text{dry}}}(T_k + T_{k-1})}\left\{1 - c_{p_{\text{dry}}}\rho_{k-1/2}\frac{(T_k - T_{k-1})}{(p_k - p_{k-1})}\right\} \tag{4.26}$$

(ii) The definition of the mean wind components in the layer $\mu < z < 2\mu$

$$U_{\text{LOW}} = \frac{\sum_{k=\mu}^{k=2\mu} U_k \Delta p_k}{\sum_{k=\mu}^{k=2\mu} \Delta p_k} \tag{4.27}$$

and similarly for V_{LOW}; likewise the mean static stability, N_{LOW}, and the mean density, ρ_{LOW} are calculated.

(iii) The calculation of necessary geometry pertaining to geographical orientation of subgrid-scale orography and wind direction,

$$\varphi_k = \tan^{-1}\left(\frac{V_k}{U_k}\right) \tag{4.28}$$

$$\psi_k = \theta - \varphi_k \tag{4.29}$$

$$\bar{\varphi} = \tan^{-1}\left(\frac{V_{\text{LOW}}}{U_{\text{LOW}}}\right) \tag{4.30}$$

and $\bar{\psi} = \theta - \bar{\varphi}$. Also computed are the parameters B and C (4.17).

(iv) The calculation of the vertical wind-profile in the plane of the gravity wave stress. Defining

$$\hat{U}_k = \frac{U_{\rm LOW}}{|\mathbf{V}_{\rm LOW}|}U_k + \frac{V_{\rm LOW}}{|\mathbf{V}_{\rm LOW}|}V_k$$

and similarly for $\hat{V}_k$, where $\mathbf{V}_{\rm LOW} = (U_{\rm LOW}, V_{\rm LOW})$, then the wind profile is defined level-by-level as

$$V_k^{\rm G} = \frac{(\hat{U}_k D_1 + \hat{V}_k D_2)}{\sqrt{(D_1^2 + D_2^2)}} \tag{4.31}$$

where $D_1 = B - (B - C)\sin^2\bar{\psi}$ and $D_2 = (B - C)\sin\bar{\psi}\cos\bar{\psi}$; the values of $V_k^{\rm G}$ are also used to compute half level values $V_{k+1/2}^{\rm G}$ etc. by linear interpolation in pressure.

(v) The calculation of basic flow Richardson Number

$$\overline{Ri}_{k-1/2} = N_{k-1/2}^2 \left\{ \frac{p_k - p_{k-1}}{g\rho_{k-1/2}(V_k^G - V_{k-1}^G)} \right\}^2$$

(vi) The calculation of the blocked layer depth (4.4), given by the value of $Z_{\rm blk}$ that is the solution to the finite-difference form of the equation

$$\int_{Z_{\rm blk}}^{3\mu} \frac{N_k}{\hat{U}_k}\,{\rm d}z \geq H_{n_{\rm crit}} \tag{4.32}$$

(vii) The calculation of the layer in which low-level wave-breaking occurs (if any). This is given by the value of Δz that is the solution to the finite difference form of the equation

$$\int_{Z_{\rm blk}}^{Z_{\rm blk}+\Delta z} \frac{N_k}{\hat{U}_k}\,{\rm d}z = \frac{\pi}{2} \tag{4.33}$$

the value of $(Z_{\rm blk} + \Delta z)$ is not allowed to be less than 4μ.

(viii) The calculation of the assumed vertical profile of the sub-grid scale orography needed for the 'blocking' computations (4.10), for $z < Z_{\rm blk}$,

$$z_k^{\rm DEP} = \sqrt{\frac{Z_{\rm blk} - z_k}{z_k + \mu}} \tag{4.34}$$

4.4.2 GWPROFIL

This routine computes the vertical profile of gravity-wave stress by constructing a local wave Richardson number which attempts to describe the onset of turbulence due to the gravity waves becoming convectively unstable or encountering critical layers. This local Richardson number can be written in the form

$$\tilde{R}i = \overline{Ri}\left\{ \frac{1 - \alpha}{(1 + \overline{Ri}^{1/2}\alpha)^2} \right\}$$

where $\overline{Ri}$ is the Richardson number of the basic flow. The parameter $\alpha = N|\delta z|/V_k^{\rm G}$ in which $|\delta z|$ represents the amplitude. By requiring that $\tilde{R}i$ never falls below a critical value $\tilde{R}i_{\rm crit}$ (currently equal to 0.25), values of wave stress are defined progressively from the top of the blocked layer upwards.

When low-level breaking occurs the relevant depth is assumed to be related to the vertical wavelength. Hence a linear (in pressure) decrease of stress is included over a depth Δz given by the solution of (4.33). The linear decrease of gravity wave stress is written as

$$\tau_{wave_{p_k}} = \tau_{wave_{z_{\rm blk}}} + (\tau_{wave_{z_{\rm blk}+\Delta z}} - \tau_{wave_{z_{\rm blk}}})\frac{p_k - p_{z_{\rm blk}}}{p_{z_{\rm blk}+\Delta z} - p_{z_{\rm blk}}} \tag{4.35}$$

4.4.3 GWDRAG

This is the main routine. The total (TOT) tendency due the dynamics (DYN), vertical diffusion (VDF), wave drag, and blocking drag is given by

$$\left(\frac{\partial u}{\partial t}\right)_{\mathrm{TOT}} = \left(\frac{\partial u}{\partial t}\right)_{\mathrm{wave}} + \left(\frac{\partial u}{\partial t}\right)_{\mathrm{blk}} + \left(\frac{\partial u}{\partial t}\right)_{\mathrm{DYN+VDF}} = \alpha_{\mathrm{u}} - \beta u^{n+1} + \left(\frac{\partial u}{\partial t}\right)_{\mathrm{DYN+VDF}} \tag{4.36}$$

where α_{u} and β are the explicit gravity wave drag tendency coefficient and implicit blocking drag tendency coefficient respectively. A similar equation is apparent for the v component. As stated above, these tendencies are computed in the vertical diffusion routine.

(*a*) *Gravity wave drag component*

Using (4.19) the surface gravity-wave stress is computed in the form,

$$\tau_{\mathrm{wave}} = \rho_{\mathrm{LOW}}(H_{\mathrm{eff}}^2/9)(\sigma/\mu)G(U_{\mathrm{LOW}}^2 + V_{\mathrm{LOW}}^2)^{1/2}(D_1^2 + D_2^2)^{1/2}N_{\mathrm{LOW}} \tag{4.37}$$

where G is a function of the mountain sharpness. As Z_{blk} is able to reach a maximum height of 3μ (4.32), we must choose $H = 3\mu$. However, the surface stress must be scaled to a mountain height of 2μ, so the denominator of (4.37) is divided by 9 rather than 4 (4.19) (i.e. for $Z_{\mathrm{blk}} = 0$ both equations are identical). Following this, GWPROFIL is called to compute the vertical profile of gravity wave stress.

For $z > Z_{\mathrm{blk}}$ the gravity wave tendency coefficient is defined level by level as,

$$\left(\frac{\partial u}{\partial t}\right)_{\mathrm{wave}} = -g\frac{\tau_{wave_{k+1}} - \tau_{wave_k}}{p_{k+1} - p_k} f_{\mathrm{u}}(\psi) = \alpha_{\mathrm{u}} \tag{4.38}$$

where $f_{\mathrm{u}}(\psi)$ is the necessary geometric function to generate components. A similar equation exists for α_{v}. Here $\beta = 0$.

To avoid excessive tendencies at the top of the model, the remaining momentum flux above 9.9 *Pa* is spread over the layer between 9.9 *Pa* and the top of the model according to the following expression

$$\left(\frac{\partial u}{\partial t}\right)_{\mathrm{wave}} = -g\frac{\tau_{wave_{ktop}} - \tau_{wave_1}}{p_{ktop} - p_1}^2 (p_{k+1} - p_k) f_{\mathrm{u}}(\psi) \tag{4.39}$$

where *ktop* is the index of the first level above 9.9 *Pa*.

(*b*) *Blocking drag component*

For $z \leq Z_{\mathrm{blk}}$ the blocking drag tendency is defined level by level as

$$\left(\frac{\partial u}{\partial t}\right)_{\mathrm{blk}} = -C_{\mathrm{d}} \max\left(2 - \frac{1}{r}, 0\right) \frac{\sigma}{2\mu} \sqrt{\frac{Z_{\mathrm{blk}} - z}{z + \mu}} (B\cos^2\psi + C\sin^2\psi) \frac{U|U|}{2} \tag{4.40}$$

Here $\alpha_{\mathrm{u,v}} = 0$. This equation is evaluated in the following partially implicit manner by writing it in the form

$$\left(\frac{\partial u}{\partial t}\right)_{\mathrm{blk}} = \frac{U^{n+1} - U^n}{\Delta t} = -A|U^n|U^{n+1} = -\beta_{\mathrm{u}} U^{n+1}$$

with $U^{n+1} = U^n/(1+\beta)$ and $\beta = \beta_{\mathrm{u}}\Delta t$, with $\beta_{\mathrm{u}} = A|U^n|$. Here

$$\beta_{\mathrm{u}} = C_{\mathrm{d}} \max\left(2 - \frac{1}{r}, 0\right) \frac{\sigma}{2\mu} \sqrt{\frac{Z_{\mathrm{blk}} - z}{z + \mu}} (B\cos^2\psi + C\sin^2\psi) \frac{|U|}{2} \tag{4.41}$$

(*c*) *Evaluation of tendencies*

The tendency coefficients are passed to CALLPAR where they are jointly implicitly computed in the vertical diffusion code with momentum tendency coefficients from the TOFD scheme. The actual tendencies are given as

$$\left(\frac{\partial u}{\partial t}\right)_{\text{wave+blk}} = \left(\frac{\partial u}{\partial t}\right)_{\text{TOT}} - \left(\frac{\partial u}{\partial t}\right)_{\text{DYN+VDF}} \tag{4.42}$$

Finally the tendencies are incremented. Local dissipation heating is calculated in the form

$$\left(\frac{\partial u}{\partial t}\right)_{\text{wave+blk}} = \frac{1}{c_p}\frac{DISS}{\Delta t} \tag{4.43}$$

with $DISS = 0.5((U^n)^2 + (V^n)^2 - \hat{U}^2 - \hat{V}^2)$, where $\hat{U} = U^n + \Delta t(\partial u/\partial t)_{\text{wave+blk}}$ and $\hat{V} = V^n + \Delta t(\partial v/\partial t)_{\text{wave+blk}}$.

APPENDIX A. LIST OF SYMBOLS

a	half mountain width in the cross-ridge or x-direction
B, C	functions of the mountain anisotropy
b	half mountain width in the along-ridge or y-direction
C_{d}	drag coefficient
$c_{p_{\text{dry}}}$	specific heat capacity
D_{blk}	blocked-flow drag
g	gravitational acceleration
G	function of the mountain sharpness
H	maximum mountain height
H_{eff}	effective mountain height
$h(x, y)$	mountain height profile
H_{n}	non-dimensional mountain height $(= NH/\lvert U\rvert)$
$H_{\text{n}_{\text{crit}}}$	critical non-dimensional mountain height
L	length scale of the grid-point region
$l(z)$	horizontal width of mountain seen by the upstream flow
N	Brunt–Väisälä frequency
N_{H}	(=N_{LOW}) mean Brunt–Väisälä frequency of low-level flow between $z = \mu$ and $z = 2\mu$
p_{k}	model level air pressure
$\overline{Ri}$	Richardson number of the basic flow
$\tilde{R}i$	local Richardson number
$\tilde{R}i_{\text{crit}}$	critical Richardson number
T	temperature
U	wind speed
$U_{\text{LOW}}, V_{\text{LOW}}$	horizontal components of mean low-level flow between $z = \mu$ and $z = 2\mu$
U_{H}	mean wind speed of low-level flow between $z = \mu$ and $z = 2\mu$
U_{p}	component of the wind speed in the direction of U_H
U_τ	component of wind speed in the direction of the stress τ
u, v	horizontal wind components
$U_{\text{k}}, V_{\text{k}}$	level-by-level horizontal wind components
V_{k}^{G}	level-by-level wind profile in the plane of gravity wave stress
Z_{blk}	depth of blocked layer
$\alpha_{\text{u,v}}$	explicit gravity wave tendency coefficient
β	$(= \beta_u \Delta t)$ implicit blocking drag tendency coefficient
γ	anisotropy of the orography $(= a/b \leq 1)$
θ	orientation of the orography

μ	standard deviation of orography
ρ_{k}	model level air density
ρ_0	density of air at the surface
ρ_{H}	(=ρ_{LOW}) mean density of low-level flow between $z=\mu$ and $z=2\mu$
σ	slope of the orography
τ_{blk}	stress due to blocked flow
τ_{wave}	surface stress due to gravity waves
ψ	angle between incident flow and orographic principal axis
$\bar{\psi}$	$(=\psi_{\mathrm{H}})$ mean value of ψ between $z=\mu$ and $z=2\mu$
φ	angle between low-level wind and the x-axis
$\bar{\varphi}$	mean value of φ between $z=\mu$ and $z=2\mu$

Chapter 5

Non-orographic gravity wave drag

Table of contents

5.1 Introduction
5.2 History
5.3 Launch spectrum
5.4 Discretisation
5.5 Critical level filtering
5.6 Nonlinear dissipation
5.7 Tendencies
5.8 Parameter settings
5.9 Code
Appendix A. List of symbols

5.1 INTRODUCTION

Gravity waves have an important influence on the climate of the middle atmosphere, comprising the stratosphere and the mesosphere. The middle atmosphere is dominated by a westerly jet in the winter hemisphere and an easterly jet in the summer hemisphere, and a meriodional circulation with upwelling in the tropics and downwelling over the winter pole, referred to as the Brewer-Dobson circulation. This circulation is driven by the momentum deposited by breaking Rossby and small-scale non-orographic gravity waves. Furthermore, non-orographic gravity waves form the dominant source of momentum in the mesosphere and the thermosphere, and are also important in driving the variability of the tropical stratosphere, most prominent are the quasi-biennial oscilation and the semi-annual oscillation.

Non-orographic gravity waves are forced by dynamical motions such as convection, frontogenesis, and jet stream activity (e.g Fritts and Nastrom, 1980). They have vertical wavelengths which vary from less than one to many tens of kilometres and horizontal wavelengths which vary from tens to thousands of kilometres (Ern *et al.*, 2004). Thus these waves are generally unresolved or under-resolved by the model as the generating process is often poorly represented, and therefore have to be parametrized.

Prior to Cy35r3 (September 2009) the effect of small-scale non-orographic gravity waves has been parametrized in the simplest possible manner by Rayleigh friction above the stratopause, which is formulated as a drag force proportional to the mean flow. The parametrization scheme adopted since then is that of Scinocca (2003). The description is kept short and the effects of the parametrization on the middle atmosphere circulation in the IFS are not discussed as all material is described in detail, inluding an extensive literature list, in Orr *et al.* (2010).

5.2 HISTORY

The Scinocca (2003) scheme, hereafter referred to as S03 scheme, is a spectral scheme that follows from the Warner and McIntyre (1996) scheme which represents the three basic wave mechanisms that are conservative propagation, critical level filtering, and non-linear dissipation. However, the full non-hydrostatic and rotational wave dynamics considered by Warner and McIntyre (1996) is too costly for operational models, and therefore only hydrostatic and non-rotational wave dynamics is employed.

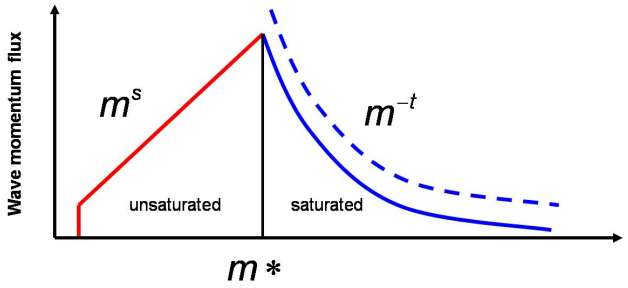

Figure 5.1 *Schematic of the gravity wave spectrum as a function of vertical wavenumber at constant intrinsic frequency $\tilde{\omega}$ showing the different spectral shapes, separated by $m_\star$ for large and small m. The saturation spectrum is denoted by the dashed line.*

5.3 LAUNCH SPECTRUM

The dispersion relation for a hydrostatic gravity wave in the absence of rotation is

$$m^2 = \frac{k^2 N^2}{\tilde{\omega}^2} = \frac{N^2}{\tilde{c}^2} \tag{5.1}$$

where k, m are horizontal and vertical wavenumbers, $\tilde{\omega} = \omega - kU$ and $\tilde{c} = c - U$ are the intrinsic frequency and phase speed (with c the ground based phase speed and U the background wind speed in the direction of propagation), and N is the Brunt–Väisälä frequency (here expressed in height coordinate z for a better tangent-linear approximation and not in pressure coordinates as in the original code)

$$N^2 = \frac{g^2}{c_p T} + \frac{g\partial T}{T\partial z}; \qquad N \geq 10^{-12} \tag{5.2}$$

with g the gravity constant and c_p the specific heat of dry air at constant volume.

The launch spectrum is given by the total wave energy per unit mass in each azimuth ϕ following Fritts and Nastrom (1993), and is globally uniform and constant

$$\tilde{E}(m, \tilde{\omega}, \phi) = \mathrm{B}\left(\frac{m}{m_\star}\right)^{\mathrm{s}} \frac{N^2 \tilde{\omega}^{-\mathrm{p}}}{1 - \left(\frac{m}{m_\star}\right)^{\mathrm{s}+3}} \tag{5.3}$$

where B, s and p are constants, and $m_\star = 2\pi/L$ is a transitional wavelength (see Section 5.8 for an overview of the parameter settings).

Observation and theory suggest p values in the range $1 \leq \mathrm{p} \leq 2$. The spectrum is separable in terms of both m and $\tilde{\omega}$ and is displayed in Fig. 5.1 for a given value of $\tilde{\omega}$.

However, instead of the total wave energy the momentum flux spectral density $\rho\tilde{F}(m, \tilde{\omega}, \phi)$ is required, where ρ is the air density. It is obtained through the group velocity rule

$$\rho\tilde{F}(m, \tilde{\omega}, \phi) = \rho c_{\mathrm{g}} \frac{k}{\tilde{\omega}} E(m, \tilde{\omega}, \phi) \tag{5.4}$$

where $c_{\mathrm{g}} = \partial\tilde{\omega}/\partial m = \tilde{\omega}/m$ is the group velocity for hydrostatic dynamics. However as shown in S03, in the $(m, \tilde{\omega})$ coordinate framework the wave momentum flux is not conserved in the absence of dissipative processes as the spectrum propagates vertically through height varying background winds and buoyancy frequencies, but it is conserved in the (k, ω) coordinate framework. Performing a coordinate transformation on (5.4) and using the dispersion relation (5.1), one obtains the expression of the unscaled momentum flux density or Eliassen-Palm flux density as a function of the independent variable c

$$\rho F^{\star}(\hat{c},\phi) = \rho \frac{\hat{c}-\hat{U}}{N}\left(\frac{\hat{c}-\hat{U}}{\hat{c}}\right)^{2-\mathrm{p}} \frac{1}{1+\left(\frac{m_{\star}(\hat{c}-\hat{U})}{N}\right)^{s+3}} \tag{5.5}$$

where $\hat{U} = U^{(\phi)} - U_0^{(\phi)}$ and $\hat{c} = c - U_0^{(\phi)}$, with $U^{(\phi)} = u\cos(\phi) + v\sin(\phi)$ the velocity in the direction of the azimuth ϕ and the subscript 0 referring to the launch level. Note that at the launch level $\hat{U} = 0$ so that the transformation renders the wave flux independent of azimuth. In the current formulation the departure spectrum is globally constant, therefore identical for each model column.

The final result for the scaled momentum or Eliassen-Palm flux density (having units ρ m^{2}s$^{-2}/d\hat{c} = \rho$ ms^{-1}) at the launch level $\hat{F}$ is obtained through scaling with $\rho_0 F_{\text{launch}}$ which is the imposed launch momentum flux, and the most important free model parameter

$$\rho\hat{F}(\hat{c},\phi) = \rho F^{\star}(\hat{c},\phi) * A; \qquad A = (\rho_0 F_{\text{launch}}) / \int (\rho F^{\star}(\hat{c},\phi_1))d\hat{c} \tag{5.6}$$

Prior to cycle 38r2 the launch momentum flux has been set to a globally uniform value $\rho_0 F_{\text{launch}} = \rho_0 F^0_{\text{launch}}$. However, it was recognized that lower values are preferable for the tropics while the higher latitudes require larger values to control the polar night jets. Furthermore, it was recognized that the subgrid momentum flux should decrease with resolution in order to keep the otal (resolved + subgrid) momentum flux roughly unchanged. The latitude and resolution scaled launch momentum flux is

$$\rho_0 F_{\text{launch}} = \rho_0 F^0_{\text{launch}}\left[1 - a_\lambda \exp\left(\frac{-\lambda^2}{\lambda_0^2}\right)\right]\left[1 - min\left(1, \text{atan}\left(\frac{max(dx^{-1}, x_a) - x_a}{x_b - x_a}\right)\right)\right] \tag{5.7}$$

with λ the latitude, dx the horizontal grid spacing, $x_a = (29\times10^3\text{m})^{-1}$ and $x_b = (3.5\times10^3\text{m})^{-1}$. The latitude dependency has been introduced in cycle 38r2. The horizontal resolution dependency with decreasing subgrid momentum fluxes below dx=29 km and vanishing fluxes below dx=1 km has been introduced in cycle 41r2.

5.4 DISCRETISATION

The wave fluxes are defined at half model levels. Therefore, all variables like U, N (temperature) etc. required in the computation of the fluxes have to be interpolated to half-levels.

The wave spectrum is discretised in n_c phase speed bins, and n_ϕ equally spaced azimuths. The wave momentum flux is initialised at the model level just below the launch level height p_{launch}.

As it is the small-m portion of the spectrum which is associated with large values of momentum flux it is important to apply a coordinate stretch in order to obtain higher resolution and better accuracy at large phase speeds (i.e. small m). The problem is solved in the space of the transformed variable $\bar{X}$ having uniform resolution $d\bar{X}$. Taking as untransformed variable

$$X = \frac{1}{\hat{c}} \tag{5.8}$$

the coordinate stretch under the constraint $X_{\min} \le X \le X_{\max}$ and and $X_{\min} \le \bar{X} \le X_{\max}$ is defined by

$$X = B_1 e^{(\bar{X}-X_{\min})/\Gamma} + B_2 \tag{5.9}$$

and

$$B_1 = \frac{X_{\max} - X_{\min}}{e^{(X_{\max}-X_{\min})/\Gamma} - 1}; \qquad B_2 = X_{\min} - B_1 \tag{5.10}$$

The free parameters are the half-width of the stretch Γ, as well as $\hat{c}_{\min}$ with $X_{\max} = 1/\hat{c}_{\min}$, and $\hat{c}_{\max}$ with $X_{\min} = 1/\hat{c}_{\max}$. In discretised space this means one uses $\bar{X}_i = X_{\min} + (X_{\max} - X_{\min})(i/n_c)$ instead of $\hat{c}_i = \hat{c}_{\min} + (\hat{c}_{\max} - \hat{c}_{\min})(i/n_c)$, and the space element $d\hat{c}$ then becomes

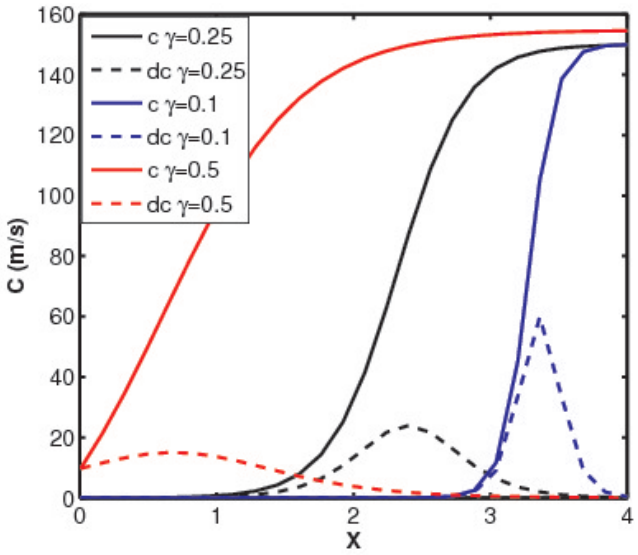

Figure 5.2 *Schematic of the coordinate stretch with phase speed $\hat{c}$ and phase element $d\hat{c}$ as a function of $\bar{X}$ for different values of* Γ.

$$d\hat{c} = \frac{d\hat{c}}{dX}\frac{dX}{d\bar{X}}d\bar{X} = X^{-2}\frac{B_1}{\Gamma}e^{(\bar{X}-X_{\min})/\Gamma}d\bar{X} \tag{5.11}$$

The coordinate stretch is displayed in Fig. 5.2 for different values of Γ.

5.5 CRITICAL LEVEL FILTERING

Waves that encounter critical levels are filtered from the wave spectrum, depositing their momentum to the mean flow in this layer. In practice one checks for each azimuth bin in each layer z above the departure level and for each phase speed. Critical level filtering is encountered if U increases such with height that $\hat{U}_1 > \hat{U}_0$ and $\hat{U}_0 \leq \hat{c} \leq \hat{U}_1$. Then all momentum flux in the corresponding $(\hat{c}, \phi)$ bin is removed from $\rho\bar{F}(\hat{c}, \phi)$. Note that at the departure level $\hat{U}_0 = 0$ which sets an aboslute lower bound for critical filtering of $\hat{c} = \hat{c}_{\min}$.

The consequence of critical level filtering is that, as the waves propagate vertically through stratospheric westerlies (easterlies) as in the middle latitude winter (summer) hemisphere, the spectrum becomes more and more asymmetric with height leaving only the easterly (westerly) phase speed component. In contrast, in the tropical atmosphere winds change from easterlies to westerlies or vice versa and both wind directions are filtered, leaving little zonal momentum flux.

The portions of the wave spectrum that survive critical level filtering undergo conservative propagation to the next model level where they are checked for nonlinear dissipation.

5.6 NONLINEAR DISSIPATION

Nonlinear dissipation is simply modelled by assuming that waves are dissipative in nature and employing 'saturation' theory (Lindzen, 1981) such that the amplitude of the parametrized wave field is limited to some treshold value (thought to be associated with the onset of instability). This is dealt with empricially by limiting the growth of the gravity wave spectrum at large-m (short wavelengths) so as not to exceed the observed m^{-3} dependence. The saturation momentum flux is written as

$$\rho\hat{F}^{\text{sat}}(\hat{c}, \phi) = \rho C^{\star} A \frac{\hat{c} - \hat{U}}{N}\left(\frac{\hat{c} - \hat{U}}{\hat{c}}\right)^{2-\text{p}} \tag{5.12}$$

where $C^\star$ is a tuning parameter introduced by McLandress and Scinocca (2005). The saturation momentum flux is depicted in Fig. 5.1. It decreases with height as a consequence of decreasing density, iit is therefore not conserved. Nonlinear dissipation is formulated as the constraint $\rho\hat{F}(\hat{c},\phi) \leq \rho\hat{F}^{\text{sat}}(\hat{c},\phi)$. When the wave momentum flux exceeds the saturated value $\rho\hat{F}(\hat{c},\phi)$ is set equal to $\rho\hat{F}^{\text{sat}}$ meaning that the excess momentum flux is deposited to the flow. Increasing the parameter $C^\star$ means pushing the onset of nonlinear dissipation to higher amplitudes and therefore to greater heights.

Finally, at the model top momentum conservation is achieved by depositing any remaining momentum from the wave field to the mean flow, i.e. the upper boundary condition is zero wave momentum flux.

5.7 TENDENCIES

The tendencies for the u, v wind components are given by the divergence of the net eastward $\rho\bar{F}_{\text{E}}$, and northward, $\rho\bar{F}_{\text{N}}$ momentum fluxes, which are obtained through summation of the total momentum flux (i.e. integrated over all phase speed bins) in each azimuth ϕ_i projected onto the east and north directions, respectively.

$$\left.\begin{array}{ll} \frac{\partial u}{\partial t} = g\frac{\partial(\rho\bar{F}_{\text{E}})}{\partial p}; & \bar{F}_{\text{E}} = \sum_{i=1}^{n_\phi}(\rho\hat{F}(\phi_i))\cos\phi_i \\ \frac{\partial v}{\partial t} = g\frac{\partial(\rho\bar{F}_{\text{N}})}{\partial p}; & \bar{F}_{\text{N}} = \sum_{i=1}^{n_\phi}(\rho\hat{F}(\phi_i))\sin\phi_i \end{array}\right\} \tag{5.13}$$

The dissipation of the non-orographic gravity waves (an external wave source) is also taken into account as a heat source for the model

$$\frac{\partial T}{\partial t} = -\frac{1}{c_p}\left(u\frac{\partial u}{\partial t} + v\frac{\partial v}{\partial t}\right) \tag{5.14}$$

5.8 PARAMETER SETTINGS

- $\hat{c}_{\text{min}} = 0.25$ m s^{-1}, $\hat{c}_{\text{max}} = 100$ m s^{-1}: minimum and maximum intrinsic phase speed
- $\Gamma = 0.25$: half width of the stretch in (5.9)
- $L = 2000$ m: transitional wavelength
- $p = 1$: the $\tilde{\omega}$ exponent in (5.5) and (5.12)
- $s = 1$: the small m spectral slope in (5.5) and (5.12)
- p_{launch}=450 hPa: launch elevation (Pa)
- n_ϕ=4 (=N, S, E, W): number of equally spaced azimuths
- n_c=32: number of spectral intervals for phase speed
- $C^\star$=1: non-dimensional constant for saturation spectrum in (5.12)
- $\rho_0 F^0_{\text{launch}} = 3.75 \times 10^{-3}$ (Pa): launch momentum flux in (5.7)
- $\lambda_0 = 20^\circ$ in (5.7)
- $a_\lambda = 0.75$ in (5.7)

The most important tuning for future applications (in particular higher horizontal resolutions) would require a reduction of the amplitude of the launch momentum flux with increasing resolution so that as the resolved gravity wave momentum flux increases the parametrised flux decreases, and the total flux remains fairly constant. A reduction of the launch momentum flux would also increase the period of the models 'Quasi-Biennial Oscillation' which is currently too short. Further tuning could also include a time-dependent and horizontally variable amplitude of the launch momentum flux, but this is probably fairly difficult to achieve.

5.9 CODE

The principal routine is GWDRAG_WMS, which is called from CALLPAR. The tunable parameters are defined in the setup routine SUGWWMS which is called from SUPHEC. To save computing time routine GWDRAG_WMS is not called every time step, but typically every few time steps (i.e. every hour for

spectral truncations >255 and every 2 hours for truncations < 255. Therefore, the tendencies due to non-orographic gravity wave dissipation are stored in buffers (GFL arrays), and the total physics tendencies are incremented every time step inside routine GWDRAG_WMS.

APPENDIX A. LIST OF SYMBOLS

A	scaling factor for momentum flux density
B	formal dimensional constant, not actually used
c	phase speed
$\tilde{c}$	intrinsic phase speed $= c - U$
$\hat{c}$	intrinsic phase speed using departure level Doppler shift$= c - U_0$
c_g	group velocity
$\hat{c}_{max}$	maximum intrinsic phase speed
$\hat{c}_{min}$	minimum intrinsic phase speed
c_p	specific heat at constant pressure
$C_\star$	parameter
dx	horizontal grid spacing
F	wave momentum flux (without density factor)
F^{sat}	saturation value of wave momentum flux
g	gravity constant
Γ	parameter
k	horizontal wavenumber
L	transitional wavelength
m	vertial wavenumber
n_c	number of phase speed bins
n_ϕ	number of azimuth bins
N	Brunt–Väisälä frequency
p	constant, the ω exponent
p	pressure
s	constant, the small m spectral slope
t	time
T	temperature
u	west-east component of wind speed
U	wind speed in direction of wave
v	south-north component of wind speed
x_a	upper bound for resolution dependency
x_b	lower bound for resolution dependency
X	Transform for spectral discretisation
z	height
ϕ	azimuthal direction
λ	latitude
ω	frequency

Chapter 6
Convection

Table of contents

6.1 Introduction
6.2 Large-scale budget equations
6.3 Cloud model equations
6.3.1 Updraughts
6.3.2 Downdraughts
6.4 Convection initiation and convective types
6.4.1 Deep convection
6.4.2 Shallow convection
6.4.3 Mid-level convection
6.5 Sub-cloud layer
6.6 Cloud microphysics
6.6.1 Condensation rate in updraughts
6.6.2 Freezing in convective updraughts
6.6.3 Generation of precipitation
6.6.4 Fallout of precipitation in the updraught
6.6.5 Evaporation of rain
6.6.6 Melting and freezing of precipitation
6.7 Link to cloud scheme
6.8 Momentum transport and kinetic energy dissipation
6.9 Vertical discretization of the model equations
6.10 Temporal discretization
6.11 Diagnostics for post-processing: CAPE and CIN and other convective indices
6.12 Tropopause pressure
6.13 Lightning diagnostics
6.14 Structure of code
Appendix A. List of symbols

6.1 INTRODUCTION

Cumulus convection is parametrized by a bulk mass flux scheme which was originally described in Tiedtke (1989). The scheme considers deep, shallow and mid-level convection. Clouds are represented by a single pair of entraining/detraining plumes which describes updraught and downdraught processes. Momentum and tracer transport is also included.

6.2 LARGE-SCALE BUDGET EQUATIONS

The contributions from cumulus convection to the large-scale budget equations of heat moisture, momentum, and chemical tracers are

$$\left.\begin{aligned}
\left(\frac{\partial \bar{s}}{\partial t}\right)_{\mathrm{cu}} &= g\frac{\partial}{\partial p}[M_{\mathrm{up}}s_{\mathrm{up}} + M_{\mathrm{down}}s_{\mathrm{down}} - (M_{\mathrm{up}} + M_{\mathrm{down}})\bar{s}] \\
&\quad + L(c_{\mathrm{up}} - e_{\mathrm{down}} - e_{\mathrm{subcld}}) - (L_{\mathrm{subl}} - L_{\mathrm{vap}})(M_{\mathrm{elt}} - F_{\mathrm{rez}}) \\
\left(\frac{\partial \bar{q}}{\partial t}\right)_{\mathrm{cu}} &= g\frac{\partial}{\partial p}[M_{\mathrm{up}}q_{\mathrm{up}} + M_{\mathrm{down}}q_{\mathrm{down}} - (M_{\mathrm{up}} + M_{\mathrm{down}})\bar{q}] \\
&\quad - (c_{\mathrm{up}} - e_{\mathrm{down}} - e_{\mathrm{subcld}}) \\
\left(\frac{\partial \bar{u}}{\partial t}\right)_{\mathrm{cu}} &= g\frac{\partial}{\partial p}[M_{\mathrm{up}}u_{\mathrm{up}} + M_{\mathrm{down}}u_{\mathrm{down}} - (M_{\mathrm{up}} + M_{\mathrm{down}})\bar{u}] \\
\left(\frac{\partial \bar{v}}{\partial t}\right)_{\mathrm{cu}} &= g\frac{\partial}{\partial p}[M_{\mathrm{up}}v_{\mathrm{up}} + M_{\mathrm{down}}v_{\mathrm{down}} - (M_{\mathrm{up}} + M_{\mathrm{down}})\bar{v}] \\
\left(\frac{\partial \bar{C}^i}{\partial t}\right)_{\mathrm{cu}} &= g\frac{\partial}{\partial p}[M_{\mathrm{up}}C^i_{\mathrm{up}} + M_{\mathrm{down}}C^i_{\mathrm{down}} - (M_{\mathrm{up}} + M_{\mathrm{down}})\bar{C}^i]
\end{aligned}\right\} \tag{6.1}$$

where M_{up}, M_{down} are the net contributions from all clouds to the updraught and downdraught mass fluxes, c_{up} and e_{down} are the condensation/sublimation in the updraughts, and the evaporation in the downdraughts. s_{up}, s_{down}, q_{up}, q_{down}, u_{up}, u_{down}, v_{up}, v_{down}, C^i_{up} and C^i_{down} are the weighted averages of the dry static energy $\bar{s}$, the specific humidity $\bar{q}$, the horizontal wind components $\bar{u}$ and $\bar{v}$ and the passive chemical tracer $\bar{C}^i$ from all updraughts and downdraughts within a grid box (although individual convective elements are not considered) obtained from the bulk cloud model described below. L_{subl} and L_{vap} are latent heats of sublimation and vaporization, and L is the effective latent heat for an ice–water mix (an empirical function of temperature 6.53). e_{subcld} is the evaporation of precipitation in the unsaturated sub-cloud layer, M_{elt} is the melting rate of snow and F_{rez} is the freezing rate of condensate in the convective updraught. In addition to (6.1) the precipitation fluxes are defined as

$$\begin{aligned}
P^{\mathrm{rain}}(p) &= \int_{P\mathrm{top}}^{p} (G^{\mathrm{rain}} - e^{\mathrm{rain}}_{\mathrm{down}} - e^{\mathrm{rain}}_{\mathrm{subcld}} + M_{\mathrm{elt}} - D^{\mathrm{rain}}_{\mathrm{up}})\frac{dp}{g} \\
P^{\mathrm{snow}}(p) &= \int_{P\mathrm{top}}^{p} (G^{\mathrm{snow}} - e^{\mathrm{snow}}_{\mathrm{down}} - e^{\mathrm{snow}}_{\mathrm{subcld}} - M_{\mathrm{elt}} - D^{\mathrm{snow}}_{\mathrm{up}})\frac{dp}{g}
\end{aligned} \tag{6.2}$$

where P^{rain} and P^{snow} are the fluxes of precipitation in the forms of rain and snow at level p. G^{rain} and G^{snow} are the conversion rates from cloud water into rain and cloud ice into snow, M_{elt} denotes melted precipitation and $D^{\mathrm{rain,snow}}_{\mathrm{up}}$, the detrained rain and snow from the updraught. The evaporation of precipitation in the downdraughts e_{down}, and below cloud base e_{subcld}, have been split into water and ice components, $e^{\mathrm{rain}}_{\mathrm{down}}$, $e^{\mathrm{snow}}_{\mathrm{down}}$, $e^{\mathrm{rain}}_{\mathrm{subcld}}$, and $e^{\mathrm{snow}}_{\mathrm{subcld}}$. The microphysical terms in (6.1) and (6.2) referring to the updraught are explained in detail in Section 6.6, those referring to the downdraught are defined in (6.17).

6.3 CLOUD MODEL EQUATIONS

6.3.1 Updraughts

The updraught of the cloud ensemble is assumed to be in a steady state. Then the bulk equations for mass, heat, moisture, cloud water content, momentum and tracers are

$$\left.\begin{aligned} -g\frac{\partial M_{\rm up}}{\partial p} &= E_{\rm up} - D_{\rm up} \\ -g\frac{\partial (M_{\rm up} s_{\rm up})}{\partial p} = E_{\rm up}\bar{s} - D_{\rm up} s_{\rm up} + L c_{\rm up}, \quad -g\frac{\partial (M_{\rm up} q_{\rm up})}{\partial p} &= E_{\rm up}\bar{q} - D_{\rm up} q_{\rm up} - c_{\rm up} \\ -g\frac{\partial (M_{\rm up} l_{\rm up})}{\partial p} = -D_{\rm up} l_{\rm up} + c_{\rm up} - G, \quad -g\frac{\partial (M_{\rm up} r_{\rm up})}{\partial p} &= -D_{\rm up} r_{\rm up} + G - S_{\rm fallout} \\ -g\frac{\partial (M_{\rm up} u_{\rm up})}{\partial p} = E_{\rm up}\bar{u} - D_{\rm up} u_{\rm up}, \quad -g\frac{\partial (M_{\rm up} v_{\rm up})}{\partial p} &= E_{\rm up}\bar{v} - D_{\rm up} v_{\rm up} \\ -g\frac{\partial (M_{\rm up} C^i_{\rm up})}{\partial p} &= E_{\rm up}\bar{C}^i - (D_{\rm up} + P_{\rm up} Z^i_{\rm scav}) C^i_{\rm up} \end{aligned}\right\} \tag{6.3}$$

where $E_{\rm up}$ and $D_{\rm up}$ are the rates of mass entrainment and detrainment, $l_{\rm up}$ is the updraught cloud water/ice content, and $r_{\rm up}$ is precipitating rain and snow. The vertical integration of (6.3) requires knowledge of the cloud-base mass flux and of the mass entrainment and detrainment rates. The cloud-base mass flux is determined for the various types of convection from the closure assumptions discussed in Section 6.4.

Entrainment of mass into convective plumes is assumed to occur (1) through turbulent exchange or inflow of mass through the cloud edges; and detrainment is assumed to occur (1) through turbulent exchange and (2) through organized outflow at cloud top. The superscripts (1) and (2) are used to denote the different components of the entrainment and detrainment processes

$$E_{\rm up} = E^{(1)}_{\rm up}, \quad D_{\rm up} = D^{(1)}_{\rm up} + D^{(2)}_{\rm up} \tag{6.4}$$

(*a*) *Entrainment rates*

Entrainment rates (s^{-1}) are parametrized as

$$E^{(1)}_{\rm up} \cong \varepsilon^{(1)}_{\rm up} \frac{M_{\rm up}}{\bar{\rho}} f^{(1)}_{\rm scale} \tag{6.5}$$

where the fractional entrainment (m^{-1}) traditionally inversely depends on cloud radius $(R_{\rm up})$ following (Simpson and Wiggert, 1969; Simpson, 1971), i.e.

$$\varepsilon^{(1)}_{\rm up} \sim \frac{0.2}{R_{\rm up}} \tag{6.6}$$

With Cy36r4 the updraught entrainment formulation has been simplified to retain only one entrainment process/formulation representing both "turbulent" and "organized" mass exchanges. Entrainment above cloud base is applied to positively buoyant convection only. Observations show that mid-tropospheric relative humidity strongly controls the cloud top heights, and it could be even shown through cloud resolving simulations (Stirling and Derbyshire, private communication)that dry environments lead to larger entrainment, probably through evaporative cooling and inflow effects. The simplest way to represent this sensitivity and to increase the mass fluxes in unstable buoyant situations, is a formulation depending on the environmental relative humidity RH

$$E^{(1)}_{\rm up} = \varepsilon^{(1)}_{\rm up} f_\varepsilon \frac{M_{\rm up}}{\bar{\rho}} \Big(1.3 - RH\Big) f^{(1)}_{\rm scale}, \quad \varepsilon^{(1)}_{\rm up} = 1.75 \times 10^{-3} \mathrm{m}^{-1}, \quad f^{(1)}_{\rm scale} = \left(\frac{q_{\rm sat}(\bar{T})}{q_{\rm sat}(\bar{T}_{\rm base})}\right)^3 \tag{6.7}$$

This entrainment formulation is able to reasonably represent the tropical variability of convection (Bechtold *et al.*, 2008). It is applied to all types of convection and only distinguishes between the different

types by the factor f_ε which takes the value of one for deep convection and 2 for shallow and mid-level convection. The vertical scaling function $f^{(1)}_{\text{scale}}$ in (6.7) is supposed to mimic the effects of a cloud ensemble and/or the effect of increasing (R_{up}) with height. As the scaling function strongly decreases with height the detrainment rate will become eventually larger than the entrainment rate, and the mass flux starts to decrease with height. Together with the detrainment (see below) the formulation produces on average a vertical distribution of the convective mass flux that broadly follows that of the large-scale ascent which is partly supported by diagnostic studies for tropical convection (e.g. Cheng *et al.*, 1980; Johnson, 1980). Finally, note that in cycles prior to 32r3 the "organized" entrainment has been linked to the large-scale moisture convergence as first advocated by Lindzen (1981). However, the imposed strong coupling between the large-scale and the convection had a detrimental effect on the forecasts ability to represent tropical variability. Only since Cy32r3, using entrainment rates scaled by a vertical function together with a relative humidity based organized entrainment, and a variable convective adjustment time-scale (see below), the model is able to maintain a realistic level of tropical variability.

(*b*) *Detrainment rates and updraught kinetic energy*

Turbulent detrainment rates (s^{-1}) for deep convection are parametrized as

$$D^{(1)}_{\text{up}} = \delta^{(1)}_{\text{up}} \frac{M_{\text{up}}}{\bar{\rho}} \Big(1.6 - RH\Big); \qquad \delta^{(1)}_{\text{up}} = 0.75 \times 10^{-4}\ \text{m}^{-1} \tag{6.8}$$

whereas turbulent detrainment rates for shallow convection are parametrized as

$$D^{(1)}_{\text{up}} = E^{(1)}_{\text{up}} \Big(1.6 - RH\Big) \tag{6.9}$$

The updraught kinetic energy K_{up} is obtained from

$$\frac{\partial K_{\text{up}}}{\partial z} = -\frac{\mu_{\text{up}}}{M_{\text{up}}}(1 + \beta C_{\text{d}})2K_{\text{up}} + \frac{1}{f(1+\gamma)} g \frac{T_{\text{v,up}} - \bar{T}_{\text{v}}}{\bar{T}_{\text{v}}} \tag{6.10}$$

with

$$K_{\text{up}} = \frac{w^2_{\text{up}}}{2} \tag{6.11}$$

where $w_{\text{up}}\bar{\rho}$ is the updraught vertical velocity, $T_{\text{v,up}}$ is the virtual temperature of the updraught and $\bar{T}_{\text{v}}$ the virtual temperature of the environment. μ_{up} is a mixing coefficient which is equal to the entrainment rate $(E_{\text{up}}\bar{\rho})$, or the detrainment rate $(D_{\text{up}}\bar{\rho})$ if the former is zero. As entrainment is weak in the upper part of the cloud layer, detrainment in this region better represents the effect of mixing and vertical pressure gradients , therefore reducing vertical velocity and reducing overshoot of convective towers into the lower stratosphere.

$\gamma = 0.5$ is the virtual mass coefficient (Simpson and Wiggert, 1969), the factor $f = 2$ is introduced because the flow is highly turbulent (Cheng *et al.*, 1980) and for the drag coefficient a value of $C_{\text{d}} = 0.506$ is used (Simpson and Wiggert, 1969). The value for β is 1.875. The cloud base value of the updraught velocity is chosen as 1 m s^{-1}.

w_{up} enters the scheme in several ways: (i) for the generation and fallout of rain (Section 6.6), (ii) to determine the top of the updraught (cloud) as the level where w_{up} reduces to zero and where the tropospheric stability $\partial\bar{T}\partial z \leq -3 \times 10^{-3}$ (G. Zängl private communication), and (iii) to specify organized detrainment below inversion layers and the top of the updraught.

The organized detrainment is set proportional to the decrease in updraught vertical velocity with height

$$\frac{M_{\text{up}}(z+\Delta z)}{M_{\text{up}}(z)} = \Big(1.6 - RH\Big)\sqrt{\frac{K_{\text{up}}(z+\Delta z)}{K_{\text{up}}(z)}}; \qquad D^{(2)}_{\text{up}} = \frac{M_{\text{up}}}{(\bar{\rho}\Delta z)}\left[1 - \Big(1.6 - RH\Big)\sqrt{\frac{K_{\text{up}}(z+\Delta z)}{K_{\text{up}}(z)}}\right] \tag{6.12}$$

where a relative humidity dependent factor has been introduced assuring a more gradual detrainment, in particular in the vicinity of inversions. The mean value of this proportionality factor roughly corresponds to the value derived by Derbyshire *et al.* (2011) from cloud resolving model data.

6.3.2 Downdraughts

Downdraughts are considered to be associated with convective precipitation from the updraughts and originate from cloud air influenced by the injection of environmental air. Following Fritsch and Chappell (1980) and Foster (1958), the Level of Free Sinking (LFS) is assumed to be the highest model level (below the level of minimum moist static energy) where a mixture of equal parts of cloud and saturated environmental air at the wet-bulb temperature becomes negative buoyant with respect to the environmental air. The downdraught mass flux is assumed to be directly proportional to the upward mass flux. Following Johnson (1976, 1980) the mass flux at the LFS is specified from the updraught mass flux at cloud base as

$$(M_{\text{down}})_{\text{LFS}} = -\eta (M_{\text{up}})_{\text{base}} \quad \text{with} \quad \eta = 0.3 \tag{6.13}$$

The vertical distribution of the downdraught mass flux, dry static energy, moisture, horizontal momentum and passive tracers below the LFS are determined by entraining/detraining plume equations similar to those for the updraught:

$$\left.\begin{aligned}
g\frac{\partial M_{\text{down}}}{\partial p} &= E_{\text{down}} - D_{\text{down}} \\
g\frac{\partial (M_{\text{down}} s_{\text{down}})}{\partial p} &= E_{\text{down}}\bar{s} - D_{\text{down}} s_{\text{down}} + L e_{\text{down}} \\
g\frac{\partial (M_{\text{down}} q_{\text{down}})}{\partial p} &= E_{\text{down}}\bar{q} - D_{\text{down}} q_{\text{down}} - e_{\text{down}} \\
g\frac{\partial (M_{\text{down}} u_{\text{down}})}{\partial p} &= E_{\text{down}}\bar{u} - D_{\text{down}} u_{\text{down}} \\
g\frac{\partial (M_{\text{down}} v_{\text{down}})}{\partial p} &= E_{\text{down}}\bar{v} - D_{\text{down}} v_{\text{down}} \\
g\frac{\partial (M_{\text{down}} C^i_{\text{down}})}{\partial p} &= E_{\text{down}}\bar{C}^i - D_{\text{down}} C^i_{\text{down}}
\end{aligned}\right\} \tag{6.14}$$

e_{down} is the evaporation of convective rain to maintain a saturated descent; the moistening and cooling of the environmental air injected at the LFS is also due to evaporating rain.

Entrainment and detrainment in downdraughts are highly uncertain as relevant data are not available. As for the updraught, both turbulent and organized entrainment/detrainment are considered.

(*a*) *Turbulent entrainment and detrainment*

For turbulent mixing

$$\varepsilon^{(1)}_{\text{down}} = \delta^{(1)}_{\text{down}} = 2 \times 10^{-4}\ \text{m}^{-1} \tag{6.15}$$

(*b*) *Organized entrainment and detrainment*

Organized entrainment for the downdraught is based upon a formulation suggested by Nordeng (1994) so that

$$\varepsilon^{(2)}_{\text{down}} = \frac{\left\{ g\frac{T_{\text{v,down}} - T_{\text{down}} r_{\text{down}} - \bar{T}_{\text{v}}}{\bar{T}} \right\}}{(w^{\text{LFS}}_{\text{down}})^2 - \int_{z_{\text{LFS}}}^{z} \left\{ g\frac{T_{\text{v,down}} - T_{\text{down}} r_{\text{down}} - \bar{T}_{\text{v}}}{\bar{T}} \right\} \text{dz}} \tag{6.16}$$

where $w^{\text{LFS}}_{\text{down}}$ is the vertical velocity in the downdraught at the LFS (set to -1 ms^{-1}). The total evaporation rate in the downdraft corresponds to the total downdraft precipitation rate that is simply given as

$$\sum_{k=\text{LFS}}^{\text{nlev}} e_{\text{down}} = \sum_{k=\text{LFS}}^{\text{nlev}} \frac{g}{\Delta p}(q_{\text{down,k}} - \hat{q}_{\text{down,k}}) M_{\text{down,k}} \tag{6.17}$$

where $q_{\text{down,k}}$ is the value of the downdraft humidity computed from (6.14) without saturation adjustment, and $\hat{q}_{\text{down,k}}$ is the humidity after the saturation adjustment. The value of the rain water

content in the downdraft used in (6.16) is estimated as $r_{\rm down} = e_{\rm down}\Delta p/(gM_{\rm up})$, for the definition of the pressure thickness Δp of layer k see (6.61).

Organized detrainment from the downdraught occurs when either the downdraught becomes positively buoyant or approaches the surface. If the downdraught remains negatively buoyant until it reaches the surface then the mass flux is decreased linearly over the lowest 60 hPa of the atmosphere. However, if a downdraught becomes positively buoyant during its descent, it is detrained over one level, except where this occurs at cloud base. In this case the downdraught fluxes are decreased linearly (deep convection) or quadratically (mid-level convection) to zero at the surface.

6.4 CONVECTION INITIATION AND CONVECTIVE TYPES

The first important task of a convection parametrization is to decide if convection is active or not in a model grid column. This is done in a very simplified "first-guess" updraught computation that implies the determination of the cloud base level, i.e. the Lifting Condensation Level (LCL), and of the properties of the cloud (updraught) at cloud base. Furthermore, in using a bulk mass flux scheme, as opposed to a scheme which considers an ensemble of convective clouds (such as that of Arakawa and Schubert, 1974), some determination of convective cloud type must be made so that appropriate choices can be made for the cloud properties.

The scheme first tests for the occurrence of shallow convection by computing the ascent of a surface parcel. The following simplified updraught equation is applied

$$\frac{\partial \phi_{\rm up}}{\partial z} = \varepsilon_{\rm up}^{\rm ini}(\bar{\phi} - \phi_{\rm up}) \tag{6.18}$$

where ϕ stands either for the dry static energy or the total water specific humidity. Similar to Jakob and Siebesma (2003) the entrainment rate for the test parcel for shallow convection is set to $\varepsilon_{\rm up}^{\rm ini} = (0.8z^{-1} + 3\times10^{-4})$ and is the same as that used for the updraught parcel in the boundary-layer scheme (Chapter 3). Additionally, a temperature $\Delta T_{\rm up}$ and moisture excess $\Delta q_{\rm up}$ with respect to the environment is given to the test parcel at the two lowest model level depending on the surface sensible and latent turbulent heat fluxes

$$\Delta T_{\rm up}^{\rm shal} = max\left(0.2, -1.5\frac{J_s}{\bar{\rho}c_p w_*}\right) \quad \text{and} \quad \Delta q_{\rm up}^{\rm shal} = max\left(1\times10^{-4}, 1.5\frac{J_q}{\bar{\rho}L w_*}\right) \tag{6.19}$$

limited to $\Delta T_{\rm up}^{\rm shal} \leq 1$K and $q_{\rm up}^{\rm shal} \leq 5\times10^{-4}$kgkg^{-1}, respectively. The convective-scale velocity w_* is given as

$$w_* = 1.2\left(u_*^3 - 1.5\frac{gz\kappa}{\bar{\rho}\bar{T}}\left[\frac{J_s}{c_p} + \varepsilon'\bar{T}\frac{J_q}{L_{\rm vap}}\right]\right)^{\frac{1}{3}} \tag{6.20}$$

with $\kappa = 0.4$ the von Kármán constant and $\varepsilon' \approx 0.61$. The friction velocity u_* is defined in the turbulence scheme (3.9), with a minimum value of 0.1 ms^{-1}. The convective-scale velocity w_* is also used to initialize the updraft vertical velocity at the first model level. A grid column is then identified as shallow convective if a LCL is found for the surface parcel, if the updraft vertical velocity at the LCL (obtained by solving the kinetic energy equation (6.10)) is positive, and if the cloud thickness is smaller than 200 hPa.

Next, the occurrence of deep convection is tested for by repeating the updraught computations but starting at the next higher model level. However, the entrainment rate is now set as similar to the first full updraught computation, i.e. $\varepsilon_{\rm up}^{\rm ini} = 0.4\times\varepsilon_{\rm up}^{(1)}\left(q_{\rm sat}(\bar{T})/q_{\rm sat}(\bar{T}_{\rm surf})\right)^3$. Simplified microphysics is taken into account by removing at each level 50% of the condensed water. The parcel perturbations for the first departure level of deep convection (i.e the second lowest model level) are the same as in (6.19) for shallow convection, while constant perturbations are applied to all higher departure levels, except for humidity below 700 hPa, where an additional positive perturbation from moisture advection is taken into account with a fixed time-scale of $\tau_{\rm adv} = 600$ s.

$$\Delta T_{\rm up}^{\rm deep} = 0.2\ {\rm K} \quad \text{and} \quad \Delta q_{\rm up}^{\rm deep} = 1\times10^{-4} + \min\left(3\times10^{-4}, \frac{\partial \bar{q}_{\rm v}}{\partial t}\Big|_{\rm adv}\tau_{\rm adv}\right){\rm kgkg}^{-1} \tag{6.21}$$

The updraught vertical velocity at the departure level is initialized to 1 ms^{-1}. Furthermore, in the lowest 60 hPa of the atmosphere that typically correspond to the mixed-layer depth over oceanic regions, the updraught values of the dry static energy (or humidity) at the departure level k are initialised as $s_{\mathrm{up},k} = \tilde{s}_k + c_p \Delta T_{\mathrm{up}}^{\mathrm{deep}}$, where the tilde symbol represents a 50 hPa layer average, instead of $s_{\mathrm{up},k} = \bar{s}_k + c_p \Delta T_{\mathrm{up}}^{\mathrm{deep}}$ as for departure levels above the assumed 60 hPa mixed-layer. The idea behind is that deep convection requires a sufficiently deep source layer, this procedure also avoids spurious convection in the early morning hours when the surface-layer undergoes strong heating. A grid-column is then identified as deep-convective, if a LCL is found and the resulting cloud (the top being defined as the level where the updraught vertical velocity vanishes) is thicker than 200 hPa. If this criterion is verified the cloud is identified as deep and the results obtained for the shallow convective test parcel are ignored (only one cloud type can exist). If no deep convective cloud is found for the given departure level, the procedure is repeated starting from the next higher model level and so on, as long as the departure level of the test parcel is below 350 hPa. A summary of this procedure, and a discussion of the consequences for the simulation of the diurnal cycle of convection over land is given in Bechtold *et al.* (2004).

Finally, if neither deep nor shallow convection has been found, elevated (or mid-level) convection is tested for (see Subsection 6.4.3). Also, at the end of this procedure and if a column has been identified as convective, the computed values of the updraught vertical velocity, dry static energy, liquid water and specific humidity at cloud base are used to initialise the following full updraught computation at cloud base. The updraught values of the horizontal wind components at cloud base are simply set to the environmental values at the departure level.

In the following, the determination of the convective activity (as controlled by the cloud-base mass flux) is discussed separately for each type of convection.

6.4.1 Deep convection

Following the derivation in Bechtold *et al.* (2014) that included earlier work by Donner and Philips (2003), Nordeng (1994) and Gregory *et al.* (2000), an equilibrium is assumed between the large-scale and boundary-layer forcing (generating convective available potential energy CAPE) and convection (reducing the CAPE). As a measure for the CAPE (J kg^{-1}) we use the density weighted buoyancy integral of an entraining ascending air parcel, denoted as PCAPE (J m^{-3})

$$\mathrm{PCAPE} = -\int_{p_{\mathrm{base}}}^{p_{\mathrm{top}}} \left(\frac{T_{\mathrm{v,up}} - \bar{T}_{\mathrm{v}}}{\bar{T}_{\mathrm{v}}} - l_{\mathrm{up}} \right) dp \tag{6.22}$$

The advantage of PCAPE over an entraining CAPE is the density scaling that more readily relates the time derivative of PCAPE to the convective mass flux. Furthermore, assuming that convection reduces PCAPE over a time-scale τ toward a reference value $\mathrm{PCAPE}_{\mathrm{bl}}$, one can relate the reduction in PCAPE to the convective tendency expressed as the vertical advection of the environmental virtual temperature by the mass flux.

$$\begin{aligned} \left(\frac{\partial \mathrm{PCAPE}}{\partial t} \right)_{\mathrm{cu}} &= -\frac{\mathrm{PCAPE} - \mathrm{PCAPE}_{\mathrm{bl}}}{\tau} = \\ &- \int_{z_{\mathrm{base}}}^{z_{\mathrm{top}}} \frac{g}{\bar{T}_{\mathrm{v}}} \bar{\rho} \left(\frac{\partial \bar{T}_{\mathrm{v}}}{\partial t} \right)_{\mathrm{cu}} \mathrm{d}z \approx -\int_{z_{\mathrm{base}}}^{z_{\mathrm{top}}} M \frac{g}{\bar{T}_{\mathrm{v}}} \left(\frac{\partial \bar{T}_{\mathrm{v}}}{\partial z} + \frac{g}{c_p} \frac{\bar{T}_{\mathrm{v}}}{\bar{T}} \right) \mathrm{d}z \end{aligned} \tag{6.23}$$

where

$$M = M_{\mathrm{up}} + M_{\mathrm{down}} = \frac{M_{\mathrm{base}}}{M^*_{\mathrm{base}}} M^\star \tag{6.24}$$

The ratio between the actual (final) cloud base mass flux, and the unit (initial) cloud base mass flux $M_{\mathrm{base}}/M^*_{\mathrm{base}}$ is the convective scaling or closure factor. The initial mass flux profile M^* is known from the updraught computation starting at cloud base with value $M^\star_{\mathrm{base}} = 0.1 \Delta p_{\mathrm{base}}/(g \Delta t)$, with Δt the model time step.

Substituting (6.24) in (6.23) results in an expression for the cloud base mass flux given by

$$M_{\text{base}} = M^{\star}_{\text{base}} \frac{\text{PCAPE} - \text{PCAPE}_{\text{bl}}}{\tau} \frac{1}{\int_{z_{\text{base}}}^{z_{\text{top}}} \frac{g}{\bar{T}_{\text{v}}} M^{\star} \left(\frac{\partial \bar{T}_{\text{v}}}{\partial z} + \frac{g}{c_p} \frac{\bar{T}_{\text{v}}}{\bar{T}} \right) \text{d}z}; \quad M_{\text{base}} \geq 0 \tag{6.25}$$

The convective adjustment time scale τ is determined as follows. In cycles prior to 32r3 it was set close to or larger than the model time step. From cycle 32r3 onward it is set proportional to the convective turnover time scale τ_{c}

$$\tau = \frac{H}{\bar{w}_{\text{up}}} \alpha_{\text{x}} = \tau_{\text{c}} \alpha_{x} \qquad 720 \leq \tau \leq 10800 \text{ s} \tag{6.26}$$

where H is the cloud depth, $\bar{w}_{\text{up}}$ is the updraught velocity averaged over the cloud depth, and α_{x} is a scaling function depending on the horizontal grid spacing dx. The scaling is defined as

$$\begin{aligned} \alpha_{\text{x}} &= 1 + 1.60 \frac{dx}{dx_{\text{ref}}}, \quad dx_{\text{ref}} = 125 \times 10^3 \text{ m} \quad dx \geq 8 \times 10^3 \text{ m} \\ \alpha_{\text{x}} &= 1 + \left(\ln \left(\frac{8 \times 10^3 \text{ m}}{dx} \right) \right)^2, \qquad\qquad dx < 8 \times 10^3 \text{ m} \end{aligned} \tag{6.27}$$

It covers two regimes, one for $dx > 8$ km where the scaling factor converges to one and where the adjustment time scale decreases to the convective turnover time scale (and convective mass flux increases) when the resolution and large-scale forcing increases. The regime below $dx < 8$ km denotes the so called "grey zone" where deep convective motions become more and more resolved and the subgrid convective fluxes have to vanish in the limit of infinite resolution. The scaling factor α_{x} can be derived theoretically from the following equation in Malardel and Bechtold (2019)

$$\overline{\rho w' \psi'} = M_{\text{up}} \left(1 - \frac{w_{\text{env}}}{w_{\text{up}}} \right) (\psi_u - \overline{\psi}) = M_{\text{up}} \alpha_{\text{x}} (\psi_u - \overline{\psi}) \tag{6.28}$$

which shows that the basic mass flux equations are valid, even in the limit of non-negligible environmental vertical velocity w_{e}, i.e in the small area or small dx limit. The grey zone scaling we have used in (6.27) is an empricial scaling that has been developed by the Deutsche Wetterdienst over Europe using a large range of model resolutions.

However, comparison with observed rainfall distributions reveals (Becker *et al.*, 2021) that (6.25) underestimates the mass flux (rainfall) extremes and convective variability, impeding the propagation of mesoscale convective systems, especially when instability is weak, but vertical and horizontal advection is strong as in the mature phase of convective systems (Raymond and Fuchs-Stone, 2021). We therefore expanded in Cy47r3 (6.25) by adding the integrated and scaled total (vertical+horizontal) advective moisture tendency to PCAPE and recompute PCAPE in order not to double count these grid-scale effects. The final cloud base mass flux then writes as

$$M_{\text{base}} = M^{\star}_{\text{base}} \frac{\text{PCAPE}' + \text{QCV} - \text{PCAPE}_{\text{bl}}}{\tau} \frac{1}{\int_{z_{\text{base}}}^{z_{\text{top}}} \frac{g}{\bar{T}_{\text{v}}} M^{\star} \left(\frac{\partial \bar{T}_{\text{v}}}{\partial z} + \frac{g}{c_p} \right) \text{d}z}; \quad M_{\text{base}} \geq 0 \tag{6.29}$$

where

$$\text{PCAPE}' = (1 - \alpha_{\text{qcv}}) \, \text{PCAPE} + \alpha_{\text{qcv}} \, \text{PCAPE}'' \tag{6.30}$$

$$\text{PCAPE}'' = - \int_{p_{\text{base}}}^{p_{\text{top}}} \left(\frac{T_{\text{v,up}} - \bar{T}'_{\text{v}}}{\bar{T}'_{\text{v}}} - l_{\text{up}} \right) dp; \quad \bar{T}'_{\text{v}} = \left(\bar{T} - \frac{\partial \bar{T}}{\partial t}|_{\text{adv}} \Delta t \right) \left(1 + \varepsilon' \left(\bar{q} - \frac{\partial \bar{q}}{\partial t}|_{\text{adv}} \Delta t \right) \right) \tag{6.31}$$

and

$$\mathrm{QCV} = -\alpha_{\mathrm{qcv}} L_{\mathrm{vap}} \tau_c \frac{1}{g\,H} \int_{p_{\mathrm{surf}}}^{60\mathrm{hPa}} \left(\frac{\bar{q}}{\bar{q}_{\mathrm{sat}}}\right) \frac{\partial \bar{q}}{\partial t}|_{\mathrm{adv}} dp; \qquad \alpha_{\mathrm{qcv}} = 0.8 \tag{6.32}$$

However, we do not apply the moisture convergence term QCV in the extreme limit of the transition from parametrized to resolved convection, that is e.g. in the inner core of tropical cyclones, when the average saturation fraction integrated from the surface to the cloud top exceeds a value of 0.94.

The $\mathrm{PCAPE}_{\mathrm{bl}}$ term requires further elaboration. In model cycles prior to 40r1 this term has not been considered, implying that deep convection removes all PCAPE Gregory *et al.* (2000). This assumption obviously fails in non-equilibrium situations with rapidly varying boundary-layer forcing such as the diurnal cycle of convection and the convection tied to advective boundary-layers. As shown in Shutts and Gray (1999) deep convection scales with the surface buoyancy flux and therefore for convection rooting in the boundary-layer (lowest 50 hPa). Bechtold *et al.* (2014) have expressed the departure from equilibrium by $\mathrm{PCAPE}_{\mathrm{bl}}$ but using the integrated tendencies instead of the surface flux

$$PCAPE_{\mathrm{bl}} = -\tau_{\mathrm{bl}} \frac{1}{T_\star} \int_{p_{\mathrm{surf}}}^{p_{\mathrm{base}}} \left.\frac{\partial \bar{T}_{\mathrm{v}}}{\partial t}\right|_{\mathrm{bl}} dp \tag{6.33}$$

The tendency $\partial \bar{T}_{\mathrm{v}}/\partial t|_{\mathrm{bl}}$ includes all boundary-layer processes other than convection, i.e. turbulent diffusion, radiation and advection; therefore the corresponding tendencies must be available before the call of the convection scheme. The temperature scale $T_\star = c_p^{-1} g H$ is set to 1 and different boundary-layer time-scales τ_{bl} are used for land and water, i.e. over land the convective turnover time-scale is used and for water the advective time-scale

$$\begin{array}{ll} \tau_{\mathrm{bl}} = \tau_{\mathrm{c}} & \text{land} \\ \tau_{\mathrm{bl}} = \frac{z_{\mathrm{base}}}{\bar{u}_{\mathrm{bl}}} & \text{water} \end{array} \tag{6.34}$$

where z_{base} is the cloud base height and $\bar{u}_{\mathrm{bl}}$ the average horizontal wind speed in the subcloud layer bounded to a lower limit of 2 m s^{-1}. With this definition $\mathrm{PCAPE}_{\mathrm{bl}}$ can also be seen as an efficient sine filter on PCAPE. $\mathrm{PCAPE}_{\mathrm{bl}}$ is set to zero for convection rooting above the boundary-layer.

Once M_{base} is computed all deep convective updraught and downdraught fluxes of mass, energy, momentum and water are rescaled by the closure factor $M_{\mathrm{base}}/M^*_{\mathrm{base}}$.

6.4.2 Shallow convection

A distinction between deep and shallow convection is made on the basis of the first-guess convective cloud depth. If the cloud extends over more than 200 hPa then convection is classified as deep, and shallow otherwise. This distinction is only necessary for the closure and the specification of the entrainment rates that are a factor of two larger for shallow convection (see Section 6.3.1). Typical examples of shallow convection are trade-wind cumuli under a subsidence inversion, convection occurring in the ridge region of tropical easterly waves, daytime convection over land and in oceanic regions during cold air outbreaks. This type of convection is effectively controlled by the surface fluxes. In fact, most of the diagnostic studies carried out for trade-wind cumuli show that the net upward moisture flux at cloud-base level is nearly equal to the turbulent moisture flux at the surface (Le Mone and Pennell, 1976).

As shown in Bechtold *et al.* (2014) the shallow convective mass flux can be derived in a similar way to the deep convective mass flux but using a balance assumption for the subcloud-layer. Using the moist static energy budget one obtains

$$\frac{1}{g}\int_{p_{\mathrm{surf}}}^{p_{\mathrm{base}}} \left.\frac{\partial \bar{h}}{\partial t}\right|_{\mathrm{cu}} dp = \left|_{p_{\mathrm{surf}}}^{p_{\mathrm{base}}} F_h|_{\mathrm{cu}} = M^\star_{\mathrm{base}}(h_{\mathrm{up}} - \bar{h})_{\mathrm{base}} = -\frac{1}{g}\int_{p_{\mathrm{surf}}}^{p_{\mathrm{base}}} \left.\frac{\partial \bar{h}}{\partial t}\right|_{\mathrm{bl}} dp; \quad M^\star_{\mathrm{base}} \geq 0 \right. \tag{6.35}$$

with F_h the convective moist static energy flux (assumed to be zero at the surface) and

$$\bar{h} = c_p \bar{T} + L\bar{q} + gz \tag{6.36}$$

The rhs of 6.35, i.e. the integrated tendency of the moist static energy contains the contributions from the advection, the radiation and the boundary-layer diffusion (surface fluxes). The final mass flux M_{base} is quasi-identical to the initial mass flux $M^{\star}_{\text{base}}$ apart from a correction due to downdraught effects

$$M_{\text{base}} = \frac{-\frac{1}{g}\int_{p_{\text{surf}}}^{p_{\text{base}}} \frac{\partial \bar{h}}{\partial t}\Big|_{\text{bl}} dp}{[h_{\text{up}} - \beta h_{\text{down}} - (1-\beta)\bar{h}]}; \qquad \beta = (M_{\text{down}}/M^{\star})_{\text{base}} \tag{6.37}$$

In certain cases the denominator in (6.37) can become very small and the cloud base mass flux unrealistically large. Therefore, when the cloud base mass flux exceeds the CFL stability limit (see 6.70) and the denominator is small, we limit the denominator to a value of $dh >= 0.75 c_{\text{p}}$. The mass flux scaling depends on the choice of the variable. Using h assures that $(h_{\text{up}} - \bar{h})$ is positive but produces larger mass flux than when considering the budget for q instead. One cannot use the budget for T_{v} as the updraught buoyancy excess at cloud base is mostly negative, but we could have also used the scaling in (6.33) to obtain very similar mass fluxes to (6.35).

Again, once M_{base} is computed all convective updraught and downdraught fluxes of mass, energy, momentum and water are rescaled by the closure factor $M_{\text{base}}/M^{\star}_{\text{base}}$.

6.4.3 Mid-level convection

Mid-level convection is considered to occur at rain bands at warm fronts and in the warm sector of extra-tropical cyclones (Browning *et al.*, 1973; Houze *et al.*, 1976; Herzegh and Hobbs, 1980). These cells are probably formed by the lifting of low level air until it becomes saturated (Wexler and Atlas, 1959) and the primary moisture source for the clouds is from low-level large-scale convergence (Houze *et al.*, 1976). This occurs often in connection with mesoscale circulations which might be related to conditionally symmetric instability (Bennets and Hoskins, 1979; Bennets and Sharp, 1982) or a wave-CISK mechanism (Emanuel, 1982).

Here we use a parametrization which in a simple way considers the finding of the diagnostic studies mentioned above. We assume that mid-level convection can be activated in a height range between $0 < z < 1 \times 10^4$ m when there is a large-scale ascent, and the environmental air is sufficiently moist, i.e. of relative humidity in excess of 80%.

However, in practice mid-level convection is often activated in moist layers near the top of the boundary-layer if no shallow convection is found. In order to assure a continuity with the shallow closure, the convective mass flux is set to the maximum of the contribution by either the large-scale vertical mass transport or the surface enthalpy flux

$$M_{\text{base}} = max\left(-\bar{\omega}_{\text{base}}, (J_s + J_q)/(g z_{\text{base}})\right); \quad M_{\text{base}} \geq 10^{-6} \tag{6.38}$$

with ω the large-scale vertical velocity in pressure coordinates. The mid-level closure is the only place in the scheme where the convection is directly linked to the grid-scale vertical velocity field.

6.5 SUB-CLOUD LAYER

The first level at which convective mass, momentum and thermodynamic fluxes are estimated is cloud base. To represent the effects of convective updraughts on the sub-cloud layer a simple scaling of cloud base fluxes is applied in which they decrease to zero at the surface through the sub-cloud layer.

Care must be taken to ensure that fluxes of liquid water are zero below cloud base. Through the cloud base level an interpolation of the fluxes of liquid water static energy and total water content is used to estimate fluxes of dry static energy and water vapor mixing ratio in the level immediately below cloud

base;

$$\begin{aligned}(Ms)_{\rm up}^{\rm base+1} &= (Z^n)(Ms)_{\rm up}^{\rm base} - L(Ml)_{\rm up}^{\rm base}\\ (Mq)_{\rm up}^{\rm base+1} &= (Z^n)(Mq)_{\rm up}^{\rm base} + (Ml)_{\rm up}^{\rm base}\\ (Ml)_{\rm up}^{\rm base+1} &= 0\end{aligned} \tag{6.39}$$

where $\phi^{\rm base+1}$ refers to the value of ϕ at the level immediately below cloud base. Z is given by

$$Z = \left(\frac{p_{\rm surf} - p_{\rm base+1}}{p_{\rm surf} - p_{\rm base}}\right)^m \tag{6.40}$$

and $p_{\rm surf}$ is the surface pressure.

For deep and shallow convection m is set to 1 (implying a linear decrease in the flux with pressure below cloud base) while for mid-level convection m is equal to 2 (implying a quadratic reduction in flux below cloud base).

For the remainder of the sub-cloud layer, fluxes at level 'B + 1' are reduced to zero at the surface using Z recomputed as

$$Z = \left(\frac{p_{\rm surf} - p_k}{p_{\rm surf} - p_{\rm base+1}}\right)^m \tag{6.41}$$

where p_k is the pressure at level model k. However, for the current numerical solver it is required that the total mass flux remains positive, i.e. the downdraught mass flux cannot exceed the updraught mass flux. To avoid reducing the downdraught mass fluxes in this case, we reset $m = 1/2$ and rescale the updraught mass fluxes in the subcloud layer if the downdraught reaches the surface and its near surface mass flux exceeds 50% of the near surface updraught mass flux (computed with m=1).

The cloud-mass and momentum fluxes in the sub-cloud layer are treated in a similar manner.

6.6 CLOUD MICROPHYSICS

6.6.1 Condensation rate in updraughts

The updraught condensation rate $c_{\rm up}$ is computed through a saturation adjustment

$$c_{\rm up} = \frac{g}{\Delta p}(q_{\rm up} - \hat{q}_{\rm up})M_{\rm up} \tag{6.42}$$

where $q_{\rm up}$ is the value of the specific humidity before the saturation adjustment, and $\hat{q}_{\rm up}$ is the specific humidity at saturation after the adjustment.

6.6.2 Freezing in convective updraughts

We assume that shallow convective clouds remain in the liquid phase (since Cy45r1). For deep convection condensate in the convective updraughts freezes in the temperature range $T_{\rm ice} \le T \le T_0$, with $T_0 = 273.16$ K the triple point temperature and $T_{\rm ice} = 235.16$ K. Therefore, the fraction of total condensate in the ice phase is expressed by the factor $\alpha_{\rm T}$

$$\begin{aligned}\alpha_{\rm T} &= 0 && T \le T_{\rm ice}\\ \alpha_{\rm T} &= \left(\frac{T - T_{\rm ice}}{T_0 - T_{\rm ice}}\right)^2 && T_{\rm ice} < T < T_0\\ \alpha_{\rm T} &= 1 && T \ge T_0\end{aligned} \tag{6.43}$$

which is also used to evaluate the saturation specific humidity and the latent heat as an interpolation of their values with respect to water and ice.

6.6.3 Generation of precipitation

The conversion from cloud water/ice to rain/snow is treated in a consistent way with that in the large-scale precipitation scheme by using a formulation following Sundqvist (1978)

$$G^{\text{precip}} = \frac{M_{\text{up}}}{\bar{\rho}} \frac{c_0}{0.75 w_{\text{up}}} l_{\text{up}} [1 - \exp\{-(l_{\text{up}}/l_{\text{crit}})^2\}] \tag{6.44}$$

where c_0 is the autoconversion rate with increased values for the liquid phase, $c_0 = c_{00}(1 + 0.3\alpha_{\text{T}})$, $c_{00} = 1.4 \times 10^{-3}$ s^{-1} and $l_{\text{crit}} = 0.5$ g kg^{-1}. w_{up} is the updraught vertical velocity and is limited to a maximum value of 15 m s^{-1} in (6.44). Conversion only proceeds if l_{up} is greater than a threshold liquid water content of 0.3 g kg^{-1} over water and 0.5 g kg^{-1} over land to prevent precipitation generation from small water contents. With this autoconversion rate the updraft condensate content is probably still overestimated. However, with even larger values of the conversion coefficient the precipitation efficiency of the convection scheme would be too high, and the detrainment of cloud condensate too low. In Cy50r1, the autoconversion rate is multiplied by 0.8 over land and 0.9 over ocean for shallow and mid-level convection, while for deep convection it is multiplied by 1.11, if more than ζ=10% of precipitation produced by deep convection is handed over to the resolved scale (6.56).

Sundqvist (1978) takes into account the Bergeron–Findeisen process for temperatures below $-5°$C through a temperature dependent modification of c_0 and l_{crit} given by

$$\begin{aligned} c_0' &= c_0 c_{\text{BF}} \\ l_{\text{crit}}' &= l_{\text{crit}}/c_{\text{BF}} \end{aligned} \tag{6.45}$$

where

$$\begin{aligned} c_{\text{BF}} &= 1 + 0.5\sqrt{\min(T_{\text{BF}} - T_{\text{up}}, T_{\text{BF}} - T_{\text{ice}})} \quad \text{for } T < T_{\text{BF}} \\ c_{\text{BF}} &= 1 \quad \text{for } T > T_{\text{BF}} \end{aligned} \tag{6.46}$$

with $T_{\text{BF}} = 268.16$ K.

Equation (6.44) is integrated analytically in the vertical using the generic differential equation $dl/dz = -al + b$, where l is the cloud water, $a = G^{\text{precip}}\bar{\rho}/(l_{up} M_{\text{up}})$, and $b = c_{\text{up}}\Delta t$. The analytical solution is then given by $l = l_0 \exp^{-az} + b/a(1 - \exp^{-az})$.

6.6.4 Fallout of precipitation in the updraught

The fallout of rain water/snow in the updraught is parametrized as (e.g. Kuo and Raymond, 1980)

$$S_{\text{fallout}} = \frac{g}{\Delta p} M_{\text{up}} \frac{V}{w_{\text{up}}} r_{\text{up}} \tag{6.47}$$

where Δp is the model layer depth. The terminal velocity V is parametrized as (Liu and Orville, 1969)

$$V = 21.18 r_{\text{up}}^{0.2} \tag{6.48}$$

Since the fall speed of ice particles is smaller than that of water droplets, only half the value of V calculated with (6.48) is used for ice. In estimating the fallout of precipitation in the mixed phase region of the cloud a weighted mean of the fall speed for ice and water precipitation is used. Equation (6.47) is integrated in the vertical with the same analytical framework as (6.44).

6.6.5 Evaporation of rain

The evaporation rate of convective rain below cloud base is activated when the critical relative humidity RH_{cr} in the environment drops below 85% (90%) over water and 70% (75%) over land in the case of deep (shallow) convection. The different values for deep and shallow convection account for larger drops and less evaporation in deep convective rainfall compared to shallow. The evaporation rate is parametrized following Kessler (1969), where the evaporation is assumed to be proportional to the saturation deficit

$(RH_{\rm cr}\bar{q}_{\rm sat} - \bar{q})$ and to be dependent on the density of rain $\rho_{\rm rain}$ (gm^{-3})

$$e_{\rm subcld} = \alpha_1 (RH_{\rm cr}\bar{q}_{\rm sat} - \bar{q})\rho_{\rm rain}^{13/20} \tag{6.49}$$

where α_1 is a constant being zero for $\bar{q} > RH_{\rm cr}\bar{q}_{\rm sat}$.

As the density of rain $\rho_{\rm rain}$ is not given by the model it is convenient to express it in terms of the precipitation flux P(kg m^{-2} s^{-1}) as

$$P = \rho_{\rm rain} V_{\rm rain} \tag{6.50}$$

where $V_{\rm rain}$ is the mean fall speed of rain drops which again is parametrized following Kessler (1969).

$$V_{\rm rain} = \alpha_2 \rho_{\rm rain}^{1/8} / \sqrt{p/p_{\rm surf}} \tag{6.51}$$

(Note that this is different from the formulation used in the estimation of the fallout of precipitation.)

Considering that the convective rain takes place only over a fraction $C_{\rm conv}$ of the grid area, the evaporation rate at level k becomes

$$e_{\rm subcld} = C_{\rm conv}\alpha_1 (RH_{\rm cr}\bar{q}_{\rm sat} - \bar{q}) \left[\frac{\sqrt{p/p_{\rm surf}}}{\alpha_2} \frac{P}{C_{\rm conv}} \right]^{\alpha_3} \tag{6.52}$$

where the constants have the following values (Kessler, 1969)

$$\alpha_1 = 5.44 \times 10^{-4}\ {\rm s}^{-1} \quad \alpha_2 = 5.09 \times 10^{-3} \quad \alpha_3 = 0.5777$$

The fractional area of precipitating clouds is assumed constant for deep convection $C_{\rm conv} = 0.05$, whereas for shallow convection the fractional cover is assumed to vary between 5 and 45% depending on the average relative humidity in the cloud layer $C_{\rm conv,shal} = C_{\rm conv}(1 + (max(0.8, \bar{RH}) - 0.8)/0.025)$.

6.6.6 Melting and freezing of precipitation

Melting of snow falling across the freezing level T_0 is parametrized by a simple relaxation towards T_0 so that

$$M_{\rm elt} = \frac{c_p}{L_{\rm f}} \frac{(\bar{T}_{\rm w} - T_0)}{\tau} \tag{6.53}$$

where $M_{\rm elt}$ is the rate of melting, $\bar{T}_{\rm w}$ is the wet-bulb temperature and $\tau_{\rm melt}$ is a relaxation time scale which decreases with increasing temperature

$$\tau_{\rm melt} = \frac{\tau_{\rm m}}{\{1 + 0.5(\bar{T}_{\rm w} - \bar{T}_0)\}} \tag{6.54}$$

where $\tau_{\rm m} = 11800$ s. The wet-bulb temperature (in the melting parametrization, not that in the downdraught evaporation computation) is approximated as in the cloud scheme by

$$\bar{T}_w = \bar{T} - (q_{\rm sat}(\bar{T}) - \bar{q})(A + B(p - C) - D(\bar{T} - E)) \tag{6.55}$$

where $A = 1329.31$, $B = 0.0074615$, $C = 0.85 \times 10^5$, $D = 40.637$, and $E = 275$.

The parametrization may produce melting over a deeper layer than observed (Mason, 1971) but this has been intentionally introduced to account implicitly for the effects of vertical mixing which may develop in response to the production of negative buoyancy.

All liquid precipitation flux at temperatures $T < T_0$ is eventually frozen, while part of the heating directly drives the updraught. The term $F_{\rm rez}$ in 6.1 corresponds to the sum of frozen liquid precipitation and liquid condensate freezing during the ascent.

6.7 LINK TO CLOUD SCHEME

Before the introduction of the prognostic cloud scheme (see Chapter 7 'Clouds and large-scale precipitation') water detrained from convection ($D_{\rm up}l_{\rm up}$) was evaporated instantaneously. However with the prognostic cloud scheme, water detrained from convection is a source of cloud mass, increasing the water content of clouds, while the environmental mass flux subsidence is a sink term. In Cy43r3 we also included sources/sinks for the precipitating species (rain and snow), and in Cy50r1 we extended this to handing over ζ=0.4 (40%) of precipitation produced by deep convection to the resolved scale

$$\begin{aligned}\left(\frac{\partial \bar{l}}{\partial t}\right)_{\rm cu} &= g\frac{\partial}{\partial p}[M_{\rm up}l_{\rm up} - (M_{\rm up}+M_{\rm down})\bar{l})] = D_{\rm up}l_{\rm up} - g\frac{\partial}{\partial p}[(M_{\rm up}+M_{\rm down})\bar{l}] \\ \left(\frac{\partial \bar{r}}{\partial t}\right)_{\rm cu} &= g\frac{\partial}{\partial p}[M_{\rm up}r_{\rm up} - (M_{\rm up}+M_{\rm down})\bar{r})] = D_{\rm up}r_{\rm up} + \zeta G^{\rm precip} - g\frac{\partial}{\partial p}[(M_{\rm up}+M_{\rm down})\bar{r}]\end{aligned} \tag{6.56}$$

where $\bar{l}$ is the grid-box mean cloud water and $\bar{r}$ is the grid-box mean rain+snow content. Three important remarks apply to (6.56). First, the simplified rhs stems from the assumption that $E_{\rm up}=0$ for cloud species. Second, the mass flux subsidence term (last term on the rhs) is not included in the convective tendencies, as instead it is applied in the cloud scheme (7.96) within the implicit solver that handles subsidence and evaporation together. Third, the handover of precipitation to the resolved scale allows for hydrometeors to be advected and thus improves precipitation over coastal regions and orography. To compensate for additional rain evaporation in the cloud scheme, the evaporation of deep convective rain below cloud base is now deactivated, and autoconversion is increased for deep convection (Section 6.6.3). In the cloud scheme, in grid points where deep convection is active, cloud fraction is ensured to be at least 0.3 and snow fall speed is increased by 50%. Finally, maintaining a convective-to-large-scale precipitation ratio comparable to pre-Cy50r1 values (globally averaged) is achieved through a rescaling of precipitation fluxes, which is important for both the microwave operator in data assimilation and for forecasting. In a first step, all precipitation that was handed over to the resolved scale but remained in the same grid cell becomes convective precipitation again, and in a second step, at all grid points where deep convection is active, 50% of large-scale rain and 70% of large-scale snow becomes convective.

6.8 MOMENTUM TRANSPORT AND KINETIC ENERGY DISSIPATION

Equation set (6.3) includes a treatment of the vertical transport of horizontal momentum by convection. Studies have shown that for deep convection momentum transports are overestimated by the plume models unless the effects of cloud scale horizontal pressure gradients are included (Gregory *et al.*, 1997). For unorganized convection the effects of the pressure gradients are to adjust the in-cloud winds towards those of the large-scale flow. Pressure gradient effects might be represented by an enhanced entrainment rate in the updraught equations. For mass continuity the detrainment rate must then also be increased by an equivalent amount

$$\begin{aligned}E_{\rm up}^{(u,v)} &= E_{\rm up} + \lambda D_{\rm up} \\ D_{\rm up}^{(u,v)} &= D_{\rm up} + \lambda D_{\rm up}\end{aligned} \tag{6.57}$$

where $D_{\rm up}$ is given by (6.4).

Prior to Cy40r3 $\lambda=2$ for deep and mid-level convection and $\lambda=0$ otherwise (Gregory, 1997). However, the revision of the organized detrainment in Cy40r3 has allowed to set $\lambda=0$ for all types of convection. The momentum formulation limits the momentum transports to be downgradient. Upgradient transports by highly organized convective systems (e.g. African squall lines) are not captured by this method.

The definition of the horizontal wind in the updraught and downdraught at and below cloud base and LFS is not well known. For the updraught, the value at cloud base is set to the environmental value at the departure level. For the downdraught, the initial values at the LFS are set equal to the average

values of the winds in the updraught and those of the large-scale flow. The updraught values below cloud base are derived assuming a linear decrease of the fluxes from their cloud base value to zero at the surface. Finally, in order to correct for an apparent low-bias in the near surface wind speeds with the present linear flux relation (quasi-linear in case of an implicit time discretization see Section 6.10), the updraught velocities are decreased by a constant perturbation $u_{\rm pert}$=0.3 m s^{-1}

$$\begin{aligned} u_{\rm up} &= u_{\rm up} - min\left(u_{\rm pert}, |u_{\rm up}|\right)\ \ {\rm sign}(u_{\rm up}) \\ v_{\rm up} &= v_{\rm up} - min\left(u_{\rm pert}, |v_{\rm up}|\right)\ \ {\rm sign}(v_{\rm up}). \end{aligned} \tag{6.58}$$

Finally, with the introduction of Cy36r4 we have included the dissipation of the kinetic energy as a consequence of the convective momentum transport as an additional large-scale heat source as the convective momentum transport conserves momentum but not energy. The total kinetic energy dissipation D_{st} (W m^{-2}) in a model column can be estimated as

$$D_{\rm st} \approx -\left(\frac{\partial K}{\partial t}\right)_{\rm cu} \approx \int_{P_{surf}}^{0} \left(\bar{u}\left(\frac{\partial u}{\partial t}\right)_{\rm cu} + \bar{v}\left(\frac{\partial v}{\partial t}\right)_{\rm cu}\right)\frac{dp}{g} \tag{6.59}$$

A more precise formulation of the dissipation and discussion is provided in Steinheimer *et al.* (2007). Unfortunately one does not really know where the dissipation actually occurs. But one can reasonably distribute the dissipation over the model column using the module of the tendencies to obtain an additional convective heating due to kinetic energy dissipation as

$$\left(\frac{\partial \bar{T}}{\partial t}\right)_{\rm cu} = c_p^{-1} D_{\rm st} g f(p); \qquad f(p) = \frac{\sqrt{\left(\frac{\partial u}{\partial t}\right)_{\rm cu}^2 + \left(\frac{\partial v}{\partial t}\right)_{\rm cu}^2}}{-\int_{P_{surf}}^{0} \sqrt{\left(\frac{\partial u}{\partial t}\right)_{\rm cu}^2 + \left(\frac{\partial v}{\partial t}\right)_{\rm cu}^2} dp} \tag{6.60}$$

6.9 VERTICAL DISCRETIZATION OF THE MODEL EQUATIONS

The flux divergence in the large-scale budget equations (6.1) and in the cloud equations (6.3) and (6.14) are approximated by centred finite differences as

$$g\frac{\partial(M\phi)}{\partial p} = \frac{g}{\Delta p}(M_{k+1/2}\phi_{k+1/2} - M_{k-1/2}\phi_{k-1/2}), \quad \Delta p = p_{k+1/2} - p_{k-1/2} \tag{6.61}$$

Furthermore, the updraught/downdraught equations (6.3) and (6.14) including the entrainment/ detrainment terms are discretized as

$$\begin{aligned} \frac{g}{\Delta p}(M_{{\rm up},k-1/2}\phi_{{\rm up},k-1/2} - M_{{\rm up},k+1/2}\phi_{{\rm up},k+1/2}) &= E_{\rm up}\bar{\phi}_{k+1/2} - D_{\rm up}\phi_{{\rm up},k+1/2} \\ \frac{g}{\Delta p}(M_{{\rm down},k+1/2}\phi_{{\rm down},k+1/2} - M_{{\rm down},k-1/2}\phi_{{\rm down},k-1/2}) &= E_{\rm down}\bar{\phi}_{k-1/2} - D_{\rm down}\phi_{{\rm down},k-1/2} \end{aligned} \tag{6.62}$$

The updraught equation is solved for $\phi_{{\rm up},k-1/2}$ and the downdraught equation for $\phi_{{\rm down},k+1/2}$. Note that with the definition (6.5) the terms $E_{\rm down}$ and $D_{\rm down}$ are negative. For the horizontal wind components and for tracers, the half-level environmental values are defined as shifted full-level values, i.e. $\bar{\phi}_{k+1/2} = \bar{\phi}_k$ and $\bar{\phi}_{k-1/2} = \bar{\phi}_{k-1}$. Moreover, for tracers, in the updraught equation of (6.62), the last term includes the precipitation production $P_{\rm up}$ multiplied by the scavenging coefficient $Z^i_{\rm scav}$, as shown in equation (6.3). For temperature (dry static energy) and humidity, the half-level environmental values are determined by downward extrapolation from the next full level above along a cloud-ascent through that level giving

$$\left.\begin{aligned} \bar{T}_{k+1/2} &= \bar{T}_k + \left(\frac{\partial \bar{T}}{\partial p}\right)_{h_{\rm sat}}(p_{k+1/2} - p_k) \\ \bar{q}_{k+1/2} &= \bar{q}_k + \left(\frac{\partial \bar{q}}{\partial p}\right)_{h_{\rm sat}}(p_{k+1/2} - p_k) \end{aligned}\right\} \tag{6.63}$$

where $h_{sat} = c_p T + gz + Lq_{sat}$ is the saturation moist static energy. Using an extrapolation like (6.63) for calculating the subsidence of environmental air assures smooth profiles, and is also more consistent with the calculation of the updraughts where cloud air is transported upwards through level $k + 1/2$ with the thermal state below that level and equally with the downdraughts which depend only on values of s and q above that level. Similarly, because of (6.63) the subsidence of environmental air through the same level accounts now only for thermal properties above that level. The choice of a moist adiabat for extrapolation is dictated by the property of the moist static energy which is, by convection in the absence of downdraughts, only changed through the fluxes of moist static energy

$$\left(\frac{\partial \bar{h}}{\partial t}\right)_{cu} = g\frac{\partial}{\partial p}[M_{up}(h_{up} - \bar{h})] \tag{6.64}$$

As the lines of the saturation moist static energy h_{sat} through point $(p_{k+1/2}, \bar{T}_{k-1/2})$ and the updraught moist static energy are almost parallel, apart from entrainment effects, the difference $h_{up} - \bar{h}$ is little affected by the vertical discretization.

The ascent in the updraughts is obtained by vertical integration of (6.3). Starting at the surface the condensation level (equal to the lowest half-level which is saturated or supersaturated and where updraught velocity is positive) is determined from an adiabatic ascent. The cloud profile above cloud base is determined layer by layer by first doing a dry adiabatic ascent with entrainment and detrainment included and then adjusting temperature and moisture towards a saturated state, taking into account condensation and freezing processes. The buoyancy of the parcel is calculated taking into account the effects of cloud and precipitation water loading so that

$$B = T_{up}(1 + 0.608q_{up} - l_{up} - r_{up}) - \bar{T}(1 + 0.608q_e) \tag{6.65}$$

Special care has to be taken in the discretization of (6.10) because of overshooting effects. A centred differencing scheme is used so that

$$\begin{aligned}\frac{K_{up,k-1/2} - K_{up,k+1/2}}{z_{k-1/2} - z_{k+1/2}} = &\frac{E_{up,k}}{M_{up,k+1/2}}(1 + \beta C_d)\{K_{up,k-1/2} + K_{up,k+1/2}\} \\ &+ \frac{1}{f(1+\gamma)}\frac{g}{2}\left[\frac{\{T_{v,up} - \bar{T}_v\}_{k-1/2}}{\{T_v\}_{k-1/2}} + \frac{\{T_{v,up} - \bar{T}_v\}_{k+1/2}}{\{T_v\}_{k+1/2}}\right]\end{aligned} \tag{6.66}$$

Finally, we mention that for numerical reasons the environmental air must not be convectively unstably stratified so

$$\bar{s}_{k-1/2} \geq \bar{s}_{k+1/2} \tag{6.67}$$

In fact, one of the forecasts with the ECMWF global model became numerically unstable when (6.65) was not imposed.

6.10 TEMPORAL DISCRETIZATION

The convective tendencies for the environmental values can be obtained either by an explicit solution of the advection equation (6.1) written in flux form

$$\left(\frac{\partial \bar{\phi}}{\partial t}\right)_{cu} = \frac{g}{\Delta p}\left[M_{up}\phi_{up} + M_{down}\phi_{down} - (M_{up} + M_{down})\bar{\phi}\right]\Big|_{k-1/2}^{k+1/2} \tag{6.68}$$

or by an implicit formulation

$$\left(\frac{\partial \bar{\phi}}{\partial t}\right)_{cu} = \frac{\bar{\phi}_k^{n+1} - \bar{\phi}_k^n}{\Delta t} = \frac{g}{\Delta p}\left[M_{up}\phi_{up} + M_{down}\phi_{down} - (M_{up} + M_{down})\bar{\phi}^{n+1}\right]\Big|_{k-1/2}^{k+1/2} \tag{6.69}$$

where Δt denotes the time step and n the time instant. However, in order for the explicit solution to be stable it must satisfy the Courant–Friedrich–Levy (CFL) criterion, and therefore the mass flux values should be limited to

$$M_{up} + M_{down} \leq \frac{\Delta p}{g\Delta t} \tag{6.70}$$

It turned out that this mass flux limit is frequently reached in the case of shallow convection and long model time steps and that the application of this mass flux limiter contributed to a sensitivity of model results to the model time step.

With cycle Cy31r1 onwards the convective transports are solved implicitly for chemical tracers and horizontal winds, whereas a semi-implicit formulation is used for specific humidity and dry static energy. With the "shifted" vertical discretization for tracers and horizontal winds $\bar{\phi}_{k+1/2} = \bar{\phi}_k$ and $\bar{\phi}_{k-1/2} = \bar{\phi}_{k-1}$, (6.69) constitutes a bi-diagonal linear system with unknowns $\bar{\phi}_k^{n+1}$ and $\bar{\phi}_{k-1}^{n+1}$.

The implicit formulation for specific humidity and dry static energy (temperature) is less straightforward, as the half-level values are non-linear functions of the full-level values (6.65). Expressing the half-level values as a linear function of the full-level values

$$\begin{aligned} \bar{s}_{k-1/2}^{n+1} &= \bar{s}_{k-1}^{n+1} + \alpha_{k-1/2}^{(s)} \bar{s}_k^n \\ \bar{q}_{k-1/2}^{n+1} &= \bar{q}_{k-1}^{n+1} + \alpha_{k-1/2}^{(q)} q_{\text{sat}}(\overline{T}_k^n), \end{aligned} \tag{6.71}$$

with the coefficients $\alpha^{(s)}$ and $\alpha^{(q)}$ precomputed from

$$\begin{aligned} \bar{s}_{k-1/2}^{n} &= \bar{s}_{k-1}^{n} + \alpha_{k-1/2}^{(s)} \bar{s}_k^n \\ \bar{q}_{k-1/2}^{n} &= \bar{q}_{k-1}^{n} + \alpha_{k-1/2}^{(q)} q_{\text{sat}}(\overline{T}_k^n) \end{aligned} \tag{6.72}$$

the same bi-diagonal linear equation system as for tracers and momentum is obtained. Note that only the temperature and not the geopotential term of the dry static energy is formulated implicitly, and that the saturation specific humidity $q_{\text{sat}}(\overline{T}_k^n)$ has been preferred to q_k^n as it is smoother and positive definite.

Overall the implicit solution provides a stable and smoother solution through its inherent diffusivity. The mass flux CFL limit for temperature and humidity is set to 3, while for momentum and tracers a CFL limit of 1 is retained in order to prevent too strong mixing, resulting e.g. in too strong surface winds. Finally, an absolute mass flux limit of 2 kg $\text{m}^{-2}\text{s}^{-1}$ is applied.

6.11 DIAGNOSTICS FOR POST-PROCESSING: CAPE AND CIN AND OTHER CONVECTIVE INDICES

Grib code	Short Name	Description	Units
59.128	CAPE	Convective available potential energy	J kg^{-1}
232.228	CIN	Convective inhibition	J kg^{-1}
044.228	CAPES	CAPE-Shear	J kg^{-1}
231.228	MLCAPE50	CAPE from 50 hPa near surface mixed-layer	J kg^{-1}
232.228	MLCIN50	CIN from 50 hPa near surface mixed-layer	J kg^{-1}
233.228	MLCAPE100	CAPE from 100 hPa near surface mixed-layer	J kg^{-1}
234.228	MLCIN100	CIN from 100 hPa near surface mixed-layer	J kg^{-1}
235.228	MUCAPE	Maximum convective available potential energy	J kg^{-1}
237.228	PDEPL	Parcel Departure Level for updraught corresponding to CIN and MUCAPE	hPa
123.260	TOTALX	Convective Total Totals Index	K
121.260	KX	Convective K Index	K

As the CAPE computed in the convection routines is only computed for convectively active model columns, but taking into account lateral entrainment and liquid water loading (6.22) it was decided to provide to forecasters a diagnostic CAPE product that is horizontally more homogeneous and close in line with the actual WMO definition (i.e the CAPE corresponding to a pseudo-adiabatic ascent)

$$\text{CAPE} = \int_{p_{\text{LCL}}}^{p_{\text{top}}} -\left(\frac{\theta_{\text{v,up}} - \bar{\theta}_{\text{v}}}{\bar{\theta}_{\text{v}}}\right) \frac{\mathrm{d}p}{\bar{\rho}} \approx \int_{p_{\text{LCL}}}^{p_{\text{top}}} -\left(\frac{\theta_{\text{e,up}} - \bar{\theta}_{\text{esat}}}{\bar{\theta}_{\text{e,sat}}}\right) \frac{\mathrm{d}p}{\bar{\rho}}; \quad \theta_{\text{e,up}} - \bar{\theta}_{\text{e,sat}} > 0 \tag{6.73}$$

The pressure at the LCL, $p_{\rm LCL}$ is computed with the aid of the empirical formula by Davies-Jones (1983) which gives the adiabatic saturation temperature using the temperature and dewpoint temperature $T_{\rm d}$ at the departure model level $k_{\rm dep}$

$$\begin{aligned} T_{\rm LCL} &= T_{{\rm d},k_{\rm dep}} - \left(0.212 + 1.571\times10^{-3}(T_{{\rm d},k_{\rm dep}} - T_0) - 4.36\times10^{-4}(T_{k_{\rm dep}} - T_0)\right)(T_{k_{\rm dep}} - T_{{\rm d},k_{\rm dep}}) \\ p_{\rm LCL} &= p_0(T_{\rm LCL}/\theta_{k_{\rm dep}})^{c_{\rm p}/R_d} \end{aligned} \tag{6.74}$$

For reasons of numerical efficiency (avoiding the saturation adjustments) the CAPE has been approximated by the rhs of (6.73) using the updraught equivalent potential temperature $\theta_{\rm e} = T\left(\frac{p_0}{p}\right)^{R_{\rm d}/c_p}\exp\left(\frac{{\rm L}q}{c_{\rm p}T}\right)$ which is conserved during pseudo-adiabatic ascent, and the environmental saturated equivalent potential temperature $\theta_{\rm e,sat}$ which is a function of the environmental temperature only. The above integral is evaluated for parcels ascending from all model levels below 350 hPa of the atmosphere and initialising $\theta_{\rm e,up} = \theta_{{\rm e},k_{\rm dep}}$. For parcels ascending in the lowest 60 hpa, 30 hPa moving average mixed layer values are used. The CAPE value retained is the maximum value from the different ascents. This is the definition of CAPE in the operational archive and in the ERA5 reanalysis. However, in order to have a more accurate formulation of "CAPE" that better compares between the different weather Centres, we recompute with Cy47r3 the CAPE for the most unstable parcel using $\Theta_{\rm v}$ and the lhs of (6.73) and it is called MUCAPE. The departure level (hPa) of the most unstable parcel is stored in PDEPL. Furthermore, we provide with Cy47r3 additional diagnostics that correspond to the CAPE from a parcel ascent of a near surface 50 and 100 hPa mixed-layer, denoted as MLCAPE50 and MLCAPE100. The computation is the same as for MUCAPE and uses $\Theta_{\rm v}$.

The Convective Inhibition (CIN) is computed for the departure level producing the maximum CAPE only, and by retaining the negative part of the integral between the departure level and the level of free convection. The accurate computation of CIN requires using the virtual potential temperature $\Theta_{\rm v}$. Unfortunately prior to Cy47r1 and in the ERA5 $\Theta_{\rm v}$ was used and the results were only of limited use.

$$\text{CIN} = \int_{p_{\rm dep}}^{p_{\rm LFC}} \left(\frac{\theta_{\rm v,up} - \bar{\theta}_{\rm v}}{\bar{\theta}_{\rm v}}\right)\frac{{\rm d}p}{\bar{\rho}}; \quad \theta_{\rm v,up} - \bar{\theta}_{\rm v} < 0 \tag{6.75}$$

where LFC is the Level of Free Convection, approximated as the level where CAPE exceeds a small threshold. CIN is therefore positive definite. As for MLCAPE50 and MLCAPE100 we have also introduced with Cy47r3 the corresponding mixed-layer CIN values, MLCIN50 and MLCIN100.

As requested by forecasters additional stability indices for convection are provided. The CAPE-Shear parameter (CAPES) is defined as the product of the 500-925 hPa wind-shear and the square root of PCAPE. It aims at depicting areas with potential for organised long-lived mesoscale convection. The Total Totals Index (TOTALX) and K Index (KX) are defined as

$$\begin{aligned} \text{TOTALX} &= T(P_{850}) - T_{\rm d}(P_{850}) - 2T(P_{500}) \\ \text{KX} &= T(P_{850}) - T(P_{500}) + T_{\rm d}(P_{850}) - T(P_{700}) + T_{\rm d}(P_{700}) \end{aligned} \tag{6.76}$$

where $T_{\rm d}$ is the dewpoint temperature. These indices are actually evaluated on model levels that for a standard atmosphere correspond to the pressure levels in (6.76)

6.12 TROPOPAUSE PRESSURE

Grib code	Short Name	Description	Units
045.260	TRPP	Pressure of stability (thermal) tropopause	Pa

The pressure of the stability tropopause largely follows the method used in Santer *et al.* (2004). It is derived in isentropic coordinates using the identity

$$\frac{P}{\theta}\frac{d\theta}{dp} = \frac{P}{T}\frac{dT}{dp} - \frac{R_{\rm d}}{c_{\rm p}} \tag{6.77}$$

together with

$$\frac{P}{\theta}\frac{d\theta}{dp} = \frac{P}{\theta}\frac{d\theta}{dz}\frac{dz}{dp} = -\frac{R_d T}{g^2}\frac{g}{\theta}\frac{d\theta}{dz} = -\frac{R_d T}{g^2}N_0^2 \tag{6.78}$$

where N_0 is the Brunt-Vaisälä frequency. Using a transition value of $N_0^2 = 2.5 \times 10^{-4}$ s^{-2} and starting at 70 hPa, going downward, the tropopause is then defined as the level where the criterium

$$\frac{P}{T}\frac{dT}{dp} + \frac{R_d T}{g^2}N_0^2 \geq \frac{R_d}{c_p} \tag{6.79}$$

is first met. The tropopause is supposed to be in between 70 and 500 hPa. Note that this procedure is somewhat different from the WMO standard, where computations start near the surface and where the tropopause is defined as the lowest level at which the lapse rate dT/dz decreases to 2 K km^{-1} or less, provided that the average lapse rate between this level and all higher levels within 2 km does not exceed this value. However, the current procedure, using isentropes and the buoyancy frequency instead of the lapse rate is simpler and more robust than the WMO procedure.

6.13 LIGHTNING DIAGNOSTICS

Grib code	Short Name	Description	Units
50.228	LITOTI	Instantaneous total lightning flash density	km^{-2} day^{-1}
51.228	LITOTA1	Averaged total lightning flash density in last hour	km^{-2} day^{-1}
57.228	LITOTA3	Averaged total lightning flash density in last 3 hours	km^{-2} day^{-1}
58.228	LITOTA6	Averaged total lightning flash density in last 6 hours	km^{-2} day^{-1}

A parametrization able to diagnose lightning activity from some convective predictors from the model is available (Lopez, 2016). The diagnosed quantity is the density of "total" lightning flashes, which means that there is at present no discrimination between cloud-to-cloud (CC) and cloud-to-ground (CG) lightning flashes. The parametrization is based on the following predictors:

- CAPE (in J kg^{-1}),
- the vertical profile of convective frozen precipitation flux (P_f; in kg m^{-2} s^{-1}),
- the profile of cloud condensate amount within the convective updraft (q_{cond}; in kg kg^{-1}),
- the convective cloud base height (z_{base}; in km).

First, the respective amounts of graupel (q_{graup}; in kg kg^{-1}) and snow (q_{snow}; in kg kg^{-1}) are diagnosed from the following partitioning of P_f for each model vertical level:

$$q_{graup} = \beta\frac{P_f}{\overline{\rho}\, V_{graup}} \tag{6.80}$$

$$q_{snow} = (1-\beta)\frac{P_f}{\overline{\rho}\, V_{snow}} \tag{6.81}$$

where $\overline{\rho}$ denotes air density (kg m^{-3}) and V_{graup} and V_{snow} are typical terminal velocities for graupel and snow, which are set to 3.0 and 0.5 m s^{-1}, respectively. The dimensionless partitioning coefficient β is set equal to 0.7 over land and 0.45 over sea to account for the observed lower graupel contents over oceans. Prescribing two fixed values of β over land and ocean is probably rather crude, but the lack of reliable observations of frozen hydrometeor amounts on the global scale prevents going beyond this level of complexity.

Then a quantity, Q_R, assumed to provide a proxy for the charging rate resulting from the collisions between graupel and other types of hydrometeors inside the charge separation region, is empirically computed as

$$Q_R = \int_{z_0}^{z_{-25}} q_{graup}\left(q_{cond} + q_{snow}\right)\overline{\rho}\, dz \tag{6.82}$$

where z_0 and z_{-25} are the heights of the 0°C and −25°C isotherms, respectively. The inclusion of cloud liquid water through q_{cond} as well as the multiplication of graupel content by the contents in other

hydrometeors are expected to represent hydrometeor interactions involved in the process of charge separation.

Finally, the total (CC plus CG) lightning flash density (f_T; in km^{-2} day^{-1}), is determined as

$$f_T = \alpha_L Q_R \sqrt{CAPE} \ \min\left(z_{base}, 1.8\right)^2 \tag{6.83}$$

where α_L is a constant set to 37.5, which was obtained after calibrating the global mean lightning flash density from the model with the LIS/OTD satellite lightning climatology produced by Cecil *et al.* (2014). The dependence of f_T on $\sqrt{CAPE}$ is included to account for the observed correlation of total lightning frequency with updraft vertical velocity. The term in z_{base} can be seen as a proxy for the horizontal extent of the convective ascent, which is assumed here to increase with z_{base}^2, before becoming constant once z_{base} exceeds 1.8 km.

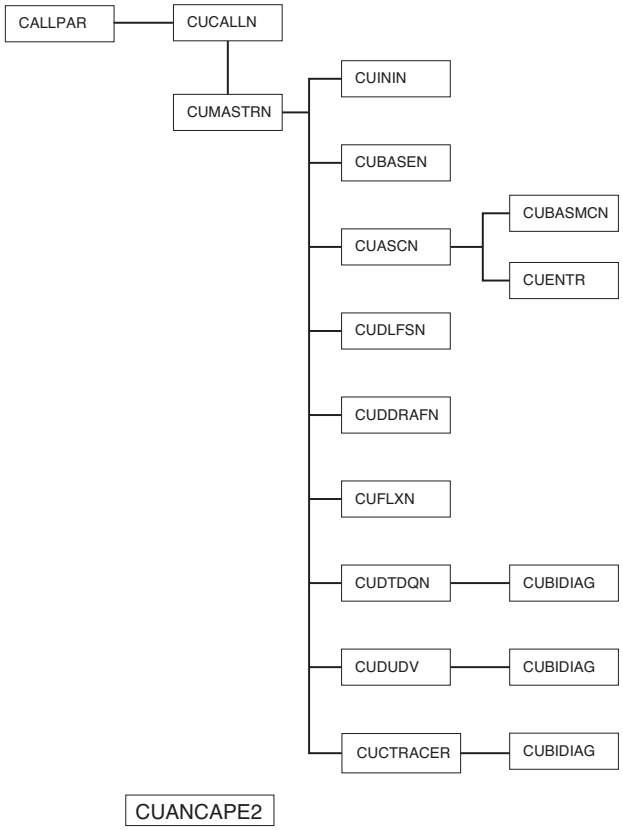

Figure 6.1 *Structure of convection scheme.*

6.14 STRUCTURE OF CODE

The parametrization of cumulus convection is performed in subroutines shown in Fig. 6.1.

CUCALLN: Provides interface of routines for cumulus parametrization. It takes the input values through arguments from CALLPAR and returns updated tendencies of T, q, l, u, v and chemical Tracers, as well as convective precipitation rates.

CUMASTRN: Master routine for convection scheme. Also performs the convective closure and with Cy32r3 computes the momentum in the convective draughts.

CUININ: Initializes variables for convection scheme (including vertical interpolation to the half model levels).

CUBASEN: First Guess updraught. Calculates condensation level, and sets updraught base variables and first guess cloud type.

CUASCN: Calculates ascent in updraughts. Before Cy32r3 CUASCN has been called twice as part of an iterative procedure. With cycle 32r3 CUASCN is only called once and the mass flux scaling is done in routine CUMASTRN. Routines CUENTR and CUBASMCN are called from CUASCN.

CUENTR: Calculates turbulent entrainment and detrainment rates.

CUBASMCN: Calculates cloud base properties of mid-level convection.

CUDLFSN: Calculates the level of free sinking for downdraughts.

CUDDRAFN: Calculates the downdraught descent.

CUFLXN: Calculates final convective fluxes and surface precipitation rates taking into account of melting/freezing and the evaporation of falling precipitation.

CUDTDQN: Calculates the tendencies of T and q from convection.

CUDUDV: Calculates the tendencies of u and v from convection.

CUADJTQ: Calculates super/sub saturation and adjusts T and q accordingly.

CUCTRACER: Calculates convective tendencies for chemical Tracers.

CUBIDIAG: Solver for bi-diagonal linear equation system.

CUANCAPE2: Computes CAPE/CIN diagnostics.

DIAG CLOUD: Computes Total Totals, K index and cloud base/top heights.

CULIGHT: Computes lightning diagnostics.

TROPLEV: Computes tropopause pressure.

EXTERNALS

Subroutine SATUR for calculating saturation mixing ratio.

PARAMETERS

Defined in subroutine SUCUM called from INIPHY.

APPENDIX A. LIST OF SYMBOLS

CAPE	Convective available potential energy
CIN	Convective inhibition
PCAPE	Entraining and density weighted convective available potential energy
$\mathrm{PCAPE}_{\mathrm{bl}}$	Boundary-layer production of PCAPE
QCV	Integrated total advective moisture tendency
C^i	Convective chemical Tracer no. i
C^i_{down}	Convective Tracer concentration in updraught
C^i_{down}	Convective Tracer concentration in downdraught
C_{d}	Drag coefficient
C_{conv}	Fraction of grid square occupied by convection
c_p	Specific heat at constant pressure for dry air
c_{up}	Condensation/sublimation in the updraughts
c_0	Autoconversion coefficient
c_{00}	Autoconversion coefficient base value
D_{up}	Rate of mass detrainment in the updraughts
D_{down}	Rate of mass detrainment in the downdraughts
D_{st}	Total kinetic energy dissipation in model column
dx	Horizontal grid spacing
dx_{ref}	Reference horizontal grid spacing
E_{up}	Rate of mass entrainment in the updraughts
E_{down}	Rate of mass entrainment in the downdraughts
e^{rain}	Evaporation of rain
e_{down}	Evaporation of precipitation (rain and snow) in the downdraughts
$e^{\mathrm{rain}}_{\mathrm{down}}$	Evaporation of rain in the downdraughts
$e^{\mathrm{snow}}_{\mathrm{down}}$	Evaporation of snow in the downdraughts
$\tilde{e}_{\mathrm{subcld}}$	Evaporation of precipitation (rain and snow) in the unsaturated sub-cloud layer
f_ε	multiplicative entrainment factor for shallow/mid-level convection
f_{scale}	vertical scaling function for the entrainment
f_{T}	Cloud-to-cloud plus cloud-to-ground lightning flash density
$\tilde{e}^{\mathrm{rain}}_{\mathrm{subcld}}$	Evaporation of rain in the unsaturated sub-cloud layer
$\tilde{e}^{\mathrm{snow}}_{\mathrm{subcld}}$	Evaporation of snow in the unsaturated sub-cloud layer
F_{rez}	Freezing rate of condensate in the updraughts
F_{h}	moist static energy flux
g	gravity constant
G^{precip}	Conversion rate from cloud (water+ice) into precipitation (rain+snow)
G^{rain}	Conversion rate from cloud water into rain
G^{snow}	Conversion rate from cloud ice into snow
H	Height of convective cloud top
$\bar{h}$	Moist static energy $(= c_p\bar{T} + L\bar{q} + gz)$ in the environment
$\bar{h}_{\mathrm{sat}}$	Saturated moist static energy in the environment
h_{up}	Moist static energy in the updraughts
h_{down}	Moist static energy in the downdraughts
J_s	Surface turbulent sensible heat flux
J_q	Surface turbulent latent heat flux
k	model level
k_{dep}	model level from which updraught departs
K_{up}	Kinetic energy in the updraughts
L	Effective latent heat for an ice/water mix
L_{fus}	Latent heat of fusion
L_{subl}	Latent heat of sublimation
L_{vap}	Latent heat of vaporization
CFL	Courant–Friedrich–Levy criterium
LCL	Lifting Condensation Level

LFC	Level of Free Convection
$l_{\rm up}$	Cloud water/ice content in the updraughts
$l_{\rm crit}$	Cloud water/ice content above which autoconversion occurs
$M_{\rm elt}$	Melting rate of snow
M	Net mass flux in the convective clouds (updraughts + downdraughts)
$M^{\star}_{\rm cld}$	First-guess net mass flux
$M_{\rm up}$	Updraught mass flux
$M_{\rm down}$	Downdraught mass flux
N_0	Buoyancy frequency
n	index for time discretization
nlev	number of vertical model levels (nlev denotes the first layer above surface)
$P^{\rm rain}$	Net flux of precipitation in the form of rain
$P^{\rm snow}$	Net flux of precipitation in the form of snow
$P_{\rm up}$	Net precipitation production (rain and snow) in updraughts
$P^{\rm f}$	Flux of frozen precipitation
p	Pressure
p_0	Reference pressure=1000 hPa
$\bar{q}$	Specific humidity of the environment
$q_{\rm up}$	Specific humidity in the updraughts
$q_{\rm down}$	Specific humidity in the downdraughts
$q_{\rm snow}$	Snow content diagnosed from the convective frozen precipitation flux
$q_{\rm graup}$	Graupel content diagnosed from the convective frozen precipitation flux
$q_{\rm cond}$	Convective cloud condensate content
$Q_{\rm R}$	Proxy for the charging rate
R	Rain intensity
R_{rmd}	Gas cosntant for dry air
RH	Relative humidity
$RH_{\rm cr}$	Critical relative humidity for rain evaporation
$\bar{r}$	Rain+snow) in the environment
$r_{\rm up}$	Precipitation (rain+snow) in the updraughts
$r_{\rm down}$	Precipitation (rain+snow) in the downdraughts
$S_{\rm fallout}$	Fall-out of rain/snow
$\bar{s}$	Dry static energy in the environment
$s_{\rm up}$	Dry static energy in the updraughts
$s_{\rm down}$	Dry static energy in the downdraughts
$\bar{T}_{\rm v}$	Virtual temperature in the environment
$\bar{T}_0$	Temperature at triple point or melting
$\bar{T}_{\rm ice}$	Temperature for which all condensate will be in ice phase
$T_{\rm d}$	Dewpoint temperature
$T_{\rm v,up}$	Virtual temperature in the updraughts
$T_{\rm w}$	wet-bulb temperature
$\bar{u}$	u component of wind in the environment
$u_{\rm up}$	u component of wind in the updraughts
$u_{\rm down}$	u component of wind in the downdraughts
$u_{\rm pert}$	additional updraught perturbation velocity
V	Mean terminal velocity of precipitation (rain+snow)
$V_{\rm rain}$	Mean terminal velocity of rain drops
$V_{\rm snow}$	Mean terminal velocity of snow
$V_{\rm graup}$	Mean terminal velocity of graupel
$\bar{v}$	v component of wind in the environment
$v_{\rm up}$	v component of wind in the updraughts
$v_{\rm down}$	v component of wind in the downdraughts
$\bar{w}$	Grid-mean vertical velocity, approximately environment
$w_{\rm up}$	Vertical velocity in the updraughts
$w_{\rm env}$	Vertical velocity in the environment

w_*	Convective velocity scale
z	height
z_{base}	Convective cloud base height
Z^i_{scav}	Scavenging coefficient
$\alpha_1, \alpha_2, \alpha_3$	Microphysical constants
α_{x}	Horizontal resolution dependency of the deep convective adjustment time
α_{qcv}	constant in moisture convergence contribution to PCAPE
$\alpha^{(s)}, \alpha^{(q)}$	Interpolation coefficients for half-level values
α_{T}	Interpolation coefficient between the liquid and ice phase as function of temperature
α_{L}	Constant in lightning strike production
δ	Detrainment per unit length
ε	Entrainment per unit length
ε'	$(R_{\text{v}}/R_{\text{d}}) - 1$
ζ	Fraction of convective precipitation (rain+snow) handed over to resolved scale
η	Updraught mass flux fraction to initialise downdraught
κ	von Karman constant
ψ	Generic prognostic quantity
ρ	Density of air
ρ_{rain}	Density of rain
τ	Adjustment time scale
τ_{c}	Cloud turnover time scale
τ_{m}	Melting time scale
θ	Potential temperature
θ_{e}	Equivalent potential temperature
θ_{v}	Virtual potential temperature
ω	Omega (large-scale) vertical velocity
Δp	Pressure difference between two model half-levels
Δt	Model time step

Chapter 7

Clouds and large-scale precipitation

Table of contents

7.1 Introduction
7.2 Basic assumptions and subgrid cloud scheme
7.2.1 Definitions
7.2.2 Budget equations
7.2.3 Saturation adjustment and subgrid cloud source and sink terms
7.3 Microphysical processes
7.3.1 Microphysical hydrometeor assumptions
7.3.2 Autoconversion/accretion of cloud water to rain
7.3.3 Evaporation of rain
7.3.4 Aggregation of ice to snow
7.3.5 Ice crystal growth by deposition in mixed phase clouds
7.3.6 Depositional growth of snow particles
7.3.7 Sublimation of snow
7.3.8 Collection (accretion) of rain, snow and ice
7.3.9 Riming - collection of cloud water by snow
7.3.10 Melting of ice and snow
7.3.11 Freezing of rain
7.3.12 Freezing of cloud water droplets
7.3.13 Sedimentation
7.4 Numerics
7.4.1 Integration of the equations
7.4.2 Calculation of $\mathrm{d}q_{\mathrm{sat}}/\mathrm{d}t$
7.4.3 Convective cloud source
7.4.4 Final moist adjustment
7.5 Description of output fields: Humidity, clouds and precipitation
7.5.1 Prognostic variables
7.5.2 Relative humidity
7.5.3 Cloud
7.5.4 Precipitation
7.6 Code
Appendix A. History of key cloud scheme developments
Appendix B. List of symbols

7.1 INTRODUCTION

Cloud and large-scale precipitation processes are described by prognostic equations for cloud liquid water, cloud ice, rain, snow and a grid box fractional cloud cover. This new scheme was implemented in IFS Cycle 36r4 and is significantly modified from the previous version which had just two prognostic cloud variables (cloud condensate and cloud fraction). The philosophy of the original scheme (Tiedtke, 1993) is retained with regards to the prognostic cloud fraction and sources/sinks of all cloud variables due to the major generation and destruction processes, including detrainment from convection and

boundary layer turbulence. However, liquid and ice water contents are now independent, allowing a more physically realistic representation of super-cooled liquid water and mixed-phase cloud. Rain and snow precipitation are also now able to precipitate with a determined terminal fall speed and can be advected by the three-dimensional wind. A multi-dimensional implicit solver is used for the numerical solution of the cloud and precipitation prognostic equations. Figure 7.1 shows a schematic to highlight the differences between the current and previous (pre-36r4) cloud parametrization schemes. Further discussion of the changes and impacts on the IFS forecasts can be found in Forbes and Tompkins (2011) and Forbes *et al.* (2011).

Section 7.2 describes the basic equations and the assumptions for the subgrid cloud scheme. Section 7.3 describes the microphysical parametrizations for the cloud and precipitation processes. Section 7.4 discusses the numerical aspects of the parametrization formulation and Section 7.6 outlines the code structure. The Appendices provide further information on relevant diagnostics available, the history of key changes to the IFS cloud scheme and a list of symbols used in this documentation.

7.2 BASIC ASSUMPTIONS AND SUBGRID CLOUD SCHEME

7.2.1 Definitions

(*a*) ***Specific water contents and cloud fraction***

The grid-mean specific water content for cloud liquid (kg kg^{-1}) is defined as

$$q_{\mathrm{l}} = \frac{1}{V}\int_V \frac{\rho_{\mathrm{l}}}{\rho}\,\mathrm{d}V \tag{7.1}$$

where ρ_{l} is the mass of cloud water per unit volume (density, kg m^{-3}), ρ is the density of moist air (kg m^{-3}) and V is the volume of the grid box (m^{-3}). The variables for specific humidity (q_{v}), cloud ice (q_{i}), rain (q_{r}) and snow (q_{s}) follow a similar definition. The fraction of the grid box covered by clouds is defined as

$$a = \frac{1}{V}\int_V \delta\,\mathrm{d}V, \qquad \delta = \begin{cases} 1, & \text{in clouds} \\ 0, & \text{otherwise} \end{cases} \tag{7.2}$$

Furthermore, the definition of the specific cloud water content per cloud area (in-cloud water/ice content) is

$$q_{\mathrm{l}}^{\mathrm{cld}} = \frac{q_{\mathrm{l}}}{a} \tag{7.3}$$

The above applies also to cloud ice and the precipitation variables, rain and snow, where the cloud fraction, a, is replaced with precipitation fraction, a_{P}.

(*b*) ***Saturation specific humidity***

The saturation specific humidity is expressed as a function of saturation water vapour pressure as

$$q_{\mathrm{sat}} = \frac{\frac{R_{\mathrm{dry}}}{R_{\mathrm{vap}}}e_{\mathrm{sat}}(T)}{p - \left(1 - \frac{R_{\mathrm{dry}}}{R_{\mathrm{vap}}}\right)e_{\mathrm{sat}}(T)} \tag{7.4}$$

where the saturation water vapour pressure is expressed with the Teten's formula

$$e_{\mathrm{sat}}(T) = a_1 \exp\left\{a_3\left(\frac{T - T_0}{T - a_4}\right)\right\} \tag{7.5}$$

with the parameters set according to Buck (1981) for saturation over water ($a_1 = 611.21$ Pa, $a_3 = 17.502$ and $a_4 = 32.19$ K) and to the AERKi formula of Alduchov and Eskridge (1996) for saturation over ice ($a_1 = 611.21$ Pa, $a_3 = 22.587$ and $a_4 = -0.7$ K), with $T_0 = 273.16$ K.

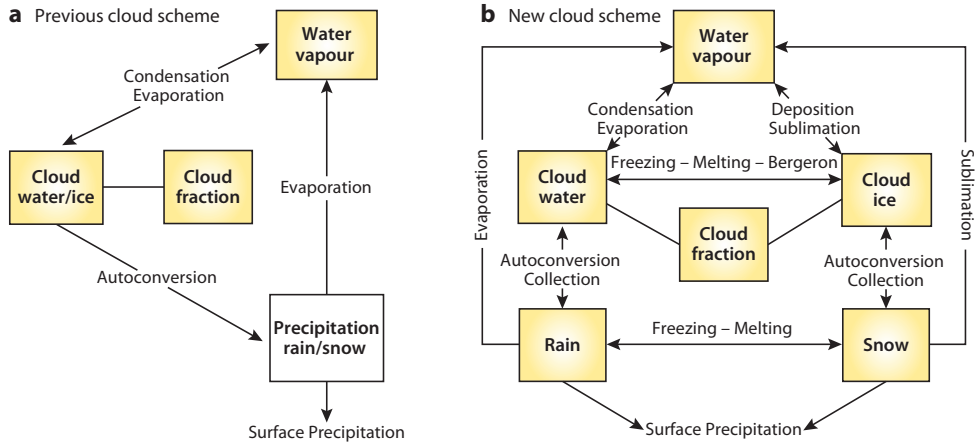

Figure 7.1 *Schematic of the IFS cloud scheme: (a) the original Tiedtke (1993) scheme with three moisture related prognostic variables, operational from 1995 to 2010 (before IFS Cy36r4) and (b) the current cloud scheme with six moisture related prognostic variables (Cy36r4 onwards). Shaded boxes indicate prognostic variables.*

(*c*) *Mixed phase*

With separate prognostic variables for cloud liquid and cloud ice, both can coexist in cloud at temperatures below freezing in variable amounts dependent on the different sources and sinks (see section 7.2.3). However, there are still some cloud generating processes, such as the detrainment of convective cloud, that diagnose the phase of the cloud source as a function of temperature (as in Tiedtke (1993)). For these processes the fraction of liquid water in the total condensate is described as

$$\begin{aligned} \alpha &= 0 && T \le T_{\mathrm{ice}} \\ \alpha &= \left(\frac{T - T_{\mathrm{ice}}}{T_0 - T_{\mathrm{ice}}}\right)^2 && T_{\mathrm{ice}} < T < T_0 \\ \alpha &= 1 && T \ge T_0 \end{aligned} \tag{7.6}$$

where T_{ice} and T_0 represent the threshold temperatures between which a mixed phase is allowed to exist and are chosen as $T_{\mathrm{ice}} = 250.16$ K and $T_0 = 273.16$ K.

7.2.2 Budget equations

With the above definitions and the assumption that clouds extend vertically over the whole model layer depth, the equations for the time change of the grid-box averaged cloud liquid, cloud ice, rain and snow water contents are

$$\frac{\partial q_{\mathrm{l}}}{\partial t} = A(q_{\mathrm{l}}) + S^{\mathrm{liq}}_{\mathrm{conv}} + S^{\mathrm{liq}}_{\mathrm{cond}} + S^{\mathrm{ice}}_{\mathrm{melt}} - S^{\mathrm{ice}}_{\mathrm{dep}} - S^{\mathrm{liq}}_{\mathrm{evap}} - S^{\mathrm{rain}}_{\mathrm{auto}} - S^{\mathrm{snow}}_{\mathrm{rime}} \tag{7.7}$$

$$\frac{\partial q_{\mathrm{i}}}{\partial t} = A(q_{\mathrm{i}}) + S^{\mathrm{ice}}_{\mathrm{conv}} + S^{\mathrm{ice}}_{\mathrm{dep}} + S_{\mathrm{iacr}} - S^{\mathrm{ice}}_{\mathrm{melt}} - S^{\mathrm{ice}}_{\mathrm{evap}} - S^{\mathrm{snow}}_{\mathrm{auto}} \tag{7.8}$$

$$\frac{\partial q_{\mathrm{r}}}{\partial t} = A(q_{\mathrm{r}}) + S^{\mathrm{rain}}_{\mathrm{conv}} - S^{\mathrm{rain}}_{\mathrm{evap}} + S^{\mathrm{rain}}_{\mathrm{auto}} + S^{\mathrm{snow}}_{\mathrm{melt}} - S^{\mathrm{rain}}_{\mathrm{frz}} - S_{\mathrm{sacr}} - S_{\mathrm{iacr}} \tag{7.9}$$

$$\frac{\partial q_{\mathrm{s}}}{\partial t} = A(q_{\mathrm{s}}) + S^{\mathrm{snow}}_{\mathrm{conv}} - S^{\mathrm{snow}}_{\mathrm{subl}} + S^{\mathrm{snow}}_{\mathrm{auto}} - S^{\mathrm{snow}}_{\mathrm{melt}} + S^{\mathrm{rain}}_{\mathrm{frz}} + S^{\mathrm{snow}}_{\mathrm{rime}} + S^{\mathrm{snow}}_{\mathrm{dep}} + S_{\mathrm{iacr}} \tag{7.10}$$

and for the cloud fraction,

$$\frac{\partial a}{\partial t} = A(a) + \delta a_{\mathrm{conv}} + \delta a_{\mathrm{strat}} - \delta a_{\mathrm{evap}} \tag{7.11}$$

The terms on the right-hand side of Eqns. (7.7) to (7.11) represent the following processes:

- $A(q), A(a)$ – rate of change of water contents and cloud area due to transport through the boundaries of the grid volume (advection, sedimentation).
- $S_{\text{conv}}, \delta a_{\text{conv}}$ – rate of detrainment of cloud water/ice/rain/snow and cloud area by convective processes.
- S_{cond} – rate of formation of cloud water by stratiform condensation processes.
- δa_{strat} – rate of change of cloud area by stratiform condensation processes.
- S_{evap} – rate of evaporation of cloud water/ice, rain/snow.
- S_{dep} – rate of depositional growth of ice/snow.
- S_{subl} – rate of sublimation of ice/snow.
- S_{auto} – rate of generation of precipitation from cloud water/ice (autoconversion).
- S_{melt} – rate of melting ice/snow.
- S_{rime} – rate of snow riming (collection of cloud liquid drops).
- S_{iacr} – rate of ice accretion of rain.
- S_{sacr} – rate of snow accretion of rain.
- S_{frz} – rate of freezing of rain.
- δa_{evap} – rate of decrease of cloud area due to evaporation.

The large-scale budget equations for specific humidity q_v, and dry static energy $s = c_p T + gz$ in the cloud scheme are

$$\frac{\partial q_{\text{v}}}{\partial t} = A(q_{\text{v}}) - S_{\text{cond}} - S_{\text{dep}} + S_{\text{evap}} + S_{\text{subl}} \tag{7.12}$$

and

$$\frac{\partial s}{\partial t} = A(s) + L_{\text{vap}}(S_{\text{cond}} - S_{\text{evap}}) + L_{\text{dep}}(S_{\text{dep}} - S_{\text{subl}}) + L_{\text{fus}}(S_{\text{frz}} + S_{\text{rime}} + S_{\text{sacr}} + S_{\text{iacr}} - S_{\text{melt}}) \tag{7.13}$$

where $A(q_v)$ and $A(s)$ represent all processes except those related to clouds, L_{vap} is the latent heat of condensation/evaporation, L_{fus} is the latent heat of freezing/melting and L_{dep} is the latent heat of deposition/sublimation ($= L_{\text{vap}} + L_{\text{fus}}$) .

7.2.3 Saturation adjustment and subgrid cloud source and sink terms

(*a*) ***Convection***

Clouds formed by convective processes are parametrized by considering them to be condensates produced in cumulus updraughts and detrained into the environmental air. This approach, besides being part of the cloud parametrization, represents also an important extension of the model's cumulus parametrization. It is applied for all types of convection, namely deep, shallow and mid-level. The source of cloud water/ice content is

$$S_{\text{conv}} = D_{\text{up}} l_{\text{up}} + \frac{M_{\text{up}}}{\rho} \frac{\partial q_{\text{l}}}{\partial z} \tag{7.14}$$

and is partitioned between ice and water diagnostically according to Eq. 7.6. The source of cloud area is described as

$$\delta a_{\text{conv}} = D_{\text{up}} + \frac{M_{\text{up}}}{\rho} \frac{\partial a}{\partial z} \tag{7.15}$$

where D_{up} (s^{-1}) is the detrainment of mass from cumulus updraughts, l_{up} (kg kg^{-1}) is the specific cloud water/ice content in cumulus updraughts and M_{up} is the updraught mass flux (see Chapter 6). The first term in (7.14) and (7.15) represents the detrainment of cloud from the convective updraughts and the second term represents the advection of cloud in the vertical due to compensating subsidence in the environmental air. The evaporation due to this subsidence is represented by term E_1 described in subsection *(e)* below.

From Cycle 50r1, a proportion of the convective precipitation is passed to the cloud scheme to improve the advection in coastal regions and orography (controlled by parameter RMFDPREC which defines the proportion, default 0.4, i.e. 40%). Two adjustments are made to the cloud scheme for grid columns where the deep convection parametrization is active to reduce evaporation if the grid box is partially cloudy

and to be more representative of convective precipitation: (1) for the calculation of the area fraction of precipitation in the clear sky part of the grid box, a minimum cloud cover of 30% is assumed between 800 hPa and cloud top (or 350 hPa if cloud top is higher); (2) the fallspeed of snow hydrometeors is increased by a factor of 1.5 to better represent rimed particles.

(*b*) ***Formation of stratiform clouds***

Here the formation of clouds by non-convective processes (e.g. large-scale lifting of moist air, radiative cooling etc.) is considered. The parametrization is based on the principle that condensation processes are determined by the rate at which the saturation specific humidity decreases. This rate is linked to vertical motions and diabatic cooling through

$$\frac{\mathrm{d}q_{\mathrm{sat}}}{\mathrm{d}t} = \left(\frac{\mathrm{d}q_{\mathrm{sat}}}{\mathrm{d}p}\right)_{\mathrm{ma}} (\bar{w} + gM_{\mathrm{Cu}}) + \left(\frac{\mathrm{d}q_{\mathrm{sat}}}{\mathrm{d}T}\right)\left(\frac{\mathrm{d}T}{\mathrm{d}t}\right)_{\mathrm{diab}} \tag{7.16}$$

where $(\mathrm{d}q_{\mathrm{sat}}/\mathrm{d}p)_{\mathrm{ma}}$ is the change of q_{sat} along a moist adiabat through point (p, T), $\bar{w}$ is the area-mean generalized vertical velocity, gM_{Cu} is the cumulus-induced subsidence between the updraughts, and $(\mathrm{d}T/\mathrm{d}t)_{\mathrm{diab}}$ is the net temperature tendency due to radiative and turbulent mixing processes. The changes in any existing cloudy part of the grid box (increase in condensate, C_1) and in the clear part of the grid box (formation of new cloud, C_2) are treated separately.

$$S_{\mathrm{cond}} = C_1 + C_2 \tag{7.17}$$

The condensation rate in already existing clouds (C_1) is described as

$$C_1 = -a\frac{\mathrm{d}q_{\mathrm{sat}}}{\mathrm{d}t} \qquad \frac{\mathrm{d}q_{\mathrm{sat}}}{\mathrm{d}t} < 0 \tag{7.18}$$

The formation of new clouds (C_2) is more complex due to the assumption of subgrid heterogeneity of humidity in the clear air. New clouds are assumed to form when the grid-averaged relative humidity exceeds a threshold value, defined as a function of height,

$$\begin{aligned} RH_{\mathrm{crit}} &= RH_{\mathrm{c}} + (1 - RH_{\mathrm{c}})\left(\frac{\sigma - \sigma_1}{1 - \sigma_1}\right)^2 \qquad \sigma > \sigma_1 \\ RH_{\mathrm{crit}} &= RH_{\mathrm{c}} \qquad \sigma < \sigma_1 \end{aligned} \tag{7.19}$$

where $RH_{\mathrm{c}} = 0.8$, $\sigma = p/p_{\mathrm{surf}}$ with p being the pressure and p_{surf} the pressure at the surface and $\sigma_1 = 0.8$. The increase in cloud cover is determined by how much of the cloud-free area exceeds saturation in one time step which in turn depends on the moisture distribution in the cloud-free area and how fast saturation is approached. The vapour is assumed to be evenly distributed within the range $[\{q_{\mathrm{v}}^{\mathrm{env}} - (q_{\mathrm{sat}} - q_{\mathrm{v}}^{\mathrm{env}})\}, q_{\mathrm{sat}}]$ around the mean environmental value $q_{\mathrm{v}}^{\mathrm{env}}$, while the approach to saturation is determined by $\mathrm{d}q_{\mathrm{sat}}/\mathrm{d}t$. The rate of increase in cloud cover then becomes

$$\delta a_{\mathrm{strat}} = \frac{1}{2}\frac{-(1-a)}{(q_{\mathrm{sat}} - q_{\mathrm{v}}^{\mathrm{env}})}\frac{\mathrm{d}q_{\mathrm{sat}}}{\mathrm{d}t} \qquad \frac{\mathrm{d}q_{\mathrm{sat}}}{\mathrm{d}t} < 0 \tag{7.20}$$

which can be expressed in terms of grid averages (using the definition $q_{\mathrm{v}} = aq_{\mathrm{sat}} + (1-a)q_{\mathrm{v}}^{\mathrm{env}}$) as

$$\delta a_{\mathrm{strat}} = \frac{-(1-a)^2}{2}\frac{1}{(q_{\mathrm{sat}} - q_{\mathrm{v}})}\frac{\mathrm{d}q_{\mathrm{sat}}}{\mathrm{d}t} \qquad \frac{\mathrm{d}q_{\mathrm{sat}}}{\mathrm{d}t} < 0 \tag{7.21}$$

For the application of (7.21) at values of q_{v} close to saturation, the constraint $\delta a_{\mathrm{strat}} < (1-a)/\Delta t$ is imposed to ensure realistic values of a.

The generation rate of cloud water/ice in newly formed clouds is then as for the generation rate in existing cloud (Eq. 7.18), except for half the total change in cloud fraction ($\Delta a_{\mathrm{strat}} = \delta a_{\mathrm{strat}} \Delta t$) due to the sub-grid variability assumption in the clear sky:

$$C_2 = -\frac{1}{2}\Delta a_{\mathrm{strat}}\frac{\mathrm{d}q_{\mathrm{sat}}}{\mathrm{d}t} \qquad \frac{\mathrm{d}q_{\mathrm{sat}}}{\mathrm{d}t} < 0 \tag{7.22}$$

(*c*) ***Ice crystal nucleation and supersaturation with respect to ice*** ($T < -38°C$)

Ice crystal nucleation contrasts sharply with the equivalent process for liquid cloud droplets, since the nucleation process is not activated at small supersaturations with respect to the ice saturation vapour pressure. At cold temperatures, where the difference between the liquid water and ice saturation vapour pressures is large, the relative humidity (RH) with respect to ice can exceed 150% before the onset of the nucleation process, and supersaturations with respect to ice are commonly observed by in-situ and remote sensing techniques (e.g. Heymsfield *et al.*, 1998; Gierens *et al.*, 1999, 2000, 2004; Spichtinger *et al.*, 2003).

The formulation for cloud generation outlined above is modified to allow supersaturation with respect to ice in the clear sky portion of the grid-cell. For temperatures below the homogeneous freezing temperature (defined as -38°C), the scheme assumes ice nucleation initiates when the RH measured with respect to ice saturation *locally* reaches the threshold RH_{homo} specified by Kärcher and Lohmann (2002), or water saturation, whichever is lower:

$$RH_{\text{homo}} = MIN\left(2.583 - \frac{T}{207.8}, \frac{q_{\text{sat(w)}}}{q_{\text{sat(i)}}}\right) \tag{7.23}$$

where T is the temperature in Kelvin. For temperatures warmer than $-38°$C), the liquid water saturation mixing ratio is reached first, at which point liquid water droplets will nucleate (see discussion on mixed phase processes in subsection 7.3.5).

In Cycle 48R1, to avoid too high humidity in the upper troposphere, the above RH threshold is reduced to be half way between the homogeneous nucleation limit and ice saturation. Hence the RH threshold is adjusted to be $RH_{\text{lim}} = 0.5(RH_{\text{homo}} + RH_{\text{sat(i)}})$. This only has a small impact on the shape of the supersaturation PDF, but does reduce the overall humidity in supersaturated regions. This assumption will be revised in the future.

An additional consideration for ice cloud formation, as for the warm phase, is the clear-sky humidity fluctuations that are assumed to be uniformly distributed with a fixed constant variance. Thus nucleation can occur when the grid-mean RH exceeds a threshold that is lower than this local criterion, and is given by $RH_{\text{crit}} \times RH_{\text{lim}}$. The relative humidity threshold for cloud formation to begin also takes into account the assumption in partially cloudy grid boxes that the cloudy part is at ice saturation.

Figure 7.2 shows the various thresholds in terms of relative humidity with respect to ice as a function of temperature.

Once ice cloud is formed, the deposition process is considered to be sufficiently rapid relative to the model time-step that it can be approximated by a diagnostic adjustment to exactly ice saturated conditions inside the cloud. This assumption is necessary, since to allow ice supersaturation both within the pure ice cloud and in the clear sky environment would either require a separate prognostic variable to monitor the evolution of the water vapour inside the cloud, or a diagnostic assumption would have to be used to divide the grid-mean humidity between the two regions, which can generate large artificial horizontal sub-grid humidity fluxes (see Tompkins *et al.*, 2007, for more detail). In any case, this assumption appears to be reasonably justified in a wide range of updraught situations by modelling of the homogeneous nucleation process (Khvorostyanov and Sassen, 1998). The obvious drawback is that pure ice clouds may not exist in a subsaturated or supersaturated state, and no information concerning the ice crystal number concentration is available.

Thus, if $T < T_0$ and the relative humidity exceeds the threshold given by RH_{lim}, the scheme calculates the increase in cloud fraction from (7.21) but with a relaxation time of 2 hours to avoid immediately reaching overcast conditions. The associated change in cloud ice mass is calculated in two stages. The first source term is derived using (7.22). This generation term for ice mass reduces RH back to the threshold, RH_{lim}, and leaves the newly generated cloudy region in an ice supersaturated state. This is then corrected by condensing the supersaturation to bring the grid-mean humidity back to the limit of

$$q_v^{max} = q_s(a + (1-a)RH_{lim}) \tag{7.24}$$

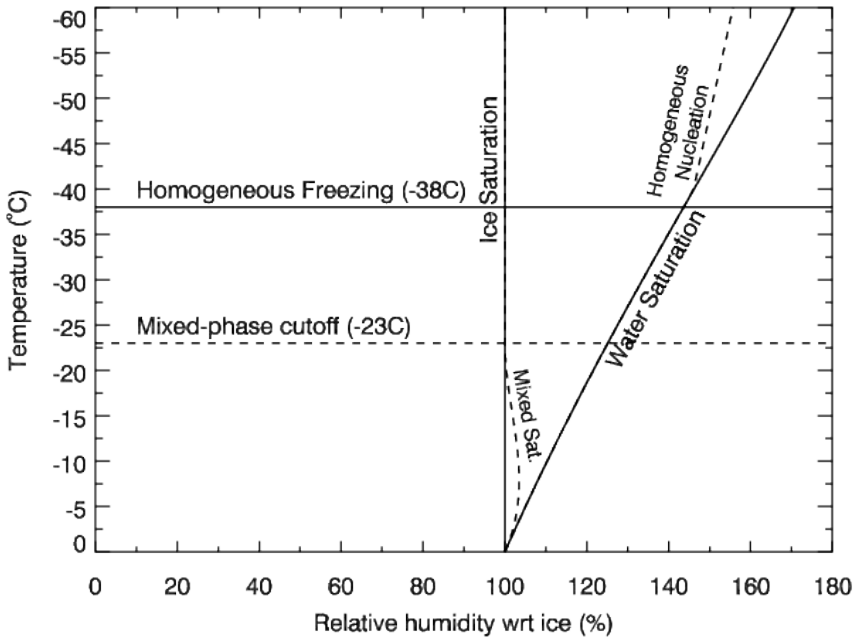

Figure 7.2 *Relative humidity with respect to ice as a function of temperature (below 0°C) showing ice saturation, water saturation, mixed-phase saturation and the homogeneous nucleation threshold defining the maximum possible supersaturation. The temperatures of the homogeneous freezing of water droplets and mixed phase function are also shown.*

This term has the effect of reducing the in-cloud humidity to the ice saturated value within one time-step, but allowing supersaturation in the clear air part of the grid box.

Tompkins *et al.* (2007) show that the supersaturation scheme, while simple, reproduces very well the climatological PDF of upper tropospheric RH derived from MOZAIC aircraft observations (Gierens *et al.*, 1999), as well as the geographical distribution of ice supersaturation given by MLS retrievals (Spichtinger *et al.*, 2003).

(*d*) ***Evaporation of cloud water/ice***

The scheme describes evaporation of clouds by two processes; (i) in connection with large-scale and cumulus-induced descent and diabatic heating and (ii) by turbulent mixing of cloud air with unsaturated environmental air. The evaporation rate is defined as

$$S_{\text{evap}}^{\text{liq/ice}} = E_1 + E_2 \tag{7.25}$$

The first process (E_1) is accounted for in the same way as the stratiform cloud formation except that $\mathrm{d}q_{\text{sat}}/\mathrm{d}t > 0$. Hence

$$E_1 = a\frac{\mathrm{d}q_{\text{sat}}}{\mathrm{d}t} \qquad \frac{\mathrm{d}q_{\text{sat}}}{\mathrm{d}t} > 0 \tag{7.26}$$

Before Cy50r1, evaporation did not affect cloud fraction until all the condensate had evaporated (homogeneous in-cloud assumption). From Cy50r1, evaporation due to warming/drying of the air reduces the cloud fraction linearly with the proportion of the condensate evaporated to the total cloud water content, so the rate of decrease of cloud fraction is:

$$\delta a_{\text{evap}} = \frac{aE_1}{(q_l + q_i)} \tag{7.27}$$

The second process (E_2) represents the parametrization of cloud dissipation as cloud air mixes with environmental air (cloud edge erosion). It is described as a diffusion process proportional to the

saturation deficit of the air:

$$E_2 = \alpha a(1-a)K(q_{\text{sat}} - q_{\text{v}}) \tag{7.28}$$

where the diffusion coefficient K is 6×10^{-6} s^{-1}, increased to 1.2×10^{-4} s^{-1} when deep convection is active, and 12×10^{-4} s^{-1} when shallow convection is active and the boundary layer estimated inversion strength (EIS) is less than 10. This latter threshold is to limit the erosion where the boundary layer inversion is strong and stratocumulus cloud is present. Here the $\alpha a(1-a)$ term is associated with the cloud edge perimeter ($\alpha = 0.333$) following Morcrette (2012).

The rate of decrease in cloud cover is parametrized as

$$\delta a_{\text{evap}} = 0.5 \frac{E_2}{q^{\text{cld}}} \tag{7.29}$$

where q^{cld} is the specific cloud water/ice content per cloud area as defined in (7.3). Note that because of (7.3) the parametrizations (7.28) and (7.29) imply a slower reduction in cloud area than for condensate so the in-cloud condensate decreases with erosion.

(*e*) *Precipitation fraction and overlap*

Precipitation processes are treated separately in clear and cloudy skies. This owes to the fact that the microphysical processes in these two regions are very distinct from each other, with conversion, collection and accretion processes being relevant in clouds whereas evaporation of precipitation is the relevant process outside clouds. Therefore the precipitation flux is written as

$$P = P^{\text{cld}} + P^{\text{clr}} \tag{7.30}$$

with

$$P^{\text{cld}} \equiv \frac{1}{A} \int P \cdot H(a)\, dA \tag{7.31}$$

and

$$P^{\text{clr}} \equiv \frac{1}{A} \int P \cdot (1 - H(a))\, dA \tag{7.32}$$

where the step function, $H(a)$, marks the portion of the grid-cell containing cloud and A is the area of the grid-cell.

The precipitation fraction in the grid-box is then described as

$$a_P = a_P^{\text{cld}} + a_P^{\text{clr}} \tag{7.33}$$

with

$$a_P^{\text{cld}} \equiv \frac{1}{A} \int H(a) H(a_P)\, dA \tag{7.34}$$

and

$$a_P^{\text{clr}} \equiv \frac{1}{A} \int (1 - H(a)) H(a_P)\, dA \tag{7.35}$$

Whereas cloud fraction (for cloud liquid and cloud ice) is a prognostic variable, precipitation fraction (for rain and snow) is still treated diagnostically. The treatment of precipitation fraction in the previous cloud scheme (Jakob and Klein, 2000) in IFS cycles prior to 36r4 needed to be updated for the new prognostic microphysical treatment, since snow and rain are now prognostic variables and can survive from one timestep to the next. So the previous complex two-stream treatment is replaced by a simpler treatment where the total precipitation fraction a_P is calculated using a maximum-random overlap treatment of the cloud fraction, so that at level k:

$$a_{P,k} = 1 - \left(\frac{(1 - a_{P,k-1})(1 - MAX[a_k, a_{k-1}])}{1 - MIN[a_{k-1}, 1 - \epsilon]} \right) \tag{7.36}$$

where ϵ is equal to a small number (10^{-6}) and a_k is the cloud cover at level k. The clear sky precipitation fraction is then given by

$$a_P^{clr} = a_P - a \tag{7.37}$$

The precipitation flux is proportionally divided between the clear-sky and the in-cloud component.

Rain and snow are prognostic variables and can be advected by the wind out of the column that they were produced, but precipitation fraction is still a diagnostic. Therefore a precipitation fraction needs to be specified when there is no cloud fraction in the column above. At present, this is set as a minimum precipitation coverage of 10%.

7.3 MICROPHYSICAL PROCESSES

7.3.1 Microphysical hydrometeor assumptions

For each of the hydrometeor categories, there are assumptions about the particle size distribution, mass-diameter relationship and terminal velocity that are used in the parametrization of microphysical processes. At present, this is limited to the rain evaporation and snow riming but in subsequent versions they will be consistently used for the other microphysical processes. The general formulations are given below for a particle of diameter D for hydrometeor x and the constants for each hydrometeor category are shown in Tables 7.1, 7.2 and 7.3.

(*a*) ***Mass-diameter relationship***

The mass of a particle is defined by a power law:

$$m_x(D) = a_x D^{b_x} \tag{7.38}$$

(*b*) ***Particle size distribution***

The number concentration (m^{-3}) of particles is:

$$N_x(D) = N_{0x} exp(-\Lambda D) \tag{7.39}$$

where Λ is the slope of the particle size distribution and N_{0x} is the intercept parameter, assumed to be either constant or a function of Λ:

$$N_{0x} = n_{ax} \Lambda^{n_{bx}} \tag{7.40}$$

The specific mass integrated over all particle sizes (i.e. the prognostic variable) can therefore be described by:

$$q_x = \frac{1}{\rho} \int_{D=0}^{\infty} N_x(D) m_x(D) dD = \frac{1}{\rho} \int_{D=0}^{\infty} n_{ax} \Lambda^{n_{bx}} a_x D^{b_x} exp(-\Lambda D) dD \tag{7.41}$$

Integrating and rearranging gives the slope of the particle size distribution Λ as a function of the prognostic specific mass (q_x):

$$\Lambda = \left(\frac{n_{ax} a_x \Gamma(b_x + 1)}{q_x \rho} \right)^{1/(b_x + 1 - n_{bx})} \tag{7.42}$$

where the generalised factorial function is defined as:

$$\Gamma(y) = \int_{D=0}^{\infty} D^{y-1} exp(-D) dD \tag{7.43}$$

(*c*) ***Terminal velocity of hydrometeor sedimentation***

The terminal velocity of a hydrometeor particle is defined by a power law:

$$\nu_x(D) = c_x D^{d_x} \left(\frac{\rho_0}{\rho} \right)^{0.4} \tag{7.44}$$

where c_x and d_x are constants defined for each hydrometeor in Table 7.3. The last term accounts for the decreased drag (and therefore higher terminal velocities) in less dense air where ρ_0 is a reference air density (=1 kg m^{-3}).

The mass weighted fallspeed is determined by integrating over the particle size spectra

$$V_x = \frac{\int_{D=0}^{\infty} \nu_x(D) m_x(D) N_x(D) dD}{\int_{D=0}^{\infty} m_x(D) N_x(D) dD} \tag{7.45}$$

In Cycle 50r1, the ice fallspeed is defined as $V_i = 0.7 \rho q_i^{0.17}$ based on Heymsfield (1977), and equivalent particle size distribution, mass-diameter and fall speed parameters are included in the tables below.

Hydrometeor	n_{ax}	n_{bx}	References
Rain	0.22	2.2	Abel and Boutle (2012)
Ice	2×10^8	0.0	
Snow	2×10^6	0.0	

Table 7.1 *List of particle size distribution parameters for each hydrometeor.*

Hydrometeor	a_x	b_x
Rain	$\pi/6$	3.0
Ice	0.069	2.0
Snow	0.069	2.0

Table 7.2 *List of mass-diameter relationship parameters for each hydrometeor.*

Hydrometeor	c_x	d_x	References
Rain	386.8	0.67	Sachidananda and Zrnic (1986)
Ice	8.4	0.527	for sedimentation, equivalent to $V_i = 0.7\rho q_i^{0.17}$
Snow	1.0	0.0	for sedimentation, constant fallspeed
	1.5	0.0	(increased when deep convection active)
Snow	16.8	0.527	for snow deposition ventilation coefficient

Table 7.3 *List of hydrometeor terminal velocity parameters for each hydrometeor.*

7.3.2 Autoconversion/accretion of cloud water to rain

Autoconversion describes the formation of rain from cloud droplets through the collision-coalesence process. Accretion represents the collection process where larger rain drops falling through the cloud drops coalesce and grow. Two options are available for the parametrization of autoconversion and accretion and Option 2 is used operationally.

Option 1: Parametrization based on Sundqvist (1978)

Following (Sundqvist, 1978) the rate of generation of precipitation due to autoconversion and accretion is parameterized as

$$S_{\text{auto}}^{\text{rain}} = a c_0 q_l^{\text{cld}} \left[1 - \exp\left\{ -\left(\frac{q_l^{\text{cld}}}{q_l^{\text{crit}}} \right)^2 \right\} \right] \tag{7.46}$$

where c_0^{-1} represents a characteristic time scale for conversion of cloud liquid droplets into rain drops and q_l^{crit} is a typical cloud water content at which the generation of precipitation begins to be efficient. The critical liquid water content is different over ocean and land to take account of the differences in cloud condensation nuclei (CCN) in clean and polluted air. Cleaner air over the ocean has fewer CCN, hence larger drops and an onset of precipitation at lower cloud liquid water contents than in the more polluted air over land. These disposable parameters are defined as

$$c_0 = c_0^* F_1 \tag{7.47}$$

and

$$q_l^{\text{crit}} = \frac{q_l^{\text{crit}*}}{F_1} \tag{7.48}$$

to take into account the effect of collection (accretion) of cloud droplets by raindrops falling through the cloud (F_1). Here F_1 is defined as

$$F_1 = 1 + b_1 \sqrt{P_{\text{loc}}} \tag{7.49}$$

where P_{loc} is the local cloudy precipitation rate ($P_{\text{loc}} = P^{\text{cld}}/a_P^{\text{cld}}$). For a definition of precipitation fraction overlapping with cloud (a_P^{cld}), see the section on precipitation fraction below. The values for the constants are $b_1 = 100\ (\text{kg m}^{-2}\ \text{s}^{-1})^{-0.5}$ and $c_0^* = 1.67 \times 10^{-4}\ \text{s}^{-1}$. The critical liquid water content, $q_{\text{l}}^{\text{crit}*}$ is set to 0.25 g kg^{-1} over ocean and 0.55 g kg^{-1} over land. Currently, any rain that is formed at temperatures colder than zero is assumed to freeze and is converted to the snow hydrometeor category.

Option 2: Parametrization based on Khairoutdinov and Kogan (2000) (operational)

The second autoconversion/accretion parameterization is a non-linear function of the mass of both liquid cloud and rain water. The formulation follows Khairoutdinov and Kogan (2000) which is derived from large eddy simulation studies of drizzling stratocumulus clouds. Given the large uncertainties in the autoconversion/accretion process, it is assumed here that this parameterization is at least as valid as the Sundquist scheme for cloud regimes other than stratocumulus.

The rates for autoconversion (S_{aut}) and accretion (S_{acc}) are parameterized as:

$$S_{aut} = 1350 q_l^{2.47} N_c^{-1.79} F_{aut} \tag{7.50}$$

and

$$S_{acc} = 67 q_l^{1.15} q_r^{1.15} F_{acc} \tag{7.51}$$

where N_c is the cloud droplet number concentration and q_r is the rain water content. The droplet number concentration is considered to be constant within the grid box with a value of 50 cm^{-3} over ocean and 300 cm^{-3} over land. F_{aut} and F_{acc} are the inhomogeneity enhancement factors for the autoconversion and accretion processes respectively, which account for the subgrid variance and covariance of the cloud liquid water and cloud rain water content inhomogeneities. At present these are fixed values ($F_{aut} = 1.5$ and $F_{acc} = 3$) in reasonable agreement with observations (Boutle *et al.*, 2013), but in the future could depend on other prognosed quantities such as cloud fraction.

The rate of conversion of cloud liquid to rain is more non-linear than in the Sundqvist scheme, creating a stronger contrast between the slow production of rain for low liquid water clouds and more rapid conversion to rain for high liquid water clouds. The accretion rate depletes clouds with higher precipitation rates more quickly than clouds with low precipitation rates.

This process can occur at sub-freezing temperatures if supercooled cloud liquid is present. The process forms supercooled rain drops, which can then subsequently freeze through riming processes if ice or snow is present (see later subsections). Otherwise supercooled rain drops from the collision-coalescence process that reach the surface are defined as the "freezing drizzle" precipitation type.

7.3.3 Evaporation of rain

The rate of change of mass of a raindrop due to evaporation in subsaturated air is given by:

$$\frac{dm}{dt} = \frac{4\pi C(S_w - 1)F}{A'' + B''} \tag{7.52}$$

where C is the capacitance of the particle assumed to be spherical ($C = D/2$), $S_w = e/e_{sw}$ is the saturation ratio with respect to water, and F is the ventilation factor given by Beard and Pruppacher (1971)

$$F = 0.78 + 0.31 S_c^{1/3} R_e^{1/2} \tag{7.53}$$

where $S_c = 0.6$ is the Schmidt Number and the Reynolds number $R_e = \nu(D)D\rho/\mu$ where μ is the kinematic viscosity of air.

Terms A'' and B'' represent heat conduction and vapour diffusion respectively,

$$A'' = \frac{L_{vap}}{K_a T}\left(\frac{L_{vap}}{R_v T} - 1\right) \tag{7.54}$$

$$B'' = \frac{R_v T}{\chi e_{sw}} \tag{7.55}$$

where K_a is the heat conductivity of air and χ is the diffusivity of water vapour in air (which varies inversely with pressure as $\chi = 2.21/p$), L_{vap} is the latent heat of vaporization and R_v is the gas constant for water vapour.

Integrating over the particle size distribution for raindrops (see section 7.2.3) gives the following evaporation rate equation for rain:

$$S_{evap}^{rain} = c_{phase}^{r} \frac{(S_w - 1)}{\rho(A'' + B'')} \tag{7.56}$$

where

$$c_{phase}^{r} = \frac{2\pi n_{ar}}{\rho}\left(0.78\frac{\Gamma(2-n_{br})}{\Lambda_r^2} + 0.31\left(\frac{c_r}{\mu}\right)^{0.5} S_c^{1/3}(\rho\rho_0)^{1/4}\frac{\Gamma(0.5d_r+2.5)}{\Lambda_r^{(0.5d_r+2.5-n_{br})}}\right) \tag{7.57}$$

The formulation implicitly assumes an exponential droplet size distribution, but with the Abel and Boutle (2012) formulation of the intercept as described in Eq. 7.40 that increases the number of smaller particles for lower rain rates. This is in closer agreement to aircraft observations in drizzling cloud, and results in higher evaporation rates for light precipitation.

Sub-grid heterogeneity assumption

There is a sub-grid heterogeneity assumption defined by a limit in moist environments to prevent the gridbox saturating when only part of the gridbox has evaporating precipitation. Therefore evaporation of rain/snow only takes place when the grid mean relative humidity is below a threshold value. The choice of the threshold value is not straightforward for numerical reasons. Here, the assumption is made that the clear-sky relative humidity (which is equal to the grid mean relative humidity in the absence of clouds) that can be reached by evaporation of precipitation is a function of the fractional coverage with precipitation of the clear sky part of the grid-box. There is also a limit in the lower troposphere to reduce evaporation in moist environments. For rain evaporation to occur, the relative humidity must be below the following threshold:

$$RH_{\text{crit},E_P} = MIN(0.7 + 0.3\frac{a_P^{\text{clr}}}{(1-a)}, RH_{\text{crit},bl}, 0.9) \tag{7.58}$$

where $RH_{\text{crit},bl}$ is defined similarly to Eq. 7.19 but with a value of 0.8 above a sigma level of 0.7, increasing linearly to 1 at the surface.

7.3.4 Aggregation of ice to snow

The ice phase is currently represented with two separate prognostic variables for "cloud ice" and "snow". This formulation requires a parametrization representing the aggregation process where ice particles collide to form larger "snow" particles. The parametrization of this ice to snow "autoconversion" process follows the Sundqvist (1978) approach, with the rate of generation of precipitation defined as in (7.46) but with parameters appropriate for ice. The rate coefficient (c_0) is based on Lin *et al.* (1983),

$$c_0 = 10^{-3} e^{0.03(T-273.15)} \tag{7.59}$$

where T is the temperature in Kelvin. Note the exponent multiplier of 0.03 is slightly larger than the 0.025 in Lin *et al.* (1983).

For this process, Lin *et al.* (1983) set q_{i}^{crit} to 10^{-3}kg kg^{-1} in their cloud resolving model (note they were using a Kessler-type scheme rather than the Sundqvist form, but the sensitivities to c_0 and $q_{\text{i}}^{\text{crit}}$ are likely to be similar in both schemes). A lower value is appropriate for a GCM sized grid box (unless sub-grid

cloud variability is explicitly taken into account; Rotstayn, 2000; Pincus and Klein, 2000), and based on model tuning q_i^{crit} is set to 2×10^{-5}kg kg^{-1}.

7.3.5 Ice crystal growth by deposition in mixed phase clouds

The scheme allows supercooled liquid water to exist at temperatures warmer than the homogeneous nucleation threshold of -38°C. At temperatures colder than this water droplets are assumed to freeze instantaneously. When supercooled liquid and ice are coexistent, they are assumed to be well mixed and distributed uniformly through the cloud (see Rotstayn *et al.* (2000) for a discussion of alternative assumptions). The ice crystals can then grow at the expense of the water droplets through the Wegener-Bergeron-Findeisen process. If water droplets are present, the ice crystals are in an environment supersaturated with respect to ice and grow by deposition, reducing the water vapour and leading to subsaturation with respect to water. Water droplets then evaporate and the process continues with ice growth until the water droplets are completely evaporated. Thus in mixed phase clouds, the deposition process acts as a sink of cloud liquid and a source of ice cloud. A description of the consequences of various assumptions in the formulation of this parametrization can be found in Forbes and Ahlgrimm (2014).

Following Pruppacher and Klett (1997) and Rotstayn *et al.* (2000), the rate of growth of an ice crystal of mass M_i is:

$$\frac{dM_i}{dt} = \frac{4\pi C(S_i - 1)}{A'' + B''} \tag{7.60}$$

where C is the capacitance of the particle (related to the shape) and $S_i = e/e_{si}$ is the saturation ratio with respect to ice. Terms A'' and B'' represent heat conduction and vapour diffusion respectively,

$$A'' = \frac{L_{subl}}{K_a T}\left(\frac{L_{subl}}{R_v T} - 1\right) \tag{7.61}$$

$$B'' = \frac{R_v T}{\chi e_{si}} \tag{7.62}$$

where K_a is the heat conductivity of air and χ is the diffusivity of water vapour in air, which varies inversely with pressure as $\chi = 2.21/p$. If the ice crystal number concentration is N_i and the ice crystals are assumed to be monodispersed with all particles having equal diameter D_i and equal mass M_i (and therefore also equal density ρ_i), then the cloud ice specific water content $q_i = M_i N_i/\rho$. If the air is at water saturation, then $S_i = (e_{sl} - e_{si})/e_{si}$, and from (7.60) the rate of change of q_i is

$$\frac{dq_i}{dt} = \frac{N_i}{\rho}\frac{4\pi C}{(A'' + B'')}\frac{(e_{sl} - e_{si})}{e_{si}} \tag{7.63}$$

The capacitance term C assumes ice crystals are spherical ($C = D_i/2$) where $D_i = (6M_i/\pi\rho_i)^{1/3}$. Elimination of C from (7.63) then gives

$$\frac{dq_i}{dt} = c_{vd}^s q_i^{1/3} \tag{7.64}$$

where

$$c_{vd}^s = \left(\frac{N_i}{\rho}\right)^{2/3}\frac{7.8}{\rho_i^{1/3}(A'' + B'')}\frac{(e_{sl} - e_{si})}{e_{si}} \tag{7.65}$$

The analytical treatment of Rotstayn *et al.* (2000) is used, which assumes the temperature dependent quantities in (7.65) can be approximated as constant through the timestep. The ice condensate amount at time t can then be calculated by integrating (7.64) with respect to time, giving

$$q_i^t = \left(\frac{2}{3} c_{vd}^s \Delta t + (q_i^{t-1})^{2/3}\right)^{3/2} \tag{7.66}$$

and the deposition rate, $S_{\text{dep}} = (q_i^t - q_i^{t-1})/\Delta t$.

There is no prognostic equation for ice crystal concentration, and thus N_i is given diagnostically assuming the air is at water saturation according to Meyers *et al.* (1992):

$$N_i = 1000 exp[12.96(e_{sl} - e_{si})/e_{si} - 0.639] \tag{7.67}$$

As the formulation uses only the saturation vapour pressures for water and ice, the ice crystal concentration is effectively only a function of temperature.

To initiate the glaciation process, at each gridbox, a minimum ice mass mixing ratio is assumed of

$$q_i^{min} = \frac{m_{i0} N_i}{\rho} \tag{7.68}$$

where m_{i0} is the initial mass of an ice particle and is set to 10^{-12}kg. The glaciation process also can only occur if the temperature is colder than -5°C.

Once the supercooled liquid water reservoir in the cloud is exhausted through the deposition process, there is a complication to consider. At the point the cloud becomes completely glaciated, the in-cloud vapour pressure is equal to e_{sl}. From this point the ice crystals would continue to grow by deposition of water vapour, until the in-cloud vapour pressure is reduced to the saturation value with respect to ice (or an equilibrium value exceeding the saturation value in the presence of strong updraughts, see Ren and Mackenzie, 2005, for example). However, unlike the mixed phase situation, where the "memory" for the vapour reservoir is provided by the prognostic cloud liquid water variable, there is no memory for the water vapour content in the cloudy region of the gridbox to model the deposition process in glaciated clouds. So, the new cloud follows the same assumption as before for pure ice cloud (see previous subsection) and the deposition of the remaining water vapour in excess of ice saturation occurs within a single timestep, bringing the cloud to exactly ice saturation.

So, in mixed phase clouds with supercooled liquid water present, the cloud is assumed to be exactly at saturation with respect to water (and therefore supersaturated with respect to ice), and when only ice is present, the cloud is assumed to be exactly at saturation with respect to ice. However, supersaturation is permitted in the clear sky portion of a gridcell in all cases.

It is this process of deposition that largely determines the partition between liquid and ice in mixed phase clouds in the scheme.

A modification to the parametrization of ice deposition rate is additionally included to represent the effects of unresolved microphysical processes in the region of cloud top. The small scale dynamical and microphysical processes are unique at cloud top due to radiative cooling enhancing turbulent production of supercooled water, the rate of ice nucleation controlling the depletion of the liquid water through the Wegener-Bergeron-Findeison mechanism, and the fall out of the growing ice crystals reducing the number of crystals and limiting the amount of ice mass in the shallow layer at cloud top. In the model, if there is sufficient resolved vertical motion or vertical transport by the sub-grid parametrizations, or local longwave radiative cooling for the model grid-box to reach water saturation, then supercooled water is produced. Ice nucleation will then occur and the deposition process will start to evaporate the supercooled water and increase the ice mass. The sedimentation term then removes a proportion of the ice from the grid box, depending on the assumed fallspeed for the ice, the depth of the model layer and time step of the model. For a model with high vertical grid resolution and a well-resolved cloud layer, the sedimentation may reduce the ice content in the layers at the top of the cloud significantly, reducing the deposition rate substantially and allowing supercooled liquid water to persist. For a model with low vertical grid resolution and a poorly resolved cloud layer, only a small portion of the total ice in the grid box may be removed due to sedimentation, and the remaining ice is implicitly redistributed vertically throughout the grid box, as the model cloud is always assumed to

homogeneously fill each model layer in the vertical. Thus, the amount of ice at "cloud top" will be much higher in the low resolution case, leading to higher deposition rates than the vertically resolved case near cloud top, and less supercooled liquid water.

One solution is implemented here by finding cloud top and decreasing the deposition rate over a specified depth scale near the top of the cloud. The impact is to reduce the sink of liquid water to ice and increase the amount of supercooled liquid water at cloud top. The deposition rate is multiplied by a factor, F_{dep}, which reduces the conversion rate from supercooled liquid water to ice near cloud top, defined as

$$F_{dep} = MIN[f_{nuc} + (1 - f_{nuc})(F_{ref} + \Delta z_{cldtop}/\Delta z_{refdep}), 1] \tag{7.69}$$

where f_{nuc} is a function of the activated ice nuclei concentration, F_{ref} is a reference deposition rate factor set to 0.1, Δz_{cldtop} is the distance in metres of the model layer from the cloud top layer (cloud top defined by the presence of supercooled liquid water and a cloud fraction threshold of 1%) and Δz_{refdep} is a reference depth of 500m.

The formulation has two components. The first represents the reduced deposition rate near cloud top due to the unresolved microphysical processes of ice nucleation, growth and fallout, controlled by the parameters F_{ref} and Δz_{refdep}. The formulation in terms of distance from cloud top gives the parametrization some independence of vertical grid resolution. If the model layer depths at a particular altitude are of the same magnitude as Δz_{refdep}, then only the top cloud layer will be modified, but if the vertical resolution is higher, then the deposition rate factor increases linearly with layer distance from the diagnosed cloud top.

The second component represents the reduced effect of the parametrization as the number of activated ice nuclei increases with higher supersaturation. This is represented by the function f_{nuc} defined as

$$f_{nuc} = MIN(N_i/15000, 1) \tag{7.70}$$

where N_i is the number of activated ice nuclei given by (7.67). As discussed earlier, N_i in this application is only dependent on temperature and the function f_{nuc} gives a value increasing from 0.035 at 0°C to 1 at -23°C; the latter defined to be consistent with the previous diagnostic scheme mixed-phase temperature threshold. This term therefore reduces the effect of the deposition rate modification with decreasing temperature (increasing altitude) as the number of activated ice nuclei increases.

An additional assumption is made for the spatial overlap of the supercooled liquid water and ice in the cloud. An overlap of 0.65 is assumed, which acts to reduce the ice deposition rate.

7.3.6 Depositional growth of snow particles

The equations are similar to those for the evaporation of rain, but for snow particle growth in supersaturated air with respect to ice, using the latent heat of sublimation/deposition, a particle capacitance of D/4 (Westbrook *et al.*, 2008), the snow particle parameters given in Tables 7.1/7.2/7.3, and ventilation factor F given by Thorpe and Mason (1966)

$$F = 0.65 + 0.44 S_c^{1/3} R_e^{1/2} \tag{7.71}$$

where $S_c = 0.6$ is the Schmidt Number and the Reynolds number $R_e = \nu(D)D\rho/\mu$ where μ is the kinematic viscosity of air.

7.3.7 Sublimation of snow

The sublimation of snow (i.e. from solid to vapour) currently uses the Kessler (1969) formulation for precipitation evaporation in the clear air part of the grid-box using the saturation deficit with respect to ice.

The sublimation rate for snow is assumed to be proportional to the saturation deficit $(q_{\mathrm{sat(i)}} - q_{\mathrm{v}}^{\mathrm{env}})$ and dependent on the snow water content in the clear air (environment), $\rho_{\mathrm{s}}^{\mathrm{clr}}$ (gm^{-3}),

$$S_{\mathrm{subl}} = \alpha_1 (q_{\mathrm{sat(i)}} - q_{\mathrm{v}}^{\mathrm{env}})(\rho_{\mathrm{s}}^{\mathrm{clr}})^{13/20} \tag{7.72}$$

where α_1 is a constant.

Even though the snow water content can be calculated directly from the prognostic specific snow water content, this version of the parametrization calculates the snow water content indirectly from the precipitation flux, $P_{\mathrm{s}}^{\mathrm{clr}}$(kg m^{-2} s^{-1}),

$$\rho_{\mathrm{s}}^{\mathrm{clr}} = P_{\mathrm{s}}^{\mathrm{clr}} / V_{\mathrm{s}} \tag{7.73}$$

where V_{s} is the mean fall speed of snow particles which again is parametrized following Kessler (1969),

$$V_{\mathrm{s}} = \alpha_2 (\rho_{\mathrm{s}}^{\mathrm{clr}})^{1/8} / \sqrt{p/p_0} \tag{7.74}$$

Considering that the sublimation only takes place in the clear-sky precipitation fraction a_P^{clr}, the sublimation rate becomes

$$S_{\mathrm{subl}} = a_P^{\mathrm{clr}} \alpha_1 (q_{\mathrm{sat(i)}} - q_{\mathrm{v}}^{\mathrm{env}}) \left[\frac{\sqrt{p/p_0}}{\alpha_2} \frac{P_{\mathrm{s}}^{\mathrm{clr}}}{a_P^{\mathrm{clr}}} \right]^{\alpha_3} \tag{7.75}$$

where the constants have the following values (Kessler, 1969),

$$\alpha_1 = 5.44 \times 10^{-4}\ \mathrm{s}^{-1}, \qquad \alpha_2 = 5.09 \times 10^{-3}, \qquad \alpha_3 = 0.5777$$

Another option with a more physical basis for snow hydrometeor sublimation is available and will be tested for future implementation.

7.3.8 Collection (accretion) of rain, snow and ice

This process represents the collision/collection (accretion) ice and snow by rain drops leading to freezing of the rain water. If the snow particles are large and rain drops small (drizzle) the resulting particles will be lightly rimed and retain the characteristics of snow. If there is heavier riming of the snow particles, then this would ideally form graupel (but this version of the scheme does not have a hydrometeor category for graupel).

The process is only active if both rain and snow/ice are present and the temperature is below freezing ($< 0^{\circ}$C) as it shouldn't be active in the melting layer, where the rain/snow prognostic variables are used to represent the degree of melting of individual particles rather than separate rain and snow particles. We start with generalised equations for arbitrary hydrometeor types. The collection of hydrometeor type y by hydrometeor type x can be defined by integrating over the joint particle size distributions:

$$S_{xacy} = \frac{1}{\rho} \int_{Dx=0}^{\infty} \int_{Dy=0}^{\infty} E_{xacy} \frac{\pi}{4} (D_x + D_y)^2 |V_y(D_y) - V_x(D_x)| \\ M_y(D_y) n_y(D_y) M_x(D_x) n_x(D_x) dD_y dD_x \tag{7.76}$$

The rate of collisions is dependent on the relative difference in fallspeeds and ideally this would evaluate the double integral for relative fallspeeds across both the rain and snow size distributions. In practice this is difficult to analytically integrate and the differential fall velocity is simplified, often with the following approximation:

$$|V_y(D_y) - V_x(D_x)| = |\overline{V_y} - \overline{V_x}| \tag{7.77}$$

However this approximation gives an underestimation when the two fall velocities are close to each other To avoid the differential approximation going to zero the following form is assumed here following Wilson and Ballard (1999),

$$|V_y(D_y) - V_x(D_x)| = f(\overline{V_y}, \overline{V_x}) = MAX[(|\overline{V_y} - \overline{V_x}|, (\overline{V_y} + \overline{V_x})/8] \tag{7.78}$$

Subsitituting this into Eq. 7.76 gives

$$\begin{aligned} S_{xacy} =& \frac{1}{\rho}\frac{\pi}{4}E_{xacy}f(\overline{V_y}, \overline{V_x}) \\ & \int_{Dx=0}^{\infty}\int_{Dy=0}^{\infty}(D_y + D_x)^2 M_y(D_y)n_y(D_y)M_x(D_x)n_x(D_x)dD_y dD_x \\ =& \frac{1}{\rho}\frac{\pi}{4}E_{xacy}f(\overline{V_y}, \overline{V_x}) \\ & \int_{Dx=0}^{\infty}\int_{Dy=0}^{\infty}(D_y + D_x)^2 a_y D_y^{b_y} n_{ay}\Lambda^{n_{by}} exp(-\Lambda D_y) a_x D_x^{b_x} n_{ax}\Lambda^{n_{bx}} exp(-\Lambda D_x) dD_y dD_x \end{aligned} \tag{7.79}$$

The accretion rate (S_{sacr}) of snow and rain hydrometeor categories (x and y respectively in Eq. 7.79) is calculated by evaluating the double integral over the rain and snow particle size distributions using the respective mass and fall velocity assumptions for each hydrometeor type, yielding

$$S_{sacr} = \pi^2 \frac{\rho_w}{\rho} E_{sacr} f(\overline{V_r}, \overline{V_s}) n_{0r} n_{0s} \left(\frac{5}{\Lambda_r^6 \Lambda_s} + \frac{2}{\Lambda_r^5 \Lambda_s^2} + \frac{0.5}{\Lambda_r^4 \Lambda_s^3}\right) \tag{7.80}$$

Similarly the accretion rate (S_{iacr}) of ice and rain hydrometeors is parametrized with the microphysical parameters for snow replaced by those for ice (number concentration, density and fall speed relationships):

$$S_{iacr} = \pi^2 \frac{\rho_w}{\rho} E_{iacr} f(\overline{V_r}, \overline{V_i}) n_{0r} n_{0i} \left(\frac{5}{\Lambda_r^6 \Lambda_i} + \frac{2}{\Lambda_r^5 \Lambda_i^2} + \frac{0.5}{\Lambda_r^4 \Lambda_i^3}\right) \tag{7.81}$$

The collection efficieny E_{sacr} for snow and rain is set to 1.0, and E_{iacr} for ice and rain is set to 0.1.

7.3.9 Riming - collection of cloud water by snow

This process represents the collection and freezing of cloud liquid water drops by falling snow particles and by assuming that the cloud droplets have negligible size and fall speed compared to the snow hydrometeors ($D_r \ll D_s$ and $V_r \ll V_s$), the collection equation (Eq. 7.79) can be simplified to

$$S_{rime} = \frac{1}{\rho}\int_{Dl=0}^{\infty} M_l(D_l)n_l(D_l)dD_l E_{rime}\frac{\pi}{4}(D_s)^2 \int_{Ds=0}^{\infty} V_s(D_s)M_s(D_s)n_s(D_s)dD_s \tag{7.82}$$

If the liquid drops are assumed to have zero fallspeed and are represented by spheres of diameter, D, then this becomes,

$$S_{rime} = E_{rime}\frac{\pi}{4}q_l \int_{D=0}^{\infty} n_{as}\Lambda^{n_{bs}} exp(-\Lambda D) c_s D^{d_s} \left(\frac{\rho_0}{\rho}\right)^{0.5} dD \tag{7.83}$$

Integrating over the particle size distribution gives

$$S_{rime} = E_{rime}\frac{\pi}{4}q_l \frac{n_{as} c_s \Gamma(3 + d_s)}{\Lambda^{3+d_s}} \left(\frac{\rho_0}{\rho}\right)^{0.5} \tag{7.84}$$

The collection efficieny E_{rime} is assumed to be 0.3.

The riming of ice particles (collection of cloud water droplets by ice particles) is assumed to be negligible and is therefore currently not represented.

7.3.10 Melting of ice and snow

The melting of ice and snow hydrometeors is parametrized by allowing the part of the grid box that contains precipitation to cool to T_{melt} over a time scale τ, that is

$$S_{\text{melt}} = (a_P^{\text{cld}} + a_P^{\text{clr}}) \frac{c_p}{L_{\text{fus}}} \frac{T_w - T_{\text{melt}}}{\tau} \tag{7.85}$$

where $T_{\text{melt}} = 0°\text{C}$, T_w is the wet-bulb temperature and

$$\tau = \frac{\tau_m}{1 + 0.5(T_w - T_{\text{melt}})}$$

where $\tau_m = 7200$ s. The wet-bulb temperature is used in order to account for the thermal (cooling) effect of evaporation on the melting process in sub-saturated air. The evaporation counteracts the latent heating due to melting and allows snow particles to survive to slightly warmer temperatures when the relative humidity of the air is low. The wet-bulb temperature is approximated as in the scheme described by Wilson and Ballard (1999)

$$T_w = T - (q_{sat(w)} - q_v)(A + B(p - C) - D(T - E)) \tag{7.86}$$

where $A = 1329.31$, $B = 0.0074615$, $C = 0.85 \times 10^5$, $D = 40.637$, and $E = 275$.

7.3.11 Freezing of rain

If rain (containing no ice) falls into sub-zero temperatures, it will become supercooled. The probability of a rain drop freezing then depends exponentially on the temperature difference of the air below 0°C and on the volume of the drop, with larger drops more likely to freeze than smaller drops (Bigg, 1953; Wisner *et al.*, 1972).

Following Bigg (1953), the probability of a water drop of diameter D freezing in a second is proportional to its volume:

$$P_f = \frac{\pi}{6} D^3 B_B (e^{-A_B T_c} - 1) \tag{7.87}$$

where A_B and B_B are constant parameters determined from laboratory experiment. The rate of freezing of the rain mass is then determined by integrating over the rain drop size distribution,

$$\begin{aligned} S_f &= \frac{1}{\rho} \int P_f(D) M(D) n(D) dD \\ &= \frac{\pi}{6} D^3 B_B (e^{-A_B T_c} - 1) n_{0r} \frac{\Gamma(4 + d_r)}{\lambda_r^4} \end{aligned} \tag{7.88}$$

If rain drops are not completely melted, they will contain an ice core which leads to rapid refreezing if the melting particles fall from an elevated above-freezing layer into a layer of sub-zero temperatures below. In this case, the rate of freezing is faster and is parametrized with a similar functional form to the melting of snow (Eq. 7.85), with a timescale of 7200s. It is assumed that at least 20% of the precipitation mass must be in the ice phase at the base of the warm layer for refreezing to be rapid. Otherwise, if more than 80% of the precipitation mass at the base of the warm layer is rain, the slower timescale for supercooled rain drops is applied in the column below and freezing rain can be diagnosed at the surface.

7.3.12 Freezing of cloud water droplets

All liquid cloud drops are assumed to freeze instantaneously to ice crystals at temperatures below the homogeneous freezing temperature of -38°C.

7.3.13 Sedimentation

The numerical formulation of the hydrometeor sedimentation follows an implicit upstream approach. The rain, snow and ice hydrometeor categories are allowed to sediment.

With the potential for hydrometeors to settle through many model layers in a single timestep, using a mass related fall speed formulation can lead to numerical 'shocks' when long timesteps are necessary if the numerics of the process are not carefully formulated. At present the fallspeed for ice and snow are set to a constant ($V_i = 0.13$ m s^{-1}, $V_s = 1$ m s^{-1}). A mass-weighted terminal fallspeed for rain is parametrized following Eq. 7.44 with parameters defined in Table 7.3. Revision of the sedimentation term for ice and snow will be a topic for future development.

7.4 NUMERICS

7.4.1 Integration of the equations

The microphysics parametrization is a multi-species scheme with $m = 5$ prognostic equations for water vapour, cloud liquid water, rain, cloud ice and snow (i.e. the single cloud condensate equation in the previous version is replaced by four variables). The equation governing each prognostic cloud variable within the cloud scheme is

$$\frac{\partial q_x}{\partial t} = A_x + \frac{1}{\rho}\frac{\partial}{\partial z}\left(\rho V_x q_x\right) \tag{7.89}$$

where q_x is the specific water content for category x (so $x = 1$ represents cloud liquid, $x = 2$ for rain, and so on), A_x is the net source or sink of q_x through microphysical processes, and the last term represents the sedimentation of q_x with fall speed V_x.

The solution to this set of equations uses the upstream approach. Writing the advection term in mass flux form and collecting all fast processes (relative to a GCM timestep) into an implicit term, gives

$$\frac{q_x^{n+1} - q_x^n}{\Delta t} = A_x + \sum_{x=1}^{m} B_{xy} q_y^{n+1} - \sum_{x=1}^{m} B_{yx} q_x^{n+1} + \frac{\rho_{k-1} V_x q_{x,k-1}^{n+1} - \rho V_x q_x^{n+1}}{\rho \Delta Z} \tag{7.90}$$

for timestep n. The subscript "$k-1$" refers to a term calculated at the model level above the present level k for which all other terms are being calculated. The matrix $\widetilde{B}$ (with terms B_{xx}, B_{xy}, B_{yx}) represents all the implicit microphysical pathways such that $B_{xy} > 0$ represents a sink of q_y and a source of q_x. Matrix $\widetilde{B}$ is positive-definite off the diagonal, with zero diagonal terms since $B_{xx} = 0$ by definition. Some terms, such as the creation of cloud through condensation resulting from adiabatic motion or diabatic heating, are more suitable for an explicit framework, and are retained in the explicit term A.

For cloud fraction, there are no multi-dimensional dependencies, so the equation simplifies to

$$\frac{a^{n+1} - a^n}{\Delta t} = A + B a^{n+1} \tag{7.91}$$

However, for the cloud and precipitation variables in (7.90), a matrix approach is required. Due to the cross-terms q_y^{n+1}, (7.90) is rearranged to give a straight forward matrix equation which can be solved with standard methods (the scheme currently uses the LU decomposition method). As long as the solution method is robust the choice for solution is not critical as the number of microphysical prognostic equations is small ($m = 5$), in contrast to chemical models with typically O(100) species. The solution method is simplified by assuming the vertical advection terms due to convective subsidence and sedimentation act only in the downward direction, allowing the solution to be conducted level by level from the model top down.

The matrix on the LHS has the microphysical terms in isolation off the diagonal, with the sedimentation term on the diagonal, thus the matrix equation for a 3-variable system is

$$\begin{pmatrix} 1 + \Delta t(\frac{V_1}{\Delta z} + B_{21} + B_{31}) & -\Delta t B_{12} & -\Delta t B_{13} \\ -\Delta t B_{21} & 1 + \Delta t(\frac{V_2}{\Delta z} + B_{12} + B_{32}) & -\Delta t B_{23} \\ -\Delta t B_{31} & -\Delta t B_{32} & 1 + \Delta t(\frac{V_3}{\Delta z} + B_{13} + B_{23}) \end{pmatrix} \cdot \begin{pmatrix} q_1^{n+1} \\ q_2^{n+1} \\ q_3^{n+1} \end{pmatrix} =$$
$$\left[q_1^n + \Delta t \left(A_1 + \frac{\rho_{k-1} V_1 q_{1,k-1}^{n+1}}{\rho \Delta Z} \right), q_2^n + \Delta t \left(A_2 + \frac{\rho_{k-1} V_2 q_{2,k-1}^{n+1}}{\rho \Delta Z} \right), q_3^n + \Delta t \left(A_3 + \frac{\rho_{k-1} V_3 q_{3,k-1}^{n+1}}{\rho \Delta Z} \right) \right] \tag{7.92}$$

There are some aspects that require attention. Firstly, although implicit terms are unable to reduce a cloud category to zero, the explicit can, and often will, achieve this. Thus safety checks are required to ensure that all end-of-timestep variables remain positive definite, in addition to ensuring conservation. Practically, to aid the conservation requirement, the explicit source and sink terms are thus also generalised from a vector $\vec{A}$ to an anti-symmetric matrix $\widetilde{A}$,

$$\widetilde{A} = \begin{pmatrix} A_{11} & A_{21} & A_{31} \\ -A_{12} & A_{22} & A_{32} \\ -A_{13} & -A_{23} & A_{33} \end{pmatrix} \tag{7.93}$$

Thus $A_{xy} > 0$ represents a source of q_x and a sink of q_y, and the original vector for A can be obtained by summing over the rows. Although this matrix approach involves a degree of redundancy, it is a simple method of ensuring conservation properties. The matrix diagonals A_{xx} contain the 'external' sources of q_x such as the cloud water detrainment terms from the convection scheme.

In order to simultaneously guarantee conservation and positive-definite properties, the sum of all sinks for a given variable are scaled to avoid negative values. This solution is not accurate, seen from the consideration of the simple case of a variable in equilibrium, with a small initial value subjected to a large source and an equal and opposing sink: the sink will be clipped first and the variable will increase. However, this is deemed preferable to any method that attempts to account for variable sources, which must invoke a sensitivity to the order in which the variables are considered.

The impact on the temperature budget is calculated from the change in cloud variables due to each process after the cloud scheme 'solver' has been applied, and then collecting the terms together that are associated with latent heating/cooling. With the fully implicit solver it is thus easier to use conserved variables to govern the temperature budget; the scheme uses the liquid water temperature T_L defined as:

$$T_L = T - \frac{L_{vap}}{C_p}(q_l + q_r) - \frac{L_{subl}}{C_p}(q_i + q_s) \tag{7.94}$$

Since $dT_L/dt = 0$, the temperature change is thus given by

$$\frac{\partial T}{\partial t} = \sum_{x=1}^{m} \frac{L(x)}{C_p}\left(\frac{dq_x}{dt} - D_{q_x} - \frac{1}{\rho}\frac{\partial}{\partial z}\left(\rho V_x q_x\right)\right) \tag{7.95}$$

The first term on the right in the brackets is the rate of change of species q_x due to *all* processes, including the convective detrainment term D_{q_x} and the advective flux terms, which are then subtracted separately since they represent a net T_L flux not associated with latent heating.

7.4.2 Calculation of $\mathrm{d}q_{\mathrm{sat}}/\mathrm{d}t$

Special care has to be taken in the numerical calculation of $\mathrm{d}q_{\mathrm{sat}}/\mathrm{d}t$ from (7.16). Since the saturation water vapour pressure depends exponentially on temperature, straightforward numerical integration of (7.16) would produce large truncation errors. Therefore the average of $\mathrm{d}q_{\mathrm{sat}}/\mathrm{d}t$ over the time step is determined by the means of moist adjustment (e.g. Haltiner and Williams, 1980) , adjusting temperature and moisture toward saturation conditions.

7.4.3 Convective cloud source

The vertical discretisation of (7.14) and (7.15) is achieved with a simple upstream scheme, that is

$$S_{\mathrm{conv}} = D_{\mathrm{up},k} l_{\mathrm{up},k+1/2} - gM_{\mathrm{up},k-1/2}\frac{q_{\mathrm{l}_{k-1}} - q_{\mathrm{l}_k}}{z_{k-1} - z_k} \tag{7.96}$$

and

$$\delta a_{\mathrm{conv}} = D_{\mathrm{up},k} - gM_{\mathrm{up},k-1/2}\frac{a_{k-1} - a_k}{z_{k-1} - z_k} \tag{7.97}$$

The convective source is treated explicitly to ensure conservation. As stated earlier, cloud fraction is treated implicitly.

7.4.4 Final moist adjustment

In the case where semi-Lagrangian advection is not used, a final test for supersaturation is performed after the calculation of the cloud tendencies and the corresponding tendencies of temperature and moisture. If any supersaturation is found, the grid box is re-adjusted to saturation (using the moist adjustment formulation) and the moisture excess is converted into precipitation. When the semi-Lagrangian averaging of physics process tendencies (SLAVEPP) scheme is utilized however, there is an additional check after the averaging to condense any remaining supersaturation above the defined threshold. See Section 3.10 of Chapter 3 "Semi-Lagrangian formulation" for a more detailed description. Note, that small amounts of non-physical supersaturation due to numerical approximations may remain in the postprocessed fields and that supersaturation with respect to ice is allowed as described in Section 7.2.3.

7.5 DESCRIPTION OF OUTPUT FIELDS: HUMIDITY, CLOUDS AND PRECIPITATION

7.5.1 Prognostic variables

Grib code	Short Name	Description	Units
248.128	CC	Cloud fraction	(0-1)
246.128	CLWC	Cloud liquid specific water content	(kg kg^{-1})
247.128	CIWC	Cloud ice specific water content	(kg kg^{-1})
75.128	CRWC	Precipitation rain specific water content	(kg kg^{-1})
76.128	CSWC	Precipitation snow specific water content	(kg kg^{-1})
130.128	T	Temperature	(K)
133.128	Q	Specific humidity	(kg kg^{-1})

These define the cloud/precipitation related prognostic (predicted) variables in the IFS. Humidity/cloud/precipitation are grid-box mean specific quantities (mass of water) / (mass of moist air), where the latter is defined as the mass of dry air plus the mass of the cloud liquid, ice, rain and snow in the grid box.

[Note: Rain (CRWC) and snow (CSWC) were introduced into operations in IFS Cycle 36r4 and are therefore not available in ERA-Interim. 3D fields of convective precipitation are not currently available.]

7.5.2 Relative humidity

Grib code	Short Name	Description	Units
157.128	R	Relative humidity	(%)

Relative humidity is calculated on model levels from the 3D specific humidity, temperature and pressure fields. It is defined as a mixed water/ice relative humidity: with respect to water for temperatures warmer than 0°C, with respect to ice for temperatures colder than -23°C, and a quadratic interpolation of the two in the 0°C to -23°C temperature range. This follows the diagnostic mixed-phase parametrization assumption for saturation vapour pressure in parts of the IFS.

The definition of relative humidity is the ratio of the partial pressure of water vapour (e) to the saturation partial pressure of water vapour ($e_{\mathrm{sat}}(T)$)over a plane of liquid water/ice at temperature T, given by:

$$\frac{e}{e_{\mathrm{sat}}(T)} = \frac{pq\frac{1}{\epsilon}}{e_{\mathrm{sat}}(T)\left(1+q(\frac{1}{\epsilon}-1)\right)} \tag{7.98}$$

where p is the atmospheric pressure, q is the specific humidity and ϵ is the ratio of the molar masses of water and dry air ($= R_{\mathrm{dry}}/R_{\mathrm{vap}} = 0.621981$). this is multiplied by 100 to convert to a percentage.

The saturation vapour pressure is defined as

$$e_{\mathrm{sat}}(T) = \alpha e_{\mathrm{sat(w)}}(T) + (1-\alpha)e_{\mathrm{sat(i)}}(T) \tag{7.99}$$

where $e_{\mathrm{sat(w)}}(T)$ and $e_{\mathrm{sat(i)}}(T)$ are the saturation partial pressures of water vapour with respect to water and ice, respectively, given by Tetens formula

$$e_{\mathrm{sat}}(T) = a_1 \exp\left\{a_3\left(\frac{T-T_0}{T-a_4}\right)\right\} \tag{7.100}$$

with the parameters set according to Buck (1981) for saturation over water ($a_1 = 611.21$ Pa, $a_3 = 17.502$ and $a_4 = 32.19$ K) and to the AERKi formula of Alduchov and Eskridge (1996) for saturation over ice ($a_1 = 611.21$ Pa, $a_3 = 22.587$ and $a_4 = -0.7$ K), with $T_0 = 273.16$ K.

The mixed phase parameter α is a function of temperature:

$$\begin{aligned} \alpha &= 0 && T \leq T_{\text{ice}} \\ \alpha &= \left(\frac{T - T_{\text{ice}}}{T_0 - T_{\text{ice}}}\right)^2 && T_{\text{ice}} < T < T_0 \\ \alpha &= 1 && T \geq T_0 \end{aligned} \tag{7.101}$$

where T_{ice} and T_0 represent the threshold temperatures between which a mixed phase is allowed to exist and are chosen as $T_{\text{ice}} = 250.16$ K and $T_0 = 273.16$ K.

Supersaturation with respect to ice is represented in the IFS; significant supersaturations can be observed at cold temperatures in the atmosphere. Relative humidity can therefore be greater than 100% and the maximum possible supersaturation increases with decreasing temperature, although with decreasing frequency of occurrence (about 120% at -20°C to about 140% at -40°C).

7.5.3 Cloud

(*a*) ***Cloud cover***

Grib code	Short Name	Description	Units
164.128	TCC	Total cloud cover	(0-1)
186.128	LCC	Low cloud cover	(0-1)
187.128	MCC	Mid-level cloud cover	(0-1)
188.128	HCC	High cloud cover	(0-1)

The total, high, mid-level and low cloud cover are 2D fields calculated from the 3D field of predicted subgrid cloud cover using a diagnostic assumption ("exponential-random") for overlap in the vertical based on observations (Hogan and Illingworth, 2000; Mace and Benson-Troth, 2002; Barker, 2008). A generalised overlap is applied within a contiguous cloud where the degree of overlap randomness between two cloudy levels increases exponentially with increasing vertical separation, and a random overlap is applied between cloud layers separated in the vertical. The overlap algorithm is the same as used in the IFS McICA radiation scheme (IFS Documentation, Part IV, Chapter 2) and is based on the stochastic cloud generator described in Räisänen *et al.* (2004). The diagnostics for low, medium and high cloud cover are calculated from the prognostic cloud cover (CC) field over the relevant vertical atmospheric slab. In sigma coordinates these slabs are defined as follows.

LCC	Low cloud cover	$p > 0.8p_s$
MCC	Mid-level cloud cover	$0.45p_s \leq p \leq 0.8p_s$
HCC	High cloud cover	$p < 0.45p_s$

where p is the pressure and p_s is the surface pressure.

[Note: Before IFS Cycle 33R1, the low cloud cover (LCC) is underestimated if there is both cloud in the profile either side of the the medium cloud cover (MCC/LCC) boundary and the cloud fraction is less in the lower layer than in the higher layer. This problem also applies to MCC for the high cloud cover (HCC/MCC) boundary. This was fixed in Cycle 33R1 onwards, but it affects ERA-Interim, which will therefore underestimate LCC/MCC in deep cloud systems. The total cloud cover (TCC) is unaffected.]

(*b*) ***Cloud height***

Grib code	Short Name	Description	Units
23.228	CBH	Cloud base height	(m)
109.260	CEIL	Ceiling	(m)
46.228	HCCT	Height of convective cloud top	(m)

These are 2D fields evaluated in meters above ground, which are of special interest for aviation. The cloud base height and the ceiling are defined as the height of the model level, starting from the ground, when a certain threshold of the total condensate and/or cloud fraction is first exceeded. For the cloud base height this threshold is 1% cloud fraction and a total condensate specific mass content of 10^{-6} kg kg^{-1}. If no cloud base is found, but the convection scheme diagnoses a convective cloud base, then the cloud base height is set to the convective cloud base. The ceiling is defined by a threshold of 50% cloud fraction. The height of convective cloud top is output from the convection scheme as the height where the convective updraught (velocity) vanishes.

(*c*) ***Vertically integrated cloud and precipitation***

Grib code	Short Name	Description	Units
136.128	TCW	Total column water	(kg m^{-2})
137.128	TCWV	Total column water vapour	(kg m^{-2})
78.128	TCLW	Total column liquid water	(kg m^{-2})
79.128	TCIW	Total column ice water	(kg m^{-2})
88.228	TCSLW	Total column supercooled liquid water	(kg m^{-2})
89.228	TCRW	Total column rain water	(kg m^{-2})
90.228	TCSW	Total column snow water	(kg m^{-2})

These are 2D fields vertically integrated throughout each grid column to give the mass of water in the column per metre squared for each category. The total column water is the sum of the water vapour, cloud water, cloud ice, rain and snow. ($TCW = TCWV + TCLW + TCIW + TCRW + TCSW$). [Note for IFS Cycles before 36r4 including ERA-Interim the precipitation is excluded so $TCW = TCWV + TCLW + TCIW$).]

The total column supercooled liquid water (TCSLW) is the part of the total column liquid water present at temperatures below 0°C.

7.5.4 Precipitation

(*a*) ***Accumulated precipitation***

Grib code	Short Name	Description	Units
142.128	LSP	Acc. large-scale (stratiform) precipitation (rain+snow)	m
143.128	CP	Acc. precipitation (rain+snow) from convective updraughts	m
144.128	SF	Acc. snowfall (water equivalent) (stratiform + convective)	m
228.128	TP	Acc. total precipitation (CP + LSP)	m
216.228	FZRA	Acc. freezing rain	m
50.128	LSPF	Acc. large-scale surface precipitation fraction	(0-1) × s

These parameters are for precipitation falling at the surface and are accumulated from the start of the forecast. The IFS represents precipitation with four variables, convective rainfall and snowfall from the convection parametrization, and stratiform rainfall and snowfall from the large-scale (or stratiform) cloud parametrization. The accumulated parameters give different combinations of the accumulated precipitation, and snowfall is always defined as the mass-of-water equivalent accumulation. For the individual contributions, precipitation rates at the output timesteps are available (see below).

The amount of precipitation accumulation (LSP+CP) that is diagnosed as "freezing rain" or "freezing drizzle" at the surface (FZRA) is made available as a separate quantity for assessing hazardous weather.

The IFS predicts the fractional area of a grid box that is covered by the large-scale precipitation at each timestep (see ILSPF below). The LSPF parameter is this fractional area accumulated from the start of the forecast. Dividing by the accumulation time (in seconds) gives a time-average precipitation fraction.

Grib code	Short Name	Description	Units
217.228	ILSPF	Instantaneous large-scale surface precipitation fraction	0-1
218.228	CRR	Convective rainfall rate	kg m^{-2} s^{-1}
219.228	LSRR	Large scale rainfall rate	kg m^{-2} s^{-1}
220.228	CSFR	Convective snowfall rate	kg m^{-2} s^{-1}
221.228	LSSFR	Large scale snowfall rate	kg m^{-2} s^{-1}
260.048	TPRATE	Total precipitation rate (CRR+LSRR+CSFR+LSSFR)	kg m^{-2} s^{-1}
222.228	MXTPR3	Maximum total precipitation rate in the last 3 hours	kg m^{-2} s^{-1}
223.228	MNTPR3	Minimum total precipitation rate in the last 3 hours	kg m^{-2} s^{-1}
224.228	MXTPR6	Maximum total precipitation rate in the last 6 hours	kg m^{-2} s^{-1}
225.228	MNTPR6	Minimum total precipitation rate in the last 6 hours	kg m^{-2} s^{-1}

(*b*) ***Precipitation rates***

The precipitation rates are the surface precipitation fluxes valid at the specified output time. There are four predicted precipitation variables, convective rainfall (CRR) and snowfall (CSFR) from the convection parametrization, and stratiform rainfall (LSRR) and snowfall (LSSFR) from the large-scale (or stratiform) cloud parametrization. The fractional grid-box area covered by the large-scale precipitation (LSRR+LSSFR) at the specified time is ILSPF. The total precipitation rate at the output time is available (TPRATE) and equal to the sum of the four components; CRR+LSRR+CSFR+LSSFR. In addition, there are a number of parameters that record the maximum and minimum precipitation rate in the last 3 hours and the last 6 hours of the output time. There is additional information on the predicted type of the precipitation at the output time in the PTYPE parameter described below.

(*c*) ***Precipitation type***

Grib code	Short Name	Description (WMO Code Table 4.201)	Units
015.260	PTYPE	Precipitation type	0-12
320.260	PTYPE_FREQ1H	Precipitation type (most frequent) in the last 1 hour	0-12
321.260	PTYPE_FREQ3H	Precipitation type (most frequent) in the last 3 hours	0-12
339.260	PTYPE_FREQ6H	Precipitation type (most frequent) in the last 6 hours	0-12
318.260	PTYPE_SEV1H	Precipitation type (most severe) in the last 1 hour	0-12
319.260	PTYPE_SEV3H	Precipitation type (most severe) in the last 3 hours	0-12
338.260	PTYPE_SEV6H	Precipitation type (most severe) in the last 6 hours	0-12

Precipitation type (WMO Code Table 4.201)		Severity order (most severe first)	
0	Not defined (no precipitation)	3	Freezing rain
1	Rain	12	Freezing drizzle
3	Freezing rain	6	Wet snow
5	Snow	5	Snow
6	Wet snow	8	Ice pellets
7	Mixture of rain and snow	7	Mixture of rain and snow
8	Ice pellets	1	Rain
12	Freezing drizzle	0	Not defined (no precipitation)

"Precipitation type" describes the diagnosed type of precipitation at the surface valid at the output time. A precipitation type is assigned wherever total precipitation rate is essentially non-zero (defined by $> 10^{-10}$ kg m^{-2} s^{-1}). The precipitation type should be interpreted alongside the total precipitation rate (i.e. the sum of the convective and large scale rainfall and snowfall rates TPRATE=CRR+LSRR+CSFR+LSSFR) or the total accumualted precipiation (TP) over the appropriate accumulation period for the most-frequent and most-severe precipitatoion types in the last 1, 3 or 6 hours..

The type of winter precipitation can be challenging to predict correctly as small uncertainties in the temperature profile and precipitation processes can affect the type of precipitation at the surface. The

IFS ensemble will provide some estimate of this uncertainty. For a more detailed discussion of winter precipitation-type, and in particular freezing rain predictions from the IFS, see the article in ECWMF Newsletter 141 (Forbes *et al.*, 2014).

Precipitation type is represented as an integer value defined by WMO Code Table 4.201. The precipitation types used in the IFS are described in the table above. As this is an integer field, plotting should be by nearest grid point without interpolation. As the IFS only explicitly predicts liquid or frozen precipitation (rain or snow), additional assumptions have been used to diagnose the precipitation type at the surface. The relative contributions of coexisting rain and snow at the surface are combined with the knowledge of the precipitation processes in the vertical column above (particularly melting and freezing - for information on the process parametrizations see *IFS Documentation Part IV, Section 7.3*).

As precipitation type can vary on the time steps between output times, the "most-frequent" (mode) and "most-severe" precipitation type in the last 1, 3 or 6 hours are defined that take input from every timestep of the model during the specified time period. The order of severity for the "most-severe" precipitation type is defined in the above table with freezing rain the most severe. As an example, even if there is only one time step when freezing rain occurs and snow occurs on every other time step in the period, freezing rain would be reported as the most-severe precipitation type during the period, and snow would be reported as the most-frequent. For the most-frequent precipitation type, if the frequency of occurrence of two precipitation types is equal during the time period, then the precipitation type with the lower value is reported. For example, if rain (precip type 1) and snow (precip type 5) have equal frequency of occurrence during the period, rain will be reported as the most-frequent.

The diagnosis of each of the precipitation types at each timestep is described below. Note that hail and graupel are not currently diagnosed in the IFS.

Figure 7.3 shows schematic temperature profiles for some of precipitation types. Figure 7.4 shows an illustration of the precipitation type diagnosis and how this has changed across IFS Cycles. Figure 7.5 shows an idealised cross section to illustrate varying precipitation type that would be diagnosed across a warm front with an elevated warm layer.

Precip Type 1: Rain

A precipitation type of "rain" is diagnosed when the 2m temperature is warmer than 0°C and the percentage ratio of rainfall to snowfall at the surface is greater than 80%.

Precip Type 3: Freezing rain

The "freezing rain" precipitation type represents supercooled rain drops that can freeze on impact at the surface if below 0°C. If the precipitation is heavy or prolonged then a glaze of ice can build up on exposed surfaces.

Freezing rain can occur when there is snow falling into an elevated layer of air that is warmer than 0°C with a sub-freezing layer below. This is often associated with warm air advection aloft ahead of a warm front. As snow particles fall into the layer, they will start to melt. If the layer is deep enough for the snow particles to completely melt to rain drops before they reach the sub-freezing layer near the ground, they can remain in supercooled liquid form all the way to the surface (Fig. 7.3d). The layer of cold air near the surface is typically only a few degrees below freezing, so it is generally not cold enough for significant homogeneous or heterogeneous freezing of the rain drops to occur (although this process is represented in the IFS). It is the presence of the elevated warm (melting) layer that is necessary for the formation of freezing rain. The formation of supercooled rain/drizzle drops from the collision-coalescence of supercooled cloud liquid droplets, which does not need an elevated melting-layer, is described below in the "freezing drizzle" category.

Freezing rain at the surface is diagnosed if the 2-metre temperature is below 0°C, at least 1% of the precipitation rate is in the liquid phase at the base of the elevated melting layer and more than 50% is supercooled rain when it reaches the surface. Freezing rain can therefore be diagnosed even if there is a high frozen precipitation fraction at the base of the elevated melting layer, which may not be realistic, but this situation rarely occurs in the IFS.

Precip Type 5: Snow / Dry snow

The "snow" precipitation type represents ice particles (aggregates of crystals) when the whole temperature profile is colder than 0°C (in practice up to 1% meltwater is allowed for this precipitation type). (See Fig. 7.3a). This category is also diagnosed if the 2 metre temperature is below 0°C with up to 50% supercooled water, depending on the precipitation type aloft. However, occurrence of this is rare and would indicate a complex mix of processes in the vertical column with snow particles mixed with ice pellets, and supercooled rain or drizzle which would freeze at the surface.

Precip Type 6: Wet snow

As snow particles fall into air with a wet-bulb temperature warmer than 0°C, they start to melt. In the model this process is parametrized as a transfer of mass from the snow category to the rain category. Wet snow is diagnosed if the 2m temperature is greater than 0°C and particles have between 1% and 20% meltwater. In reality "wet snow" particles of the same size can have different fall speeds due to small differences in melt-water content (Yuter *et al.*, 2006). Aggregation can therefore be an efficient process forming large snow particles with the potential for greater surface accumulations if the ground is at or below the freezing point. This is the main reason why there is a separate "wet snow" precipitation type.

Melting and evaporation act to cool the air, so with prolonged snowfall a near-zero degree isothermal layer can develop, sometimes up to a few hundred metres deep. This deep melting layer can intersect the surface over a large spatial area resulting in a wide region of precipitation diagnosed as "wet snow", or a "rain/snow mix".

Precip Type 7: Mixture of rain and snow / Melting snow / Sleet

As the "wet snow" falls into warmer air, it rapidly melts with increasing amounts of melt water and a reducing core of ice in each particle. In reality, there is often a mix of rain drops and partially melted ice particles. In the model, if the 2m temperature is greater than 0°C and the rain to snow ratio at the surface is between 20% and 80%, then the surface is diagnosed as intersecting the main part of the melting layer and the precipitation type is diagnosed as a "mix of rain and snow" ("melting snow" or "sleet" depending on the preferred term). (See Fig. 7.3b).

Precip Type 8: Ice pellets

As for freezing rain, ice pellet formation also requires an elevated layer warmer than 0°C. Where this layer is shallow or close to 0°C throughout the depth, the snow particles falling in to the layer may only partially melt before they enter the sub-freezing layer below. In this case the supercooled mixed-phase particles contain an ice core and refreezing is rapid, forming ice pellets before reaching the surface (Fig. 7.3c). The ice pellet precipitation type is therefore diagnosed if the 2-metre temperature is below 0°C and at least 20% of the precipitation rate is from frozen particle (i.e. in the snow hydrometeor category) at the base of the elevated melting layer, and more than 50% of the precipitation reaching the surface is frozen. If ice pellets occur, then quite often they will be in a narrow band between a region of freezing rain and snow where the nose of the elevated warm layer is shallow and only partial melting occurs (Fig. 7.5).

Precip Type 12: Freezing drizzle

The "freezing drizzle" precipitation type represents supercooled rain/drizzle drops formed from collision-coalescence of supercooled cloud liquid droplets at sub-freezing temperatures (represented by parametrized autoconversion and accretion processes in the model). This can occur in relatively shallow clouds that have not glaciated and therefore often results in relatively light rain (drizzle), hence the name "freezing drizzle". When the supercooled drizzle drops impact a surface that is below 0°C they can freeze and if the precipitation is prolonged then a glaze of ice can build up on exposed surfaces.

Freezing drizzle at the surface is diagnosed if the 2-metre temperature is below 0°C, at least 50% of the precipitation rate is from rain and there is no melting layer (T$>$ 0°C) aloft.

History of changes to Precipitation Type

- **Cycle 41r1**: Precipitation type introduced.
- **Cycle 47r3**: Change to the thresholds for diagnosis of snow, ice pellets and freezing rain when the 2m temperature is below 0°C (See Fig. 7.4).
- **Cycle 48r1**: Addition of freezing drizzle precipitation type and output diagnostics for the "most-frequent" and "most-severe" precipitation types in the last 1/3/6 hours.

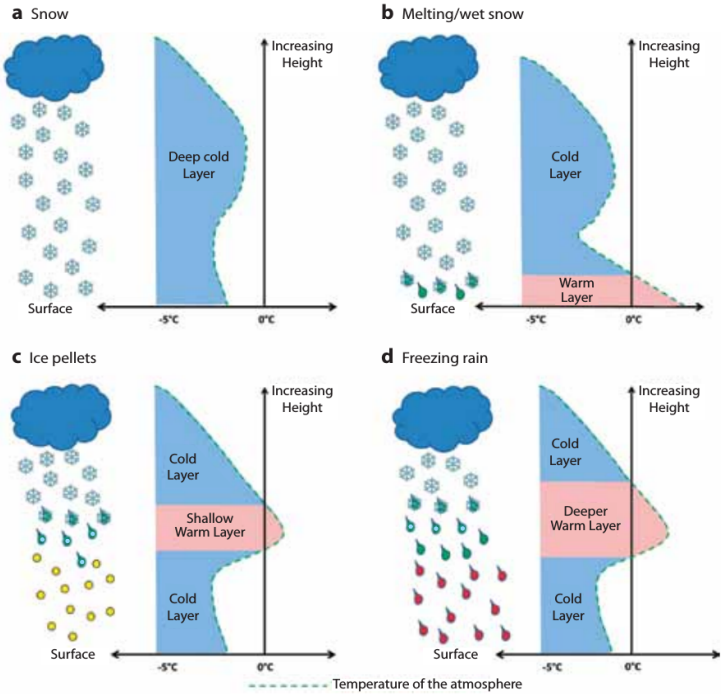

Figure 7.3 *Schematic of typical temperature profiles for different precipitation types: (a) snow, (b) melting/wet snow, (c) ice pellets and (d) freezing rain (all assuming 100% relative humidity).*

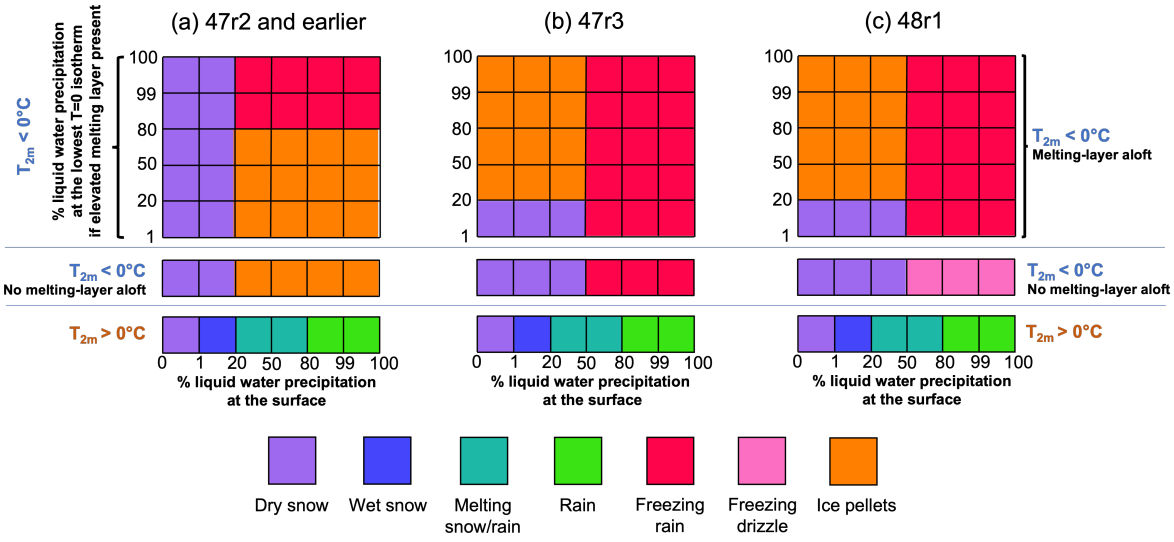

Figure 7.4 *Diagnosis of precipitation type from 2m temperature, percentage liquid water content of hydrometeors at the surface and at the lowest T=0°C isotherm of an elevated melting layer (if present), for (a) Cycles 47r2 and earlier, (b) Cycle 47r3, (c) Cycle 48r1.*

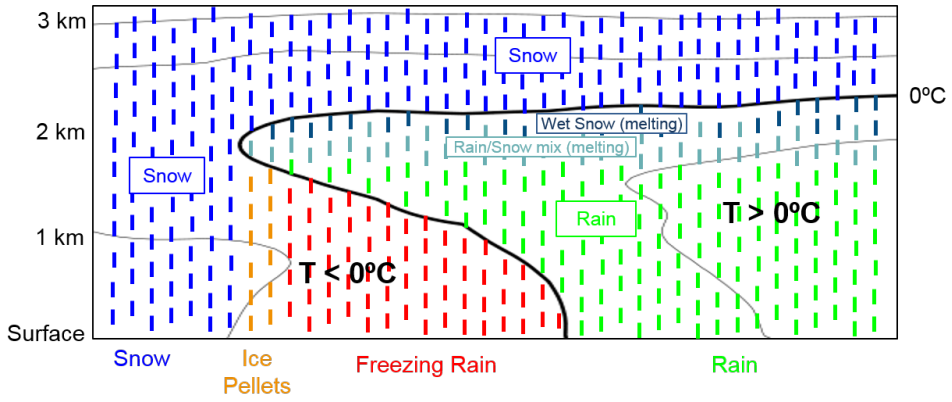

Figure 7.5 *Schematic cross section of precipitation type across a warm front with elevated warm layer above 0°C and a sub-freezing layer below showing the change of precipitation type that would be seen at the surface.*

7.6 CODE

The parametrization of cloud and large-scale precipitation processes is performed in the following routines.

CLOUD_SATADJ

- calculation of $\mathrm{d}q_{\mathrm{sat}}/\mathrm{d}t$ (see Subsection 7.4.2]
- large-scale evaporation (7.26)
- large-scale cloud formation [(7.18), (7.21) and (7.22)]
- check to condense any supersaturation over defined limit (CLOUD_SUPERSATCHECK)

CLOUD_SUPERSATCHECK

- perform supersaturation check over defined limit and condense to liquid/ice

CLOUDSC This routine carries out all calculations necessary to solve (7.7) to (7.11). The calculations are carried out in the following order.

(i) Section 1: Calculate initial input profiles
(ii) Section 2: Initial setup
(iii) Section 3: Subgrid cloud sources and sinks
- convective detrainment and subsidence [(7.14) and (7.15)]
- erosion of clouds by turbulent mixing [(7.28) and (7.29)]

(iv) Section 4: Microphysical processes
- ice sedimentation
- calculation of precipitation overlap
- autoconversion of cloud water droplets to rain
- accretion of cloud water droplets by rain
- evaporation of rain
- growth of ice by vapour deposition
- growth of snow by vapour deposition
- autoconversion of cloud ice to snow
- melting of snow and ice (7.85)
- freezing of rain
- freezing of cloud water
- riming of snow by cloud water (7.84)
- accretion of rain by snow (7.80)
- accretion of rain by ice (7.81)
- sublimation of snow

(v) Section 5: Numerical solvers
- analytical integration of the equation for cloud fraction, a
- truncate explicit sinks to avoid negative values
- LU decomposition for cloud condensate/precipitation

(vii) Section 6: Update tendencies
- final tendency calculations of all thermodynamic quantities
- check to condense any supersaturation over defined limit (CLOUD_SUPERSATCHECK)

(viii) Section 7: Flux calculations for diagnostics and budget terms

CLDPP

This routine calculates total, high, mid-level and low cloud cover for postprocessing diagnostics.

DIAG_CLOUDS

This routine diagnoses the precipitation type, freezing rain accumulation and various other cloud-related diagnostic quantities.

APPENDIX A. HISTORY OF KEY CLOUD SCHEME DEVELOPMENTS

There have been a number of modifications to the cloud scheme since the operational implementation of the Tiedtke (1993) scheme in 1995. Here are some of the changes since Cycle 31r1:

- **Cycle 31r1**: Change to an implicit upstream ice sedimentation formulation and separate ice to snow autoconversion process to reduce vertical resolution sensitivity. Allow ice supersaturation in clear air.
- **Cycle 33r1**: The cloud cover diagnostics (total, high, medium, low) changed to use an exponential overlap assumption (consistent with McICA radiation scheme implemented in Cycle 32r2). This corrected low and medium cloud cover diagnostics resulting in an increase in occurrence of medium and low cloud cover in deeper cloud.
- **Cycle 35r1**: Increase melting rate for snow to reduce snowfall at warmer temperatures.
- **Cycle 36r4**: New prognostic microphysics scheme (separate cloud liquid, cloud ice, rain, snow prognostic variables) and multi-phase numerical solver.
- **Cycle 37r2**: Numerical limiter reinstated for cloud condensation in existing cloud, allow humidity heterogeneity close to tropopause by reducing critical relative humidity threshold.
- **Cycle 37r3**: Supersaturation term in temperature range 0 to -40°C changed to source of liquid phase and passed to ice deposition term. Reduction of deposition rate at cloud top and dependence on diagnosed ice nuclei concentration to improve representation of super-cooled liquid water layers in mixed-phase cloud.
- **Cycle 38r1**: Modified sedimentation fallspeed profiles for ice/snow/rain, include a timescale for the freezing of rain to allow supercooled rain in low level sub-zero temperature inversions. Remove excessive clear-air supersaturations in partially cloudy grid boxes. Convert melting ice to rain rather than liquid (ice particles near 0°C assumed to be large enough to form rain droplets), removing unrealistic liquid water cloud generation at the melting level.
- **Cycle 40r3/41r1**: New warm-rain autoconversion and accretion parametrization based on Khairoutdinov and Kogan (2000)
  New rain evaporation formulation with enhanced evaporation for small droplets, based on Abel and Boutle (2012)
  New riming parametrization for snow (collection of liquid water drops by falling snow particles). Included a slower timescale for the freezing of rain to allow supercooled rain and a faster timescale for the freezing of partially melted particles with an ice core.
  Corrected the precipitation fraction formulation for rain and snow evaporation.
  Modified the ice to snow autoconversion to increase ice water content at cold temperatures (tropical upper troposphere).
  Additional diagnostics for ”instantaneous” precipitation rates, maximum and minimum over different time periods, precipitation area fraction, precipitation type and total column supercooled liquid water.
- **Cycle 45r1**: Removal of liquid water content threshold for warm-rain autoconversion and accretion parametrizations. Changed the inhomogeneity enhancement factor for accretion from 2 to 3. Fall speed for rain changed from fixed 4 m/s to variable mass-weighted terminal fall speed based on Sachidananda and Zrnic (1986). Revised cloud edge erosion based on Morcrette (2012). Addition of reduced overlap of supercooled liquid water and ice for mixed phase in convective clouds.
- **Cycle 47r3**: Removal of the first-guess call to the cloud scheme. Major revision of the subgrid cloud saturation adjustment, with move of relevant processes from cloudsc to cloud_satadj, called sequentially before the microphysics. Added microphysical parametrization of depositional growth of snow particles. Revision of precipitation-type for diagnosis of ice pellets and freezing rain. Cloud cover diagnostics (total, high, medium, low) changed to an exponential-random overlap assumption. Various modifications to erosion rate, ice fall speed, ice deposition rate, ice autoconversion.
- **Cycle 48r1**: Supercooled rain/drizzle formed from the collision-coalescence of liquid water droplets no longer freezes instantly, allowing supercooled rain/drizzle drops. New collision-collection-freezing processes for ice/snow and rain. Additional precipitation type ”freezing drizzle”. Additional output diagnostics for ”most-frequent” and ”most-severe” precipitation in the last 1, 3, and 6 hours.

APPENDIX B. LIST OF SYMBOLS

$A(\,)$	advective transport through the boundaries of the grid box
a	fraction of grid box covered by clouds (0-1)
$a_{\rm P}$	fraction of grid box covered by precipitation (0-1)
$a_{\rm up}$	fractional area of updraughts (0-1)
c_p	specific heat capacity at constant pressure (J kg^{-2} K^{-1})
$D_{\rm up}$	detrainment in the cumulus updraughts (s^{-1})
$e_{\rm sat}$	saturation vapour pressure (Pa)
$e_{\rm sl}$	saturation vapour pressure with respect to water (Pa)
$e_{\rm si}$	saturation vapour pressure with respect to ice (Pa)
g	acceleration of gravity (m s^{-2})
K	diffusion coefficient
K_a	conductivity of heat in air
L	latent heat (J kg^{-1})
$L_{\rm fus}$	latent heat of fusion (J kg^{-1})
$L_{\rm subl}$	latent heat of sublimation (J kg^{-1})
$L_{\rm vap}$	latent heat of vaporization (J kg^{-1})
$l_{\rm up}$	specific cloud water/ice content in the cumulus updraughts (kg kg^{-1})
$M_{\rm Cu}$	cumulus-induced subsidence mass flux
P	precipitation rate (kg m^{-2} s^{-1})
$P_{\rm loc}$	local precipitation rate (kg m^{-2} s^{-1})
p	pressure (Pa)
$q^{\rm env}$	environmental specific humidity (kg kg^{-1})
$q_{\rm v}$	grid-mean specific humidity (kg kg^{-1})
$q_{\rm l}$	grid-mean specific cloud liquid water content (kg kg^{-1})
$q_{\rm l}^{\rm cld}$	in-cloud specific cloud liquid water content (kg kg^{-1}) or per cloud area
$q_{\rm i}$	grid-mean specific cloud ice water content (kg kg^{-1})
$q_{\rm r}$	grid-mean specific precipitating rain water content (kg kg^{-1})
$q_{\rm s}$	grid-mean specific precipitating snow water content (kg kg^{-1})
$q_{\rm sat}$	saturation specific humidity (kg kg^{-1})
$q_{\rm sat(i)}$	saturation specific humidity with respect to ice (kg kg^{-1})
$q_{\rm sat(w)}$	saturation specific humidity with respect to water (kg kg^{-1})
$q_{\rm up}$	specific humidity in the convective updraughts (kg kg^{-1})
$R_{\rm cld}$	radiative heating rate in cloudy air
$R_{\rm clear}$	radiative heating rate in cloud-free air
$R_{\rm dry}$	gas constant for dry air
$R_{\rm vap}$	gas constant for water vapour
RH_c	= 0.8 (in the free troposphere)
$RH_{\rm crit}$	threshold value of the relative humidity for condensation
$RH_{\rm homo}$	threshold relative humidity for homogenous nucleation
$S_{\rm auto}$	rate of generation of precipitation in the form of rain/snow (kg kg^{-1} s^{-1})
$S_{\rm evap}$	rate of evaporation of cloud water/ice/rain/snow (kg kg^{-1} s^{-1})
$S_{\rm conv}$	rate of formation of cloud water/ice by convective processes (kg kg^{-1} s^{-1})
$S_{\rm rime}$	rate of snow riming (collection of cloud liquid drops) (kg kg^{-1} s^{-1})
$S_{\rm iacr}$	rate of ice accretion of rain (kg kg^{-1} s^{-1})
$S_{\rm sacr}$	rate of snow accretion of rain (kg kg^{-1} s^{-1})
$S_{\rm cond}$	rate of formation of cloud water/ice by stratiform condensation processes (kg kg^{-1} s^{-1})
$S_{\rm bl}$	rate of formation of cloud water/ice by boundary-layer processes (kg kg^{-1} s^{-1})
$S_{\rm frz}$	rate of freezing of rain (kg kg^{-1} s^{-1})
$S_{\rm melt}$	rate of melting of ice/snow (kg kg^{-1} s^{-1})
s	dry static energy
$s_{\rm v}$	virtual dry static energy
T	temperature

T_0	= 273.16 K
T_{ice}	= 250.16 K
T_{melt}	= 0° C
$\bar{w}$	area-mean generalized vertical velocity
w	terminal fall speed of hydrometeors
w_{up}	updraught velocity
α	fraction of condensate held as liquid water
δa_{bl}	rate of increase of cloud area by boundary-layer processes
δa_{conv}	rate of increase of cloud area by convective processes
δa_{strat}	rate of increase of cloud area by stratiform condensation processes
δa_{evap}	rate of decrease of cloud area due to evaporation
ρ	density of moist air (kg m^{-3})
ρ_{l}	cloud water content (kg m^{-3})
ρ_{s}	snow water content (kg m^{-3})

Chapter 8

Surface parameterisation

Table of contents

8.1 Introduction
8.2 Tiles and surface fluxes
8.2.1 Tile and vegetation characteristics
8.2.2 Surface momentum flux
8.2.3 Surface heat and evaporation fluxes
8.3 Surface energy balance and land coupling
8.4 Snow
8.4.1 Energy and water budget
8.4.2 Snow vertical discretisation
8.4.3 Prognostic snow density
8.4.4 Prognostic snow albedo
8.4.5 Additional details
8.5 Land-ice
8.5.1 Ice albedo
8.5.2 Ice melting and runoff
8.5.3 Surface energy balance for land-ice
8.6 Soil heat transfer
8.6.1 Discretisation and choice of parameters
8.6.2 Soil-water phase changes
8.7 Soil-water budget
8.7.1 Interception
8.7.2 Soil properties
8.7.3 Runoff
8.7.4 Water transport in frozen soil
8.7.5 Discretisation and the root profile
8.8 The ecosystem exchanges parameterisation
8.8.1 The A-gs photosynthesis scheme
8.8.2 The Farquhar photosynthesis scheme
8.8.3 Ecosystem respiration and Gross Primary Production
8.8.4 Vegetation description
8.8.5 The wetland methane scheme
8.9 Urban
8.9.1 Urban Radiation
8.9.2 Urban Roughness
8.9.3 Thermal Properties
8.9.4 Urban Hydrology
8.10 Lakes and other inland water bodies
8.10.1 Lake prognostic and ancillary variables
8.10.2 Lake temperature and self-similarity
8.10.3 Lake freezing and melting
8.11 Sea ice
8.12 Ocean boundary conditions for temperature and specific humidity

8.12.1 The cool skin
8.12.2 The warm layer
8.12.3 Salinity effect on q_s
8.13 Numerical solution of the surface equations
8.13.1 Recap of the analytical equations
8.13.2 Implicit numerical solution
8.14 Code

8.1 INTRODUCTION

The parameterisation scheme described in this chapter represents the surface fluxes of energy and water and, where appropriate, corresponding sub-surface quantities. Fig. 8.1 summarizes the main features of the land part of the model; the main surface scheme parameterisation structures are provided by the Tiled ECMWF Scheme for Surface Exchanges over Land (Van den Hurk *et al.*, 2000; Viterbo and Beljaars, 1995; Viterbo *et al.*, 1999) or TESSEL scheme. At the interface between the surface and the atmosphere, each grid-box is divided into fractions (tiles), with up to nine fractions over land (bare ground, low and high vegetation, intercepted water, shaded and exposed snow, glaciers, lake and urban) and up to two fractions over sea and freshwater bodies (open and frozen water). Each fraction has its own properties defining separate heat and water fluxes used in an energy balance equation solved for the tile skin temperature. Special attention is devoted to the different physical mechanisms limiting evaporation of bare ground and vegetated surfaces. A revised land surface hydrology (hereafter referred as HTESSEL, Balsamo *et al.*, 2009) has been introduced to address shortcomings of the previous land surface scheme version, specifically the lack of surface runoff and the choice of a global uniform soil texture. New infiltration and runoff schemes are introduced with a dependency on the soil texture and standard deviation of orography. Until CY47R3, the snowpack is represented with a single-layer, taking into account its thermal insulation properties and a physical representation of density, the interception of liquid rain and a variation of albedo with time based on the snow conditions (Dutra *et al.*, 2010a and Balsamo *et al.*, 2011b). Since CY48R1, a multi-layer snow scheme of intermediate physical complexity is used (Arduini *et al.*, 2019), representing the evolution with time of snow temperature, snow mass, liquid water content and density in up to 5 layers, as well as surface snow albedo. Since CY50R1, glaciers and ice sheets are represented with an explicit land-ice tile allowing fractional coverage within a grid-box, a 4-layer ice column with its own thermodynamics, and dynamic snow processes (mass, density, albedo) over glaciated surfaces (Arduini *et al.*, 2026). A model to represent inland water bodies both for resolved lakes and sub-grid coastal water in liquid and frozen state is used with a dedicated water tile.

Over land, the skin temperature is in thermal contact with the underneath medium. This can be soil, snow or ice, depending on the presence of snow and if the grid point is on a glacier or ice-sheet. The soil heat budget follows a Fourier diffusion law, modified to take into account the thermal effects of soil water phase changes. The energy equation is solved discretising the soil in 4 layers, with a net ground heat flux as the top boundary condition and a zero-flux at the bottom. The ice column is discretised in 4 layers and is on top of the soil column; the energy equation is solved with the same top boundary condition as the soil and a thermal contact with the underlying soil at the bottom. The snow temperature varies due to the combined effect of top energy fluxes, basal heat flux and the melt energy. The snow mantle is discretised in up to 5 layers, and the energy equation is solved with the same top boundary condition as the soil and a thermal contact with the underlying soil or ice at the bottom.

Snowfall is collected in the snow mantle, which in turn is depleted by snowmelt, contributing to surface runoff and soil infiltration, and evaporation. A fraction of the rainfall is collected by an interception layer, where the remaining fraction (throughfall) is partitioned between surface runoff and infiltration. Subsurface water fluxes are determined by Darcy's law, used in a soil water equation solved with a four-layer discretisation shared with the heat budget equation. Top boundary condition is infiltration plus surface evaporation, free drainage is assumed at the bottom; each layer has an additional sink of water in the form of root extraction over vegetated areas. The seasonal evolution of the vegetation development modulates the evapotranspiration (Boussetta *et al.*, 2013a), and revised formulation of the

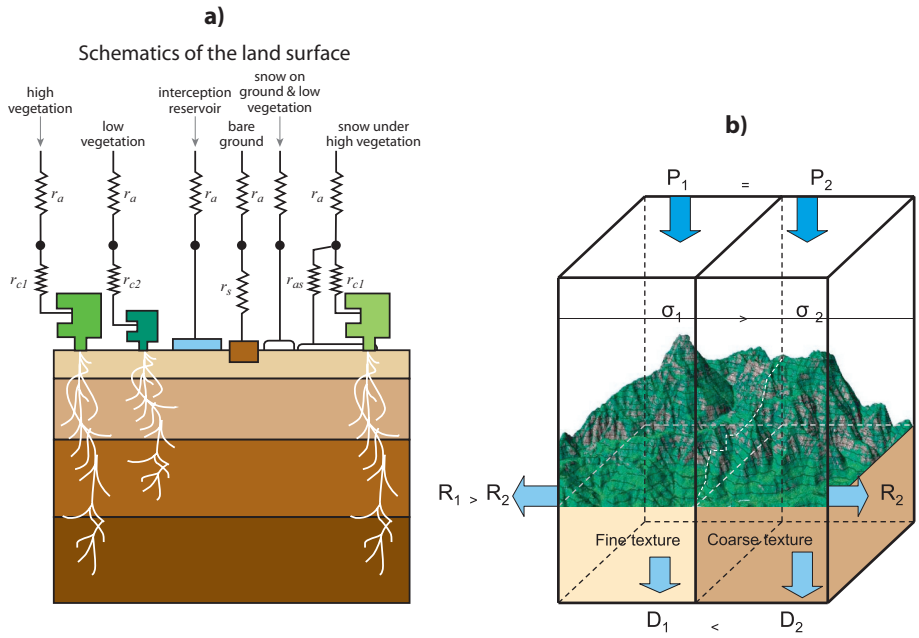

Figure 8.1 *Schematic representation of the structure of (a) TESSEL land-surface scheme and (b) spatial structure added in HTESSEL (for a given precipitation $P_1 = P_2$ the scheme distributes the water as surface runoff and drainage with functional dependencies on orography and soil texture respectively).*

bare soil evaporation allowed to improved the realism of soil-atmosphere water transfer over sparsely vegetated areas and deserts (Albergel *et al.*, 2012).

The land surface exchange of carbon dioxide (CO_2) which represents an essential component of the green-house-gases global budget has been added (Boussetta *et al.*, 2013b) to enable the interaction with atmospheric CO_2 concentration in environmental forecasting applications. The land CO_2 responds to meteorological and climate disturbances, modulated by the natural biomes diversity and their stress conditions. The main photosynthesis processes fixing carbon dioxide into biomass and releasing carbon dioxide via land biogenic processes are parametrised, while land carbon stocks are made dependent on land-use. The carbon parameterisation is modular to the HTESSEL water cycle parameterisation and it introduces the capability of interacting with the atmospheric CO_2 concentrations for global monitoring and prediction purposes. We refer to the CO_2-enabled land surface scheme version as CHTESSEL.

Finally, open water points classified as lakes and any subgrid water area are treated by a dedicated mixed layer model (Dutra *et al.*, 2010b, Balsamo *et al.*, 2012, Balsamo, 2013). Open ocean points have a specified surface temperature driven by initial and boundary conditions that in ocean uncoupled simulations are driven by the ocean model tendency. Sea-ice occupies a fraction of the grid box specified by a sea-ice cover, while lakes and coastal ice is treated by dedicated prognostic variables in the lake model. The sea ice prognostic temperatures are evolving in the forecast following the heat budget of a four-layer ice model in thermal contact with an underlying ocean at freezing temperature. The lakes and coastal ice temperatures are evolving following a single layer ice scheme with an underlying water at freezing temperature.

With a continuous increase in spatial resolution and more broad applications of LSMs, as well as the growing availability of a range of diverse observations, a clear need for a more complex and accurate process representation is emerging. This continuous research effort aims at improving the land surface model parameterisation for better surface prediction and ultimately better NWP and atmospheric composition forecasts. The current improvements are targeting different components of the land surface model, namely, the vegetation parameterisation, the snow component, the soil hydrology, the open water/lake parameterisation and also the representation of urban areas. An efficient and scalable land surface system is essential for a routine NWP and service environment and can facilitate a paradigm shift for an Earth-Observation driven model development under an Earth System framework, while linking

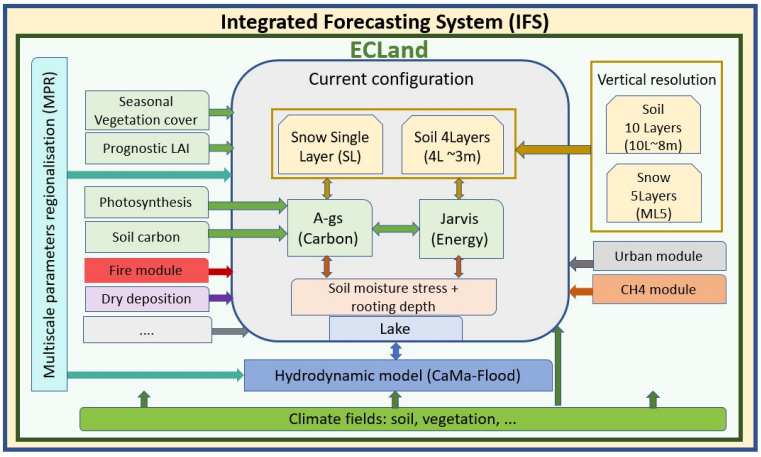

Figure 8.2 *Simplified representation of the main ECLand system components and its prospective evolution (inner light green box) as part of the full Integrated Forecasting System (outer yellow box) where the current ECLand main components are within the light grey box).*

with new possibilities brought by machine learning and Artificial Intelligence (AI) tools. The ECMWF land surface model has evolved as a modelling system: **ECLand** (Boussetta *et al.*, 2021) that would facilitate such modular extensions for the benefit of efficient developments and external collaborations. Fig. 8.2 illustrates the main ECLand system components and its prospective evolution elements that would facilitate its interaction with external projects and modular added services and being part of the full Integrated forecasting system. ECLand is being openly externalised under the following git repository https://github.com/ecmwf-ifs/ecland (available from cycle 48R1).

8.2 TILES AND SURFACE FLUXES

8.2.1 Tile and vegetation characteristics

Grid-box surface fluxes are calculated separately for the different subgrid surface fractions (or "tiles"), leading to a separate solution of the surface energy balance equation and skin temperature for each of these tiles. This is an analogue of the "mosaic" approach of Koster and Suarez (1992). Note that the tiles at the interface soil-atmosphere are in energy and hydrological contact with one single atmospheric profile above and one single soil profile below. Each grid box is divided into ten fractions: two vegetated fractions (high and low vegetation without snow), one bare soil fraction, three snow/ice fractions (snow on bare ground/low vegetation, high vegetation with snow beneath, and sea-ice or land-ice, respectively), three water fractions (interception reservoir, oceans and lakes) and urban fraction. The tile for "high vegetation with snow beneath" is a combined tile with a separate energy balance and evaporation model for the high vegetation and the underlying snow. A mixture of land and water (ocean/inland water) tiles is not allowed, i.e. a grid box is either 100% land or 100% sea. Since CY50R1, the ice tile is also used for land-ice (glaciers and ice sheets) over land grid-boxes. A glacier mask provides the fractional land-ice coverage, f_{gl}, continuously between 0 (no glaciers) and 1 (grid-point fully covered by land-ice). As the model employs a binary land-sea mask, a sea-ice fraction cannot coexist on the same grid-box with a land-ice fraction.

In each grid box two vegetation types are present: a high and a low vegetation type. An external climate database, based on the Global Land Cover Characteristics (GLCC) data that has been derived using one year of Advanced Very High Resolution Radiometer (AVHRR) data and ancillary information (Loveland *et al.*, 2000; http://edcdaac.usgs.gov/glcc/glcc.html; see also Chapter 11). The nominal resolution is 1 km. The data used provides for each pixel a biome classification based on the Biosphere-Atmosphere Transfer Scheme (BATS) model (Dickinson *et al.*, 1993), and four parameters have been derived for each

Table 8.1 *Vegetation types and parameter values (see text). H/L refer to the distinction between high and low vegetation.*

Index	Vegetation type	H/L	$r_{s,min}$ (sm^{-1})	c_{veg}	g_D (hPa^{-1})	a_r	b_r
1	Crops, mixed farming	L	125	0.90	0	5.558	2.614
2	Short grass	L	80	0.85	0	10.739	2.608
3	Evergreen needleleaf trees	H	395	0.90	0.03	6.706	2.175
4	Deciduous needleleaf trees	H	320	0.90	0.03	7.066	1.953
5	Deciduous broadleaf trees	H	215	0.90	0.03	5.990	1.955
6	Evergreen broadleaf trees	H	320	0.99	0.03	7.344	1.303
7	Tall Grass/mixed crops	L	100	0.70	0	8.235	1.627
8	Desert	–	250	0	0	4.372	0.978
9	Tundra	L	45	0.50	0	8.992	8.992
10	Irrigated crops	L	110	0.90	0	5.558	2.614
11	Semidesert/sparse vegetation	L	45	0.10	0	4.372	0.978
12	Ice caps and glaciers	–	–	–	–	–	–
13	Bogs and marshes	L	130	0.60	0	7.344	1.303
14	Inland water	–	–	–	–	–	–
15	Ocean	–	–	–	–	–	–
16	Evergreen shrubs	L	230	0.50	0	6.326	1.567
17	Deciduous shrubs	L	110	0.40	0	6.326	1.567
18	Mixed Forest/woodland/Broad Savanah	H	180	0.90	0.03	4.453	1.631
19	Interrupted forest	H	175	0.90	0.03	4.453	1.631
20	Water and land mixtures	L	150	0.60	0	–	–

grid box: dominant vegetation type, T_H and T_L, and the area fraction, A_H and A_L, for each of the high- and low-vegetation components, respectively.

The coverage C_i for the tile i depends on the type and relative area of low and high vegetation, and the presence of snow and intercepted water. In the absence of snow and interception, the vegetation coverage of high (c_H) and low (c_L) vegetation are calculated as $A_H c_{veg}(T_H)$ and $A_L c_{veg}(T_L)$, respectively, with c_{veg} a vegetation type dependent coverage (see Table 8.1). The bare ground fraction c_B is the residual.

$$\begin{aligned} c_H &= A_H c_{veg}(T_H) \\ c_L &= A_L c_{veg}(T_L) \\ c_B &= (1 - c_H - c_L) \end{aligned} \tag{8.1}$$

Each vegetation type is characterized by a series of (fixed) parameters as detailed in Table 8.1.

(i) A minimum canopy resistance, $r_{s,min}$.
(ii) A leaf area index, LAI.
(iii) A vegetation coverage, c_{veg}.
(iv) A coefficient, g_D, for the dependence of the canopy resistance, r_c, on water vapour pressure deficit.
(v) The root distribution over the soil layers, specified by an exponential profile involving attenuation coefficients, a_r, and b_r.

The numerical values for the parameters of Table 8.1 are based both on experiments conducted as described in Van den Hurk *et al.* (2000) and on literature review, in particular Mahfouf *et al.* (1995), Manzi and Planton (1994), Giard and Bazile (2000), Dorman and Sellers (1989), Bonan (1994), Pitman *et al.* (1991), and Zeng *et al.* (1998a). The values for minimum canopy resistance have been revised for crops, needle-leaf forest and short-grass in Boussetta *et al.* (2013b).

The presence of snow and intercepted water dynamically modifies the coverage fractions. The coverage of snow, c_{sn}, has been revised following Niu and Yang (2007), and it is a non linear function of the snow mass S (units kg m^{-2}) and snow density ρ_{sn} (units kg m^{-3}), to account for the hysteresis characterizing snow accumulation and melting processes.

The interception reservoir fraction, c_1, is given by W_1/W_{1m}, with W_{1m}, the maximum value for the intercepted water in the grid box, defined from the leaf area index contributions from the high and low vegetation tiles. The water contents of the interception reservoir, W_1 (units m), and S are prognostic quantities in the model. Snow cover is assumed to be overlying vegetation and bare ground with the same fraction. The interception reservoir occupies an identical fraction of all snow-free tiles.

$$\begin{aligned} c_{sn} &= \min\left(1, \tanh\left[\frac{S_{tot}/\rho_{sn,eq}}{2.5\, z_{0,c}\, (\rho_{sn,eq}/\rho_{0,c})}\right]\right) \\ W_{1m} &= W_{lmax}[c_B + c_H \cdot LAI(T_H) + c_L \cdot LAI(T_L)] \\ c_1 &= \min\left(1, \frac{W_1}{W_{lm}}\right) \end{aligned} \tag{8.2}$$

with $z_{0,c} = 0.01$ m and $\rho_{0,c} = 100$kg m^{-3}. S_{tot} is the total snow mass of the snowpack, and $\rho_{sn,eq}$ is the equivalent total snow density of the snowpack, i.e. the single-layer density giving the same snow depth (in m) for a given S_{tot}:

$$\begin{aligned} S_{tot} &= \sum_i^N S_i \\ \rho_{sn,eq} &= \frac{S_{tot}}{\sum_i^N (S_i/\rho_{sn,i})} \quad , \end{aligned} \tag{8.3}$$

with N the number of snow layers and S_i, $\rho_{sn,i}$, the snow mass and density of each snow layer, respectively; see also Sect. 8.4 for more details on the treatment of snow. In the Eq. 8.2 above the minimum snow depth that ensures complete coverage of the grid box depends on the value of $\rho_{sn,eq}$; for a value of $\rho_{sn,eq} = 300$kg m^{-3} (corresponding to well settled snow on the ground), the value of snow depth resulting in the grid-box completely snow-covered is $D_{cr} = 0.20$ m. The maximum water over a single layer of leaves or over bare ground is $W_{1\,max} = 0.0002$ m. The leaf area index LAI, is prescribed from a MODIS satellite-based dataset as detailed in Boussetta *et al.* (2013b). The full set of fractional tile coverages is given by (8.4) and (8.6), where the indexing of the tiles is detailed in Table 8.2. Since a mixture of land and ocean tiles is not allowed, a grid box is either 100% water (open water and ice, with ice fraction c_i):

$$\begin{aligned} C_1 &= 1 - c_i \\ C_2 &= c_i \\ C_i &= 0, i \in [3, N_T] \end{aligned} \tag{8.4}$$

or 100% land: tiles 3 to N_T (where $N_T = 10$ is the number of tiles) represent the non-glaciated land surface, while tile 2 is also used over land to represent the land-ice fraction f_{gl} from the glacier mask, with a continuous coverage between 0 (no glaciers) and 1 (fully glaciated). Because a binary land-sea mask is used, sea-ice and land-ice fractions cannot coexist within the same grid-box. The vegetation and bare-soil fractions are defined over the non-glaciated portion of the grid-box by introducing effective fractions:

$$\begin{aligned} c'_L &= c_L\,(1 - f_{gl}) \\ c'_H &= c_H\,(1 - f_{gl}) \\ c'_B &= (1 - c_L - c_H)\,(1 - f_{gl}) \end{aligned} \tag{8.5}$$

The tile fractions for land grid-boxes are then given by:

$$\begin{aligned} C_1 &= 0 \\ C_2 &= f_{\mathrm{gl}} \cdot (1 - c_{\mathrm{sn}}) \\ C_3 &= (1 - c_{\mathrm{sn}}) \cdot c_1 \cdot (1 - f_{\mathrm{gl}}) \\ C_4 &= (1 - c_{\mathrm{sn}}) \cdot (1 - c_1) \cdot c'_{\mathrm{L}} \\ C_5 &= c_{\mathrm{sn}} \cdot (c'_{\mathrm{B}} + c'_{\mathrm{L}} + f_{\mathrm{gl}}) \\ C_6 &= (1 - c_{\mathrm{sn}}) \cdot (1 - c_1) \cdot c'_{\mathrm{H}} \\ C_7 &= c_{\mathrm{sn}} \cdot c'_{\mathrm{H}} \\ C_8 &= (1 - c_{\mathrm{sn}}) \cdot (1 - c_1) \cdot c'_{\mathrm{B}} \end{aligned} \tag{8.6}$$

Tile 2 represents the snow-free land-ice surface (exposed ice). The snow tile (tile 5) covers the bare-soil, low-vegetation and land-ice fractions when snow is present, i.e. snow accumulates on top of the ice column. For $f_{\mathrm{gl}} = 0$ the equations reduce to the pre-CY50R1 formulation. The land-ice thermodynamics are described in Sect. 8.5.

Apart from the fractional gridbox coverage, each tile has a couple of additional parameters (see Table 8.2). Both the lake and urban fraction are based on their grid cell fraction. The urban fraction is reduced to accomodate the wet tile fraction and snow fraction when appropriate.

(i) The skin conductivity, Λ_{sk}, provides the thermal connection between the skin level and the soil or snow deck. For high vegetation, Λ_{sk}, is different for a stable and unstable stratification of the temperature gradient between the skin level and the upper soil or snow layer. This difference is considered to represent the asymmetric coupling between the ground surface and the tree canopy layer: an effective convective transport within the tree trunk space for unstable conditions, and a limited turbulent exchange for stable stratification (Bosveld *et al.*, 1999).

(ii) A small fraction $f_{R_{\mathrm{s}}}$ of net short-wave radiation that is transmitted directly to the top soil or snow layer. The remaining fraction of the short-wave radiation $(1 - f_{R_{\mathrm{s}}})$ is absorbed by the skin layer.

Finally, the surface albedo, α_i, is similar for all land tiles within a grid box except for those covered with snow (see the snow scheme description below) and land-ice. The climate database provides the snow-free background albedo on a monthly basis. Long-wave emissivity, ε, outside the window region is equal to 0.99 for all tiles; emissivity in the window region is tile dependent and varies between 0.93 and 0.98 (see Section 2.4.5 for more details). The remaining surface characteristics (roughness length for momentum, $z_{0\mathrm{m}}$, and heat, $z_{0\mathrm{h}}$) are similar for all land tiles within a grid box and specified in the climate database (Chapter 11).

8.2.2 Surface momentum flux

The roughness lengths for momentum and heat are prescribed as constant values depending on each vegetation type following Mahfouf *et al.* (1995) since cycle 31r1 as used in ERA-Interim re-analysis. In Cy37r3 some of these values were revised based on a study by Sandu *et al.* (2011). This study emphasized that the model generally tends to overestimate the 10-m winds compared to routine observations and that the forecast errors depend on the vegetation type because the representation of the 10-m wind speed is mainly controlled by the value of the momentum roughness length associated with each vegetation type. This parameter is difficult to determine from observations and the values used so far in the ECMWF model were empirically chosen as 20% and 10% of the vegetation height for forests and respectively for the other vegetation types (Mahfouf *et al.*, 1995). The overestimation of the near-surface wind speed for most of the vegetation types suggests that the values used for the momentum roughness length were too low. They were therefore revised based on theoretical considerations and synop observations of wind speed at 10 m. The basic idea was to search, for each vegetation type, for a new value of the momentum roughness length for which the mean 10-m wind speed forecast error with respect to synop observations drops to zero. This calibration showed that the momentum roughness length values should be increased for nine and decreased for one of the 18 vegetation types

Table 8.2 *The resistance scheme describes the way of coupling with the atmosphere: P=Potential denotes atmospheric resistance only; R=Resistance denotes aerodynamic resistance in series with a canopy or soil resistance; In presence of snow on high vegetation R_s=Canopy and snow resistance a canopy resistance for the vegetation and an extra aerodynamic coupling to the snow surface are used (see Figs 8.1–8.3 and Subsection 8.2.3).*

Type	*Vegetation type*	Λ_{sk} unstable ($Wm^{-2}K^{-1}$)	Λ_{sk} stable ($Wm^{-2}K^{-1}$)	f_{R_s} –	Scheme –
1	Crops, mixed farming	10.0	10.0	0.05	R
2	Short grass	10.0	10.0	0.05	R
3	Evergreen needleleaf	10.0	10.0	0.03	R,R_s
4	Deciduous needleleaf	10.0	10.0	0.03	R,R_s
5	Deciduous broadleaf	10.0	10.0	0.03	R,R_s
6	Evergreen broadleaf	10.0	10.0	0.035	R,R_s
7	Tall grass/mixed crops	10.0	10.0	0.05	R
8	Desert	15.0	15.0	0.	R
9	Tundra	10.0	10.0	0.05	R
10	Irrigated crops	10.0	10.0	0.05	R
11	Semidesert/sparse vegetation	10.0	10.0	0.05	R
12	Ice caps and glaciers	58.0	58.	0.	P
13	Bogs and marshes	10.0	10.0	0.05	R
14	Inland water	∞	∞	0.	P
15	Ocean	∞	∞	0.	P
16	Evergreen shrubs	10.0	10.0	0.05	R
17	Deciduous shrubs	10.0	10.0	0.05	R
18	Mixed Forest/woodland/Broad Savanah	10.0	10.0	0.03	R,R_s
19	Interrupted forest	10.0	10.0	0.03	R,R_s
20	Water -land mixtures	∞	∞	0.	P

characterizing land areas. The newly derived values for ten of the vegetation types were introduced in CY37r3 (Table 8.3). As the roughness length for momentum was on average increased, the roughness length for heat was decreased in order to account for terrain heterogeneity (Table 8.3).

The wet skin tile obtains values that are weighted between low and high vegetation according to their fractional cover. The exposed snow tile is set to table entry 12 (ice caps and glaciers), the snow under high vegetation tile has the roughness length of the high vegetation and the bare soil tile is set to the roughness length of table entry 8 (desert). The model uses the roughness lengths for the individual tiles and aggregates the fluxes. For postprocessing also an aggregated roughness length field is computed by tile averaging the neutral transfer coefficients and backing out the aggregated roughness lengths z_{oma} and z_{oha}.

$$\frac{1}{(ln10/z_{oma})^2} = \Sigma_i \frac{Fr_i}{(ln10/z_{omi})^2} \qquad \frac{1}{(ln10/z_{oha})^2} = \Sigma_i \frac{Fr_i}{(ln10/z_{ohi})^2} \tag{8.7}$$

The result with the T1279 model is shown in Figs 11.19–11.20 for 1 August 2012.

8.2.3 Surface heat and evaporation fluxes

A resistance parameterisation is used to calculate the turbulent fluxes. Momentum exchange is parametrised with the same roughness length for all tiles, but with a different stability correction for each tile. The resistance scheme for water vapour and heat exchanges is different for different tiles (see Fig. 8.3). For ocean, sea ice and snow on low vegetation, the turbulent fluxes of heat and water vapour are given by

$$H_i = \rho_a c_{pd} |U_L| C_{H,i} (T_L + g z_L / c_{pd} - T_{sk,i}) \tag{8.8}$$

$$E_i = \rho_a |U_L| C_{H,i} [q_L - q_{sat}(T_{sk,i})] \tag{8.9}$$

Table 8.3 *Roughness lengths for momentum and heat associated with high and low vegetation types.*

Index	Vegetation type	H/L veg	z_{0m}	z_{0h}
1	Crops, mixed farming	L	0.25	$0.25\ 10^{-2}$
2	Short grass	L	0.1	$0.1\ 10^{-2}$
3	Evergreen needleleaf trees	H	2.0	2.0
4	Deciduous needleleaf trees	H	2.0	0.2
5	Deciduous broadleaf trees	H	2.0	2.0
6	Evergreen broadleaf trees	H	2.0	2.0
7	Tall grass/mixed crops	L	0.5	$0.5\ 10^{-2}$
8	Desert	–	0.013	$0.013\ 10^{-2}$
9	Tundra	L	0.03	$0.03\ 10^{-2}$
10	Irrigated crops	L	0.5	$0.5\ 10^{-2}$
11	Semidesert/sparse vegetation	L	0.03	$0.03\ 10^{-2}$
12	Ice caps and glaciers	–	$1.3\ 10^{-3}$	$1.3\ 10^{-4}$
13	Bogs and marshes	L	0.25	$0.25\ 10^{-2}$
14	Inland water	–	–	–
15	Ocean	–	–	–
16	Evergreen shrubs	L	0.5	$0.5\ 10^{-2}$
17	Deciduous shrubs	L	0.1	$0.1\ 10^{-2}$
18	Mixed Forest/woodland/Broad Savanah	H	1.5	$1.5\ 10^{-2}$
19	Interrupted forest	H	1.1	1.1
20	Water and land mixtures	L	–	–

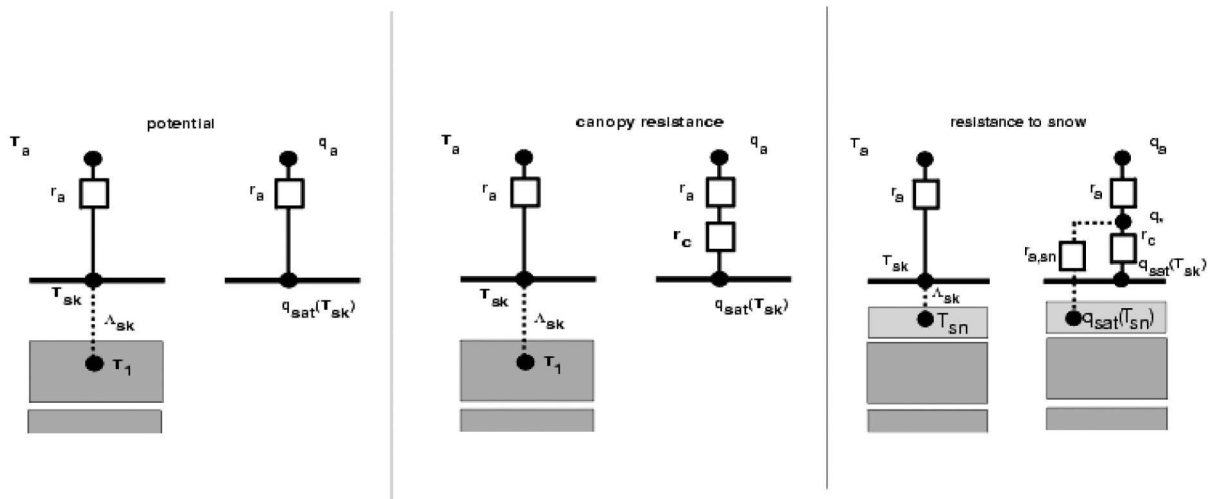

Figure 8.3 *Resistance scheme for three categories of coupling. Potential refers to ocean, sea ice and snow on low vegetation; (Canopy) resistance to dry low and dry high vegetation, bare soil, and interception reservoir when potential evaporation exceeds the maximum reservoir content; Resistance to snow to snow under high vegetation.*

with ρ_a the air density, c_{pd} the heat capacity of dry air, g the acceleration of gravity, $|U_L|$, T_L, q_L, z_L the wind speed, temperature, humidity and height of the lowest atmospheric model level, and $C_{H,i}$ the turbulent exchange coefficient, that varies from tile to tile because of different atmospheric stabilities. See Chapter 3 for a description of the exchange coefficients where different roughness lengths for heat and momentum are assumed and a Monin–Obukhov formulation is adopted for the stability dependence.

For high and low vegetation, an additional canopy resistance r_c is added with

$$E_i = \frac{\rho_a}{r_a + r_c}[q_L - q_{sat}(T_{sk,i})] \tag{8.10}$$

with $r_a = (|U_L|C_{H,i})^{-1}$ and i indicating the high or low vegetation tiles. r_c is a function of downward short-wave radiation R_s, leaf area index LAI, average unfrozen root soil water $\tilde{\theta}$, atmospheric water

Table 8.4 *Root distribution per vegetation type (in %) over the four layers. Vegetation indexes refer to Table 8.1.*

Vegetation index	1	2	3	4	5	6	7	8	9	10	11	13	16	17	18	19
Layer 1	24	35	26	26	24	25	27	100	47	24	17	25	23	23	19	19
Layer 2	41	38	39	38	38	34	27	0	45	41	31	34	36	36	35	35
Layer 3	31	23	29	29	31	27	27	0	8	31	33	27	30	30	36	36
Layer 4	4	4	6	7	7	14	9	0	0	4	19	11	11	11	10	10

vapour deficit D_a and a minimum stomatal resistance $r_{s,min}$, following Jarvis (1976) given by

$$r_c = \frac{r_{S,min}}{LAI} f_1(R_s) f_2(\bar{\theta}) f_3(D_a) \tag{8.11}$$

With the introduction of the new CLMS-based LAI and ESACCI-based LULC maps (Chapter 11), and given that the bareground is explicitly defined in the original ESA-CCI maps, in CY49R1 the LAI value was scaled by C_{veg}.

f_1 is a hyperbolic function of downward short-wave radiation only so that

$$\frac{1}{f_1(R_s)} = \min\left[1, \frac{bR_s + c}{a(bR_s + 1)}\right] \tag{8.12}$$

where $a = 0.81$, $b = 0.004\ \mathrm{W^{-1}m^2}$ and $c = 0.05$.

The soil moisture stress function f_2 is modified in CY49R1 to better follow the soil matric behaviour which allows more evapotranspiration under drier conditions according to Ronda *et al.* (2001):

$$f_2 = 2f_{2orig} - f_{2orig}^2 \tag{8.13}$$

And f_{2orig} is the original soil moisture stress function defined as:

$$\frac{1}{f_{2orig}(\bar{\theta})} = \begin{cases} 0 & \bar{\theta} < \theta_{pwp} \\ \dfrac{\bar{\theta} - \theta_{pwp}}{\theta_{cap} - \theta_{pwp}} & \theta_{pwp} \le \bar{\theta} \le \theta_{cap} \\ 1 & \bar{\theta} > \theta_{cap} \end{cases} \tag{8.14}$$

where the soil moisture at permanent wilting point and at field capacity, θ_{pwp} and θ_{cap}, respectively, are defined in Table 8.8. $\bar{\theta}$ is a weighted average of the unfrozen soil water given by

$$\bar{\theta} = \sum_{k=1}^{4} R_k \max[f_{liq,k}\theta_k, \theta_{pwp}] \tag{8.15}$$

where R_k is the fraction of roots in layer k and the fraction of unfrozen soil water, $f_{liq,k} = 1 - f_{fr}(T_k)$, is a parametrised function of the soil temperature of layer k, T_k, as specified in Subsection 8.6.2. Table 8.1 lists the coefficients a_r and b_r which are used to calculate the root fraction R_k according to Zeng *et al.* (1998a):

$$R_k = 0.5[\exp(-a_r z_{k-1/2}) + \exp(-b_r z_{k-1/2}) - \exp(-a_r z_{k+1/2}) - \exp(-b_r z_{k+1/2})] \tag{8.16}$$

where $z_{k+1/2}$ is the depth of the bottom of layer k (in m; $z_{1/2} = 0$ m). Contributions from levels exceeding the column depth are added to the deepest soil layer in order to ensure that $\sum R_k = 1$. Table 8.4 lists the distribution of the roots over the four soil layers.

A dependence on atmospheric humidity deficit ($D_a = e_{sat}(T_L) - e_L$, with e the vapour pressure) is included according to

$$\frac{1}{f_3(D_a)} = \exp(-g_D D_a) \tag{8.17}$$

where g_D depends on the vegetation type (Table 8.1), and is non-zero for high vegetation only.

Evaporation from the interception reservoir is given by (8.9) only when the amount of water in the interception reservoir, W_1, is sufficient to sustain potential evaporation during the entire time step Δt. If W_1 is limited, an additional resistance r_1, analogue to r_c in (8.10), is introduced. r_1 is calculated from the potential evaporation of the previous time step. Note that this type of flux-limiter is a time-step dependent feature of the model numerics.

The evaporation from non-vegetated areas responds to a different physical mechanism compared to densely vegetated areas. Over bare soil the vaporisation of water in the soil pores takes place in a thin layer close to the surface-atmosphere interface as a direct effect of incoming solar radiation providing the latent heat requirements 2.5106 J/kg. Atmospheric conditions (e.g. air temperature, humidity, wind velocity and radiation) as well as soil conditions (e.g. water content, roughness length) all play a role in modulating the evaporation processes.

The relationship between soil moisture and bare soil evaporation is generally parametrised in land surface models and several formulations have been compared in the study by (Mahfouf and Noilhan, 1991). They found that in all cases the bare soil evaporation formulation stops when the soil is completely dry (for soil moisture close to zero). In the TESSEL scheme (Van den Hurk *et al.*, 2000; Viterbo and Beljaars, 1995; Viterbo *et al.*, 1999) the soil-moisture-evaporation link was assumed to be varying linearly between the wilting point and the field capacity values for soil moisture. With the introduction of a tiling approach, the same stress function was applied to both vegetated and non-vegetated tiles, neglecting the fact that wilting point is a soil moisture threshold that applies uniquely to vegetated areas. A justification for this approach is that the soil underneath the surface tiles is still a unique column for both vegetated and non-vegetated fractions. In the most recent version of the HTESSEL scheme (Balsamo *et al.*, 2011a), included in IFS Cy36r4 and operational since 10 November 2010), the formulation of the bare soil evaporation has been revisited to allow a smooth transition between vegetated and non-vegetated areas and to realign the formulation of bare ground evaporation with studies in the literature.

The soil evaporation resistance, r_{soil}, is

$$r_{soil} = r_{soil,min} f_{2b}(f_{liq}\theta_1) \tag{8.18}$$

with $r_{soil,min} = 50$ s m^{-1}. By this parameterisation, evaporation from bare ground is treated similar to a single leaved canopy with a minimum resistance $r_{soil,min}$, extracting water from the upper soil layer only, and not experiencing any additional stress due to limited radiation or dry air. In case of a vegetated tile the canopy resistance is formulated according to Jarvis (1976) and the soil moisture inhibition function (see (8.10)), which depends on the root-zone soil wetness, normalized between the wilting point and the field capacity, for non-vegetated tiles is uniquely dependent on the soil moisture of the first soil layer and a minimum soil resistance.

In the new formulation the f_2b for bare ground is calculated as

$$\frac{1}{f_{2b}(\theta_1)} = \frac{\theta_1 - \theta_{min}}{\theta_{cap} - \theta_{min}} \tag{8.19}$$

where θ_1 is the unfrozen soil water in the first soil layer and θ_{min} is a vegetation-weighted average of the wilting point and a residual soil moisture content (θ_{res} which is a function of the soil textural class, as defined in Table 8.6). The weights are given by the vegetation cover veg (Van den Hurk *et al.*, 2000) over the gridbox, so that

$$\theta_{min} = veg\theta_{pwp} + (1 - veg)\theta_{res} \tag{8.20}$$

This modification of the soil moisture inhibition function allows a much lower level of soil moisture to be reached in dry areas as a consequence of direct bare ground evaporation under strong insulation. Also results are more consistent with the soil moisture values observed, for instance, over deserts.

A special treatment is included in the calculation of evaporation over high vegetation with snow underneath (see Fig. 8.3). Evaporation takes place from both the canopy component in the tile ($E_{veg,7}$)

and from the snow lying under the vegetation. The canopy evaporation uses a canopy resistance and saturation specific humidity at the canopy skin temperature, while the snow evaporation $E_{sn,7}$ is parametrised with an additional constant aerodynamic resistance $r_{a,sn}$ and saturation specific humidity at snow temperature T_{sn}. The evaporation from tile 7 is the combination of the canopy transpiration and the snow evaporation so that

$$E_7 = \rho_a \frac{q_L - q_*}{r_a} = \rho_a \frac{q_* - q_{sat}(T_{sn})}{r_{a,sn}} + \rho_a \frac{q_* - q_{sat}(T_{sk})}{r_c} \tag{8.21}$$

where q_* is the humidity at the connection point of the three resistances (Fig. 8.3). After elimination of q_*, E_7 can be rewritten as

$$E_7 = \rho_a \frac{q_L - q_{sat}(T_{sk})}{r_a + r_c + r_c \frac{r_a}{r_{a,sn}}} + \rho_a \frac{q_L - q_{sat}(T_{sn})}{r_a + r_{a,sn} + r_{a,sn} \frac{r_a}{r_c}} \tag{8.22}$$

The first term in the equation above is interpreted as $E_{veg,7}$ and is treated in the standard way (i.e., implicit in the tile skin temperature). The second term is interpreted as evaporation from snow ($E_{sn,7}$) and is handled explicitly. The values of $r_{a,sn}$ depend on the stability of the subcanopy layer and are functions of $\Lambda_{a,u}$ and $\Lambda_{a,s}$ (see Table 8.2); $r_{a,sn} = 67$ sm^{-1} and $r_{a,sn} = 220$ s m^{-1} for an unstable and stable subcanopy layer, respectively. In spring, the latent heat flux of that tile, $L_v E_{veg,7} + L_s E_{sn,7}$ will be dominated by snow evaporation since the frozen soil under the snow deck will lead to very large values of r_c.

The grid box total sensible and latent heat fluxes are expressed as an area weighted average:

$$H = \sum_{i=1}^{8} C_i H_i \tag{8.23}$$

$$E = \sum_{i=1}^{8} C_i E_i \tag{8.24}$$

with H_i given by (8.8), and E_i by (8.9) for ocean, sea-ice and snow on low vegetation, (8.10) for dry high and low vegetation, the interception reservoir (with r_c replaced by r_1) and for bare soil (with r_c replaced by r_{soil}) and (8.22) for high vegetation with underlying snow.

8.3 SURFACE ENERGY BALANCE AND LAND COUPLING

A skin temperature T_{sk} forms the interface between the soil and the atmosphere. As detailed in Section 3.6, it is calculated for each grid box tiles separately, by scanning the surface energy balance solver over the eight tiles, assuming a complete coverage of the specific tile. For a single tile, this procedure is very similar to the derivation of the Penman–Monteith equation in which the skin temperature is eliminated from the surface energy balance equation. The numerical approach used in HTESSEL has the advantage that the feedback of skin temperature on net radiation and ground heat flux is included (see Section 3.6). The input radiation and reference atmospheric temperature (T_L), specific humidity (q_L) and wind speed (U_L) are identical for each tile. The surface fluxes "seen" by the atmosphere are calculated as an area-weighted average over the tiles (see (8.23) and (8.24)). For the high vegetation with snow underneath, the skin temperature is that of the high vegetation; the temperature of the underlying snow is calculated separately.

The energy balance equation solved for each tile takes into account partial absorption of net short-wave radiation, $1 - f_{Rs,i}$, in the skin layer (see Table 8.2). The remaining energy is directly passed to the soil or snow so that

$$(1 - f_{Rs,i})(1 - \alpha_i) R_s + \varepsilon (R_T - \sigma T_{sk,i}^4) + H_i + L_{v,s} E_i = \Lambda_{sk,i} (T_{sk,i} - T_1) \tag{8.25}$$

where i denotes the tile index, R_s and R_T are downward short-wave radiation and long-wave radiation, respectively, σ is the Stefan–Bolzman constant, T_1 the temperature of the upper soil or snow layer, H_i the sensible heat flux, and $L_{v,s} E_i$ the latent heat flux from the skin layer, and $\Lambda_{sk,i}$, the skin conductivity for tile i. Latent heat of evaporation, L_v, is used for all evaporation terms except snow evaporation, while

L_s, the latent heat of sublimation, is used for evaporation of snow (i.e., tile 5 and the contribution $E_{sn,7}$ from tile 7, defined by (8.22)).

The tiled surface is thermally coupled to the snow deck, when present, and to a single soil profile. The net flux into the soil is a weighted average of the flux from each tile.

For exposed snow, a special procedure is applied to avoid the skin temperature over snow to be greater than T_f, the triple-point temperature for water. If $T_{sk,5} > T_f$ over a grid-point, the surface energy balance equation is solved a second time, setting $\Lambda_{sk,5} = \Lambda_{sk,L}$ and $T_1 = T_f$. This forces $T_{sk,5}$ to stay close to T_f and the updated net heat flux into the snowpack is used to warm or melt the snow layer.

The solution of (8.25) is performed inside the code for turbulent exchanges in the atmosphere (Chapter 3). The atmospheric vertical diffusion equations yield a tridiagonal system of equations, with the coupling to the skin temperature given by the matrix row corresponding to the lowest model level. The first step for the solution of the system of equations, an LU decomposition, is followed by the solution of (8.25) before back-substitution. Details of the computations can be found in Chapter 3.

Due to the linearisation performed in (8.25) the net long-wave radiation $R_{LW} = \varepsilon(R_T - \sigma T_{sk}^4)$ for each tile is re-computed at the end of the energy balance by linearising it around the new skin temperature so that

$$\begin{aligned} R_{LW,i} &= R_{LW} - \varepsilon 4\sigma T_{sk}^3 (T_{sk,i} - T_{sk}) \\ T_{sk} &= \sum_i Fr^i T_{sk,i} \end{aligned} \tag{8.26}$$

where T_{sk} is the mean grid-box skin temperature and $R_{LW,i}$ the tiled net long-wave radiation used to compute the net energy passed to the remaining surface processes.

8.4 SNOW

The snow scheme represents an additional medium on top of the upper soil layer, with an independent, prognostic, thermal and mass contents. Since CY50R1, snow can also accumulate and melt on top of the land-ice column over glacier and ice sheet grid-points (see Sect. 8.5). Before CY48R1, a single-layer snow scheme was used to simulate the snowpack; description of that scheme can be found in previous versions of the IFS documentation. Since CY48R1, a multi-layer snow scheme (ML5) is used to simulate the snowpack. A schematic of the scheme is shown in Fig. 8.4. The multi-layer snow scheme (ML5 hereafter) introduced in ecLand is an intermediate complexity snow scheme following the definition by Boone and Etchevers (2001). It represents the vertical structure and evolution of snow temperature, T_{sn}, mass per unit area (snow mass for short), S, density ρ_{sn}, liquid water content, S_l, on a variable number of active layers N ($N = 1$ to 5), and of surface snow albedo, α_{sn}. The net energy flux at the top of the snow pack, G_{sn}^T, is the residual of the skin energy balance from the snow covered tiles (considering as well the penetration of a fraction of solar radiation within the snowpack itself) and the snow evaporation from the tile with high vegetation over snow (see (8.21)). The basal heat flux, G_{sn}^B, is given by a resistance formulation. For grid-points partially covered with land-ice, the grid-box average basal heat flux between the snowpack and the underlying surface is computed as the weighted average of the soil and ice top-layer temperatures. The absorbed energy is used to change the snow temperature or melt the snow, when T_{sn} exceeds the melting point.

The heat capacity of each snow layer is a function of its depth, and snow density, and is modified in the presence of liquid water. The snow thermal conductivity changes with changing snow density and a term accounting for water vapor diffusion effects, adapted from Sun *et al.* (1999). Snow density changes due to overburden and thermal metamorphisms (Anderson, 1976; Boone and Etchevers, 2001), compaction related to melt water retained in the snowpack, adapted from Lynch-Stieglitz (1994), and related to wind, adapted from Decharme *et al.* (2016). The snow albedo changes exponentially with snow age. For snow on low vegetation it ranges between 0.50 for old snow and 0.85 for fresh snow. The albedo for high vegetation with snow underneath depends on vegetation type adapted from Moody *et al.* (2007). More details of the multi-layer snow scheme can be found in Arduini *et al.* (2019).

In this section, all fluxes are per unit area and apply only to the snow area (i.e. tile 5 and 7). The snow mass S applies to the entire grid square, as well as the snowfall flux from the atmospheric model. As a general rule, all quantities with subscript sn refer to the snow area. For instance, snow evaporation (see Eq. 8.38) is defined as

$$c_{sn} E_{sn} = c_5 E_5 + c_7 E_7 \tag{8.27}$$

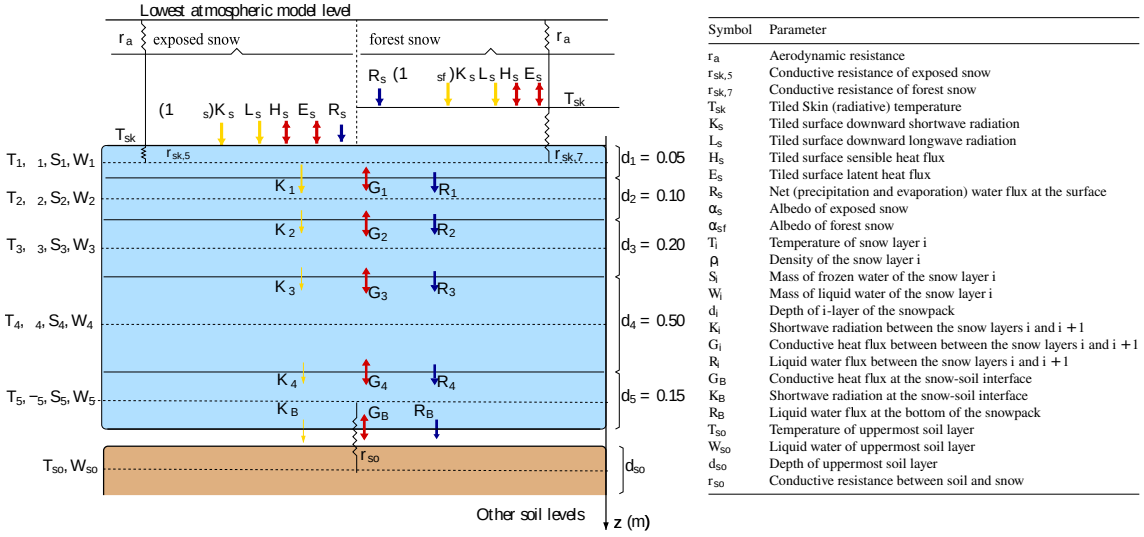

Symbol	Parameter
r_a	Aerodynamic resistance
$r_{sk,5}$	Conductive resistance of exposed snow
$r_{sk,7}$	Conductive resistance of forest snow
T_{sk}	Tiled Skin (radiative) temperature
K_s	Tiled surface downward shortwave radiation
L_s	Tiled surface downward longwave radiation
H_s	Tiled surface sensible heat flux
E_s	Tiled surface latent heat flux
R_s	Net (precipitation and evaporation) water flux at the surface
α_s	Albedo of exposed snow
α_{sf}	Albedo of forest snow
T_i	Temperature of snow layer i
ρ	Density of the snow layer i
S_i	Mass of frozen water of the snow layer i
W_i	Mass of liquid water of the snow layer i
d_i	Depth of i-layer of the snowpack
K_i	Shortwave radiation between the snow layers i and i +1
G_i	Conductive heat flux between between the snow layers i and i +1
R_i	Liquid water flux between the snow layers i and i +1
G_B	Conductive heat flux at the snow-soil interface
K_B	Shortwave radiation at the snow-soil interface
R_B	Liquid water flux at the bottom of the snowpack
T_{so}	Temperature of uppermost soil layer
W_{so}	Liquid water of uppermost soil layer
d_{so}	Depth of uppermost soil layer
r_{so}	Conductive resistance between soil and snow

Figure 8.4 *Schematic representation of the multi-layer snow scheme.*

8.4.1 Energy and water budget

The temporal evolution of snow temperature in the absence of snow melt is expressed as

$$(\rho C)_{\mathrm{sn}} \frac{\partial T_{sn}}{\partial t} = -\frac{\partial}{\partial z}\left(\kappa_{sn} \frac{\partial T_{sn}}{\partial z}\right) - \frac{\partial R_{\mathrm{sn,tr}}}{\partial z}\,, \tag{8.28}$$

where $(\rho C)_{\mathrm{sn}}$ is the snow volumetric heat capacity (J m^{-3}K^{-1}), T_{sn} κ_{sn}, R are snow temperature, snow thermal conductivity and transmitted shortwave radiation, respectively, in each snow layer. The equation states that temperature changes below freezing point of each snow layer are due to the heat conduction between layers and the absorption of solar radiation in each layer.

Snow heat conductivity controls the heat transfer within the snowpack. In ML5 this quantity is parametrised as

$$\kappa_{sn} = \kappa_c + \kappa_{wv} = \left[a_1\,\rho^2 - a_2\,\rho + a_3\right] + \left(\frac{P_{sfc}}{P_0}\right)\left(b_1 - \frac{b_2}{T_{sn} - b_3}\right). \tag{8.29}$$

κ_c follows the parameterisation proposed Calonne *et al.* (2011), which closely follows the one proposed by Douville *et al.* (1995). κ_{wv} takes into account the water vapor diffusion effects on the thermal conductivity, which depends on surface pressure P_{sfc} and T_{sn} (Sun *et al.*, 1999). κ_{wv} can be particularly important at high altitude and very cold conditions. The remaining free parameters of Eq. 8.29 are constants, with values $a_1 = 2.5\,10^{-6}$, $a_2 = 1.23\,10^{-4}$, $a_3 = 0.024$ and $P_0 = 1000$ hPa, $b_1 = -0.06023$ W m^{-1} K^{-1}, $b_2 = 2.5425$ W m^{-1} and $b_3 = 289.99$ K.

Penetration of solar radiation is not negligible in the top $10 - 20$ cm of the snowpack (see for example Sud and Mocko, 1999), therefore adding a heat source in the top snow layers. Transmission of solar radiation into the snowpack ($R_{\mathrm{sn,tr}}$) decreases exponentially with depth and it is parametrised using a formulation adapted from Jordan (1991),

$$R_{\mathrm{sn,tr}}(z) = R_{\mathrm{s,sn}}\,(1 - \alpha_{sn})\,e^{-k_a z}\,, \tag{8.30}$$

with $R_{\mathrm{s,sn}}$ the shortwave solar radiation at the surface over the snow tiles, α_{sn} is the broadband snow albedo and k_a is the solar extinction coefficient within the snowpack, the latter being a complex quantity that depends on the optical properties of snow grains and snow density (Bohren and Barkstrom, 1974). To avoid the introduction of additional prognostic variables such as the snow optical depth, the solar extinction coefficient is parametrised as a function only of the snow density, using a relationship proposed by Anderson (1976):

$$k_a = \max(k_{a,\min}, \min(k_{a,\max}, 0.0038\rho_{sn}/g_{sn}^2)) \\ \text{with } g_{sn} = \min(g_{sn,\max}, g_{sn,1} + g_{sn,2}\,\rho_{sn}^4); \tag{8.31}$$

$k_{a,\min} = 5.0$, $k_{a,\max} = 50.0$; g_{sn} is the grain size, as a function of snow density, with $g_{sn,\max} = 2.796 \times 10^{-3}$, $g_{sn,1} = 0.16 \times 10^{-3}$ and $g_{sn,2} = 0.11 \times 10^{-12}$. For thin snow layers, solar radiation can penetrate throughout the entire snowpack. In these cases, the residual radiative heat flux is passed to the soil as additional basal heat flux.

Within the snowpack, the heat budget is solved with an implicit solver inverting a tridiagonal matrix, as described for instance in Press *et al.* (1996). The solution of the surface energy balance provides the conductive heat flux used as the upper boundary condition, i.e.

$$G_{\mathrm{sn}}^{\mathrm{T}} = R_{\mathrm{sn}}^{\mathrm{N}} + L_{\mathrm{s}}E_{\mathrm{sn}} + H_{\mathrm{sn}} - R_{\mathrm{sn,tr}}^{\mathrm{T}} \tag{8.32}$$

where $R_{\mathrm{sn}}^{\mathrm{N}}$, H_{sn} are the net radiation (shortwave and longwave) and sensible heat flux (W m^{-2}), respectively; the mass flux E_{sn} is the snow sublimation (kg m^{-2}s^{-1}) associated with the latent heat of sublimation L_{s} (J kg^{-1}); $R_{\mathrm{sn,tr}}^{\mathrm{T}}$ is the solar radiation (W m^{-2}) trasmitted through the topmost snow layer. For forested area, the skin heat conductivity in the surface energy balance calculation is modified following Beljaars *et al.* (2017) to ensure numerical stability, see for more details also Sect. 8.4.4(a).

The heat conductivity on half levels is used to solve the heat budget equation (Eq. 8.28). This is computed as the weighted average of the heat conductivity of two adjacent layers, namely

$$\kappa_{i-\frac{1}{2}} = \frac{\kappa_{i-1}\Delta z_{sn,i-1} + \kappa_i \Delta z_{sn,i}}{\Delta z_{sn,i-1} + \Delta z_{sn,i}} \text{ for } i = 2, .., N. \tag{8.33}$$

The bottom boundary condition is the residual solar radiation at the bottom of the snowpack and the basal heat flux (G_B) between the snow and soil interface. In ML5 this quantity is written as a finite difference

$$G_{\mathrm{sn},B} \;=\; \lambda_B \left(T_{\mathrm{sn},N} - T_{so}\right), \tag{8.34}$$

where $T_{\mathrm{sn},N}$ is the temperature of the snow layer in contact with the soil, T_{so} is the temperature of the top soil layer and λ_B (W m^{-2} K^{-1}) is the conductance between the bottom snow layer and the top soil layer. The conductance between the two media is computed as the weighted average of the two conductance,

$$\lambda_B = \frac{1}{l_B(z_{\mathrm{sn},N} + \Delta z_{so,1})} \frac{\Delta z_{\mathrm{sn},N}\kappa_{\mathrm{sn},N} + \Delta z_{so,1}\lambda_{so,1}}{\Delta z_{\mathrm{sn},N} + \Delta z_{so,1}}, \tag{8.35}$$

where $\Delta z_{\mathrm{sn},N}$ is the thickness of the bottom active snow layer N, $\Delta z_{so,1}$ the thickness of the top soil layer, $\lambda_{so,1}$ the soil heat conductivity and l_B is a parameter controlling the depth considered to compute the conductance, which is set to 1. In the ideal case in which the snow attaches perfectly to the soil interface, $l_B = 0.5$ and the calculation of the conductance considers only half of the bottom and top snow and soil layer, respectively. However, often this is not the case as vegetation or organic material could form an additional insulating layer between the snow and the soil, therefore decreasing the heat conduction between the two medium. This effect is taken into account setting l_B to a higher value than 0.5.

Melting and freezing processes are diagnosed in ML5 by computing the heat content, H_{sn}, of each snow layer sequentially from top (surface) to bottom (soil) after that Eq. 8.28 is solved and a preliminary snow temperature computed. The heat available for melting and freezing in the ith layer (H_i) is defined as

$$H_{\mathrm{sn},i} \;=\; (\rho C)_{\mathrm{sn},i}\Delta z_{\mathrm{sn},i}\,(T_{\mathrm{sn},i}^{*} - T_0), \tag{8.36}$$

where $T^*_{\mathrm{sn,i}}$ is the snow temperature of the ith layer resulting from the solution of Eq. 8.28 and $\Delta z_{\mathrm{sn},i}$ the thickness of the ith layer. Melting occurs if $T^*_{\mathrm{sn},i} > T_0$, whereas freezing occurs if $T^*_{\mathrm{sn},i} < T_0$ and liquid water is available in the layer. The latent heat released in this process is then used to change the snow temperature of the layer accordingly. In the case the value of $H_{\mathrm{sn},i}$ is larger (in absolute value) than the energy required to melt or freeze the entire amount of ice or liquid water in the layer, the residual energy is transmitted to the following layer.

The snow heat capacity in each layer is approximated as

$$(\rho C)_{\mathrm{sn},i} = \frac{(\rho C)_{\mathrm{ice}}}{\rho_{\mathrm{ice}}}\rho_{\mathrm{sn},i} + C_w \frac{S_{\mathrm{l},i}}{\Delta z_{\mathrm{sn},i}} \,, \tag{8.37}$$

with $(\rho C)_{\mathrm{ice}}$ the volumetric heat capacity of ice ρ_{ice} the ice density and C_w the heat capacity of water.

The water budget of the snowpack reads

$$\frac{\partial S}{\partial t} = F + F_l + E_{sn} + R_{sn} \,. \tag{8.38}$$

where $S = S_{\mathrm{f}} + S_{\mathrm{l}}$ is the total mass of the snowpack, sum of the frozen (S_{f}) and liquid (S_{l}) water contents, F is snowfall, F_l is rainfall E_{sn} is snow sublimation and evaporation and R_{sn} is liquid water (melted snow), which goes into runoff or infiltrates into the soil at the snow/soil interface. Rainfall is considered to reach the snowpack at T_f. The maximum snow mass that can accumulate over a grid point is capped at $S_{\mathrm{gl}} = 10^4$ kg m^{-2} (10 m of snow water equivalent).

Movement of liquid water between layers is taken into account using a bucket-type formulation. This means that liquid water is retained in the ith layer until it reaches the liquid water holding capacity. Any excess of water above this threshold is transferred to the ith+1 layer. The snow liquid water holding capacity of a snow layer is approximated as a function of S and ρ_{sn}, following Anderson (1976)

$$S^c_{\mathrm{l}} = S[r_{\mathrm{l,min}} + (r_{\mathrm{l,max}} - r_{\mathrm{l,min}})\,\max(0, \rho_{\mathrm{sn,l}} - \rho_{\mathrm{sn}})/\rho_{\mathrm{sn,l}}] \tag{8.39}$$

with the constants $r_{\mathrm{l,min}}$ =0.03, $r_{\mathrm{l,max}}$ =0.1 and $\rho_{\mathrm{sn,l}} = 200$ kgm^{-3}. This equation is a simple parameterisation of a very complex phenomenon and has been used in other snow schemes, for example, Boone and Etchevers (2001).

Runoff is defined as the rate at which liquid water leaves the snowpack and parametrised as follows:

$$R_{\mathrm{sn}} = c_{sn} M_{\mathrm{sn}} \,, \tag{8.40}$$

where M_{sn} is liquid water not retained within the snowpack (for $S_{\mathrm{l}} > S^c_{\mathrm{l}}$), either resulting from melted snow or rainfall interception.

8.4.2 Snow vertical discretisation

The number of active snow layers and their thicknesses is computed diagnostically at the beginning of each time-step before the prognostic snow fields are updated. The snow thickness of each layer is computed using the relationship between snow mass and snow depth

$$\Delta z_{\mathrm{sn},i} = \frac{1}{c_{\mathrm{sn}}}\frac{S_i}{\rho_{\mathrm{sn},i}} \tag{8.41}$$

where Δz_i is snow depth of the ith layer for the snow-covered area (units m; note that Δz_i is not a grid-averaged quantity). The maximum thermal depth allowed in each layer, $\Delta Z^{\mathrm{max}}_{\mathrm{sn}}$, in the calculation of the temporal evolution of snow temperature, Eq. 8.28, is equal to 1 m, as in the pre-CY48R1 single-layer snow scheme. This avoids large thermal inertia to enter the heat budget calculation.

The total snow depth D_{sn} in the snowpack is the sum of the thicknesses of all active layers, N,

$$D_{\mathrm{sn}} = \sum_{i}^{N} \Delta z_{\mathrm{sn},i}, \tag{8.42}$$

with $1 < N < N_{\max}$, with $N_{\max} = 5$, depending on the total snow depth. Multiple layers are used when $D_{\rm sn} = \geq 0.125$ m. A different discretisation algorithm is applied over flat terrain and complex terrain regions, the latter defined as regions with the standard deviation of the sub-grid-scale orography ($\sigma_{\rm or}$) greater than 50 m. Over flat terrain, for $D_{sn} < 0.125$ one layer is used; for $D_{sn} \geq 0.125$ m the thickness of the topmost layer in contact with the atmosphere is fixed to 0.075 m and the thickness of the other active snow layers results from

$$\Delta z_{{\rm sn},i=2,..,N_{max}} = \begin{cases} 0, & \text{if } D_{sn} < \sum_{j=1}^{j=i} \Delta z^{j}_{{\rm sn},min} \\ \min\left[\frac{D_{sn}-\Delta z_{{\rm sn},1}}{N-1}\ ,\ \Delta z^{i}_{{\rm sn},max}\right], & \text{if } D_{sn} > \sum_{j=1}^{j=i} \Delta z^{j}_{{\rm sn},min} \end{cases} . \tag{8.43}$$

$\Delta z^{i}_{{\rm sn},min} = (0.05,\ 0.05,\ 0.05,\ 0.05)$ is the minimum layer depth allowed to activate layer 2, 3, 4 and 5, respectively; $\Delta z^{i}_{{\rm sn},max} = (0.10,\ 0.20,\ \infty,\ 0.15)$ is the maximum snow depth allowed for layer 2, 3, 4 and 5, respectively. This definition of $\Delta z_{{\rm sn},max}$ implies that the layer $N_{max} - 1$ is used as the accumulation layer for thick snowpack, enabling to have a relatively high vertical resolution for the layers at the interfaces with the atmosphere above and the soil underneath. An example of the vertical discretisation of a 1.0 m-thick snowpack is shown in Fig. 8.5.

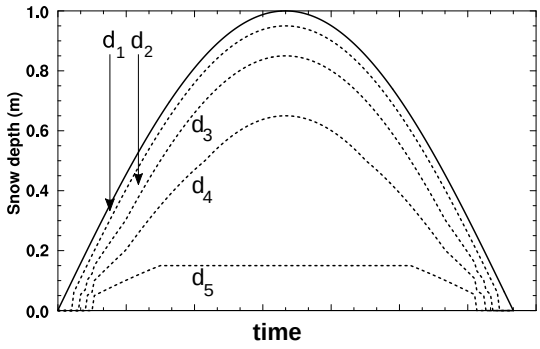

Figure 8.5 *Schematic representation of layering over flat terrain.*

Over complex terrains, for $D_{sn} < 0.25$ m the same vertical discretisation as described for a flat terrain is used. For a snowpack with $D_{sn} \geq 0.25$ m, the minimum ($\Delta z_{min,i}$) and maximum ($\Delta z_{max,i}$) thicknesses of each layer varies with snow depth as follows:

$$\Delta z^{i}_{{\rm sn},min} = \min(\ 0.25, 0.10 + \alpha_o\ (D_{sn} - 0.25)) \quad \text{if } i = 1...N_{\max}$$

$$\Delta z^{i}_{{\rm sn},max} = \begin{cases} \min(\ 0.25, 0.10 + \alpha_o\ (D_{sn} - 0.25)) & \text{if } i = 1 \\ \min(\ 0.30, 0.15 + \alpha_o\ (D_{sn} - 0.25)) & \text{if } i = 2...N_{max} \end{cases}$$

with α_o set to 0.10. This means that the thickness of the topmost layer varies between 0.10 m, for $0.25 \leq D_{sn} < 1.75$ m, and 0.25 m, for $D_{sn} \geq 1.75$ m; for the other layers (i=2...N_{max}), $\Delta z_{{\rm sn},max}$ varies between 0.15 m and 0.30 m. This implies that for a thick snowpack over complex terrain the snow layers are thicker than a snowpack with same depth over a flat region. For complex terrain, the same discretisation equation (Eq. 8.43) is used, with $\Delta z_{{\rm sn},i=1} = \Delta z^{i=1}_{{\rm sn},max}$.

If the total snow depth changes from one step to the following one (as a result of snowfall, snow melt or compaction) it may occur that the number of active layers varies, or one layer reaches the maximum allowed layer depth. In these case, the prognostic snow variables are reweighted based on the updated discretisation at the new time step.

(*a*) *Snow discretisation over glaciers and ice sheets*

Over glacier and ice sheet grid-points the snowpack has a different vertical discretisation compared to seasonal snow over land. Each active layer has a minimum thickness of $\Delta z_{\rm gl} = 0.50$ m. The thickness of the topmost layer (in contact with the atmosphere) and the three layers immediately below is fixed at

0.50 m whenever these layers are active. The depth of the bottom layer (in contact with the underlying ice, see Sect. 8.5) is unconstrained and acts as an accumulation layer. The maximum number of layers is $N_{max} = 5$, as for non-glaciated surfaces.

8.4.3 Prognostic snow density

Snow density is computed for each active layer i, and the rate of density change is parametrised as

$$\frac{1}{\rho_{sn}}\frac{\partial \rho_{sn}}{\partial t} = \frac{\sigma_{sn}}{\eta_{sn}(T_{sn},\rho_{sn})} + \xi_{sn}(T_{sn},\rho_{sn}) + \frac{\max(0,(S_l^{t+1}-S_l^t)}{S} + \frac{\max(0,\rho_{wc}-\rho_{sn})}{\tau_{sn}} \tag{8.44}$$

where the first two terms in (8.44) represent overburden and thermal metamorphism (Anderson, 1976; Boone and Etchevers, 2001), respectively, the third term represents the compaction related to meltwater retained in the snowpack, adapted from Lynch-Stieglitz (1994), and the last term represents wind-driven compaction, adapted from Decharme *et al.* (2016), which is active only for $\rho_{sn} < \rho_{wc}$, with $\rho_{wc} = 350$ kg m^{-3}.

In the overburden term (first term on the rhs of (8.44)), σ_{sn} and η_{sn} are the pressure of the overlying snow (Pa) and snow viscosity (Pa s), respectively. Melted water retained in the snowpack leads to a decrease of snow depth while keeping S constant. In snowfall conditions snow density is updated as the ratio between the new snow mass and new snow depth using the snowfall mass (ΔtF) and density (ρ_{new})

$$\rho_{sn}^{*} = \frac{S+\Delta tF}{\frac{S}{\rho_{sn}^{t}}+\frac{\Delta tF}{\rho_{new}}} \tag{8.45}$$

where ρ_{sn}^{*} is an updated snow density. Snowfall density ρ_{new} is given by an expression from CROCUS (Brun *et al.*, 1989, 1992) were fresh snow density is a function of near surface air temperature and wind speed

$$\rho_{new} = a_{sn} + b_{sn}(T_{air}-T_f) + c_{sn}(V_a)^{1/2} \tag{8.46}$$

where T_{air} and V_a are the near surface air temperature (K) and wind speed (ms^{-1}), respectively. The coefficients are $a_{sn} = 109$ kg m^{-3}, $b_{sn} = 6$ kg m^{-3}K^{-1}, and $c_{sn} = 26$ kg m$^{-7/2}$s$^{1/2}$. Snow density is constrained to be between $\rho_{min} = 50$ and $\rho_{max} = 500$ kg m^{-3}.

The snow viscosity in (8.44) is formulated following Anderson (1976)

$$\eta_{sn} = \eta_0 \exp\left(a_\eta(T_f - T_{sn}) + b_\eta \rho_{sn}\right) \tag{8.47}$$

where $\eta_0 = 3.7\times10^7$ (Pa s), $a_\eta = 8.1\times10^{-2}$ K^{-1} and $b_\eta = 1.8\times10^{-2}$ m^{3}kg^{-1}. The pressure of the overlying snow is given by $\sigma_{sn} = \frac{1}{2}Sg$, where g is the standard gravity (m^{2}s^{-2}).

The thermal metamorphism (second term in the rhs of (8.44)) is parametrised as

$$\xi_{sn} = a_\xi \exp\left[-b_\xi(T_f - T_{sn}) - c_\xi \max(0,\rho_{sn}-\rho_\xi)\right] \tag{8.48}$$

using the constant values $a_\xi = 2.8\times10^{-6}$ s^{-1}, $b_\xi = 4.2\times10^{-2}$, $c_\xi = 0.046$ m^3 kg^{-1} and $\rho_\xi = 150$ kg m^{-3}.

The wind driven compaction (fourth term in the rhs of (8.44)) can be particularly effective for polar snow, for which snow temperature is extremely low throughout the winter. The compaction rate τ_{sn} is defined for each layer as

$$\tau_{sn,i} = \frac{2\tau_1}{\tau_{wc,i}}, \text{ with } \quad \tau_{wc,i} = \max(0,\Gamma_{wc,i}) \exp\left[-a_\tau \sum_{j=1}^{i}[\Delta z_j(b_\tau - \Gamma_{wc,j})]\right], \tag{8.49}$$

where $\tau_1 = 86400$ s, $a_\tau = 10.0$, $b_\tau = 3.25$ and Γ_{wc} is the wind-driven compaction index. The latter is defined as

$$\Gamma_{wc} = 1 - a_\Gamma \exp\left(-b_\Gamma \kappa_{wc} V_a\right) + \Gamma_{mob} \text{ with } \quad \Gamma_{mob} = a_{mob}\left[1 - \max\left(0, \frac{\rho_{sn} - \rho_{min}}{\rho_{mob}}\right)\right], \tag{8.50}$$

where $a_\Gamma = 2.868$, $b_\Gamma = 0.085$ s m^{-1}, $\kappa_{wc} = 1.25$ and Γ_{mob} is a mobility index with constants $\rho_{mob} = 295$ kg m^{-3} and $a_{mob} = 1.25$.

(*a*) *Snow density over glaciers and ice sheets*

Snow density is allowed to vary dynamically over glaciated surfaces using the same formulation as for seasonal snow over land (Eq. 8.44). However, the density of the top snow layer over glacier and ice sheet grid-points is constrained to vary between $\rho_{min,top} = 280$ kg m^{-3} (for freshly fallen snow) and $\rho_{max,top} = 315$ kg m^{-3} (for relatively older snow) (Arduini *et al.*, 2026). The maximum snow density for the deeper layers is $\rho_{max} = 500$ kg m^{-3}, the same as for non-glaciated surfaces.

8.4.4 Prognostic snow albedo

Snow albedo in exposed areas evolves according to the formulation of Baker *et al.* (1990), Verseghy (1991), Douville *et al.* (1995) and Dutra *et al.* (2010a). For melting and non melting-conditions:

$$\alpha_{sn}^{t+1} = \begin{cases} \alpha_{sn}^{t} - \tau_a \Delta t / \tau_1 & M_{sn} = 0 \\ (\alpha_{sn}^{t} - \alpha_{min}) \exp(-\tau_f \Delta t / \tau_1) + \alpha_{min} & M_{sn} > 0 \end{cases} \tag{8.51}$$

where $\tau_a = 0.008$, which will decrease the albedo by 0.1 in 12.5 days, $\alpha_{min} = 0.5$ and $\alpha_{max} = 0.85$. The timescales $\tau_1 = 86400$ s, and $\tau_f = 0.24$ corresponding to an e-folding time of about 4 days (see Table 8.5).

A continuous reset is applied to snow albedo after snowfall events:

$$\alpha_{sn}^{t+1} = \alpha_{sn}^{t} + \min\left(1, \frac{F\Delta t}{10}\right)(\alpha_{max} - \alpha_{sn}^{t}) \tag{8.52}$$

This formulation assumes that 10 kg m^{-2} of fresh snowfall are needed to reset the snow albedo to its maximum value ($\alpha_{max} = 0.85$). The spectral albedo in the UV/Vis band, used by the radiation scheme, is interpolated from the broadband snow albedo, assuming a range of albedo values from Moody *et al.* (2007). The near-infrared value is then computed as a residual from the interpolated UV/Vis value, in order to ensure that the average value is equal to α_{sn}:

$$\begin{aligned} \alpha_{uv/vis} &= \frac{\alpha_{s1}(\alpha_{b2} - \alpha_{sn}) + \alpha_{s2}(\alpha_{sn} - \alpha_{b1})}{(\alpha_{b2} - \alpha_{b1})} \\ \alpha_{nir} &= \frac{\alpha_{sn} - \alpha_{uv/vis} s_{f,uv}}{s_{f,ni}}, \end{aligned} \tag{8.53}$$

where $s_{f,uv}$ and $s_{f,ni}$ are the solar fraction in the UV/Vis and near-infrared parts of the spectrum, respectively, and constants $\alpha_{s1} = 0.57$, $\alpha_{s2} = 0.89$, $\alpha_{b1} = 0.47$ and $\alpha_{b2} = 0.74$. The above formulae are inadequate to describe the evolution of the surface albedo of snow cover with high vegetation. Observations suggest a dependence on forest type but, by and large, the albedo changes from a value around 0.3 just after a heavy snowfall to a value around 0.2 after a few days (see Betts and Ball, 1997 and the discussion in Viterbo and Betts, 1999). This change reflects the disappearance of intercepted snow, due to melt (for sufficiently warm temperatures) or wind drift (for cold temperatures). Ways of describing those two mechanisms would involve either a separate albedo variable for the snow in the presence of high vegetation, or the introduction of an interception reservoir for snow. In the absence of any of the two, an explicit climatological albedo is used for the high vegetation and ground snow albedo is used for the residual bare fraction.

(*a*) *Snow albedo over glaciers and ice sheets*

The snow albedo over glacier and ice sheet grid points is allowed to vary dynamically (Arduini *et al.*, 2026). For grid points partially covered with land-ice, a weighted average between the snow albedo over

Table 8.5 *Snow-related parameters.*

Symbol	Parameter	Value
ΔZ_{sn}^{max}	Maximum snow thermal depth, per layer	1.00 m
D_{cr}	Threshold value for grid box coverage of snow	0.1 m
α_{min}	Minimum albedo of exposed snow	0.50
α_{max}	Maximum albedo of exposed snow	0.85
λ_{ice}	Ice heat conductivity	2.2 W m^{-1}K^{-1}
ρ_{ice}	Ice density	920 kg m^{-3}
$(\rho C)_{ice}$	Ice volumetric heat capacity	2.05×10^6 J m^{-3}K^{-1}
τ_a	Linear coefficient for decrease of albedo of non-melting snow	0.008
τ_f	Coefficient for exponential decrease of snow density and melting snow albedo	0.24
τ_1	Length of day	86400 s
$\Lambda_{sk,L}$	$\Lambda_{sk,5}$ in case of surface melting	100 W m^{-2}K^{-1}
S_{gl}	Maximum snow mass over a grid point	10^4 kg m^{-2}
	Glacier and ice sheet parameters	
$\alpha_{max,gl}$	Maximum snow albedo over glaciers	0.82
$\alpha_{min,gl}$	Minimum snow albedo over glaciers	0.65
$\tau_{sn,gl}$	Albedo decay parameter over glaciers	0.085 s
T_{gl}	Temperature threshold for glacier snow albedo change	-5 °C
$\rho_{min,top}$	Minimum snow density, top layer over glaciers	280 kg m^{-3}
$\rho_{max,top}$	Maximum snow density, top layer over glaciers	315 kg m^{-3}
Δz_{gl}	Fixed snow layer thickness over glaciers (layers 1–4)	0.50 m
α_I	Albedo of exposed land-ice	0.4
$\Lambda_{sk,I}$	Skin conductivity for land-ice melting	10^6 W m^{-2}K^{-1}
$D_{I,gl}$	Ice layer depths (top to bottom)	0.07, 0.21, 0.72, 9.86 m
$(\rho C)_I$	Volumetric heat capacity of land-ice	1.88×10^6 J m^{-3}K^{-1}
λ_I	Thermal conductivity of land-ice	2.03 W m^{-1}K^{-1}

land ($\alpha_{sn,l}$) and over land-ice ($\alpha_{sn,gl}$) is computed:

$$\alpha_{sn} = f_{gl}\,\alpha_{sn,gl} + (1 - f_{gl})\,\alpha_{sn,l}\,, \tag{8.54}$$

where f_{gl} is the glacier fraction and $\alpha_{sn,l}$ is given by Eq. (8.51). The snow albedo over glaciers, $\alpha_{sn,gl}$, evolves as

$$\alpha_{sn,gl} = \alpha_{min,gl} + (\alpha_{sn}^{t-1} - \alpha_{min,gl}) \exp\left(-\tau_{sn,gl}\,\Delta t \,/\, \tau_{day}\right) \qquad \text{for } T_{sn} > T_{gl}\,, \tag{8.55}$$

with $\alpha_{min,gl} = 0.65$, $\tau_{sn,gl} = 0.085$ s, $\tau_{day} = 86400$ s, and a temperature threshold $T_{gl} = -5$ °C (see Table 8.5). α_{sn}^{t-1} is the albedo value at the previous time-step. The fresh snow albedo reset (Eq. 8.52) is applied as for seasonal snow over land, but using $\alpha_{max,gl} = 0.82$.

8.4.5 Additional details

(*a*) *Numerical stability of the snow scheme*

Considering the snow scheme is adopting an explicit-flux boundary condition, occasional numerical instability can occur with long timesteps and very thin snowpack. This is particularly the case since the conductivity between the forest canopy and the underlying snow (skin layer conductivity for tile 7) has increased (since the IFS cycle 39r1). The snow tiles for cases with only one active layer, as in the case of a thin snowpack, are represented in Fig. 8.6.

A standard solution for stability problems would imply the coupled formulation to be fully implicit. However a simpler solution that does not require the heat flux G and the snow temperature T_{sn}^{n+1} at

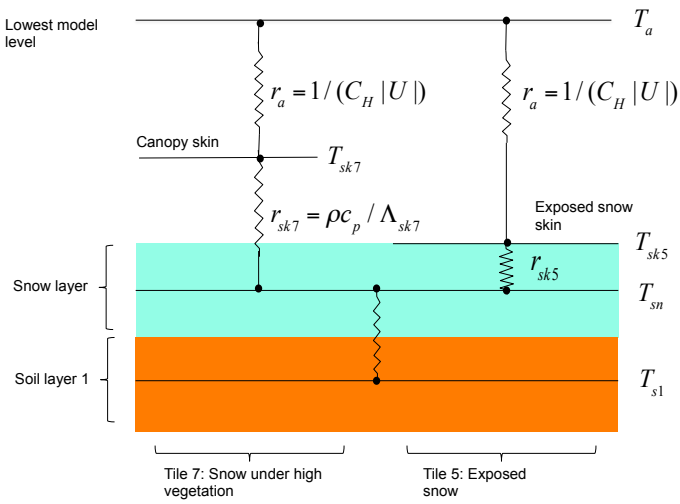

Figure 8.6 *Schematic representation of the snow tiles for cases with only one active layer.*

time level $n+1$ was found. This assumes that the temperature of the topmost snow layer, T_{sn}, responds to the heat flux G, and it consider a simplified version of the snow energy equation 8.28 with the linear relation

$$\frac{\partial T_{sn}}{\partial t} = A_{sn} + B_{sn} G \,. \tag{8.56}$$

In this case the snow heat flux is approximated as

$$\begin{aligned} G &= \Lambda_{sk}[T_{sk}^{n+1} - T_{sn}^{n+1}] \\ &= \Lambda_{sk}[T_{sk}^{n+1} - T_{sn}^{n} - (A_{sn} + B_{sn} G)\Delta t] \,, \\ G &= \frac{\Lambda_{sk}}{1 + \Lambda_{sk} B_{sn} \Delta t}[T_{sk}^{n+1} - T_{sn}^{n} - A_{sn}\Delta t] \,. \end{aligned} \tag{8.57}$$

The coefficients A_{sn} and B_{sn} can only be calculated correctly by the snow scheme, so a call to the snow scheme would be necessary before the surface energy balance is called involving a substantial redesign effort. A simplified estimate of A_{sn} and B_{sn} is used instead with $A_{sn} = 0$ and that $B_{sn} = (D(\rho C)_{sn})^{-1}$ as it was found efficient to prevent oscillatory evolution of the snow temperature.

For introducing the numerical stability term is sufficient to replace $\Lambda_{\mathrm{sk},i}$ in the surface energy balance equation 8.25 of tile 5 and tile 7 with the $\Lambda_{\mathrm{sks},i}$ given by the formulation below

$$\Lambda_{sks} = \frac{\Lambda_{sk}}{1 + \Lambda_{sk} B_{sn} \Delta t} \,. \tag{8.58}$$

Equation (8.58) enhances the original Λ_{sk} to guarantee numerical stability and it mimics a fully implicit formulation provided the approximated estimate of A_{sn} and B_{sn} withstand.

(*b*) *Treatment of phase changes*

As explained in Sect. 8.4.1, melting and refreezing processes are considered using the cold content, see Eq. 8.36. Energy available for melting and refreezing are defined as follows

$$\begin{aligned} Q_{\mathrm{melt},i} &= \max(0, \min(H_{\mathrm{sn},i}, L_f \Delta t S_{\mathrm{f},i})) \quad \text{melting} \\ Q_{\mathrm{frz},i} &= \min(0, \max(H_{\mathrm{sn},i}, L_r \Delta t S_{\mathrm{l},i})) \quad \text{freezing} \,. \end{aligned} \tag{8.59}$$

These are used to update the preliminary snow temperature, $T^*_{\rm sn}$:

$$T^{**}_{{\rm sn},i} = T^*_{{\rm sn},i} - \frac{(Q_{{\rm melt},i} + Q_{{\rm frz},i})}{A_1}$$
$$\text{with } A_1 = (\rho C)_{{\rm sn},i} \Delta z_{{\rm sn},i} \Delta t \,. \tag{8.60}$$

In case $T^{**}_{{\rm sn},i} <= T_0$, then $T^{t+1}_{{\rm sn},i} = T^{**}_{{\rm sn},i}$. Otherwise, the excess of energy is passed to the next snow layer (or the soil layer in case of the last snow layer) and $T^{t+1}_{{\rm sn},i} = T_0$. In the case of the bottom snow layer in contact with the soil, any excess of energy is added to the snow basal heat flux (Eq. 8.32).

Frozen and liquid water content are updated consistently

$$S^{t+1}_{{\rm f},i} = S^t_{{\rm f},i} + \frac{(Q_{{\rm melt},i} + Q_{{\rm frz},i})}{L_r} \Delta t$$
$$S^{t+1}_{{\rm l},i} = S^t_{{\rm l},i} + \frac{(Q_{{\rm melt},i} + Q_{{\rm frz},i})}{L_f} \Delta t \,, \tag{8.61}$$

where $S_{\rm f} = S - S_{\rm l}$. The total snow mass S^{t+1} is the sum of the frozen and liquid water parts at $t+1$.

(*c*) *Numerical solution for 1 active layer*

In case only 1 layer is active, e.g. $D_{\rm sn} < 0.125$ m, the solution of Eq. 8.28 is given by

$$T^*_{\rm sn} = \frac{c_{\rm sn} G^{\rm T}_{\rm sn} + A_1 T^t_{\rm sn} + A_2 T_1}{(A_1 + A_2)}$$
$$\text{with} \quad A_1 = \frac{(\rho C)_{\rm sn} \Delta z_{\rm sn}}{\Delta t}$$
$$\text{and} \quad A_2 = c_{\rm sn} \lambda_B \,, \tag{8.62}$$

where $T^*_{\rm sn}$ is the preliminary snow temperature (before checking for melting conditions). The basal snow heat flux to be used as input for the thermal budget of the soil (in the snow covered fraction only) is

$$G_B = c_{\rm sn} \lambda_B (T^*_{\rm sn} - T_{\rm so}) \,. \tag{8.63}$$

If $T^*_{\rm sn} \leq T_0$ then $T^{t+1}_{sn} = T^*_{\rm sn}$.

(*d*) *Numerical solution in case of melting in the top layer*

In case of melting occurring in the topmost snow layer after the T^* is computed, a special procedure is applied. Melting conditions are diagnosed if $T^*_{\rm sn}(i=1) > T_0$. In case of multiple active snow layers, the tridiagonal solver is called a second time, after setting $T^{t+1}_{sn}(i=1) = T_0$, to provide a new preliminary snow temperatures for the layers snow 1 to N; the basal heat flux is recomputed with the new preliminary snow temperature; finally, the preliminary snow temperature for layer 1, used for diagnosing the meltwater, is recomputed using an explicit formulation:

$$T^{*,n}_{sn}(i=1) = \frac{c_{\rm sn} G^{\rm T}_{\rm sn} + A_1 T^t_{sn}(i=1) - \lambda_B (i=1)(T^*_{sn}(i=1) - T^*_{sn}(i=2))}{A_1}$$
$$\text{with } A_1 = \frac{(\rho C)_{\rm sn}(i=1) \Delta z_{\rm sn}(i=1)}{\Delta t} \,. \tag{8.64}$$

In case of one snow layer active, the basal heat flux is recomputed setting the snow temperature to T_0 and the preliminary snow temperature T^* is recomputed as follows

$$G_{{\rm sn},B} = c_{\rm sn} \lambda_B (T_0 - T_{\rm so})$$
$$T^{t+1}_{sn} = \frac{c_{\rm sn} G^{\rm T}_{\rm sn} + A_1 T^t_{\rm sn} - G_{{\rm sn},B}}{A_1}$$
$$\text{with } A_1 = \frac{(\rho C)_{\rm sn} \Delta z_{\rm sn}}{\Delta t} \,. \tag{8.65}$$

(*e*) *Treatment of glaciers and ice sheets*

Since CY50R1, snow over glaciers and ice sheets is treated with dynamic snow processes: snow mass, density, albedo and liquid water content evolve prognostically using the same formulations as for seasonal snow, with the glacier-specific modifications described in Sect. (a) (vertical discretisation), Sect. (a) (density) and Sect. (a) (albedo). The underlying land-ice thermodynamics, surface energy balance and melt processes are described in Sect. 8.5. In previous cycles, glacier points were assigned a fixed snow mass ($S_{\rm gl} = 10^4$ kg m^{-2}), a fixed density ($\rho_{\rm gl} = 300$ kg m^{-3}) and a fixed albedo ($\alpha_{\rm gl} = 0.82$), and no snow mass balance was computed.

(*f*) *Initialisation of multi-layer snow fields from a single-layer*

An initialization procedure is generally needed for new parameterizations with an increased number of prognostic variables in NWP models, to enable the initialization of the additional fields from previous model versions using a smaller amount of prognostic variables. This consists of a parameterization routine called at the initial step of each forecast, which uses the one-layer snow fields, the skin temperature and the upper soil temperature fields to generate the vertical profiles of the fields needed by the multi-layer snow scheme.

The algorithm is based on the assumption that the snow temperature and density profiles can be approximated using simple exponential functions as

$$\begin{aligned} T_{sn}(z) &= A_T + B_T\, e^{-C_T\, z} \\ \rho_{sn}(z) &= A_\rho + B_\rho\, e^{-C_\rho\, z} \end{aligned} \tag{8.66}$$

for snow temperature and density, respectively.

The coefficients in Eqs. 8.66 are estimated offline using surface-only model simulations using a single-layer snow scheme and a multi-layer snow scheme, on a set of snow-dominated sites sampling different climate conditions. 27 set of parameters are estimated for different conditions of input skin temperature, soil temperature, snow temperature and density from simulations using a single-layer snow scheme. These are clustered using a k-means clustering algorithm (explained in more details below) to represent a variety of possible snow conditions.

Values for parameters A_T and B_T can be constrained assuming $T_{sn}(z=0) = T_{sk}$ and $T_{sn}(z = D_{sn} + 0.5\, d_{so}) = T_{so}$, with T_{sk} the skin (surface) temperature and T_{so} the temperature of the top soil layer. Parameters for density are more difficult to constrain as there are no a-priori physical boundaries for the top and bottom values. Therefore, a statistical approach is used to estimate the value of the top density layer using a multi-linear regression against the input snow albedo and snow density (single-layer). Both variables are highly correlated with the density of the top snow layer (linear correlation coefficient is larger than 0.90 in most cases considered). Hence, values of A_ρ and B_ρ in Eq. 8.66 can be constrained using the estimated values of density of the top snow layer and the single-layer snow density, assuming the latter as representative of the density of the middle of the snowpack. The free parameters of Eqs. 8.66 are determined using a non-linear regression algorithm which uses as predictors $T_{sk} - \overline{T_{sn}}$, $T_{so} - \overline{T_{sn}}$ and $\overline{\rho}/\rho_{min}$, where $\overline{T_{sn}}$, $\overline{\rho}$ are the single-layer snow temperature and density, respectively, and ρ_{min} is the minimum snow density allowed (50 kg m^{-3}). The predictor variables are clustered in 27 clusters using a k-means clustering approach. A sensitivity to the number of clusters showed that the error in the parameterisation was increasing with a lower number of clusters. Therefore, 27 was found as a compromise between increasing the error and over-fitting. For each cluster, a least-square non-linear regression is performed, to estimate a pair of values of C_T and C_ρ for each of them. The non-linear regression enables a spread (standard deviation) of the C_T and C_ρ values to be estimated. This is used to find the pair of coefficients minimizing the errors in the snowpack.

The initialization algorithm of snow multi-layer fields is organized in the following main steps:

(I) The closest cluster centroid to the initial set of predictors is computed and the coefficients to use are selected;
(II) A first-guess of the profiles is estimated using Eqs. 8.66.

(III) Conservation of mass of the snowpack is used to find an optimal set of coefficients for the snow density which minimizes the error in the mass;
(IV) Snow liquid water is computed using the diagnostic formulation from Dutra *et al.* (2010a);

8.5 LAND-ICE

Glaciers and ice sheets are represented using the ice tile of ecLand, as described in Arduini *et al.* (2026). Land-ice is represented by 4 vertical layers of fixed depth on top of the soil column, with layer thicknesses of 0.07, 0.21, 0.72 and 9.86 m (from top to bottom). The heat transfer within the ice column is governed by the heat conduction equation

$$(\rho C)_{\mathrm{I}} \frac{\partial T_{\mathrm{I}}}{\partial t} = \frac{\partial}{\partial z}\left[\lambda_{\mathrm{I}} \frac{\partial T_{\mathrm{I}}}{\partial z}\right] \tag{8.67}$$

where $(\rho C)_{\mathrm{I}} = 1.88 \times 10^6$ J m^{-3} K^{-1} is the volumetric ice heat capacity, T_{I} is the ice temperature, and $\lambda_{\mathrm{I}} = 2.03$ W m^{-1} K^{-1} is the ice thermal conductivity. This is the same equation as used for sea-ice (Eq. 8.189), but with different boundary conditions: in the absence of snow, the flux boundary condition at the top of the ice column is the conductive flux from the surface energy balance for the ice tile; at the bottom, the soil (ground) temperature is used as boundary condition to compute the ice basal heat flux. When snow is present on top of the ice, the snow basal heat flux provides the upper boundary condition for the ice column (see Sect. 8.4.1).

8.5.1 Ice albedo

The albedo of exposed land-ice (i.e. in the absence of snow) is fixed to $\alpha_{\mathrm{I}} = 0.4$, to account for the presence of impurities and debris on the ice surface.

8.5.2 Ice melting and runoff

If the ice surface is exposed (i.e. the overlying snow has completely melted) and the temperature of the top ice layer exceeds the melting point ($T_{\mathrm{I}} > T_0$), ice melting occurs. The amount of ice that melts is diagnosed from the energy available for melting, as for snow melting (see Sect. (b)). The runoff generated from ice melt is added to the surface runoff over the grid-box, weighted by the glacier fraction, assuming that the meltwater does not infiltrate into the ice column. The change in mass (thickness) of the ice column is not considered in the model.

8.5.3 Surface energy balance for land-ice

The surface energy balance calculation for the land-ice tile follows the approach used for exposed snow (see Sect. 8.3). If the diagnosed surface temperature over land-ice exceeds the melting point ($T_{\mathrm{sk}} > T_0$), the surface energy balance equation (8.25) is solved a second time, setting the skin conductivity to $\Lambda_{\mathrm{sk}} = 10^6$ W m^{-2} K^{-1} and the subsurface temperature to the melting point T_0. This forces the skin temperature to remain close to T_0 and provides a physically realistic estimate of the energy available for melting.

8.6 SOIL HEAT TRANSFER

In the absence of internal phase changes, the soil heat transfer is assumed to obey the following Fourier law of diffusion

$$(\rho C)_{\mathrm{soil}} \frac{\partial T}{\partial t} = \frac{\partial}{\partial z}\left[\lambda_T \frac{\partial T}{\partial z}\right] \tag{8.68}$$

where $(\rho C)_{\mathrm{soil}}$ is the volumetric soil heat capacity (J m^{-3}K^{-1}), T is the soil temperature (units K), z is the vertical coordinate (i.e. the distance from the surface, positive downwards – units m), and λ_{T} is the thermal conductivity (W m^{-1}K^{-1}). The above equation assumes that heat fluxes are predominantly in the vertical direction, that the effects of phase changes in the soil and the heat transfer associated

Table 8.6 *Parameters in the land-surface scheme. See Table 8.5 for snow-related parameters.*

Symbol	Parameter	Value
b_I	Interception efficiency	0.25
D_1	Depth of soil layer 1	0.07 m
D_2	Depth of soil layer 2	0.21 m
D_3	Depth of soil layer 3	0.72 m
D_4	Depth of soil layer 4	1.89 m
$F_{\rm cv}$	Fraction of gridbox covered by convective rainfall	0.5
k	Heterogeneity factor for convective precipitation	0.5
$T_{\rm f1}$	Highest temperature for existence of ice water	T_0+1
$T_{\rm f2}$	Lowest temperature for existence of liquid water	T_0-1
$w_{1\,\rm max}$	Maximum water amount on single leaf	0.0002 m

with the vertical movement of water in the soil can be neglected (De Vries, 1975), and that the effects of hysteresis can be neglected (Milly, 1982).

The boundary condition at the bottom, no heat flux of energy, is an acceptable approximation provided that the total soil depth is large enough for the time-scales represented by the model or, in other words, the bottom of the soil is specified at a depth where the amplitude of the soil heat wave is a negligible fraction of its surface amplitude (see De Vries, 1975 and next Section 8.7).

8.6.1 Discretisation and choice of parameters

For the solution of (8.68) the soil is discretized in four layers, of depths D_k $(k=1,2,3,4)$, the temperatures are defined at full layers (T_k), and the heat fluxes, at half layers ($\hat{G}_{k+1/2}$ is the heat flux, positive downwards, units W m^{-1}, at the interface between layer k and $k+1$). An energy-conserving implicit algorithm is used, leading to a tridiagonal system of equations with solution detailed in Section 8.10.

The boundary condition at the bottom is

$$G_{4+1/2}=0 \tag{8.69}$$

At the top, the boundary condition is the soil heat flux at the surface, computed as a weighted average over the tiles. For the snow free tiles, the flux into the soil consists of two parts. Apart from the diffusion of heat governed by $\Lambda_{{\rm sk},i}(T_{{\rm sk},i}-T_1)$ (see (8.25)), the net short-wave radiation not absorbed by the skin layer ($f_{{\rm Rs},i}$) provides energy to the soil. Table 8.2 lists the values of $\Lambda_{{\rm sk},i}$ and $f_{{\rm Rs},i}$ for each of the tiles. For the snow tiles, the heat flux into the soil is the snow basal flux, calculated using a resistance formulation and modified in the case of melting (see Eq.8.32 and Sect.8.4.5(b)).

The net heat flux into the soil is given by

$$G_{1/2}=\sum_i C_i[\Lambda_{{\rm sk},i}(T_{{\rm sk},i}-T_1)+f_{{\rm Rs},i}(1-\alpha_i)R_{\rm s}]+c_{\rm sn}G^{\rm B}_{\rm sn} \tag{8.70}$$

where the summation scans all snow free tiles.

The volumetric soil heat capacity is assumed constant, with value 2.19×10^6 J m^{-3}K^{-1} (see Table 8.6 for a list of constants used by the model). The heat conductivity, λ, depends on the soil-water content following Peters-Lidard *et al.* (1998) (see also Farouki, 1986; Johansen, 1975) and is given by a combination of dry $\lambda_{\rm dry}$ and saturated $\lambda_{\rm sat}$ values, weighted by a factor known as the Kersten number, $K_{\rm e}$, so that

$$\lambda=K_{\rm e}(\lambda_{\rm sat}-\lambda_{\rm dry})+\lambda_{\rm dry} \tag{8.71}$$

where $\lambda_{\rm dry}=0.190$ W m^{-1} K^{-1} and

$$\lambda_{\rm sat}=\lambda_{\rm sm}^{1-\theta_{\rm sat}}\lambda_{\rm w}^{\theta} \tag{8.72}$$

where the heat conductivity of the soil matrix, $\lambda_{\rm sm}=3.44$ W m^{-1} K^{-1} and the thermal conductivity of water is $\lambda_{\rm w}=0.57$ W m^{-1} K^{-1}. Equation (8.72) represents a simplification of Peters-Lidard formulation,

neglecting the changes in conductivity due to ice water and assuming the quartz content typical of a loamy soil. Finally, the Kersten number for fine soils was selected in Peters-Lidard *et al.* (1998) as

$$K_e = \log_{10}\left[\max\left(0.1, \frac{\theta}{\theta_{\text{sat}}}\right)\right] + 1 \tag{8.73}$$

The depths of the soil layers are chosen in an approximate geometric relation (see Table 8.6), as suggested in Deardorff (1978). Warrilow *et al.* (1986) have shown that four layers are enough for representing correctly all timescales from one day to one year. Using the numerical values of the heat capacity and soil depths defined in Table 8.6, the amplitude and phase response of the numerical solution of (8.68) were analysed by Viterbo and Beljaars (1995) for typical values of soil moisture in (8.71), and for harmonic forcings at the surface with periods ranging from half a day to two years. The analysis points to an error in the numerical solution of less than 20% in amplitude and 5% in phase for forcing periods between one day and one year.

8.6.2 Soil-water phase changes

At high and mid latitudes the phase changes of water in the soil have an important effect on the water and energy transfer in the soil. A proper consideration of the solid phase of soil water requires modifications including, in order of importance, the following.

(i) The thermal effects related to the latent heat of fusion/freezing (e.g. Rouse, 1984).
(ii) Changes in the soil thermal conductivity due to the presence of ice (e.g. Penner, 1970, not included in TESSEL as mentioned in the previous section).
(iii) Suppression of transpiration in the presence of frozen ground (e.g. Betts *et al.*, 1998) and already described in (8.15).
(iv) Soil water transfer dependent on a soil water potential including the effects of frozen water (e.g. Lundin, 1989), represented in a proxy way by (8.95).

The latent-heat effects are described in the following. The main impact will be to delay the soil cooling in the beginning of the cold period, and to delay the soil warming in spring, although the latter effect is less important because it occurs when the solar forcing is significant. Both effects make the soil temperatures less responsive to the atmospheric forcing and damp the amplitude of the annual soil temperature cycle. More details on the soil-freezing scheme and its impact on forecasts and the model climate are described in Viterbo *et al.* (1999).

The soil energy equation, (8.68), is modified in the presence of soil water phase changes as

$$(\rho C)_{\text{soil}} \frac{\partial T}{\partial t} = \frac{\partial}{\partial z}\left[\lambda_T \frac{\partial T}{\partial z}\right] + L_{\text{fus}}\rho_{\text{w}} \frac{\partial \theta_{\text{I}}}{\partial t} \tag{8.74}$$

where θ_{I} is the volumetric ice-water content. Without loss of generality, for the grid squares characteristic of NWP models it can be assumed that

$$\theta_{\text{I}} = \theta_{\text{I}}(\theta, T) = f(T)\theta \tag{8.75}$$

where θ is the total soil-water content (liquid + ice), and

$$\begin{array}{ll} f_{\text{fr}}(T) = 0 & T > T_{\text{f1}} \\ 0 < f_{\text{fr}}(T) < 1 & T_{f1} \leq T \leq T_{\text{f2}} \\ f_{\text{fr}}(T) = 1 & T < T_{\text{f2}} \end{array} \tag{8.76}$$

where T_{f1} and T_{f2} are characteristic temperatures limiting the phase change regime. In reality, the values of T_{f1} and T_{f2} and the function $f_{\text{fr}}(T)$ have complicated dependencies on soil texture and composition (see e.g. Williams and Smith, 1989), but here they are approximated in a simple way. For an idealized homogeneous, one-component soil, $f_{\text{fr}}(T)$ would be a step-function. According to Williams and Smith (1989) physical reasons for having an interval over which melting/freezing is active, rather than a threshold temperature, include the following.

(i) Adsorption, resulting from forces between the mineral parts of the soil and the water.
(ii) Capillarity, related to the fact that the water-free surface is not plane.
(iii) Depression of the freezing point due to the effect of dissolved salts.
(iv) Soil heterogeneity.

To avoid an undesirable coupling between the temperature and water equations in the soil, (8.75) is simplified to

$$\theta_I = f_{fr}(T)\theta_f \tag{8.77}$$

where θ_f is a constant, representing the amount of soil water that can be frozen (thawed). For simplicity, $\theta_f = (c_H + c_L)\theta_{cap}$. The scaling with the vegetated fractions is the simplest way of distinguishing between dry (vegetation-sparse areas, e.g. deserts) and wet (vegetated) areas. Combining (8.77) with (8.74) results in

$$\left[(\rho C)_{soil} - L_{fus}\rho_w \frac{\partial f_{fr}}{\partial T}\right]\frac{\partial T}{\partial t} = \frac{\partial}{\partial z}\left[\lambda_T \frac{\partial T}{\partial z}\right] \tag{8.78}$$

showing that the effect of freezing can be interpreted as an additional soil heat capacity, sometimes referred in the literature as the 'heat-capacity barrier' around freezing; not considering the process of soil water freezing/melting can lead to very large artificial temperature changes that do not occur in nature when sufficient soil water is available.

Finally, function $f_{fr}(T)$, is given by

$$f_{fr}(T) = \begin{cases} 0 & T > T_{f1} \\ 0.5\left\{1 - \sin\left[\dfrac{\pi(T - 0.5T_{f1} - 0.5T_{f2})}{T_{f1} - T_{f2}}\right]\right\} & T_{f2} \geq T \geq T_{f1} \\ 1 & T < T_{f2} \end{cases} \tag{8.79}$$

with $T_{f1} = T_0 + 1$, $T_{f2} = T_0 - 3$.

8.7 SOIL-WATER BUDGET

The vertical movement of water in the unsaturated zone of the soil matrix obeys the following equation (see Richards (1931), Philip (1957), Hillel (1982) and Milly (1982) for the conditions under which (8.80) and (8.81) are valid) for the volumetric water content θ:

$$\rho_w \frac{\partial \theta}{\partial t} = -\frac{\partial F_w}{\partial z} + \rho_w S_\theta \tag{8.80}$$

ρ_w is the water density (kg m^{-3}), F_w is the water flux in the soil (positive downwards, kg m^{-2}s^{-1}), and S_θ is a volumetric sink term (m^{3}m^{-3}s^{-1}), corresponding to root extraction. Using Darcy's law, F_w can be specified as

$$F_w = \rho_w\left(\lambda\frac{\partial \theta}{\partial z} - \gamma\right) \tag{8.81}$$

λ (m^2 s^{-1}) and γ (m s^{-1}) are the hydraulic diffusivity and hydraulic conductivity, respectively.

Replacing (8.81) in (8.80), specifying $S_\theta = S_\theta(\theta, z)$, and defining parametric relations for λ and γ as functions of soil water, a partial differential equation for θ is obtained; it can be numerically integrated if the top boundary condition is precipitation minus evaporation minus surface runoff. The bottom boundary condition assumes free drainage. Abramopoulos *et al.* (1988) specified free drainage or no drainage, depending on a comparison of a specified geographical distribution of bedrock depth, with a model-derived water-table depth. For the sake of simplicity the assumption of no bedrock everywhere has been adopted.

8.7.1 Interception

The interception reservoir is a thin layer on top of the soil/vegetation, collecting liquid water by the interception of rain and the collection of dew, and evaporating at the potential rate. The water in the interception reservoir, W_1, obeys

$$\rho_w \frac{\partial W_l}{\partial t} = c_1 E_1 + D + I \tag{8.82}$$

where $C_1 E_1$ is the water evaporated by the interception reservoir (or dew collection, depending on its sign), D represents the dew deposition from other tiles, and I (kg m^{-2} s^{-1}) is the interception—the fraction of precipitation that is collected by the interception reservoir and is later available for potential evaporation. Because the interception reservoir has a very small capacity (a maximum of the order of 1 mm, see (8.2)), it can fill up or evaporate completely in one time step; special care has to be taken in order to avoid numerical problems when integrating (8.82). In addition, since E_1 is defined in the vertical diffusion code, it might impose a rate of evaporation that depletes entirely the interception layer in one time step. In order to conserve water in the atmosphere-intercepted water–soil continuum, the mismatch of evaporation of tile 3 plus dew deposition from the other tiles (which is not explicitly dealt with by the vertical diffusion) as seen by the vertical diffusion and the intercepted water has to be fed into the soil.

The equation is solved in three fractional steps: evaporation, dew deposition, and rainfall interception. The solver provides the following as outputs.

(i) Interception layer contents at time step $n+1$, W_i^{n+1}.
(ii) Throughfall (i.e. rainfall minus intercepted water).
(iii) The evaporation effectively seen by the intercepted layer in each tile i.

First, the upward evaporation ($E_1 < 0$) contribution is considered; because $C_1 E_1$ depends linearly on W_1 (see (8.2)), an implicit version of the evaporating part of (8.82) is obtained by linearizing $C_1(W_1)E_1$ giving

$$\rho_w \frac{W_1^* - W_1^t}{\Delta t} = C_1(W_1^t)E_1 + \frac{E_1}{W_{1m}}(W_1^* - W_1^t) \tag{8.83}$$

where W_1^* is the new value of interception-reservoir content after the evaporation process has been taken into account. After solving for W_1^*, a non-negative value of evaporation is obtained and the evaporation seen by this fractional time step is calculated

$$\begin{aligned} W_1^1 &= \max(0, W_1^*) \\ E^1 &= \rho_w \frac{W_1^1 - W_1^t}{\Delta t} \end{aligned} \tag{8.84}$$

The dew deposition is dealt with explicitly for each non-snow tile in succession, for tiles 3, 4, 6, 7, 8, where tile 7 is also considered because in the exposed snow tile, the canopy is in direct evaporative contact with the atmosphere. When the evaporative flux is downwards ($E_1 > 0$)

$$\begin{aligned} W^2 &= W^1 + \min\left(W_{1m} - W^1, \frac{\Delta t}{\rho_w} c_i D_i\right) \\ D_i &= \rho_w \frac{W_{1,i}^2 - W_1^1}{\Delta t} \end{aligned} \tag{8.85}$$

where superscript 2 denotes the final value at the end of the this fractional time step.

The interception of rainfall is considered by applying the following set of equations to large-scale and convective rainfall

$$\begin{aligned} W_1^3 &= W_1^2 + \min\left(W_{1\mathrm{m}} - W_1^2, \frac{\Delta t}{\rho_\mathrm{w}} b_\mathrm{I}(c_\mathrm{H} + c_\mathrm{L}) R_{1\mathrm{s}}\right) \\ T_{1\mathrm{s}} &= R_{1\mathrm{s}} - \rho_\mathrm{w} \frac{W_1^3 - W_1^2}{\Delta t} \\ W_1^{t+1} &= W_1^3 + \min\left(W_{1\mathrm{m}} - W_1^3, \frac{\Delta t}{\rho_\mathrm{w}} b_\mathrm{I}(c_\mathrm{H} + c_\mathrm{L}) \frac{R_\mathrm{cv}}{F_\mathrm{cv}}\right) \\ T_\mathrm{cv} &= R_\mathrm{cv} - \rho_\mathrm{w} \frac{W_1^{t+1} - W_1^3}{\Delta t} \end{aligned} \tag{8.86}$$

$R_\mathrm{cv}/F_\mathrm{cv}$ is a modified convective rainfall flux, computed by applying the heterogeneity assumption that convective rainfall only covers a fraction $F_\mathrm{cv} = 0.5$ of the grid box, $b_\mathrm{I} = 0.5$ is a coefficient of efficiency of interception of rain. The total evaporation seen by the interception reservoir is D_i for tiles 4, 6, 7, and 8 and $c_1 E_1 + D_i$ for tile 3.

The interception reservoir model described in this section is probably the simplest water-conserving formulation based on Rutter's original proposition (Rutter *et al.*, 1972, 1975). For more complicated formulations still based on the Rutter concept see, for instance, Mahfouf and Jacquemin (1989), Dolman and Gregory (1992) and Ridder (2001).

8.7.2 Soil properties

Integration of (8.80) and (8.81) requires the specification of hydraulic conductivity and diffusivity as a function of soil-water content. In the previous TESSEL the parametric relations of Clapp and Hornberger (1978) (see also Cosby *et al.*, 1984) were adopted (still available as option). These are given by

$$\begin{aligned} \gamma &= \gamma_\mathrm{sat}\left(\frac{\theta}{\theta_\mathrm{sat}}\right)^{2b+3} \\ \lambda &= \frac{b\gamma_\mathrm{sat}(-\psi_\mathrm{sat})}{\theta_\mathrm{sat}}\left(\frac{\theta}{\theta_\mathrm{sat}}\right)^{b+2} \end{aligned} \tag{8.87}$$

where b is a non-dimensional exponent, γ_sat and ψ_sat are the values of the hydraulic conductivity and matric potential at saturation, respectively. A minimum value is assumed for λ and γ corresponding to permanent wilting-point water content.

Cosby *et al.* (1984) tabulate best estimates of b, γ_sat, Ψ_sat and θ_sat, for the 11 soil classes of the US Department of Agriculture (USDA) soil classification, based on measurements over large samples. Since the model described here specifies only one soil type everywhere, and because the determination of the above constants is not independent of the values of θ_cap and θ_pwp, the following procedure is adopted.

A comprehensive review of measurements of θ_cap and θ_pwp may be found in Patterson (1990). Starting from Patterson's estimates of θ_cap and θ_pwp for the 11 USDA classes, a mean of the numbers corresponding to the medium-texture soils (classes 4, 5, 7, and 8, corresponding to silt loam, loam, silty clay loam and clay loam, respectively) is taken. The resulting numbers are $\theta_\mathrm{cap} = 0.3\dot{2}3$ m^3 m^{-3} and $\theta_\mathrm{pwp} = 0.171$ m^3 m^{-3}. Averaging the values of Cosby *et al.* (1984) for soil moisture and soil-water conductivity at saturation for the same classes gives the numerical values $\gamma_\mathrm{sat} = 0.57 \times 10^{-6}$ m s^{-1} and $\theta_\mathrm{sat} = 0.472$ m^3 m^{-3} . The Clapp and Hornberger expression for the matric potential is

$$\psi = \psi_\mathrm{sat}\left(\frac{\theta}{\theta_\mathrm{sat}}\right)^{-b} \tag{8.88}$$

is used with $\psi(\theta_\mathrm{pwp}) = -153$ m (-15 bar) and $\psi(\theta_\mathrm{cap}) = -3.37$ m (-0.33 bar) (see Hillel, 1982; Jacquemin and Noilhan, 1990) to find the remaining constants b and ψ_sat. The results are $b = 6.04$ and $\Psi_\mathrm{sat} =$

Table 8.7 *Van Genuchten soil parameters.*

Texture	α	l	n	γ_{sat}
Units	m^{-1}	-	-	10^{-6}m/s
Coarse	3.83	1.250	1.38	6.94
Medium	3.14	-2.342	1.18	1.16
Medium-Fine	0.83	-0.588	1.25	0.26
Fine	3.67	-1.977	1.10	2.87
Very Fine	2.65	2.500	1.10	1.74
Ext.Trop. Organic	1.30	0.400	1.20	0.93
Trop. Organic	3.14	-2.342	1.18	1.16

Table 8.8 *Values for the volumetric soil moisture in Van Genuchten and Clapp-Hornberger (CH, loamy; bottom row), at saturation, θ_{sat}, field capacity, θ_{cap}, permanent wilting point, θ_{pwp}, and θ_{res}, residual moisture. Last column reports the plant available soil moisture. Units are $[m^3m^{-3}]$.*

Texture	θ_{sat}	θ_{cap}	θ_{pwp}	θ_{res}	$\theta_{cap}-\theta_{pwp}$
Coarse	0.403	0.244	0.059	0.025	0.185
Medium	0.439	0.347	0.151	0.010	0.196
Medium-Fine	0.430	0.383	0.133	0.010	0.251
Fine	0.520	0.448	0.279	0.010	0.170
Very Fine	0.614	0.541	0.335	0.010	0.207
Ext.Trop. Organic	0.766	0.663	0.267	0.010	0.396
Trop. Organic	0.439	0.347	0.151	0.010	0.196
Old-Loamy (CH)	0.472	0.323	0.171	-	0.151

-0.338 m. The above process ensures a soil that has an availability corresponding to the average value of medium-texture soils, and yields a quantitative definite hydraulic meaning to θ_{cap} and θ_{pwp} compatible with the Van Genuchten relations (see Table 8.7 for a summary of the soil constants).

The van Genuchten (1980) formulation used in HTESSEL provides a closed-form analytical expression for the conductivity, given as a function of the pressure head, h, as

$$\gamma = \gamma_{sat}\frac{[(1+(\alpha h)^n)^{1-1/n}-(\alpha h)^{n-1}]^2}{(1+(\alpha h)^n)^{(1-1/n)(l+2)}} \tag{8.89}$$

where α, n and l are soil-texture dependent parameters. Pressure head h is linked to the soil moisture by the expression

$$\theta(h) = \theta_r + \frac{\theta_{sat}-\theta_r}{(1+(\alpha h)^n)^{1-1/n}} \tag{8.90}$$

The VG scheme is recognized among soil physicists as capable of reproducing both the soil water retention and the hydraulic conductivity, and has shown good agreement with observations in intercomparison studies (Shao and Irannejad, 1999). Table 8.7 lists parameter values for six soil textures for the VG scheme. HTESSEL uses the dominant soil texture class for each gridpoint. This information is taken from the FAO (FAO, 2003) dataset as detailed in Chapter 11. The permanent wilting point and the soil field capacity are obtained by a specified matric potential of $\psi(\theta_{pwp}) = -15$ bar and $\psi(\theta_{cap}) = -0.10$ bar, respectively. In Table 8.8 the volumetric soil moistures associated with each soil class are shown for saturation, field capacity, wilting point, and residual moisture. Also shown is the plant available water content and the percentage of land points in each class. The last row shows the corresponding values for the single loamy soil used in the CH formulation in TESSEL. Note that the plant available soil water is greater for all the new soil classes in HTESSEL. Figure 8.7 shows the soil hydraulic diffusivity and conductivity for the TESSEL CH formulation and the six VG soil texture classes in HTESSEL. In TESSEL those were not allowed to fall below their wilting point values. At saturation, TESSEL has the highest diffusivity and conductivity. The reduced values for fine soils in HTESSEL reduces the infiltration of water and consequently the baseflow.

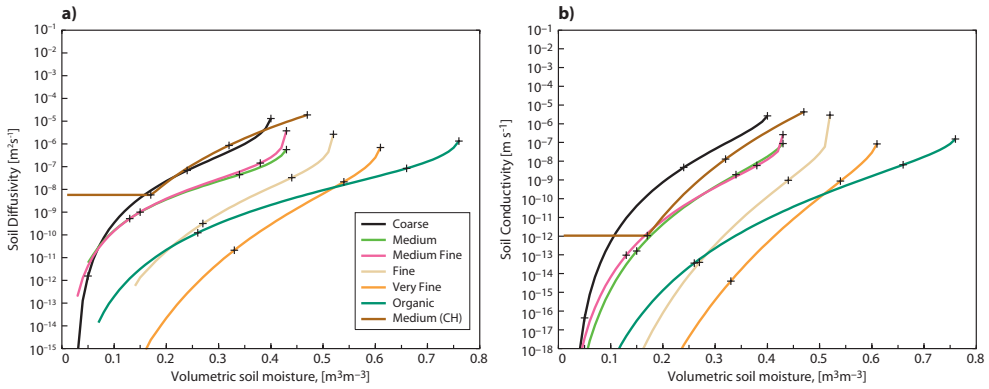

Figure 8.7 *Hydraulic properties of TESSEL and HTESSEL: (a) Diffusivity and (b) conductivity. The (+) symbols on the curves highlight (from high to low values) saturation, field capacity permanent wilting point.*

8.7.3 Runoff

In general when the water flux at the surface exceeds the maximum infiltration rate, the excess water is put into surface runoff. A general formulation of surface runoff can be written as:

$$R = T + M - I_{\max} \tag{8.91}$$

where $I_{\max}$ is the maximum infiltration rate, T the throughfall precipitation and M the snow melting. Different runoff schemes differ in the formulation of the infiltration. In TESSEL a maximum infiltration

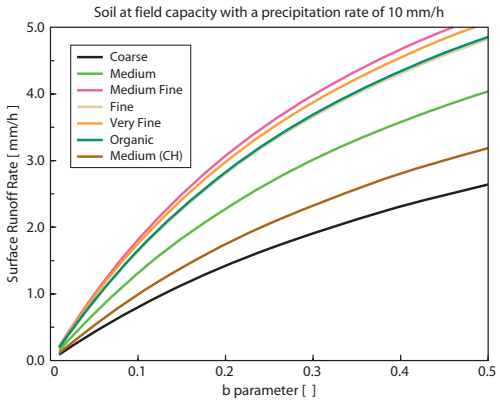

Figure 8.8 *Surface runoff generation (rate mm/h) as a function of the b parameter (accounting for sub-grid effects of orography), when exposed to a precipitation rate of* 10 *mm/h.*

rate at the surface, defined by the maximum downward diffusion from a saturated surface was used to define the runoff term. The maximum infiltration rate $I_{\max}$ is calculated as

$$I_{\max} = \rho_w \left(\frac{b_c \gamma_{sat}(-\psi_{sat})}{\theta_{sat}} \frac{\theta_{sat} - \theta_1}{z_1/2} + \gamma_{sat} \right) \tag{8.92}$$

where ρ_w is the water density, and z_1 is the depth of the first soil model layer (7 cm). At typical NWP model resolutions this scheme is active only in the presence of frozen soil, when downward soil water transfer is inhibited, otherwise it hardly ever produces runoff, as shown in Boone *et al.* (2004).

In HTESSEL A variable infiltration rate, first introduced in the so-called Arno scheme by Dümenil and Todini (1992), accounts for the sub-grid variability related to orography and considers that the runoff can (for any precipitation amount and soil condition) occur on a fraction s of the grid-point area S.

$$\frac{s}{S} = 1 - \left(1 - \frac{W}{W_{sat}}\right)^b \qquad b = \frac{\sigma_{or} - \sigma_{min}}{\sigma_{or} + \sigma_{max}} \tag{8.93}$$

where W and W_{sat} are vertically integrated soil water contents (θ and θ_{sat}) over the first 50 cm of soil defined as an effective depth for surface runoff. Parameter b is spatially variable, depends on standard deviation of orography (σ_{or}), and is allowed to vary between 0.01 and 0.5. The parameters σ_{min} and σ_{max} are set to 100 m and 1000 m respectively as in Van den Hurk and Viterbo (2003).

The surface runoff is obtained by the Hortonian runoff formulation by integrating (8.93) over the gridbox.

$$I_{max} = -(W_{sat} - W) + \max\left[0, W_{sat}\left[\left(1 - \frac{W}{W_{sat}}\right)^{\frac{1}{b+1}} - \left(\frac{T+M}{(b+1)W_{sat}}\right)\right]^{b+1}\right] \tag{8.94}$$

Whenever rain or snow melt occurs, a fraction of the water is removed as surface runoff. The ratio runoff/precipitation scales with the standard deviation of orography, and therefore depends on the complexity represented in the gridbox, as well as on soil texture and soil water content via W and W_{sat}.

In Figure 8.8 the response to a 10 mm/h rain rate for the six VG soil types and for the CH case in TESSEL is shown as a function of the b parameter. At field capacity, the surface runoff may vary from roughly 1% to 50% of the rainfall (snow melting) rate, generally increasing with finer textures and orographic complexity.

8.7.4 Water transport in frozen soil

Finally, the water transport is limited in the case of a partially frozen soil, by considering the effective hydraulic conductivity and diffusivity to be a weighted average of the values for total soil water and a very small value (for convenience, taken as the value of (8.87) at the permanent wilting point) for frozen water.

8.7.5 Discretisation and the root profile

A common soil discretisation is chosen for the thermal and water soil balance for ease of interpretation of the results, proper accounting of the energy involved in freezing/melting soil water, and simplicity of the code. Equations (8.80) and (8.81) are discretized in space in a similar way to the temperature equations, i.e., soil water and root extraction defined at full layers, θ_k and $\rho_w S_{\theta,k}$, and $F_{k+1/2}$ the flux of water at the interface between layer k and $k+1$. The resulting system of equations represents an implicit, water-conserving method.

For improved accuracy, the hydraulic diffusivity and conductivity are taken as (see Mahrt and Pan, 1984)

$$\begin{aligned} \lambda_{k+1/2} &= (1 - f^*_{fr})\lambda[\max(\theta^n_k, \theta^n_{k+1})] + f^*_{fr}\lambda(\theta_{pwp}) \\ \lambda_{k+1/2} &= (1 - f^*_{fr})\gamma[\max(\theta^n_k, \theta^n_{k+1})] + f^*_{fr}\gamma(\theta_{pwp}) \end{aligned} \tag{8.95}$$

where $f^*_{fr} = \min[f_{fr}(\theta_k), f_{fr}(\theta_{k+1})]$. The boundary conditions are given by

$$\begin{aligned} F_{4+1/2} &= \rho_w \gamma_4 \\ F_{1/2} &= T + M_{sn} - y_{sfc} + E_{1/2} \end{aligned} \tag{8.96}$$

The difference between throughfall T and surface runoff Y_{sfc} (kg m^{-2} s^{-1}) is the soil infiltration at the surface:

$$\begin{aligned} T &= T_{1s} + T_{cv} \\ y_{sfc} &= \max(0, T_{1s} + M_{sn} - I_{f,mx}) + \frac{\max(0, F_{cv} + T_{cv} - I_{f,mx})}{F_{cv}} \\ I_{f,mx} &= \rho_w \left[\lambda_{1/2}\frac{(\theta_{sat} - \theta_1)}{0.5 D_1} + \gamma_{1,2}\right] \end{aligned} \tag{8.97}$$

and $\lambda_{1/2} = f^*_{fr}\lambda(\theta_{pwp}) + (1 - f^*_{fr})\lambda(\theta_{sat})$, with a similar equation for $\gamma_{1/2}$. The evaporation at the top of the soil layer, $E_{1/2}$, is computed as the sum of the evaporations of tile 8 plus the contributions necessary to conserve water with the solver of the interception layer.

(i) Tile 3 mismatch (after the evaporated water used by the interception reservoir for the given tile is subtracted).
(ii) When the evaporative fluxes are downward (i.e., dew deposition), the evaporation for tiles 4, 6 and the canopy evaporation of tile 7.

Root extraction is computed as sum of the transpiration contributions (expressed in kgm^{-2}) over tiles i and soil layers j divided by the layer depth, such as

$$\rho_w S_{\theta,k} = \sum_i C_i \frac{E_i}{D_k} \frac{R_k \theta_k}{\sum_j R_j \theta_j} \tag{8.98}$$

where the sum over tiles i is done for tiles 4, 6, and 7. In case of dew deposition (i.e., tile downward evaporative flux), $S_{\theta,k} = 0$.

8.8 THE ECOSYSTEM EXCHANGES PARAMETERISATION

In order to obtain the net exchange of CO_2 between the land surface and atmosphere by a NWP model, the Gross Primary Production (GPP) and the ecosystem respiration (R_{eco}) needs to be represented. In CHTESSEL (Boussetta *et al.*, 2013b) the GPP [kg CO_2 m^{-2} s^{-1}] is parametrised following the so-called A-gs (Goudriaan *et al.*, 1985) or Farquhar *et al.* (1980) approach while R_{eco} [kg CO_2 m^{-2} s^{-1}] is parametrised as a function of soil temperature, soil moisture, snow depth and vegetation type rather than prognostically computed. Schemes relying on prognostic land carbon "pools" (CLM-DGVM, Levis *et al.*, 2004; JULES, Clark *et al.*, 2011; ORCHIDEE, Krinner *et al.*, 2005) are less practical for NWP purposes because they are difficult to initialize without a very long spin-up. The Net Ecosystem Exchange (NEE) of CO_2 [kg CO_2 m^{-2} s^{-1}] between the surface and atmosphere is then given by

$$NEE = GPP - R_{eco} \tag{8.99}$$

This quantity is the main observed variable in field site experiments.

8.8.1 The A-gs photosynthesis scheme

The A-gs approach is based on plant physiological considerations and describes the plant photosynthesis process and its dependence on CO_2, temperature and soil moisture (Jacobs, 1994; Jacobs *et al.*, 1996; Calvet *et al.*, 1998; Calvet *et al.*, 2004). The stomatal conductance is active for regulating both water vapor and CO_2 fluxes. The gross CO_2 assimilation by the canopy A_g [kg CO_2 $m^{-2}s^{-1}$] is calculated using a photosynthesis module following Goudriaan *et al.* (1985). The net assimilation A_n [kg CO_2 $m^{-2}s^{-1}$] (i.e. the net flow of CO_2 through the stomata) is A_g minus the dark respiration R_d [kg CO_2 $m^{-2}s^{-1}$]. Once the net assimilation is known, the stomatal conductance for CO_2, g_{sc} [m s^{-1}] can be derived by Kirchhoff's resistance/conductance analogy. It is defined as the net flow of CO_2 through the stomata divided by the difference between the CO_2 concentration outside the leaves C_s [kg CO_2 m^{-3}] and the concentration in the intercellular cavities C_i [kg CO_2 m^{-3}] (see Fig. 8.9):

$$g_{sc} = \frac{A_n(Env)}{C_s - C_i(Env)} \tag{8.100}$$

where the functions (Env) indicate the dependence of A_n and C_i on the different environment factors. In future version, it is planned that the stomatal conductance from the carbon module would be used for water vapor transpiration, which leads to a full coupling between carbon and water vapor fluxes.

The basics of the A-gs model are described by Jacobs (1994) and Jacobs *et al.* (1996). Further details of the current extended formulation are given in publications by Calvet *et al.* (1998) and Calvet *et al.* (2004). For the description of the canopy conductance to CO_2, g_{sc}, a stepwise approach is followed with: (i) the definition of the temperature dependent parameters, (ii), the radiation response, (iii) the calculation of the ratio between internal and external CO_2 concentration, (iv) the computation of stomatal conductance, (v) inclusion of the soil moisture response and (vi) the vertical integration over the canopy.

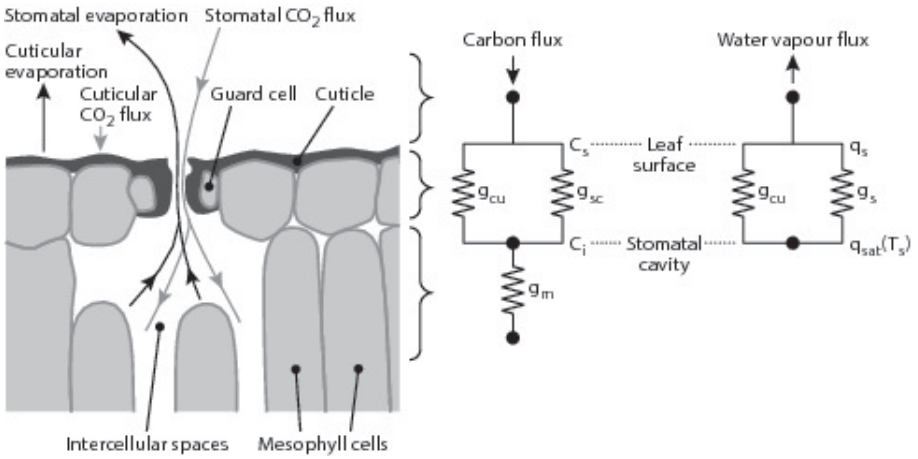

Figure 8.9 *Schematic representation of a leaf with the resistance analogies for carbon and water vapor, where g_{cu} is the cuticular conductance, g_{sc} the stomatal conductance to CO_2, g_s the stomatal conductance to water vapor, g_m the mesophyll conductance, C_s and C_i the CO_2 concentration at the canopy surface and inside the leaf cavity respectively, q_s and $q_{sat}(T_s)$ the humidity at the canopy surface and the saturated humidity at the temperature T_s of the canopy surface respectively.*

(i) Temperature responses

There are several parameters in the photosynthesis model that are temperature dependent, namely the compensation point, the mesophyll conductance and the maximum photosynthetic capacity. The compensation point Γ is defined as the CO_2 concentration at which the net CO_2 assimilation of a fully lit leaf becomes zero. It can be measured in a laboratory by exposing plants to a variable CO_2 concentration. The mesophyll conductance g_m describes the transport of CO_2 from the substomatal cavities to the mesophyll cells where the carbon is fixed. It includes the representation of physical and chemical processes. The maximum photosynthetic capacity $A_{m,max}$ is specified as an absolute upper limit to the photosynthesis rate in full sunlight and non-limiting CO_2 concentration. The temperature dependence is described with so-called Q_{10} functions, where Q_{10} represents the proportional increase of a parameter for a 10° increase in temperature (Berry and Raison, 1982).

For the compensation point the formulation is:

$$\Gamma(T_s) = \Gamma(25^o) Q_{10\Gamma}^{(T_s-25)/10} \tag{8.101}$$

where $\Gamma(25^o)$ is the compensation point at 25° C, $Q_{10\Gamma}$ is the Q_{10}-constant and $T_s$is the leaf surface temperature. For g_m and $A_{m,max}$, the temperature dependence is further adjusted by the inhibition functions after Collatz *et al.* (1992):

$$g_m(T_s) = \frac{g_m(25^o) Q_{10gm}^{(T_s-25)/10}}{(1+e^{0.3(T_{1gm}-T_s)})(1+e^{0.3(T_s-T_{2gm})})} \tag{8.102}$$

$$A_{m,max}(T_s) = \frac{A_{m,max}(25^o) Q_{10Am,max}^{(T_s-25)/10}}{(1+e^{0.3(T_{1am,max}-T_s)})(1+e^{0.3(T_s-T_{2am,max})})} \tag{8.103}$$

where Q_{10gm}, $Q_{10Am,max}$, T_{1gm}, T_{2gm}, $T_{1Am,max}$, $T_{2Am,max}$, are constants affecting the sensitivity to the plant surface temperature T_s. Parameter $g_m(25^o)$ depends on soil moisture stress and will be further described in the following sections. Its unstressed value $g_m^*(25^o)$ is optimized here with the help of observations. The constants in these functions are vegetation type dependent and are listed in Table 8.9 and Table 8.10.

(ii) Radiation and CO_2 response

For A_n, two regimes are distinguished: the radiation limiting regime and the CO_2 limiting regime (Goudriaan *et al.*, 1985; Jacobs, 1994). In the radiation limiting regime with sufficient CO_2, A_n is

Table 8.9 *Parameter values as specified in the optimized CTESSEL model. The vegetation types are from the GLCC database and used in the same way as in TESSEL Van den Hurk et al. (2000)*

Type	*Vegetation type*	R_0 [$mgCO_2$ $m^{-2}s^{-1}$]	g_m*(25) [mm s^{-1}]	g_c [mm s^{-1}]	*Dmax** [kg kg^{-1}]	*Am,max*(25) [$mgCO_2$ m^{-2} s^{-1}]	$f_0{}^*$ [-]	$\Gamma(25)$ [ppm]
1	Crops, mixed farming	0.100	1.3	0.15	Eq.8.118	2.20	0.85	42
2	Short grass	0.080	1.3	0.20	Eq.8.118	3.00	0.65	42
3	Evergreen needleleaf	0.360	0.8	0.20	0.124	2.20	Eq.8.122	42
4	Deciduous needleleaf	0.330	0.8	0.20	0.124	2.20	Eq.8.122	42
5	Deciduous broadleaf	0.280	1.4	0.00	0.109	1.83	Eq.8.122	42
6	Evergreen broadleaf	0.270	1.1	0.25	0.124	1.83	Eq.8.122	42
7	Tall grass	0.150	2.3	0.20	Eq.8.118	1.83	0.70	2.6
8	Desert	-	-	-	-	-	-	-
9	Tundra	0.360	2.0	0.25	Eq.8.118	3.00	0.95	42
10	Irrigated crops	0.096	1.4	0.25	Eq.8.118	1.83	0.92	42
11	Semidesert	0.019	1.0	0.25	Eq.8.118	1.83	0.80	42
12	Ice caps and glaciers	-	-	-	-	-	-	-
13	Bogs and marshes	0.270	0.5	0.25	Eq.8.118	1.83	0.96	42
14	Inland water	-	-	-	-	-	-	-
15	Ocean	-	-	-	-	-	-	-
16	Evergreen shrubs	0.110	0.9	0.15	Eq.8.118	1.83	0.72	2.6
17	Deciduous shrubs	0.080	1.9	0.20	Eq.8.118	1.83	0.96	42
18	Mixed forest- Wood	0.420	1.0	0.00	0.124	2.20	Eq.8.122	42
19	Interrupted forest	0.160	0.8	0.10	0.124	2.20	Eq.8.122	42
20	Water -land mixtures	0.270	1.0	0.25	Eq.8.118	1.83	0.95	42

Table 8.10 *CTESSEL temperature response, quantum use efficiency and soil moisture stress parameters*

Parameter	Value	Notes
$Q_{10\Gamma}$	2	
Q_{10gm}	2	
$Q_{10Am,max}$	2	
T_{1gm} (^{o}C)	5	(13 for veg. types 7 and 16)
$T_{1Am,max}$(^{o}C)	8	(13 for veg. types 7 and 16)
T_{2gm}(^{o}C)	36	
$T_{2Am,max}$(^{o}C)	38	
a	2.381	(5.323 for veg.types 7 and 16
b	0.6103	(0.8923 for veg.types 7 and 16)
D^X_{max}(g/kg)	300	
ε_o (mg CO_2/J PAR)	0.0142	(0.0117 for vegetation types 7 and 16)

controlled by the amount of photosynthetically active radiation (PAR) I_a

$$A_n = \varepsilon I_a - R_d \tag{8.104}$$

where R_d is the dark respiration and where ε is the quantum efficiency expressed according to

$$\varepsilon = \varepsilon_o \frac{C_i - \Gamma}{C_i + 2\Gamma} \tag{8.105}$$

Parameter ε_o is the maximum quantum use efficiency and C_s is the ambient CO_2 concentration at the leaf surface.

At high radiation intensities, net assimilation saturates at a level A_m and becomes CO_2 limited according to $A_m = (C_i - \Gamma)\ g_m$ with C_i the CO_2 concentration inside the leaf cavities (see below). An absolute limit to account for the maximum photosynthetic capacity of the leaves is further applied as follows

$$A_m = A_{m,max}\ [1 - \exp\{-g_m\ (C_i - \Gamma)\ / A_{m,max}\}] \tag{8.106}$$

The radiation and CO_2 limiting regimes are combined via a smooth exponential transition function

$$A_n = (A_m + R_d)\left[1 - \exp\left(\frac{-\varepsilon I_a}{A_m + R_d}\right)\right] - R_d \tag{8.107}$$

The autotrophic dark respiration is simply parametrised according to Van Heemst (1986) and includes the respiration from the leaves only

$$R_d = A_m/9 \tag{8.108}$$

The respiration from other parts of the vegetation is included in the parametrised heterotrophic respiration.

(iii) The C_i/C_s ratio

The CO_2 concentration inside the leaf cavities C_i needs to be known in order to derive the stomatal conductance from the net assimilation. Observations indicate that the ratio C_i/C_s is a rather conservative quantity for moist atmospheric conditions and that increasing humidity deficit exerts a strong stomatal control affecting this ratio. Therefore C_i/C_s is specified as a function of atmospheric moisture deficit D_s at the leaf surface.

$$\frac{C_i}{C_s} = f + (1-f)\frac{\Gamma}{C_s} \tag{8.109}$$

where f is the coupling factor defined by:

$$f = f_o\left(1 - \frac{D_s}{D_{max}}\right) + f_{min}\frac{D_s}{D_{max}} \tag{8.110}$$

and f_o is the value of f at D_s, D_{max} is the maximum saturation deficit and

$$f_{min} = \frac{g_{cu}}{g_{cu} + g_m} \tag{8.111}$$

The transport of CO_2 is maintained in the situation where $f = f_{min}$ through the leaf cuticle or because of imperfect closure of the stomata. This process is represented by the cuticule with conductance g_{cu}.

(iv) Stomatal conductance

The first computation of the stomatal conductance for CO_2, g^1_{sc} is achieved by dividing net assimilation by the difference between CO_2 concentration in and outside the leaves. It is modified here to account for the limiting cases of very dry air and dark respiration:

$$g^1_{sc} = \frac{A_n - A_{min}\left(\frac{D_s}{D_{max}}\frac{A_n+R_d}{A_m+R_d}\right) + R_d\left(1 - \frac{A_n+R_d}{A_m+R_d}\right)}{C_s - C_i} \tag{8.112}$$

where A_{min} represents the residual photosynthesis rate (at full light intensity) associated with cuticular transfers when the stomata are closed because of a high specific humidity deficit:

$$A_{min} = g_m(C_{min} - \Gamma) \tag{8.113}$$

In this equation, C_{min} is the value of C_i at maximum specific humidity deficit:

$$C_{min} = \frac{g_{cu}C_s + g_m\Gamma}{g_{cu} + g_m} \tag{8.114}$$

The diffusion of CO_2 through the stomatal openings interacts with that of water vapour and therefore stomatal conductance to CO_2 is corrected for this interaction by an iterative refinement:

$$g_{sc} = g^1_{sc} + E\frac{M_a}{\rho_a M_v}\frac{C_s + C_i}{2(C_s - C_i)} \tag{8.115}$$

where M_v and M_a are molecular masses of water vapour and air respectively, ρ_a is the air density and E is the leaf transpiration based on the previous guess of the stomatal conductance:

$$E = (1.6g^1_{sc})D_s\rho_a \tag{8.116}$$

Finally, the stomatal conductance to water vapour g_s is given by:

$$g_s = 1.6 g_{sc} \tag{8.117}$$

The total conductance used by the transpiration scheme is $g_s + g_{cu}$, where g_{cu} is the vegetation type dependent cuticular conductance (Table 8.9).

(v) Soil moisture stress response

Among other possible A-gs formulations for which the soil moisture stress response is directly applied to the gross assimilation A_g (Ronda *et al.*, 2001) or the net assimilation A_n (Sala and Tenhunen, 1996), Calvet (2000) found that the soil moisture stress response is driven in a complex way through the mesophyll conductance g_m, the maximum specific humidity deficit tolerated by the vegetation D_{max}, and the ratio C_i/C_s controlled by f. The soil moisture response behaves differently for high and low vegetation. In CHTESSEL the adopted soil moisture stress response follow the function described in Calvet (2000) and Calvet *et al.* (2004) and based on a meta-analysis of several herbaceous and woody vegetation types.

Low vegetation formulation:

Calvet (2000) found that the mesophyll conductance g_m and the maximum atmospheric moisture deficit D_{max} vary with soil moisture but that they remain correlated according to:

$$\ln\left(g_m(25^\circ)\right) = a - b \ \ln(D_{max}) \tag{8.118}$$

where $g_m(25^\circ)$ in [mm s^{-1}] and D_{max} in [g kg^{-1}]

Therefore this equation is used to derive D^*_{max} (maximum saturation deficit without soil moisture stress) from the tabulated $g^*_m(25^\circ)$, where superscript * indicates optimal soil moisture conditions and a and b are tabulated empirical coefficients (Table 8.10). Then the soil moisture stress index F_2 ($F_2 = 1/f_2$, see 8.14) is applied to find D_{max}in stressed conditions according to a bilinear function with a breakpoint at a critical soil moisture stress index f_{2c}:

$$\begin{aligned} D_{max} &= D^X_{max}\frac{F_2}{f_{2c}} && for\ F_2 < f_{2c} \\ D_{max} &= D^X_{max} + (D^*_{max} - D^X_{max})\frac{F_2 - f_{2c}}{1 - f_{2c}} && for\ F_2 \geq f_{2c} \end{aligned} \tag{8.119}$$

where D^X_{max} is the maximum value of D_{max} corresponding to f_{2c}. The resulting D_{max} is substituted in (8.118) to find $g_m(25^\circ)$.

High vegetation formulation:

Observations show that $g_m(25^\circ)$ is well correlated with the coupling factor f_0 according to the following empirical expression (Calvet *et al.*, 2004):

$$\ln\left(g^*_m(25^\circ)\right) = 4.7 - 7.0 f^*_0 \tag{8.120}$$

where $g_m(25^\circ)$ is in [mm s^{-1}]. In this case (8.120) is used to derive $g^*_m(25^\circ)$ from the value f^*_0 as tabulated according to vegetation type (Table 8.9). Subsequently a soil moisture stress function is applied to find $g_m(25^\circ)$:

$$\begin{aligned} g_m(25^\circ) &= g^N_m\frac{F_2}{f_{2c}} && for\ F_2 < f_{2c} \\ g_m(25^\circ) &= g^N_m + (g^*_m(25^\circ) - g^N_m)\frac{F_2 - f_{2c}}{1 - f_{2c}} && for\ F_2 \geq f_{2c} \end{aligned} \tag{8.121}$$

where g^N_m is the stressed value of g_m derived from Calvet *et al.* (2004) meta-analysis with the following empirical function:

$$\ln\left(g^N_m\right) = 2.8 - 7.0 f^*_0 \tag{8.122}$$

g^N_m is in [mm s^{-1}].

After computing $g_m(25^\circ$ according to (8.121), the stressed value for f_0 is derived with

$$\ln\left(g_m(25^\circ)\right) = 2.8 - 7.0 f_0 \tag{8.123}$$

$g_m(25°)$ is in [mm s^{-1}].

Further details on the soil stress parameterisation can be found in Calvet (2000), Calvet *et al.* (2004) and Voogt *et al.* (2006).

(vi) Vertical integration from leaf to canopy

The net CO_2 assimilation calculated at the leaf scale is upscaled to the canopy scale assuming that leaf parameters do not vary with height in the canopy, and that the attenuation of the incoming shortwave radiation in the canopy can be computed using a simple radiative extinction model. The incoming PAR above the vegetation ($I_a(h)$, with h the canopy height) is assumed to be 48% of the incoming shortwave radiation and then further attenuated in the canopy. The dependence of PAR on height z within the canopy is described by Roujean (1996) according to:

$$I_a(z) = I_a(h)(1 - K(z)) \tag{8.124}$$

where K is the extinction function given by:

$$K(z) = \delta(\mu_s)K_{df}(z) + (1 - \delta(\mu_s)K_{dr}(z)) \tag{8.125}$$

$K_{df}(z)$ and $K_{dr}(z)$ are the extinction coefficients of diffuse and direct light, respectively:

$$K_{df}(z) = 1 - e^{\left(\frac{-0.8bLAI(h-z)}{h}\right)}, \tag{8.126}$$

$$K_{dr}(z) = 1 - e^{\left(-\frac{G_l}{\cos(\mu_s)}\frac{bLAI(h-z)}{h}\right)} \tag{8.127}$$

where μ_s is the solar zenith angle and G_l is a parameter that describes the distribution of leaves (a spherical angular distribution is assumed with $G_l = 0.5$), δ is the ratio of diffuse to total downward shortwave radiation at the top of the canopy, $LAI(h - z)$ is the cumulative leaf area index above height z and b is the foliage scattering coefficient given by:

$$b = 1 - \frac{1 - \sqrt{1 - \omega}}{1 + \sqrt{1 - \omega}} \tag{8.128}$$

based on the leaf single scattering albedo ω (=0.2) for the solar spectrum corresponding to the PAR. Parameter δ is given by:

$$\delta(\mu_s) = \frac{0.25}{0.25 + \cos(\mu_s)} \tag{8.129}$$

Assuming a homogeneous leaf vertical distribution, the integrated canopy net CO_2 assimilation, dark respiration and conductance can be written as:

$$A_{nI} = LAI \int_0^1 A_n d(z/h) \tag{8.130}$$

$$R_{dI} = LAI \int_0^1 R_d d(z/h) \tag{8.131}$$

$$g_c = LAI \int_0^1 g_s d(z/h) \tag{8.132}$$

In the above equations, LAI is defined as the ratio of leaf area covering a unit of ground area (m^2 m^{-2}).

The integrations are parametrised with a three-point Gaussian quadrature method following Goudriaan (1986):

$$A_{nI} = LAI \sum_{i=1}^{3} W_i A_n(z_i) \tag{8.133}$$

$$R_{dI} = LAI \sum_{i=1}^{3} W_i R_d(z_i) \tag{8.134}$$

$$g_c = LAI \sum_{i=1}^{3} W_i g_s(z_i) \tag{8.135}$$

where W_i and z_i are the Gauss weights and levels, respectively.

8.8.2 The Farquhar photosynthesis scheme

The leaf photosynthesis scheme developed by Farquhar, von Caemmerer and Berry (Farquhar *et al.*, 1980) (FvCB) has been implemented in the IFS as an alternative to the A-gs scheme described in section 8.8.1. The FvCB scheme is more widely used than the A-gs scheme because it includes a more mechanistic approach to the different photosynthesis limiting processes, which allows then the coupling of photosynthesis-based radiative transfer models for the simulation of Solar Induced Fluorescence (SIF). As described in van Diepen *et al.* (2022), the FvCB model considers rate-limiting processes due to Rubisco capacity and electron transport in parallel, whereas the A-gs model considers Rubisco activity which is then scaled with quantum use efficiency. The models also differ fundamentally in terms of the parameterisation of dark respiration.

There are two major steps in the implementation of the FvCB model. The firt step is the calculation of the photosynthesis together with the water/carbon coductance at the leaf level, i.e. for a given canopy layer with specific light and meteorological conditions. In the second step, the leaf-level photosynthesis is integrated at the canopy level, using some hypothesis about the pentration of the light within the plan canopy. Such approach is based on a vertical discretisation of the canopy in several layer. This is a common approach in most models, even if the overall exchange with the atmosphere corresponds to the so-called "big leaf" approach.

For the light-independent reactions (i.e. the Calvin Cycle), we can distinguish three phases:

- Carbon fixation (phase 1): this phase relies on the Rubisco enzyme to fix the CO_2 that has entered the leaves and has diffused up to carboxylation sites, through the mesophyll. Such phase is associated to the so-called V_{cmax} parameter (maximum photosynthetic capacity).
- Carbon reduction (phase 2): this phase concerns the reduction of the CO_2 into the first organics compounds containing three carbon atoms. The energy that is consumed during the different reactions of this phase is provided by ATP molecules.
- Enzyme regeneration (phase 3): this phase concerns the absorption of the light to regenerate the Rubisco enzyme and produce the ATP and ADP molecules needed in phase 2. It is associated to the so-called V_{jmax} parameter (light limitation photosynthesis rate).

The following two subsections describe the leaf level photosynthesis implementation that use the numerical approach of Yin and Struik (2009).

(*a*) *C3 photosynthesis model*

The Farquhar–von Caemmerer–Berry model predicts the net CO2 assimilation rate (A) as the minimum of the Rubisco-limited rate (A_c) and electron-transport-limited rate (A_j).

$$A = min(A_c, A_j) \tag{8.136}$$

These two parts of the model can be written in a single equation as:

$$A = \frac{(C_c - \Gamma_*)\chi_1}{C_c + \chi_2} - R_d \tag{8.137}$$

where for the Rubisco-limited part $\chi_1 = V_{cmax}$ and $\chi_2 = K_{mC}(1 + C_o/K_{mO})$, for the electron-transport-limited part $\chi_1 = J/4$ and $\chi_2 = 2\Gamma_*$; C_c and C_o are the carbon dioxide and oxygen partial pressures at the carboxylation sites, Γ_* is the CO_2 compensation point in the absence of dark respiration (R_d). This latter case assumes a purely linear electron transport (LET). The dark respiration at 25^oC (R_{d25}) is parametrised as follows:

$$R_{d25} = 0.01 V_{cmax25} F_2 \tag{8.138}$$

where F_2 is the soil moisture stress index used in this version of the FvCB model ($F_2 = min(1.0, Khrel/f_2)$), based on the $1/f_2$ soil moisture stress index defined in equation 8.14 using a PFT-dependent *Khrel* scaling parameter to reduce the stress for dry conditions. The soil moisture stress index F_2 is also applied to other FvCB parameters (g_{m25}, g_0,f_{VPD},V_{cmax25} defined in Table 8.11).

Following Farquhar and Wong (1984), the rate of electron transport (J) is described as a non-rectangular hyperbolic function of irradiance:

$$J = \frac{\alpha_{LL} I_{abs} + J_{max} - \sqrt{(\alpha_{LL} I_{abs} + J_{max})^2 - 4\theta J_{max} \alpha_{LL} I_{abs}}}{2\theta} \tag{8.139}$$

where α_{LL} is the conversion efficiency of absorbed light into J at strictly limiting light, J_{max} is the maximum capacity of e–transport, and θ is the convexity factor for response of J to absorbed irradiance.

The leaf photosynthesis is coupled with the stomatal conductance (gs) on the base of the following phenomenological approach:

$$g_s = g_0 + \frac{(A + R_d)}{(C_i - (\Gamma_* - R_d/g_m)} f_{vpd}(4) \tag{8.140}$$

where g_0 is the residual stomatal conductance when irradiance approaches zero; C_i is the intercellular CO_2 partial pressure and g_m is the mesophyll conductance.

For describing the effect of leaf-to-air vapor pressure difference (VPD) on stomatal conductance the following factor is introduced:

$$f_{vpd} = \frac{1}{1/(a_1 - b_1 VPD) - 1} \tag{8.141}$$

where a1 and b1 are empirical constants.

According to the first diffusion law of Fick, the CO2 transfer from Ca (ambient CO2 partial pressure) to Cc can be written as:

$$C_i = C_a - A(1/g_b + 1/g_s) \tag{8.142}$$

$$C_c = C_i - A/g_m \tag{8.143}$$

where g_b is the boundary-layer conductance.

The three equations 8.137, 8.140 and 8.143 with the three unknowns A, g_s and C_c form the system to be solved for C3 plants.

(*b*) *C4 photosynthesis model*

For C4 plants, CO_2 is fixed by phosphoenolpyruvate (PEP) carboxylase in the mesophyll cell into a C4 compound, which then goes into a bundle-sheath cell, where it is decarboxylated to provide CO_2 to Rubisco. The CO_2 concentration in the bundle-sheath is high, thus preventing photorespiration.

$$A = V_p - L - R_m \tag{8.144}$$

where V_p is the rate of PEP carboxylation, R_m is the mitochondrial respiration in the mesophyll and fixed to $0.5R_d$ and L is the leakage of CO_2 from the bundle-sheath to the mesophyll through the bundle-sheath conductance g_{bs}:

where V_P is the rate of PEP carboxylation, R_m is the mitochondrial respiration in the mesophyll and fixed to $0.5R_d$ and L is the leakage of CO_2 from the bundle-sheath to the mesophyll through the bundle-sheath conductance g_{bs}:

$$L = g_{bs}(C_c - C_i) \tag{8.145}$$

V_P is limited by the PEP carboxylation rate or the electron transport rate; in the former case, we have:

$$V_P = min(k_P C_i, V_{Pmax}) \tag{8.146}$$

where k_P is the initial carboxylation efficiency of the PEP carboxylase, and V_{Pmax} is the maximum rate of PEP carboxylation at the saturated C_i.

For the electron transport-limited case of C4 plants, we also consider f_{cyc}, a fraction of electrons at photosystem I (PSI) that follow a cyclic electron transport (CET) around PSI, and f_{pseudo}, a fraction of electrons at PSI that follow a pseudocyclic electron transport (PET), that are not used for carbon reduction and photorespiration (which is negligible in C4 plants). Similarly, f_Q, a fraction of electrons at reduced plastoquinone that follow the Q-cycle, is not transferred to the plastocyanin. f_{pseudo} and f_Q are PFT-dependent constants.

Based on this, we have:

$$f_{cyc} = 1 - \frac{(4(1-\chi)(1+f_q) + 3hf_{pseudo}}{3h - 4(1-\chi)} \tag{8.147}$$

where χ is the fraction of electron transport rate partitioned to the mesophyll reactions and set at 0.4, and h is the number of protons required to produce one ATP and set at 4.

$$J = J_2 \left(1 - \frac{f_{pseudo}}{1 - f_{cyc}}\right) \tag{8.148}$$

$$V_p(J_2) = \frac{(\chi J_2(2 + f_Q - f_{cyc})}{2h(1 - f_{cyc})} = \frac{\chi J_2 z)}{2} \tag{8.149}$$

As for C3 plants, the Rubisco-based assimilation of CO_2 follows equation 8.136 and we have an equivalent to equation 8.137:

$$A = \frac{(C_c - \gamma_* O_{bs})\chi_1}{C_c + \chi_2 O_{bs} + \chi_3} - R_d \tag{8.150}$$

where O_{bs} is the oxygen partial pressure in the bundle-sheath, $\gamma_* = 0.5/S_{c:o}$, $S_{c:o}$ is the relative CO_2 $/O_2$ specificity factor for Rubisco. For the rubisco-limited rate, we have: $\chi_1 = V_{cmax}$, $chi_2 = K_{mC}/K_{mO}$, $\chi_3 = K_{mC}$, and for the electron transport limited rate: $\chi_1 = (1-\chi)J_2 z/3$, $\chi_2 = 7\gamma_*/3$, $\chi_3 = 0$.

The oxygen partial pressures between intercellular air-space and bundle-sheath are linked through the following equation:

$$O_{bs} = \frac{\alpha A}{0.047 g_{bs}}) + O_i \tag{8.151}$$

where α is the fraction of PSII activity in the bundle sheath and 0.047 accounts for the diffusivities for O_2 and CO_2 in water and their respective Henry constants.

The equation for the stomatal conductance is slightly different from the C3 case:

$$g_s = g_0 + \frac{A + R_d}{C_s - (C_{i*} - R_d/g_{s,C_i*})} f_{vpd} \tag{8.152}$$

where g_{s,C_i*} is the stomatal conductance at C_{i*}:

$$C_{i*} = \frac{g_{bs}\gamma_* O_i - (1 + \gamma_* \alpha/0.047)R_d + R_m}{g_{bs} + k_p} \tag{8.153}$$

The three equations 8.150, 8.152 and 8.145 with the three unknowns A, g_s and C_c form the system to be solved for C4 plants.

(*c*) *Analytical solution for the coupled model*

For both C3 and C4 plants, the three equations coupling photosynthesis, stomatal conductance and the CO2 partial pressure at the carboxylation site can be combined into the form of a standard cubic equation for A:

$$A^3 + pA^2 + qA + r = 0 \tag{8.154}$$

The analytical solution for this form is given in Yin and Struik (2009) in the Appendixes A (general solution), B (for C3 photosynthesis) and C (for C4 photosynthesis).

(*d*) *Up-scaling at the canopy level*

The assimilation A is computed per canopy layer to account for the light profile extinction, which follows the Beer-Lambert law. Because the light profile follows an exponential decrease, we consider thin canopy layers at the top of the canopy, and thick ones at the bottom. Thus, the canopy is discretized in a given number of layers of exponentially growing LAI thickness from the top of canopy. LAI at level i is calculated as:

with $LAI_{\max}$, the maximum LAI value (equal to 12 m^2m^{-2}) and $n_{\mathrm{LAI,max}}$ the maximum number of layers (equal to 20). Thus, the top layer has a thickness of $\sim 0.1 m^2m^{-2}$ and the bottom layer (in case of a vegetation with a LAI of 12 m^2m^{-2} a thickness of 1.5 m^2m^{-2}. The total LAI from top to bottom canopy (LAI_{tot}) is a variable computed independently by the model. As a consequence, the number of layers over which the assimilation is computed (nLAI) varies over time and between ecosystem types in order to ensure that $LAI_{\mathrm{tot}} = \sum_{n=i}^{n_{\mathrm{LAI}}} LAI_{\mathrm{i}}$.

The light fraction of light is calculated for each LAI step, the available light follows a simple Beer extinction law:

$$f_{\mathrm{light}} = \exp(-c_{\mathrm{ext}} LAI) \tag{8.155}$$

where c_{ext} is a PFT-dependent extinction coefficient. The photon flux density absorbed by leaf photosynthetic pigments (I_{abs}) is calculated as:

$$I_{abs} = SW_{\mathrm{down}} c_{\mathrm{ext}} f_{\mathrm{light}} \tag{8.156}$$

Apart from the light amount, the other environmental parameters that drive the photosynthesis (temperature, ambient CO_2, air humidity) are held constant along the canopy depth. We only account for a leaf nitrogen-related reduction of V_{cmax} along the canopy depth, assuming that leaf nitrogen content decreases from top to bottom of the canopy, as in equation 8.155. The overall photosynthesis will thus be the integral over all layers and canopy-mean values for CO_2 fluxes (A_n) and other relevant parameters (g_s, R_d) is also derived.

The light propagates through the canopy following a decreasing exponential Beer-Lambert law. The canopy is discretized accordingly in LAI with growing thickness from top to bottom. To implicitly account for the reduction of nitrogen availability through the canopy, a decreasing function is applied to the maximum rate of carboxylation and the maximum rate of electron transport. The assimilation and stomatal conductances are computed for each layer and then integrated at canopy level by a weighted sum over the LAI layers.

The temperature dependence of R_{d}, K_{mC}, K_{mO}, $S_{\mathrm{C/O}}$, Γ_* is described by an Arrhenius function normalized with respect to their values at 25^oC (P_{25}):

$$P = P_{25} \exp\left(\frac{(T-25)E}{(298R(T+273)}\right) \tag{8.157}$$

where T is leaf temperature; E is the activation energy, defining the responsiveness of the relevant parameter P to temperature; R is the universal gas constant (8.314).

Table 8.11 *Main variables involved in the FvCB photosynthesis calculation*

Variable	Description	Units
A	Net photosynthesis rate	$\mu mol\,/\,(m^2 s)$
A_c	Net photosynthesis rate limited by Rubisco activity	$\mu mol\,/\,(m^2 s)$
A_j	Net photosynthesis rate limited by electron transport	$\mu mol\,/\,(m^2 s)$
f_{vpd}	Factor for describing the effect of leaf-to-air vapour difference on gs	–
g_0	Residual stomatal conductance when irradiance approaches zero	$\mu mol\,/\,(m^2 s\ bar)$
g_b	Leaf boundary-layer conductance	$\mu mol\,/\,(m^2 s\ bar)$
g_m	Mesophyll diffusion conductance	$\mu mol\,/\,(m^2 s\ bar)$
g_s	Stomatal conductance	$\mu mol\,/\,(m^2 s\ bar)$
I_{abs}	Photon flux density absorbed by leaf photosynthetic pigments	$\mu mol\,/\,(m^2 s)$
J	Rate of electron transport	$\mu mol\,/\,(m^2 s)$
J_{max}	Maximum value of J under saturated light	$\mu mol\,/\,(m^2 s)$
K_{mC}	Michaelis–Menten constant of Rubisco for CO_2	μbar
K_{mO}	Michaelis–Menten constant of Rubisco for O_2	μbar
R_d	Day respiration (respiratory CO2 release other than by photorespiration)	$\mu mol\,/\,(m^2 s)$
$S_{C/O}$	Relative CO2 / O2 specificity factor for Rubisco	$bar\,/\,bar$
V_{cmax}	Maximum rate of Rubisco activity-limited carboxylation	$\mu mol\,/\,(m^2 s)$
Γ_*	Ci-based CO2 compensation point in the absence of Rd	μbar
Khrel	Scaling factor for soil water stress function (virtual parameter)	–

Table 8.12 *Main constants involved in the FvCB photosynthesis calculation*

Constant	Description	Units	Value
LAI_{depth}	Depth of LAI level	–	0.15
LAI_{max}	Maximal LAI used for splitting LAI into nlai layers	m^2/m^2	12
n_{LAI}	Number of LAI levels	–	20

The response of other parameters (V_{cmax}, J_{max}, g_m) is described with a modified Arrhenius function:

$$P = P_{25} \exp\left(\frac{(T-25)E}{298R(T+273)}\right) \frac{1+\exp(\frac{298S-D}{298R})}{1+\exp\left(\frac{(T+273)S-D}{R(T+273)}\right)} \tag{8.158}$$

where S is an entropy term; D is the deactivation energy. For V_{cmax} and J_{max} it is assumed that the entropy term acclimates to temperature:

$$S = a_S + b_S\, max(11, min(T, 35)) \tag{8.159}$$

where a_S and b_S are the linear regression coefficients. The growth temperature, as tested by Kattge and Knorr (2007), range from 11^oC to 35^oC, so we limit the relationship between these lower and upper limits.

(*e*) *FvCB model parameters*

Main variables and constants involved in the FvCB photosynthesis calculation are listed in Tables 8.11 and 8.12. The PFT-dependent parameters of the FvCB photosynthesis model have been optimised using equivalent parameters in the ORCHIDEE model (used as prior values) to minimise the error of the model with respect to the GPP eddy covariance data at FLUXNET2015 sites (Pastorello *et al.*, 2020). The optimised values are shown in Table 8.14.

8.8.3 Ecosystem respiration and Gross Primary Production

The ecosystem respiration R_{eco} is given by two terms: the autotrophic dark respiration R_{dI} (8.108), and $R_{soilstr}$ which represents both heterotrophic respiration from the soil and autotrophic respiration from

Table 8.13 *Main parameters involved in the FvCB photosynthesis calculation*

Parameter	Description	Units	Value for C3 PFTs	Value for C4 PFTs
a_1	Empirical constant involved in the calculation of f_{vpd}	–	0.85	0.72
a_{rJV}	a coefficient of the linear regression $(a+bT)$ defining the J_{max25}/V_{cmax25} ratio	$\mu mol\ e-/(\mu molCO_2)$	2.59	1.715
a_{SJ}	a coefficient of the linear regression $(a+bT)$ defining the entropy term for J_{max}	$J/(Kmol)$	0.14	0.2
b_1	Empirical constant involved in the calculation of f_{vpd}	0.14 –	0.2	
b_{rJV}	b coefficient of the linear regression $(a+bT)$ defining the J_{max25}/V_{cmax25} ratio	$\mu mole-/(\mu molCO_2\ ^oC)$	–0.035	0
b_{SJ}	b coefficient of the linear regression $(a+bT)$ defining the Entropy term for J_{max}	$J/(Kmol^oC)$	–0.75	0
b_{SV}	b coefficient of the linear regression $(a+bT)$ defining the Entropy term for V_{cmax}	$J/(Kmol^oC)$	–1.07	0
c_{ext}	Extinction coefficient of the Monsi–Seaki relationship	– –	0.5 0.5	0.5 0.5
D_{gm}	Deactivation energy for g_m	J/mol	437400	–
D_{Jmax}	Deactivation energy for J_{max}	J/mol	200000	192000
D_{Vcmax}	Deactivation energy for V_{cmax}	J/mol	200000	192000
$E_{\blacksquare_*}$	Activation energy for Γ_*	J/mol	37830	37830
E_{gm}	Activation energy for g_m	J/mol	49600	–
$E_{J_{max}}$	Activation energy for J_{max}	J/mol	49884	77900
$E_{K_{mC}}$	Activation energy for K_{mC}	J/mol	79430	79430
$E_{K_{mO}}$	Activation energy for K_{mO}	J/mol	36380	36380
E_{R_d}	Activation energy for R_d	J/mol	46390	46390
$E_{Sc/o}$	Activation energy for S_S/O	J/mol	-24460	-24460
$E_{V_{rmcmax}}$	Activation energy for V_{cmax}	J/mol	71513	67300
f_{pseudo}	Fraction of electrons at PSI that follow pseudocyclic transport	–	–	0.1
f_{psir}	Fraction of PSI electron transport rate partitioned to the C4 cycle	–	–	0.4
f_Q	Fraction of electrons at reduced plastoquinone follow Q-cycle	–	–	1
g_0	Residual stomatal conductance when irradiance approaches zero	$mol/(m^2sbar)$	0.00625	0.01875
g_{bs}	Bundle-sheath conductance	$mol/(m^2sbar)$	–	0.003
g_{m25}	Mesophyll diffusion conductance at 25 ^oC	$mol/(m^2sbar)$	0.4 (C3)	–
h_{proton}	Number of protons required to produce one ATP	mol/mol	4	4
K_{mC25}	Michaelis–Menten constant of Rubisco for CO_2 at 25^oC	μbar μbar	404.9 404.9	650 650
K_{mO25}	Michaelis–Menten constant of Rubisco for O_2 at 25^oC	μbar	278400	450000
k_p	Initial carboxylation efficiency of the PEP carboxylase	$mol/(m^2sbar)$	–	0.7
S_{gm}	Entropy term for g_m	$J/(Kmol)$	1400	–
$S_{c/o25}$	Relative CO_2/O_2 specificity factor for Rubisco at 25^oC	bar/bar	2800	2590
$T_{photo,max}$	Maximum photosynthesis temperature	^oC	55	55
$T_{photo,min}$	Minimum photosynthesis temperature	^oC	-4	-4
α	Fraction of PSII activity in the bundle sheath	–	–	0.1
α_{LL}	Conversion efficiency of absorbed light into J at strictly limiting light	$mole-/(molphoton)$	0.3	0.3
γ_{*25}	Ci-based CO_2 compensation point in the absence of R_d at 25^oC	μbar	42.75	42.75
θ	Convexity factor for response of J to irradiance	–	0.7	0.7

Table 8.14 *Farquhar model parameters dependent on vegetation type*

Vegetation type	Index	V_{cmax}	hrel	a_1	b_1	g_0	g_{m25}	$E_{V_{cmax}}$	$E_{J_{max}}$
C3 Crops, mixed farming	1	49.0	4.00	0.9460	0.130	0.006990	0.513	72801.3	64849.2
C4 Crops$^{(*)}$	1	70.5	2.06	0.8640	0.168	0.021900	0.400	80090.2	101270.0
C3 Short grass	2	48.7	3.32	0.8880	0.117	0.006640	0.657	50059.1	41459.5
C4 Short grass$^{(*)}$	2	40.3	3.52	0.6680	0.210	0.017000	0.657	47110.0	54530.0
Evergreen needleleaf trees	3	62.2	2.93	0.6800	0.168	0.005330	0.100	59880.2	35048.2
Deciduous needleleaf trees	4	35.0	1.00	0.8500	0.140	0.006250	0.400	71513.0	49884.0
Deciduous broadleaf trees	5	41.9	3.25	0.9775	0.112	0.007696	0.719	92966.9	34918.8
Evergreen broadleaf trees	6	33.9	4.00	0.9775	0.138	0.007838	0.387	67706.1	34918.8
Tall grass	7	40.3	3.52	0.6680	0.210	0.017000	0.657	47110.0	54530.0
Tundra	9	70.0	4.00	0.9775	0.112	0.008125	0.800	50059.1	34918.8
Irrigated crops	10	60.0	1.00	0.9775	0.140	0.006250	0.400	71513.0	49884.0
Semidesert	11	50.0	1.00	0.7200	0.200	0.018750	0.400	67300.0	77900.0
Bogs and marshes	13	48.6	4.00	0.9190	0.126	0.007390	0.590	72906.6	34918.8
Evergreen shrubs	16	58.4	2.63	0.8640	0.206	0.014200	0.400	47110.0	54530.0
Deciduous shrubs	17	44.5	4.00	0.9775	0.112	0.007730	0.724	50059.1	52755.6
Mixed forest/woodland	18	42.2	1.73	0.7220	0.153	0.005430	0.404	67899.3	34918.8
Interrupted forest	19	50.0	1.00	0.8500	0.140	0.006250	0.400	71513.0	49884.0

the above and below ground structural biomass. It is parametrised following a modified formulation of Norman *et al.* (1992) as a function of soil temperature, soil moisture, snow depth and vegetation type:

$$R_{\text{soilstr}} = R_0(25) Q_{10\text{Ro}}^{\left(\frac{T_{\text{soil}}-25}{10}\right)} f_{\text{sm}} f_{\text{sn}} \tag{8.160}$$

In this equation f_{sn} and f_{sm} are snow and soil moisture attenuation functions respectively defined as:

$$f_{\text{sn}} = 1 - C_{\text{vs}}(1 - e^{-\alpha z_{\text{snow}}}) \tag{8.161}$$

C_{vs} is the surface fraction covered by snow, α is a constant expressing the attenuation of the soil carbon emission within the snow pack and z_{snow} is the snow depth. The soil moisture stress function for soil respiration is defined following a study by Albergel *et al.* (2010) as:

$$f_{\text{sm}} = \frac{\bar{\theta}}{\theta_{\text{cap}}} \tag{8.162}$$

$Q_{10\text{Ro}}$ represents the proportional increase of a parameter for a 10$^{\text{o}}$ increase in temperature (Berry and Raison, 1982), this case, given its variability with climate regimes, $Q_{10\text{Ro}}$ is defined as a function of soil temperature after McGuire *et al.* (1992). The vegetation types are affecting the ecosystem respiration through a reference respiration at 25°C, $R_0(25)$, estimated by minimizing the root mean square errors between simulated and observed R_{eco} for each vegetation type.

Finally, the gross primary production GPP and the ecosystem respiration are given by:

$$GPP = A_{\text{nI}} + R_{\text{dI}} \tag{8.163}$$

$$R_{\text{eco}} = R_{\text{dI}} + R_{\text{soilstr}}. \tag{8.164}$$

These two quantities are often derived from flux-tower NEE observations and used for evaluation of the two main CO_2 processes.

8.8.4 Vegetation description

The state of vegetation is given by the Leaf Area Index; crucial for deriving the plant assimilation and transpiration activity. Currently a satellite observation-based climatology was considered for the representation of LAI. The satellite product (MOD15A2) is derived from the Moderate Resolution Imaging Spectroradiometer (MODIS) instrument on board of TERRA. It is produced daily for the

land surfaces at 1 km spatial resolution from MODIS spectral reflectance with a global coverage, and synthesized on an 8-day time interval based on simultaneously retrieved maximum Fraction of Absorbed Photosynthetically Active Radiation (FAPAR) in order to remove the atmospheric noise (Myneni *et al.*, 1992). The collection 5 of the product (released in 2008 available from February 2000 to present) is used. To derive the climatological time series, 9 years of data (2000–2008) were re-projected from the sinusoidal to a geographic regular latitude/longitude projection, spatially averaged to 1/12th degree resolution, then temporally smoothed, monthly averaged (Jarlan *et al.*, 2008) and finally interpolated to the IFS reduced Gaussian grid. The MODIS LAI products were analyzed and validated in previous studies (Garrigues *et al.*, 2008; MODIS Land team http://landval.gsfc.nasa.gov/, Weiss *et al.*, 2012). After a positive assessment within the IFS system (Boussetta *et al.*, 2013b), this product was adopted by ECMWF for operational use. This climatology is used within CHTESSEL to drive the surface carbon exchange module.

The land use classification follows from the Global Land Cover Characteristics (GLCC) data (Loveland *et al.*, 2000) according to the Biosphere-Atmosphere Transfer Scheme (BATS) classification to assign dominant high and low vegetation types and associated parameters within each grid box (as detailed in Table 8.9,and Table 8.10).

8.8.5 The wetland methane scheme

Wetland methane (CH_4) emissions calculation is implemented in the ECLand model following Bloom *et al.* (2017), where it is estimated by a simple formulation:

$$F(t,x) = sA(t,x)R(t,x)q_{10,ch4}^{\frac{T(t,x)-25.0}{10}} \tag{8.165}$$

where F is wetland CH_4 emissions at time t and location x, s is global scaling factor, A is wetland extent fraction, R is heterotrophic respiration, $q_{10,ch4}$ is temperature dependency factor, T_{soil} is soil temperature.

This formulation has been adapted following additional assumptions:

- The heterotrophic respiration R is based on the formulation of the CO_2 soil respiration (see section 8.8.3):

  $$R(t,x) = f_{\text{sm}} f_{\text{sn}} R_0(25) \tag{8.166}$$

  Thus, the heterotrophic respiration has been substituted with its defining terms: reference respiration tabulated by vegetation type ($R_0(25)$), scaling factor accounting for soil moisture effect on respiration (f_{sm}) and attenuation function for snow pack (f_{sn}). $R(t,x)$ is modulated by its own temperature dependency, expressed through a factor $q_{10,ch4}$ corresponding to the $Q_{10\text{Ro}}$ (in equation 8.160) scaled by the relative CH_4:CO_2 respiration for a 10 ^{o}C increase).
- Instead of the surface skin temperature, the first soil layer temperature is used, calculated in the model as the variable PTSOIL. This allows more smooth temporal variations of the wetland CH_4 emissions.
- The temperature dependency factor $q_{10,ch4}$ is made independent on the CHTESSEL plant functional type (PFT). It is set to the same value for each of the 15 vegetated PFTs and to zero for 5 non-vegetated land use types. The $q_{10,ch4}$ factor has been optimised using FLUXNET-CH4 eddy covariance observations. The optimal posterior $q_{10,ch4}$ value has been found to be 2.337.
- The global scaling factor s has been optimized by scaling the budget to match the observed global methane growth rate in 2018 using the standard CAMS configuration for the other components of the budget. This scaling factor has been tested for other years, showing an improved fit to observations compared to the LPJ-HYME climatology (Spahni *et al.*, 2011) used in CY48R1. In the future, the s scaling factor will be optimized using atmospheric observations of CH_4 in an atmospheric inversion framework.

One of the most important aspects of the wetland model is the wetland extend fraction A(t,x). The wetland cover is based on a combination of the Global Inundation Extent from Multi-Satellites (GIEMS) dataset (v3.1, Prigent *et al.* (2007)) and inundation derived using the Catchment-based Macro-scale

Table 8.15 *Global urban parameters*

Variable	Symbol	Value	Units
Road Albedo	α_{road}	0.05	$(-)$
Roof Albedo	α_{roof}	0.16	$(-)$
Wall Albedo	α_{wall}	0.6	$(-)$
Road Emissivity	σ_{road}	0.99	$(-)$
Roof Emissivity	σ_{roof}	0.96	$(-)$
Wall Emissivity	σ_{wall}	0.96	$(-)$
Road Vol. Heat Cap.	VHC_{road}	3.0	$MJm^{-3}K^{-1}$
Roof Vol. Heat Cap.	VHC_{roof}	2.0	$MJm^{-3}K^{-1}$
Wall Vol. Heat Cap.	VHC_{wall}	3.0	$MJm^{-3}K^{-1}$
Road Thermal Cond.	TC_{road}	1.4	$Wm^{-1}K^{-1}$
Roof Thermal Cond.	TC_{roof}	0.7	$Wm^{-1}K^{-1}$
Wall Thermal Cond.	TC_{wall}	1.4	$Wm^{-1}K^{-1}$
Average Bui. Height	H	8.0	m
Height-Width Ratio	$\frac{H}{W}$	1.0	$(-)$
Road-Bui. Ratio	$\frac{R}{B}$	1.0	$(-)$
Vol. Moi. Saturation	θ_{sat}	0.15	m^3m^{-3}

Floodplain model (CaMa-Flood, Yamazaki *et al.* (2011)) coupled to the IFS. GIEMS is processed as an annual climatology based on monthly averages between 1992 and 2020 and interpolated from 0.25 degree resolution to 0.1 degree. Monthly inundation from CaMa-Flood is taken from a 4km IFS simulation interpolated to 0.1 degree for 2019. For all points the maximum wetland fraction between the two products is selected, providing a global monthly climatology of wetland extent. The resulting wetland map is converted for use as a climate field at all resolutions required from climate.v021 onwards.

8.9 URBAN

The urban scheme represents the impact of urban areas on both the land surface interface with the atmosphere, through the introduction of an urban tile and the sub-surface impact by generate a hybrid urban-soil top soil layer. The scheme described by McNorton *et al.* (2021) adopts a single-layer urban canopy assumption, which provides a simplified representation of buildings and urban surfaces as elements affecting surface energy exchanges. The scheme treats urban areas as obstacles that modify the fluxes of heat, moisture, and momentum between the surface and atmosphere. The scheme accounts for both impervious surfaces (roads, buildings) and their heat storage capacity.

The scheme considers radiation using an infinite canyon assumption, accounting for shadowing, which is dependent on urban parameters and the solar zenith angle. The surface roughness is generated using building properties and information on canyon geometry, removing any concept of canyon orientation. Thermal and hydrological properties are also defined by several urban parameters, accounting for not only land-atmosphere exchange but also sub-surface exchanges of both heat and water. The scheme consists of both time varying (e.g., albedo based on solar zenith angle) and fixed variables (e.g., thermal heat capacity of a building) defind in Table 8.15.

8.9.1 Urban Radiation

The radiation scheme used is based upon previous schemes, Oleson *et al.* (2008) and Porson *et al.* (2010). The solar-radiation scheme for the roof fraction of the tile follows a surface albedo simple incoming/reflected exchange. For the canyon fraction of the tile, the impact of shadowing based on the solar zenith, building height, and aspect ratio is considered along with the albedo of the wall and street. The canyon bulk albedo, α_{can}, which is the same for both direct and diffuse solar radiation is derived using

$$\alpha_{\text{can}} = 1 - \left[((1-\chi_{\text{f}})\chi_{\text{r}} + Q_{\text{S,r}}) + \frac{2H}{W} ((1-\chi_{\text{w}})\chi_{\text{w}} + Q_{\text{S,w}}) \right] \tag{8.167}$$

where χ_{f} is the fraction of solar radiation scattered by the sky (estimated at 0.3), χ_{r} and χ_{w} are the shadowing factors of streets and walls (following Masson, 2000), $Q_{\text{S,r}}$ and $Q_{\text{S,w}}$ are the net radiation exchange for the road and wall, following Harman *et al.* (2004) and $\frac{H}{W}$ is the building height to street width ratio.

For bulk emissivity, ϵ, a similar approach is adopted for longwave radiation using material emissivity. The bulk emissivity for the canyon is influenced by the building height to canyon width ratio but in a different way to albedo. The code has been written to calculate bulk emissivity based on $\frac{H}{W}$ of the canyon and such that it would satisfy the net longwave radiation, $R_{L,c}$, using

$$R_{L,c} = \epsilon(Lw\downarrow - \sigma T_c^4) \tag{8.168}$$

where $Lw\downarrow$ is the downward longwave radiation, σ is the Stefan-Boltzmann constant and $sigmaT_c$ is the canyon temperature, which is assumed to be equal to the surface temperature. The long and shortwave radiation routine used here assumes building azimuthal orientation is random and accounts for all possible directions equally. Here, as a simplification, albedo, and emissivity are assumed to be spectrally constant in both long and shortwave, additionally gas absorption/emission in the longwave is ignored.

8.9.2 Urban Roughness

The roughness length for momentum and heat exchange with the atmosphere is calculated based on the Macdonald *et al.* (1998) formulation, where roughness is a function of $\frac{H}{W}$ and the ratio of street width to building width $\frac{R}{B}$. The estimated displacement height, D is calculated based on a calibrated coefficient for staggered arrays ($A = 4.43$) and drag coefficient, $\beta = 1$. These formulations are

$$D = 1 - \frac{R}{B}(A^{\frac{R}{B}}) \tag{8.169}$$

$$z = (\beta(1-D)\frac{2\frac{H}{W}\frac{R}{B}}{k^2})^{-0.5} \tag{8.170}$$

$$Z_m = H(1-D)e^{-z} \tag{8.171}$$

The approach to estimate roughness length for heat uses morphometric methods relating to aerodynamic parameters based on empirical relations. It uses previously defined flow regimes of isolated roughness, wake interference, and skimming (Harman *et al.*, 2004). These regimes separate the infinite canyon into recirculation and ventilated regions. Full details of the roughness length calculation can be found in Harman *et al.* (2004). As with the radiation, a random orientation assumption is made for the infinite length canyon model used. This formulation is dependent on bulk resistance of both the canyon and roof calculated using the formulation of Porson *et al.* (2010). This results in a roughness length for heat which is several order magnitudes smaller than the roughness length for momentum in agreement with similar studies (e.g., Kanda *et al.* (2005)).

8.9.3 Thermal Properties

Urban thermal properties are implemented following a similar methodology to the radiation, whereby individual properties are defined for the urban wall, roof, and street structure. These combine to provide bulk properties weighted by the fraction of the urban tile covered by each. These bulk variables, thermal conductivity, and volumetric heat content, are used to compute the transfer of heat from the atmosphere and between the upper most and second soil layer, broadly corresponding to concrete aggregates (Wonorahardjo *et al.*, 2020).

8.9.4 Urban Hydrology

As with previous properties, the impervious nature of the urban environment is represented as a weighted fraction of the total tile. An increased urban fraction results in a low saturation point of the top-soil layer, resulting in an increased surface run-off generation. The volumetric soil moisture values for the top-soil layer become a hybrid of the default values and updated urban ones weighted by urban cover. Simple assumptions are also made regarding drainage whereby 30% of precipitation is removed over the urban fraction of the tile.

8.10 LAKES AND OTHER INLAND WATER BODIES

The representation of inland water bodies (lakes, reservoirs, rivers and coastal waters) is important in order to account for the thermal inertia effects and specific albedo and roughness characteristics associated to open water and to account for phase change during freezing/melting. This is simulated by the Fresh-water Lake model FLake (Mironov *et al.*, 2010), which was chosen to be included in the IFS for its intermediate complexity, particularly adapted for numerical weather prediction and climate applications. Moreover FLake benefits from a large research community efforts, contributing to validation and development (see http://www.flake.igb-berlin.de/papers.shtml).

The FLake implementation in the HTESSEL surface scheme has been introduced in subsequent steps, with ad-hoc simplifications that are necessary at global scale due to the lack of detailed knowledge of the lake conditions, i.e. turbidity or presence of lake bottom sediments. A freezing parameterization and specific ice prognostic variables with their energy and mass balance allows FLake to be used in all climate conditions. At present there are is no account for a water balance equation and lake depth and surface area (or fractional cover) are kept constant in time.

The offline implementation and surface testing at global scale is presented in Dutra *et al.* (2010b). Balsamo *et al.* (2010) performed a sensitivity study on the lake depth parameter, which is most directly related to lake thermal inertia. The ancillary conditions such as global lake cover and bathymetry and lake initial conditions are described in Chapter 11. The forecast sensitivity of FLake in the IFS is evaluated in Balsamo *et al.* (2012), while the preparation of a retrospective lake reanalysis for initial conditions together with the coupled data assimilation impact assessment is provide in Balsamo (2013).

Previously to the introduction of FLAKE only grid-scale lakes (lake fraction larger than 50%) were considered in the IFS and treated similarly to ocean-points. In these grid points, the surface temperature was prescribed, and evolved daily during integration according to climatological temperatures (derived from ERA-40), without diurnal changes of surface temperature and inter-annual variability. With the activation of FLAKE both partial lake cover within a grid-box and fully resolved lakes are modelled prognostically and evolve with the same timestep and spatial grid resolution used to the atmospheric and land surface processes in the IFS.

A new tile (tile 9) was created in HTESSEL to represent the lakes interface with the atmosphere. The FLake model has been extensively modified removing components that were already part of HTESSEL scheme such as the turbulent fluxes calculation in the tiling scheme, and the omission of parameterization for the treatment of lake bottom sediments for which global dataset are not available. The treatment of snow cover is omitted although the HTESSEL snow scheme can be coupled to the lake tile over resolved lakes allowing a consistent representation of snow cover over frozen lakes (Dutra *et al.*, 2010b).

8.10.1 Lake prognostic and ancillary variables

FLake meets the requirements for physical parameterizations in weather forecast systems, in terms of both physical realism and numerical efficiency. Mironov *et al.* (2010) presented a brief description of FLake, in its implementation into a limited-area atmospheric model. FLake adopts a similar concept to force-restore (Deardorff, 1978) in land surface models, since it has intermediate features between purely bulk models and multi-layer one-dimensional models.

The vertical temperature profile specified in FLake consists of a top mixed layer, with uniform distribution of temperature, and a thermocline with its upper boundary located at the mixed

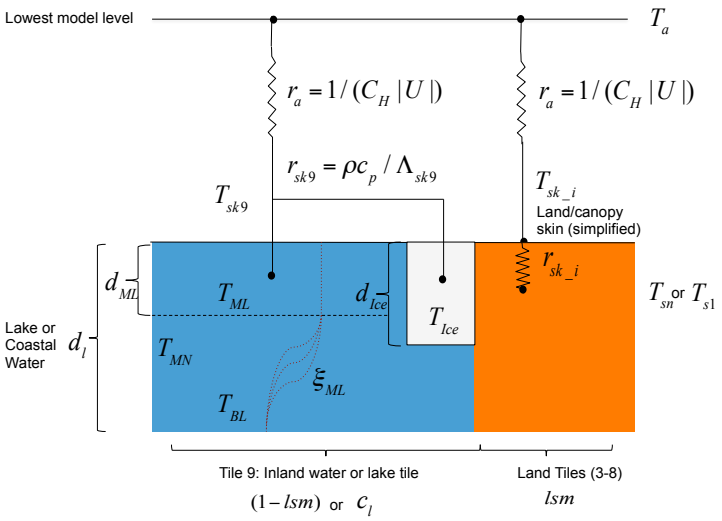

Figure 8.10 *Schematic representation of the lake model.*

layer bottom, and the lower boundary at the lake bottom. The profile in the thermocline is parameterized according to the self-similarity concept, which has been supported by many theoretical and observational studies (see Mironov, 2008 for a discussion).

In the IFS implementation of FLake the surface fluxes of heat, moisture and momentum are computed by the HTESSEL routines. A new lake tile (tile 9) has been introduced to enable Flake to run on any single surface grid-point in the surface scheme, independently from the lake fractional cover. This is desirable to ease the interoperability of lake output at diverse spatial resolutions where the ratio of resolved/unresolved lakes and coastal water varies.

The prognostic variables included in FLake are: mixed-layer temperature T_{ML}, mixed-layer depth d_{ML}, bottom temperature T_{BL}, mean temperature of the water column T_{MN}, shape factor ζ_{ML} (with respect to the temperature profile in the thermocline), temperature at the ice upper surface T_{Ice}, and ice thickness d_{Ice}, which correspond to the schematic representation of Fig. 8.10.

The ancillary variables prescribed to characterize the lakes are the lake depth d_{l} and the lake cover c_{l} reported in Chapter 11.

8.10.2 Lake temperature and self-similarity

The self-similarity assumption leeds to a significant simplification in comparison with multi-layer one-dimensional models, while still retaining a more realistic physics than bulk models. In particular, the unrealistic assumption of fully mixed temperature profile in a lake, applied in many bulk models, can be avoided. The mixed layer depth is calculated taking into account both wind and thermally driven mixing (Mironov, 2008), that follows from the volumetric heating of the water column by solar radiation. The structure of the stratified layer between the upper mixed-layer and the lake bottom, the thermocline, reposes on the concept of self-similarity (assumed shape) of a temperature-depth curve. The same concept is used to describe the temperature structure of the lake ice. Considering fresh water density as

$$\rho_{\mathrm{w}} = \rho_{\mathrm{r}} \left[1 - \frac{1}{2} \alpha_{\mathrm{tl}} (T_{\mathrm{MN}} - T_{\mathrm{MNr}})^2 \right] \tag{8.172}$$

where ρ_w is the water density, $\rho_r = 999.98 kg m^{-3}$ is the maximum density of fresh water at the temperature $T_{MNr} = 277.13K$, and $\alpha_{tl} = 1.6509\ K^{-2}$ is an empirical coefficient. According to 8.172, the thermal expansion coefficient α_{tl} and a buoyancy parameter β depend on the water temperature according to:

$$\beta(T_l) = g\alpha_{T_l} = g\ a_T(T_l(z) - T_r) \tag{8.173}$$

where g is the acceleration due to gravity. The following two-layer parametric representation of the evolving temperature profile $T_l(z)$is adopted

$$T_l(z) = \begin{cases} T_{ML} & \text{if } 0 < z \leq d_{ML} \\ T_{ML} - (T_{ML} - T_{BL})\Phi_{T_l}(\zeta) & \text{if } d_{ML} < z \leq d_l \end{cases} \tag{8.174}$$

as a function of depth z, where T_{ML} is the temperature of the upper mixed layer of depth d_{ML}. T_{BL} is the temperature at the bottom of the water body ($z = d_l$), and $\Phi_T = [T_{ML} - T_l(z,t)]/[T_{ML} - T_{BL}]$ is a dimensionless function of dimensionless depth $\zeta = [z/d_{ML}(t)]/[d_l/d_{ML}(t)]$ that satisfies the boundary conditions $\Phi_T(0) = 0$ and $\Phi_T(1) = 1$.

The mean temperature of the water column T_{MN} is obtained integrating 8.174, and relates d_{ML} , d_l, T_{ML}, T_{BL} as

$$T_{MN} = T_{ML} - \xi_{ML}\left(1 - \frac{d_{ML}}{d_l}\right)(T_{ML} - T_{BL}) \tag{8.175}$$

where ξ_{ML} is the shape factor with respect to the temperature profile in the thermocline.

The equation for the mean temperature of the water column is obtained by integrating one-dimensional heat transfer equation over z from 0 to d_l, and it reads as

$$d_l \frac{dT_{MN}}{dt} = \frac{1}{\rho_w c_w}\Big[G_s + I_s - G_{BL} - I(d_l)\Big] \tag{8.176}$$

where $c_w = 4.2\ 10^3 J\ kg^{-1}K^{-1}$ is the specific heat of water, G_s and I_s are the values at the surface of the vertical heat flux and of the heat flux due to solar radiation, respectively, and G_{BL} is the heat flux through the lake bottom. The radiation heat flux I that penetrates into the water is the surface value of the incident solar radiation flux from the atmosphere multiplied by $1 - \alpha_w$, where α_w is the albedo of the water surface with respect to solar radiation. The surface flux G_s is a sum of the sensible and latent heat fluxes and the net heat flux due to long-wave radiation at the air-water interface. The equation of heat budget of the mixed layer reads as

$$d_{ML} \frac{dT_{ML}}{dt} = \frac{1}{\rho_w c_w}\Big[G_s + I_s - G_{ML} - I(d_{ML})\Big] \tag{8.177}$$

where G_{ML} is the heat flux at the bottom of the mixed layer, and assumes two variants for stationary/retreating or deepening mixed layers as detailed in Mironov *et al.* (2010) . In the case of the mixed-layer being stationary or retreating, $d\ d_{ML}/dt \leq 0$, the bottom temperature is

$$\frac{dT_{BL}}{dt} = 0 \tag{8.178}$$

In the case of the mixed-layer deepening, $d\ d_{ML}/dt > 0$, the following equation is used:

$$\begin{aligned} \tfrac{1}{2} \quad & (d_l - d_{ML})^2 \frac{dT_{ML}}{dt} - \frac{d}{dt}\Big[C_P(d_l - d_{ML})^2(T_{ML} - T_{BL})\Big] = \\ = \quad & \frac{1}{\rho_w c_w}\Big[C_G(d_l - d_{ML})(G_{ML} - G_{BL}) + (d_l - d_{ML})I_{ML} - I_{ML_BL}\Big] \end{aligned} \tag{8.179}$$

Where C_P and C_G are dimensionless parameters. If $d_{ML} = d_l$ both T_{ML} and T_{BL} are equal to T_{MN} and the water column profile is isothermal. The depth of a stably or neutrally stratified wind-mixed layer is determined from:

$$\frac{d\, d_{ML}}{dt} = \frac{d_{EQ} - d_{ML}}{d_{EQ}} C_{rh} u^* \tag{8.180}$$

where u^* is the surface friction velocity, $C_{rh} = 0.03$ is a dimensionless constant, and d_{EQ} is a mixed-layer depth in radiative equilibrium (Mironov *et al.*, 2010).

8.10.3 Lake freezing and melting

The parameterisation of lake freezing is essential for treating inland water bodies in global models as mid-latitude and high-altitude lakes are often subject to extensive frozen periods especially when characterized by a shallow depth.

In the current implementation the snow accumulation over ice is not allowed and the existence of fractional ice condition on a give grid-point is not contemplated. The approach used to describe the temperature structure of the lake ice is conceptually similar to the approach used to describe the temperature structure of the lake thermocline. The following parametric representation of the evolving temperature profile within the ice is adopted (cf. 8.174):

$$T_{ice} = T_f - (T_f - T_{sk,i})\Phi_{ice}(\zeta_i) \text{ if } -d_{ice} < z \leq 0 \tag{8.181}$$

where z is the vertical co-ordinate (positive downward) with the origin at the ice-water interface, $d_{ice}(t)$ is the ice thickness, $T_f = 273.15\ K$ is the fresh-water freezing point, and $T_{sk,i}(t)$ is the temperature at the ice upper surface. The dimensionless universal function $\Phi_{ice} = [T_f - T_{ice}(z,t)]/[T_f - T_{sk,i}]$ of dimensionless depth $\zeta_i = z/d_{ice}(t)$ satisfies the boundary conditions $\Phi_{ice}(0) = 0$ and $\Phi_{ice}(1) = 1$. The equation of the heat budget of the ice layer is

$$\begin{aligned} \tfrac{d}{dt} \quad & \left\{\rho_{ice} c_i d_{ice}[T_f - C_i(T_f - T_{ice})]\right\} - \rho_{ice} c_i T_{ice} \frac{d\, d_{ice}}{dt} = \\ = \quad & G_s + I_s - I(0) + \kappa_i \frac{T_f - T_{ice}}{d_{ice}} \Phi'_{ice}(0) \end{aligned} \tag{8.182}$$

where $\rho_{ice} = 9.1\ 10^2 kg\ m^{-3}$, $c_i = 2.1\ 10^3 J\ kg^{-1}\ K^{-1}$ and $\kappa_i = 2.29\ J\ m^{-1} s^{-1} K^{-1}$ are the ice mean property for density, specific heat and heat conductivity, respectively. G_s and I_s are the values of G and I, respectively, at the ice upper surface $z = d_{ice}(t)$, and $\Phi'_{ice}(0) = d\Phi_{ice}/d\zeta_i$ at $\zeta_i = 0$. The radiation heat flux I_s that penetrates into the ice medium is the surface value of the incident solar radiation flux from the atmosphere multiplied by $1 - \alpha_i$, where α_i is the ice surface albedo with respect to solar radiation and C_i dimensionless parameter representing the shape factor with respect to the temperature profile within the ice.

Equation 8.182 serves to determine T_{ice} when this temperature is below the freezing point T_f, i.e. when no melting at the ice upper surface takes place. During the ice melting from above, T_{ice} remains equal to T_f. During the ice growth or ice melting from below (these occur as $T_{ice} < T_f$), the ice thickness is computed as:

$$L_f \frac{d(\rho_{ice} d_{ice})}{dt} = G_w + \kappa_{ice} \frac{T_f - T_{ice}}{d_{ice}} \Phi'_{ice}(0) \tag{8.183}$$

where $L_f = 3.3\ 10^5\ J\ kg^{-1}$ is the latent heat of fusion, and G_w is the heat flux in the near-surface water layer just beneath the ice. If the right-hand side of 8.183 is negative (this may occur due to a negative G_w), ice ablation takes place. During the ice melting from above, the following equation is used:

$$L_f \frac{d(\rho_{ice} d_{ice})}{dt} = G_w - (G_s + I_s) + I(0) \tag{8.184}$$

that holds as the atmosphere heats the ice upper surface and T_{ice} is equal to T_f. The evolution of the temperature profile beneath the ice is described as follows. The temperature at the ice-water interface is fixed at the freezing point, $T_{ML} = T_f$. The mean temperature of the water column is computed from 8.183, where G_s and I_s are replaced with G_w and $I(0)$, respectively. If the bottom temperature is less than the temperature of maximum density, ρ, the mixed-layer depth and the shape factor with respect to the temperature profile in the thermocline are kept unchanged, $d\, d_{ML}/dt = 0$ and $\xi/dt = 0$, and the bottom temperature is computed from 8.175. If the entire water column appears to be mixed at the moment of freezing, i.e. $d_{ML} = d_l$ and $T_{ML} = T_{BL}$, the mixed layer depth is reset to zero, $d_{ML} = 0$, and the shape factor is reset to its minimum value, $\xi_{ML} = \xi_{min}$.

As the bottom temperature reaches the temperature of maximum density, its further increase is prevented and is kept constant equal to ρ_r. If $d_{ML} > 0$, the shape factor ξ_{ML} is kept unchanged, and the mixed-layer depth is computed from 8.175. As the mixed-layer depth approaches zero, 8.175 is used to compute the shape factor ξ_{ML} that in this regime increases towards its maximum value, $\xi_{ML} = \xi_{max}$ (the values of $\xi_{min} = 0.5$ and $\xi_{max} = 0.8$ are used). If $d_{ML} = 0$, the heat flux from water to ice is estimated from

$$G_w = -\kappa_w \frac{T_b - T_{ice}}{d_l} max[1, \Phi_w(0)] \tag{8.185}$$

where $\kappa_w = 5.46\, 10^{-1} J\, m^{-1}\, s^{-1}\, K^{-1}$ is the molecular heat conductivity of water, and $\Phi'_w(0) = d\Phi_w/d\zeta$ at $\zeta = 0$. Note that as soon as a mixed layer is formed ($d_{ML} > 0$) the above water flux is neglected ($G_w = 0$).

The shape factor with respect to the temperature profile in the thermocline is computed from

$$\frac{d\xi_{\mathrm{ML}}}{dt} = sign(d\, d_{ML}/dt) \frac{\xi_{max} - \xi_{min}}{t_{rc}} \tag{8.186}$$

where *sign* is the sign function [$sign(x) = x > 0$]. The shape factor ξ_{ML} evolves towards its maximum value during the mixed-layer deepening, and towards its minimum value during the mixed-layer stationary state or retreat. The adjustment occurs on a relaxation time scale t_{rc} estimated using the buoyancy frequency in the thermocline (Mironov *et al.*, 2010).

The exponential approximation of the decay law for the flux of solar radiation is used:

$$I = I_s \Sigma_{k=1}^{n} a_k e^{-\gamma_k (z + d_{ice})} \tag{8.187}$$

where I_s is the surface value of the incident solar radiation heat flux multiplied by $1 - \alpha$ with α being the albedo of the water surface or of the ice surface with respect to solar radiation, n is the number of wavelength bands, α_k are fractions of the total radiation flux for different wavelength bands, and a_k are attenuation coefficients for different bands. The attenuation coefficients are piece-wise constant functions of z, i.e. they have different values for water and ice but remain constant within each media. The following parameterization of the ice surface albedo with respect to solar radiation is adopted:

$$\alpha_i = \alpha_i{}^{max} - (\alpha_i{}^{max} - \alpha_i{}^{min}) e^{-C_\alpha (T_f - T_{ice})/T_f} \tag{8.188}$$

where $\alpha_i{}^{max} = 0.7$ and $\alpha_i{}^{min} = 0.4$ are maximum and minimum values of the ice albedo, respectively, and $C_\alpha = 95.6$ is a fitting coefficient. The presence of snow over lake ice and its seasonal changes are parametrised in 8.188 as a function of T_{ice}. During the melting season, the ice surface temperature is close to the fresh-water freezing point. The presence of wet snow, puddles, melt-water ponds is again parametrised implicitly and results in a decrease of the area-averaged surface albedo. The water surface albedo with respect to solar radiation, $\alpha_w = 0.07$, is assumed to be constant.

8.11 SEA ICE

Points that are not defined as land or lakes (i.e., a grid point with land cover less or equal 0.5 and lake cover is not dominant) are sea/ocean points and can have two tile fractions, open water and ice. A surface analysis defines the ice fraction, c_I, and the temperature of the open water fraction. All forecast systems are coupled to an ocean-ice model which evolves the SST and sea ice cover using the NEMO model (see the Part 5 on ensemble prediction for more details). No distinction is made between surface and skin temperature for the open water fraction (see Table 8.2).

The ice fraction is modelled as an ice slab, with open water underneath and a skin temperature for the thermal contact with the atmosphere. The main caveats in the sea ice parameterisation are as follows.

(i) Fixed depth of the slab, which can be relaxed once there is a reliable data set to specify its geographic distribution.
(ii) No snow accumulation on top of the ice (although one of the main effects of snow, i.e., a markedly different surface albedo, is partially emulated by the prescribed seasonal albedo outlined in Section 2.4.5).

The ice heat transfer is assumed to obey the following Fourier law of diffusion

$$(\rho C)_I \frac{\partial T_I}{\partial t} = \frac{\partial}{\partial z}\left[\lambda_I \frac{\partial T_I}{\partial z}\right] \tag{8.189}$$

where $(\rho C)_I = 1.88 \times 10^6$ J m^{-3} K^{-1} is the volumetric ice heat capacity, T_I is the ice temperature, $\lambda_I = 2.03$ W m^{-1} K^{-1} and is the ice thermal conductivity. The boundary condition at the bottom is the temperature of the frozen water, $T_{fr} = T_0 - 1.7$ and the top boundary condition is the net heat flux at the surface, obtained from the solution of the ice skin thermal budget.

Equation (8.189) is solved with the ice discretized in four layers, with the depth of the top three layers as in the soil model and the depth of the bottom layer defined as

$$D_{I,4} = D_I - \sum_{j=1}^{3} D_{I,j} \tag{8.190}$$

and the total depth of the ice slab, D_I, is prescribed as 1.5 m. In order to ensure a constant ice fraction, the solution of the ice thermal budget is capped to the ice melting temperature, $T_{m1} = T_0$ at all levels. the details of the numerical discretisation can be found in Section 8.13.

8.12 OCEAN BOUNDARY CONDITIONS FOR TEMPERATURE AND SPECIFIC HUMIDITY

The SST and sea ice cover is evolved during the forecast using the NEMO model (see the Part 5 on ensemble prediction for more details). In the operational system, the sea surface temperature (SST) is specified from an analysis provided by OCEAN5 in the Tropics and OSTIA elsewhere. The OSTIA analysis is a blend of satellite retrievals and in situ observations from ships. The idea is to have a detailed horizontal distribution from satellite and to anchor this temperature fields to the rather sparse ship observations. It means that that the analyzed SST fields are calibrated as if they are ship observations and therefore they represent bulk SST fields (i.e. measured a few metres deep)

The ocean skin temperature is not always the same as the bulk SST. A very shallow layer (less then 1 *mm* thick) is cooler because of the turbulent and long wave radiative heat loss to the atmosphere which has to be compensated for by the inefficient molecular transport in the water skin. Solar radiation has only a small effect on the cool skin because the solar absorption in such a thin layer is small. However, at low winds, solar radiation can create a so-called warm layer with a depth of a few metres.

Parameterisations of three different near surface ocean effects are included in the code: 1. the cool skin, 2. the warm layer and 3. salinity effects on the saturation specific humidity at the surface. These parameterisations can be controlled through namelist NAEPHY. The namelist parameters are

LEOCCO (default:TRUE), LEOCWA (default:FALSE when coupled), and LEOCSA (default:TRUE), for the cool skin, the warm layer and salinity effects respectively. So, all three effects are activated in this cycle (cool skin and warm layer are activated since Cy35r1). Details of the cool skin and warm layer parameterisations are given in Beljaars (1997) and Zeng and Beljaars (2005).

8.12.1 The cool skin

The cool ocean skin is the result of heat loss to the atmosphere which is balanced by thermal conduction in the quasi-laminar sublayer near the water surface. Scaling arguments for the skin layer lead to the following expression for the temperature difference over the skin layer (cf. Fairall *et al.*, 1996)

$$T_{\rm sk} - T_{-\delta} = \frac{\delta}{\rho_{\rm w} c_{\rm w} k_{\rm w}} (Q + R_{\rm s} f_{\rm s}) \tag{8.191}$$

$$\text{with } Q = H + \lambda E + LW \tag{8.192}$$

where $T_{\rm sk}$ is the skin temperature, $T_{-\delta}$ is the temperature below the cool skin, $R_{\rm s}$ is the net solar radiation at the surface, $f_{\rm s}$ is the fraction of solar radiation absorbed in the skin, H is the sensible heat flux, λE is the latent heat flux, LW is the net long wave radiation at the surface, $\rho_{\rm w}$ (=1025 kgm^{-3}) is the density of sea water (at the surface), $c_{\rm w}$ (=4190 Jkg^{-1}K^{-1}) is the volumetric heat capacity of water, and $k_{\rm w}$ (=0.6 Wm^{-1}K^{-1}) is the molecular thermal conductivity of water. The fraction of solar absorbed radiation is given by

$$f_{\rm s} = 0.065 + 11\delta - \frac{6.6\,10^{-5}}{\delta}\left(1 - e^{-\delta/0.0008}\right) \tag{8.193}$$

$$\tag{8.194}$$

The thickness of the skin layer δ is (Fairall *et al.*, 1996)

$$\delta = c_{\rm S}\left[1 + \left(\frac{-16 g \alpha_{\rm w} \nu_{\rm w}^3}{u_{*\rm w}^4 k_{\rm w}^2 \rho_{\rm w} c_{\rm w}}(Q + R_{\rm s} f_{\rm s})\right)^{3/4}\right]^{-1/3} \tag{8.195}$$

where $c_{\rm S} = 6$ is the Saunders constant, g is the acceleration of gravity, $\alpha_{\rm w} = \max(10^{-5}, 10^{-5}(T_{-\delta} - 273))$ is the thermal expansion coefficient of water and $\nu_{\rm w}$ =1.7558 10^{-6} − 5.1029 $10^{-8} * (T_{-\delta} - T_0)$ + 6.4864 $10^{-10} * (T_{-\delta} - T_0)^2$ (m^{2}s^{-1}) is the kinematic viscosity, with $T_0 = 273.16$ K.

8.12.2 The warm layer

The near ocean warm layer is caused by solar absorption in the top few meters of the ocean during day time. This warm layer can develop when the wind mixing is not strong enough to prevent a stable layer to build up. The result is a diurnal cycle in the surface temperature which is commonly observed by satellite, but not seen in routine bulk SST observations from ships. The warm layer is typically a few meters deep. Although wind mixing erodes the warm later at night, in very low wind conditions a residual warm layer may survive until the next day, and therfore a prognostic variable is needed. The model variable $T_{\rm sk}$ (which is diagnostic over land) is used as a prognostic variable over the ocean.

In the IFS a simple bulk formulation is used based on similarity temperature profiles. It results in the following differential equation for the difference between the temperature just below the cool skin (less than a millimetres deep) $T_{-\delta}$ and the ocean bulk temperature a few metres deep T_{-d}

$$\frac{\partial(T_{-\delta} - T_{-d})}{\partial t} = \frac{Q + R_{\rm s} - R(-d)}{d\rho_{\rm w} c_{\rm w} \nu/(\nu+1)} - \frac{(\nu+1) k u_{*\rm w}}{d\phi_t(d/L)}(T_{-\delta} - T_{-d}) \tag{8.196}$$

where d (=3 m) is the depth scale of the warm layer, ν (=0.3) is the profile shape parameter and $\phi_t(d/L)$ is the stability function with L for the Obukhov length. The solar radiation at depth $-d$ is

$$R(-d) = R_{\rm s}\Sigma_{i=1}^{3} a_i e^{-d b_i} \tag{8.197}$$

with $(a_1, a_2, a_3) = (0.28, 0.27, 0.45)$ and $(b_1, b_2, b_3) = (71.5, 2.8, 0.06\,\mathrm{m}^{-1})$. The stability function is

$$\begin{aligned} \phi_t(-z/L) &= 1 + 5\frac{-z}{L} \qquad for \frac{-z}{L} \geq 0 \\ &= (1 - 16\frac{-z}{L})^{-1/2} \; for \; \frac{-z}{L} < 0 \end{aligned} \tag{8.198}$$

The Obukhov length is

$$L = \rho_w c_w u_{*w}^3 / (kF_d) \tag{8.199}$$

The buoyancy flux F_d is

$$\begin{aligned} F_d &= g\alpha_w[Q + R_s - R(-d)] \qquad for\,(T_{-\delta} - T_{-d}) \leq 0 \\ &= \left(\frac{\nu g \alpha_w}{5d}\right)^{1/2} \rho_w c_w u_{*w}^2 (T_{-\delta} - T_{-d})^{1/2} \quad for\,(T_{-\delta} - T_{-d}) > 0 \end{aligned} \tag{8.200}$$

Equation (8.196) is integrated in time with a fully implicit scheme using $(T_{-\delta} - T_{-d})$ as the prognostic variable. Every time step, the differences $(T_{-\delta} - T_{-d})$ from (8.196) and the difference $(T_{sk} - T_{-\delta})$ from (8.192) are added to the ocean bulk temperature to obtain the ocean skin temperature T_{sk}. With the schemes switched off (by default), the differences are zero and the skin temperature is equal to the bulk SST.

8.12.3 Salinity effect on q_s

Many models use the saturation specific humidity at ocean surface temperature as boundary condition for humidity. However, salinity reduces the saturation value and a reasonable approximation for a salinity of 34 parts per thousand is (Sverdrup *et al.*, 1942)

$$q_s = 0.98\, q_{sat}(T_{sk}) \tag{8.201}$$

The 2% difference due to salinity may look a small effect, but it should be seen as a fraction of the air-sea specific humidity difference, which is typically 15% in relative humidity. So a 2% change in saturation value at the surface is equivalent to a change of 2/0.15=13% in air-sea transfer (see Zeng *et al.*, 1998b for an intercom-parison of schemes).

8.13 NUMERICAL SOLUTION OF THE SURFACE EQUATIONS

8.13.1 Recap of the analytical equations

The water budget ((8.80) and (8.81) with boundary conditions given by (8.96)), the soil energy budget ((8.68) with boundary conditions given by (8.69) and (8.70)) and the ice energy budget (8.189) can be rewritten in a generalised form as

$$\frac{\partial \Psi}{\partial t} = \frac{1}{C}\frac{\partial}{\partial z}\left(\lambda \frac{\partial \Psi}{\partial z} - \gamma\right) + S_\Psi \tag{8.202}$$

The meaning of the different variables in each individual equations is summarized Table 8.16, together with the respective upper and lower boundary conditions, F_Ψ.

8.13.2 Implicit numerical solution

Equation (8.202) is time discretized using

$$\frac{\Psi^{t+1} - \Psi^t}{\Delta t} = \frac{1}{C}\frac{\partial}{\partial z}\left(\lambda \frac{\partial \hat{\Psi}}{\partial z} - \gamma\right) + S_\Psi \tag{8.203}$$

where

$$\hat{\Psi} = \alpha_{impl}\Psi^{t+1} + (1 - \alpha_{impl})\Psi^t \tag{8.204}$$

Table 8.16 *Variables in the generalized soil/ice temperature and water equation.*

Equation	Ψ	C	λ	γ	S_Ψ	UBC	LBC
Soil moisture	θ	1	λ_θ	γ_θ	S_θ	$F_\theta = If - c_8 E_8$	$F_\theta = \gamma_\theta$
Soil temperature	T	$(\rho C)_{\text{eff}}$	λ_T	0	0	$F_T = H^N$	$F_T = 0$
Ice temperature	T_I	$(\rho C)_I$	λ_I	0	0	$F_I = H^N$	$F_{Ns+1} = T_{0,I}$
UBC and LBC stand for upper and lower boundary condition, respectively							

and the semi-implicit coefficient, $\alpha_{\text{impl}} = 1$. If the prognostic variable Ψ is defined at full levels and the fluxes F_Ψ are defined at half-levels (the interface between layers), (8.203) can be discretized in space to give

$$\begin{aligned}
\frac{\hat{\Psi}-\Psi^t}{\alpha_{\text{impl}}} &= \frac{\Delta t}{C_k}\left(\frac{\lambda_{k-1/2}(\hat{\Psi}_{k-1}-\hat{\Psi}_k)}{\Delta z_k \Delta z_{k-1/2}} - \frac{\lambda_{k-1/2}(\hat{\Psi}_k-\hat{\Psi}_{k+1})}{\Delta z_k \Delta z_{k+1/2}} + \frac{\gamma_{k-1/2}-\gamma_{k+1/2}}{\Delta z_k}\right) + \Delta t S_{\Psi,k} \quad k = 2,\ldots,Ns-1 \\
\frac{\hat{\Psi}-\Psi^t}{\alpha_{\text{impl}}} &= \frac{\Delta t}{C_k}\left(\frac{F_\Psi^T}{\Delta z_k} - \frac{\lambda_{k-1/2}(\hat{\Psi}_k-\hat{\Psi}_{k+1})}{\Delta z_k \Delta z_{k+1/2}} + \frac{\gamma_{k-1/2}-\gamma_{k+1/2}}{\Delta z_k}\right) + \Delta t S_{\Psi,k} \quad k = 1 \\
\frac{\hat{\Psi}-\Psi^t}{\alpha_{\text{impl}}} &= \frac{\Delta t}{C_k}\left(\frac{\lambda_{k-1/2}(\hat{\Psi}_{k-1}-\hat{\Psi}_k)}{\Delta z_k \Delta z_{k-1/2}} - \underbrace{\frac{\lambda_{k-1/2}(\hat{\Psi}_k-\hat{\Psi}_{k+1})}{\Delta z_k \Delta z_{k+1/2}}}_{I} + \frac{\gamma_{k-1/2}-\gamma_{k+1/2}}{\Delta z_k}\right) + \Delta t S_{\Psi,k} \quad k = Ns
\end{aligned} \tag{8.205}$$

where the horizontal brace means that the term exists only for the ice temperature equation (because of the bottom temperature boundary condition for ice) and $\Delta z_k, z_k, z_{k-1/2}$, and $z_{k+1/2}$ represent the thickness of layer k, and the depths of its centre, the top and the bottom interface, respectively:

$$\begin{aligned}
\Delta z_k &= D_k = z_{k+1/2} - z_{k-1/2} \\
\Delta z_{k+1/2} &= z_{k+1} - z_k
\end{aligned} \tag{8.206}$$

Equation (8.205) leads to a tridiagonal system of equations

$$\begin{aligned}
&\frac{\hat{\Psi}_{k-1}}{\alpha_{\text{impl}}}\left(\frac{\hat{\lambda}_{k-1/2}}{C_k \Delta z_k}\right) + \frac{\hat{\Psi}_k}{\alpha_{\text{impl}}}\left(1 + \frac{\hat{\lambda}_{k-1/2}}{C_k \Delta z_k} + \frac{\hat{\lambda}_{k+1/2}}{C_k \Delta z_k}\right) - \frac{\hat{\Psi}_{k+1}}{\alpha_{\text{impl}}}\left(\frac{\hat{\lambda}_{k+1/2}}{C_k \Delta z_k}\right) \\
&\quad = \left(\frac{\Psi_k^t}{\alpha_{\text{impl}}} + \Delta t\left(\frac{\gamma_{k-1/2}-\gamma_{k+1/2}}{C_k \Delta z_k}\right) + \Delta t S_{\Psi,k}\right) \qquad k = 2,\ldots,Ns-1 \\
&\frac{\hat{\Psi}_k}{\alpha_{\text{impl}}}\left(1 + \frac{\hat{\lambda}_{k+1/2}}{C_k \Delta z_k}\right) - \frac{\hat{\Psi}_{k+1}}{\alpha_{\text{impl}}}\left(\frac{\hat{\lambda}_{k+1/2}}{C_k \Delta z_k}\right) - \frac{F_\Psi^T}{C_k \Delta z_k} \\
&\quad = \frac{\Psi_k^t}{\alpha_{\text{impl}}} + \Delta t\left(\frac{\gamma_{k-1/2}-\gamma_{k+1/2}}{C_k \Delta z_k}\right) + \Delta t S_{\Psi,k} \qquad k = 1 \\
&\frac{\hat{\Psi}_{k-1}}{\alpha_{\text{impl}}}\left(\frac{\hat{\lambda}_{k-1/2}}{C_k \Delta z_k}\right) - \frac{\hat{\Psi}_k}{\alpha_{\text{impl}}}\left(1 + \frac{\hat{\lambda}_{k-1/2}}{C_k \Delta z_k} + \underbrace{\frac{\hat{\lambda}_{k+1/2}}{C_k \Delta z_k}}_{I}\right) - \underbrace{\frac{\hat{\Phi}_{k+1}}{\alpha_{\text{impl}}}\left(\frac{\hat{\lambda}_{k+1/2}}{C_k \Delta z_k}\right)}_{I} \\
&\quad = \frac{\Psi_k^t}{\alpha_{\text{impl}}} + \Delta t\left(\frac{\gamma_{k-1/2}-\gamma_{k+1/2}}{c_k \Delta z_k}\right) + \Delta t S_{\Psi,k} \qquad k = Ns
\end{aligned} \tag{8.207}$$

with the generalized modified diffusivities, $\hat{\lambda}_{k-1/2}$, defined as

$$\begin{aligned}
\hat{\lambda}_{k-1/2} &= \frac{\Delta t \alpha_{\text{impl}} \lambda_{k-1/2}}{\Delta z_{k-1/2}} \\
I &\begin{cases} \Delta z_{Ns+1/2} & = D_{Ns}/2 \\ \hat{\Psi}_{Ns+1} & = T_{0,I} \end{cases}
\end{aligned} \tag{8.208}$$

where D_{Ns} is the depth of the deepest soil layer. The discretisation above conserves water (energy) and is linearly stable. The coefficients λ and γ are a function of variable at the current time step, Ψ^n.

8.14 CODE

The surface code is fully externalized and it communicates with the rest of the code via interfaces. The architecture of the surface code is organized in modules which contain the parameterisations and normally belong to the surface library only (internal routines).

- ROUTINE_MOD.F90. The module which contains the routine's code ROUTINE with the parameterisation.

Routines which need to be called from anywhere outside the surface code are duplicated as externals. For a given external routine there are associated:

- ROUTINE.h. The routine's interface which is needed in the outside routine to call the external surface routine.
- ROUTINE.F90. The external routine which uses the routine's module ROUTINE_CTL_MOD and contains the call to the surface routine ROUTINE_CTL.
- ROUTINE_CTL_MOD.F90. The module which contains the routine's code ROUTINE_CTL with the parameterisation.

The external routines, for which the above structure apply, are identified hereafter by ⋆ROUTINE⋆. This structure allows for separately compile and run the surface code (e.g. with prescribed atmospheric forcing). The access to surface parameters and fields is done by dedicated routines (⋆SURF_INQ⋆ allows for enquiry mode for scalars, and ⋆SURFBC⋆ for a given set of surface fields). The surface parameterisation computations are shared between the vertical diffusion routine (the routine ⋆SURFEXCDRIVER⋆ called by VDFMAIN, see Chapter 3) and the main surface routine, ⋆SURFTSTP⋆. In ⋆SURFEXCDRIVER⋆, the tile fluxes and skin temperatures are computed: After the elimination part of the tridiagonal system of equations is computed, the energy budget for each tile is computed before back-substitution.

At the start of the model integration, the ⋆SUSURF⋆ setup routine is called to initialize modules specific to the surface code:

- SUSCST. Setup general constants.
- SUSTHF. Setup thermodynamic function constants.
- SUSRAD. Setup radiation constants.
- SUSSOIL. Setup soil constants.
- SUSVEG. Setup vegetation constants.
- SUCOTWO. Setup surface ecosystem exchange constants.
- SUFARQUHAR_MOD. Setup surface ecosystem exchange constants for Farquhar photosynthesis model.
- SUVEXC. Setup surface exchange coefficients constants.
- SUVEXCS. Setup static stability constants.
- SUSFLAKE. Setup static mixed-layer model constants.

The main subroutine of the surface code (⋆SURFTSTP⋆) is called from CALLPAR, with: (a) values of the surface prognostic equations at time step n, convective and large-scale rainfall and snowfall, tile evaporation, sensible and latent heat fluxes, and temperatures, net surface long-wave flux, tile net short-wave flux as inputs; and (b) tendencies for the surface prognostic variables, plus a comprehensive set of diagnostic arrays as outputs. ⋆SURFTSTP⋆ does a sequence of computations and subroutine calls:

- SRFENE. Computes soil energy in each layer, considering vegetation and snow effects.
- SRFSN_DRIVER. Driver routine containing the routines for the multi-layer snow scheme. Inputs: standard deviation of sub-grid-scale orography, snow water equivalent, snow liquid water content, temperature, density and albedo at the current time step, soil temperature and moisture, wind speed and temperature at the lowest model level, turbulent sensible and latent heat fluxes, short-wave and long-wave radiation fluxes, rainfall, snowfall. Outputs: Snow water equivalent,

snow liquid water content, temperature, density and albedo at the next time step, meltwater flux and basal heat flux. SRFSN_DRIVER calls the following routines:

  - SRFSN_VGRID. Compute the vertical grid of the snowpack per each grid point given the snow mass and density at the current time step.
  - SRFSN_REGRID. Redistribute the mass and temperature of each snow layer, if the vertical grid has changed from the previous time-step.
  - SRFSN_WEBAL. Solution of the snow energy and water (frozen and liquid) budget.
  - SRFSN_RSN. Computation of the next time step density fields.
  - SRFSN_ASN. Computation of the next time step albedo fields.

- SRFSN_LWIMP. Solution of the snow energy and water budget and computation of the next time step density and albedo fields, using the single-layer snow scheme (pre-48R1). Inputs: snow depth, temperature, density and albedo at the current time step, soil temperature, short-wave and long-wave radiation fluxes, snowfall, and tile fluxes. Outputs: snow depth, temperature, density and albedo at the next time step, meltwater flux, and basal heat flux. The formulation include a diagnostic treatment of liquid water reservoir in the snow-pack.
- SRFSN. Same as SRFSN_LWIMP but using the former TESSEL snow formulation (available as an option).
- SRFRCG. Computes apparent soil heat capacity, i.e. including effects of soil freezing. Inputs: soil temperature and vegetation covers. Output is volumetric heat capacity.
- SRFT. Solution of the soil heat budget. Inputs: Soil temperature, soil moisture, long-wave radiative flux, snow basal heat flux, volumetric heat capacity, tile evaporation, sensible heat flux and short-wave radiative flux. Output: Soil temperature at the next time step. First the modified heat diffusivity, the soil energy per unit area and the right-hand side of the system of equations are computed. The generalized surface tridiagonal solver, SRFWDIF, is called to solve for the semi-implicit variable, $\hat{T}/\alpha$. The soil temperatures for the next time step are computed at the end.
- SRFI. Solution of the ice heat budget. Inputs: Ice temperature, long-wave radiative flux, tile evaporation, sensible heat flux and short-wave radiative flux. Output: Ice temperature at the next time step. First the modified heat diffusivity, the ice energy per unit area and the right-hand sice of the system of equations are computed. The generalized surface tridiagonal solver, SRFWDIF, is called to solve for the semi-implicit variable, $\hat{T}_I/\alpha$. The ice temperatures for the next time step are computed at the end.
- SRFWL. Solution of the interception layer water budget. Inputs: Interception layer contents, low and high vegetation water cover, maximum capacity of the interception layer, convective and large-scale rainfall, snow evaporation of shaded snow tile, and tile evaporation. Outputs: Interception layer at next time step, convective and large-scale throughfall and tile evaporation collected (or depleting) the interception layer.
- SRFWEXC_VG. First part of the computation of the soil water budget (i.e., computation of the coefficients of the tridiagonal system of equations for $\hat{\theta}$). This includes the partitioning of transpiration into root extraction at the different layers and soil hydraulic coefficients including the effect of frozen water. Inputs: Soil moisture and temperature, convective and large-scale throughfall, snowmelt, tile evaporation, tile evaporation collected (or depleting) the interception layer, and snow evaporation of the shaded snow tile. Outputs: Modified diffusivity for water, right-hand side of the tridiagonal system, and layer depths. Soil properties are defined according to HTESSEL scheme
- SRFWEXC. Same as SRFWEXC_VG but using the former TESSEL soil properties formulation (available as an option).
- SRFWDIF. Generalized surface tridiagonal solver. Inputs: Values of ψ at the current time step, generalized modified diffusivities, soil energy (or water) per unit area, and right-hand side of equations. Output: $\hat{\psi}/\alpha$. The routine computes the coefficients on the left-hand side of the equations and solves the equations using and LU-decomposition and back substitution in one downward scan and one upward scan.
- SRFWINC. Computation of next time step soil water. Inputs: $\hat{\theta}/\alpha$ and current time step soil water. Output: next time step soil water.
- SRFWNG. Bounded-value operator for intercepted water (limited to non-negative values and values below or equal the maximum contents of the interception layer) and soil water (limited

to non-negative values and values below or equal saturation). The "soil column" is scanned from top to bottom and the amount of water needed to satisfy physical limits in each layer are borrowed from the layer below. The water exchanged in this way is accounted for as runoff. Inputs: next time step intercepted water and soil water. Output: Bounded values of the same quantities.

- FLAKE_DRIVER. This is a communication routine between HTESSEL and a FLake routines. It assigns the FLake variables at the previous time step to their input values given by the driving model calls a routine FLAKE_RADFLUX to compute the radiation fluxes,and FLAKE_ENE that returns the updated FLake variables to the driving model. The FLAKE_DRIVER does not contain any Flake physics. It only serves as a convenient means to organize calls of Flake routines.
- SRFVEGEVOL. Performs the time evolution of vegetation parameters at solar midnight in the case of interactive vegetation .

In ⋆SURFEXCDRIVER⋆ a set of routines relevant for the vertical diffusion code are called. These are listed below and discussed in full detail in Chapter 3:

- VUPDZ0. Update of roughness lengths for heat and momentum over ocean and setup over land according to vegetation types.
- VSURF. Definition of bare soil resistance, low and high canopy resistances.
  - COTWORESTRESS. Compute the net assimilation of CO_2 and the canopy conductance with the A-gs model or the Farquhar model.
- SRFCOTWO. Post-processing of the CO_2 fluxes.
- VEXCS. Computation of aerodynamical part of exchange coefficients for heat and moisture, including stability computations.
- VEVAP. Computation of evapotranspiration for each tile.
- VSFLX. Surface fluxes for each tile, defined at time t.
- ⋆SURFSEB⋆. Computation of surface energy balance and skin temperature for each tile. This is called by ⋆SURFEXCDRIVER⋆ only the first time-step, otherwise called by the vertical diffusion (VDFDIFH, see Chapter 3).
- ⋆SURFPP⋆. Computation of quantities at the end of vertical diffusion, including post-processed weather elements and gustiness.
- VOSKIN. Computation of warm/cold skin effects over the ocean (called by ⋆SURFPP⋆).

⋆SURFWS⋆ contains the set of routines relevant for the initialisation of the multi-layer snow fields from a cold start (that is, initial conditions with 1-layer snow scheme) and it is called by CALLPAR. This calls the following routines:

- SRFSN_VGRID. Compute the vertical grid of the snowpack given the total input snow depth.
- SURFWS_INIT. Initialise constants and select parameters for the parameterization, depending among others on time-of-the-day and total snow depth.
- SURFWS_FGPROF. Generate first vertical profiles of snow density and temperature; use the updated snow density and vertical layer depth to compute snow mass of each layer.
- SURFWS_MASSADJ.Update the vertical profiles of snow density in order to conserve the total mass of the snowpack; compute vertical profile of liquid water content in each layer using diagnostic formulation.

Chapter 9

Methane oxidation

Table of contents

9.1 Introduction
9.2 Methane oxidation
9.3 The parametrization
9.3.1 Methane oxidation
9.3.2 Photolysis in the mesosphere
9.4 Code

9.1 INTRODUCTION

A study of stratospheric humidity in analyses and multi-year simulations has shown that the ECMWF system prior to 1999 was capable of producing a broadly realistic distribution of water vapour at, and immediately above, the tropopause, and that the slow upward transfer of water vapour in the tropical stratosphere could be captured quite reasonably given sufficiently fine vertical resolution in the model (Simmons *et al.*, 1999). However, values of water vapour in the tropical upper stratosphere, and throughout much of the extratropical stratosphere, were too low. This deficiency has now been remedied by the introduction of a simple parametrization of the upper-stratospheric moisture source due to methane oxidation. A sink representing photolysis in the mesosphere is also included. The scheme was derived as a simplification of an approach adopted by Peter Stott and Anne Pardaens at the Department of Meteorology, University of Edinburgh, notes on which and helpful references were supplied by Bob Harwood.

9.2 METHANE OXIDATION

Methane is produced by natural and anthropogenic sources at the earth's surface, and is well-mixed in the troposphere. Its volume mixing ratio is currently around 1.7 ppmv. It is carried upwards in the tropical stratosphere and decreases in relative density (due to oxidation) to values of around 0.2–0.4 ppmv around the stratopause. Mean stratospheric descent at higher latitudes results in relatively low values of methane at these latitudes in the middle and lower stratosphere.

Brasseur and Solomon (1984) provide an account of the chemistry of carbon compounds in the stratosphere and mesosphere. The long chain of reactions starting from methane (CH_4) ends with the production of water vapour (H_2O) and molecular hydrogen (H_2) in the stratosphere and mesosphere. This occurs such that the sum

$$2[CH_4] + [H_2O] + [H_2]$$

is approximately uniformly distributed in the absence of precipitation, where [ ] denotes a volume mixing ratio. Le Texier *et al.* (1988) provide calculations of the relative amounts of H_2O and H_2, showing that the predominant production is that of water vapour in the vicinity of the stratopause. They indicate, however, that H_2 production in the mesosphere, and relatively strong descent in winter and early spring at high latitudes, may result in the upper stratosphere being relatively dry in these seasons and latitudes.

There is, nevertheless, good observational evidence that over much of the stratosphere the quantity

$$2[CH_4] + [H_2O]$$

is quite uniformly distributed with a value somewhat over 6 ppmv. Jones *et al.* (1986) provide evidence for this from the LIMS and SAMS instruments on the Nimbus 7 satellite launched in 1978, and a

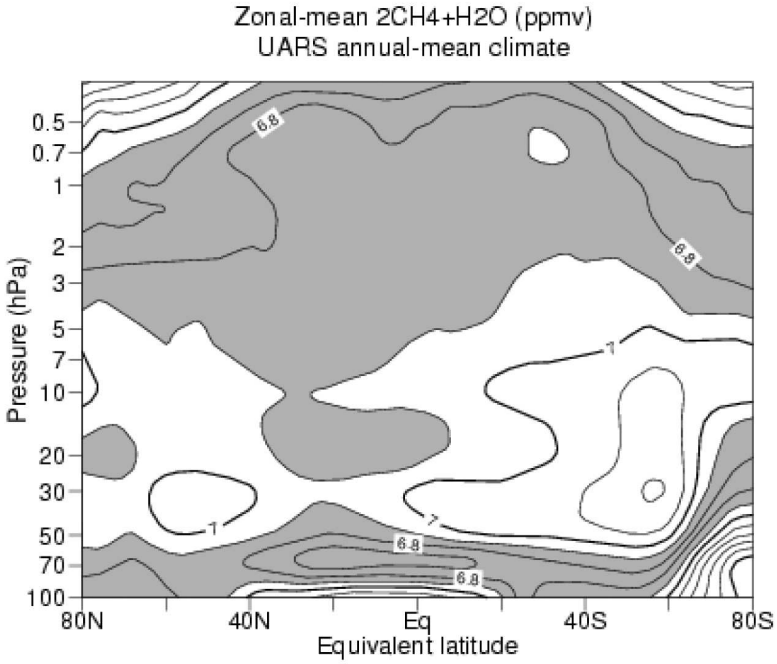

Figure 9.1 *Annual-mean distribution of the sum of twice the volume mixing ratio of methane and of the mixing ratio of water vapour (ppmv) as a function of pressure and potential vorticity (expressed as equivalent latitude), derived from UARS (HALOE, supplemented by CLAES and MLS) data analysed by Randel* et al. *(1998). The contour interval is 0.1 ppmv, and shading denotes the range 6.6–6.9 ppmv.*

particularly clear demonstration is given by Bithell *et al.* (1994) based on HALOE data from the UARS satellite. In a pressure-latitude section at about the austral spring equinox, Bithell *et al*. show the result to fail significantly only below 10 hPa in the high-latitude southern hemisphere due, presumably, to condensation at the very cold temperatures in the Antarctic polar vortex.

Prior to cycle 25r1 of the IFS (operational in 2002), the parametrization used the value 6 ppmv for the sum $2[CH_4] + [H_2O]$. This version was used in production of the ERA-40 reanalyses, which have been found to be generally drier in the stratosphere than the climatology derived by Randel *et al.* (1998) from UARS measurements. From cycle 25r1 to cycle 43r3 (operational until 2018), including ERA-Interim, the parametrization used the value 6.8 ppmv, based on Randel *et al.*'s data as presented in Fig. 9.1. From observations, there is a continuing increase in methane in the atmosphere and the IFS was subsequently showing an increasing underestimate of water vapour compared with MLS data in the stratosphere. The value of the constant $2[CH_4] + [H_2O]$ was therefore increased further in cycle 45r1 (operational in 2018) to 7.7 ppmv for closer agreement with the observations.

9.3 THE PARAMETRIZATION

9.3.1 Methane oxidation

We assume that the volume mixing ratio of water vapour $[H_2O]$ increases at a rate

$$S_{ppmv} = 2k_1[CH_4] \tag{9.1}$$

We further assume that

$$2[CH_4] = 7.7 \text{ ppmv} - [H_2O] \tag{9.2}$$

The rate of increase of volume mixing ratio of water vapour (in ppmv) is thus

$$S_{ppmv} = k_1(7.7 - [H_2O]) \tag{9.3}$$

In terms of specific humidity, q, the source is

$$S_q = k_1(Q - q) \tag{9.4}$$

where (having divided by 1.6×10^6 to convert from volume mixing ratio in ppmv to specific humidity in kg kg^{-1}) the parameter Q has the value 4.81×10^{-6} kg kg^{-1}, or 4.81 mg kg^{-1}.

The rate k_1 could be determined, for example, from a two-dimensional model with comprehensive chemistry, as in the scheme developed at Edinburgh University. However, in this first scheme for use at ECMWF we prescribe a simple analytical form for k_1 which varies only with pressure.

The photochemical life time of water vapour is of the order of 100 days near the stratopause, 2000 days at 10 hPa, and effectively infinite at the tropopause (Brasseur and Solomon, 1984). A prescription of k_1 that gives a reasonable profile up to the stratopause is provided by

$$k_1 = \frac{1}{86400\tau_1} \tag{9.5}$$

where k_1 is given in s^{-1} and the timescale, τ_1, in days, is given in terms of pressure, p, in Pa, by

$$\tau_1 = \begin{cases} 100 & p \le 50 \\ 100\left[1 + \alpha_1 \dfrac{\{\ln(p/50)\}^4}{\ln(10000/p)}\right] & 50 < p < 10000 \\ \infty & p \ge 10000 \end{cases} \tag{9.6}$$

where we define

$$\alpha_1 = \frac{19 \ln 10}{(\ln 20)^4} \tag{9.7}$$

to give a time-scale of 2,000 days at the 10 hPa level.

This parametrization moistens rising air in the tropical stratosphere. This air will earlier have been freeze-dried near the tropopause, where specific humidities can locally fall well below 1 mg/kg. Specific humidities approaching the value Q will be reached near the stratopause. Descent near the poles will bring down air with specific humidity close to Q. Expression (9.4) will then yield a source term that is weaker in polar than in tropical latitudes, so reasonable results may be obtained without imposing a latitudinal variation of k_1. (Strictly, k_1 should vanish in the polar night, where photodissociation does not produce the excited oxygen O(^{1}D), which in turn produces the OH radical, these two species being intimately involved in the production of water vapour from methane.)

9.3.2 Photolysis in the mesosphere

For model versions with an uppermost level at 0.1 hPa, or lower, there is no strong need to include the sink of water vapour that occurs in the mesosphere and above due to photolysis. However, for completeness we include a simple representation of this effect, modifying the source term (9.4) by adding a decay term $-k_2 q$ above a height of about 60 km. The full source/sink term becomes

$$k_1(Q - q) - k_2 q \tag{9.8}$$

As for k_1 we take k_2 independent of latitude with parameters chosen to match the vertical profile of photochemical lifetime presented by Brasseur and Solomon (1984). Specifically,

$$k_2 = \frac{1}{86400\tau_2} \tag{9.9}$$

with

$$\tau_2 = \begin{cases} 3 & p \le 0.1 \\ \left[\exp\left\{\alpha_2 - 0.5(\ln 100 + \alpha_2)\left(1 + \cos\dfrac{\pi \ln(p/20)}{\ln 0.005}\right)\right\} - 0.01\right]^{-1} & 0.1 < p < 20 \\ \infty & p \ge 20 \end{cases} \tag{9.10}$$

and

$$\alpha_2 = \ln\left(\frac{1}{3} + 0.01\right) \tag{9.11}$$

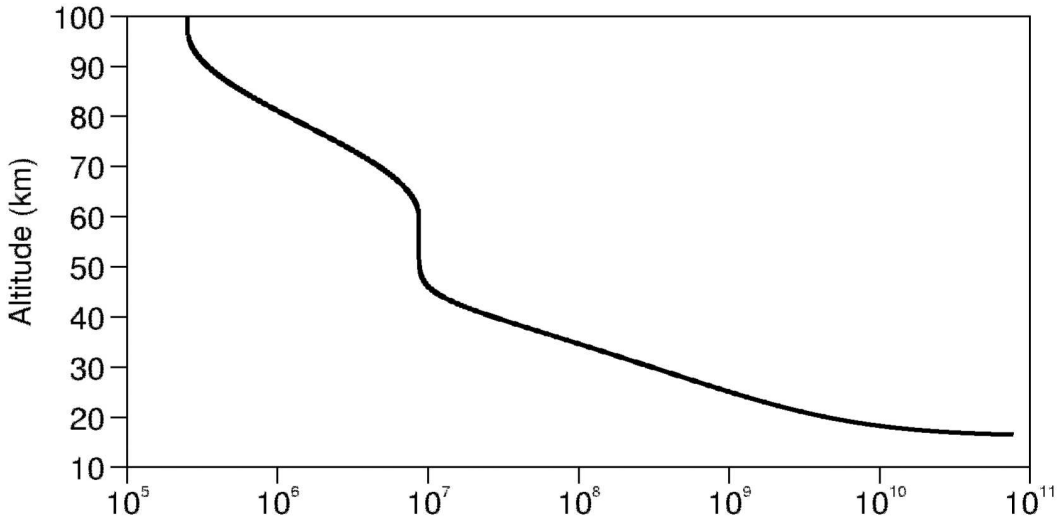

Figure 9.2 *Combined photochemical lifetime, $(k_1 + k_2)^{-1}$, as a function of altitude for the analytical specification given by Equations (9.5) to (9.7) and (9.9) to (9.11).*

The vertical profile of the photochemical lifetime of the combined scheme, $(k_1 + k_2)^{-1}$, is shown in Fig. 9.2, in which we have converted to height as a vertical coordinate assuming an isothermal atmosphere with a temperature of 240 K. Comparison of this profile with that for H_2O shown in Fig. 5.21 of Brasseur and Solomon (1984) indicates reasonable agreement.

9.4 CODE

The calculations for methane oxidation and photolysis of water vapour are performed in subroutine METHOX.

This routine calculates the tendency of water vapour due to methane oxidation and due to photolysis following (9.8). The order of the calculations is as follows.

(i) Find time-scale for methane oxidation following (9.6).
(ii) Solve first part of (9.8).
(iii) Find time-scale for water vapour photolysis following (9.10).
(iv) Solve second part of (9.8).

The setup of the constants used in METHOX is performed in SUMETHOX which is called from SUPHEC. The constants are kept in module YOEMETH. The controlling switch for the methane oxidation is LEMETHOX which is part of namelist NAEPHY.

Chapter 10

Ozone chemistry parametrization

Table of contents

10.1 Introduction
10.2 The ECMWF ozone parametrization

10.1 INTRODUCTION

Ozone is fully integrated into the ECMWF forecast model and analysis system as an additional three-dimensional model and analysis variable similar to humidity. The forecast model includes a prognostic equation for the ozone mass mixing ratio (kg kg^{-1}) given by

$$\frac{\mathrm{d}O_3}{\mathrm{d}t} = R_{O_3}, \tag{10.1}$$

where R_{O_3} is a parametrization of sources and sinks of ozone. Without such a source/sink parametrization the ozone distribution would drift to unrealistic values in integrations longer than a few weeks. The source/sink parametrization must maintain a realistic ozone distribution over several years of integration, without reducing the dynamic variability of ozone. In addition, we would like the parametrization to be able to create an Antarctic ozone hole when the conditions are right.

The parametrization used in the ECMWF model is a hybrid linear ozone model, which we refer to as HLO. Structurally, it is the same form of linear model as that introduced by Cariolle and Déqué (1986), which has been used in the ARPEGE climate model at Météo-France, and in updated form was used in the IFS up to Cy47r3. Unfortunately the ozone fields from the Cariolle scheme were not accurate enough to use in the radiation scheme, so an ozone climatology was used instead. HLO, operational from Cy48r1, is derived differently, and is considered a hybrid model because the coefficients are derived in part from reanalyses of ozone, wind and temperature, and in part from a chemistry model. This has resulted in much improved accuracy and long-term stability in the ozone fields, and as a result the predicted ozone is now used online within the radiation scheme (see Section 2.4.4).

10.2 THE ECMWF OZONE PARAMETRIZATION

The equation used assumes that the net chemical production or destruction of ozone can be described as a specified function of latitude, height and time of year, with perturbations which are locally linear functions of temperature and the total column ozone above the point concerned (as a proxy for variations in incoming UV):

$$R_{O_3} = c_0 + c_1(O_3 - \overline{O_3}) + c_2(T - \overline{T}) + c_3(O_3^{\uparrow} - \overline{O_3^{\uparrow}}), \tag{10.2}$$

where

$$O_3^{\uparrow}(p) = -\int_{p^0} \frac{O_3(p')}{g}\mathrm{d}p'. \tag{10.3}$$

Here c_0 is the mean production rate, c_1 to c_3 are the relaxation rates and $\overline{T}$, $\overline{O_3}$ and $\overline{O_3^{\uparrow}}$ are climatological mean values derived from reanalyses, in all cases functions of latitude, pressure, and month. We currently use version H1.0 of the coefficients, which used the CAMS reanalysis (EAC4) for the years

2005–2012 to define the ozone climatologies, and ERA5 for the same period to define the temperature climatology.

The mean production rate c_0 is diagnosed from a nudging run of the IFS. This used a T255L137 configuration with winds and temperature nudged to ERA5, with the specified ozone production term set to zero but with a 12h relaxation of ozone to the CAMS reanalysis. This enables the diagnosis of what the net ozone production would needed to have been, in order to reproduce the analysed ozone evolution in the presence of the transport estimated from the ERA5 nudging. This diagnosed production rate is processed to give monthly mean fields for the period 2005–2012, from which a zonal mean climatology is then derived. To give a smooth estimate of the production rate, a conservative quartic interpolation method was used to create an L137 version of the original L60 ozone input data.

The coefficients c_1 to c_3 are derived from version 2.3 of the Météo-France ozone scheme (Cariolle and Teyssèdre, 2007), but with several adjustments made to ensure consistency with the diagnosed mean production rate. In the troposphere, the damping rate is set to be at least 10 days at 500 hPa, increasing to at least 2 days at 900 hpa and below, ensuring that lower tropospheric ozone values always stay close to the imposed zonal mean climatology.

Unlike the Cariolle scheme, there is no separate representation of heterogenous chemistry. Rather, the diagnosed mean production rate c_0 includes the mean effect of heterogenous chemistry, including rapid destruction leading to the development of an ozone hole in the Antarctic spring. However, the model is unable to capture variations in this chemistry, and ozone hole variability is driven only by dynamical variability. The ozone chemistry is also the mean of that for the period 2005-2012 which, while reasonably representative of the wider period from the 1990s to the present, does not represent earlier parts of the twentieth century (in particular before the development of the ozone hole in the early 1980s), nor capture the gradual recovery of ozone expected in the decades ahead. Values for mesopheric ozone, at levels above the CAMS reanalysis, are estimated from WACCM model runs and other available data estimates.

Despite these limitations, HLO with H1.0 coefficients reproduces well both the mean state of ozone (as represented by the CAMS reanalysis) and dynamically driven variability throughout the stratsophere and mid- to upper-troposphere, and does so accurately enough for the ozone fields to be used in radiative calculations. The main limitation is an inability to capture chemically-driven interannual variability in the polar vortex of either hemisphere.

Chapter 11
Climatological data

Table of contents

11.1 Introduction
11.2 Data sets and conversion to high resolution GRIB files
11.2.1 Land-sea mask, Glaciers and Lake information
11.2.2 Surface elevation data at 30 arc seconds
11.2.3 Land Use and Land Cover data
11.2.4 Seasonal leaf area index (LAI)
11.2.5 Plants photosythesis types (C3,C4)
11.2.6 Albedo
11.3 Topographic data at target resolution
11.3.1 Smoothing operator
11.3.2 Mean orography
11.3.3 Standard deviation of filtered orography
11.3.4 Parameters for gravity-wave and low level orographic blocking schemes
11.4 Vegetation parameters
11.5 Roughness length
11.6 Albedo
11.7 Aerosols
11.8 Trace gases and ozone
11.9 Soil type
11.10 Sea surface temperature and sea ice cover

11.1 INTRODUCTION

The ECMWF model uses a series of climate fields, that do not depend on initial condition or forecast step. Examples are orography, vegetation type/cover, surface albedo and leaf area index (LAI). Most fields are constant; surface albedo and LAI are specified for 12 months to describe the seasonal cycle. Dependent on the origin, the data comes at different resolutions and different projections. The processing of the data is done offline under the surface type experiment with a series of programs that are part of the so-called "climate fields suite". All the fields are processed in two or more steps. The first step is to convert the original data to a GRIB file on a regular lat/long grid at a resolution of 30x30 arc seconds ($30''$) with 43200×21600 grid points (about 1 km at the equator). This applies to high resolution data. For data at coarser resolution than $30''$, a conversion to GRIB is performed, but the resolution of the original data is kept.

In the second processing step the GRIB data is smoothed and interpolated to the IFS model grid. The climate files are created for all resolutions that are supported by IFS. The current cycle uses a cubic octahedral grid. However, to cater for experimentation with older model versions, linear reduced Gaussian grids are created. A cubic grid has twice the resolution of the linear grid for the same spectral truncation. In the following the individual data sources and processing procedures are discussed in more details.

11.2 DATA SETS AND CONVERSION TO HIGH RESOLUTION GRIB FILES

11.2.1 Land-sea mask, Glaciers and Lake information

(*a*) *Land-Sea-mask*

The land-sea-mask (lsm) is updated in cycle 48R1 (climate.v020). The main data source is Global Surface Water Explorer (GSWE) (Pekel *et al.*, 2016) provided by the Joint Research Centre (JRC). GSWE is a 30m regular grid resolution data from Landsat 5, 7 and 8, covering from 80^{o}N to 60^{o}S and providing information on the spatial and temporal variability of surface water on the Earth since March 1984 (Choulga *et al.*, 2019). The data used for the genration of the final lsm are the updated glacier mask (see subsection II below) and the following:

- JRC Global Surface Water Mapping Layers, v1.2 (main source): The Water Transitions facet of surface water dynamics, shows changes in water classes between the first and last years in which reliable observations were obtained. Classes related to permanent water are: (0) No water – water was not detected in this place, (1) Permanent – unchanging permanent water surfaces, (2) New Permanent – conversion of a no water place into a permanent water place, and (7) Seasonal to Permanent – conversion of seasonal water into permanent water;
- JRC Global Surface Water Metadata, v1.2: The Detections facet, shows the number of water detections in the period 1984-2018; and the Valid_Obs facet, shows the number of valid observations in the period 1984-2018; both combined are used to locate valid water observation grid-cells;
- JRC Monthly Water History, v1.2: The Water facet, which shows water detection for the month, where (0) – NoData, (1) – NotWater, and (2) – Water; used to detect permanent water for years 2010-2018 on a month-by-month basis;
- MERIT DEM: The global digital elevation map at 90 m (3″) resolution (Yamazaki *et al.*, 2017) to detect islands and other land with high accuracy, data based on years 1987-2017.
  Glaciers information is added to the lsm in a consistent way to complete the global coverage north of 80^{o}N and south of 60^{o}S.

The processing procedure of the land-sea-mask emphasizing the consistency between the different products is described in Fig. 11.1.

(*b*) *Glaciers*

All upgraded glacier mask sources were interpolated or gridded on 30 m latitude/longitude regular grid. Grid-cell values vary from 0 (no glacier at all) to 1 (fully covered by glacier) depending on what size of grid-cell is covered by initial data. Data from several regional sources for Svalbard, Iceland, Greenland and Antarctica are merged together and completed globally with GLIMS project data. In addition, Antarctica region was checked for areas with no glacier further from the coast; these grid-cells were forced to be fully covered by glacier, as they might cause unrealistic values in the atmospheric model (e.g. ERA5). The different datasources are outlined below.

- Norwegian Institute data for Svalbard - shapefile with nominal resolution 1:100 000 (data loaded from https://doi.org/10.21334/npolar.2014.645336c7, last accessed 11 January 2021);
- Icelandic Meteorological Office for Iceland – from (Palmason, personal communication 2019), data for the year 2017, nominal resolution 100 m;
- GIMP for Greenland – The Greenland Ice Mapping Project- Howat *et al.* (2014), data based on years 1999-2001, nominal resolution 15 m (https://doi.org/10.5067/B8X58MQBFUPA);
- CryoSat-2 satellite for Antarctica – satellite observations Slater *et al.* (2018), data based on years 2010-2016, nominal resolution 1 km (30″) (https://doi.org/10.5194/tc-2017-223) + extra gap filling in the middle of the continent.
- GLIMS for the rest of the globe -the Global Land Ice Measurements from Space project- GLIMS and NSIDC (2005, updated 2018), data for the year 2017, polygonal boundary dataset (https://doi.org/10.7265/N5V98602).

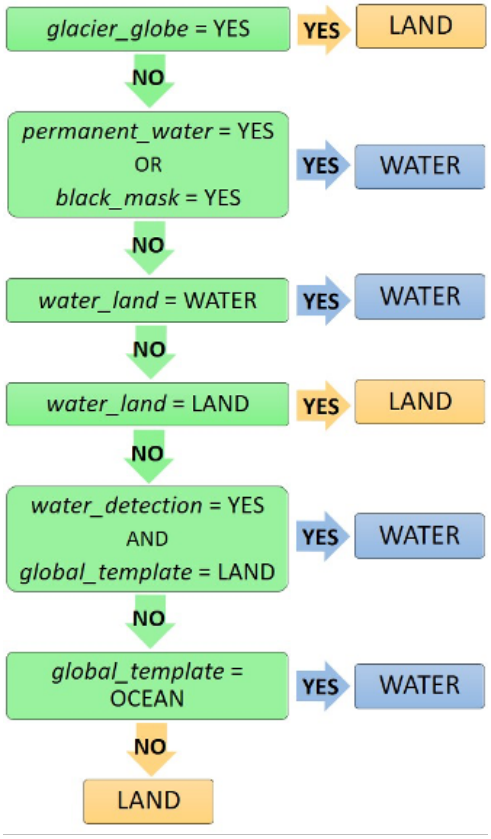

Figure 11.1 *Land-sea-mask processing procedure.*

It is important to mention that glacier cover is now set as fractional map while it was a binary 0/1 map in climate.v015.

(*c*) *Lake cover*

Inland water fractional map is generated by applying an upgraded pixel-by-pixel flooding algorithm Choulga *et al.* (2019) at 1 km resolution over the fractional land sea mask according to the following steps:

(i) fractional land-water mask is translated into "land" (if its value is more than 0.5) and "water" (if its value is 0.5 or less) binary mask;
(ii) by using innovative waterbody separation algorithm Choulga *et al.* (2019) "water" is separated into ocean and inland water bodies
  (a) The algorithm is pixel-by-pixel and iterative with two tuning parameters:
    i. the window width - the checking radius around the water pixel in question (defined in number of pixels);
    ii. the number of iterations - how many times the algorithm must be applied over each water body.

  The parameters depend on the resolution and complexity of the coastline.
  (b) At the end of all iterations an additional visual check is performed to correct significant freshwater coastal lagoons where needed.
  (c) the Azov sea and Maracaibo lake are also considered separately as they are better represented by lake parametrization in IFS.

New approach of fractional inland water mask generation is designed so that it would be as automated as possible and fast and easy to apply with new dataset. Further these consistent lake cover and land sea mask fields are interpolated to the required resolution and grid Choulga *et al.* (2019).

(*d*) *Lake depth*

The lake depth is derived at a 30 arc seconds resolution by combining GEBCO (General Bathymetric Charts of the Ocean) Weatherall *et al.* (2015) over the Caspian Sea and the Azov Sea, Global Relief Model (ETOPO1) Amante and Eakins (2009) over the Great Lakes, GLDBv3 (Global Lake DataBase version 3) Choulga *et al.* (2014) over rest of the globe and indirect estimates based on geological origin of lakes Choulga *et al.* (2014) over grid-cells with missing data.

11.2.2 Surface elevation data at 30 arc seconds

The model orography in the IFS is based on five orographic data sets:

- SRTM30 is the 30″ version of the Shuttle Radar Topography Mission and is the primary data set for the IFS (ftp://topex.ucsd.edu/pub/srtm30_plus/README.V6.0.txt). However, it exists only between 60^oN and 60^oS. The 30″ resolution version of SRTM is provided as an average of the original 30m resolution observations over 30″ × 30″ areas. Although not used in the IFS, SRTM30 is available as a global product through the use of GTOPO30 data (see: http://edcwww.cr.usgs.gov/landdaac/gtopo30/gtopo30.html) north of 60^oN and south of 60^oS.
- GLOBE data (http://www.ngdc.noaa.gov/mgg/topo/globe.html) replaces the areas North of $60^o N$ in SRTM30. GLOBE data is used rather than GTOPO30 because it is believed to be of better quality.
- Antarctic RAMP2 (Radarsat Antarctic Mapping Project DEM Version 2, http://nsidc.org/data/docs/daac/nsidc0082_ramp_dem_v2.gd.html) provided as raw binary data on a 1km grid in Polar Stereographic coordinates is used south of 60^oS.
- BPRC for Greenland (Byrd Polar Research Center, Ohio State University, http://bprc.osu.edu/rsl/greenland_data/dem/index.html) provided as raw binary data on a 1km grid in Polar Stereographic coordinates.
- Iceland Digital Elevation Model (DEM) by IMO (Icelandic Meteorological Service) and NLSI (National Land Survey of Iceland) provided as raw binary data on a 0.5 km grid in Lambert Conformal Conic coordinates.

To obtain a combined global data set on a regular lat/long grid of 30″ resolution, the following processing is applied:

(i) Both SRTM30 and GLOBE are already at the desired 30″ grid, so they are simply merged by replacing in SRTM30 the points North of 60^oN by the GLOBE points. The ocean is not identified in a particular way and is coded with elevation 0.

(ii) The Greenland (BPRC), Iceland, and Antarctica (RAMP2) data are combined and projected on the global 30″ grid. The adopted procedure is to transform the positions of the 30″ latitude/longitude grid into the map coordinates of each of the three DEMs where then a nearest neighbour interpolation is applied. Because the void data surrounding the orography in the three DEMs overlapped with some orography of SRTM30/GLOBE, a modification (cutting/fitting) of the raw data was necessary before interpolation. Also, for consistency with the other DEMs, the Iceland DEM is bi-linearly interpolated from the 0.5 km to the 1 km grid in the map coordinates before inclusion.

(iii) In the merged SRTM30/GLOBE data, all the existing points of the combined RAMP2/BPRC/Iceland data set are used to replace the SRTM30/GLOBE points.

Note: With the land-sea-mask update and a fix in the reading of the original elevation data, a spatial shift could be visible when comparing the new orography fields (climate.v020 for cycle 48R1) with previous cycles versions.

11.2.3 Land Use and Land Cover data

The land use/land cover (LULC) data for ECLand are now updated in CY49R1 based on the ESA-CCI dataset (Defourny, 2014). This dataset provides consistent maps of land cover, based on

Table 11.1 *Land use classification according to BATTS.*

Index	Vegetation type	H/L veg
1	Crops, Mixed Farming	L
2	Short Grass	L
3	Evergreen Needleleaf Trees	H
4	Deciduous Needleleaf Trees	H
5	Deciduous Broadleaf Trees	H
6	Evergreen Broadleaf Trees	H
7	Tall Grass/mixed crops	L
8	Desert	-
9	Tundra	L
10	Irrigated Crops	L
11	Semidesert/sparse vegetation	L
12	Ice Caps and Glaciers	–
13	Bogs and Marshes	L
14	Inland Water	–
15	Ocean	–
16	Evergreen Shrubs	L
17	Deciduous Shrubs	L
18	Mixed Forest/woodland/Broad Savana	H
19	Interrupted Forest	H
20	Water and Land Mixtures	L

the 22 classes from the land cover classification system developed by the United Nations Food and Agriculture Organization (UNLCCS). The latter are derived by combining remotely sensed surface reflectance (AVHRR, SPOT- VEGETATION, MERIS and PROBA-V satellite) and in situ observations which are made consistent throughout the whole 1992-2019 period. The LULC dataset has a 300m spatial resolution, annually available from 1992 to 2019 and provided throught the Copernicus Climate change platform (C3S). A detailed description of the original data is available at https://cds.climate.copernicus.eu/cdsapp#!/dataset/satellite-land-cover?tab=doc. For CY49R1, to represent as best as possible the current LULC status the latest available year (2019) is used.

The ESA-CCI data processing is performed in three steps:

(i) Aggregation of ESA-CCI land cover classes (UNLCCS) from 300m to the target resolution: All pixels at 300m are aggregated to the nearest target resolution grid point generating a fractional cover for each of the ESA-CCI land cover classes by counting the number of 300 m pixels of each class occurring within each grid-cell of the target grid. This step creates maps of fraction cover for each ESA-CCI land cover type at the target grid.

(ii) Conversion to the IFS vegetation types: The output of the target resolution aggregated data from previous step is then loaded and a cross- walking table is applied transforming the fraction cover of each of ESA-CCI land cover classes into fraction cover of the ECLand BATS-based vegetation types (see Table 11.1). The new ECLand land cover types fractions are processed to compute the fractional cover of low and high vegetation, as well as the dominant types of low and high vegetation attributed to each grid point.

(iii) Consistency with the land sea mask: For the target resolution final product, a consistency with the land sea mask is ensured by setting all points where the input land sea mask indicates water ($lsm \leq 0.5$) to 0.

11.2.4 Seasonal leaf area index (LAI)

The MODIS-based monthly LAI climatology (Boussetta *et al.*, 2011) is updated in CY49R1 based on the Copernicus Land Monitoring Service (CLMS) LAI data (GEOV2 LAI) brokered through the C3S platform (Verger *et al.*, 2023).

The total LAI data is processed in 3 steps:

(i) A climatology for the period 2010-2019 was computed at the original resolution of 1 km.
(ii) The climatology (or the original data) total LAI is aggregated to the target grid and disaggregated into low and high vegetation.
(iii) The disaggregation of low/high LAI is further processed for consistency with the land cover map and to conserve the total LAI. For the spatial aggregation and the low/high disaggregation, each 1 km pixel of CLMS LAI (laihr) is aggregated to the target grid total LAI (lai), while the low and high LAI (lai_lv, lai_hv) are derived considering the low vegetation fraction (cvl), high vegetation fraction (cvh), and land sea mask (lsm). The cvl, cvh, and lsm, are derived from aggregating the 300 m ESA-CCI land cover to the CLMS 1 km grid, by applying the same cross-walking table (as described in the previous section). For a particular target grid-cell, the aggregated lai, lai_lv, and lai_hv, consider all the 1 km pixels that fall inside the grid-cell (i.e., i = 1, n pixels, where lsm ¿ 0.5). Each 1 km pixel is then assigned to high or low vegetation, depending on cvl and cvh, and average weighted on cvl or cvh to derive the low and high vegetation lai:

$$lai = \frac{1}{n}\sum_{i=1}^{n} laihr_i \tag{11.1}$$

$$lai\_lv = \frac{1}{W}\sum_{i=1}^{n} w_i \times laihr_i \quad W = \sum_{i=1}^{n} w_i; w_i = \begin{cases} cvl_i & cvl_i > cvh_i \\ 0 & cvl_i \leq cvh_i \end{cases} \tag{11.2}$$

$$lai\_hv = \frac{1}{W}\sum_{i=1}^{n} w_i \times laihr_i \quad W = \sum_{i=1}^{n} w_i; w_i = \begin{cases} cvh_i & cvh_i > cvl_i \\ 0 & cvh_i \leq cvl_i \end{cases} \tag{11.3}$$

A further processing is applied to reinforce land cover consistency and to guarantee total LAI conservation. The low and high vegetation lai for each vegetation type are scaled to guarantee consistency in term of annual maximum. For each vegetation type and grid-point, the maximum annual LAI is computed, and the median of the distribution is taken as representative for that vegetation type lai. A new lai is then computed by scaling the maximum lai in each grid-cell by that median value, weighted by the vegetation fraction:

$$lai_{vty\_max} = \max\left(lai_{vty}\right) \tag{11.4}$$

$$lai_{vty\_max\_med} = median(lai_{vty\_max}) \tag{11.5}$$

$$\alpha = \min(5, \max(0.2, \frac{lai_{vty\_max\_med}}{lai_{vty\_max}})) \tag{11.6}$$

$$lai_{vty} = (1 - cv) \times \alpha \times lai_{vty} + cv \times lai_{vty} \tag{11.7}$$

Finally the updated lai_lv and lai_hv for each calendar month are scaled to conserve the total lai:

$$lai^* = \frac{cvl \times lai\_lv + cvh \times lai\_hv}{cvl + cvh} \tag{11.8}$$

$$\beta = \min(5, \max(0.2, \frac{lai}{lai^*})) \tag{11.9}$$

$$lai\_lv = \beta \times lai\_lv \tag{11.10}$$

$$lai\_hv = \beta \times lai\_hv \tag{11.11}$$

More details on the LULC and LAI data processing can be found in Boussetta and Balsamo (2021) and Nogueira *et al.* (2021).

11.2.5 Plants photosythesis types (C3,C4)

C3/C4 map represent the distribuition of the plants photosynthesis types and they are used in the current ECLand under the Farkuhar module. In the current implementation, C3/C4 map from Still *et al.* (2003) and C4 from the Land-Use Harmonization data set LUH (http://luh.umd.edu/) are used to generate a dominant C3/C4 map according to the following steps:

(i) Map C3/C4 cover from C. Still
Fraction coverage of c3 low vegetation c3l and fraction coverage of c4 low vegetation c4l with resolution of 1/6x1/6 are used to compute the c3 coverage c3S as: c3S = 1 - (c4l / (c3l+c4l)). This map is linearly interpolated to a regular 0.15x0.15 grid, converted to grib, and then interpolated by mars to the target gaussian grid.

(ii) Map c4 from LUH
LUH data can be retrieved from https://luh.umd.edu/data.shtml, but the latest data used in TrendyV9 was provided by LSCE. The data was processed with cdo to reduce it's size.
A specific year can be selected, and for the current implementation, 2019 is selected. The following variables are loaded from the netcdf: 'c4ann','c4per','c3ann','c3per','c3nfx' and the c4 crops fraction (c4C) is computed as: c4C = (c4ann+c4per)/(c3ann+c4ann+c3per+c4per+c3nfx). This field c4C at the original resolution 0.25x0.25 is converted to grib and interpolated by mars to the target gaussian grid.

(iii) Generate dominant C3/C4 map
Since IFS only considers dominant type, a dominant c3/c4 map is generated based on the previous fields assuming that c3S is the the baseline, and replaced by c4C when the dominant vegetation type is crops. This procedure requires as input lsm, cvl and tvl, and the final C3/C4 maps (c3_c4) is given as:
c3_c4 = 3 : by default set as C3 in all land points (including if cvl==0) (0 in ocean points)

$$\begin{aligned} clv > 0 \ \& \ tvl = 1\,(crops) \ \& \ c4C > 0.5 : c3\_c4 = 4 : c4 \ \ from \ \ LHU \\ clv > 0 \ \& \ tvl = 1\,(crops) \ \& \ c4C \leq 0.5 : c3\_c4 = 3 : c3 \ \ from \ \ LHU \\ clv > 0 \ \& \ tvl \neq 1\,(crops) \ \& \ c3S > 0.5 : c3\_c4 = 3 : c3 \ \ from \ \ C.Still \\ clv > 0 \ \& \ tvl \neq 1\,(crops) \ \& \ c3S \leq 0.5 : c3\_c4 = 4 : c4 \ \ from \ \ C.Still \end{aligned} \tag{11.12}$$

11.2.6 Albedo

Snow free surface albedo over land is derived from a 5-year MODIS climatology (http://www.umb.edu/spectralmass/terra_aqua_modis/v006/v004; Schaaf *et al.*, 2002). The data is provided on a 0.05^o regular lat/long grid in the form of weighting parameters associated with the RossThickLiSparseReciprocal BRDF model that best describes the anisotropy of each pixel. The three parameters (f_{iso}, f_{vol}, f_{geo}) are used for the UV-visible (0.3-0.7 μm) and the near-infrared (0.7-5.0 μm). They can be used to construct a direct albedo $A_{dir}(\theta, \lambda)$ at solar zenith angel θ and diffuse albedo

$A_{\mathrm{dif}}(\lambda)$ with the following formulae:

$$\begin{aligned} A_{\mathrm{dir}}(\theta,\lambda) = \; & f_{\mathrm{iso}}(\lambda)(g_{0\mathrm{iso}} + g_{1\mathrm{iso}}\theta^2 + g_{2\mathrm{iso}}\theta^3) \\ & + f_{\mathrm{vol}}(\lambda)(g_{0\mathrm{vol}} + g_{1\mathrm{vol}}\theta^2 + g_{2\mathrm{vol}}\theta^3) \\ & + f_{\mathrm{geo}}(\lambda)(g_{0\mathrm{geo}} + g_{1\mathrm{geo}}\theta^2 + g_{2\mathrm{geo}}\theta^3) \end{aligned} \tag{11.13}$$

$$\begin{aligned} g_{0\mathrm{iso}} &= 1.0, & g_{1\mathrm{iso}} &= 0.0, & g_{2\mathrm{iso}} &= 0.0 \\ g_{0\mathrm{vol}} &= -0.007574, & g_{1\mathrm{vol}} &= -0.070987, & g_{2\mathrm{vol}} &= 0.307588 \\ g_{0\mathrm{geo}} &= -1.284909, & g_{1\mathrm{geo}} &= -0.166314, & g_{2\mathrm{geo}} &= 0.041840 \end{aligned}$$

$$\begin{aligned} A_{\mathrm{dif}}(\lambda) = \; & f_{\mathrm{iso}}(\lambda) g_{\mathrm{iso}} \\ & + f_{\mathrm{vol}}(\lambda) g_{\mathrm{vol}} \\ & + f_{\mathrm{geo}}(\lambda) g_{\mathrm{geo}} \end{aligned} \tag{11.14}$$

$$\begin{aligned} g_{\mathrm{iso}} &= 0.0 \\ g_{\mathrm{vol}} &= 0.189184 \\ g_{\mathrm{geo}} &= -1.377622 \end{aligned}$$

In the previous version of the climate software these formulae were used to construct monthly climatology at 0.05^o resolution of four albedo fields: UV-visible-direct, UV-visible-diffuse, near-infrared-direct, and near-infrared-diffuse. A solar zenith angle $\theta = 0$ is used to generate these fields.

In the new version of the climate software, given that the dependency on the solar zenith angle is now directly computed within the radiation scheme, the 6-components MODIS land-surface albedo climatology (isotropic, volumetric and geometric at the UV/Vis and Near-IR bands) are now fed into the IFS. The three components for each band are used by the IFS as described by Schaaf et al. (2002).

11.3 TOPOGRAPHIC DATA AT TARGET RESOLUTION

11.3.1 Smoothing operator

To avoid spectral aliasing in the process of going from high resolution $30''$ data to model resolution, and for filtering, a general smoothing operator is used in grid point space. The smoothing scale is specified in km rather than degrees, so the filtering scale is uniform over the globe. The smoothing operator is a top hat function with smooth edges (see Fig. 11.2):

$$\begin{aligned} h(r) &= \tfrac{1}{\Delta}, && \text{for } |r| < \Delta/2 - \delta \\ h(r) &= \tfrac{1}{2\Delta} + \tfrac{1}{2\Delta}\cos \pi(r - \Delta/2 + \delta)/2\delta, && \text{for } \Delta/2 - \delta < |r| < \Delta/2 + \delta \\ h(r) &= 0, && \text{for } |r| > \Delta/2 + \delta \end{aligned} \tag{11.15}$$

The edges reduce the amplitude of the side lobes in the spectral domain. The filter is applied by convoluting the input field in two dimensions with $h(r)$, where r is the radial distance. Parameter Δ is the width of the filter and δ is the width of the edge. Sardeshmukh and Hoskins (1984) show that a rotation symmetric smoothing is equivalent to filtering of the total wavenumber. The effect of this operation is equivalent to multiplying the spectrum by a filter function $H(k)$ where H is the square of the Fourier transform of $h(r)$. For all smoothing operations $\delta = 1$ km is selected unless otherwise stated.

11.3.2 Mean orography

Orography, or geopotential height, for the **linear grid** is derived from the $30''$ data in a few steps:

(i) The smoothing operator with a *Pre-Filter-Scale* of 5 km is applied to the $30''$ orography.

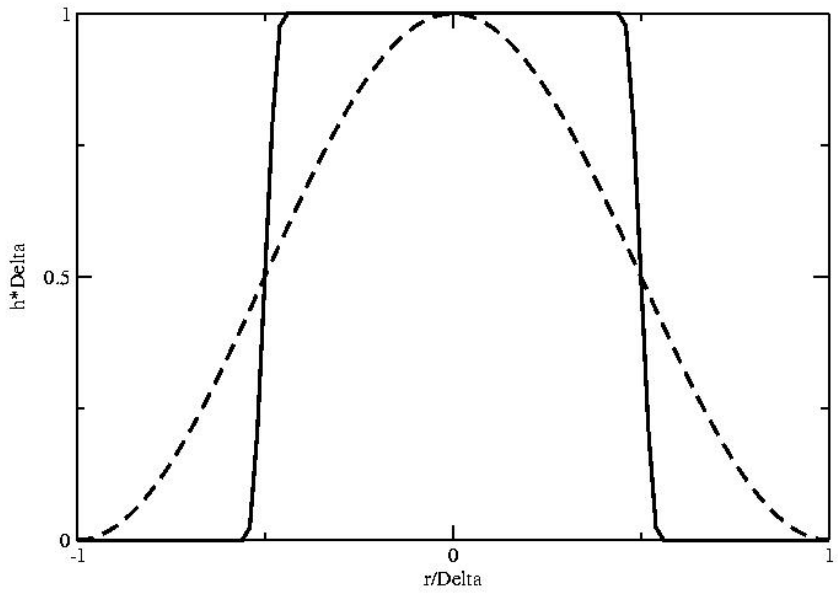

Figure 11.2 *Smoothing operators for $\delta = \Delta/20$ (solid), and $\delta = \Delta/2$ (dashed).*

(ii) The smoothed 30″ data is interpolated to a 5 km grid (reduced Gaussian grid with $NGL = 4000$). For target resolutions with 4000 grid points or more between the south and north poles ($NGL \geq 4000$), the pre-smoothing and interpolation scale of 5 km is reduced to 2 km.
(iii) The 5 km (or 2 km) resolution field is smoothed with the *Filter-Scale* listed in Table 11.2 dependent on the selected target resolution, e.g. at T1279, the linear grid has $NGL = 1280$ and a *Filter-Scale* of 16000 m.
(iv) The resulting field is interpolated to target resolution, e.g. $NGL = 1280$ for a T1279 linear grid.
(v) The grid-point orography is transformed to spectral space at target resolution, e.g. T1279.
(vi) The orographic spectrum is tapered by multiplication with $1/[1+4\{l(l+1)\}^8\{l_{\max}(l_{\max}+1)\}^{-8}]$, where l is the wave number index and $l_{\max}$ is the maximum wave number of the target resolution (e.g. 1279). This is equivalent to smoothing of the grid point field with a $5\nabla^{16}$ operator. The exponent determines the sharpness of the tapering and the factor 5 determines the filtering strength.
(vii) The spectral orography is transformed back to grid point space.

Orography for the **cubic grid** is handled slightly differently. A TL15999 spectral orography is derived first from the high resolution 30″ field, and the lower resolutions are created in spectral space. The cubic grid has twice as much resolution as the linear grid for the same spectral truncation (e.g. for T1279, the number of latitudes between south and north poles is $NGL = 1280$ for the linear grid whereas for Tco1279 $NGL = 2560$ for the cubic grid). The processing steps are as follows:

(i) The smoothing operator with a *Filter-Scale* of 2500 m is applied to the 30″ orography.
(ii) The field from step 1 is interpolated to a reduced Gaussian linear grid corresponding to TL15999 (i.e. with $NGL = 32000$) and transformed to spectral space.
(iii) To reduce the Gibbs phenomenon, a least square method is applied to constrain the curvature of the field, which is evaluated as the Laplacian of orography $\Delta h(s)$, where h is the terrain elevation and s is the horizontal coordinate. The following function is minimised

$$E(h) = \int \{\tilde{h}(s) - h(s)\}^2 ds + \lambda \int \{\Delta\tilde{h}(s)\}^2 ds \tag{11.16}$$

which is equivalent in spectral space to (http://www.ppsloan.org/publications/StupidSH36.pdf)

$$\tilde{h}_l^m = \frac{h_l^m}{1 + \lambda \{l(l+1)\}^2 \{l_{\max}(l_{\max}+1)\}^{-2}} \tag{11.17}$$

Table 11.2 *Resolution dependent parameters for the generation of orographic fields. NGL indicates the number of points between north and south poles.*

NGL	*Fact*	*Pre-Filter-Scale (m)*	*Filter-Scale (m)*
160	0.001	5000	125000
256	0.001	5000	78000
320	0.001	5000	62500
400	0.001	5000	50000
512	0.001	5000	40000
640	0.001	5000	30000
800	0.001	5000	25000
1024	0.001	5000	20000
1280	0.001	5000	16000
1600	0.01	5000	14000
1920	0.02	5000	12000
2048	0.02	5000	10000
2560	0.02	5000	8000
3200	0.02	5000	6500
4000	0.03	-	5000

where h_l^m and $\tilde{h}_l^m$ are the spectral coefficients of the orography before and after constraining the curvature. Parameter $l_{\max}$ is the highest wave number (15999 in this case). In fact this is a 4th order filter with a damping factor of λ for the highest wave number. The damping factor λ is selected such that the square of the curvature is reduced by a specified factor, i.e. $Fact = \int\{\Delta\tilde{f}(s)\}^2 ds / \int\{\Delta f(s)\}^2 ds$. Reduction factor *Fact* is selected subjectively for different target resolutions (see Table 11.2).

(iv) The TL15999 spectral orography of the previous step is truncated at target resolution.

(v) To avoid minor aliasing during the time integration in the model, the spectrum is further filtered with a sharp filter to reduce the highest wave numbers. The spectrum is multiplied by $1/[1+4\{l(l+1)\}^{16}\{l_{\max}(l_{\max}+1)\}^{-16}]$, where l is the wave number index and $l_{-\max}$ is the maximum wave number of the target resolution (e.g. 1279). This is equivalent to a smoothing of the grid point field with a ∇^{32} operation The exponent determines the sharpness of the tapering and the factor 4 determines the filtering strength.

(vi) The spectral orography is transformed back to grid point space.

Although the processing and filtering is designed to achieve a compromise between sharpness of the orography and limited rippling (Gibbs phenomenon), the spectral representation still shows some rippling near steep orography. Fig. 11.3 shows the orography at Tco1279 resolution.

11.3.3 Standard deviation of filtered orography

To compute the standard deviation of the small scale orography for well defined scales all over the globe (also in polar regions where the grid point spacing is much less than 1 km), the 30″ field is filtered twice with filter (11.15), shown in Fig. 11.2. The first time, the smallest scales are filtered out by using $\Delta_1 = 2$ km and $\delta_1 = 1$ km. The second filtering is done with $\Delta_2 = 20$ km and $\delta_2 = 1$ km, to isolate the larger scales. Subsequently the following processing steps are performed:

(i) The square of the difference is computed of the two 30″ resolution filtered fields.

(ii) For every point of the target grid, the result of (i) is averaged over the grid square of the target grid.

(iii) The square root is calculated of the target grid point.

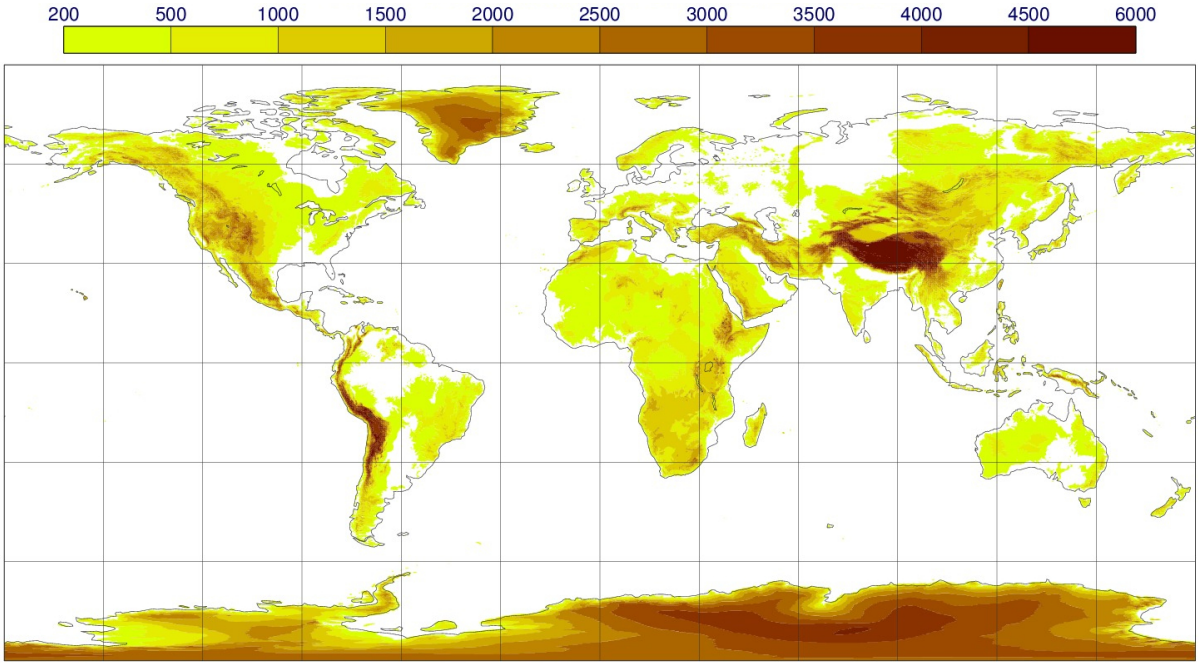

Figure 11.3 *Orography at Tco1279 resolution.*

The resulting field is shown in Fig. 11.5 for the Tco1279 model. The spectral filter for the small scale orography corresponding to the procedure described above is

$$
\begin{aligned}
H_{\mathrm{flt}}(k) = \quad & \frac{1}{\Delta_1^2}\left\{\frac{\sin(k\Delta_1/2-k\delta_1)}{k}+\frac{\sin(k\Delta_1/2+k\delta_1)}{k}\right. \\
& \left.+\frac{\cos(\pi/2+k\Delta_1/2)\sin(\pi/2+k\delta_1)}{\pi/(2\delta_1)+k}+\frac{\cos(\pi/2-k\Delta_1/2)\sin(\pi/2-k\delta_1)}{\pi/(2\delta_1)-k}\right\}^2 \\
& -\frac{1}{\Delta_2^2}\left\{\frac{\sin(k\Delta_2/2-k\delta_2)}{k}+\frac{\sin(k\Delta_2/2+k\delta_2)}{k}\right. \\
& \left.+\frac{\cos(\pi/2+k\Delta_2/2)\sin(\pi/2+k\delta_2)}{\pi/(2\delta_2)+k}+\frac{\cos(\pi/2-k\Delta_2/2)\sin(\pi/2-k\delta_2)}{\pi/(2\delta_2)-k}\right\}^2
\end{aligned}
\tag{11.18}
$$

The filter of (11.18) is shown in Fig. 11.4. The filter has the shape of a band pass filter with the lower bound determined by Δ_2, and the upper bound by Δ_1. Parameters δ_1 and δ_2 control the level of overshooting. The parameter selection is based on the following ideas. First the filter should drop off quickly near $k = 0.0012$ m^{-1}, because the spectrum has an aliasing tail (see Beljaars *et al.*, 2004b). Secondly we would like to cut off below scales of 5 km because we are interested in scales smaller 5 km for TOFD. However, this leads to a very narrow filter with noisy results. Therefore we select a longer filtering scale of about 20 km. The edges of the filter defined by $H_{\mathrm{flt}} = 0.0005$ are $k = 0.00014$ m^{-1} and $k = 0.00112$ m^{-1} respectively. These wave numbers correspond to length scales (half wave length) of 22000 m and 3000 m. The advantage of having a broad filter is that resulting standard deviations will be less noisy.

With an orography spectrum F_{o} and the band pass filtering with (11.18), the following spectrum is obtained for the small scale orography

$$F_{\mathrm{flt}}(k) = F_{\mathrm{o}}(k)H_{\mathrm{flt}}(k) \tag{11.19}$$

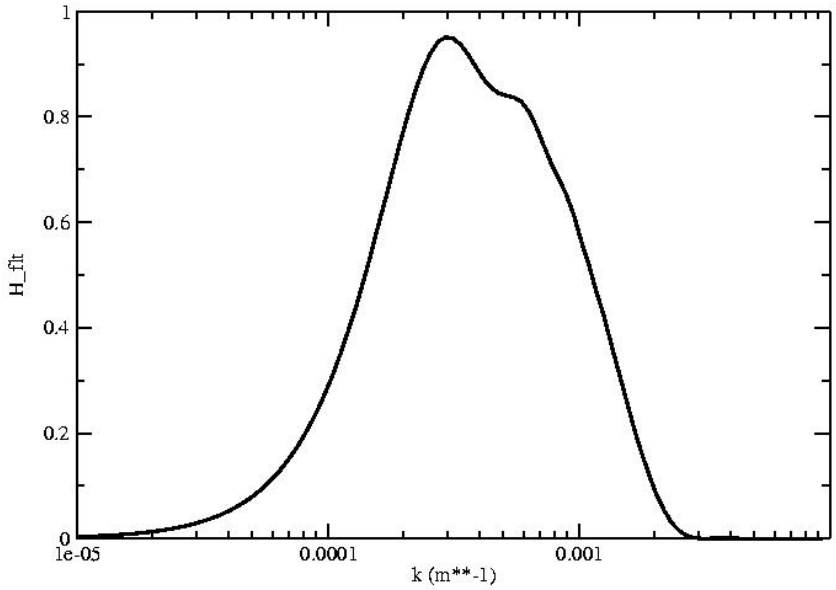

Figure 11.4 *Spectral filter corresponding to difference of two smoothing operations with:* $\Delta_1 = 2000\ m$, $\Delta_2 = 20000\ m$, $\delta_1 = 1000\ m$, $\delta_2 = 1000\ m$.

The variance of the sub-grid orography as computed from the filtered fields is

$$\sigma^2_{\text{flt}} = \int F_{\text{o}}(k) H_{\text{flt}}(k) dk \tag{11.20}$$

$$\approx F_{\text{o}}(k_{\text{flt}}) \int H_{\text{flt}}(k) dk \tag{11.21}$$

$$= F_{\text{o}}(k_{\text{flt}}) I_{\text{H}} \tag{11.22}$$

The approximation is based on the idea that the band width of the filter is small and that the spectrum of the orography does not change much over the band width of the filter. So, by computing the variance of the small scale orography σ^2_{flt}, an estimate is obtained of the orographic power spectrum at wavelength k_{flt}:

$$F_{\text{o}}(k_{\text{flt}}) = \sigma^2_{\text{flt}} / I_{\text{H}} \tag{11.23}$$

For a power spectrum with exponent n_1 in the range of the band filter, a filter wave number can be defined that satisfies (11.22) exactly

$$k^{n_1}_{\text{flt}} = \left\{ \int k^{n_1} H(k) dk \right\} \left\{ \int H(k) dk \right\}^{-1} \tag{11.24}$$

With the filter parameters $\Delta_1 = 2000$ m, $\delta_1 = 1000$ m, $\Delta_2 = 20000$ m, $\delta_2 = 1000$ m, and $n_1 = -1.9$, the following results are found from numerical integration:

$$I_{\text{H}} = 0.00102\,\text{m}^{-1},\ k_{\text{flt}} = 0.00035\,\text{m}^{-1} \tag{11.25}$$

These numbers are used in the parametrization scheme to account for the way the standard deviation of filtered orography was generated.

11.3.4 Parameters for gravity-wave and low level orographic blocking schemes

The parameters that are needed for the sub-grid orography scheme characterize the variability of the orography between horizontal scales of 5 km and up to 4 times the target resolution for cubic grids, or up to twice the target resolution for linear grids. The scales larger than 5 km are considered to be the main contributors to low level blocking and gravity wave generation. Since cycle 48r1, the subgrid

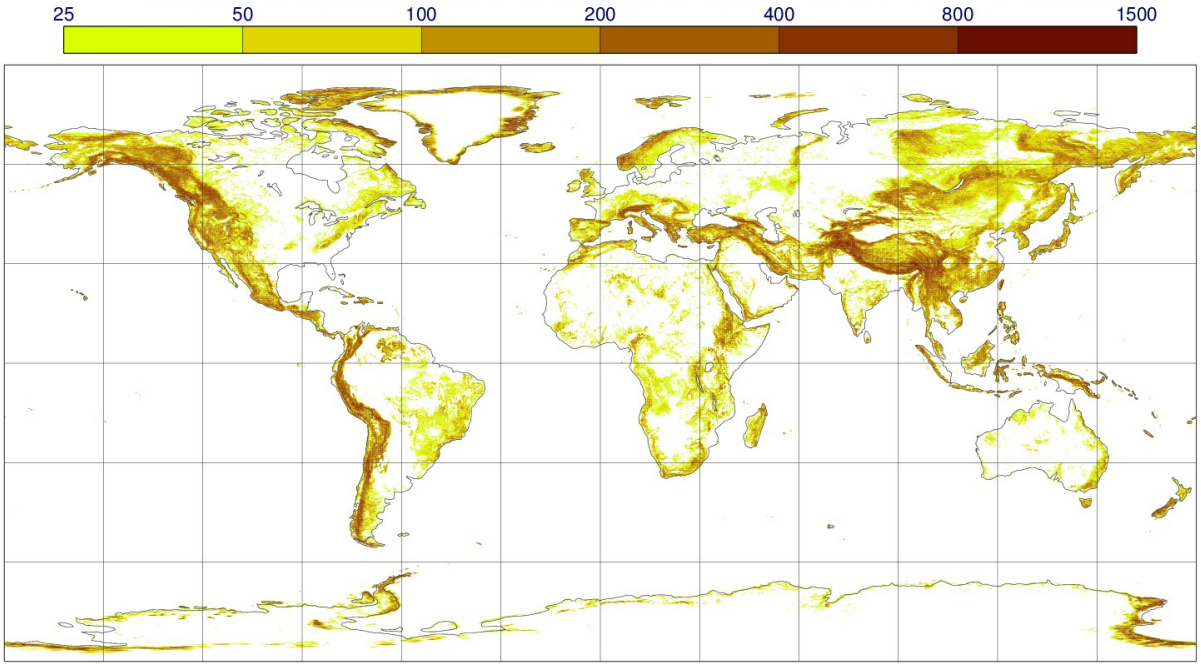

Figure 11.5 *Standard deviation of the filtered orography for the Tco1279 model, to support the TOFD parametrization.*

orography for the ororaphic flow blocking and gravity wave drag defines scales up to 4 times the target resolution as subgrid for cubic grids. This accounts for the 'effective' resolution of the model i.e. scales that are poorly resolved by the model dynamics.

The parameters are: standard deviation μ_{GW}, anisotropy γ_{GW}, orientation θ_{GW}, and slope σ_{GW}. They are computed as follows (see Lott and Miller, 1997; Baines and Palmer, 1990).

(i) The smoothing operator with a scale of *Pre-Filter-Scale*, is applied to the 30″ orography and this is interpolated to a 2′30″ grid (0.041666 by 0.041666 degree) if $NGL < 4000$, a 1′ grid if $4000 \leq NGL < 8000$ or a 30″ grid if $NGL \leq 8000$.

(ii) The smoothing operator with a scale of 4x*Filter-Scale* for cubic grids, to account for the effective resolution, or *Filter-Scale* for linear grids is applied to this pre-filtered orography. A difference between this and the result of step (i) is then taken.

(iii) For every point of the difference field, $(\partial h/\partial x)$ and $(\partial h/\partial y)$ are computed by central differencing with help of the points to the north, south, east and west.

(iv) Parameters K, L, M O, and P are computed for all the points of the 5 km (or 2 km or 1 km) grid:

$$K = \frac{1}{2}\left\{\left(\frac{\partial h}{\partial x}\right)^2 + \left(\frac{\partial h}{\partial y}\right)^2\right\}$$
$$L = \frac{1}{2}\left\{\left(\frac{\partial h}{\partial x}\right)^2 - \left(\frac{\partial h}{\partial y}\right)^2\right\}$$
$$M = \left\{\left(\frac{\partial h}{\partial x}\right)\left(\frac{\partial h}{\partial y}\right)\right\}$$
$$O = h^2$$
$$P = h$$

(v) For every point of the target grid, K, L, M, O and P are aggregated by conservative interpolation of the 5 km (or 2 km or 1 km) points, i.e. the fraction of every grid square that overlaps with the target grid square is included with the proper weight.

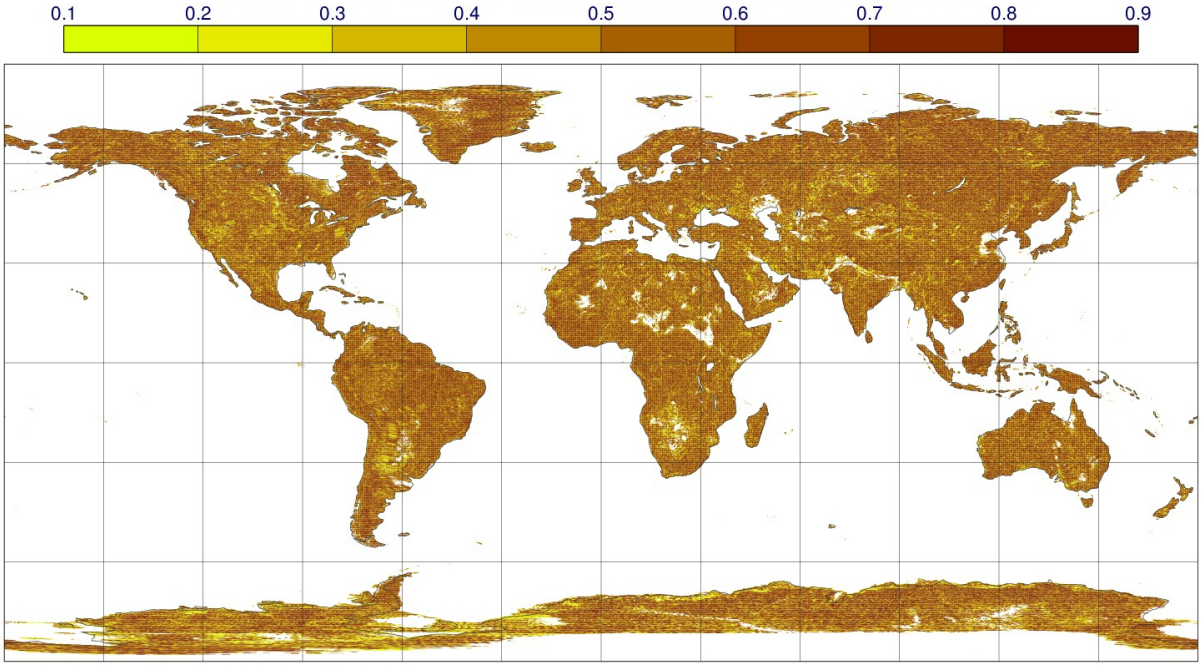

Figure 11.6 *Anisotropy γ_{GW} of sub-grid orography (1 indicates isotropic, 0 means maximum anisotropy).*

(vi) Anisotropy γ_{GW}, orientation θ_{GW}, and slope σ_{GW} are computed from K, M and L using

$$\gamma_{GW}^2 = \frac{K - (L^2 + M^2)^{1/2}}{K + (L^2 + M^2)^{1/2}}$$
$$\theta_{GW} = \frac{1}{2}\text{atan}\frac{M}{L}$$
$$\sigma_{GW}^2 = K + \sqrt{L^2 + M^2}$$

and the standard deviation μ_{GW} is computed according to

$$\mu_{GW}^2 = O - P^2$$

Results are shown in Figs 11.6, 11.7, 11.8 and 11.9.

11.4 VEGETATION PARAMETERS

Vegetation is represented by seven climatological parameters: vegetation cover of low vegetation, vegetation cover of high vegetation, low vegetation type, high vegetation type, leaf area for low vegetation, leaf area for high vegetation and C3/C4 plant photosynthesis types. The first four parameters are derived from the 300m ESA-CCI data by aggregating over the target grid squares. The fractional covers for low and high vegetation are obtained by combining the fractions from all the low and high vegetation types of Table 11.1. The index of the dominant low and high vegetation types are also coded as climatological fields for use by the land surface scheme. The latter two fields can not be interpolated by standard procedures to another resolution. The resulting fields are shown in Figs 11.10, 11.11, 11.12 and 11.13. Table 11.3 and Table 11.4 contain statistical information on the number of points in each vegetation class.

Leaf area index is based on CLMS LAI and is specified as a monthly climatology. The geographical distribution is shown for January and July in Figs 11.14, 11.15, 11.16 and 11.17. The model interprets these fields as the climatology for the 15th of the month and does a linear interpolation between months to obtain a smooth seasonal cycle.

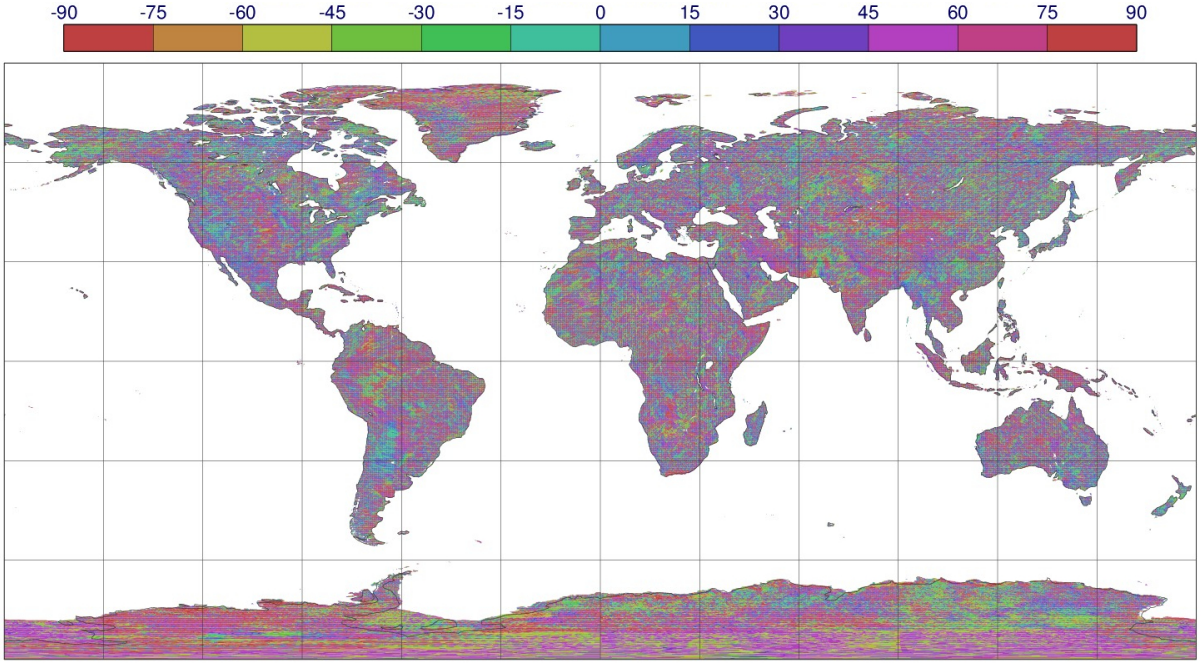

Figure 11.7 *Orientation θ_{GW} of sub-grid orography. The field is in radians and has values between $-\frac{1}{2}\pi$ and $\frac{1}{2}\pi$). For clarity the plot has been converted to degrees with values between -90 and +90.*

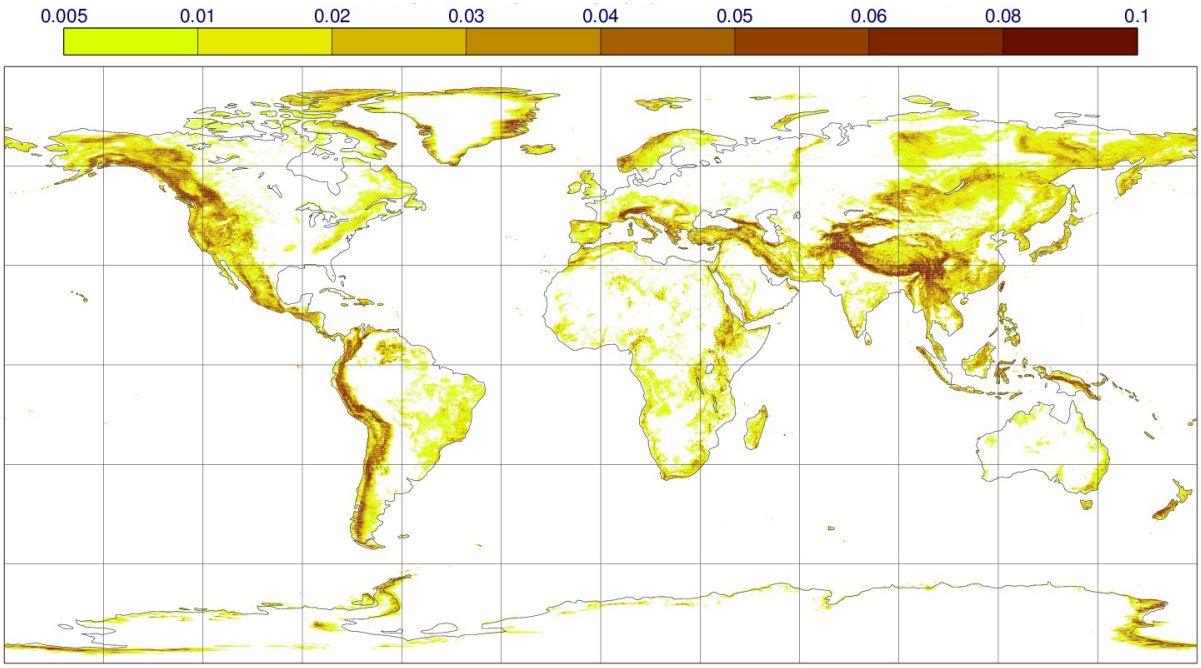

Figure 11.8 *Slope σ_{GW} of sub-grid orography.*

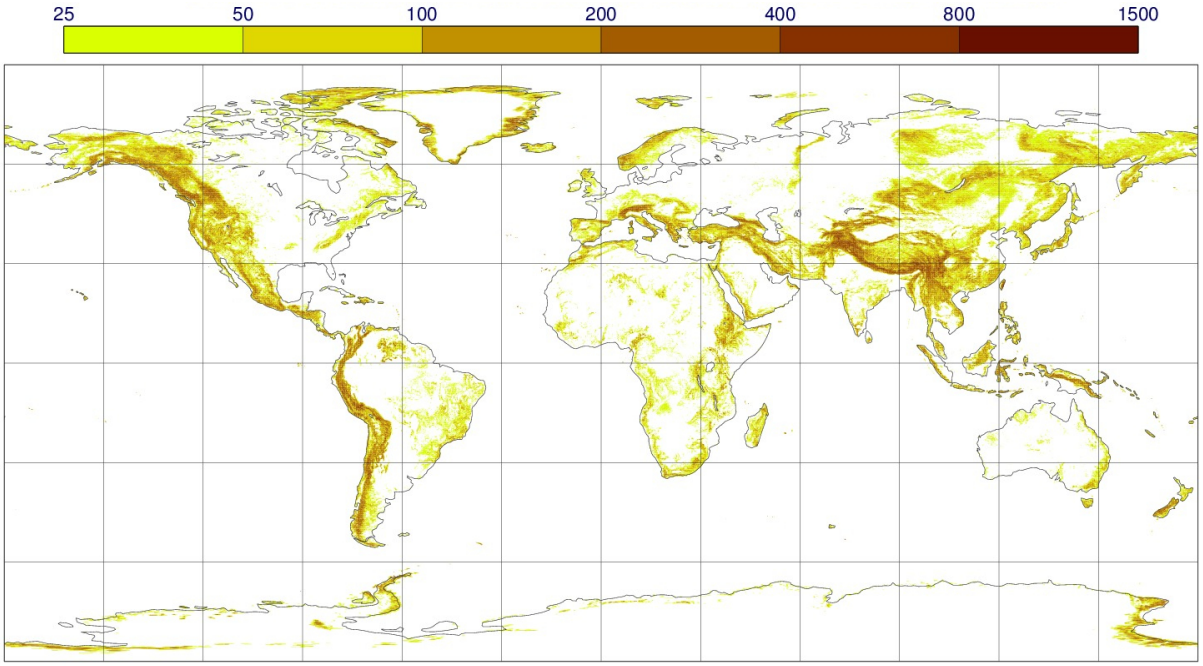

Figure 11.9 *Standard deviation μ_{GW} of sub-grid orography.*

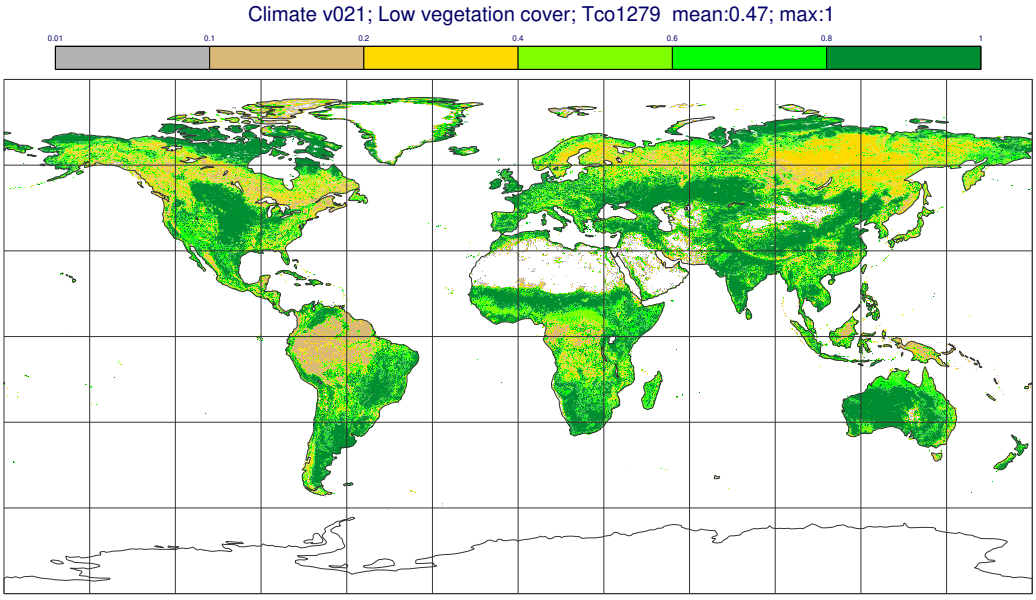

Figure 11.10 *Fractional cover of low vegetation.*

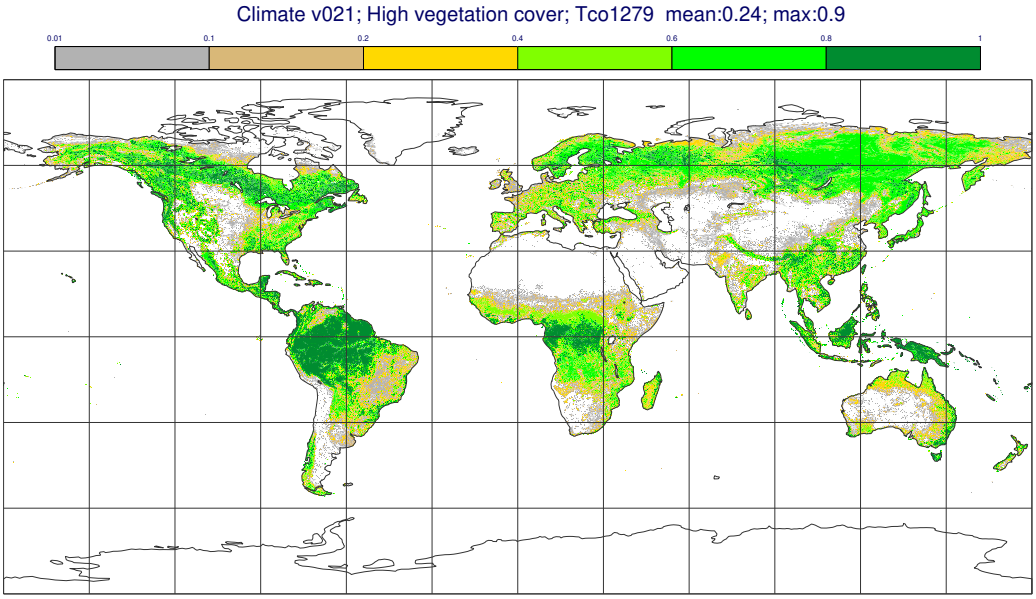

Figure 11.11 *Fractional cover of high vegetation.*

Table 11.3 *Percentage of land points at Tco1279 for each low vegetation type.*

Index	Vegetation type	Percentage of land points
1	Crops, Mixed Farming	11.5
2	Short Grass	31.8
7	Tall Grass/ Mixed crops	6.4
9	Tundra	1.3
10	Irrigated Crops	1.8
11	Sparse Vegetation	5.7
13	Bogs and Marshes	2.0
16	Evergreen Shrubs	7.3
17	Deciduous Shrubs	14.2
20	Water and Land Mixtures	0
-	Remaining land points without low vegetation	17.6

C3/C4 map are derived from Still *et al.* (2003) and C4 from the Land-Use Harmonization data set LUH (http://luh.umd.edu/) based on the dominant type procedure described above. An example of the resultant fiels is shown in Figs 11.18

11.5 ROUGHNESS LENGTH

Roughness lengths are not prepared as climatological fields, but derived in the model from vegetation type, vegetation cover, and snow cover through a correspondence table (see the Chapter on land surface modelling). Results with the Tco1279 model are shown in Figs 11.19 and 11.20 for 1 August 2017.

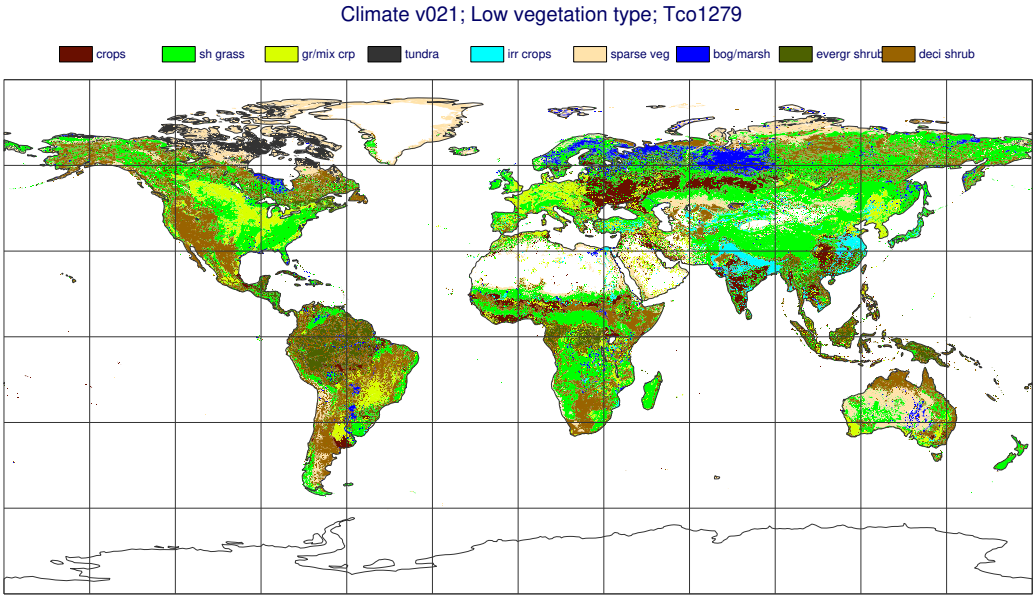

Figure 11.12 *Low vegetation type.*

Table 11.4 *Percentage of land points at Tco1279 for each high vegetation type.*

Index	Vegetation type	Percentage of land points
3	Evergreen Needleleaf Trees	13.9
4	Deciduous Needleleaf Trees	6.4
5	Deciduous Broadleaf Trees	24.7
6	Evergreen Broadleaf Trees	16.9
18	Broadleaf-Savana	7.1
19	Interrupted Forest	0.0
–	Remaining land points without high vegetation	30.7

11.6 ALBEDO

Monthly albedo fields at target resolution are derived form the pre-computed high resolution 0.05^o fields described in section 11.2.6 in the following way:

(i) The resolution field is smoothed with the *Filter-Scale* listed in Table 11.2 dependent on the selected target resolution, e.g. at Tco1279, the linear grid has $NGL = 2560$ and a *Filter-Scale* of 8000 m.
(ii) The resulting field is interpolated to target resolution.

Given that the dependency on the solar zenith angle is now directly computed within the radiation scheme, the 6-components MODIS land-surface albedo climatology (isotropic, volumetric and geometric at the UV/Vis and Near-IR bands) are now fed into the IFS. The three components for each band are used by the IFS as described by Schaaf *et al.* (2002). The fields for July are shown in Figs 11.21 to 11.26 and the corresponding previously used 4-components direct and diffuse UV/Vis and Near-IR fields are

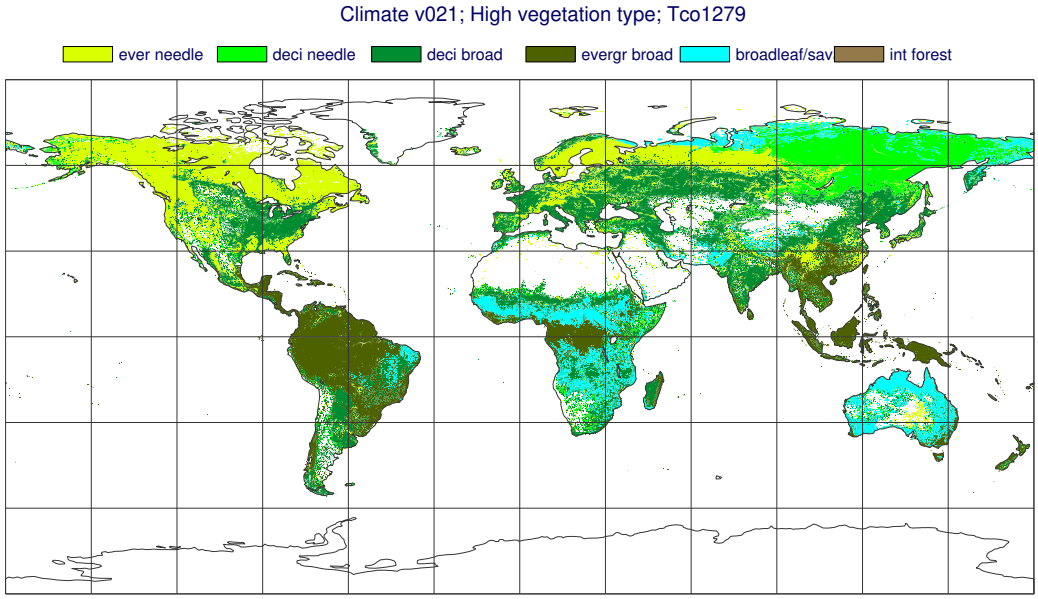

Figure 11.13 *High vegetation type.*

shown in Figs 11.27 to 11.30. To obtain a smooth evolution in time, the model does a linear interpolation between successive months, assuming that the monthly field applies to the 15th of the month.The model adapts the background albedo over water, ice and snow as documented in the chapter on radiation.

11.7 AEROSOLS

Since Cy43r3 five types of tropospheric aerosols divided into 10 species are considered in the model. The main types are sea-salt, mineral dust, organic carbon, black carbon and sulfates and the seasonal AOD geographical distribution is shown in Fig. 11.31. Sea salt and mineral dust are further divided each into 3 size bins while the organic carbon has an hydrophilic and an hydrophobic component. The aerosol climatology is derived from the aerosol model developed by the Copernicus Atmospheric Monitoring Service and coupled to the IFS, and the implementation in the IFS is described in Bozzo *et al.* (2017). Well-mixed (vertically and horizontally) tropospheric background aerosols with an optical thickness of 0.05 and stratospheric background aerosols with an optical thickness of 0.0045 are added to the climatological amounts with a rate of change of optical thickness with pressure of 0.037 and 0.233 /atm respectively. A smooth transition from troposphere to stratosphere is obtained by weighting the concentrations with a function which uses the temperature profile to compute the thickness of the stratosphere.

11.8 TRACE GASES AND OZONE

A new description of the radiatively active trace gases has been introduced in the IFS with Cy35r3 on 8 September 2009. It replaces the previous globally averaged values for CO_2, CH_4, N_2O, $CFCl_3$, CF_2Cl_2 (with possibility of defining their history since 1850) by bi-dimensional (latitude/height) climatologies derived from either the MOBIDIC model or, for CO_2, CH_4 and O_3, from the GEMS reanalysis effort. The effect of $CHFCl_2$ and CCl_4 have also been added using their globally-defined concentrations. A discussion of the impact of these new climatologies and of further model developments (dissipation

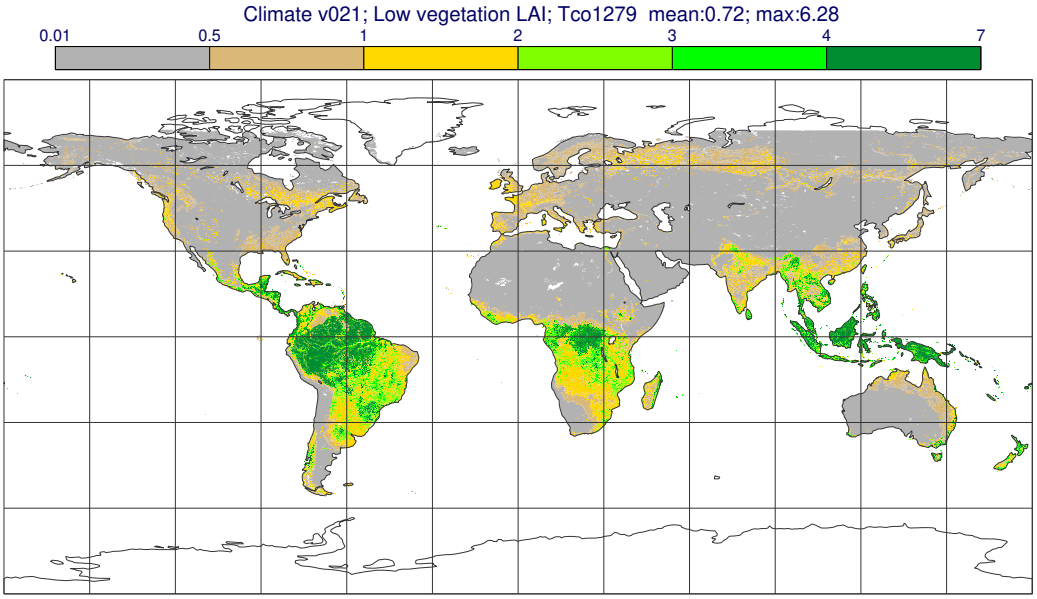

Figure 11.14 *LAI climatology for low vegetation in January.*

of non-orographic gravity-waves) can be found in Bechtold *et al.* (2009). With Cy40r3 the GEMS-based climatology for CO_2, CH_4 and O_3 has been revised and a new climatology was computed based on the MACC reanalysis for the period 2003-2011 (Inness *et al.*, 2013). In Cy43r1 the O_3 climatology was further revised using the most recent CAMS Interim Reanalysis (CAMSiRA, Flemming *et al.* (2016)) (Fig. 11.32). The CAMSiRA O_3 distribution shows better agreement with independent O_3 concentration estimates, reducing by $\sim$15% the O_3 amount between 10 hPa and 1 hPa with respect to the MACC-based climatology (Fig. 11.33). The change in O3 concentration has a direct impact on the temperature in the mid-upper stratosphere. The model climate shows a cooling in the zonal mean, annual mean temperature above 10 hPa and this reduces the positive bias against ERA40. The long-term evolution of CO_2 and CH_4 is described by yearly globally averaged volume mixing ratios over the marine surface (Hansen and Sato, 2004) and applied to the zonal-mean climatologies scaled by their global mean mixing ratio at the surface.

11.9 SOIL TYPE

Soil types are derived from the FAO/UNESCO Digital Soil Map of the World, DSMW (FAO, 2003), which exists at a resolution of $5' \times 5'$ (about 10 km). FAO DSMW provides the information on two levels of soil depth namely 0–30 cm and 30–100 cm. Since the root zone is most important for the water holding, the 30–100 cm layer is selected for H-TESSEL. To interpolate to model target resolution the INTERPOL utility is applied. INTERPOL's interpolation option is used for resolutions with $NGL \geq 2048$ (10 km), whereas the nearest neighbour option is chosen for $NGL < 2048$. In all cases, the the dominant soil type is selected, which has the advantage of preserving hydraulic properties when moving across various model resolutions (Balsamo *et al.*, 2009). The climate field used by the model has an index from 1 to 7 corresponding to the soil textures (see Fig. 11.34): 'coarse' (1),'medium' (2), 'medium fine' (3), 'fine' (4), 'very fine' (5), 'organic' (6), and 'tropical organic' (7).

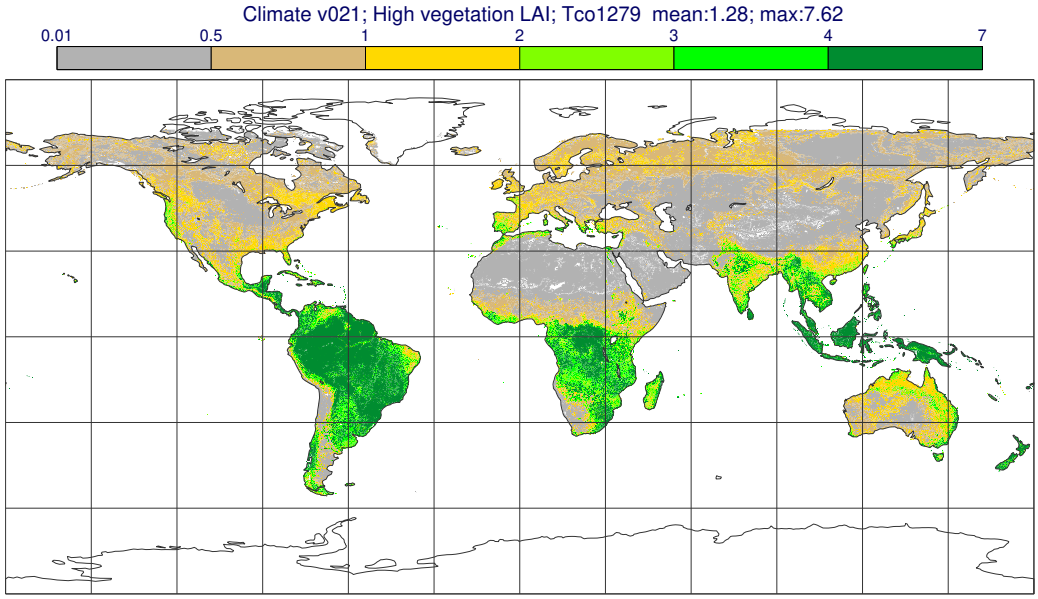

Figure 11.15 *LAI climatology for high vegetation in January.*

11.10 SEA SURFACE TEMPERATURE AND SEA ICE COVER

Sea surface temperature and sea ice climatology are used by the model to apply persistent SST anomalies to the ocean surface boundary condition. It is a daily climatology based on 40 years of ERA40 data. The INTERPOL utility is applied to interpolate from ERA40 to target resolution. INTERPOL also fills in the missing data for ocean points that do exist at target resolution and did not exist at ERA40 resolution. The same procedure is used for sea ice cover.

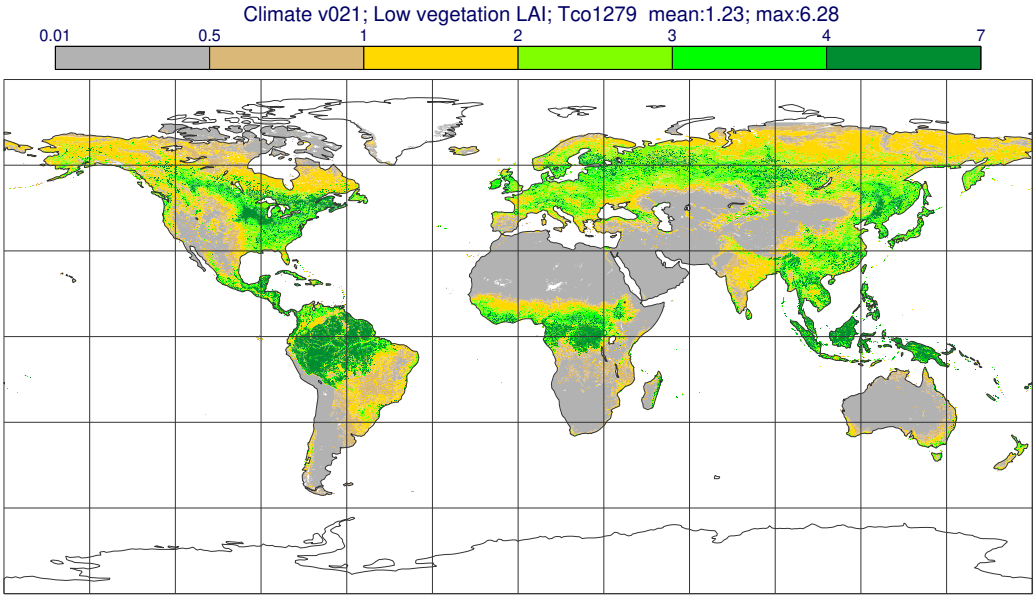

Figure 11.16 *LAI climatology for low vegetation in July.*

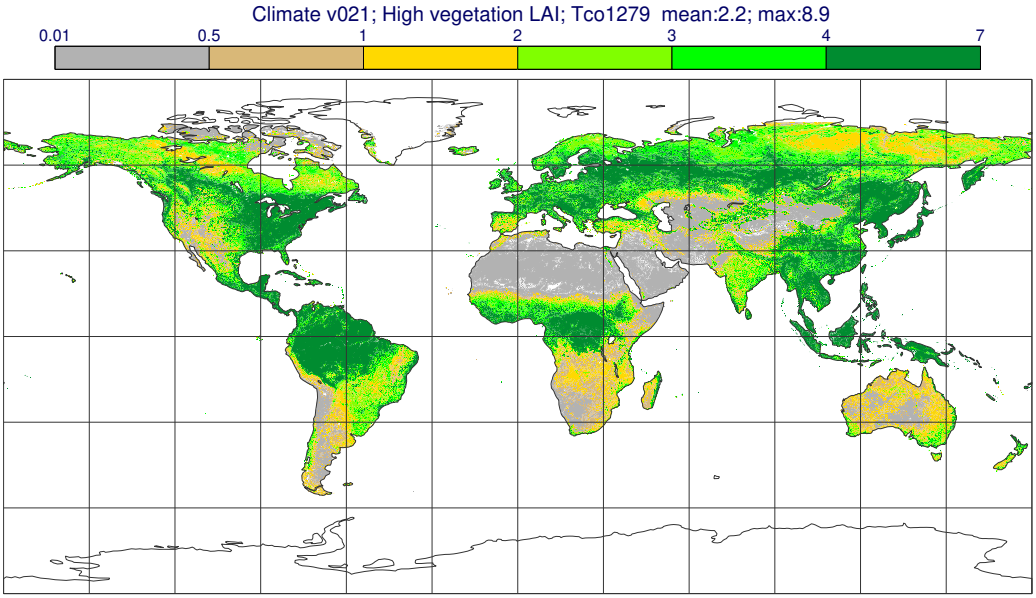

Figure 11.17 *LAI climatology for high vegetation in July.*

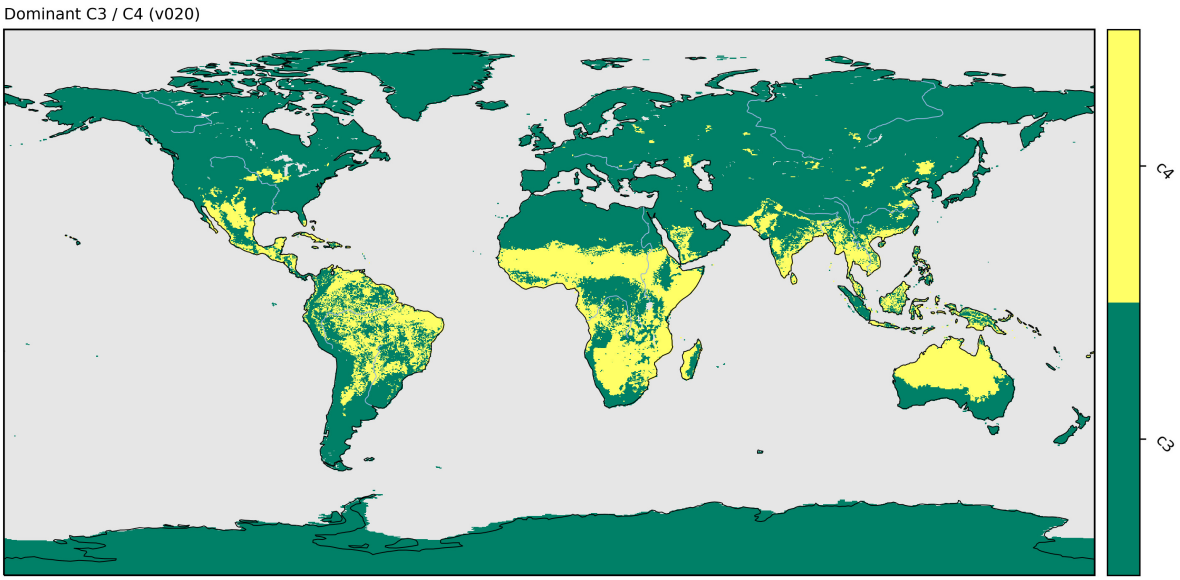

Figure 11.18 *C3/C4 plants photosynthesis types.*

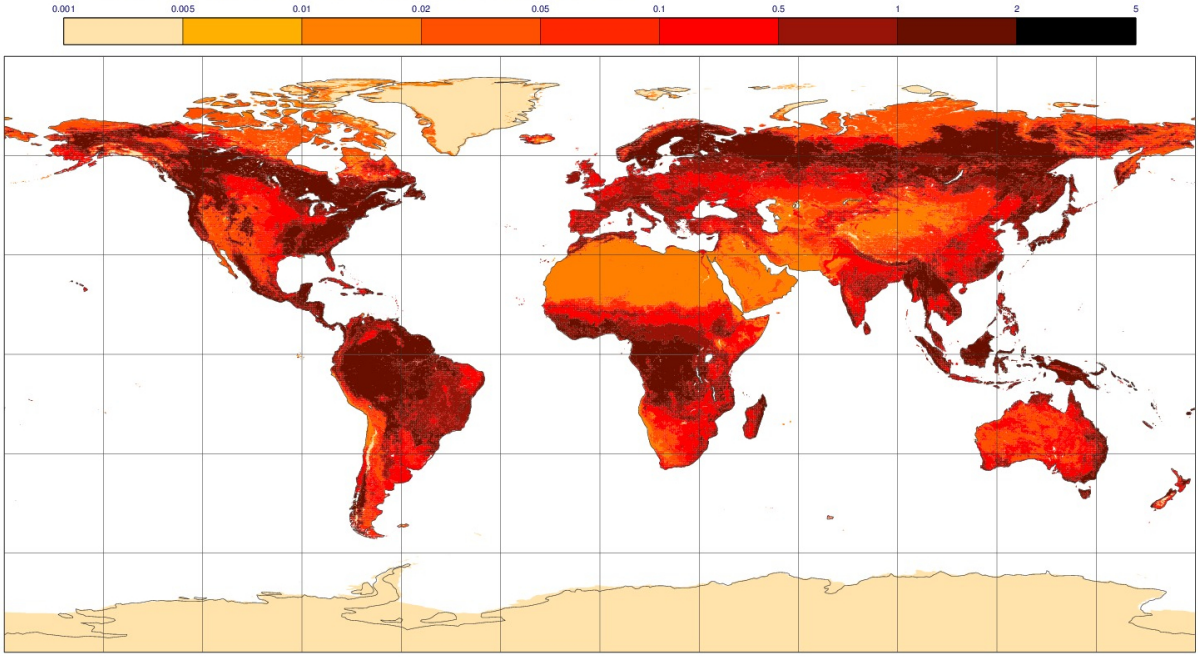

Figure 11.19 *Roughness length for momentum as produced by the Tco1279 model for 1 August 2017, using the dominant vegetation type, snow cover and correspondence Table 8.3.*

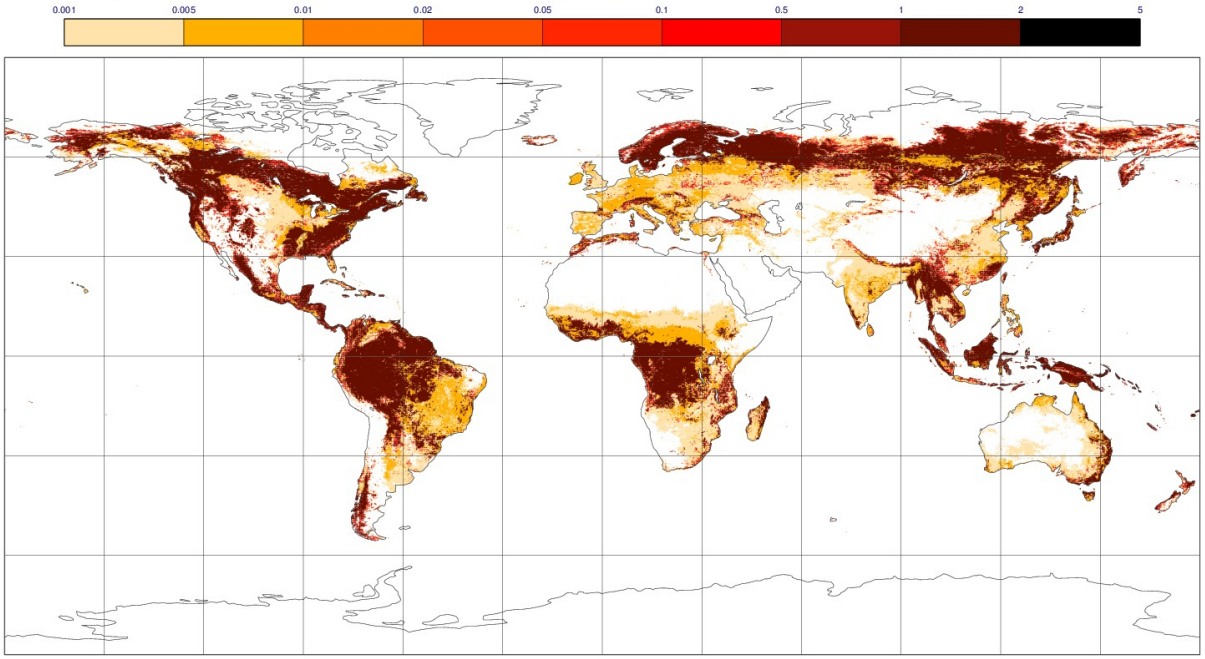

Figure 11.20 *Roughness length for heat as produced by the Tco1279 model for 1 August 2017, using the dominant vegetation type, snow cover and correspondence Table 8.3.*

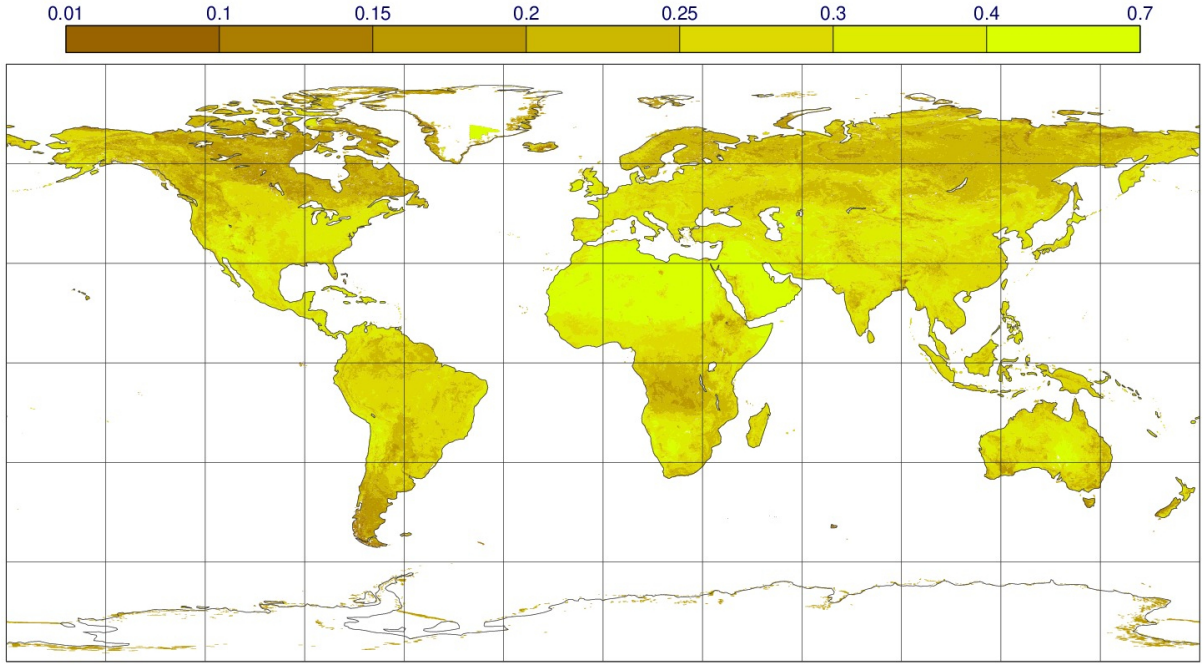

Figure 11.21 *Climatological background albedo for July (near infrared, isotropic).*

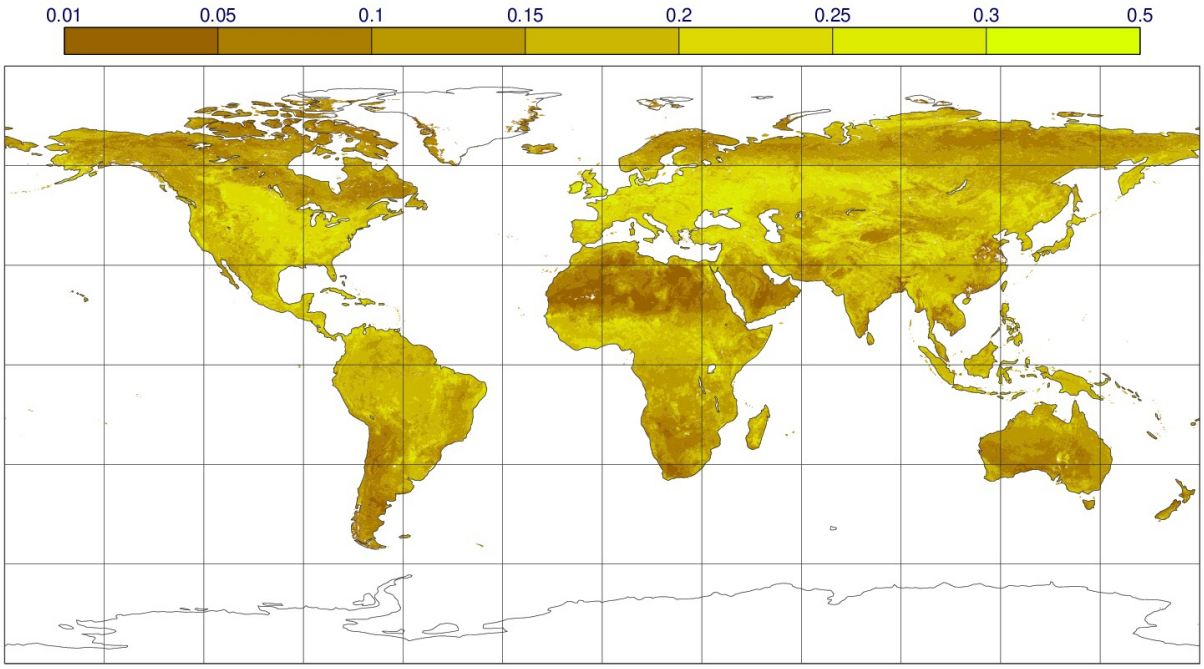

Figure 11.22 *Climatological background albedo for July (near infrared, volumetric).*

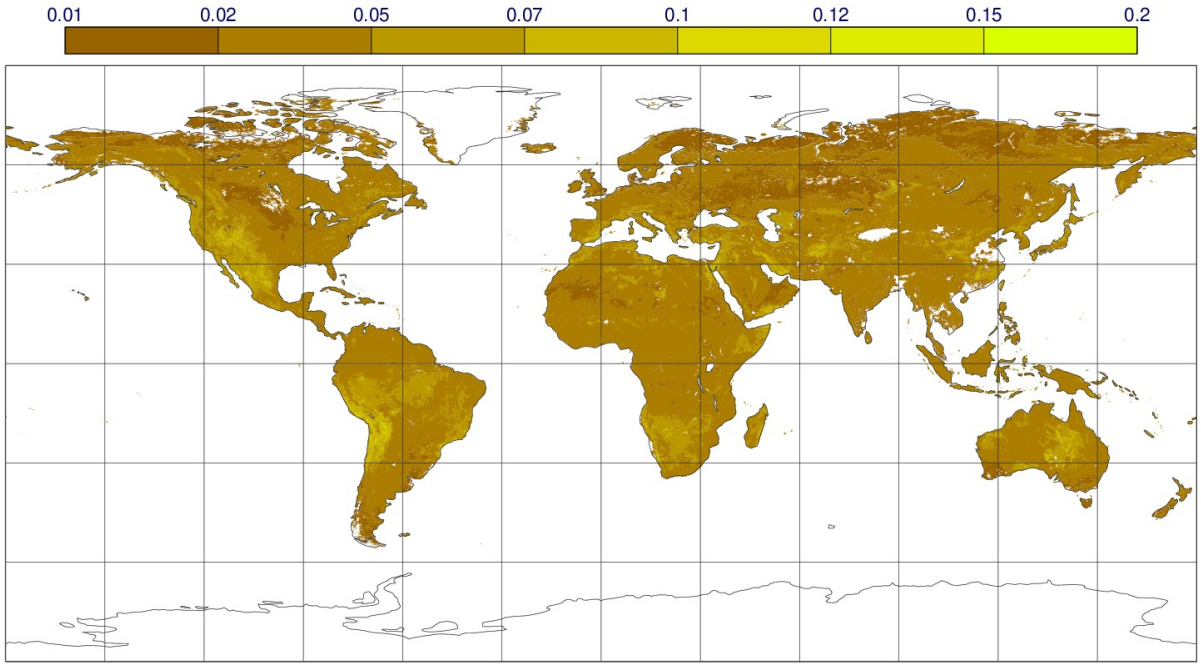

Figure 11.23 *Climatological background albedo for July (near infrared, geometric).*

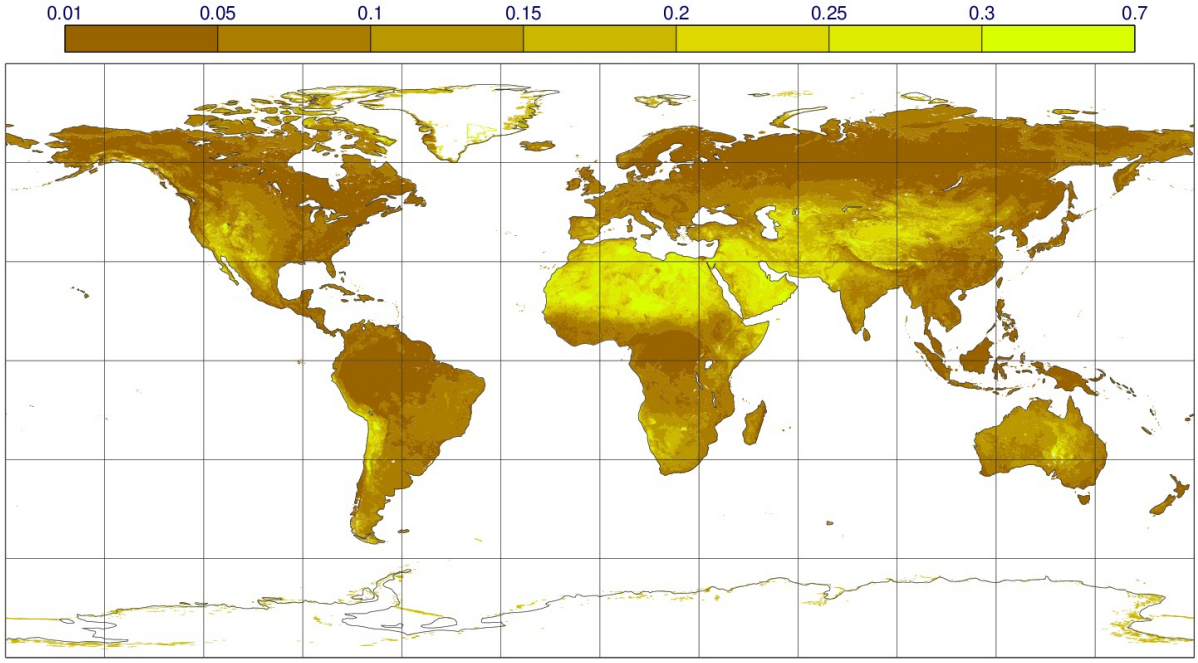

Figure 11.24 *Climatological background albedo for July (UV visible, isotropic).*

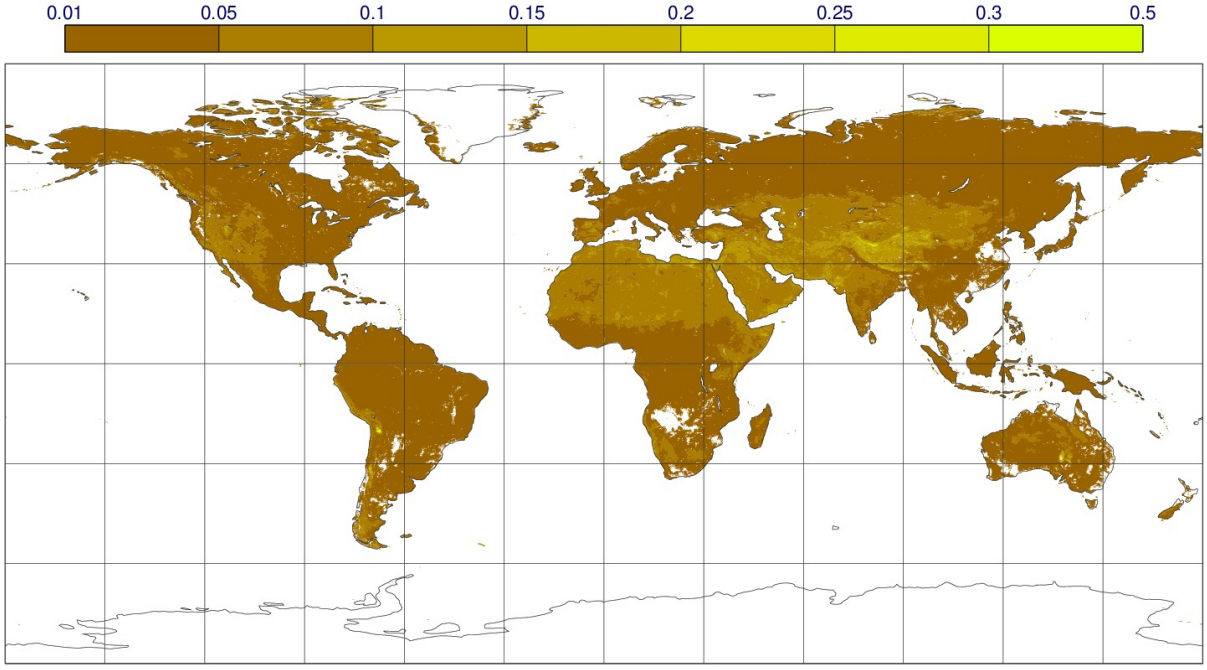

Figure 11.25 *Climatological background albedo for July (UV visible, volumetric).*

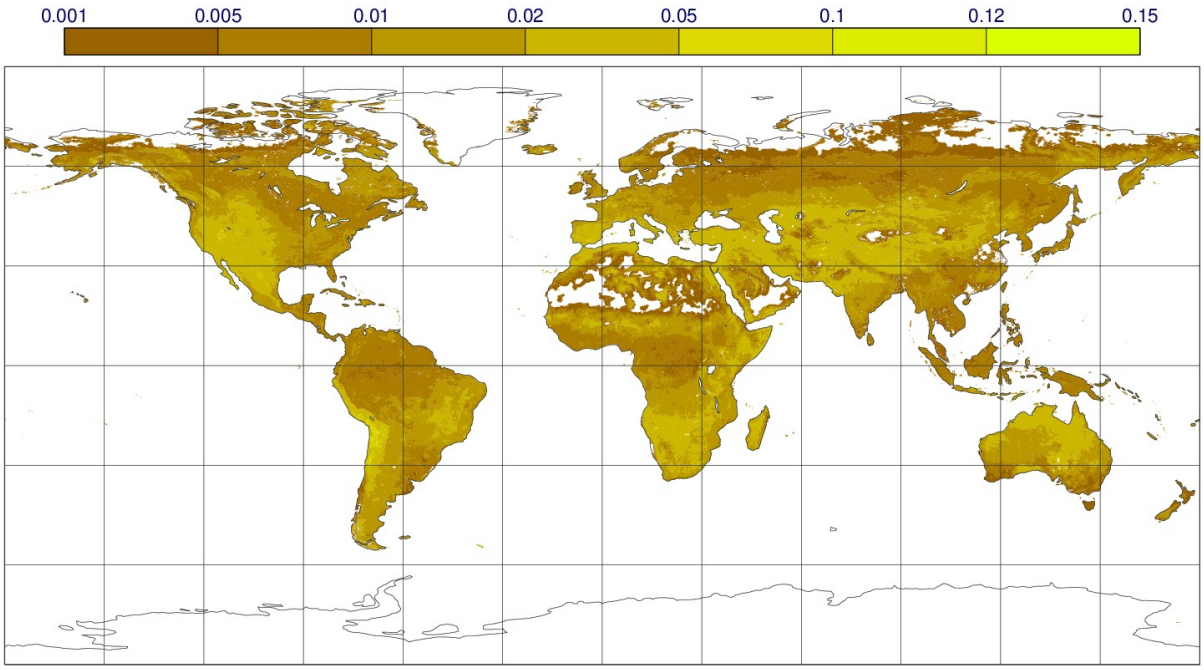

Figure 11.26 *Climatological background albedo for July (UV visible, geometric).*

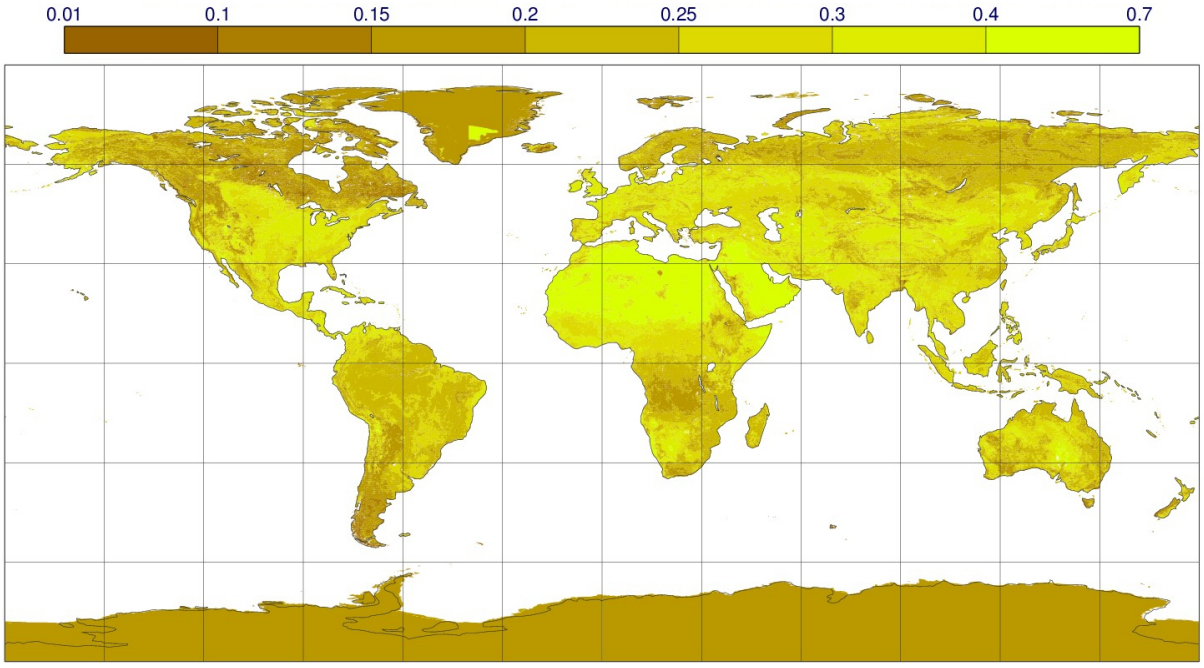

Figure 11.27 *Climatological background albedo for July (near infrared, diffuse).*

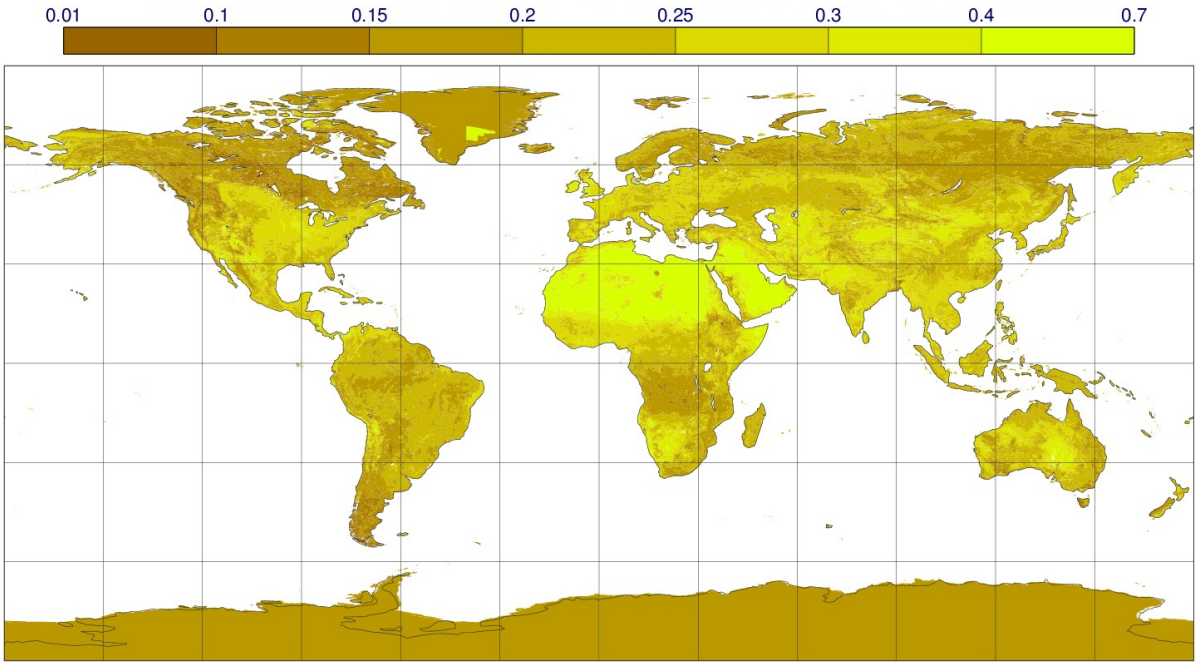

Figure 11.28 *Climatological background albedo for July (near infrared, direct).*

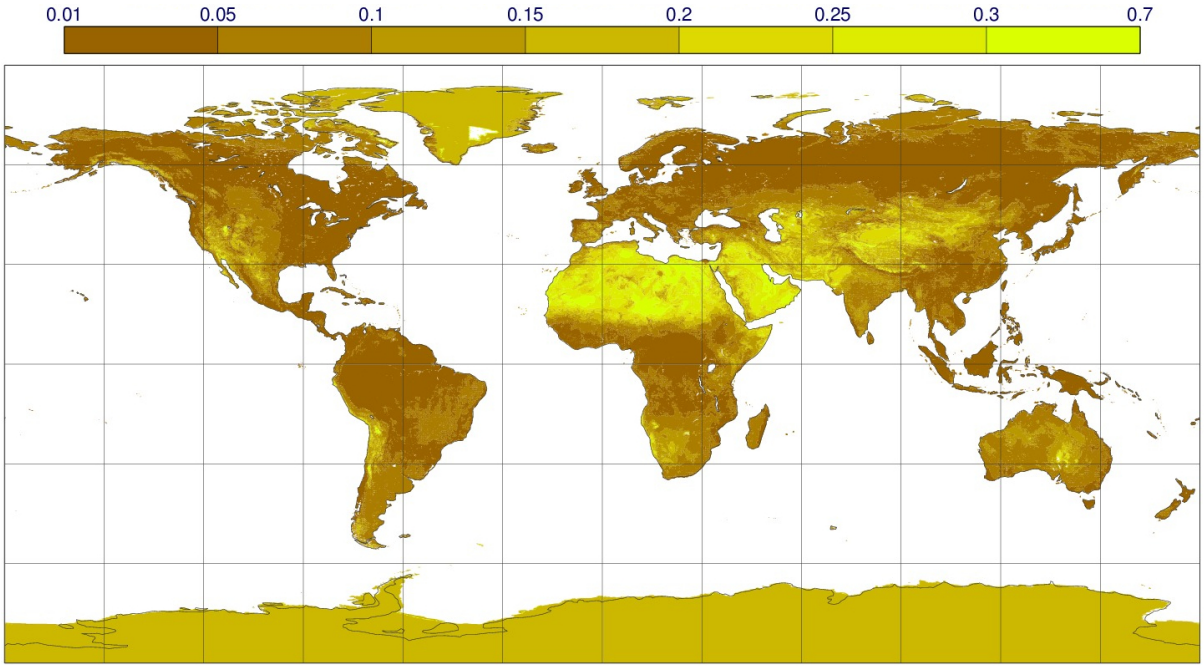

Figure 11.29 *Climatological background albedo for July (UV visible, diffuse).*

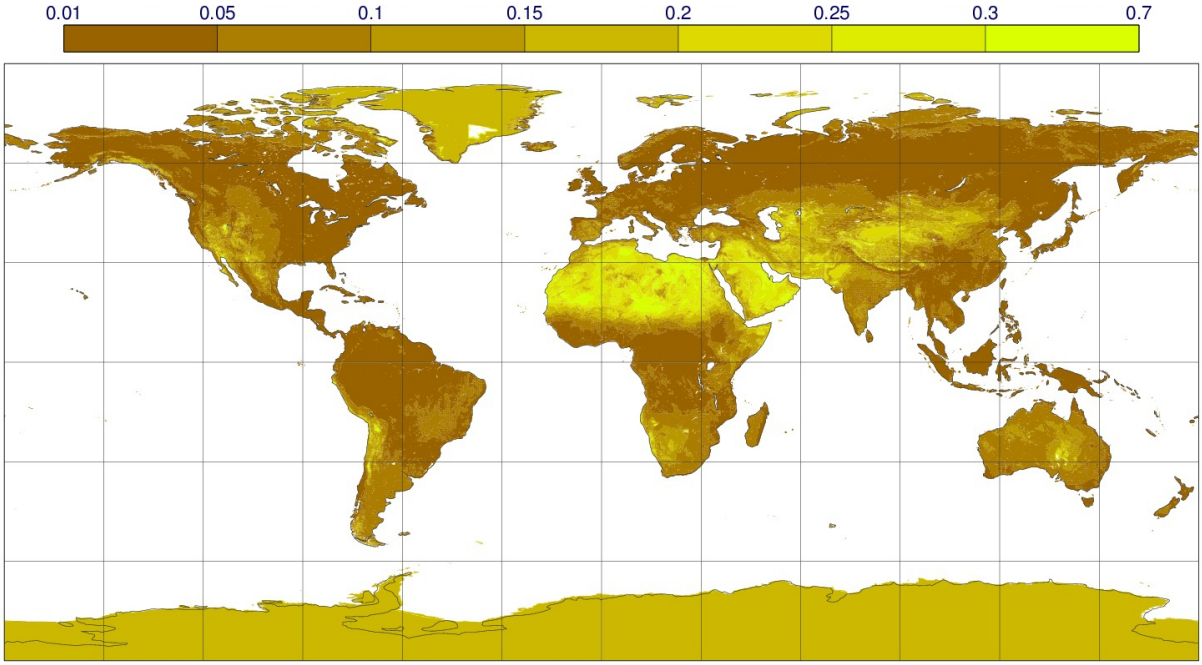

Figure 11.30 *Climatological background albedo for July (UV visible, direct).*

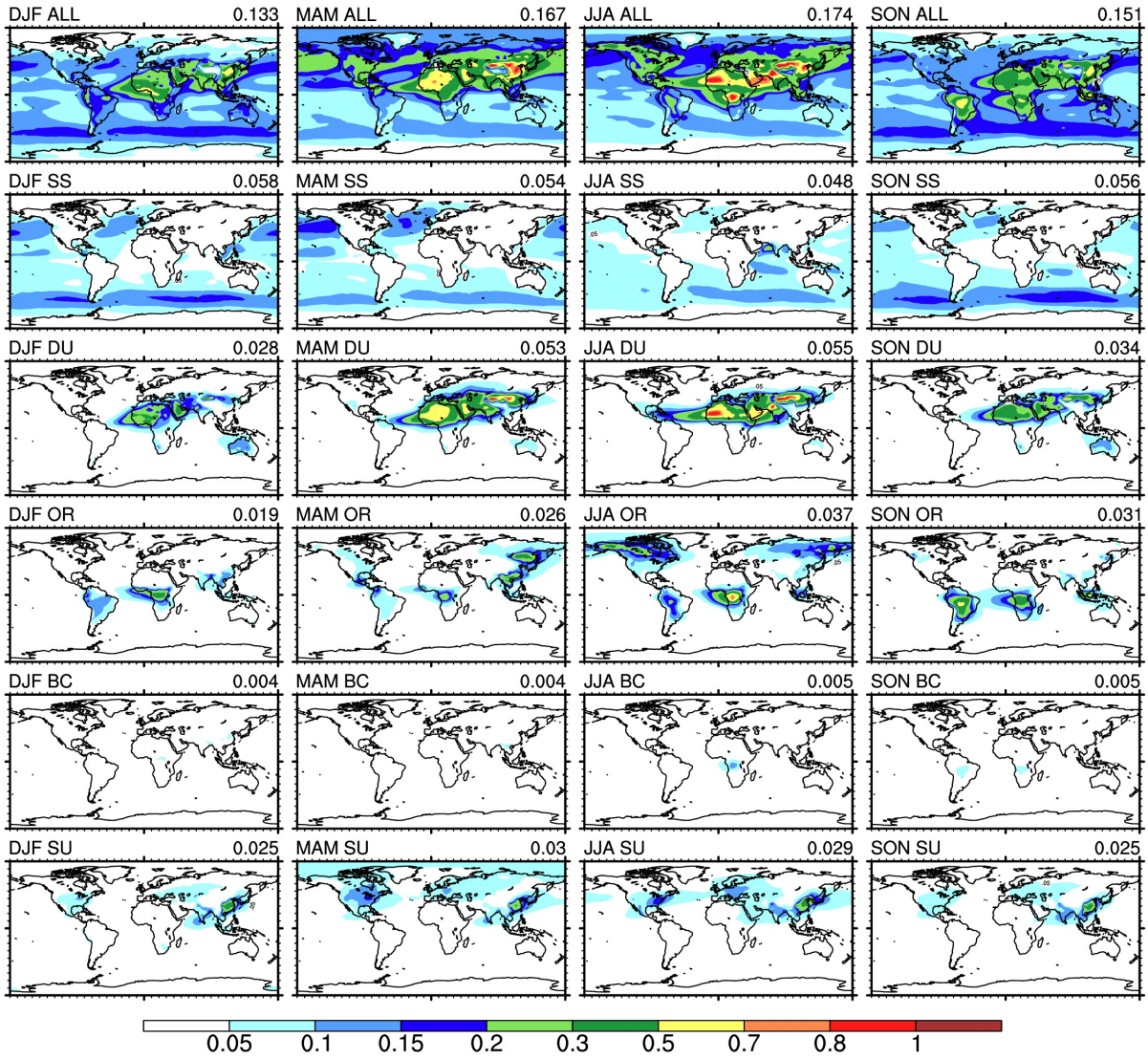

Figure 11.31 *Seasonal aerosol optical depth at 550nm from the CAMS climatology. The top row shows the total optical depth and the other rows the contribution from the single species for each season (SS=sea-salt, DU=mineral dust, OR=organic carbon, BC=black carbon, SU=sulfates). The global average is shown on the top right of each map.*

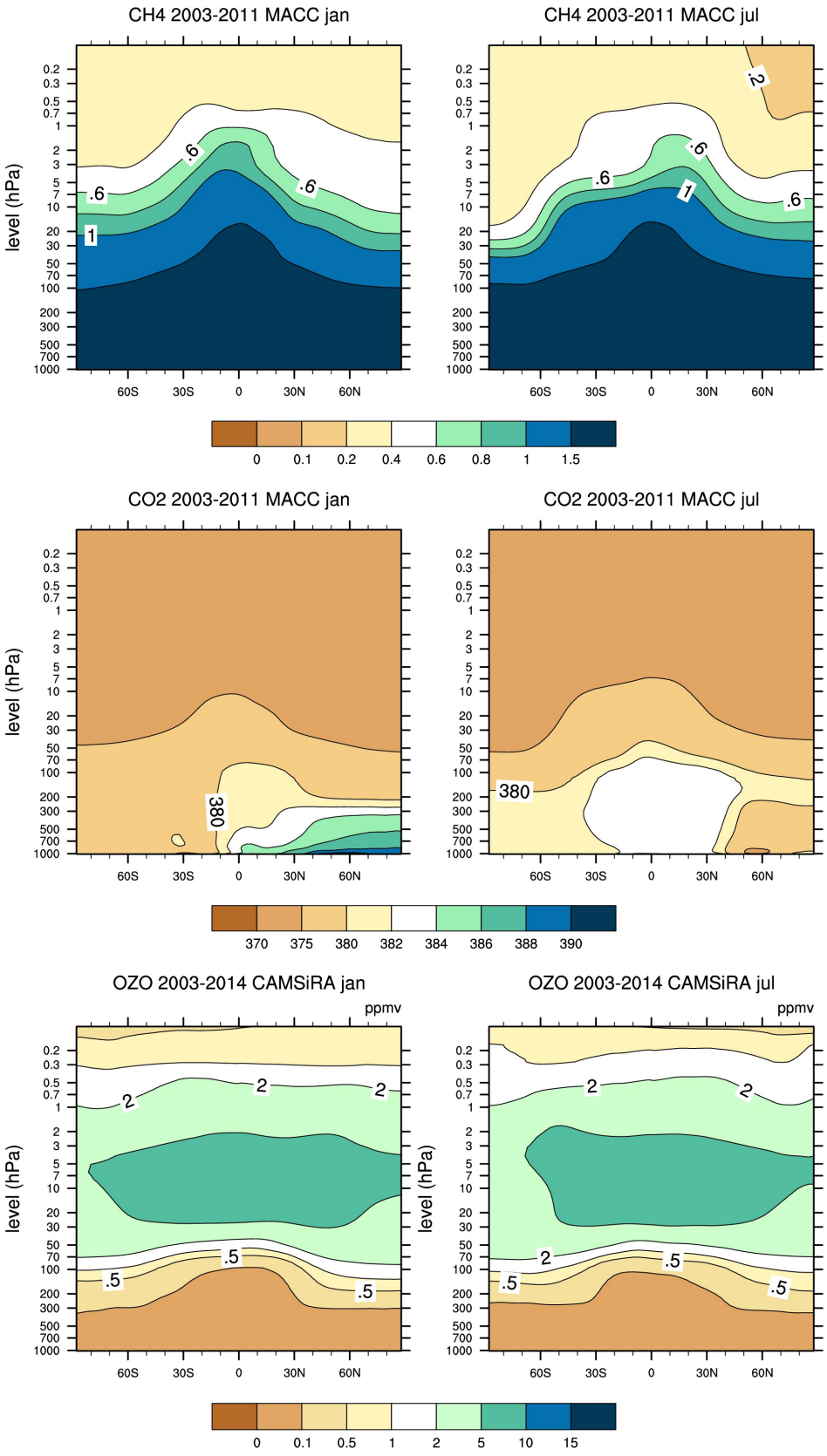

Figure 11.32 *January and July monthly-mean, zonal-mean climatologies for trace gases.* CO_2, CH_4 *are derived from the 2003-2011 MACC reanalysis and and* O_3 *is derived from the 2003-2014 CAMS Interim Reanalysis. All the concentrations are in ppmv.*

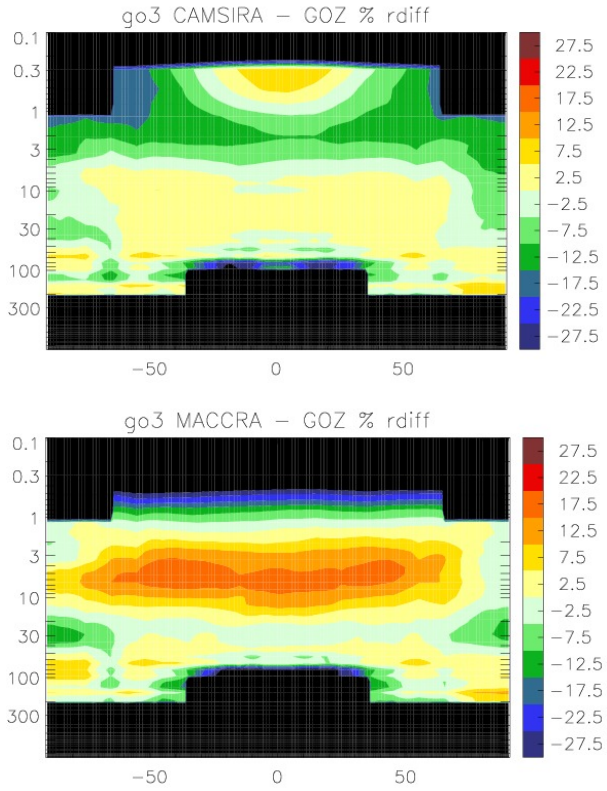

Figure 11.33 *Comparison between the observational climatology GOZCART (https://gozcards.jpl.nasa.gov/) and CAMSiRA (left) and MACC (right) climatologies. Relative difference in O3 mixing ratio.*

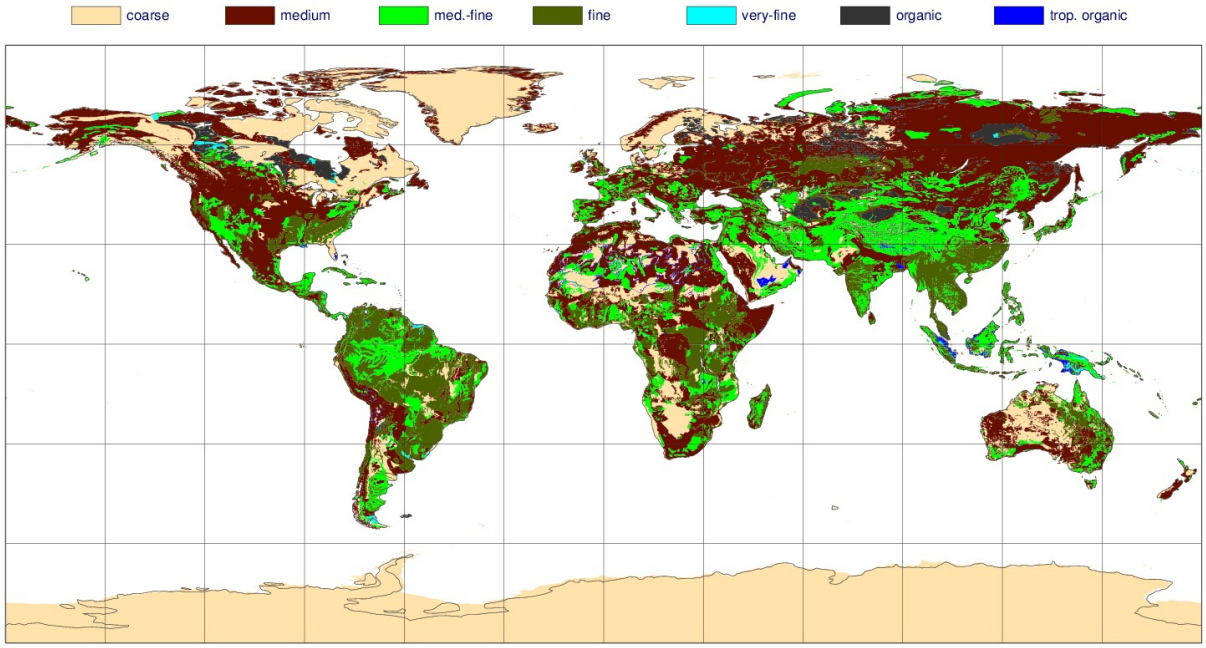

Figure 11.34 *Soil type classes as used in H-TESSEL.*

Chapter 12

Basic physical constants, thermodynamic functions, energy potentials and column integrals

Table of contents

12.1 Time
12.2 Geoid
12.3 Fundamental constants
12.4 Radiation
12.5 Thermodynamics, gas constants and specific and latent heats
12.6 Thermodynamics, basic state variables
12.7 Thermodynamics, saturation functions
12.8 Mass and enthalpy conservation
12.9 Enthalpy flux
12.10 Column integrals

12.1 TIME

length of the day d = 86400 s
length of the year y_j = 365.25 d

Taking into account the average variation in the Sun–Earth distance, the sidereal year and sidereal day are defined as

sidereal year $y_s = y_j \frac{2\pi}{6.283076}$
sidereal day $d_s = \frac{d}{1+d/d_s}$

and therefore defining the Earth's rotation rate as

$\Omega = \frac{2\pi}{d_s}$

12.2 GEOID

The Earth is supposed spherical with radius a (average value of the reference ellipsoid) and energy potentials a =6371229 m

The gravitational acceleration g is

$g = 9.80665 \text{ m s}^{-2}$

from where the geopotential height Φ is derived as $\Phi = gz$ (J kg^{-1}).

12.3 FUNDAMENTAL CONSTANTS

speed of light in vacuum	c	$= 299792458$ m s^{-1}
Planck constant	h	$= 6.6260755\ 10^{-34}$ J s
Boltzmann constant	k	$= 1.380658\ 10^{-23}$ J K^{-1}
Avogadro number	N	$= 6.0221367\ 10^{23}$ mol^{-1}

12.4 RADIATION

Stefan-Boltzmann constant	σ	$=\frac{2\pi^5 k^4}{15c^2h^3}=5.6705085\ 10^{-8}$ W m^{-2} K^{-4}
total solar irradiance	S_0	$= 1370$ W m^{-2}

12.5 THERMODYNAMICS, GAS CONSTANTS AND SPECIFIC AND LATENT HEATS

universal gas constant	R	$= Nk= 8.31451$ J K^{-1} mol^{-1}
dry air molar mass	M_d	$= 28.9644\ 10^{-3}$ kg mol^{-1}
water vapor molar mass	M_v	$= 18.0153\ 10^{-3}$ kg mol^{-1}

leading to the definition of the gas constants for dry air and water vapor

$R_d = \frac{R}{M_d} = 287.0597$ J kg^{-1} K^{-1}
$R_v = \frac{R}{M_v} = 461.5250$ J kg^{-1} K^{-1}

The specific heats at constant pressure (first subscript p) and constant volume (first subscript v) for dry air and water vapor are

$c_{pd} = \frac{7}{2}R_d = 1004.7090$ J kg^{-1} K^{-1}
$c_{vd} = \frac{5}{2}R_d = 717.6493$ J kg^{-1} K^{-1}
$c_{pv} = 4\ R_v = 1846.1$ J kg^{-1} K^{-1}
$c_{vv} = 3\ R_v = 1384.575$ J kg^{-1} K^{-1}

and the specific heats for water in its liquid and solid phase

$c_l = 4218$ J kg^{-1} K^{-1}
$c_s = 2106$ J kg^{-1} K^{-1}

c_l and c_s are supposed constant, with the above values actually valid for the triple point temperature

$T_0 = 273.16$ K

The functions for the specific heats of vaporisation and sublimation correspond to the differences in the specific enthalpies h of water vapor and liquid water, and water vapor and ice, respectively

$$L_v = h_v - h_l = L_v(T_0) + (c_{pv} - c_l)(T - T_0) \quad (12.1)$$
$$L_s = h_v - h_s = L_s(T_0) + (c_{pv} - c_s)(T - T_0) \quad (12.2)$$

However, the approximation chosen in the model physics is that of invariable specific latent heats together with invariable (independent of the water contribution) specific heat at constant pressure

$L_v \equiv L_v(T_0) = L_{v0} = 2.5008\ 10^6$ J kg^{-1}
$L_s \equiv L_s(T_0) = L_{s0} = 2.8345\ 10^6$ J kg^{-1}
$c_p \equiv c_{pd} = 1004.7090$ J kg^{-1} K^{-1}

as will be discussed further in the context of enthalpy conservation and mixed phase saturation adjustment. For a more general summary of atmospheric thermodynamics and derivations of the main constants, thermodynamic potentials and numerical procedures that apply to the IFS, see Bechtold (2015).

12.6 THERMODYNAMICS, BASIC STATE VARIABLES

The total atmospheric pressure p, specific humidity $q_{\rm v}$, specific masses of water in its liquid and ice phase $q_{\rm l,i,r,s}$, the air density ρ and virtual temperature $T_{\rm v}$ are related through

$$p = p_{\rm d} + e \tag{12.3}$$

$$q_{\rm v} = \frac{\rho_{\rm v}}{\rho} = \frac{\rho_{\rm v}}{(\rho_{\rm d}+\rho_{\rm v})} = \epsilon\frac{e}{p-(1-\epsilon)e} = \frac{\epsilon\frac{e}{p}}{1-\frac{1-\epsilon}{\epsilon}\epsilon\frac{e}{p}} = \frac{\tilde{q}}{1-\epsilon^\star\tilde{q}} \tag{12.4}$$

$$\epsilon = \frac{R_{\rm d}}{R_{\rm v}};\quad \epsilon^\star = \frac{R_{\rm v}}{R_{\rm d}} - 1 \tag{12.5}$$

$$\rho = \frac{p}{R_{\rm d}T_{\rm v}} \tag{12.6}$$

$$T_{\rm v} = T(1+\epsilon^\star q_{\rm v} - q_l - q_{\rm i} - q_{\rm r} - q_{\rm s}) \tag{12.7}$$

where the usual notation $p_{\rm v} = e$ for the water vapor pressure has been used. In the derivation of T_v the specific volume of the condensed water phases has been neglected. Nota, the complete expression of density via $T_{\rm v}$ in (12.3-12.7) taking into account all prognostic microphysical species, is used in the dynamical prognostic equations for vector wind and T, and in the model physics when buoyancy perturbations are implied (e.g updraught kinetic energy computation in the convection). However, when air density is required in the physics it is computed using $T_{\rm v} = (1+\epsilon^\star q_{\rm v})T$ only.

12.7 THERMODYNAMICS, SATURATION FUNCTIONS

The expressions for the water vapour saturation pressure over water and ice are derived from the Clausius-Clapeyron equation

$$\frac{d\ln e_{\rm sat}}{dT} = \frac{L_{\rm v}}{R_{\rm v}T^2} \tag{12.8}$$

where the specific volume of water has been neglected. Instead of integrating 12.8 between the triple point temperature $T_{\rm t}$ and T, an empirical form is used with separate functions for saturation over water and over ice

$$e_{\rm sat,l} = e_0 \quad \exp\left[17.502 \quad (T-T_0)/(T-32.19)\right] \quad \text{water} \tag{12.9}$$

$$e_{\rm sat,i} = e_0 \quad \exp\left[22.587 \quad (T-T_0)/(T+0.7)\right] \quad \text{ice} \tag{12.10}$$

$$e_0 = e_{\rm sat}(T_0) = 611.21 \quad \text{Pa} \tag{12.11}$$

Mixed-phase thermodynamics, ie when water is supposed to be present in its three forms, is represented through an interpolation as a function of temperature of the saturation functions and the latent heats

between their values with respect to water and ice

$$\alpha = \left(\frac{T - T_0 + \Delta T_i}{\Delta T_i}\right)^2; \quad T_0 \geq T \geq T_0 - \Delta T_i; \quad \Delta T_i = 23(38)\mathrm{K} \tag{12.12}$$

$$L = \alpha L_{v0} + (1-\alpha) L_{s0} \tag{12.13}$$

$$e_{sat} = \alpha e_{sat,l} + (1-\alpha) e_{sat,i} \tag{12.14}$$

$$q_{sat} = \frac{\tilde{q}_{sat}}{1 - \epsilon^\star \tilde{q}_{sat}} \quad ; \tilde{q}_{sat} = \epsilon \frac{e_{sat}}{p} \tag{12.15}$$

$$RH = \frac{e}{e_{sat}} \approx \frac{q_v}{q_{sat}} \tag{12.16}$$

where we have also introduced the definition of the relative humidity RH. Note that the mixed phase is supposed to occur in the temperature range $T_0 \geq T \geq T_0 - \Delta T_i$ with a different value of $T_i = 38$K for convection. In many cases the diagnostic mixed-phase relation might not be consistent with the mixed phase representation in the prognostic microphysics.

In case of supersaturation or evaporation of rain, the saturation adjustment process can then be formulated from the conservation of enthalpy making use of (12.5),(12.9)-(12.11) and (12.12)-(12.15)

$$c_{pd} dT = L \quad (q_v - q_{sat}(T)) \tag{12.17}$$

$$c_{pd}(T^\star - T) = L \left[q_v - \left\{ q_{sat}(T) + \frac{dq_{sat}}{dT}|_T (T^\star - T) + o(2) \right\} \right] \tag{12.18}$$

$$T^\star = T + \frac{L}{c_{pd}} \frac{q_v - q_{sat}(T)}{1 + \frac{L}{c_{pd}} \frac{dq_{sat}}{dT}|_T} \tag{12.19}$$

$$\frac{dq_{sat}}{dT} = \frac{dq_{sat}}{d\tilde{q}_{sat}} \frac{d\tilde{q}_{sat}}{dT} = \frac{1}{(1 - \epsilon^\star \tilde{q}_{sat}(T))^2} \frac{\epsilon}{p} \frac{de_{sat}}{dT}|_T \tag{12.20}$$

$$q_v^\star = q_{sat}(T^\star) \tag{12.21}$$

$$q_{l,i} = q_v - q_v^\star \tag{12.22}$$

$$q_l = \alpha q_{l,i}; \quad q_i = (1-\alpha) q_{l,i} \tag{12.23}$$

where a linearisation around the initial temperature T has been applied and superscript * denotes the adjusted values. Only one iteration of the above equation set is necessary to achieve sufficient accuracy of O(10^{-3}) K.

12.8 MASS AND ENTHALPY CONSERVATION

A conserved energy potential can be derived from the adiabatic (no exchange of heat) transformations in differential form for a closed system comprising dry air and all water species (Dufour and van Mieghem, 1975)

$$\left(m_d c_{pd} + m_v c_{pv} + (m_l + m_r) c_l + (m_i + m_s) c_s)\right) dT = -L_v dm_v + (L_s - L_v) d(m_i + m_s) + V\, dp \tag{12.24}$$

$$\left(m_d c_{pd} + m_v c_{pv} + (m_l + m_r) c l_l + (m_i + m_s) c_s)\right) dT = L_v d(m_l + m_r) + L_s d(m_i + m_s) + V\, dp \tag{12.25}$$

where $V = \rho^{-1} m_t$ is the volume, m_t the total mass and $m_{d,v,r,i,s}$ the individual masses of dry air and water species. The above equations can be integrated, writing e.g. (12.24) as

$$\begin{aligned} \left(m_d c_{pd} + m_v c_{pv} + (m_l + m_r) c_l + (m_i + m_s) c_s)\right) dT &= -d(L_v m_v) + d((L_s - L_v)(m_i + m_s)) \\ &+ m_v \frac{dL_v}{dT} dT - (m_i + m_s) \frac{d(L_s - L_v)}{dT} dT + V dp \end{aligned} \tag{12.26}$$

and using (12.1-12.2) for the temperature dependency of the latent heats, dividing by the total mass m_t and applying the hydrostatic approximation to the last term of the rhs. One then obtains two variants of the moist static energy as an expression for the moist enthalpy

$$h = [c_{pd} + q_t(c_l - c_{pd})]T + L_v q_v - (L_s - L_v)(q_i + q_s) + \Phi + h_0 \quad (12.27)$$
$$h = [c_{pd} + q_t(c_{pv} - c_{pd})]T - L_v(q_l + q_r) - L_s(q_i + q_s) + \Phi + h_0 \quad (12.28)$$
$$q_t = q_v + q_l + q_i + q_r + q_s = \frac{m_v + m_l + m_i + m_r + m_s}{m_d + m_v + m_l + m_i + m_r + m_s} \quad (12.29)$$

with q_t the total specific water content and h_0 a true integration constant that can be discarded.

The above equations have also been derived more thoroughly by Marquet (2015) for an open system using the integral form $h = (1 - q_t)h_d + q_v h_v + q_l h_l + q_i h_i$ and $h_d = h_{d0} + c_{pd}(T - T_0)$ etc, where q_t is not a constant

$$h = [c_{pd} + q_t(c_l - c_{pd})]T + L_v q_v - (L_s - L_v)(q_i + q_s) + \Phi + q_t[h_{ld0} - (c_l - c_{pd})T_0] \quad (12.30)$$
$$h = [c_{pd} + q_t(c_{pv} - c_{pd})]T - L_v(q_l + q_r) - L_s(q_i + q_s) + \Phi + q_t[h_{vd0} - (c_{pv} - c_{pd})T_0] \quad (12.31)$$

It now also includes a term on the lhs of reference enthalpies that are in factor of q_t, where the difference in the reference specific enthalpies of liquid water and dry air, and water vapor and dry air, respectively, are given by $h_{ld0} = 102$ kJ kg^{-1} and $h_{vd0} = 2373$ kJ kg^{-1}(Marquet, 2015).

The quantity conserved in the IFS is an approximation (linearisation at $T = T_0$) of (12.29), using constant specific and latent heats, as also used in the saturation adjustment (12.16)-(12.23)

$$h \equiv c_{pd}T + L_{v0}q_v - (L_{s0} - L_{v0})(q_i + q_s) + \Phi \quad (12.32)$$

Two important remarks come in here. In many places of the IFS there is the option of a moist c_p. Using this option would (i) making budgets extremely difficult as $c_p(q)$ varies between each physical process as q is updated, and (ii) be inconsistent as there is largely a cancellation with terms involving the reference values as can be seen from (12.30) setting $T = T_0$. Second, as noted by Marquet (2015), while (12.30) represents the true change of moist enthalpy created by a change in water vapor, the approximation (12.32) does not, which has consequences for the formulation of the surface enthalpy flux and the surface energy budget (Mayer *et al.*, 2017).

12.9 ENTHALPY FLUX

The enthalpy flux can be derived from (12.30) including correlations such as $\bar{T}(c_l - c_{pd})\overline{w'q'_t}$ and $\bar{q_v}\overline{w'L'_v} = \bar{q_v}(c_{pv} - c_l)\overline{w'T'}$ etc to obtain

$$\rho\,\overline{w'h'} = \rho\,\overline{w's'} + L_v\rho\,\overline{w'q'_v} - (L_s - L_v)\rho\,\overline{w'(q'_i + q'_s)} + ((c_l - c_{pd})(T - T_0) + h_{ld0})\rho\,\overline{w'q'_t} \quad (12.33)$$
$$= Fs + Fq - (L_s - L_v)\rho\,\overline{w'(q'_i + q'_s)} + ((c_l - c_{pd})(T - T_0) + h_{ld0})(Fq\,L_v^{-1} + Fprs)$$
$$s = \bar{c}_p T + \Phi; \quad c_p = (1 - q_t)c_{pd} + q_v c_{pv} + (q_l + q_r)c_l + (q_i + q_s)c_i \quad (12.34)$$

where Fs is the sensible heat flux (W m^{-2}), Fq (W m^{-2}) the latent heat flux and $Fprs = Fpr + Fps$ the rain+snow precipitation flux (kg water m^{-2} s^{-1}). Note that the sign convention for the fluxes is upward=negative, e.g. the water vapour flux, and downward=positive, e.g. precipitation flux, with the last term of the rhs of (12.33) proportional to the net moisture flux (evaporation-precipitation). The heat capacity c_p in (12.33)-(12.34) is now the mass weighted sum of the individual heat capacities and is different from that in (12.30).

In the IFS the enthalpy flux in accordance with (12.32) is approximated as

$$\rho\,\overline{w'h'} \equiv \underbrace{\rho\,\overline{w's'}}_{Fs} + \underbrace{L_{v0}\rho\,\overline{w'q'_v}}_{Fq} - (L_{s0}-L_{v0})\rho\,\overline{w'(q'_i+q'_s)} \tag{12.35}$$

$$s = c_{pd}T + \Phi \tag{12.36}$$

where the last term essentially represents the melting of snow and ice deposition. Over permanent ice and snow L_{v0} in Fq is replaced by L_{s0}. The difference between (12.33) and (12.35) amounts to about 1.4 W m^{-2} in global mean, with weaker fluxes in (12.33) mainly due to the temperature dependency of L_v in the latent heat flux term. The last term of the rhs of (12.33) involving the reference enthalpies is small in global and annual mean O(0.3 W^{-2}) but can be significant in tropical oceanic regions with either strong precipitation or evaporation (attaining up to 10-20 W^{-2} in annual mean).

12.10 COLUMN INTEGRALS

Under the approximation (12.32) the conservation of the following column integrals for water mass, enthalpy (static energy) and momentum is substantially facilitated and can be made exact:

Conservation of water

$$\frac{1}{g}\int_{p_{surf}}^{0}\left(\frac{dq_v}{dt}+\frac{dq_l}{dt}+\frac{dq_i}{dt}+\frac{dq_r}{dt}+\frac{dq_s}{dt}\right)dp_h = \frac{1}{g}\int_{p_{surf}}^{0}\frac{dq_t}{dt}dp_h = F_{prs}+F_q L_{v0}^{-1} \tag{12.37}$$

where tendencies are at full model levels and p_h denotes half-level pressure. Therefore, the change in total moisture is equal to the sum of the surface precipitation flux and the moisture flux.

Conservation of enthalpy (moist static energy)

$$\frac{c_{pd}}{g}\int_{p_{surf}}^{0}\frac{dT}{dt}dp_h + \frac{L_{v0}}{g}\int_{p_{surf}}^{0}\frac{dq_v}{dt}dp_h - \frac{L_{s0}-L_{v0}}{g}\int_{p_{surf}}^{0}\frac{(dq_i+dq_s)}{dt}dp_h = F_s+F_q-(L_{s0}-L_{v0})F_{ps}-F_{rad}^{top}+F_{rad}^{surf}-D_{diss}^{KE} \tag{12.38}$$

where $F_{rad}^{top}, F_{rad}^{surf}$ are net radiative shortwave+longwave fluxes at the top of the atmosphere and surface, respectively. D_{diss}^{KE} is the dissipation of kinetic energy (KE) due to turbulent diffusion and orographic form drag, convective momentum transport and dissipation of gravity wave momentum flux (3.97),(4.43),(6.59),(5.14); this does not include the dissipative heating due to horizontal diffusion and the dissipative kinetic energy loss in the advection scheme. Note that D_{diss}^{KE} on the archive is called "boundary-layer dissipation" and only includes the contribution from convective momentum transport (<0.2 W m^{-2}) from the ERA6 cycle 49r2 onward.

Alternatively, one can formulate the enthalpy conservation as

$$\frac{c_{pd}}{g}\int_{p_{surf}}^{0}\frac{dT}{dt}dp_h - \frac{L_{v0}}{g}\int_{p_{surf}}^{0}\left(\frac{dq_l}{dt}+\frac{dq_r}{dt}\right)dp_h - \frac{L_{s0}}{g}\int_{p_{surf}}^{0}\left(\frac{dq_i}{dt}+\frac{dq_s}{dt}\right)dp_h = F_s-L_{v0}F_{pr}-L_{s0}F_{ps}-F_{rad}^{top}+F_{rad}^{surf}-D_{diss}^{KE} \tag{12.39}$$

Note that in (12.38) the integrated moisture tendency on the lhs mirrors the latent heat flux on the rhs, while in (12.39) the integrated liquid+ice water tendencies mirror the surface precipitation flux.

The conservation of zonal and meridional momentum for the model physics is given by

$$\frac{1}{g}\int_{p_{surf}}^{0}\left(\frac{du}{dt},\frac{dv}{dt}\right)dp_h = F_{u,v} \tag{12.40}$$

where $F_{u,v}$ is the surface stress. The surface stress is positive downward and has the same sign as the wind vector. Note that the total column integral (12.40) including also the dynamical tendencies would

involve two additional rhs terms, namely the horizontal gradient of the geopotential and the Coriolis term.

Finally, the conservation of total energy in the model is given by

$$\iiint \left(\frac{\mathrm{d}h}{\mathrm{d}t} + \frac{\mathrm{d}KE}{\mathrm{d}t} \right) dV = 0 \tag{12.41}$$

In summary, the following approximations apply

- The temperature of the falling precipitation is that of the ambient air, which is itself cooled to the wet bulb value through evaporation
- The inherent dissipation from the dynamics is not included in the budget, it is estimated to be of O(0.3 W m^{-2})
- The column integral budgets above are satisfied in the physics to machine precision for moisture and to $< 0.1\%$ in heavy precipitating regions and < 1 (W m^{-2}) globally for enthalpy.

Integrating the budgets (12.38)-(12.41) globally and over time, ie an annual cycle, the lhs should be negligible, i.e. the rhs should balance. It is possible to tune the enthalpy budget of the atmosphere via tuning of the surface fluxes, likely via tuning of the air sea exchange coefficients and/or by including the temperature dependency of the latent heat. Tuning might also be accomplished via the radiation budget, i.e. via tuning of microphysical parameters.

References

Abel, S. J. and Boutle, I. A. (2012). An improved representation of the raindrop size distribution for single-moment microphysics schemes. *Q. J. R. Meteorol. Soc.*, **138**, 2151–2162, doi:10.1002/qj.1949.

Abramopoulos, F., Rosenzweig, C. and Choudury, B. (1988). Improved ground hydrology calculations for global climate models (GCMs): Soil water movement and evapotranspiration. *J. Climate*, **1**, 921–941.

Albergel, C., Balsamo, G., de Rosnay, P., Muñoz Sabater, J. and Boussetta, S. (2012). A bare ground evaporation revision in the ecmwf land-surface scheme: evaluation of its impact using ground soil moisture and satellite microwave data. *Hydrology and Earth System Sciences*, **16**(10), 3607–3620.

Albergel, C., Calvet, J.-C., Gibelin, A.-L., Lafont, S., Roujean, J.-L., Berne, C., Traulle, O. and Fritz, N. (2010). Observed and modelled ecosystem respiration and gross primary production of a grassland in south-western France. *Biogeosciences*, **7**, 1657–1668.

Alduchov, O. A. and Eskridge, R. E. (1996). Improved Magnus form approximation of saturation vapor pressure. *J. Appl. Meteorol.*, **35**, 601–609.

Amante, C. and Eakins, B. W. (2009). Etopo1 global relief model converted to panmap layer format. doi:10.1594/PANGAEA.769615, URL https://doi.org/10.1594/PANGAEA.769615.

Anderson, E. A. (1976). A point energy and mass balance model of a snow cover. *NOAA Tech. Rep.*, **19**, 150 pp.

Andreas, E., Horst, T., Grachev, A., Persson, P., Fairall, C., Guest, P. and Jordan, R. (2010). Turbulent exchange over summer sea ice and the marginal ice zone. *Q. J. R. Meteorol. Soc.*, **136**, 927–947.

Arakawa, A. and Schubert, W. H. (1974). Interaction of a cumulus cloud ensemble with the large-scale environment. Part I. *J. Atmos. Sci.*, **31**, 674–701.

Arduini, G., Balsamo, G., Dutra, E., Day, J. J., Sandu, I., Boussetta, S. and Haiden, T. (2019). Impact of a multi-layer snow scheme on near-surface weather forecasts. *J. Adv. Model. Earth Syst.*, **11**(12), 4687–4710.

Arduini, G., Rüdiger, C. and Balsamo, G. (2026). Enhancing the representation of glaciers and ice sheets in the ecland land-surface model: Impacts on surface energy balance and hydrology across scales. *The Cryosphere*, **20**(2), 1119–1137, doi:10.5194/tc-20-1119-2026, URL https://tc.copernicus.org/articles/20/1119/2026/.

Baines, P. G. and Palmer, T. N. (1990). Rationale for a new physically based parametrization of subgrid-scale orographic effects. *ECMWF Tech. Memo. No. 1699*.

Baker, D. G., Ruschy, D. L. and Wall, D. B. (1990). The albedo decay of prarie snows. *J. Appl. Meteorol.*, **29**, 179–187.

Balsamo, G. (2013). Interactive lakes in the integrated forecasting system. *ECMWF Newsletter, No. 137*, pp. 30–34.

Balsamo, G., Boussetta, S., Dutra, E., Beljaars, A., Viterbo, P. and den Hurk, B. V. (2011a). Evolution of land-surface processes in the ifs. *ECMWF Newsletter No. 127*, pp. 12–22.

Balsamo, G., Dutra, E., Stepanenko, V. M., Viterbo, P., Miranda, P. M. A. and Mironov, D. (2010). Deriving an effective lake depth from satellite lake surface temperature data: A feasibility study with modis data. *Boreal Env. Res.*, **15**, 178–190.

Balsamo, G., Pappenberger, F., Dutra, E., Viterbo, P. and van den Hurk, B. (2011b). A revised land hydrology in the ecmwf model: a step towards daily water flux prediction in a fully-closed water cycle. *Hydrological Processes*, **25**(7), 1046–1054, doi:10.1002/hyp.7808.

Balsamo, G., Salgado, R., Dutra, E., Boussetta, S., Stockdale, T. and Potes, M. (2012). On the contribution of lakes in predicting near-surface temperature in a global weather forecasting model. *Tellus A*, **64**, 15829. doi:10.3402/tellusa.v64i0.15829.

Balsamo, G., Viterbo, P., Beljaars, A., van den Hurk, B., Hirschi, M., Betts, A. K. and Scipal, K. (2009). A revised hydrology for the ECMWF model: Verification from field site to terrestrial water storage and impact in the Integrated Forecast System. *J. Hydrometeorol.*, **10**, 623–643.

Barker, H. W. (2008). Representing cloud overlap with an effective decorrelation length: An assessment using CloudSat and CALIPSO data. *J. Geophys. Res.*, **113**, D24205, doi:10.1029/2008JD010391.

Batchelor, G. K. (1967). *An Introduction to Fluid Dynamics*. Cambridge University Press, 615 pp.

Bašták Ďurán, I., Geleyn, J.-F. and Váňa, F. (2014). A compact model for the stability dependency of tke production–destruction–conversion terms valid for the whole range of richardson numbers. *Journal of the Atmospheric Sciences*, **71**(8), 3004 – 3026, doi:10.1175/JAS-D-13-0203.1.

Beard, K. and Pruppacher, H. R. (1971). A wind tunnel investigation of the rate of evaporation of small water drops falling at terminal velocity in air. *J. Atmos. Sci.*, **28**(8), 1455–1464.

Bechtold, P. (2015). Atmospheric thermodynamics. *Technical report*, ECMWF Leture Notes, "https://www.ecmwf.int/sites/default/files/elibrary/2015/16954-atmospheric-thermodynamics.pdf".

Bechtold, P. and Bidlot, J.-R. (2009). Convective gusts. *ECMWF Newsletter No. 119*, pp. 15–18.

Bechtold, P., Bramberger, M., Dörnbrack, A., Leutbecher, M. and Isaksen, L. (2021). Experimenting with a clear air turbulence (cat) index from the ifs. *ECMWF Tech. Report No. 874*, Research Department, ECMWF.

Bechtold, P., Chaboureau, J.-P., Beljaars, A., Betts, A. K., Köhler, M., Miller, M. and Redelsperger, J.-L. (2004). The simulation of the diurnal cycle of convective precipitation over land in a global model. *Q. J. R. Meteorol. Soc.*, **130**, 3119–3137.

Bechtold, P., Köhler, M., Jung, T., Leutbecher, M., Rodwell, M., Vitart, F. and Balsamo, G. (2008). Advances in predicting atmospheric variability with the ECMWF model, 2008: From synoptic to decadal time-scales. *Q. J. R. Meteorol. Soc.*, **134**, 1337–1351.

Bechtold, P., Orr, A., Morcrette, J.-J., Engelen, R., Flemming, J. and Janiskova, M. (2009). Improvements in the stratosphere and mesosphere of the IFS. *ECMWF Newsletter No. 120*, pp. 22–31.

Bechtold, P., Semane, N., Lopez, P., Chaboureau, J.-P., Beljaars, A. and Bormann, N. (2014). Representing equilibrium and non-equilibrium convection in large-scale models. *J. Atmos. Sci.*, **71**, 734–753.

Becker, T., Bechtold, P. and Sandu, I. (2021). Characteristics of convective precipitation over tropical africa in storm-resolving global simulations. *Q. J. R. Meteorol. Soc.*

Beljaars, A., Dutra, E., Balsamo, G. and Lemarié, F. (2017). On the numerical stability of surface–atmosphere coupling in weather and climate models. *Geoscientific Model Development*, **10**(2), 977–989, doi:10.5194/gmd-10-977-2017.

Beljaars, A. C. M. (1987). The influence of sampling and filtering on measured wind gusts. *J. Atmos. Oceanic Technol.*, **4**, 613–626.

Beljaars, A. C. M. (1991). Numerical schemes for parametrization. In *Proc. of ECMWF Seminar on Numerical Methods in Atmospheric Models*, Vol. 2, pp. 1–42, Reading, 9–13 September 1991.

Beljaars, A. C. M. (1994). The parametrization of surface fluxes in large-scale models under free convection. *Q. J. R. Meteorol. Soc.*, **121**, 255–270.

Beljaars, A. C. M. (1995). The impact of some aspects of the boundary layer scheme in the ECMWF model. In *Proc. of ECMWF Seminar on Parametrization of Sub-grid Scale Physical Processes*, pp. 125–161, Reading, 5–9 September 1994.

Beljaars, A. C. M. (1997). Air-sea interaction in the ECMWF model. In *Proc. of ECMWF Seminar on Atmosphere Surface Interaction*, pp. 33–52, Reading, 8–12 September 1997.

Beljaars, A. C. M., Bechtold, P., Köhler, M., Morcrette, J.-J., Tompkins, A., Viterbo, P. and Wedi, N. (2004a). The numerics of physical parametrization. In *Proc. of ECMWF Seminar on Recent Developments in Numerical Methods for Atmosphere and Ocean Modelling*, pp. 113–134, Reading, 6–10 September 2004.

Beljaars, A. C. M., Brown, A. R. and Wood, N. (2004b). A new parametrization of turbulent orographic form drag. *Q. J. R. Meteorol. Soc.*, **130**, 1327–1347.

Beljaars, A. C. M. and Viterbo, P. (1999). The role of the boundary layer in a numerical weather prediction model. In A. A. M. Holtslagkral and P. G. Duynkerke (Eds), *Clear and Cloudy Boundary Layers*, North Holland Publishers.

Bennets, D. A. and Hoskins, B. J. (1979). Conditional symmetric instability—a possible explanation for frontal rainbands. *Q. J. R. Meteorol. Soc.*, **105**, 945–962.

Bennets, D. A. and Sharp, J. C. (1982). The relevance of conditional symmetric instability to the prediction of meso-scale frontal rainbands. *Q. J. R. Meteorol. Soc.*, **108**, 595–602.

Berry, J. and Raison, J. (1982). Responses of macrophytes to temperature. *Encyclopedia of plant Physiology New Series, Physiological plant Ecology II*, **12B**, 277–388.

Best, M. J., Beljaars, A. C. M., Polcher, J. and Viterbo, P. (2004). A proposed structure for coupling tiled surfaces with the planetary boundary layer. *J. Hydr. Meteorol.*, **5**, 1271–1278.

Betts, A. K. and Ball, J. H. (1997). Albedo over the boreal forest. *J. Geophys. Res.*, **1028**, 28901–28909.

Betts, A. K., Viterbo, P. and Wood, E. (1998). Surface energy and water balance for the Arkansas–Red River basin from the ECMWF reanalysis. *J. Climate*, **11**, 19293–19306.

Bidlot, J.-R., Keeley, S. and Mogensen, K. (2014). Towards the inclusion of sea ice attenuation in an operational wave model. In *Proceedings of the 22nd IAHR International Symposium on ICE 2014 (IAHR-ICE 2014)*, available at http://rpsonline.com.sg/iahr-ice14/html/org.html.

Bigg, E. K. (1953). The supercooling of water. *Proc. Phys. Soc. London*, **B66**, 688–694.

Bithell, M., Gray, L. J., Harries, J. E., Rusell III, J. M. and Tuck, A. F. (1994). Synoptic interpretation of measurements from HALOE. *J. Atmos. Sci.*, **51**, 2942–2956.

Blackadar (1962). The vertical distribution of wind and turbulent exchange in a neutral atmosphere. *J. Appl. Meteorol*, **30**, 327–341.

Bloom, A. A., Bowman, K. W., Lee, M., Turner, A. J., Schroeder, R., Worden, J. R., Weidner, R., McDonald, K. C. and Jacob, D. J. (2017). A global wetland methane emissions and uncertainty dataset for atmospheric chemical transport models (wetcharts version 1.0). *Geoscientific Model Development*, **10**(6), 2141–2156, doi:10.5194/gmd-10-2141-2017, URL https://gmd.copernicus.org/articles/10/2141/2017/.

Bohren, C. F. and Barkstrom, B. R. (1974). Theory of the optical properties of snow. *Journal of Geophysical Research*, **79**(30), 4527–4535.

Bonan, G. B. (1994). Comparison of two land surface process models using prescribed forcings. *J. Geophys. Res.*, **99**, 25803–25818.

Boone, A. and Etchevers, P. (2001). An intercomparison of three snow schemes of varying complexity coupled to the same land surface model: Local-scale evaluation at an alpine site. *J. Hydrometeorol.*, **2**, 374–394.

Boone, A., Habets, F., Noilhan, J., Clark, D., Dirmeyer, P., Fox, S., Gusev, Y., Haddeland, I., Koster, R., Lohmann, D., Mahanama, S., Mitchell, K., Nasonova, O., Niu, G.-Y., Pitman, A., Polcher, J., Shmakin, A. B., Tanaka, K., van den Hurk, B., Vérant, S., Verseghy, D., Viterbo, P. and Yang., Z.-L. (2004). The Rhône-Aggregation Land Surface Scheme Intercomparison Project: An overview. *J. Climate*, **17**, 187–208.

Bosveld, F. C., Holtslag, A. A. M. and van den Hurk, B. J. J. M. (1999). Interpretation of crown radiation temperatures of a dense Douglas fir forest with similaty theory. *Boundary-Layer Meteorol.*, **92**, 429–451.

Boucher, O. and Lohmann, U. (1995). The sulfate-ccn-cloud albedo effect. *Tellus B: Chemical and Physical Meteorology*, **47**(3), 281–300.

Bougeault, P. and Lacarrere, P. (1989). Parameterization of orography-induced turbulence in a mesobeta–scale model. *Monthly Weather Review*, **117**(8), 1872 – 1890, doi:10.1175/1520-0493(1989)117⟨1872:POOITI⟩2.0.CO;2.

Boussetta, S. and Balsamo, G. (2021). Vegetation dataset of land use/land cover and leaf area index. *CONFESS EU project report. ECMWF*.

Boussetta, S., Balsamo, G., Arduini, G., Dutra, E., McNorton, J., Choulga, M., Agustí-Panareda, A., Beljaars, A., Wedi, N., Munõz-Sabater, J., de Rosnay, P., Sandu, I., Hadade, I., Carver, G., Mazzetti, C., Prudhomme, C., Yamazaki, D. and Zsoter, E. (2021). Ecland: The ecmwf land surface modelling system. *Atmosphere*, **12**(6), doi:10.3390/atmos12060723, URL https://www.mdpi.com/2073-4433/12/6/723.

Boussetta, S., Balsamo, G., Beljaars, A., Agusti-Panareda, A., Calvet, J., Jacobs, C., van den Hurk, B., Viterbo, P., Lafont, S., Dutra, E., Jarlan, L., Balzarolo, M., Papale, D. and van der Werf, G. (2013a). Natural land carbon dioxide exchanges in the ECMWF Integrated Forecasting System: Implementation and offline validation. *J. Geophys. Res.*, **118**, 5923–5946, DOI: 10.1002/jgrd.50488.

Boussetta, S., Balsamo, G., Beljaars, A., Kral, T. and Jarlan, L. (2011). Impact of a satellite-derived leaf area index monthly climatology in a global numerical weather prediction model. *ECMWF Tech. Memo. No. 640*.

Boussetta, S., Balsamo, G., Beljaars, A., Kral, T. and Jarlan, L. (2013b). Impact of a satellite-derived Leaf Area Index monthly climatology in a global Numerical Weather Prediction model. *Int. J. Rem. Sens.*, **34**, 3520–3542.

Boutle, I. A., Abel, S. J., Hill, P. G. and Morcrette, C. J. (2013). Spatial variability of liquid cloud and rain: Observations and microphysical effects. *Q. J. R. Meteorol. Soc.*, **140**, 583–594, doi:10.1002/qj.2140.

Bozzo, A., Benedetti, A., Flemming, J., Kipling, Z. and Rémy, S. (2020). An aerosol climatology for global models based on the tropospheric aerosol scheme in the Integrated Forecasting System of ECMWF. *Geosci. Model Dev.*, **13**, 1007–1034.

Bozzo, A., Remy, S., Benedetti, A., Flemming, J., Bechtold, P., Rodwell, M. and Morcrette, J.-J. (2017). Implementation of a cams-based aerosol climatology in the ifs. *ECMWF Tech. Memo. No. 801*.

Brasseur, G. and Solomon, S. (1984). *Aeronomy of the Middle Atmosphere*. D. Reidel Publishing Co.

Bretagnon, P. and Francou, G. (1988). Planetary theories in rectangular and spherical variables. VSOP87 solutions. *Astron. Astrophys.*, **202**, 309–315.

Browning, K. A., Hardman, M. E., Harrold, T. W. and Pardoe, C. W. (1973). The structure of rainbands within a mid-latitude depression. *Q. J. R. Meteorol. Soc.*, **99**, 215–231.

Brun, E., David, P., Sudul, M. and Brunot, G. (1992). A numerical-model to simulate snow-cover stratigraphy for operational avalanche forecasting. *J. Glaciol.*, **38**, 13–22.

Brun, E., Martin, E., Simon, V., Gendre, C. and Coleou, C. (1989). An energy and mass model of snow cover suitable for operational avalanche forecasting. *J. Glaciol.*, **35**, 333–342.

Brutsaert, W. (1982). *Evaporation in the Atmosphere*. D. Reidel.

Buck, A. L. (1981). New equations for computing vapor pressure and enhancement factor. *J. Appl. Meteorol.*, **20**, 1527–1532.

Calonne, N., Flin, F., Morin, S., Lesaffre, B., du Roscoat, S. R. and Geindreau, C. (2011). Numerical and experimental investigations of the effective thermal conductivity of snow. *Geophysical Research Letters*, **38**(23).

Calvet, J. (2000). Investigating soil and atmospheric plant water stress using physiological and micrometeorological data. *Agric. Forest Meteorol.*, **103**, 229–247.

Calvet, J., Noilhan, J., Roujean, J.-L., Bessemoulin, P., Cabelguenne, M., Olioso, A. and Wigneron, J.-P. (1998). An interactive vegetation SVAT model tested against data from six contrasting sites. *Agric. Forest Meteorol.*, **92**, 73–95.

Calvet, J., Rivalland, V., Picon-Cochard, C. and Guehl, J. (2004). Modelling forest transpiration and CO_2 fluxes response to soil moisture stress. *Agric. Forest Meteorol.*, **124**, 143–156.

Cariolle, D. and Déqué, M. (1986). Southern hemisphere medium-scale waves and total ozone disturbances in a spectral general circulation model. *J. Geophys. Res.*, **91D**, 10825–10846.

Cariolle, D. and Teyssèdre, H. (2007). A revised linear ozone photochemistry parameterization for use in transport and general circulation models: multi-annual simulations. *Atmos. Chem. and Phys. Disc.*, **7**, 1655–1697.

Cecil, D. J., Buechler, D. E. and Blakeslee, R. J. (2014). Gridded lightning climatology from TRMM-LIS and OTD: Dataset description. *J. Geophys. Res.*, **135-136**, 404–414.

Chapront, J. and Francou, G. (2003). The lunar theory ELP revisited: Introduction of new planetary perturbations. *Astron. Astrophys.*, **404**, 735–742.

Cheng, L., Yip, T.-C. and Cho, H.-R. (1980). Determination of mean cumulus cloud vorticity from GATE A/B-scale potential vorticity budget. *J. Atmos. Sci.*, **37**, 797–811.

Choulga, M., Kourzeneva, E., Balsamo, G., Boussetta, S. and Wedi, N. (2019). Upgraded global mapping information for earth system modelling: an application to surface water depth at the ecmwf. *Hydrology and Earth System Sciences*, **23**(10), 4051–4076, doi:10.5194/hess-23-4051-2019, URL https://hess.copernicus.org/articles/23/4051/2019/.

Choulga, M., Kourzeneva, E., Zakharova, E. and Doganovsky, A. (2014). Estimation of the mean depth of boreal lakes for use in numerical weather prediction and climate modelling. *Tellus A: Dynamic Meteorology and Oceanography*, **66**(1), 21295, doi:10.3402/tellusa.v66.21295, URL https://doi.org/10.3402/tellusa.v66.21295.

Clapp, R. B. and Hornberger, G. M. (1978). Empirical equations for some soil hydraulic properties. *Water Resources Res.*, **14**, 601–604.

Clark, D. B., Mercado, L., Sitch, S., Jones, C., Gedney, N., Best, M., Pryor, M., Rooney, G., Essery, R., Blyth, E., Boucher, O., Harding, R., Huntingford, C. and Cox, P. (2011). The Joint UK Land Environment Simulator (JULES), model description. part 2: Carbon fluxes and vegetation. *Geosci. Mod. Dev.*, **4**, 701–722.

Clark, P. A., Harcourt, S. A., Macpherson, B., C. T. Mathison, S. C. and Naylor, M. (2008). Prediction of visibility and aerosol within the operational Met Office Unified Model. I: Model formulation and variational assimilation. *Quart. J. Roy. Meteorol. Soc.*, **134**, 1801–1816.

Coakley Jr., J. A. and Chylek, P. (1975). The two-stream approximation in radiation transfer: Including the angle of the incident radiation. *J. Atmos. Sci.*, **32**, 409–418.

Collatz, G. J., Ribas-Carbo, M. and Ball, J. A. (1992). Coupled photosynthesis-stomatal conductance model for leaves of C4 plants. *Aust. J. Plant Physiol.*, **19**, 519–538.

Cosby, B. J., Hornberger, G. M., Clapp, R. B. and Ginn, T. (1984). A statistical exploration of the relationships of soil moisture characteristics to the physical properties of soils. *Water Resources Res.*, **20**, 682–690.

Cuxart, J., Bougeault, P. and Redelsperger, J.-L. (2000). A turbulence scheme allowing for mesoscale and large-eddy simulations. *Quarterly Journal of the Royal Meteorological Society*, **126**(562), 1–30, doi: https://doi.org/10.1002/qj.49712656202.

Davies-Jones, R. P. (1983). An accurate theoretical approximation for adiabatic condensation temperature. *Mon. Wea. Rev.*, **111**, 1119–1121.

De Vries, D. A. (1975). Heat transfer in soils. In D. A. de Vries and N. H. Afgan (Eds), *Heat and Mass Transfer in the Biosphere. Part I: Transfer Processes in the Plant Environment*, pp. 4–28, Wiley.

Deardorff, J. W. (1978). Efficient prediction of ground surface temperature and moisture, with inclusion of a layer of vegetation. *J. Geophys. Res.*, **83C**, 1889–1903.

Decharme, B., Brun, E., Boone, A., Delire, C., Le Moigne, P. and Morin, S. (2016). Impacts of snow and organic soils parameterization on northern eurasian soil temperature profiles simulated by the isba land surface model. *The Cryosphere*, **10**(2), 853–877.

Defourny, B. M. B. S. K. G. K. O. L. C. e. a., P. (2014). Algorithm theoretical basis document for land cover climate change initiative. *Eur Space Agency, ESA 191*.

Derbyshire, S. H., Maidens, A. V., Milton, S. F., Stratton, R. A. and Willett, M. R. (2011). Adaptive detrainment in a convective parametrization. *Q. J. R. Meteorol. Soc.*, **137**, 1856–1871.

Deschamps, P.-Y., Herman, M. and Tanre, D. (1983). Modelisation du rayonnement solaire reflechi par l'atmosphere et la terre, entre 0.35 et 4 microns. *Rapport ESA 4393/80/F/DC(SC)*.

Dickinson, R., Henderson-Sellers, A. and Kennedy, P. (1993). Biosphere-atmosphere transfer scheme (BATS) version 1e as coupled to the NCAR community climate model. *Technical Report NCAR/TN-387 + STR*, NCAR Boulder, Colorado.

Dolman, A. J. and Gregory, D. (1992). The parameterization of rainfall interception in GCMs. *Q. J. R. Meteorol. Soc.*, **118**, 445–467.

Donner, L. J. and Philips, V. T. (2003). Boundary-layer control on convective available potential energy: Implications for cumulus parametrization. *J. Geophys. Res.*, **108.4701**, doi:10.1029/2003JD003773.

Dorman, J. L. and Sellers, P. J. (1989). A global climatology of albedo, roughness length and stomatal resistance for atmospheric general circluation models as represented by the simple biosphere model (SB). *J. Appl. Meterol.*, **28**, 833–855.

Douville, H., Royer, J.-F. and Mahfouf, J.-F. (1995). A new snow parameterization for the Météo-France climate model. Part I: Validation in stand-alone experiments. *Climate Dyn.*, **12**, 21–35.

Dubuisson, P., Buriez, J.-C. and Fouquart, Y. (1996). High spectral resolution solar radiative transfer in absorbing and scattering media: Application to the satellite simulation. *J. Quant. Spectrosc. Radiat. Transfer*, **55**, 103–126.

Dufour, L. and van Mieghem, J. (1975). *Thermodynamique de l'atmosphère*. Institut Royal Météorologique de Belgique, 278 pp.

Dümenil, L. and Todini, E. (1992). A rainfall-runoff scheme for use in the hamburg climate model. In *Advances in theoretical hydrology, A tribute to James Dooge. P. O'Kane*, European Geophysical Society Series on Hydrological Sciences 1,Elsevier, Amsterdam.

Dutra, E., Balsamo, G., Viterbo, P., Miranda, P., Beljaars, A., Schär, C. and Elder, K. (2010a). An improved snow scheme for the ECMWF Land Surface Model: Description and offline validation. *J. Hydrometeorol.*, **11**, 7499–7506.

Dutra, E., Stepanenko, V. M., Balsamo, G., Viterbo, P., Miranda, P. M. A., Mironov, D. and Schär, C. (2010b). An offline study of the impact of lakes on the performance of the ecmwf surface scheme. *Boreal Env. Res.*, **15**, 100–112.

Dyer, A. J. (1974). A review of flux-profile relationships. *Boundary-Layer Meteorol.*, **7**, 363–372.

Ebert, E. E. and Curry, J. A. (1992). A parametrization of ice cloud optical properties for climate models. *J. Geophys. Res.*, **97D**, 3831–3836.

Ebert, E. E. and Curry, J. A. (1993). An intermediate one-dimensional thermodynamic sea ice model for investigating ice-atmosphere interactions. *J. Geophys. Res.*, **98C**, 10085–10109.

ECMWF (2023). Ifs documentation, part 8: Atmospheric composition. *ECMWF IFS Documentation, Cy48r1*, Research Department, ECMWF.

Elsasser, W. M. (1942). Heat transfer by infrared radiation in the atmosphere. *Harvard Meteorological Studies No. 6*, p. 107.

Emanuel, K. A. (1982). Inertial instability and mesoscale convective systems. Part II: Symmetric CISK in a baroclinic flow. *J. Atmos. Sci.*, **39**, 1080–1097.

Erickson, D., Merrill, J. and Duce, R. (1986). Seasonal estimates of global atmospheric sea-salt distributions. *J. Geophys. Res. Atmos.*, **91**(D1), 1067–1072.

Ern, M. P., Preusse, P. and Warner, C. D. (2004). Absolute values of gravity wave momentum flux derived from satellite data. *J. Geophys. Res.*, **109**, D20103.

Etling, D. (1989). On atmsopheric vortex streets in the wake of large islands. *Meteorol. Atmos. Phys.*, **41**, 157–164.

Fairall, C. W., Bradley, E. F., Godfrey, J. S., Wick, G. A. and Edson, J. B. (1996). Cool-skin and warm-layer effects on sea surface temperature. *J. Geophys. Res.*, **101**, 1295–1308.

FAO (2003). Digital soil map of the world (DSMW). *Technical report*, Food and Agriculture Organization of the United Nations, re-issued version.

Farouki, O. T. (1986). Thermal properties of soils. In W. R. van Wijk (Ed.), *Physics of Plant Environments*, North-Holland Publishing, Amsterdam.

Farquhar, G. D., von Caemmerer, S. and Berry, J. A. (1980). A biochemical model of photosynthetic co2 assimilation in leaves of c3 species. *Planta*, **149**(1), 78–90, doi:10.1007/BF00386231.

Farquhar, G. D. and Wong, S. (1984). An empirical model of stomatal conductance. *Australian Journal of Plant Physiology*, **11**, 191–210.

Fels, S. B. (1979). Simple strategies for inclusion of Voigt effects in infrared cooling rate calculations. *Appl. Optics*, **18**, 2634–2637.

Flemming, J., Benedetti, A., Innesas, A., Engelen, R., Jones, L., Huijnen, V., Remy, S., Parrington, M., Suttie, M., Bozzo, A., Peuch, V.-H., Akritidis, D. and Katragkou, E. (2016). The cams interim reanalysis of carbon monoxide, ozone and aerosol for 2003–2015. *Atmos. Chem. Phys. Discuss.*, **doi:10.5194/acp-2016-666, in review**.

Forbes, R. and Ahlgrimm, M. (2014). On the representation of high-latitude boundary layer mixed-phase cloud in the ECMWF global model. *Mon. Wea. Rev.*, **142**, 3425–3445, doi:10.1175/MWR-D-13-00325.1.

Forbes, R., Tvonevsky, I., Hewson, T. and Leutbecher, M. (2014). Towards predicting high-impact freezing rain events. *ECMWF Newsletter, No. 141*, pp. 15–21.

Forbes, R. M. and Tompkins, A. M. (2011). An improved representation of cloud and precipitation. *ECMWF Newsletter No. 129*, pp. 13–18.

Forbes, R. M., Tompkins, A. M. and Untch, A. (2011). A new prognostic bulk microphysics scheme for the IFS. *ECMWF Tech. Memo. No. 649*.

Foster, D. S. (1958). Thunderstorm gusts compared with computed downdraught speeds. *Mon. Wea. Rev.*, **86**, 91–94.

Fouquart, Y. (1974). Utilisation des approximants de pade pour l'etude des largeurs equivalentes de raies formees en atmosphere diffusante. *J. Quant. Spectrosc. Radiat. Transfer*, **14**, 497–508.

Fouquart, Y. (1987). Radiative transfer in climate modeling. In M. E. Schlesinger (Ed.), *NATO Advanced Study Institute on Physically-Based Modeling and Simulation of Climate and Climate Changes*, pp. 223–283, Erice, Sicily, 11–23 May 1986.

Fouquart, Y. and Bonnel, B. (1980). Computations of solar heating of the earth's atmosphere: A new parameterization. *Beitr. Phys. Atmos.*, **53**, 35–62.

Fritsch, J. M. and Chappell, C. G. (1980). Numerical prediction of convectively driven mesoscale pressure systems. Part I: Convective parametrization. *J. Atmos. Sci.*, **37**, 1722–1733.

Fritts, D. C. and Nastrom, D. D. (1980). Sources of mesoscale variability of gravity waves. Part ii: frontal, convective, and jet stream excitation. *J. Atmos. Sci.*, **49**, 111–127.

Fritts, D. C. and Nastrom, D. D. (1993). Spectral estimates of gravity wave energy and momentum fluxes. part i: Energy dissipation, acceleration, and constraints. *J. Atmos. Sci.*, **50**, 3685–3694.

Fu, Q. (1996). An accurate parameterization of the solar radiative properties of cirrus clouds. *J. Climate*, **9**, 2058–2082.

Fu, Q., Liou, K. N., Cribb, M. C., Charlock, T. P. and Grossman, A. (1997). Multiple scattering parameterization in thermal infrared radiative transfer. *J. Atmos. Sci.*, **54**, 2799–2812.

Fu, Q., Yang, P. and Sun, W. B. (1998). An accurate parametrization of the infrared radiative properties of cirrus clouds of climate models. *J. Climate*, **11**, 2223–2237.

Garrigues, S., Lacaze, R., Baret, F., Morisette, J., Weiss, M., Nickeson, J., Fernandes, R., Plummer, S., Shabanov, N., Myneni, R., Knyazikhin, Y. and Wang, W. (2008). Validation and inter-comparison of global Leaf Area Index products derived from remote sensing data. *J. Geophys. Res.*, **113**, G02028.

Geleyn, J.-F. and Hollingsworth, A. (1979). An economical analytical method for the computation of the interaction between scattering and line absorption of radiation. *Beitr. Phys. Atmos.*, **52**, 1–16.

Genthon, C. (1992). Simulations of desert dust and sea-salt aerosols in antarctica with a general circulation model of the atmosphere. *Tellus B*, **44**(4), 371–389.

Gesch, D. B. and Larson, K. S. (1998). Techniques for development of global 1-kilometer digital elevation models. In *Proc. Pecora Thirteenth Symposium*, Sioux Falls, South Dakota, August 20–22, 1996 (CD-ROM), Am. Soc. Photogrammetry Remote Sens., Bethesda, Md.

Giard, D. and Bazile, E. (2000). Implentation of a new assimilation scheme for soil and surface variables in a global NWP model. *Mon. Wea. Rev.*, **128**, 997–1015.

Gierens, K., Kohlhepp, R., Spichtinger, P. and Schrödter-Homscheidt, M. (2004). Ice supersaturation as seen from TOVS. *Atmos. Chem. Phys.*, **4**, 539–547.

Gierens, K., Schumann, U., Helten, M., Smit, H. and Marenco, A. (1999). A distribution law for relative humidity in the upper troposphere and lower stratosphere derived from three years of mozaic measurements. *Ann. Geophysicae*, **17**, 1218–1226.

Gierens, K., Schumann, U., Helten, M., Smit, H. and Wang, P. H. (2000). Ice-supersaturated regions and subvisible cirrus in the northern midlatitude upper troposphere. *J. Geophys. Res.*, **105**, 22743–22753.

Giorgetta, M. A. and Morcrette, J.-J. (1995). Voigt line approximation in the ECMWF radiation scheme. *Mon. Wea. Rev.*, **123**, 3381–3383.

GLIMS and NSIDC (2005, updated 2018). Global land ice measurements from space glacier database. doi:DOI:10.7265/N5V98602, compiled and made available by the international GLIMS community and the National Snow and Ice Data Center.

Godfrey, J. S. and Beljaars, A. C. M. (1991). On the turbulent fluxes of buoyancy, heat and moisture at the air-sea interface at low wind speed. *J. Geophys. Res.*, **96**, 22043–22048.

Goudriaan, J. (1986). A simple and fast numerical method for the computation of daily totals of crop photosynthesis. *Agric. Forest Meteorol.*, **38**, 249–254.

Goudriaan, J., Laar, H. V., Keulen, H. V. and Louwerse, W. (1985). Photosynthesis, CO_2 and plant production. In *Wheat Growth and Modelling, NATO ASI Series, Series A: Life Sciences*, Vol. 86, pp. 107–122, W., Day, and R.K., Atkin (Eds.).

Gregory, D. (1997). Parametrization of convective momentum transports in the ECMWF model: evaluation using cloud resolving models and impact upon model climate. In *Proc. ECMWF Workshop on New Insights and Approaches to Convective Parametrization*, pp. 208–227, Reading, 4–7 November 1996.

Gregory, D., Kershaw, R. and Inness, P. M. (1997). Parametrization of momentum transports by convection. II: Tests in single-column and general circulation models. *Q. J. R. Meteorol. Soc.*, **123**, 1153–1183.

Gregory, D., Morcrette, J.-J., Jacob, C., Beljaars, A. C. M. and Stockdale, T. (2000). Revision of convection, radiation and cloud schemes in the ecmwf integrated forecasting system. *Quart. J. R. Meteorol. Soc.*, **126**, 1685–1710.

Gultepe, I., Müller, M. D. and Boybeyi, Z. (2006). A new visibility parameterization for warm-fog applications in numerical weather prediction models. *J. Appl. Meteorol. Climatol.*, **45**(11), 1469–1480.

Gurevitch, M. I. (1965). *Theory of Jets in Ideal Fluids*. Academic Press.

Haltiner, G. J. and Williams, R. T. (1980). *Numerical Prediction and Dynamic Meteorology*. John Wiley and Sons, 447 pp.

Hansen, J. and Sato, M. (2004). Greenhouse gas growth rates. *Proc. Natl. Acad. Sci. USA*, **101**, 16109–16114.

Harman, I. N., Best, M. J. and Belcher, S. E. (2004). Radiative exchange in an urban street canyon. *Boundary-Layer Meteorology*, **110**, 301–316.

HAWKS (2000). The Hitran Atmospheric WorKStation. URL http://www.hitran.com.

Herzegh, P. H. and Hobbs, P. V. (1980). The mesoscale and microscale structure and organization of clouds and precipitation in mid-latitude cyclones. Part II: Warm frontal clouds. *J. Atmos. Sci.*, **37**, 597–611.

Heymsfield, A. J. (1977). Precipitation development in stratiform ice clouds: A microphysical and dynamical study. *Journal of Atmospheric Sciences*, **34**(2), 367–381.

Heymsfield, A. J., Miloshevich, L. M., Twohy, C., G. Sachse, G. and Oltmans, S. (1998). Upper-tropospheric relative humidity observations and implications for cirrus ice nucleation. *Geophys. Res. Lett.*, **25**, 1343–1346.

Hillel, D. (1982). *Introduction to Soil Physics*. Academic Press.

Hogan, R., Ahlgrimm, M., Balsamo, G., Beljaars, A., Berrisford, P., Bozzo, A., Giuseppe, F. D., Forbes, R., Haiden, T., Lang, S., Mayer, M., Polichtchouk, I., Sandu, I., Vitart, F. and Wedi, N. (2017). Radiation in numerical weather prediction. *ECMWF Tech. Memo. No. 816*.

Hogan, R. J. (2022). ecRad radiation scheme: User Guide, version 1.5. URL https://confluence.ecmwf.int/display/ECRAD.

Hogan, R. J. and Bozzo, A. (2015). Mitigating errors in surface temperature forecasts using approximate radiation updates. *J. Adv. Modeling Earth Sys.*, pp. 836–853.

Hogan, R. J. and Bozzo, A. (2016). ECRAD: A new radiation scheme for the IFS. *ECMWF Tech. Memo. No. 787*.

Hogan, R. J. and Bozzo, A. (2018). A flexible and efficient radiation scheme for the ECMWF model. *J. Adv. Modeling Earth Sys.*, **10**, 1990–2008.

Hogan, R. J. and Hirahara, S. (2016). Effect of solar zenith angle specification in models on mean shortwave fluxes and stratospheric temperatures. *Geophys. Res. Lett.*, **43**, 482–488.

Hogan, R. J. and Illingworth, A. J. (2000). Deriving cloud overlap statistics from radar. *Q. J. R. Meteorol. Soc.*, **126A**, 2903–2909.

Hogan, R. J. and Illingworth, A. J. (2003). Parameterizing ice cloud inhomogeneity and the overlap of inhomogeneities using cloud radar data. *J. Atmos. Sci.*, **60**, 756–767.

Hogan, R. J. and Matricardi, M. (2022). A tool for generating fast *k*-distribution gas-optics models for weather and climate applications. *J. Adv. Modeling Earth Sys.*, **14**, e2022MS003033.

Hogström, U. (1988). Non-dimensional wind and temperature profiles in the atmospheric surface layer: A re-evaluation. *Boundary-Layer Meteorol.*, **42**, 55–78.

Holtslag, A. A. M. (1998). Modelling of atmospheric boundary layers. In A. A. M. Holtslag and P. G. Duynkerke (Eds), *Clear and Cloudy Boundary Layers*, pp. 85–1102, Royal Netherlands Academy of Arts and Sciences.

Holtslag, A. A. M. and Bruin, H. A. R. D. (1988). Applied modelling of the night-time surface energy balance over land. *J. Appl. Meteorol.*, **27**, 689–704.

Holtslag, A. A. M. and Moeng, C.-H. (1991). Eddy diffusivity and countergradient transport in the convective atmospheric boundary layer. *J. Atmos. Sci.*, **48**, 1690–1698.

Houze, R. A., Locatelli, J. D. and Hobbs, P. V. (1976). Dynamics and cloud microphysics of the rainbands in an occluded frontal system. *J. Atmos. Sci.*, **35**, 1921–1936.

Howat, I. M., Negrete, A. and Smith, B. E. (2014). The greenland ice mapping project (gimp) land classification and surface elevation data sets. *The Cryosphere*, **8**(4), 1509–1518, doi:10.5194/tc-8-1509-2014, URL https://tc.copernicus.org/articles/8/1509/2014/.

Hrastinski, M., Mašek, J., Bašták Ďurán, I., Grisogono, B. and Brožková, R. (2025). Regime-dependent turbulence length-scale formulation for nwp models based on turbulence kinetic energy, shear, and stratification. *Monthly Weather Review*, **153**(11), 2571 – 2591, doi:10.1175/MWR-D-24-0184.1.

Iacono, M., Delamere, J., Mlawer, E., Shephard, M., Clough, S. and Collins, W. (2008). Radiative forcing by long-lived greenhouse gases: Calculations with the AER radiative transfer models. *J. Geophys. Res.*, **113D**, 13103.

Ingleby, B., Arduini, G., Balsamo, G., Boussetta, S., Ochi, K., Pinnington, E. and de Rosnay, P. (2023). Improved two-metre temperature forecasts in the 2024 upgrade. *ECMWF Newsletter No. 178*, pp. 24–29, doi:10.21957/bi49s20qa8.

Inness, A., Baier, F., Benedetti, A., Bouarar, I., Chabrillat, S., Clark, H., Clerbaux, C., Coheur, P., Engelen, R. J., Errera, Q., Flemming, J., George, M., Granier, C., Hadji-Lazaro, J., Huijnen, V., Hurtmans, D., Jones, L., Kaiser, J. W., Kapsomenakis, J., Lefever, K., Leitão, J., Razinger, M., Richter, A., Schultz, M. G., Simmons, A. J., Suttie, M., Stein, O., Thépaut, J.-N., Thouret, V., Vrekoussis, M., Zerefos, C. and the MACC team (2013). The macc reanalysis: an 8 yr data set of atmospheric composition. *Atmos. Chem. Phys.*, **13**, 4073–4109.

Jacobs, C. (1994). *Direct impact of atmospheric CO_2 enrichment on regional transpiration*. Wageningen Agricultural University, phD. Thesis.

Jacobs, C., van den Hurk, B. and de Bruin, H. (1996). Stomatal behaviour and photosynthetic rate of unstressed grapevines in semi-arid conditions. *Agric. Forest Meteorol.*, **80**, 111–134.

Jacquemin, B. and Noilhan, J. (1990). Sensitivity study and validation of a land-surface parameterization using the HAPEX-MOBILHY data set. *Boundary-Layer Meteorol.*, **52**, 93–134.

Jakob, C. and Klein, S. A. (2000). A parametrization of the effects of cloud and precipitation overlap for use in general circulation models. *Q. J. R. Meteorol. Soc.*, **126**, 2525–2544.

Jakob, C. and Siebesma, A. P. (2003). A new subcloud model for mass flux convection schemes. influence on triggering, updraught properties and model climate. *Mon. Wea. Rev.*, **131**, 2765–2778.

Janssen, P. A. E. M. (1997). Effect of surface gravity waves on the heat flux. *ECMWF Tech. Memo. No. 239*.

Janssen, P. A. E. M., Beljaars, A. C. M., Simmons, A. and Viterbo, P. (1992). The determination of the surface stress in an atmospheric model. *Mon. Wea. Rev.*, **120**, 2977–2985.

Janssen, P. A. E. M. and Bidlot, J.-R. (2018). Progress in operational wave forecasting. *Procedia IUTAM*, **26**, 14–29.

Jarlan, L., Balsamo, G., Lafont, S., Beljaars, A., Calvet, J. and Mougin, E. (2008). Analysis of Leaf Area Index in the ECMWF land surface scheme and impact on latent heat and carbon fluxes: Applications to West Africa. *J. Geophys. Res.*, **113**, D24117.

Jarvis, P. J. (1976). The interpretation of the variations in leaf-water potential and stomatal conductance found in canopies in the field. *Phil. Trans. R. Soc. London*, **B723**, 385–610.

Johansen, O. (1975). *Thermal Conductivity of Soils*. Ph.D. thesis, Trondheim, Norway.

Johnson, R. H. (1976). The role of convective-scale precipitation downdrafts in cumulus and synoptic scale interactions. *J. Atmos. Sci.*, **33**, 1890–1910.

Johnson, R. H. (1980). Diagnosis of convective and mesoscale motions during Phase III of GATE. *J. Atmos. Sci.*, **37**, 733–753.

Jones, R. L., Pyle, J. A., Harries, J. E., Zavody, A. M., Russell III, J. M. and Gille, J. C. (1986). The water vapour budget of the stratosphere studied using LIMS and SAMS satellite data. *Q. J. R. Meteorol. Soc.*, **112**, 1127–1143.

Jordan, R. (1991). A one-dimensional temperature model for a snow cover: Technical documentation for sntherm. *Technical Report CRREL Special Rep. 91-b*, Cold regions research and engineering lab, Hanover, NH.

Joseph, J. H., Wiscombe, W. J. and Weinman, J. A. (1976). The Delta-Eddington approximation for radiative flux transfer. *J. Atmos. Sci.*, **33**, 2452–2459.

Kanda, M., Kawai, T. and Nakagawa, K. (2005). A simple theoretical radiation scheme for regular building arrays. *Boundary-Layer Meteorology*, **114**, 71–90.

Kärcher, B. and Lohmann, U. (2002). A parameterization of cirrus cloud formation: Homogeneous freezing of supercooled aerosols. *J. Geophys. Res.*, **107**, doi:10.1029/2001JD000470.

Kattge, J. and Knorr, W. (2007). Temperature acclimation in a biochemical model of photosynthesis: a reanalysis of data from 36 species. *Plant, Cell & Environment*, **30**(9), 1176–1190.

Kessler, E. (1969). *On the distribution and continuity of water substance in atmopsheric circulation*, *Meteorological Monographs*, Vol. 10. Am. Meteorol. Soc., Boston, MA.

Khairoutdinov, M. and Kogan, Y. (2000). A new cloud physics parameterization in a large-eddy simulation model of marine stratocumulus. *Mon. Wea. Rev.*, **128**(1), 229–243.

Khvorostyanov, V. and Sassen, K. (1998). Cirrus cloud simulation using explicit microphysics and radiation. part ii: Microphysics, vapor and ice mass budgets, and optical and radiative properties. *J. Atmos. Sci.*, **55**, 1822–1845.

Kirchoff, G. (1876). *Vorlesungen über Mathematische Physik*. Leipzig.

Köhler, M. (2005). Improved prediction of boundary layer clouds. *ECMWF Newsletter No. 104*, pp. 18–22.

Köhler, M., Ahlgrimm, M. and Beljaars, A. (2011). Unified treatment of dry convective and stratocumulus-topped boundary layers in the ECMWF model. *Q. J. R. Meteorol. Soc.*, **137**, 43–57.

Koschmieder, H. (1924). Theorie der horizontalen sichtweite. *Beitr. Phys. Frei. Atmos.*, **12**, 171–181.

Koster, R. D. and Suarez, M. J. (1992). A comparative analysis of two land surface heterogeneity representations. *J. Climate*, **5**, 1379–1390.

Krinner, G., Viovy, N., de Noblet-Ducoudre, N., Ogae, J., Polcher, J., Friedlingstein, P., Ciais, P., Sitch, S., and Prentice, I. C. (2005). A dynamic global vegetation model for studies of the coupled atmosphere-biosphere system. *Global Biogeochem. Cycles*, **19**.

Kuo, H. L. and Raymond, W. H. (1980). A quasi-one-dimensional cumulus cloud model and parametrization of cumulus heating and mixing effects. *Mon. Wea. Rev.*, **108**, 991–1009.

Landweber, L. (1961). *Motion of Immersed and Floating Bodies. Handbook of Fluid Dynamics*. McGraw-Hill, 1st edition.

Le Mone, M. A. and Pennell, W. T. (1976). The relationship of trade wind cumulus distribution to subcloud layer fluxes and structure. *Mon. Wea. Rev.*, **104**, 524–539.

Le Texier, L., Solomon, S. and Garcia, R. R. (1988). The role of molecular hydrogen and methane oxidation in the water vapour budget of the stratosphere. *Q. J. R. Meteorol. Soc.*, **114**, 281–295.

Levis, S. G., Bonan, B., Vertenstein, M. and Oleson, K. (2004). The Community Land Model's Dynamic Global Vegetation Model (CLM-DGVM): Technical Description and User's Guide. *NCAR Tech. Note TN-459+IA*, p. 50 pp.

Lin, Y. L., Farley, R. D. and Orville, H. D. (1983). Bulk parameterization of the snow field in a cloud model. *J. Climate Appl. Meteorol.*, **22**, 1065–1092.

Lindzen, R. S. (1981). Some remarks on cumulus parametrization. *Rep. on NASA-GISS Workshop: Clouds in Climate: Modelling and Satellite Observational Studies*, pp. 42–51.

Liu, J. Y. and Orville, H. D. (1969). Numerical modeling of precipitation and cloud shadow effects on mountain-induced cumuli. *J. Atmos. Sci.*, **26**, 1283–1298.

Liu, Q. and Schmetz, J. (1988). On the problem of an analytical solution to the diffusivity factor. *Beitr. Phys. Atmos.*, **61**, 23–29.

Lock, A. P. (1998). The parameterization of entrainment in cloudy boundary layers. *Q. J. R. Meteorol. Soc.*, **124**, 2729–2753.

Lock, A. P., Brown, A. R., Bush, M. R., Martin, G. M. and Smith, R. N. B. (2000). A new boundary layer mixing scheme. part i: Scheme description and single-column model tests. *Mon. Wea. Rev.*, **128**, 3187–3199.

Lopez, P. (2016). A lightning parameterization for the ECMWF Integrated Forecasting System. *Mon. Wea. Rev.*, **144**, 3057–3075.

Lopez, P. (2024). Solar eclipses in the IFS. *ECMWF Tech. Memo. No. 920*.

Lott, F. and Miller, M. J. (1997). A new subgrid-scale orographic drag parametrization: Its formulation and testing. *Q. J. R. Meteorol. Soc.*, **123**, 101–127.

Louis, J. F., Tiedtke, M. and Geleyn, J.-F. (1982). A short history of the operational PBL parametrization at ECMWF. In *Proc. ECMWF Workshop on Boundary Layer Parametrization*, pp. 59–80, Reading, 25–27 November 1981.

Loveland, T. R., Reed, B. C., Brown, J. F., Ohlen, D. O., Zhu, Z., Youing, L. and Merchant, J. W. (2000). Development of a global land cover characteristics database and IGB6 DISCover from the 1km AVHRR data. *Int. J. Remote Sensing*, **21**, 1303–1330.

Lowenthal, D. H., Borys, R. D., Choularton, T. W., Bower, K. N., Flynn, M. J. and Gallagher, M. W. (2004). Parameterization of the cloud droplet–sulfate relationship. *Atmos. Env.*, **38**(2), 287–292.

Lundin, L.-C. (1989). Water and heat fluxes in frozen soils: Basic theory and operational modelling. In *Summary of Dissertations from the Faculty of Science*, Vol. 186, Uppsala University.

Lynch-Stieglitz, M. (1994). The development and validation of a simple snow model for the Giss GCM. *J. Climate*, **7**, 1842–1855.

Macdonald, R., Griffiths, R. and Hall, D. (1998). An improved method for the estimation of surface roughness of obstacle arrays. *Atmospheric environment*, **32**, 1857–1864.

Mace, G. G. and Benson-Troth, S. (2002). Cloud-layer overlap characteristics derived from long-term cloud radar data. *J. Climate*, **15**, 2505–2515.

Mahfouf, J. F. and Jacquemin, B. (1989). A study of rainfall interception using a land surface paramterization for mesoscale meteorological models. *J. Appl. Meteorol.*, **28**, 1282–1302.

Mahfouf, J. F., Manzi, A., Noilhan, J., Giordani, H. and Dequé, M. (1995). The land surface scheme ISBA within the Météo-France climate model ARPEGE. *J. Climate*, **8**, 2039–2057.

Mahfouf, J. F. and Noilhan, J. (1991). Comparative study of various formulations from bare soil using in situ data. *J. Appl. Meteorol.*, **30**, 1345–1365.

Mahrt, L. and Pan, H.-L. (1984). A two-layer model of soil hydrology. *Boundary-Layer Meteorol.*, **29**, 1–20.

Malardel, S. and Bechtold, P. (2019). The coupling of deep convection with the resolved flow via the divergence of mass flux in the IFS. *Q. J. R. Meteorol. Soc.*, **145**, 1832–1845.

Manners, J., Thelen, J.-C., Petch, J., Hill, P. and Edwards, J. M. (2009). Two fast radiative transfer methods to improve the temporal sampling of clouds in numerical weather prediction and climate models. *Q. J. R. Meteorol. Soc.*, **135**, 457–468.

Manzi, A. O. and Planton, S. (1994). Implementation of the ISBA parameterization scheme for land surface processes in a GCM: An annual-cycle experiment. *J. Hydrol.*, **155**, 355–389.

Marquet, P. (2008). Documentation of the tke-cbr turbulent scheme in the climate version 5.0 of arpege. *CNRM Internal Documentation, Cy32*.

Marquet, P. (2011). Definition of a moist entropy potential temperature: application to FIRE-I data flights. *Q. J. R. Meteorol. Soc.*, **137**, 768–791.

Marquet, P. (2015). On the computation of moist-air specific enthalpy. *Q. J. R. Meteorol. Soc.*, **141**, 67–84.

Marquet, P. and Bechtold, P. (2020). A new estimated inversion strength (EIS) based on the moist-air entropy. In *Research activities in Earth system modelling. Working Group on Numerical Experimentation Report No. 50. WCRP Report No.122020*, Ed. E. Astakhova, WMO, Geneva, available from http://bluebook.meteoinfo.ru/uploads/2020/docs/04_Marquet_Pascal_NewEntropyEIS.pdf.

Marquet, P. and Geleyn, J.-F. (2013). On a general definition of the squared brunt–väisälä frequency associated with the specific moist entropy potential temperature. *Quarterly Journal of the Royal Meteorological Society*, **139**(670), 85–100, doi:https://doi.org/10.1002/qj.1957.

Martin, G. M., Johnson, D. W. and Spice, A. (1994). The measurement and parameterization of effective radius of droplets in warm stratocumulus. *J. Atmos. Sci.*, **51**, 1823–1842.

Mason, B. J. (1971). *The Physics of Clouds*. Clarendon Press.

Mayer, M., Haimberger, L., Edwards, J. M. and Hyder, P. (2017). Toward consistent diagnostics of the coupled atmosphere and ocean energy budgets. *J. Climate*, **30**(22), 9225–9246.

McGuire, A., Melillo, J., Joyce, L., Kicklighter, D., Grace, A., Moore, B. and Vorosmarty, C. (1992). Interactions between carbon and nitrogen dynamics in estimating net primary productivity for potential vegetation in north america. *Golb. Biogeochem. Cyc.*, **6**, 101–124.

McLandress, C. and Scinocca, J. F. (2005). The GCM response to current parameterizations of nonorographic garvity wave drag. *J. Atmos. Sci.*, **62**, 2394–2413.

McNorton, J. R., Arduini, G., Bousserez, N., Agustí-Panareda, A., Balsamo, G., Boussetta, S., Choulga, M., Hadade, I. and Hogan, R. J. (2021). An urban scheme for the ecmwf integrated forecasting system: Single-column and global offline application. *Journal of Advances in Modeling Earth Systems*, **13**, e2020MS002375.

Meador, W. E. and Weaver, W. R. (1980). Two-stream approximations to radiative transfer in planetary atmospheres: A unified description of existing methods and a new improvement. *J. Atmos. Sci*, **37**, 630–643.

Meeus, J. (1998). *Astronomical Algorithms*. Willmann-Bell, Inc., Richmond, Virginia, USA, 2 edition, 477 pages.

Meyers, M. P., DeMott, P. J. and Cotton, W. R. (1992). New primary ice nucleation parameterization in an explicit model. *J. Appl. Meteor.*, **31**, 708–721.

Miles, J. W. and Huppert, H. E. (1969). Lee waves in a stratified flow. Part 4: Perturbation approximations. *J. Fluid Mech.*, **35**, 495–525.

Miller, M., Beljaars, A. C. M. and Palmer, T. N. (1992). The sensitivity of the ECMWF model to the parametrization of evaporation from the tropical oceans. *J. Climate*, **5**, 418–434.

Miller, M. J., Palmer, T. N. and Swinbank, R. (1989). Parametrization and influence of subgrid-scale orography in general circulation and numerical weather prediction models. *Meteorol. Atmos. Phys.*, **40**, 84–109.

Milly, P. C. D. (1982). Moisture and heat transport of hyseretic, inhomogeneous porous media: A matric head-based formulation and a numerical model. *Water Resources Res.*, **18**, 489–498.

Mironov, D. (2008). Parameterization of lakes in numerical weather prediction. description of a lake model. *COSMO Technical Report, No. 11*, p. 44 pp, Deutscher Wetterdienst, Offenbach am Main, Germany.

Mironov, D., Heise, E., Kourzeneva, E., Schneider, B. R. N. and Terzhevik, A. (2010). Implementation of the lake parameterisation scheme flake into the numerical weather prediction model cosmo. *Boreal Env. Res.*, **15**, 218–230.

Mlawer, E. J., Taubman, S. J., Brown, P. D., Iacono, M. J. and Clough, S. A. (1997). Radiative transfer for inhomogeneous atmospheres: RRTM, a validated correlated-k model for the longwave. *J. Geophys. Res.*, **102D**, 16663–16682.

Moody, E., King, M., Schaaf, C., Hall, D. and Platnick, S. (2007). Northern hemisphere five-year average (2000-2004) spectral albedos of surfaces in the presence of snow: Statistics computed from Terra MODIS land products. *Remote Sen. Environ.*, **111**, 337–345.

Morcrette, C. J. (2012). Improvements to a prognostic cloud scheme through changes to its cloud erosion parametrization. *Atmos. Sci. Lett.*, **13**(2), 95–102, doi:10.1002/asl.374.

Morcrette, J.-J. (1991). Radiation and cloud radiative properties in the ECMWF operational weather forecast model. *J. Geophys. Res.*, **96D**, 9121–9132.

Morcrette, J.-J., Barker, H., Cole, J., Iacono, M. and Pincus, R. (2008a). Impact of a new radiation package, McRad, in the ECMWF Integrated Forecasting System. *Mon. Wea. Rev.*, **136**, 4773–4798.

Morcrette, J.-J. and Fouquart, Y. (1985). On systematic errors in parametrized calculations of longwave radiation transfer. *Q. J. R. Meteorol. Soc.*, **111**, 691–708.

Morcrette, J.-J. and Fouquart, Y. (1986). The overlapping of cloud layers in shortwave radiation parameterizations. *J. Atmos. Sci.*, **43**, 321–328.

Morcrette, J.-J., Mozdzynski, G. and Leutbecher, M. (2008b). A reduced radiation grid for the ECMWF Integrated Forecasting System. *Mon. Wea. Rev.*, **136**, 4760–4772.

Morcrette, J.-J., Smith, L. and Fouquart, Y. (1986). Pressure and temperature dependence of the absorption in longwave radiation parametrizations. *Beitr. Phys. Atmos.*, **59**, 455–469.

Myneni, R. B., Hoffman, S., Knyazikhin, Y., Privette, J. L., Glassy, J., Tian, Y., Wang, Y., Song, X., Zhang, Y., Smith, G. R., Lotsch, A., Friedl, M., Morisette, J. T., Votava, P., Nemani, R. R. and Running, S. W. (1992). Global products of vegetation leaf area and fraction absorbed PAR from year one of MODIS data. *Remote Sensing Environ.*, **83**, 214–231.

Nieuwstadt, F. T. M. (1984). The turbulent structure of the stable, nocturnal boundary layer. *J. Atmos. Sci.*, **41**, 2202– 2216.

Niu, G.-Y. and Yang, Z.-L. (2007). An observation-based formulation of snow cover fraction and its evaluation over large north american river basins. *Journal of geophysical research: Atmospheres*, **112**(D21).

Nogueira, M., Boussetta, S., Balsamo, G., Albergel, C., Trigo, I. F., Johannsen, F., Miralles, D. G. and Dutra, E. (2021). Upgrading land-cover and vegetation seasonality in the ecmwf coupled system: Verification with fluxnet sites, meteosat satellite land surface temperatures, and era5 atmospheric reanalysis. *Journal of Geophysical Research: Atmospheres*, **126**(15), e2020JD034163, doi:https://doi.org/10.1029/2020JD034163, URL https://agupubs.onlinelibrary.wiley.com/doi/abs/10.1029/2020JD034163, e2020JD034163 2020JD034163.

Nordeng, T.-E. (1994). Extended versions of the convection parametrization scheme at ECMWF and their impact upon the mean climate and transient activity of the model in the tropics. *ECMWF Tech. Memo. No. 206*.

Norman, J., Garcia, R. and Verma, S. (1992). Soil surface co_2 fluxes and the carbon budget of a grassland. *J. Geophys. Res.*, **97**, 18,845–18,853.

Oleson, K. W., Bonan, G. B., Feddema, J., Vertenstein, M. and Grimmond, C. (2008). An urban parameterization for a global climate model. part i: Formulation and evaluation for two cities. *Journal of Applied Meteorology and Climatology*, **47**, 1038–1060.

Orr, A., Bechtold, P., Scinocca, J. F., Ern, M. and Janiskova, M. (2010). Improved middle atnosphere climate and forecasts in the ECMWF model through a non-orographic gravity wave drag parametrization. *J. Climate*, **23**, 5905–5926.

Ou, S. C. and Liou, K.-N. (1995). Ice microphysics and climatic temperature feedback. *Atmos. Res.*, **35**, 127–138.

Paltridge, G. W. and Platt, C. M. R. (1976). *Radiative Processes in Meteorology and Climatology*. Elsevier, New York, 318 pp.

Panofsky, H. A., Tennekes, H., Lenschow, D. H. and Wyngaard, J. C. (1977). The characteristics of turbulent velocity components in the surface layer under convective conditions. *Boundary-Layer Meteorol.*, **11**, 355–361.

Pastorello, G., Trotta, C. and et al., E. C. (2020). The fluxnet2015 dataset and the oneflux processing pipeline for eddy covariance data. *Sci Data*, **7**(225), doi:https://doi.org/10.1038/s41597-020-0534-3.

Patterson, K. A. (1990). *Global Distribution of Total and Total-available Soil Water-holding Capacities*. Master's thesis, Department of Geography, University of Delaware.

Paulson, C. A. (1970). The mathematical representation of wind speed and temperature profiles in the unstable atmospheric surface layer. *J. Appl. Meteorol.*, **9**, 857–861.

Pekel, J.-F., Cottam, A., Gorelick, N. and Belward, A. (2016). High-resolution mapping of global surface water and its long-term changes. *Nature*, **540**, doi:10.1038/nature20584.

Penner, E. (1970). Thermal conductivity of frozen soils. *Canadian J. Earth Sci.*, **7**, 982–987.

Peters-Lidard, C. D., Blackburn, E., Liang, X. and Wood, E. F. (1998). The effect of soil conductivity parametrization on surface energy fluxes and temperature. *J. Atmos. Sci.*, **55**, 1209–1224.

Philip, J. R. (1957). Evaporation and moisture and heat fields in the soil. *J. Meteorol.*, **14**, 354–366.

Phillips, S. P. (1984). Analytical surface pressure and drag for linear hydrostatic flow over three-dimensional elliptical mountains. *J. Atmos. Sci.*, **41**, 1073–1084.

Pincus, R., Barker, H. and Morcrette, J.-J. (2003). A fast, flexible, approximate technique for computing radiative transfer in inhomogeneous clouds. *J. Geophys. Res.*, **108D**, 4376.

Pincus, R. and Klein, S. A. (2000). Unresolved spatial variability and microphysical process rates in large-scale models. *J. Geophy. Res.*, **105**, 27059–27065.

Pitman, A. J., Yang, Z.-L., Cogley, J. G. and Henderson-Sellers, A. (1991). Description of bare essentials of surface transfer for the Bureau of Meteorology Research Centre AGCM. *Meteorological Research Report 32*.

Porson, A., Clark, P. A., Harman, I., Best, M. and Belcher, S. (2010). Implementation of a new urban energy budget scheme into metum. part ii: Validation against observations and model intercomparison. *Quarterly Journal of the Royal Meteorological Society*, **136**, 1530–1542.

Press, W. H., Teukolsky, S. A., Vetterling, W. T. and Flannery, B. P. (1992). *Numerical Recipes in Fortran*. Cambridge University Press.

Press, W. H., Teukolsky, S. A., Vetterling, W. T. and Flannery, B. P. (1996). *Numerical Recipes in Fortran 90 (2nd Ed.): The Art of Parallel Scientific Computing*. Cambridge University Press, ISBN 0521574390.

Prigent, C., Papa, F., Aires, F., Rossow, W. B. and Matthews, E. (2007). Global inundation dynamics inferred from multiple satellite observations, 1993–2000. *Journal of Geophysical Research: Atmospheres*, **112**(D12), doi:https://doi.org/10.1029/2006JD007847, URL https://agupubs.onlinelibrary.wiley.com/doi/abs/10.1029/2006JD007847.

Pruppacher, H. R. and Klett, J. D. (1997). *The Microphysics of Clouds and Precipitation*. Kluwer Academic Publishers, 954 pp.

Räisänen, P., Barker, H. W., Khairoutdinov, M. F., Li, J. and Randall, D. A. (2004). Stochastic generation of subgrid-scale cloudy columns for large-scale models. *Q. J. R. Meteorol. Soc.*, **130**, 2047–2067.

Räisänen, P. and Lindfors, A. V. (2019). On the computation of apparent direct solar radiation. *J. Atmos. Sci.*, **76**, 2761–2780.

Randel, W. J., Wu, F., Russell III, J. M., Roche, A. and Waters, J. W. (1998). Seasonal cycles and QBO variations in straospheric CH_4 and H_2O observed in UARS HALOE data. *J. Atmos. Sci.*, **55**, 163–185.

Raymond, D. and Fuchs-Stone, Z. (2021). Emergent properties of convection in OTREC and PREDICT. *J. Geophys. Res.*, **126**, doi:0.1029/2020JD033585.

Ren, C. and Mackenzie, A. R. (2005). Cirrus parametrization and the role of ice nuclei. *Q. J. R. Meteorol. Soc.*, **131**, 1585–1605.

Richards, L. A. (1931). Capillary conduction of liquids through porous mediums. *Physics*, **1**, 318–333.

Ridder, K. D. (2001). Rainwater storage on plant canopies. *J. Geophys. Res.*, **106**(D14), 14819–14826.

Rodgers, C. D. (1967). The radiative heat budget of the troposphere and lower stratosphere. *Report A2*, Planetary Circulation Project, Dept. of Meteorology, M.I.T., Cambridge, Mass.

Rodgers, C. D. and Walshaw, C. D. (1966). The computation of the infrared cooling rate in planetary atmospheres. *Q. J. R. Meteorol. Soc.*, **92**, 67–92.

Rodier, Q., Masson, V., Couvreux, F. and Paci, A. (2017). Evaluation of a buoyancy and shear based mixing length for a turbulence scheme. *Frontiers in Earth Science*, **Volume 5 - 2017**, doi:10.3389/feart.2017.00065.

Ronda, R., Bruin, H. D. and Holtslag, A. (2001). Representation of the canopy conductance in modelling the surface energy budget for low vegetation. *J. Appl. Meteorol.*, **40**, 1431–1444.

Rothman, L. S., Gamache, R. R., Goldman, A., Brown, L. R., Toth, R. A., Pickett, H. M., Poynter, R. L., Flaud, J.-M., Camy-Peyret, C., Barbe, A., usson, N., Rinsland, C. P. and Smith, M. A. H. (1986). The HITRAN database, 1986 edition. *Appl. Optics*, **26**, 4058–409.

Rothman, L. S., Gamache, R. R., Tipping, R. H., Rinsland, C. P. *et al.* (1992). The HITRAN database: Editions of 1991 and 1992. *J. Quant. Spectros. Radiat. Transfer*, **48**, 469–507.

Rotstayn, L., Ryan, B. and Katzfey, J. (2000). A scheme for calculation of the liquid fraction in mixed-phase stratiform clouds in large-scale models. *Mon. Wea. Rev.*, **128**, 1070–1088.

Rotstayn, L. D. (2000). On the "tuning" of autoconversion parameterizations in climate models. *J. Geophy. Res.*, **105**, 15495–15507.

Roujean, J.-L. (1996). A tractable physical model of shortwave radiation interception by vegetative canopies. *J. Geophys. Res.*, **101**, 9523–9532.

Rouse, W. R. (1984). Microclimate of the Arctic tree line. 2: Soil microclimate of tundra and forest. *Water Resources Res.*, **20**, 67–73.

Rutledge, S. A. and Hobbs, P. (1983). The mesoscale and microscale structure and organization of clouds and precipitation in midlatitude cyclones. viii: A model for the "seeder-feeder" process in warm-frontal rainbands. *J. Atmos Sci.*, **40**(5), 1185–1206.

Rutter, A. J., Kershaw, K. A., Robins, P. C. and Morton, A. J. (1972). A predictive model of rainfall interception in forests. Part I: Derivation of the model from observations in a plantation of Corsican pine. *Agric. Meteorol.*, **9**, 367–384.

Rutter, A. J., Morton, A. J. and Robins, P. C. (1975). A predictive model of rainfall interception in forests. Part II: Generalization of the model and comparison with observations in some coniferous and hardwood stands. *J. Appl. Ecol.*, **12**, 367–380.

Sachidananda, M. and Zrnic, D. S. (1986). Differential propagation phase shift and rainfall rate estimation. *Radio Sci.*, **21**(2), 235–247.

Sala, A. and Tenhunen, J. (1996). Simulations of canopy net photosynthesis and transpiration in quercus ilex l. under the influence of seasonal drought. *Agric. Forest Meteorol.*, **78**, 203–222.

Sandu, I., Beljaars, A. and Balsamo, G. (2011). Revision of the roughness length table. *ECMWF Research Memorandum*, **11104**.

Santer, B. D., Wigley, T. M. L., Simmons, A. J. and many co authors (2004). Identification of anthropogenic climate change using a second-generation reanalysis. *J. Geophys. Res.*, **109**, doi:10.1029/2004JD005075.

Sardeshmukh, P. and Hoskins, B. (1984). Spatial smoothing on the sphere. *Mon. Wea. Rev.*, **112**, 2524–2529.

Schaaf, C., Gao, F., Strahler, A., Lucht, W., Li, X., Tsang, T., Strugnell, N., Zhang, X., Jin, Y., Muller, J.-P., Lewis, P., Barnsley, M., Hobson, P., Disney, M., Roberts, G., Dunderdale, M., Doll, C., d'Entremont, R., Hu, B., Liang, S., Privette, J. and Roy, D. (2002). First operational brdf, albedo nadir reflectance products from modis. *Remote Sensing Environ.*, **83**, 135–148.

Scinocca, J. F. (2003). An accurate spectral nonorographic gravity wave drag parameterization for general circulation models. *J. Atmos. Sci.*, **60**, 667–682.

Seidel, D., Zhang, Y., Beljaars, A., Golaz, J.-C. and Medeiros, B. (2012). Climatology of the planetary boundary layer over continental United States and Europe. *J. Geophys. Res.*, **117**, D17106.

Shao, Y. and Irannejad, P. (1999). On the choice of soil hydraulic models in land-surface schemes. *Boundary-Layer Meteorol.*, **90**, 83–115.

Sharman, R. D. and Pearson, J. (2017). Prediction of energy dissipation rates for aviation turbulence. Part I: Forecasting nonconvective turbulence. *J. Appl. Meteor. Climatol.*, **56**, 317–337, doi:10.1175/JAMC–D–16–0205.1.

Shettle, E. P. and Weinman, J. A. (1970). The transfer of solar irradiance through inhomogeneous turbid atmospheres evaluated by Eddington's approximation. *J. Atmos. Sci.*, **27**, 1048–1055.

Shonk, J. K. P. and Hogan, R. J. (2008). Tripleclouds: An efficient method for representing horizontal cloud inhomogeneity in 1d radiation schemes by using three regions at each height. *J. Climate*, **21**, 2352–2370.

Shonk, J. K. P., Hogan, R. J., Edwards, J. M. and Mace, G. G. (2010). Effect of improving representation of horizontal and vertical cloud structure on the Earth's global radiation budget – 1. Review and parametrization. *Q. J. R. Meteorol. Soc.*, **136**, 1191–1204.

Shutts, G. J. and Gray, M. E. B. (1999). Numerical simulations of convective equilibrium under prescribed forcing. *Q. J. R. Meteorol. Soc*, **125**, 2767–2787.

Siebesma, P. and Cuijpers, J. W. M. (1995). Evaluation of parametric assumptions for shallow cumulus convection. *J. Atmos. Sci.*, **52**, 650–666.

Simmons, A. J., Untch, A., Jacob, C., Kallberg, P. and Under, P. (1999). Stratospheric water vapour and tropical tropopause temperatures in ECMWF analyses and muli-year simularions. *Q. J. R. Meteorol. Soc.*, **125**, 353–386.

Simpson, J. (1971). On cumulus entrainment and one-dimensional models. *J. Atmos. Sci.*, **28**, 449–455.

Simpson, J. and Wiggert, V. (1969). Models of precipitating cumulus towers. *Mon. Wea. Rev.*, **97**, 471–489.

Slater, T., Shepherd, A., McMillan, M., Muir, A., Gilbert, L., Hogg, A. E., Konrad, H. and Parrinello, T. (2018). A new digital elevation model of antarctica derived from cryosat-2 altimetry. *The Cryosphere*, **12**(4), 1551–1562, doi:10.5194/tc-12-1551-2018, URL https://tc.copernicus.org/articles/12/1551/2018/.

Slingo, A. (1989). A GCM parameterization for the shortwave radiative properties of water clouds. *J. Atmos. Sci.*, **46**, 1419–1427.

Slingo, A. and Schrecker, H. M. (1982). On the shortwave radiative properties of stratiform water clouds. *Quart. J. Roy. Meteorol. Soc.*, **108**, 407–426, doi:10.1002/qj.49710845607.

Smith, E. A. and Shi, L. (1992). Surface forcing of the infrared cooling profile over the Tibetan plateau. Part I: Influence of relative longwave radiative heating at high altitude. *J. Atmos. Sci.*, **49**, 805–822.

Spahni, R., Wania, R., Neef, L., van Weele, M., Pison, I., Bousquet, P., Frankenberg, C., Foster, P. N., Joos, F., Prentice, I. C. and van Velthoven, P. (2011). Constraining global methane emissions and uptake by ecosystems. *Biogeosciences*, **8**(6), 1643–1665, doi:10.5194/bg-8-1643-2011, URL https://bg.copernicus.org/articles/8/1643/2011/.

Spichtinger, P., Gierens, K. and Read, W. (2003). The global distribution of ice-supersaturated regions as seen by the Microwave Limb Sounder. *Q. J. R. Meteorol. Soc.*, **129**, 3391–3410.

Stackhouse, P. W. and Stephens, G. L. (1991). A theoretical and observational study of the radiative properties of cirrus: Results from FIRE 1986. **48**, 2044–2059.

Stallabrass, J. R. (1985). Measurements of the concentration of falling snow. In *Proc. Snow property measurement workshop. Tech. memorandum (Canada, 1985)*, pp. 389–410, 140, National Research Council Associate Committee on Geotechnical Research. Canada.

Steinheimer, M., Hantel, M. and Bechtold, P. (2007). Convection in Lorenz's global energy cycle with the ECMWF model. *Tellus*, **60A**, 1001–1022.

Still, C. J., Berry, J. A., Collatz, G. J. and DeFries, R. S. (2003). Global distribution of c3 and c4 vegetation: Carbon cycle implications. *Global Biogeochemical Cycles*, **17**(1), 6–1–6–14, doi:https://doi.org/10.1029/2001GB001807, URL https://agupubs.onlinelibrary.wiley.com/doi/abs/10.1029/2001GB001807.

Stoelinga, M. T. and Warner, T. T. (1999). Nonhydrostatic, mesobeta-scale model simulations of cloud ceiling and visibility for an east coast winter precipitation event. *J. Appl. Meteorol. Climatol.*, **38**(4), 385–404.

Sud, Y. and Mocko, D. (1999). New snow-phsics to complement ssib-part i: design and evaluation with islscp initiative i datasets. *J. Meteor. Soc. Japan*, **77**, 335–348.

Sun, S., Jin, J. and Xue, Y. (1999). A simple snow-atmosphere-soil transfer model. *Journal of Geophysical Research: Atmospheres*, **104**(D16), 19587–19597.

Sun, Z. (2001). Reply to comments by Greg M. McFarquhar on "Parametrization of effective sizes of cirrus-cloud particles and its verification against observations". (October B, 1999, 125, 3037-3055). *Quart J. Roy. Meteorol. Soc.*, **127**, 267–271, doi:10.1002/qj.49712757116.

Sun, Z. and Rikus, L. (1999). Parametrization of effective sizes of cirrus-cloud particles and its verification against observations. *Quart J. Roy. Meteorol. Soc.*, **125**, 3037–3055, doi:10.1002/qj.49712556012.

Sundqvist, H. (1978). A parameterization scheme for non-convective condensation including prediction of cloud water content. *Q. J. R. Meteorol. Soc.*, **104**, 677–690.

Sverdrup, H. U., Johnson, M. W. and Fleming, R. H. (1942). *The Oceans: Their Physics, Chemistry and General Biology*. Prentice Hall, 1087 pp.

Taylor, J. P., Edwards, J. M., Glew, M. D., Hignett, P. and Slingo, A. (1996). Studies with a flexible new radiation code. II: Comparisons with aircraft short-wave observations. *Q. J. R. Meteorol. Soc.*, **122**, 839–862.

Tegen, I., Hoorig, P., Chin, M., Fung, I., Jacob, D. and Penner, J. (1997). Contribution of different aerosol species to the global aerosol extinction optical thickness: Estimates from model results. *J. Geophys. Res.*, **102**, 23895–23915.

Thorpe, A. and Mason, B. (1966). The evaporation of ice spheres and ice crystals. *British J. Appl. Physics*, **17**(4), 541.

Tiedtke, M. (1989). A comprehensive mass flux scheme for cumulus parameterization in large-scale models. *Mon. Wea. Rev.*, **117**, 1779–1800.

Tiedtke, M. (1993). Representation of clouds in large-scale models. *Mon. Wea. Rev.*, **121**, 3040–3061.

Tjernstrom, M. (1993). Turbulence length scales in stably stratified free shear flow analyzed from slant aircraft profiles. *J. Appl. Meteorol.*, **32**, 948–963.

Tompkins, A. M., Bechtold, P., Beljaars, A., Benedetti, A., Cheinet, S., Janisková, M., Köhler, M., Lopez, P. and Morcrette, J. (2004). Moist physical processes in the IFS: Progress and Plans. *Technical report*, European Centre for Medium-Range Weather Forecasts.

Tompkins, A. M., Gierens, K. and Rädel, G. (2007). Ice supersaturation in the ECMWF integrated forecast system. *Q. J. R. Meteorol. Soc.*, **133**, 53–63.

Troen, I. and Mahrt, L. (1986). A simple model of the atmospheric boundary layer; sensitivity to surface evaporation. *Boundary-Layer Meteorol.*, **37**, 129–148.

Van den Hurk, B. J. J. M. and Viterbo, P. (2003). The Torne-Kalix PILPS 2(e) experiment as a test bed for modifications to the ECMWF land surface scheme. *Global and Planetary Change*, **38**, 165–173.

Van den Hurk, B. J. J. M., Viterbo, P., Beljaars, A. C. M. and Betts, A. K. (2000). Offline validation of the ERA40 surface scheme. *ECMWF Tech. Memo. No. 295*.

van Diepen, K. H. H., Goudriaan, J., de Arellano, J. V.-G. and de H. J. Boer (2022). Comparison of c3 photosynthetic responses to light and co2 predicted by the leaf photosynthesis models of farquhar et al. (1980) and goudriaan et al. (1985). *Journal of Advances in Modeling Earth Systems*, **14**(9), doi: https://doi.org/10.1029/2021MS002976.

van Genuchten, M. (1980). A closed form equation for predicting the hydraulic conductivity of unsaturated soils. *Soil Science Society of America Journal*, **44**, 892–898.

Van Heemst, H. (1986). Potential crop production. In *Modelling of Agricultural Production: Weather, Soil and Crops. Simulation Monographs*, Pudoc, Wangeningen, edited by H. van Keulen and J. Wolf.

Verger, A., Sánchez-Zapero, J., Weiss, M., Descals, A., Camacho, F., Lacaze, R. and Baret", F. (2023). "geov2: Improved smoothed and gap filled time series of lai, fapar and fcover 1 km copernicus global land products". *"International Journal of Applied Earth Observation and Geoinformation"*, **"123"**, "103479", doi:"https://doi.org/10.1016/j.jag.2023.103479", URL "https://www.sciencedirect.com/science/article/pii/S1569843223003035".

Verseghy, D. L. (1991). Class-A Canadian land surface scheme for GCMs. I: Soil model. *Int. J. Climatol.*, **11**, 111–133.

Viterbo, P. and Beljaars, A. C. M. (1995). An improved land surface parametrization scheme in the ECMWF model and its validation. *ECMWF Tech. Report No. 75*, Research Department, ECMWF.

Viterbo, P., Beljaars, A. C. M., Mahouf, J.-F. and Teixeira, J. (1999). The representation of soil moisture freezing and its impact on the stable boundary layer. *Q. J. R. Meteorol. Soc.*, **125**, 2401–2426.

Viterbo, P. and Betts, A. K. (1999). Impact on ECMWF forecasts of changes to the albedo of the boreal forests in the presence of snow. *J. Geophys. Res.*, **104**, 27803–27810.

Vogelezang, D. and Holtslag, A. (1996). Evaluation and model impacts of alternative boundary-layer height formulation. *Boundary-Layer Meteorol.*, **81**, 245–269.

Voogt, M., van den Hurk, B. and Jacobs, C. (2006). The ECMWF land-surface scheme extended with a photosynthesis and lai module tested for a coniferous site. *KNMI Scientific Report*, **WR 2006-02**, available from KNMI, De Bilt.

Wallace, J. M., Tibaldi, S. and Simmons, A. (1983). Reduction of systematic forecast errors in the ECMWF model through the introduction of an envelope orography. *Q. J. R. Meteorol. Soc.*, **109**, 683–717.

Warner, C. D. and McIntyre, M. E. (1996). An ultra-simple spectral parametrization for non-orographic gravity waves. *J. Atmos. Sci.*, **58**, 1837–1857.

Warrilow, D. L., Sangster, A. B. and Slingo, A. (1986). Modelling of land-surface processes and their influence on European climate. *UK Met Office Report, Met O 20, Tech Note 38*.

Washington, W. M. and Williamson, D. L. (1977). A description of the NCAR GCMs. In J. Chang (Ed.), *GCMs of the Atmosphere. Methods in Computational Physics*, Vol. 17, pp. 111–172, Academic Press.

Weatherall, P., Marks, K. M., Jakobsson, M., Schmitt, T., Tani, S., Arndt, J. E., Rovere, M., Chayes, D., Ferrini, V. and Wigley, R. (2015). A new digital bathymetric model of the world's oceans. *Earth and Space Science*, **2**(8), 331–345, doi:https://doi.org/10.1002/2015EA000107, URL https://agupubs.onlinelibrary.wiley.com/doi/abs/10.1002/2015EA000107.

Weiss, M., van den Hurk, B. and en W. Hazeleger, R. H. (2012). Impact of vegetation variability on potential predictability and skill of EC-Earth simulations. *Clim. Dyn*, **39**, 2733–2746.

Westbrook, C. D., Hogan, R. J. and Illingworth, A. J. (2008). The capacitance of pristine ice crystals and aggregate snowflakes. *J. Atmos. Sci.*, **65**(1), 206–219.

Wexler, R. and Atlas, D. (1959). Precipitation generating cells. *J. Meteorol.*, **16**, 327–332.

Williams, P. J. and Smith, M. W. (1989). *The Frozen Earth: Fundamentals of Geocryology*. Cambridge University Press, UK.

Wilson, D. and Ballard, S. (1999). A microphysical based precipitation scheme for the UK Meteorological Office numerical weather prediction model. *Q. J. R. Meteorol. Soc.*, **125**, 1607–1636.

Wisner, C., Orville, H. D. and Myers, C. (1972). A numerical model of hail–bearing cloud. *J. Atmos. Sci.*, **19**, 1160–1181.

Wonorahardjo, S., Sutjahja, I. M., Mardiyati, Y., Andoni, H., Thomas, D., Achsani, R. A. and Steven, S. (2020). Characterising thermal behaviour of buildings and its effect on urban heat island in tropical areas. *International Journal of Energy and Environmental Engineering*, **11**, 129–142.

Wood, N., Brown, A. R. and Hewer, F. E. (2001). Parametrizing the effects of orography on the boundary layer, an alternative to effective roughness lengths. *Q. J. R. Meteorol. Soc.*, **127**, 759–778.

Wood, N. and Mason, P. J. (1993). The pressure force induced by neutral, turbulent flow over low hills. *Q. J. R. Meteorol. Soc.*, **119**, 1233–1267.

Wood, R. (2000). Parametrization of the effect of drizzle upon the droplet effective radius in stratocumulus clouds. *Quarterly Journal of the Royal Meteorological Society*, **126**(570), 3309–3324.

Wood, R. and Bretherton, C. S. (2006). On the relationship between stratiform low cloud cover and lower-tropospheric stability. *J. Climate*, **19**, 6425–6432.

Yamazaki, D., Ikeshima, D., Tawatari, R., Yamaguchi, T., O'Loughlin, F., Neal, J. C., Sampson, C. C., Kanae, S. and Bates, P. D. (2017). A high-accuracy map of global terrain elevations. *Geophysical Research Letters*, **44**(11), 5844–5853, doi:https://doi.org/10.1002/2017GL072874, URL https://agupubs.onlinelibrary.wiley.com/doi/abs/10.1002/2017GL072874.

Yamazaki, D., Kanae, S., Kim, H. and Oki, T. (2011). A physically based description of floodplain inundation dynamics in a global river routing model. *Water Resources Research*, **47**(4), doi:https://doi.org/10.1029/2010WR009726, URL https://agupubs.onlinelibrary.wiley.com/doi/abs/10.1029/2010WR009726.

Yin, X. and Struik, P. C. (2009). C3 and c4 photosynthesis models: An overview from the perspective of crop modelling. *NJAS - Wageningen Journal of Life Sciences*, **57**(1), 27–38, doi:10.1016/j.njas.2009.07.001.

Yuter, S. E., Kingsmill, D. E., Nance, L. B. and Löffler-Mang, M. (2006). Observations of precipitation size and fall speed characteristics within coexisting rain and wet snow. *Journal of Applied Meteorology and Climatology*, **45**(10), 1450–1464, doi:10.1175/JAM2406.1.

Zdunkowski, W. G., Welch, R. M. and Korb, G. (1980). An investigation of the structure of typical two-stream methods for the calculation of solar fluxes and heating rates in clouds. *Contrib. Atmos. Phys.*, **53**, 147–166.

Zeng, X. and Beljaars, A. C. M. (2005). A prognostic scheme of sea surface skin temperature for modelling and data assimilation. *Geophys. Res. Lett.*, **32**, L14605.

Zeng, X., Dai, Y.-J., Dickinson, R. E. and Shaikh, M. (1998a). The role of root distribution for land climate simulation. *Geophys. Res. Lett.*, **25**, 4533–4536.

Zeng, X., Zhao, M. and Dickinson, R. E. (1998b). Intercom-parison of bulk aerodynamic algorithms for the computation of sea surface fluxes using the toga coare and tao data. *J. Climate*, **11**, 2628–2644.